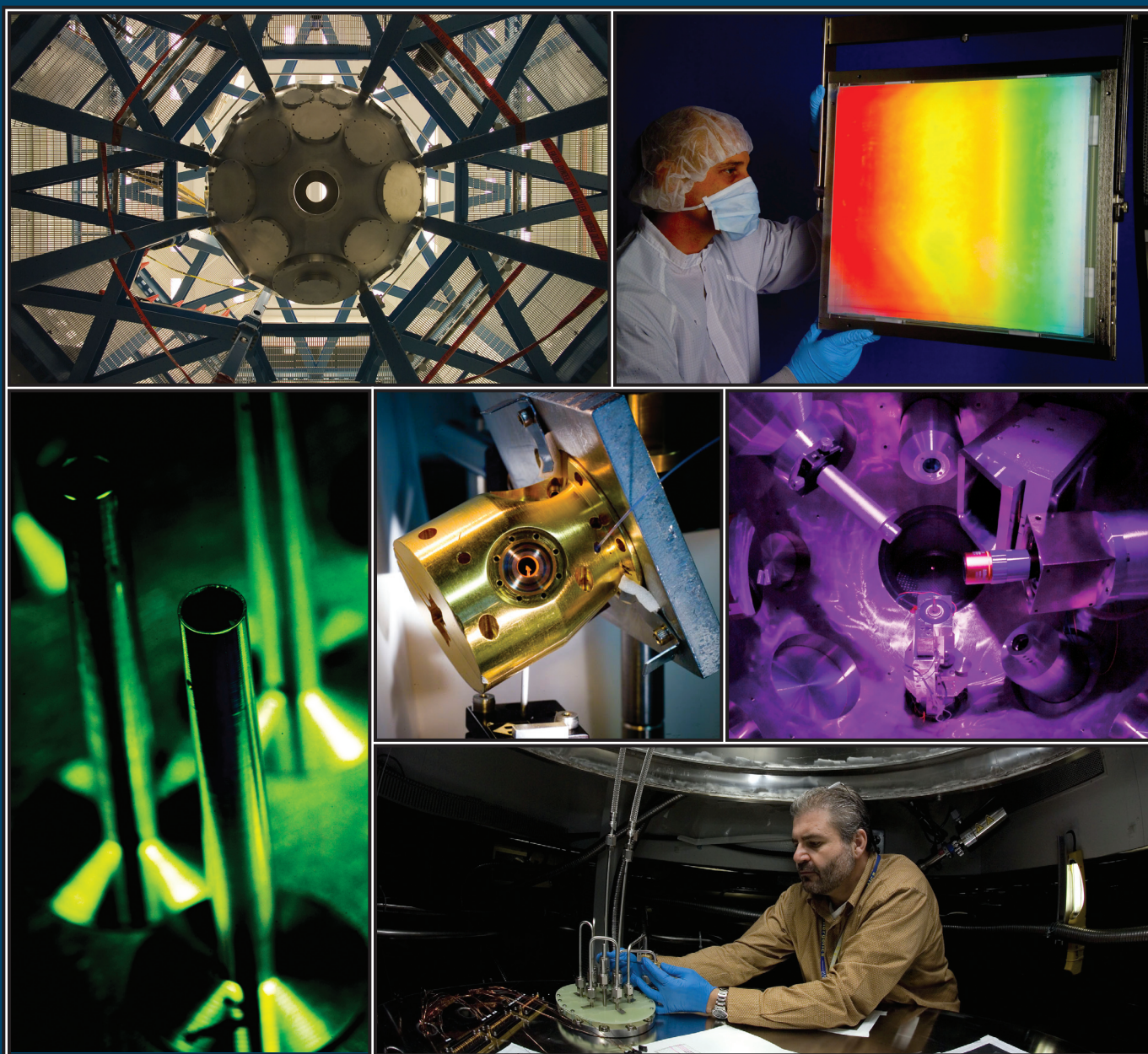


LLE 2005 Annual Report

October 2004 – September 2005



Cover Photos

Upper Left: View of the OMEGA EP target chamber as it is installed within the target chamber structure in the new OMEGA EP Facility that is currently under construction.

Upper Right: Senior Technical Associate Nelson LeBarron inspects a single full-size grating from a three-tile grating array under development for OMEGA EP.

Lower Left: Photograph of cryogenic target holders that are used to hold target assemblies in the OMEGA Cryogenic Target Handling System.

Center: A cryogenic target layering sphere undergoing optical testing to assess its ability to uniformly illuminate a target.

Middle Right: View inside the target chamber for the MTW (multi-terawatt) laser. MTW is a 10-J, 1-ps laser facility that is used to develop diagnostics for OMEGA EP.

Lower Right: Technical Associate Chad Abbott is shown making adjustments during the installation of the second fill station in LLE's target fill facility.

Prepared for
U.S. Department of Energy
San Francisco Operations Office
DOE/SF/19460-646

Distribution Category UC712
October 2004–September 2005

Printed in the United States of America
Available from
National Technical Information Services
U.S. Department of Commerce
5285 Port Royal Road
Springfield, VA 22161

Price codes: Printed Copy A12
Microfiche A01

This report was prepared as an account of work conducted by the Laboratory for Laser Energetics and sponsored by New York State Energy Research and Development Authority, the University of Rochester, the U.S. Department of Energy, and other agencies. Neither the above named sponsors, nor any of their employees, makes any warranty, expressed or implied, or assumes any legal liability or responsibility for the accuracy, completeness, or usefulness of any information, apparatus, product, or process disclosed, or represents that its use would not infringe privately owned rights. Reference herein to any specific commercial product, process, or service by trade name, mark, manufacturer, or otherwise, does not necessarily constitute or imply its endorsement, recommendation, or favoring by the United States Government or any agency thereof or any other sponsor. Results reported in the LLE Review should not be taken as necessarily final results as they represent active research. The views and opinions of authors expressed herein do not necessarily state or reflect those of any of the above sponsoring entities.

The work described in this volume includes current research at the Laboratory for Laser Energetics, which is supported by New York State Energy Research and Development Authority, the University of Rochester, the U.S. Department of Energy Office of Inertial Confinement Fusion under Cooperative Agreement No. DE-FC52-92SF19460, and other agencies.

For questions or comments, contact Laboratory for Laser Energetics
250 East River Road, Rochester, NY 14623-1299, (585) 275-5286.
Worldwide-Web Home Page: <http://www.lle.rochester.edu/>

University of Rochester
Laboratory for Laser Energetics

DOE/SF/19460-646
January 2006

LLE 2005 Annual Report

October 2004 – September 2005



**Inertial Fusion Program and
National Laser Users' Facility Program**

Contents

Executive Summary	v
Pulse Design for Relaxation Adiabatic-Shaped Targets in Inertial Fusion Implosions	1
Improved Target Stability Using Picket Pulses to Increase and Shape the Ablator Adiabatic	13
High-Spatial-Resolution Studies of UV-Laser-Damage Morphology in SiO ₂ Thin Films with Artificial Defects	23
Minimizing Artifact Formation in Magnetorheological Finishing of CVD ZnS Flats	35
A Multichannel, High-Resolution, UV Spectrometer for Laser-Fusion Applications	43
Quantum Efficiency and Noise Equivalent Power of Nanostructured, NbN, Single-Photon Detectors in the Wavelength Range from Visible to Infrared	49
Measurement of Preheat due to Fast Electrons in Laser Implosions of Cryogenic Deuterium Targets	54
The Saturn Target for Polar Direct Drive on the National Ignition Facility	61
Polar Direct Drive—Proof-of-Principle Experiments on OMEGA and Prospects for Ignition on the National Ignition Facility	67
Direct-Drive, Cryogenic Target Implosions on OMEGA	78
Stopping, Straggling, and Blooming of Directed Energetic Electrons in Hydrogenic Plasmas	87
Multidimensional Analysis of Direct-Drive, Plastic-Shell Implosions on OMEGA	92
Effects of Temporal Density Variation and Convergent Geometry on Nonlinear Bubble Evolution in Classical Rayleigh–Taylor Instability	104
High Density and High ρR Fuel Assembly for Fast-Ignition Inertial Confinement Fusion	117
Direct-Drive Fuel-Assembly Experiments with Gas-Filled, Cone-in-Shell, Fast-Ignition Targets on the OMEGA Laser	122
Planar Cryogenic Target Handling Capability for the OMEGA Laser-Fusion Facility	128
Fourier-Space, Nonlinear Rayleigh–Taylor Growth Measurements of 3-D Laser-Imprinted Modulations in Planar Targets	137
Technologies for Mitigating Tritium Releases to the Environment	142
All-Solid-State, Diode-Pumped, Multiharmonic Laser System for Timing Fiducial	155

EXAFS Measurement of Iron bcc-to-hcp Phase Transformation in Nanosecond-Laser Shocks	161
Three-Dimensional Characterization of Cryogenic Target Ice Layers Using Multiple Shadowgraph Views	169
Shock-Timing Experiments Using Double-Pulse Laser Irradiation	178
Polar Direct Drive—Ignition at 1 MJ	186
Hydrodynamic Simulations of Integrated Experiments Planned for the OMEGA/OMEGA EP Laser Systems	189
Proton Core Imaging of the Nuclear Burn in Inertial Confinement Fusion Implosions.....	196
Hot-Surface Ionic Line Emission and Cold K-Inner-Shell Emission from Petawatt-Laser-Irradiated Cu Foil Targets	208
LLE’s Summer High School Research Program	221
FY05 Laser Facility Report	223
National Laser Users’ Facility and External Users’ Programs	225
Publications and Conference Presentations	257

Executive Summary

The fiscal year ending in September 2005 concluded the third year of the second five-year renewal of Cooperative Agreement DE-FC52-92SF19460 with the U.S. Department of Energy. This report summarizes research at the Laboratory for Laser Energetics (LLE) conducted during the past fiscal year, operation of the National Laser Users' Facility (NLUF), a status report of the new OMEGA Extended Performance (EP) laser project, and programs concerning the education of high school, undergraduate, and graduate students during the year.

Progress in Laser Fusion Research

Progress in laser fusion this past year falls into five broad categories: (1) direct-drive results from OMEGA; (2) progress in the development of the cryogenic target system and experiments with cryogenic targets; (3) results for polar direct drive (the application of nonspherically disposed laser beams for direct-drive spherically symmetrically driven systems), which is of great interest for the National Ignition Facility (NIF); (4) fast ignition, which uses short-pulse (<100-ps), high-intensity ($\sim 10^{15}$ -W) laser beams to ignite a compressed thermonuclear fusion capsule; and (5) high-energy-density physics results that use inertial fusion facilities to produce matter in extreme states that are central to understanding and modeling nuclear weapons phenomena important to the National Stockpile Stewardship Program. The following sections furnish a guide to this year's results in each of these five areas.

1. Direct-Drive Results

Inertial confinement fusion (ICF) capsules with shaped adiabats are expected to exhibit hydrodynamic stability without compromising the one-dimensional (1-D) performances exhibited by flat-adiabat shells. While theoretical formulas for the adiabat profiles generated by the relaxation method of adiabat shaping have been previously derived in LLE Review 98 (pp. 106–121), the formulas presented in the article beginning on p. 1 present simplified power-law expressions to facilitate the use of the general formulas.

We have experimentally demonstrated (p. 13) that target stability improves when picket pulses are used to increase and

shape the ablator adiabat. Hydrodynamic simulations show that a picket pulse preceding the main target drive pulse in a direct-drive ICF implosion can reduce both the ablation-interface Rayleigh–Taylor (RT) instability seed and the growth rate by increasing the adiabat while maintaining a low adiabat in the inner fuel layer for optimal target compression and a minimal drive energy for ignition. Experiments show that the RT growth of nonuniformities is suppressed in both planar and spherical targets with picket-pulse laser illumination. Two types of picket pulses—a “decaying shock-wave picket” and a “relaxation” picket—are used to shape the adiabat in spherical targets. Planar growth measurements using a wide, intense picket to raise the adiabat of a CH foil showed that the growth of short-wavelength perturbations was reduced, and even stabilized, by adjusting the intensity of the picket. Planar imprint experiments showed the expected reduction of imprinting when a picket pulse is used. The data show that the imprint level is reduced when a picket is added and, for short wavelengths, is as effective as 1-D, 1.5-Å smoothing by spectral dispersion (SSD). A series of implosion experiments with a 130-ps-wide picket pulse showed a clear improvement in the performance of direct-drive implosions when the picket pulse was added to the drive pulse. Results from relaxation-picket implosions show larger yields from fusion reactions when the picket drive is used. These adiabat-shaping concepts make the likelihood of achieving ignition with direct-drive implosions on the NIF significantly more probable.

Beginning on p. 92, we provide a multidimensional analysis of direct-drive, plastic-shell implosions on OMEGA. Direct-drive, plastic-shell targets were imploded on the OMEGA Laser System with a 1-ns square pulse using the multidimensional hydrodynamic code *DRACO*. Yield degradation in “thin” shells is primarily caused by shell breakup during the acceleration phase due to short-wavelength ($\ell > 50$, where ℓ is the Legendre mode number) perturbation growth, whereas “thick” shell performance is influenced primarily by long and intermediate modes ($\ell \leq 50$). Simulation yields, the temporal history of neutron production, areal densities, and x-ray images of the core compare well with experimental

observations. In particular, the thin-shell neutron production history falls off less steeply than 1-D predictions due to shell breakup induced under compression and delayed stagnation. Thicker, more-stable shells show burn truncation due to instability-induced mass flow into the colder bubbles. Estimates of small-scale mix indicate that turbulent mixing does not influence primary neutron yields.

The effects of temporal density variations and convergent geometry on nonlinear bubble evolution in classical RT instability are discussed beginning on p. 104. Effects of temporal density variation and spherical convergence on the nonlinear bubble evolution of single-mode, classical RT instability are studied using an analytical model based on Layzer's theory. When a temporal density variation is included, the bubble amplitude in the planar geometry asymptotes to a fixed value that depends on the Layzer bubble velocity, the fluid density, and a factor to account for the two- and three-dimensional geometries. The model can be applied to spherical geometries to predict the nonlinear bubble amplitude.

Nonlinear growth measurements of 3-D broadband nonuniformities near saturation using x-ray radiography in planar foils accelerated by laser light are described on p. 137. The initial target modulations were seeded by laser nonuniformities and later amplified during acceleration by RT instability.

2. Cryogenic System and Experimental Results

We report the first measurements of electron preheat in direct-drive laser implosions of cryogenic deuterium targets (p. 54). Preheat due to fast electrons generated by nonlinear laser-plasma interactions can reduce the gain in laser-imploded fusion targets. The preheat level is derived directly from the measured hard x-ray spectrum. The fraction of the incident laser energy that preheats the deuterium fuel is found to be less than 0.1%, suggesting that preheat will have a negligible impact on target performance. These results are encouraging for the success of high-gain, direct-drive-ignition experiments on the NIF.

Direct-drive, spherical, cryogenic, D₂-filled capsules were illuminated using the 60-beam OMEGA Laser System (p. 78). The targets are energy scaled from the baseline ignition design developed for the NIF. Thin-walled (~4- μm), ~860- μm -diam deuterated (CD) polymer shells are permeation filled with D₂ gas and cooled to the triple point (~18.7 K). Cryogenic ice layers with a uniformity of ~2- μm rms are formed and maintained. The targets were imploded with high-contrast pulse shapes using full single-beam smoothing (1-THz bandwidth, 2-D SSD)

to study the effects of the acceleration- and deceleration-phase RT growth on target performance. Two-dimensional simulations show good agreement with experimental observations. Scattered-light and neutron burn-history measurements are consistent with predicted absorption and hydrodynamic coupling calculations. Time-resolved and static x-ray images show the progress of the imploding shell and the shape and temperature of the stagnating core. Particle-based instruments measure the fusion yield and rate, the ion temperature in the core, and the fuel areal density at the time of neutron production. These experiments have produced fuel areal densities up to ~100 mg/cm², primary neutron yields of ~4 × 10¹⁰, and secondary neutron yields 1% to 2% of the primary yield. These results validate the hydrocode predictions for the direct-drive ignition-point design, giving increasing confidence in the direct-drive approach to ICF ignition.

We have developed a high-performance "planar" cryogenic target handling system that has been added to LLE's OMEGA Laser Fusion Facility (p. 128). The system has demonstrated a shot-to-shot cycle interval of less than two hours and has fielded more than 125 experiments using several distinct target types. This article provides an overview of the cryogenic capabilities at LLE and then compares the operational requirements of LLE's spherical and planar cryogenic systems.

Three-dimensional characterization of cryogenic target ice layers is important in understanding experiments important to an ignition demonstration. We report (p. 169) on backlit optical shadowgraphy, the primary diagnostic for D₂ ice-layer characterization of cryogenic targets for the OMEGA Laser System. Measurement of the position of the most prominent rings, caused by the reflection and refraction of light in the ice layer, in conjunction with ray-trace model predictions, allows the construction of a 3-D ice-layer representation, an estimation of the global surface roughness, and a determination of a Legendre-mode spectrum suitable for implosion modeling.

3. Polar-Direct-Drive Results

The article beginning on p. 61 examines a design concept that is proposed for direct-drive implosions on the NIF while the facility is in its initial indirect-drive configuration. The concept differs from earlier polar-direct-drive designs by adding a low-Z ring around the capsule equator (Saturn target). Refraction in the plasma formed around this ring permits time-dependent tuning of the capsule drive uniformity. An optimized simulation shows an implosion-velocity nonuniformity at the end of the laser pulse of ~1% rms for a cryogenic

DT shell, enhancing the prospects for an early direct-drive ignition demonstration on the NIF.

In the second article on polar direct drive (p. 67), we report the results for proof-of-principle, polar-direct-drive (PDD) experiments on OMEGA and prospects for ignition on the NIF. Experiments have been carried out using 40 repointed beams of the 60-beam OMEGA Laser System to approximate the NIF PDD configuration. Backlit x-ray framing camera images of D₂-filled spherical CH capsules show a characteristic non-uniformity pattern that is in close agreement with predictions. Saturn targets increase the drive on the equator, suggesting that highly symmetric PDD implosions may be possible with appropriate tuning. Two-dimensional simulations reproduced the approximately threefold reduction in yield found for the non-Saturn PDD capsules. Preliminary simulations for a NIF Saturn design predict a high gain close to the 1-D prediction. These results increase the prospects of obtaining direct-drive ignition with the initial NIF configuration.

Designs with the objective of achieving direct-drive ignition on the NIF at 1 MJ using the x-ray-drive beam configuration are described on p. 186. The PDD approach achieves the required irradiation uniformity by repointing some of the beams toward the target equator and by increasing the laser intensity at the equator to compensate for the reduced laser coupling from oblique irradiation.

4. Fast-Ignition Progress and Results

In “High-Density and High ρR Fuel Assembly for Fast-Ignition Inertial Confinement Fusion” (p. 117), LLE authors optimize implosion parameters for fast-ignition inertial confinement fusion and design fast-ignition targets relevant to direct-drive inertial fusion energy. It is shown that a 750-kJ laser can assemble fuel with $V_I = 1.7 \times 10^7$ cm/s, $\alpha = 0.7$, $\rho = 400$ g/cc, $\rho R = 3$ g/cm², and a hot-spot volume of less than 10% of the compressed core. If fully ignited, this fuel assembly can produce energy gains of 150.

A second article (p. 122) describes recent OMEGA experiments that have studied the fuel assembly of gas-filled, cone-in-shell, fast-ignition targets. Using both fusion products and backlit images, an areal density of ~ 60 to 70 mg/cm² was inferred for the dense core assembly. The results are promising for successful integrated fast-ignition experiments on the OMEGA EP Facility, scheduled to be completed in 2007.

We present observations of a hot, $T_e \sim 2$ - to 3-keV surface plasma in the interaction of a 0.7-ps petawatt laser beam with

solid copper-foil targets at intensities $>10^{20}$ W/cm² (p. 208). These temperatures were inferred from Cu, He $_{\alpha}$, and Ly $_{\alpha}$ emission lines, which have not previously been observed with ultrafast laser pulses.

We are also developing new techniques to characterize future fast-ignition experiments and for use on the OMEGA EP Facility. The interaction of directed energetic electrons with hydrogenic plasmas was modeled analytically from fundamental principles (p. 87). The effects of stopping, straggling, and beam blooming are rigorously treated in a unified approach for the first time. Enhanced energy deposition, which occurs in the latter portion of beam penetration, is inextricably linked to straggling and beam blooming. Both effects asymptotically scale with the square root of the linear penetration. Eventually they dominate over all other sources of beam divergence; therefore, understanding their effects is critical for evaluating the requirements of fast ignition.

Simulations of integrated fast-ignition experiments on the combined OMEGA/OMEGA EP Laser Systems with the multidimensional hydrodynamic code *DRACO* are summarized beginning on p. 189. An OMEGA cryogenic DT target, designed to reach a 1-D fuel ρR of 0.5 g/cm², has been simulated in 2-D with and without nonuniformities. The neutron yield is predicted to be in excess of 10^{15} (compared to $\sim 10^{14}$ without an ignitor beam) over a synchronization range of ~ 80 ps.

The article (p. 196) describes the development of a proton emission imaging system that has been used to measure the nuclear burn regions in the cores of ICF implosions. This imaging technique relies on the penumbral imaging of 14.7-MeV D³He fusion protons. Experimental data, analysis, and error analysis are presented for a representative symmetric implosion of a fuel capsule with a 20- μ m-thick plastic shell and 18 atm of D³He gas fill.

5. High-Energy-Density Physics

In the first article in this category, we present extended x-ray absorption fine structure measurements (p. 161). These have been used to demonstrate the phase transformation from body-centered-cubic (bcc) to hexagonal-closely-packed (hcp) iron due to nanosecond, laser-generated shocks. This is a direct, atomic-level, and *in-situ* proof of shock-induced transformation in iron.

The second article (p. 178) describes velocity interferometry and optical self-emission measurements from shock waves in

polystyrene targets driven by two 90-ps pulses separated by 1.5 to 2 ns. The velocity histories, coalescence times, and transit times are unambiguously observed and are in good agreement with 1-D code predictions. The timing of multiple shock waves is crucial to the performance of ICF ignition targets.

Lasers, Optical Materials, and Advanced Technology

Crater formation in SiO₂ thin films containing artificial defects by ultraviolet (UV) pulsed-laser irradiation depends on the lodging depth of the defects (p. 23). At laser fluences close to the crater-formation threshold and for lodging depths of a few particle diameters, the dominating material-removal mechanisms are melting and evaporation. For absorbing defects lodged deeper than ~10 particle diameters, however, a two-stage material-removal mechanism occurs. The process starts with the material melting within the narrow channel volume and, upon temperature and pressure buildup, film fracture takes place.

The polishing performance of magnetorheological (MR) fluids prepared with a variety of magnetic and nonmagnetic ingredients to minimize artifact formation on the surface of CVD ZnS flats is reported on p. 35. The results show that altering the fluid composition greatly improves smoothing performance of magnetorheological finishing. A nanoalumina abrasive used with soft carbonyl iron and altered MR fluid chemistry yields surface roughnesses that do not exceed 20 nm p-v and 2-nm rms after removing 2 μm of material. Significantly, the formation of an “orange peel” and the exposure of a “pebble-like” structure inherent in ZnS from the CVD process are suppressed.

A 63-channel, high-resolution, UV spectrometer that can be used to check the tuning state of the KDP triplers has been designed and tested (p. 43). The spectrometer accepts an input energy of 1 μJ per channel, has a dispersion at the detector plane of 8.6×10^{-2} pm/μm, and has a spectral window of 2.4 nm at $\lambda = 351$ nm. The wavelength resolution varies from 2.5 pm at the center of the field of view to 6 pm at the edge.

The quantum efficiency (QE) and the noise equivalent power (NEP) of the latest-generation, nanostructured NbN, superconducting, single-photon detectors (SSPD's) operated at temperatures in the 2.0- to 4.2-K range in the wavelength range from 0.5 to 5.6 μm is discussed (p. 49). The detectors are designed as 4-nm-thick, 100-nm-wide NbN meander-shaped stripes, patterned by electron-beam lithography. Their active area is 10×10 μm². The best-achieved QE at 2.0 K for 1.55-μm photons is 17%, and the QE for 1.3-μm infrared photons reaches its saturation value of ~30%. The SSPD NEP at 2.0 K is as low

as 5×10^{-21} W/Hz^{-1/2}. These SSPD's, operated at 2.0 K, significantly outperform their semiconducting counterparts. With their gigahertz counting rate and picosecond timing jitter, they are the devices of choice for practical quantum key distribution systems and quantum optical communications.

An all-solid-state, diode-pumped Nd:YLF laser system has been developed and tested (p. 155). It produces fiducial timing signals at three wavelengths (fundamental, second, and fourth harmonics) and will be used as a primary timing reference for the OMEGA facility diagnostics. Performance results of the new OMEGA fiducial laser are reported.

Significant developments in tritium-capture technology have occurred over the past two decades (p. 142). The merits and drawbacks of the various technologies that have been developed for both air and inert gas streams are discussed.

Status and Progress on OMEGA EP

The OMEGA EP (extended performance) project continued on a fast-track schedule to complete two short-pulse beams and the scope was increased in FY05 to include two additional beams. FY06 Congressional funding has allowed the full four-beam project to proceed. This added two long-pulse beams to the originally authorized two short-pulse beams with completion in April 2008. The full OMEGA EP total estimated cost is \$89 million of which \$87 million has been appropriated through FY06. The building constructed to house the OMEGA EP equipment was completed in February 2005 at a cost of \$21 million. This building was funded by the University of Rochester and its completion enabled the start of the laser's assembly.

Prior to building completion, major assemblies were prepared for installation and work on laser technology development activities was completed. Technology development projects included optical parametric chirped-pulse amplification (OPCPA), multilayer-dielectric diffraction gratings, and coherent tiling of large-aperture gratings. These projects concluded with demonstrations of performance that meet or exceed OMEGA EP requirements. Additionally, LLE adopted plasma-electrode Pockels cell (PEPC) and adaptive optics (deformable mirrors) technology from LLNL's NIF project. The deformable mirror hardware was designed by LLNL but is operated with a LLE-developed wavefront sensor and control system. The PEPC, while similar to LLNL's, has design requirements and features specific to deployment at LLE. Both of these projects were concluded in FY05, which allowed the acquisition of prime hardware to commence.

Once the building was complete, the process of installing the infrastructure required to support the beamlines, compressors, and target chamber began. Support structure acquisitions were initiated upon completion of the beamline design and approval of the baseline change to enable four beams. Several of these structures arrived in FY05 and were placed in the OMEGA EP Laser Bay; the majority of the structures will be installed in the first quarter of FY06. The target area structure was installed and prepared for the insertion of the target chamber. The target chamber, a near replica of the OMEGA target chamber, was acquired with a grant from the New York State Energy Research and Development Authority and will be integrated at LLE in FY06. The 350,000-lb, 70-ft. \times 15-ft \times 15-ft, nine-segment grating compressor chamber (GCC) arrived from Los Angeles and was precision cleaned in the Laser Bay. Final GCC assembly and vacuum testing will be completed in FY06. Lastly, deployment of the controls system in concert with the laser hardware installation began. The control room installation is complete and operational testing for remote operation of OMEGA EP has commenced.

National Laser Users' Facility and External Users' Programs

A detailed summary of the operation and use of the National Laser Users' Facility and External User's Programs is given on p. 225. A discussion of user experiments included

- *Isentropic Compression Experiments (ICE) for Measuring EOS on OMEGA*
- *Laser-Plasma Interactions in High-Energy-Density Plasmas*
- *Three-Dimensional Study of the Spatial Structure of Direct-Drive Implosion Cores on OMEGA*
- *NLUF Proton Radiography Experiments*
- *FY05 LANL OMEGA Experimental Programs*
- *FY05 Sandia National Laboratory's Experiments on OMEGA*
- *2005 CEA Experiments on OMEGA*

FY 2005 Laser Facility Report

The use of the OMEGA Facility is reported in the article that begins on p. 223. During the year, 1461 target shots were conducted for LLE, NLUF, and external users. LLE usage accounted for less than 50% of the total target shots. Figure 1 illustrates the shot allocations during the fiscal year.

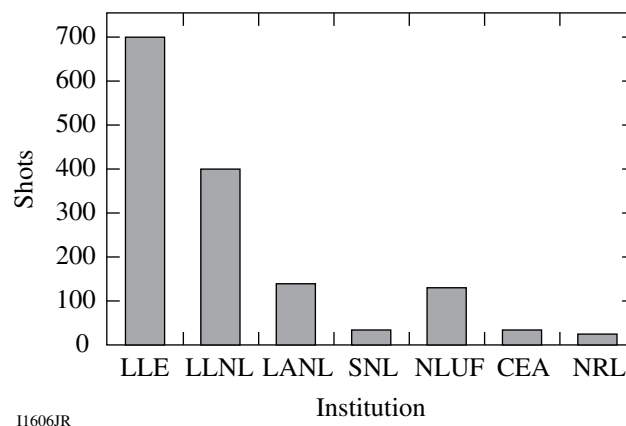


Figure 1
FY05 OMEGA usage.

Education at LLE

As the only major university participant in the National ICF Program, education continues to be an important mission for the Laboratory. A report on this year's summer high school research program is described in detail on p. 221. Fifteen students participated in this year's program. The William D. Ryan Inspirational Teacher Award was given to Mr. Stephen Locke, a chemistry teacher at Byron-Bergen High School.

Graduate students are using the world's most powerful UV laser for fusion research on OMEGA, making significant contributions to LLE's research activities. Twenty-one faculty from five departments collaborate with LLE's scientists and engineers. Presently, 102 graduate students are involved in research projects at LLE, and LLE directly sponsors 43 students pursuing Ph.D. degrees. Their research includes theoretical and experimental plasma physics, high-energy-density physics, x-rays and atomic physics, nuclear fusion, ultrafast optoelectronics, high-power-laser development and applications, nonlinear optics, optical materials and optical fabrications technology, and target fabrication. Technological developments from ongoing Ph.D. research will continue to play an important role on OMEGA.

One hundred seventy-seven University of Rochester students have earned Ph.D. degrees at LLE since its founding. An additional two undergraduate students, fourteen graduate students, two postdoctoral, and seven faculty positions from other universities were funded by NLUF grants. The most recent University of Rochester Ph.D. graduates and their thesis include the following:

Bigelow, Matthew S. *“Ultra-Slow and Superluminal Light Propagation in Solids at Room Temperature”*

Erdmann, Reinard K. *“Quantum Interference Engineered by Dispersive Parameter Design”*

Guazzotto, Luca *“Equilibrium and Stability of Axisymmetric Plasmas with Arbitrary Flow”*

Kozlov, Maxim V. *“Stimulated Brillouin Scattering in Multiple Species Plasmas”*

Rey-de-Castro, Robert C. *“Ultrafast Optical Properties and Applications of $Cd_{1-x}Mn_xTe$ Semimagnetic Semiconductors”*

Strierner, Christopher C. *“Applications of Silicon Nanostructures Compatible with Existing Manufacturing Technology”*

U’Ren, Alfred B. *“Multi-Photon State Engineering for Quantum Information Processing Applications”*

Weiss, Sharon M. *“Tunable Porous Silicon Photonic Bandgap Structures: Mirrors for Optical Interconnects and Optical Switching”*

Zheng, Lianqing *“UV-Laser-Induced Densification of Fused Silica: A Molecular Dynamics Study”*

Approximately 45 University of Rochester undergraduate students participated in work or research projects at LLE this past year. Student projects include operational maintenance of the OMEGA Laser System; work in laser development, materials, and optical-thin-film coating laboratories; and programming, image processing, and diagnostic development. This is a unique opportunity for students, many of whom will go on to pursue a higher degree in the area in which they gained experience at the Laboratory.

In addition, LLE directly funds research programs within the MIT Plasma Science and Fusion Center, the State University of New York (SUNY) at Geneseo, the University of Wisconsin, and the University of North Carolina at Chapel Hill. These programs involve a total of approximately six graduate students, twenty-seven undergraduate students, and four faculty from other universities.

Robert L. McCrory
Director, Laboratory for Laser Energetics
Vice Provost, University of Rochester

Pulse Design for Relaxation Adiabats-Shaped Targets in Inertial Fusion Implosions

Introduction

Controlling the seeds and the growth of Rayleigh–Taylor (RT) instability during the acceleration phase of imploding shells is crucial to the success of inertial confinement fusion (ICF). Since the RT growth is damped by the ablative flow off the shell’s outer surface, target performances are greatly improved by target designs with enhanced ablation velocity. A significant increase in ablation velocity and shell stability can be achieved by shaping the entropy inside the shell. Following the standard ICF notation, we measure the entropy through the so-called “adiabat” defined as the ratio of the plasma pressure to the Fermi-degenerate DT pressure: $\alpha \equiv P(\text{Mb})/2.18\rho(\text{g/cc})^{5/3}$, where the pressure is given in megabars and the density in g/cc. The optimum adiabat shape in the shell consists of a profile that is monotonically decreasing from the outer to the inner surface as qualitatively shown in Fig. 101.8 on p. 14. Large adiabat values on the shell’s outer surface increase the ablation velocity V_a , which follows a power law of the outer-surface adiabat α_{out} , $[V_a \sim \alpha_{\text{out}}^{3/5}]$, while low adiabat values on the inner surface lead to improved ignition conditions and larger burn.^{1–5} A more detailed history and target design implications of adiabat shaping can be found in the introduction of Ref. 6 by the same authors, which is devoted mostly to the adiabat shape induced by a strong decaying shock. Shaping by a decaying shock was introduced in Ref. 7 and requires a very strong prepulse aimed at launching a strong shock. This strong shock decays inside the shell shortly after the prepulse is turned off; the picket pulse is followed by the low-intensity foot of the main pulse. The decaying shock (DS) leaves behind a monotonically decreasing adiabat profile, which follows a power law of the mass coordinate

$$\alpha_{\text{DS}} = \alpha_{\text{inn}} \left(\frac{m_{\text{shell}}}{m} \right)^{\delta_{\text{DS}}}, \quad (1)$$

where m is the mass calculated from the outer surface, m_{shell} is the total shell mass, and α_{inn} is the adiabat on the shell’s inner surface. The value of δ_{DS} , calculated in Ref. 6, is approximately independent of the prepulse characteristics. Without accounting for the effect of mass ablation, δ_{DS} is about 1.3.

If mass ablation is included, δ_{DS} varies between 1.06 and 1.13, depending on the prepulse duration.⁶ Two-dimensional (2-D) simulations⁷ of all-DT, OMEGA-size-capsule implosions have confirmed that DS adiabat targets exhibit significantly reduced RT growth on the ablation surface during the acceleration phase with respect to the flat-adiabat ones. Comparisons between flat- and shaped-adiabat targets are typically carried out by designing the flat- and shaped-adiabat pulses to generate identical adiabats on the shell’s inner surface.

A different technique aimed at shaping the adiabat is the so-called shaping by relaxation (or RX shaping) first introduced in Ref. 8. The relaxation technique uses a less-energetic prepulse than the DS technique. The RX prepulse (Fig. 101.1) is used to launch a shock that may or may not decay inside the shell. In both cases, the prepulse is turned off before the prepulse shock reaches the shell’s inner surface. Since the prepulse is followed by a complete power shutoff, the outer portion of the shell expands outward, generating a relaxed density profile while the prepulse shock travels inside the shell. The prepulse shock is not intended to greatly change the shell adiabat even though

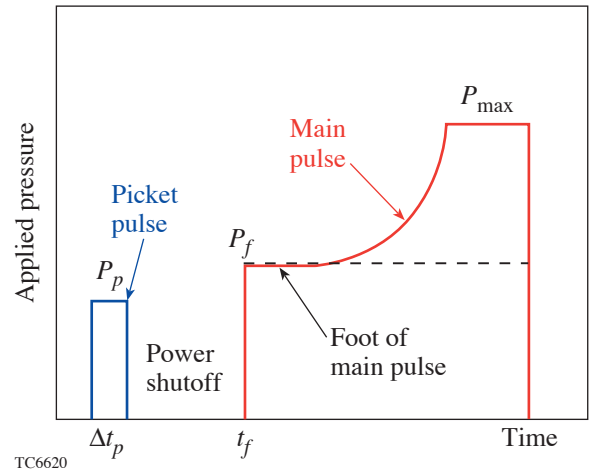


Figure 101.1
Typical pressure pulse for adiabat shaping by relaxation.

it may cause a significant adiabat modification. The main adiabat shaping occurs later in time when the foot of the main pulse starts and a strong shock travels up the relaxed density profile. The main shock first encounters the low-density portion of the relaxed profile, setting it on a very high adiabat. The adiabat develops a monotonically decreasing profile as a result of the increasing pre-shock density. Figures 101.2(a), 101.2(b), and 101.2(c) show three snapshots of the main shock propagation (m.s.) through a relaxed density profile. The density profile of an 85- μm -thick DT target is relaxed by a 60-ps, 13-Mb prepulse. The prepulse shock (p.s.) travels ahead of the main pulse shock. The latter is launched by a 15-Mb pressure applied at 1941 ps. The main shock launching time (or main pulse foot beginning time) is chosen in order to cause the main and prepulse shocks to merge on the shell's inner surface. A plot of the shaped-adiabat profile at shock breakout is shown in Fig. 101.2(d). Observe that the adiabat varies from about 2 on the inner surface to several tens on the outer surface. Two-dimensional (2-D) simulations^{8–10} of OMEGA- and NIF-size-capsule implosions have confirmed that RX-shaped targets exhibit significantly reduced RT growth on the ablation surface during the acceleration phase with respect to the flat-adiabat ones.

The RX adiabat-shaping technique can be viewed as a two-step process: the prepulse and power shutoff are needed to generate the relaxed density profile, while the foot of the main pulse shapes the adiabat. Similarly to the DS shaping, the RX adiabat profile can be approximated with a power law of the mass coordinate

$$\alpha_{\text{RX}} \approx \alpha_{\text{inn}} \left(\frac{m_{\text{shell}}}{m} \right)^{\delta_{\text{RX}}}, \quad (2)$$

where δ_{RX} can be tailored between a minimum of zero (i.e., no shaping) to a maximum value of 2.4. This upper bound, which is well above the decaying shock value, can be achieved only for weak prepulses (either low-pressure or short-duration prepulses) and by neglecting the effects of mass ablation. For realistic prepulses and including the effect of ablation, the maximum RX power index is reduced to values in the range of 1.6 to 1.8, which is still significantly larger than the 1.1 of the decaying shock. Since the steeper RX adiabat profile leads to greater values of the outer-surface adiabat with respect to the DS adiabat shaping, one can conclude that the ablation velocity will be significantly higher in RX-shaped targets than DS-shaped targets. Furthermore, the tailoring of the adiabat steepness in RX shaping is beneficial to the control of the convective instability, which is driven by the finite entropy gradients inside the shell. This instability grows at a slower rate with respect to the Rayleigh–Taylor and does not seem to cause a significant distortion of the shell.^{7,8}

Different adiabat-shaping techniques based on the tailoring of the radiation absorption in the target have also been proposed;^{11–13} however, their implementation relies on manufacturing targets with a spatially varying atomic number, a technique that is difficult in cryogenic capsules. It has also been suggested¹⁴ that some classified work on adiabat shaping was initiated in the 1980s by Verdon, Haan, and Tabak. This work

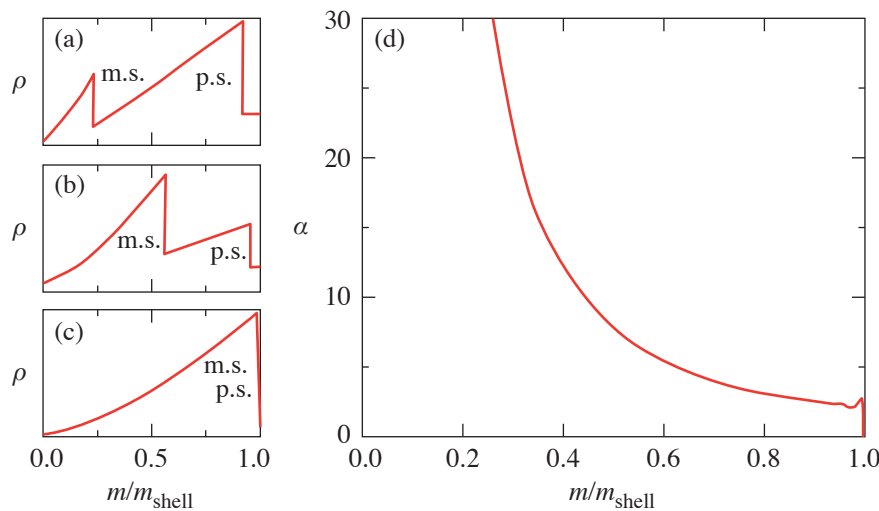


Figure 101.2
Snapshots [(a),(b), and (c)] of the density profiles at different stages of the main-shock and prepulse-shock propagation. The resulting adiabat profile left behind the main shock at breakout time is shown in (d).

TC6621

appears to be restricted, however, to the classified literature and was not accessible to Betti and Anderson (authors of the earlier published work⁸ on RX shaping and co-authors of the current article). It is also important to clarify the role of earlier work¹⁵ on the so-called “picket-fence” pulses and make a distinction between adiabat shaping and picket fence. The picket-fence pulse consists of a sequence of relatively short pulses that replace the standard isentropic continuous pulse. When plotted versus time, the laser power of such a sequence of short pulses (see Fig. 3 of Ref. 15) resembles a picket fence. Instead, both DS adiabat shaping and RX adiabat shaping make use of a single short pulse (i.e., the laser prepulse) followed by a continuous pulse. Thus, except for the prepulse, the adiabat-shaping pulses are essentially continuous. While a claim can be made that adiabat shaping and picket fence use some sort of picket pulse, it would be grossly inaccurate to think of the two techniques as equal or even similar. As stated in Ref. 15, the goal of the picket-fence pulse is to replace a continuous acceleration with an impulsive one. The rationale behind this clever idea is that the RT exponential growth turns into a sequence of linear-growth stages, thus reducing the overall growth factor (as long as the number of pickets is kept relatively low). On the contrary, adiabat shaping does not change the time evolution of the acceleration. Its primary effect is to increase the ablation velocity, thus enhancing the ablative stabilization of the RT instability. Though the physical basis and pulse design of a picket-fence pulse have little (if anything) in common with adiabat shaping, it is possible that some level of adiabat shaping may occur in picket-fence implosions due to the repeated decompressions between short pulses. Though this collateral effect was not considered in Ref. 15, it would be worth investigating the degree at which the adiabat is shaped in picket-fence implosions. It is also worth mentioning that the evolution of the laser power in Fig. 2 of Ref. 15 seems to point to a single prepulse followed by a continuous main pulse. While this pulse resembles an RX pulse, the authors of Ref. 15 do not address the possibility that adiabat shaping may occur.

Lastly, it is important to recognize that the presence of a laser prepulse could have significant consequences with regard to the level of laser imprinting. Laser imprinting is caused by the spatial nonuniformities of the laser intensity and is widely considered as the main seed for the short-wavelength RT instability in direct-drive implosions. It has been recently shown^{16–18} that the level of imprinting can be significantly reduced by tailoring the initial target density with a monotonically increasing profile varying from a lower value on the outer surface to its maximum on the shell’s inner surface. Since the

laser prepulse in RX adiabat shaping causes such a monotonically varying density profile, it is likely that RX shaping may also reduce the level of imprinting. Furthermore, it has been shown in Ref. 19 that, in the presence of a plastic (or other) coating on cryogenic capsules, the acceleration of the plastic layer against the cryogenic DT layer causes a brief exponential amplification of the imprinting level. Reference 19 also shows that this amplification can be reduced by using a sufficiently strong prepulse. Such an improvement of the imprinted nonuniformities requires a strong prepulse and may therefore be more effective in DS shaping than in RX shaping. Imprint reduction using prepulses has also been demonstrated by both simulation and experiment in single-layer targets made of aluminum.²⁰ While some encouraging results on the stability of RX-shaped capsule implosions have been obtained from 2-D simulations^{8–10} and from experiments on plastic-shell implosions,¹⁰ a more detailed 2-D analysis including the effect of RX shaping on imprinting as well as a complete description of the experiments carried out on the OMEGA laser system will be presented in a forthcoming publication.

In this article, we cite the results of the one-dimensional (1-D) hydrodynamic analysis of the relaxation adiabat profiles,^{21,22} simplify them with power-law approximations, and compare them with decaying-shock-adiabat profiles and to simulations. Furthermore, we derive formulas for relaxation pulse design and discuss nonideal effects, such as mass ablation, on the adiabat profiles.

Summary of Previously Derived Adiabat Profiles

References 21 and 22 divide relaxation adiabat shaping designs into two categories: type 1, where the prepulse shock and rarefaction merge at the rear surface of the shell; and type 2, where the rarefaction merges with the prepulse shock within the shell. These two designs yield different adiabat profiles. An accurate description of the type-1 adiabat profile is well approximated by the following set of equations from Eqs. (75)–(77) and (46b), respectively, of Ref. 22:

$$S = S_{\text{inn}} \left(\frac{m_{\text{shell}}}{m} \right)^{\frac{2\gamma}{\gamma+1}} \frac{\chi(1)}{\chi\left(\frac{m}{m_{\text{shell}}}\right)}, \quad (3)$$

where

$$S_{\text{inn}} = \frac{(\gamma-1)^{2\gamma}}{\gamma\chi(1)(\gamma+1)^{2\gamma-1}} \frac{P_f}{\rho_0^\gamma} \quad (4)$$

is the entropy on the shell's inner surface and ρ_0 is the initial shell density. The function $\chi(x)$ represents the corrections due to the finite main shock strength

$$\chi(x) = \tilde{\rho} \left\{ \frac{\gamma P_p \Theta(x)}{(\gamma+1)P_f \left[\frac{x}{\Sigma(x)} \right]^{\frac{2\gamma}{\gamma+1}}} \right\}^{\gamma} \frac{\Theta(x)}{\Sigma(x)^{\frac{2\gamma}{\gamma+1}}}, \quad (5)$$

$$\tilde{\rho}(\hat{\pi}) = \frac{1 + \frac{\gamma-1}{\gamma+1} \hat{\pi}}{1 + \frac{\gamma+1}{\gamma-1} \hat{\pi}} \approx 1 - \frac{4\gamma}{\gamma^2-1} \hat{\pi} + \mathcal{O}(\hat{\pi}^2), \quad (6)$$

and where $\beta \approx 2/(\gamma+1)$ and $\hat{\pi} = P_p/P_f$ is the ratio of the prepulse pressure to the pressure of the foot of the main pulse.

The type-2 adiabat profiles are steeper than the type-1 profiles and can be approximated as

$$S(m) \approx \frac{\omega_* P_f}{\rho_M^\gamma} \left(\frac{z_{\text{shell}}}{z} \right)^{\gamma\mu} [1 + D(z)(z-1)] \hat{s}(z), \quad (7)$$

$$\hat{s}(z) = \frac{\left\{ 1 - \phi \hat{m}_*^\phi \sqrt{\frac{2(\gamma-1) P_p}{(\gamma+1)\omega_* P_f}} [\sigma(z_{\text{shell}}) - \sigma(z)] \right\}^{\frac{\gamma\mu}{\phi}}}{\left\{ \tilde{\rho} \left[\frac{P_p}{\omega_* P_f} \frac{\hat{m}_*^{\mu\gamma} z^{-\mu\gamma-\delta}}{1 + D_0(z)(z-1)} \right] \right\}^{\gamma}}, \quad (8)$$

$$\omega_* = \omega_0 \left[1 - \frac{2\beta(\gamma+2)}{3(2-\beta)} \sqrt{\frac{2\gamma P_p}{\omega_0(\gamma+1)P_f}} \left(\frac{m_*}{m_{\text{rf}}^0} \right)^{1-\frac{\beta}{2}} \right], \quad (9)$$

where $D(x) = D_0(x) + D_1(x)$,

$$D_0(x) = \frac{2(x^\mu - 1) + \mu(x-3)(x-1) - \mu^2(x-1)^2}{(\mu-2)(\mu-1)(x-1)^3}, \quad (10)$$

$$D_1(x) = -\mu \sqrt{\frac{\gamma-1}{\gamma+1} \frac{P_p}{\omega_* P_f} \frac{\hat{m}_*^\phi (z_s^M)^\mu}{(z_s^M - 1)^3}} \times \int_1^{z_s^M} \sqrt{\frac{(x-1)^4 + D_0(x)(x-1)^5}{x^{3\mu}}} dx, \quad (11)$$

and $\tilde{\rho}(x)$ is given by Eq. (6). These formulas are derived in Ref. 22 as Eqs. (100a), (100b), (90), (82), and (94), respectively.

In practical terms, these formulas for the relaxation-adiabat profiles are cumbersome and provide no intuitive comparison with decaying-shock-adiabat profiles. Therefore, in the following section, simple power-law approximations to these formulas are calculated.

Simplified Formulas for RX Adiabat Shapes and Comparison with DS Shapes

The theoretical results derived in the previous section can be simplified by fitting the adiabat shapes with a simple power law in the mass coordinate. It has been shown in Ref. 6 that the power-law approximation works extremely well for the adiabat shape left behind by a decaying shock (DS shaping). In an ideal fluid with adiabatic index $\gamma = 5/3$ and neglecting the effects of mass ablation, the adiabat profile left behind by a decaying shock follows the power law $\alpha_{\text{DS}} \sim 1/m^{1.315}$ for $m_* < m < 10 m_*$. It is worth mentioning that the power index is approximately independent of the prepulse characteristics.

Adiabat shaping by relaxation leads to a tunable adiabat profile ranging from a rather shallow profile for RX shaping of type 1 to a steeper profile with RX shaping of type 2. In the case of RX shaping of type 1, the shaping function given in Eqs. (3)–(5) can be well approximated for $\gamma = 5/3$ by the following power law of the mass coordinate:

$$\alpha_{\text{RX1}} = \alpha_{\text{inn}}^{\text{RX1}} \left(\frac{m_{\text{shell}}}{m} \right)^{\delta_{\text{RX1}}}, \quad (12)$$

where the power index δ_{RX1} and the inner-surface adiabat $\alpha_{\text{inn}}^{\text{RX1}}$ are functions of prepulse/main-pulse pressure ratio $r_p \equiv P_p/P_f$. A straightforward numerical fit leads to the following fitting functions:

$$\alpha_{\text{inn}}^{\text{RX1}} \approx 7.2 \cdot 10^{-3} \frac{P_f (\text{Mb})}{\rho_0 (\text{g/cc})^{5/3}} \times \left(1 - 1.12 r_p^{0.52} + 6.54 r_p^{1.15} \right), \quad (13)$$

$$\delta_{\text{RX1}} \approx 1.25 - 4.14 r_p^{0.95} + 3.05 r_p^{1.61}, \quad (14)$$

where ρ_0 is the initial shell density. These approximate formulas have been derived by fitting the adiabat profile over the range $0.2 < m/m_{\text{shell}} < 1$ and $0 < r_p < 0.75$. Observe that the steepest profile of the first kind behaves as $1/m^{1.25}$ and occurs for $r_p \rightarrow 0$. For typical values of prepulse- to foot-pressure ratios in the range $0.05 < r_p < 0.2$, the power index of the adiabat profile is within the range 0.60 to 1.04, which is well below the decaying shock value of 1.315, thus indicating that the DS shaping leads to notably steeper adiabat profiles than the relaxation method of type 1.

In RX shaping of type 2, the adiabat profile left behind by the main shock [Eqs. (7)–(11)] can also be approximated by a power law of the mass coordinate

$$\alpha_{\text{RX2}} \approx \alpha_{\text{inn}}^{\text{RX2}} \left(\frac{m_{\text{shell}}}{m} \right)^{\delta_{\text{RX2}}}, \quad (15)$$

where

$$\alpha_{\text{inn}}^{\text{RX2}} = 2.46 \cdot 10^{-2} \frac{P_f (\text{Mb})}{\rho_0 (\text{g/cc})^{5/3}} \times \left(1.19 + 1.76 r_p^{0.8} \hat{m}_*^{2.15} - 1.11 \hat{m}_*^{0.25} \right), \quad (16)$$

$$\delta_{\text{RX2}} \approx 2.105 - 3.469 r_p^{0.62} \hat{m}_*^{1.31}, \quad (17)$$

and where $m_* = 2.09 \Delta t_p \sqrt{P_p \rho_0}$, Δt_p is the prepulse duration, and $m_{\text{shell}} = \rho_0 d_0$ (d_0 is the initial shell thickness). It is important to emphasize that Eqs. (15)–(17) have been derived by fitting Eqs. (7)–(11) for an ideal fluid (no ablation) with $\gamma = 5/3$ and pulse/target characteristics satisfying $0.2 < r_p < 1$ and $0.05 < \hat{m}_* < 0.4$. It is also interesting to note that the power

index δ_{RX2} is maximum for short prepulses and/or weak prepulses ($\hat{m}_* \ll 1$, $r_p \ll 1$). For $\hat{m}_* \rightarrow 0$, the RX adiabat profile of Eqs. (7)–(11) reduces to a power law with a power index $\delta_{\text{RX2}} \approx 2.4$, well above the power index of the decaying shock shaping $\delta_{\text{DS}} \approx 1.315$. However, the ratio m_*/m_{shell} cannot be arbitrarily small for RX shaping since the pressure behind the prepulse shock at its arrival on the inner surface, which is approximately $P_p \hat{m}_*^{1.3}$, must be large enough to keep the prepulse shock in the strong shock regime and to ionize the target material. Typical values of δ_{RX2} are mostly in the range 1.7 to 2.0, which is still significantly larger than the 1.315 of the decaying shock.

It has been shown in Ref. 6 that ablation causes the adiabat profile induced by a decaying shock to become shallower. This is because the shock decays more slowly due to the residual ablation pressure and the fact that the supporting pressure moves closer to the shock. In the relaxation method of type 2, the relaxed density profile is produced by a decaying shock driven by the pressure prepulse. Since ablation causes a slow-down of the shock decay, it follows that the relaxed profile is “less relaxed” because of ablation. Therefore, the adiabat shape induced by the main shock is less steep than in the ideal case without ablation. Typical ablation-induced reductions of the adiabat profile power index δ_{RX} are small (of the order of 10%) and lead to a power index in the range $\delta_{\text{RX2}} \approx 1.6$ to 1.8.

Pulse Design

To induce the desired adiabat profile, one needs to design the appropriate applied pressure pulse. The pressure pulse (Fig. 101.1) consists of a constant prepulse of pressure P_p and duration Δt_p followed by a main pulse of pressure P_f applied at time t_f . Typically, the pulse is designed to induce the desired value of the inner-surface adiabat α_{inn} . The latter is a design parameter that needs to satisfy the one-dimensional ignition and gain requirements of the implosion. Another design constraint is the merging of the prepulse and main shocks on the shell’s inner surface. This is required in order to keep the adiabat profile monotonically decreasing. For the relaxation pulse of type 1, another requirement is the merging of the rarefaction wave with the prepulse and main shocks on the shell’s inner surface. Therefore, given the four pulse parameters (P_p , P_f , Δt_p , and t_f), the type-1 relaxation has three constraints and one free parameter, while the type-2 relaxation has two constraints and two free parameters. Since different pulse parameters lead to different adiabat decay rates, another design parameter can be identified as the adiabat profile’s spatial decay rate. By approximating the adiabat profile with a power law $S \sim 1/m^\Delta$, the power index Δ defines the decay

rate and can be assigned as a design parameter (within the appropriate limits), thus further reducing the degrees of freedom. Furthermore, technical limits on the prepulse and foot pressure as well as prepulse duration are imposed by the pulse-shaping capabilities of a given laser system. Such limitations are not discussed in this article but need to be taken into account when designing an adiabat-shaping pulse. In this section we proceed to determine the relevant parameters needed to design a pressure pulse for RX adiabat shaping.

1. Pulse Design for RX Shaping of Type 1

The pulse design for a relaxation shaping of type 1 is highly constrained since the prepulse shock, the rarefaction wave, and the main shock must all merge on the shell's rear surface. By combining the Hugoniot condition on the shock velocity

$$\dot{m}_s^M = \sqrt{(\gamma+1)P_{ps}\rho_{bs}/2},$$

the type-1 post-main-shock pressure from Eqs. (73) of Ref. 22

$$P_{ps}^M = P_M/\Theta(\eta_s), \quad (18a)$$

$$\Theta(x) = 1 + \frac{2\beta(\gamma+2)}{3(2-\beta)} \sqrt{\frac{2\gamma P_p}{(\gamma+1)P_M}} x^{1-\frac{\beta}{2}}, \quad (18b)$$

and the pre-shock density $\rho_{bs}^M = \rho_p (m_s^M/m_{rf})^\beta$, with $m_{rf} = m_{shell}\tau$ and

$$\tau = t/\Delta t_*, \quad (19)$$

$$\Delta t_* = \frac{\Delta t_p}{\sqrt{2\gamma/(\gamma-1)-1}} \quad (20)$$

from Eqs. (12)–(13) of Ref. 22, one can easily derive the following ordinary differential equation for the main-shock propagation:

$$\frac{d\eta_s^M}{d\tau} = \frac{\gamma+1}{\gamma} \sqrt{\frac{P_f}{2P_p\Theta(\eta_s^M)} \left(\frac{\eta_s^M}{\tau}\right)^\beta}, \quad (21)$$

where $\eta_s^M = m/m_{shell}$ and Θ is derived from Eq. (18b) for $\beta = 2/(\gamma+1)$, leading to

$$\Theta = 1 + \frac{2(\gamma+2)}{3(\gamma+1)} \sqrt{\frac{2P_p}{P_f}} (\eta_s^M)^{\frac{\gamma}{\gamma+1}}. \quad (22)$$

A straightforward integration of Eq. (21) for $\eta_s^M \in [0,1]$ and $\tau \in [\tau_f, 1]$ leads to the following expression for the beginning time of the foot pulse:

$$t_f = \Delta t_p + \tau_f \Delta t_*, \quad (23a)$$

$$\tau_f = \left\{ 1 - \frac{\gamma}{\gamma+1} \sqrt{\frac{2P_p}{P_f}} \left[1 + \frac{\gamma+2}{6(\gamma+1)} \sqrt{\frac{2P_p}{P_f}} \right] \right\}^{\frac{\gamma+1}{\gamma}}, \quad (23b)$$

where Δt_* is proportional to the prepulse duration Δt_p through Eq. (20). The main-shock breakout time coincides with the prepulse shock and rarefaction-wave breakout time on the inner surface given by the simple relation

$$t_{b.o.} = \Delta t_p + \Delta t_*. \quad (24)$$

The inner-surface adiabat induced by such a pulse is given by Eq. (13) and is primarily dependent on the foot pressure. If the inner-surface adiabat is an assigned design parameter, then Eq. (13) is used to constrain the foot pressure P_f . Note that the prepulse pressure and duration are related by the rarefaction wave/prepulse shock overtaking time, $m_* = m_{shell} \equiv \rho_0 d_0$ or

$$\Delta t_p \sqrt{P_p} = \sqrt{\rho_0} d_0 \frac{\sqrt{2\gamma - \sqrt{\gamma-1}}}{\sqrt{\gamma(\gamma+1)}}. \quad (25)$$

It follows that, for an assigned prepulse pressure (or duration) and inner-surface adiabat, there is only one foot pressure that would shape the adiabat with a profile of type 1 [Eqs. (12)–(14)]. As an example, we consider a 100- μm -thick DT shell ($\rho_0 = 0.25 \text{ g/cc}$, $d_0 = 100 \mu\text{m}$) and design a type-1 RX shaping pulse using a prepulse given by $P_p = 5 \text{ Mb}$, requiring an inner-surface adiabat $\alpha_{inn} = 3$. Equation (25) yields a prepulse duration of $\Delta t_p \approx 1070 \text{ ps}$, while the foot pressure can be determined from Eq. (13) by setting $\alpha_{inn} = 3$. A straightforward calculation yields the foot pressure $P_f \approx 29.7 \text{ Mb}$. The foot pressure is applied at the time t_f obtained from Eq. (23),

yielding $t_f \approx 1442$ ps. The shock-breakout time on the inner surface is given by Eq. (24), yielding $t_{b.o.} \approx 1936$ ps. The corresponding adiabat profile has an approximate power-law behavior [Eq. (12)] with power index $\delta_{RX1} \approx 0.67$ given by Eq. (14). Observe that Eq. (23b) suggests that a critical value of P_p/P_f exists that makes $\tau_f = 0$. Though such a critical value is not accurately predicted by the weak prepulse theory ($P_p \ll P_f$) derived in this article, it is intuitive that an upper limit in the ratio P_p/P_f must exist in the design of a relaxation pulse of the first kind. Indeed, for a given prepulse pressure, the foot pressure must be sufficiently large to cause the main shock to catch the prepulse shock on the shell's rear surface.

2. Pulse Design Shaping for RX Shaping of Type 2

The shock-merging constraint requires that both the prepulse and the main shock merge at the rear surface. The prepulse-shock breakout time ($t_{b.o.}$) on the rear surface can be easily obtained from Eq. (32) of Ref. 22,

$$z_s^p(\tau) = \left[1 + \left(1 + \frac{\delta}{2} \right) \sqrt{\frac{\gamma-1}{2\gamma}} (\tau-1) \right]^{\frac{2}{2+\delta}}, \quad (26)$$

by setting $z_s^p = z_{shell} \equiv m_{shell}/m_*$, thus leading to

$$t_{b.o.} = \Delta t_p + \Delta t_* \tau_{b.o.}, \quad (27a)$$

$$\tau_{b.o.} \equiv 1 + \frac{2}{2+\delta} \sqrt{\frac{2\gamma}{\gamma-1}} \left[z_{shell}^{(2+\delta)/2} - 1 \right], \quad (27b)$$

where Δt_* is given in Eq. (20) and m_* in Eq. (14) of Ref. 22:

$$m_* = \Delta t_* \rho_p a_p = \Delta t_* \sqrt{\gamma P_p \rho_p}. \quad (28)$$

The main shock must also arrive on the rear surface at time $t_{b.o.}$ by traveling through the $m > m_*$ and $m < m_*$ regions. The main shock's traveling time through the $m > m_*$ region can be easily derived by integrating Eq. (91) of Ref. 22:

$$\dot{m}_s^M = \sqrt{\frac{\gamma-1}{2} \omega_* P_f \rho_M \left(\frac{m_s^M}{m_s^p} \right)^\mu \left[1 + D(z_s^M) (z_s^M - 1) \right]}. \quad (29)$$

A straightforward manipulation yields the following traveling time:

$$\Delta t_{m>m_*}^M = \Delta t_* \Delta \tau_{m>m_*}^M, \quad (30a)$$

where

$$\Delta \tau_{m>m_*}^M = \sqrt{\frac{2\gamma}{\gamma+1} \frac{P_p}{\omega_* P_f}} \times \int_1^{z_{shell}} \frac{(z_s^p)^{\mu/2} dz_s^M}{\sqrt{(z_s^M)^\mu \left[1 + D(z_s^M) (z_s^M - 1) \right]}}, \quad (30b)$$

z_s^p is a function of z_s^M [Eqs. (96)–(97) of Ref. 22],

$$(z_s^p)^\phi - z_{shell}^\phi = \phi \sqrt{\frac{2(\gamma-1)}{\gamma+1} \frac{P_p}{\omega_* P_f}} \left[\sigma(z_s^M) - \sigma(z_{shell}) \right], \quad (31)$$

where $z_s^p = m_s^p/m_*$, $z_{shell} = z_{shell} = m_{shell}/m_*$, and

$$\sigma(\xi) = \sqrt{\frac{(\mu-2)\xi^{1-\mu} - (\mu-1)\xi^{2-\mu} + 1}{(\mu-2)(\mu-1)}}, \quad (32)$$

and $D(x)$, ω_* are given in Eqs. (10), (11), and (9). It follows that the time when the main shock is at $m = m_*$ is $t_{m=m_*}^M = \Delta t_p + \Delta t_* \tau_{m=m_*}$, where $\tau_{m=m_*} \equiv \tau_{b.o.} - \Delta \tau_{m>m_*}^M$. Before arriving at m_* , the main shock travels through the region $0 < m < m_*$, where the density profile is given by Eq. (44) of Ref. 22,

$$\rho(z < 1) \approx \rho_p \left(\frac{z}{\tau} \right)^\beta = \rho_p \left(\frac{m}{m_{rf}} \right)^\beta, \quad (33)$$

and the post-shock pressure follows Eq. (18) with $\eta = m_s^M/m_{rf}^0$ and m_{rf}^0 given in Eq. (89) of Ref. 22,

$$m_{\text{if}}^0 = m_* \left\{ 1 + \frac{2}{2 + \delta} \sqrt{\frac{2\gamma}{\gamma - 1}} \left[\tau_{\text{shell}}^{(2+\delta)/2} - 1 \right] \right\}. \quad (34)$$

The shock-evolution equation is given by the Hugoniot condition [Eq. (10) of Ref. 22]

$$\dot{m}_s = \sqrt{\frac{(\gamma + 1)}{2}} [P_{\text{ps}} \rho_{\text{bs}}]_{m_s}, \quad (35)$$

which can be integrated between the main-shock launching time (or main-pulse foot beginning time t_f) and the arrival time at $m = m_*$. A short calculation yields the launching time

$$t_f = \Delta t_* \tau_f + \Delta t_p, \quad (36a)$$

$$\tau_f \equiv \left[\tau_{m=m_*}^{(2-\beta)/2} - \left(1 - \frac{\beta}{2} \right) \theta \sqrt{\frac{2\gamma}{\gamma + 1}} \frac{P_p}{\omega_0 P_f} \right]^{2-\beta}, \quad (36b)$$

where

$$\theta = \int_0^1 dx \frac{1}{\chi^{\beta/2}} \times \left[1 - \frac{2\beta(\gamma + 2)}{3(2 - \beta)} \sqrt{\frac{2\gamma P_p}{(\gamma + 1)\omega_0 P_f}} \left(\frac{x m_*}{m_{\text{if}}^0} \right)^{\frac{2-\beta}{\beta}} \right]^{-\frac{1}{2}}. \quad (36c)$$

Observe that Eqs. 36 provide the beginning time of the foot of the main pulse once the prepulse pressure P_p , foot pressure P_f , and prepulse duration Δt_p are assigned. The time t_f is derived by timing the prepulse and main shock so that they merge on the shell's inner surface. As an example, we consider a 100- μm -thick DT shell ($\rho_0 = 0.25 \text{ g/cc}$, $d_0 = 100 \mu\text{m}$) and design a type-2 RX shaping pulse using a $P_p = 18 \text{ Mb}$, $\Delta t_p = 100\text{-ps}$ prepulse and requiring an inner-surface adiabat $\alpha_{\text{inn}} \approx 3$. Using the definition $m_{\text{shell}} = \rho_0 d_0$ and Eqs. (20) and (28) to find m_* , one can easily compute the parameter $\hat{m}_* = 0.177$. The foot pressure can be determined by using $\alpha_{\text{inn}} = 3$ into Eq. (16), yielding $P_f \approx 24 \text{ Mb}$. The time when the foot pressure is applied can be computed from Eqs. (36) using $\gamma = 5/3$, $\omega_0 \approx 1.5$, and $\beta = 0.75$, leading to $t_f = 1256 \text{ ps}$. The shocks' breakout/merging time is determined through Eqs. (27), leading to $t_{\text{b.o.}} = 1993 \text{ ps}$. The corresponding adiabat profile has an

approximate power-law behavior [Eq. (15)] with power index $\delta_{\text{RX2}} \approx 1.80$, which is significantly larger than in the case of the decaying-shock shaping.

It is important to recognize that typical laser pulses are designed so that the laser power reaches its peak at shock breakout. The corresponding laser pressure starts from the foot level (P_f) and increases monotonically to its maximum value P_{max} (Fig. 101.1). The laser power (and pressure) is raised at a low-enough rate to avoid strengthening the main shock and to prevent increasing the adiabat after the main shock. Since the resulting adiabat shape is set by the main shock driven by P_f , the theory derived in this article is valid for realistic ICF pulses with a laser-power raise after the foot (Fig. 101.1).

This concludes the analysis of the pulse design. A detailed comparison of the adiabat shapes and pulse-design parameters with the results of numerical simulation is carried out in the next section.

Comparison with Simulations

The results of the analytic theory derived in this article are compared to the numerical results calculated by a one-dimensional Lagrangian hydrodynamics code, using ideal gas equation of state and an imposed pressure boundary condition to simulate the relaxation drive pulses. We have chosen the case of $\alpha_{\text{inn}} = 3$ as a case of interest, where adiabat shaping is expected to demonstrate significantly improved performance and to constrain our capsule and pulse designs to such as would be implementable on the OMEGA laser system.

Using the pulse-design formulas given in the **Pulse Design for RX Shaping of Type 1** section (p. 6), a type-1 RX pulse shape was designed for a typical OMEGA cryogenic capsule of density $\rho_0 = 0.25 \text{ g/cm}^3$ and thickness $d_0 = 100 \mu\text{m}$ using the parameters described in the example on pp. 6–7: $P_p = 5 \text{ Mb}$, $\Delta t_p = 1070 \text{ ps}$, $P_f = 29.7 \text{ Mb}$, and $t_f = 1442 \text{ ps}$. The shocks' breakout time is $t_{\text{b.o.}} = 1936 \text{ ps}$, and the resulting adiabat shape can be approximated with the power law $\alpha \approx 3.04(m_{\text{shell}}/m)^{0.67}$. The pulse parameters have been used as input to the one-dimensional Lagrangian code that solves the equation of motion over a mesh of 2000 grid points. Figure 101.3 compares the adiabat profiles from the numerical simulation (solid curve) with the power-law approximation (dashed curve) and the full analytic formula in Eqs. (3)–(5) (dotted curve). Observe that the theoretical pulse parameters described on pp. 6–7 produce a monotonically decreasing adiabat profile with an inner-surface adiabat of about $\alpha_{\text{inn}} \approx 3$. Furthermore, the simulated adiabat profile compares favorably with the full

analytic formula as well as the power-law approximation described in the **Simplified Formulas for RX Adiat Shapes and Comparison with DS Shapes** section (p. 4) for type-1 relaxation.

Similarly, a type-2 RX pulse shape is designed in the **Pulse Design for RX Shaping of Type 2** section (p. 7) for the same target with $\alpha_{\text{inn}} = 3$. The pulse parameters shown on p. 8 are $P_p = 18$ Mb, $P_f = 24$ Mb, $\Delta t_p = 100$ ps, and $t_f = 1256$ ps. The shocks' breakout time is $t_{\text{b.o.}} = 1993$ ps, and the adiabat profile can be approximated with the power law $\alpha \approx 3.0(m_{\text{shell}}/m)^{1.8}$. Figure 101.4 compares the adiabat profiles from the numerical simulation (solid curve) with the power-law approximation

(dashed curve) and the full analytic formula in Eqs. (7)–(11) (dotted curve). Observe that the theoretical pulse parameters (p. 8) induce a monotonically decreasing adiabat profile with an inner-surface adiabat of about $\alpha_{\text{inn}} \approx 3$. Even in this case, the simulated adiabat profile compares favorably with both the full analytic formula as well as the power-law approximation for type-2 relaxation.

Nonideal Effects on RX Adiat Shaping

In realistic ICF implosions, quantifying the adiabat profile generated in a relaxation-design capsule is further complicated by other physical processes and constraints, such as radiation, thermal conduction, mass ablation, laser absorption and laser system constraints, realistic equations of state (EOS's), and spherical convergence. Radiation and thermal conduction effects may invalidate the assumption of isentropic flow away from the shocks. Mass ablation alters the position where the laser-induced shocks are launched and therefore affects the shock timing. In typical pulse designs, the laser-absorption histories, and hence applied pressure histories, are not constant over the duration of either the prepulse or the foot, as has been assumed in the previous analysis. Realistic EOS's yield different results for compressibility, shock and rarefaction speeds, and post-shock flow velocity than the ideal-gas approximation. A thorough theoretical treatment of these processes is beyond the scope of this article; however, an attempt is made here to quantify their effects on the shell's adiabat profile through simple reasoning and simulation.

In ICF capsules, the radiation emitted from the hot coronal plasma can penetrate the shell, heating the dense shell material up to a significant depth. This inevitably causes a "natural" shaping of the adiabat near the ablation front,^{11–13} even when the laser pulse is designed to induce a flat adiabat. This effect may indeed be noticeable for capsules with high or moderate average atomic number, e.g., polystyrene plastic²³ (CH, $\langle Z \rangle = 3.5$). However, for the hydrogenic capsules ($Z = 1$) of interest for direct-drive ICF, the radiation shaping is typically negligible when compared with the laser-induced shaping discussed here.

Thermal conduction plays an essential role in ICF capsule implosions since the heat conducted from the laser-absorption region to the ablation surfaces determines the ablation pressure. At the ablation surface, the shell material absorbs heat rapidly, raising its adiabat quickly as it ablates off the shell. Once this shell material has been ablated, however, its adiabat is no longer relevant to the capsule stability since the ablation velocity is determined only by the local value of the adiabat at

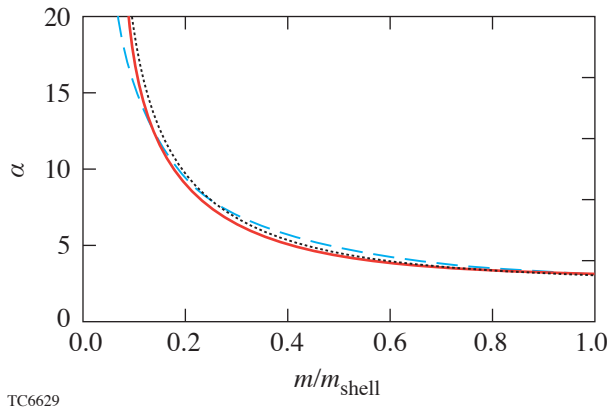


Figure 101.3
A comparison of the simulated adiabat shape of type 1 (solid) with the full analytic formula [Eqs. (3)–(5)] (dotted) and the power-law approximation [Eqs. (12)–(14)] (dashed).

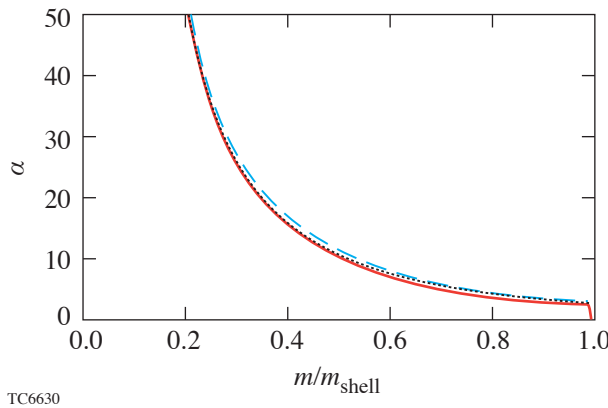


Figure 101.4
A comparison of the simulated adiabat shape of type 2 (solid) with the full analytic formula [Eqs. (7)–(11)] (dotted) and the power-law approximation [Eqs. (15)–(17)] (dashed).

the ablation surface. Furthermore, the contribution of heat conduction to the adiabat in the bulk of the shell is very small compared to the shock-induced adiabat since both the temperature and temperature gradients are small in the unablated shell. Therefore, thermal conduction effects on the adiabat profile (with the exception of mass ablation) may also be neglected.

Mass ablation occurs during the prepulse as well as the foot of the main pulse. While the mass ablated during the prepulse is negligible, a significant fraction ranging from 20% to 30% of the total shell mass is ablated during the foot of the main pulse. Since the mass m_* undertaken by the rarefaction wave before the interaction with the prepulse shock is small in type-2 adiabat shaping, the ablated mass m_{abl} often exceeds m_* . When this happens, the foot-pressure amplification through the region $0 < m < m_*$ is eliminated. In the absence of mass ablation, the applied foot pressure is amplified from P_f at $m = 0$ to $\omega_* P_f$ at m_* , where $\omega_* \approx 1.5$ is given in Eq. (9). If the mass m_* is quickly removed by mass ablation during the foot, then the main shock is launched with the pressure P_f instead of $\omega_* P_f$. Therefore, the validity of Eqs. (15)–(17) for the design of type-2 adiabat shaping can be easily extended to the ablative case by replacing the applied pressure P_f with $P_f/\omega_* \approx P_f/1.5$.

When dealing with thick cryogenic targets, spherical convergence effects should also be taken into account for an accurate estimate of the adiabat shapes. They can be easily included by replacing the areal mass coordinate m with the total mass coordinate $m^{\text{sph}} = \int_0^{\bar{r}} \bar{r}'^2 \rho(\bar{r}', 0) d\bar{r}'$. This requires a redefinition of m_* as follows:

$$m_*^{\text{sph}} = \frac{\rho_0}{3} (R_{\text{out}}^3 - R_*^3),$$

where R_{out} is the initial outer radius of the shell and

$$R_*^{\text{sph}} = \sqrt{4P_p/3\rho_0} (\Delta t_p + \Delta t_*)$$

is the radial coordinate of the rarefaction–shock merging.

To quantitatively account for all these effects, simulations were performed using *LILAC*,²⁴ a 1-D Lagrangian ICF code. The *LILAC* simulations used *SESAME* EOS in a spherical geometry, while modeling laser absorption by ray trace and inverse bremsstrahlung, thermal conduction using a flux-limited local thermodynamic equilibrium treatment, and radiation transport using multigroup diffusion. The target is an 85- μm -thick, solid-DT shell. The laser pulse, designed in

accordance with pulse-shaping capabilities of the OMEGA laser system,²⁵ consists of an 80-ps, 15-TW square prepulse, with a finite ramp-up and ramp-down in intensity, followed by a 7-TW foot with finite ramp-up launched at about 950 ps. The average prepulse pressure found by *LILAC* is 23 Mb. The ablation pressure of the foot pulse at the time of shock generation is approximately 34 Mb. The resulting adiabat profile is shown in Fig. 101.5 (solid) and compared with the prediction of Eqs. (15)–(17) (dashed), including the above modifications, indicating good agreement between theory and simulation. Note that the optimal foot-pulse turn-on time predicted by theory is 800 ps, whereas the value in simulation was 950 ps, indicating that some retuning of the pulse was necessary.

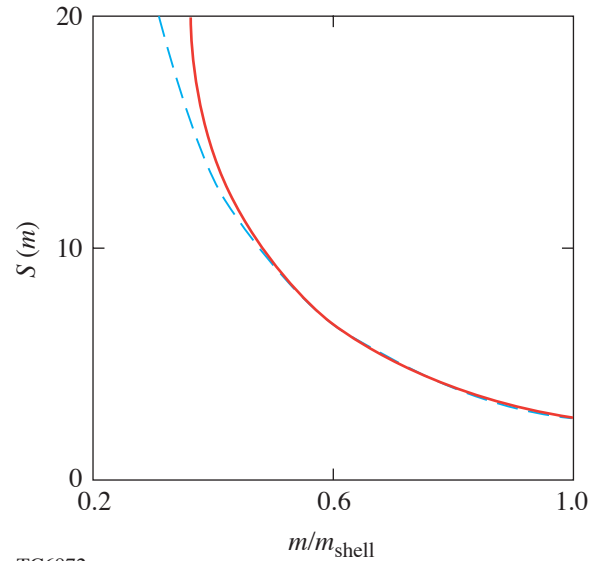


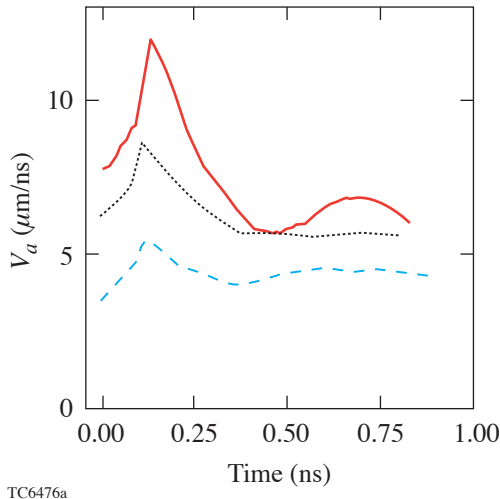
Figure 101.5

A comparison of the simulated adiabat shape predicted by *LILAC* (solid) with the analytic formula [Eqs. (15)–(17)] (dashed) for an OMEGA-scale design.

To estimate the increase in ablation velocity, it is important to recognize that in realistic ICF implosions, a significant fraction of the target material is ablated off during the foot of the laser pulse. For an RX pulse shape, about 20% to 30% of the target mass is ablated before the shock-breakout time, thus causing the shell's outer surface to shift inward. The shell acceleration starts shortly after the shock-breakout time when the laser power reaches its peak. The relevant outer-surface adiabat determining the ablation velocity is the adiabat at the ablation front, which moves deeper inside the target as more mass is ablated off. In mass coordinates, the ablation-front position is equal to the amount of mass ablated, $m_a(t)$. It follows that the ablation velocity for a shaped-adiabat implosion is determined by the following simple scaling law:

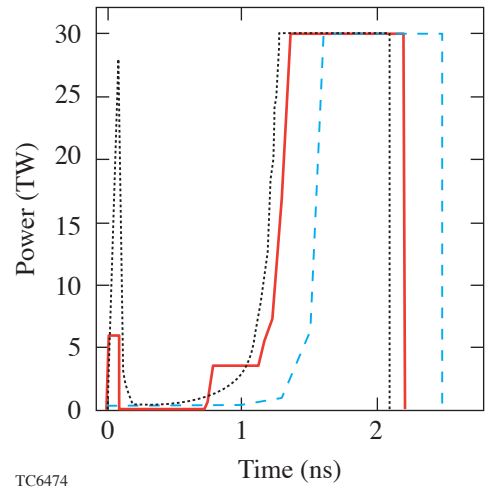
$$V_a^{\text{shaped}} \approx V_a^{\text{flat}} \left(\frac{m_{\text{shell}}}{m_a(t)} \right)^{\frac{3}{5} \delta}, \quad (37)$$

where V_a^{flat} is the ablation velocity for a flat-adiabat implosion with $\alpha = \alpha_{\text{inn}}$ and δ equal to δ_{RX1} , δ_{RX2} , or δ_{DS} , depending on the shaping method. During the acceleration phase, V_a is maximum at the beginning [low $m_a(t)$] and decreases in time as more mass is ablated and $m_a(t)$ increases. At the beginning of the acceleration phase when $m_a \sim 0.3 m_{\text{shell}}$, the shaped-adiabat ablation velocity is roughly 2 times the flat-adiabat value for the decaying-shock shaping ($\delta_{\text{DS}} \approx 1.1$), about 1.5 times V_a^{flat} for type-1 RX shaping ($\delta_{\text{RX1}} \sim 0.7$), and over 3 times V_a^{flat} for type-2 RX shaping ($\delta_{\text{RX2}} \sim 1.6$ to 1.8). Figure 101.6 shows the time evolution of the ablation velocities computed by *LILAC* for a typical OMEGA-size cryogenic DT shell of 85- μm thickness and 345- μm inner radius. The three curves represent the three pulse designs: flat adiabat with $\alpha = 3$ (dashed), shaped adiabat by decaying shock (dotted), and shaped adiabat by RX-2 shaping (solid). The corresponding laser time histories are shown in Fig. 101.7, and the time axis in Fig. 101.6 is adjusted to fit the different acceleration phases (i.e., maximum laser power intervals) of the three designs. Observe that the RX-2 design leads to the largest ablation velocity, approaching 3 times the flat-adiabat value at the beginning of the acceleration phase.



TC6476a

Figure 101.6
Time evolution of the ablation velocities during the laser pulse's flattop for flat $\alpha = 3$ (dashed), decaying-shock-shaped (dotted), and type-2 relaxation-shaped (solid) implosions.



TC6474

Figure 101.7
Laser pulse for a flat $\alpha = 3$ design (dashed), a decaying-shock design (dotted), and a type-2 relaxation design (solid) of comparable 1-D performance.

Conclusions

Analytic forms of the relaxation adiabat shapes have been derived for two cases: type 1, where the prepulse is long enough that the rarefaction wave catches the prepulse shock at the shell's inner surface; and type 2, the case of short prepulses, where the rarefaction wave/shock interaction occurs inside the shell. The analytic relaxation adiabat profiles derived here are in excellent agreement with simulations. Results indicate that the adiabat profiles for both type-1 and type-2 designs are well approximated by a power law for ICF-relevant values of the prepulse to main-pulse pressure ratio. The power-law indices for RX designs have been shown to be highly tunable, giving the possibility for tailoring adiabat profiles to desired design specifications. The type-2 relaxation designs also allow for power-law indices, which are substantially higher than those generated by decaying-shock designs (see Ref. 6), resulting in the possibility of higher ablation velocities and higher RT mitigation in RX designs, while maintaining similar one-dimensional compression and yield. In addition, formulas to aid in the design of RX implosions have been provided, and nonideal effects on RX adiabat shaping have been estimated.

ACKNOWLEDGMENT

This work was supported by the U.S. Department of Energy Office of Inertial Confinement Fusion under Cooperative Agreement No. DE-FC52-92SF19460, the University of Rochester, and the New York State Energy Research and Development Authority. The support of DOE does not constitute an endorsement by DOE of the views expressed in this article.

REFERENCES

1. W. K. Levedahl and J. D. Lindl, *Nucl. Fusion* **37**, 165 (1997).
2. M. M. Basko and J. Johner, *Nucl. Fusion* **38**, 1779 (1998).
3. M. C. Herrmann, M. Tabak, and J. D. Lindl, *Nucl. Fusion* **41**, 99 (2001).
4. A. Kemp, J. Meyer-ter-Vehn, and S. Atzeni, *Phys. Rev. Lett.* **86**, 3336 (2001).
5. R. Betti, K. Anderson, V. N. Goncharov, R. L. McCrory, D. D. Meyerhofer, S. Skupsky, and R. P. J. Town, *Phys. Plasmas* **9**, 2277 (2002).
6. K. Anderson and R. Betti, *Phys. Plasmas* **10**, 4448 (2003).
7. V. N. Goncharov, J. P. Knauer, P. W. McKenty, P. B. Radha, T. C. Sangster, S. Skupsky, R. Betti, R. L. McCrory, and D. D. Meyerhofer, *Phys. Plasmas* **10**, 1906 (2003).
8. K. Anderson and R. Betti, *Phys. Plasmas* **11**, 5 (2004).
9. L. J. Perkins, M. Tabak, J. Lindl, D. Bailey, J. Harte, A. Schmitt, S. Obenschain, and R. Betti, *Bull. Am. Phys. Soc.* **47**, 101 (2002).
10. K. Anderson, R. Betti, J. P. Knauer, and V. N. Goncharov, presented at the 34th Anomalous Absorption Conference, Gleneden Beach, OR, 2–7 May 2004.
11. J. H. Gardner, S. E. Bodner, and J. P. Dahlburg, *Phys. Fluids B* **3**, 1070 (1991).
12. S. E. Bodner *et al.*, *Phys. Plasmas* **7**, 2298 (2000).
13. L. Phillips *et al.*, *Laser Part. Beams* **17**, 225 (1999).
14. R. P. J. Town and L. J. Perkins, Lawrence Livermore National Laboratory, private communication (2003); M. Tabak, Lawrence Livermore National Laboratory, private communication (1987).
15. J. D. Lindl and W. C. Mead, *Phys. Rev. Lett.* **34**, 1273 (1975).
16. N. Metzler, A. L. Velikovich, and J. H. Gardner, *Phys. Plasmas* **6**, 3283 (1999).
17. N. Metzler *et al.*, *Phys. Plasmas* **9**, 5050 (2002).
18. N. Metzler *et al.*, *Phys. Plasmas* **10**, 1897 (2003).
19. T. J. B. Collins and S. Skupsky, *Phys. Plasmas* **9**, 275 (2002).
20. A. B. Isakov *et al.*, *Phys. Rev. E* **61**, 842 (2000); E. Krousky *et al.*, *Laser Part. Beams* **18**, 87 (2000).
21. Laboratory for Laser Energetics LLE Review **98**, 106, NTIS document No. DOE/SF/19460-527 (2004). Copies may be obtained from the National Technical Information Service, Springfield, VA 22161.
22. R. Betti, K. Anderson, J. P. Knauer, T. J. B. Collins, R. L. McCrory, P. W. McKenty, and S. Skupsky, “Theory of Laser-Induced Adiabatic Shaping in Inertial Confinement Fusion Implosions: The Relaxation Method,” submitted to *Physics of Plasmas*.
23. K. Anderson, R. Betti, J. P. Knauer, and V. N. Goncharov, *Bull. Am. Phys. Soc.* **49**, 210 (2004).
24. M. C. Richardson, P. W. McKenty, F. J. Marshall, C. P. Verdon, J. M. Soures, R. L. McCrory, O. Barnouin, R. S. Craxton, J. Delettrez, R. L. Hutchison, P. A. Jaanimagi, R. Keck, T. Kessler, H. Kim, S. A. Letzring, D. M. Roback, W. Seka, S. Skupsky, B. Yaakobi, S. M. Lane, and S. Prussin, in *Laser Interaction and Related Plasma Phenomena*, edited by H. Hora and G. H. Miley (Plenum Publishing, New York, 1986), Vol. 7, pp. 421–448.
25. T. R. Boehly, D. L. Brown, R. S. Craxton, R. L. Keck, J. P. Knauer, J. H. Kelly, T. J. Kessler, S. A. Kumpan, S. J. Loucks, S. A. Letzring, F. J. Marshall, R. L. McCrory, S. F. B. Morse, W. Seka, J. M. Soures, and C. P. Verdon, *Opt. Commun.* **133**, 495 (1997).

Improved Target Stability Using Picket Pulses to Increase and Shape the Ablator Adiat

Introduction

The minimum energy required for ignition of the imploding capsule in inertial confinement fusion¹ is a strong function of the fuel adiabat α_{stag} (the ratio of the shell pressure to the Fermi-degenerate pressure) at the time of maximum compression: $E_{\text{min}} \sim a_{\text{stag}}^{1.9}$ (Refs. 2 and 3). The shell must be driven on the lowest-possible adiabat to minimize this energy. The performance of low-adiabat implusions is limited by hydrodynamic instabilities that tend to disrupt the shell during the acceleration phase. The most important instability is the Rayleigh–Taylor^{4,5} (RT) instability that is seeded by single-beam nonuniformities and surface roughness. The RT growth is reduced by mass ablation from the target surface^{6–9} characterized by the ablation velocity V_a .

Interface perturbations grow exponentially ($a = a_0 e^{\gamma t}$) during the “linear” phase of the RT instability and reach a saturation phase (when $a \sim \lambda/10$) where the growth continues at a reduced rate.¹⁰ Here, a is the amplitude of the perturbation, a_0 is the initial perturbation amplitude (the seed), γ is the growth rate, and λ is the wavelength of the perturbation.

A great deal of effort has gone into reducing the seeds (a_0) caused by illumination nonuniformities (imprinting) and target imperfections. The effect of imprinting has been reduced by a number of beam-smoothing techniques, including distributed phase plates (DPP’s),¹¹ polarization smoothing (PS) with birefringent wedges,^{12,13} smoothing by spectral dispersion (SSD),¹⁴ and induced spatial incoherence (ISI).¹⁵ The effect of the RT instability can also be reduced by lowering the RT growth rate. It has been shown that the ablation-surface RT growth rate is reduced by the ablation process. Theoretical work that includes the effect of thermal transport⁹ shows that the RT-growth-rate dispersion formula for a DT target is given by

$$\gamma_{\text{DT}} = \sqrt{A_T(L_0, \nu)kg - A_T^2(L_0, \nu)k^2 V_a V_{bo}} - [1 + A_T(L_0, \nu)]kV_a,$$

where $A_T(L_0, \nu)$ is the Atwood number, a function of L_0 and ν ; k is the perturbation spatial wave number; g is acceleration; L_0 is ablation interface thickness; V_a is ablation velocity; V_{bo} is the “blowoff” velocity; and ν is the thermal transport index. V_{bo} is equal to V_a times the ratio of the blowoff plasma density to the ablation surface density. The ablation velocity, in turn, increases with the adiabat α in the ablation region as $V_a \propto \alpha^{3/5}$ (Ref. 16). This is the compromise that faces target designers—lowering α reduces the minimum energy required for ignition, but increases the effects of the RT instability. This article describes recent results using a shaped adiabat that increases the ablation-surface adiabat while maintaining a low adiabat for the compressed fuel.

This article is divided into five sections: (1) the motivation for adiabat shaping; (2) the results from the planar growth and imprint experiments; (3) data from spherical implusions with the decaying-shock-wave picket and the relaxation picket; (4) simulations showing the extension of the picket pulses to cryogenic implusions; and (5) conclusions.

Adiabat Shaping

The conflicting requirements of the lower-adiabat fuel at the maximum compression and the higher-adiabat ablation region can be achieved by shaping the adiabat inside the shell. A schematic of a shaped shell adiabat is shown in Fig. 101.8, where the shell is represented as a region of constant density and the adiabat varies from 1.5 to 4. The shaded region is the portion of the shell that remains at the end of the acceleration phase of the implosion. The inner fuel region is on a low adiabat while the adiabat in the ablated mass is high. The first published work on adiabat shaping used the absorption of low-energy x rays¹⁷ to increase the adiabat at the ablation surface.

A short, high-intensity picket pulse, as seen in Fig. 101.9(a), can be used to shape the shell adiabat by creating a decaying shock wave.^{18,19} This technique modifies the adiabat by modifying the pressure inside the shell. The ablation pressure from the picket pulse creates a shock wave that raises the pressure at the ablation surface and propagates into the shell. A rarefaction

wave propagates toward the shock wave at the end of the picket pulse. The shock-wave pressure then decays after the rarefaction wave overtakes it, reducing the pressure and lowering the adiabat for the inner sections of the shell.

The shell adiabat can also be shaped by propagating a strong shock wave in a fluid where the density increases from the ablation surface to the inner shell.²⁰ This density shape is created by a low-intensity, narrow picket pulse that causes the shell to decompress after it is turned off. This pulse shape is shown in Fig. 101.9(b). Shell decompression creates a density profile that is low at the ablation interface and high in the inner shell. The pulse shape needs to be timed so that the shock wave from the drive pulse reaches the shell–gas interface at the same time as the rarefaction wave from the picket pulse.

Picket-pulse shapes are not new to inertial confinement fusion (ICF); Lindl and Mead mentioned picket pulses in Ref. 21. This work showed that multiple picket pulses used in a simulation showed reduced target distortions during implosion. This was attributed to the impulsive nature of the picket drive with no mention of adiabat shaping. In the 1980s, simulations done at Lawrence Livermore National Laboratory (LLNL) and LLE²² showed that if a picket pulse is used with a low-adiabat drive, the acceleration RT growth is reduced.

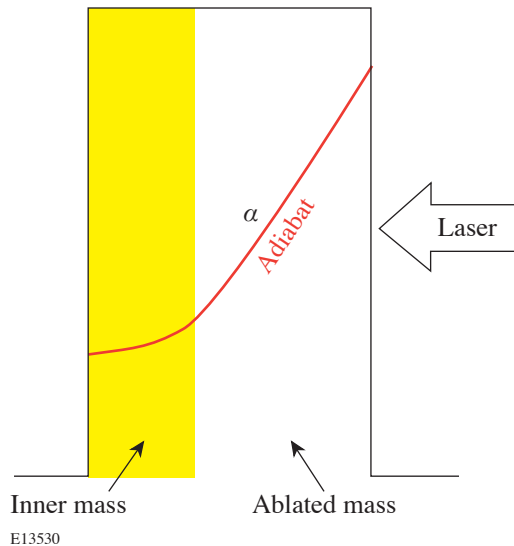


Figure 101.8 Schematic of a shell showing a shaped adiabat between the ablation surface and the inner surface. The shaded region is the portion of the shell that is not ablated. The adiabat is higher in the ablated material and therefore reduces the RT growth of ablation-interface perturbations.

LLE has done planar RT growth experiments²³ with picket pulses and established an analytical understanding of adiabat shaping with picket pulses.^{18–20} Picket pulses are being actively studied to improve direct-drive target performance.

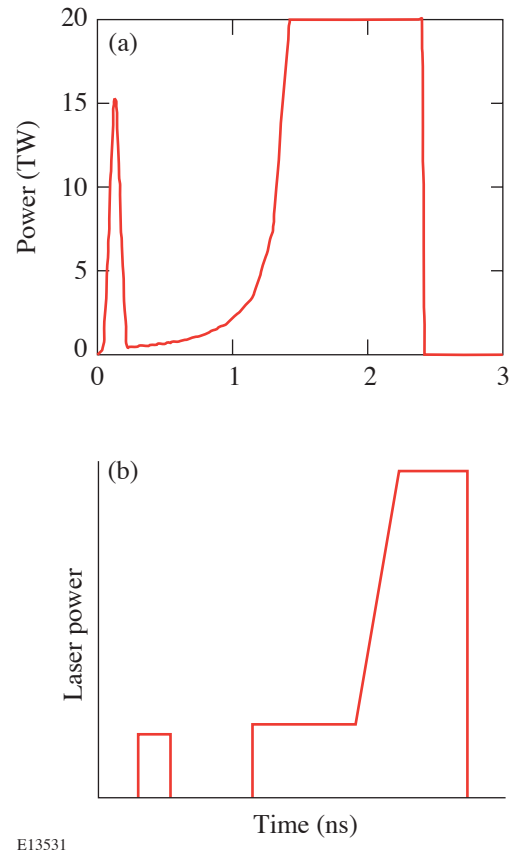


Figure 101.9 Laser pulse shapes for a decaying-shock-wave picket and a relaxation picket. In (a) the decaying shock wave is created by the short picket at the beginning of the pulse shape. The adiabat is shaped as the shock wave decays. The pulse shape for a relaxation picket drive is shown in (b). The low-intensity, narrow picket in front creates a spatial-density profile that is low at the ablation region and high inside the shell. The strong shock wave resulting from the high foot intensity then propagates through this density profile, shaping the shell’s adiabat.

Planar Experiments

Acceleration interface perturbation growth due to the RT instability has been routinely studied in planar targets. A non-converging planar target allows the whole foil to be placed on a high adiabat to study how the adiabat affects the RT growth. The mass-modulated accelerated foil was composed of a 20- μm -thick CH foil with perturbations imposed on the side irradiated by the laser.²⁴ This thickness was chosen because it has about two attenuation depths for the 1.0- to 1.5-keV x rays

used for radiography. The initial perturbations were (1) a wavelength of $\lambda = 60 \mu\text{m}$ and amplitude of $a = 0.25 \mu\text{m}$; (2) $\lambda = 30 \mu\text{m}$ and $a = 0.125$ and $0.25 \mu\text{m}$; and (3) $\lambda = 20 \mu\text{m}$ and $a = 0.05$ and $0.25 \mu\text{m}$. The perturbation amplitudes decreased with decreasing wavelength to ensure that the growth was measured in the “linear” ($a < \lambda/10$) phase of the RT instability. The $0.25\text{-}\mu\text{m}$ -amplitude perturbation at wavelengths of $30 \mu\text{m}$ and $20 \mu\text{m}$ was used to study the stability of this perturbation for large picket intensities where little or no growth was expected and the smaller amplitude perturbation was below the detection threshold.

Planar targets with imposed mass perturbations were accelerated using ten laser beams overlapped with a total overlapped peak intensity of $1.7 \times 10^{14} \text{ W/cm}^2$. Each of the drive beams was focused to a spot size with a diameter of $\sim 930 \mu\text{m}$ (at the 5% intensity contour) and used all of the beam smoothing available on OMEGA. The use of distributed phase plates, polarization smoothing, and SSD resulted in a laser-irradiation nonuniformity relative to the intensity envelope of $<1\%$ over a $600\text{-}\mu\text{m}$ -diam region defined by the 90% intensity contour. Two pulse shapes were used for the drive beams: first, a pulse with a Gaussian rise to a 2-ns constant intensity (referred to as the drive pulse) and, second, this same pulse with a Gaussian picket placed ~ 2 ns ahead of the time when the drive pulse reaches constant intensity. The pulse shape is shown in Fig. 101.10(a). The maximum drive intensity was designed to be the same for irradiation with and without a picket.

A comparison of the calculated and measured amplitudes of the fundamental Fourier mode of the optical-depth modulation for a $20\text{-}\mu\text{m}$ -wavelength perturbation is shown in Fig. 101.10(b), for a drive pulse only, a picket 50% of the drive-pulse intensity, and a picket 100% of the drive intensity. The data with and without the picket have been temporally shifted to match the start of the measured drive pulse. Multiple shots were performed at each wavelength, with the x-ray diagnostics using different temporal windows covering the duration of the drive pulse. A clear reduction in the $20\text{-}\mu\text{m}$ -wavelength perturbation growth rate is seen for the 50% I_p/I_d data. Data for a picket with an intensity of 100% of the drive pulse show that the ablation velocity during the drive pulse is large enough to stabilize the RT growth at this wavelength. Two-dimensional (2-D) hydrodynamic simulations of the experiment agree with the experimental data without and with picket pulses with intensities equal to 50% of the drive pulse.

A picket pulse is also effective in reducing the imprint seed for the RT instability in cryogenic implosions.²² Current cryo-

genic targets are thin ($\sim 3\text{-}$ to $5\text{-}\mu\text{m}$) CH shells with a $100\text{-}\mu\text{m}$ layer of DT or D_2 ice. The density mismatch between the CH shell and the hydrogenic layer causes a pressure gradient to be established during the constant-intensity foot portion of the

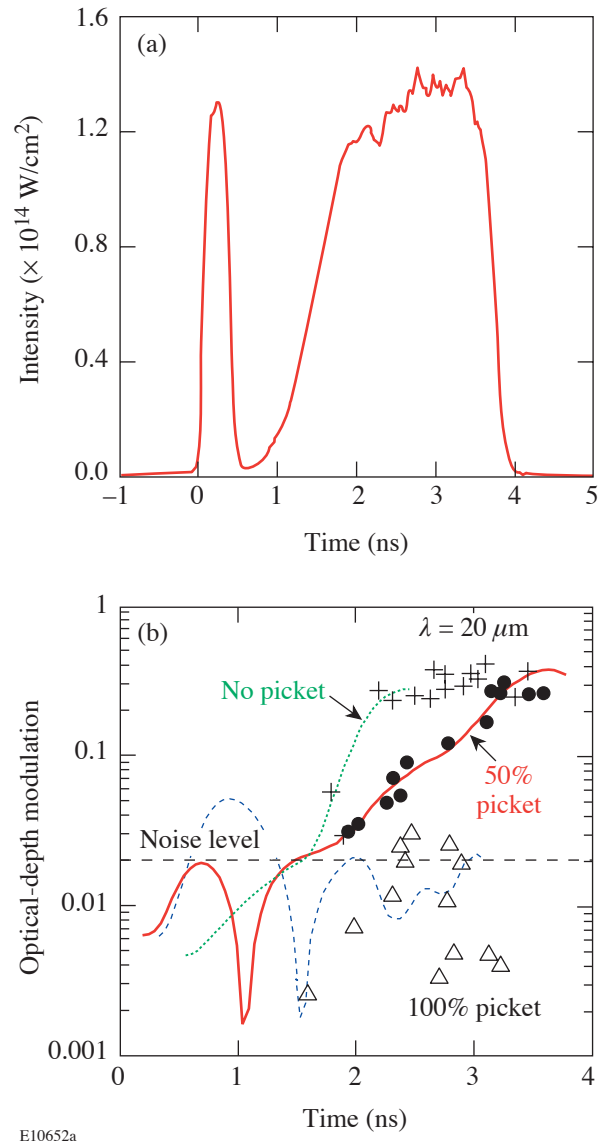


Figure 101.10

Planar RT growth experiments used the pulse shape shown in (a). The 300-ps-wide picket caused the foil to decompress, lowering the ablation-interface density and raising the ablation velocity. The modulation in optical depth is shown in (b) for an imposed $20\text{-}\mu\text{m}$ -wavelength perturbation. Data without a picket are shown as plus (+) symbols, data for a picket with an intensity of 50% of the drive are shown as filled circles, and data for a picket with an intensity of 100% of the drive are shown as triangles. Lines indicate 2-D hydrodynamic simulations of the experiments with the dotted line for no picket, the solid line for a 50% picket, and the dashed line for a 100% picket.

laser illumination. The ablation surface is accelerated as a result of the pressure gradient, and the laser imprint is amplified by the RT instability. A picket pulse mitigates the pressure gradient and reduces the RT amplification of the laser nonuniformities and thus reduces the RT seed from imprinting for the target implosion.

Planar experiments were done to study imprint reduction with picket pulses for layered targets. The planar targets were

constructed with a 5- μm -thick, solid-density CH layer and a 90- μm -thick CH foam layer with a density of 0.18 g/cm³. This foil target acts as a surrogate for a section of a cryogenic spherical target. Intensity perturbations with wavelengths of 120, 90, 60, and 30 μm using specifically designed DPP's in a single beam were imposed on these planar foils. Figures 101.11 and 101.12 show the experimental optical-depth-modulation amplitude for these perturbations. Data in Figs. 101.11(a) and 101.11(b) show little reduction in the imprinting for long-

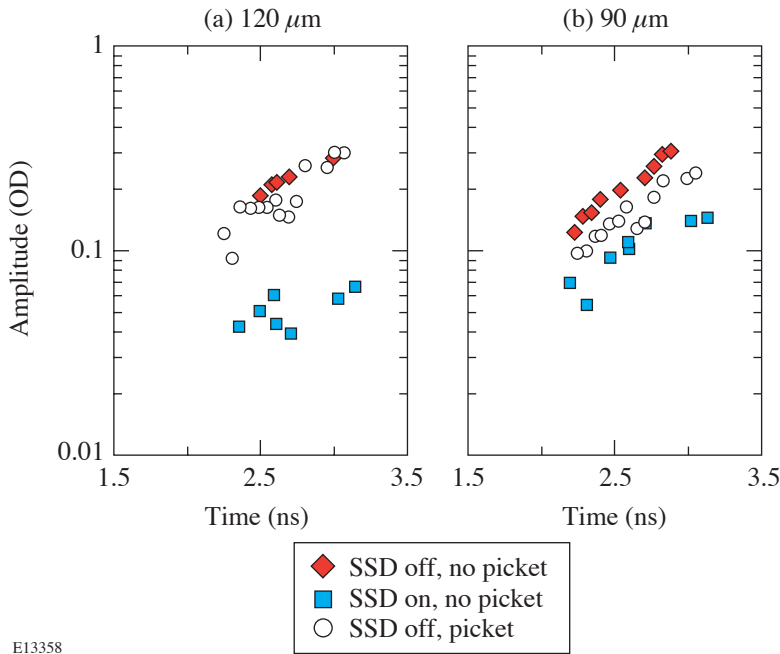


Figure 101.11
Imprinting data for 120- μm and 90- μm intensity perturbations. Data with SSD off and no picket are plotted as diamonds, data with SSD on and no picket as squares, and data with SSD off and with the picket as circles.

E13358

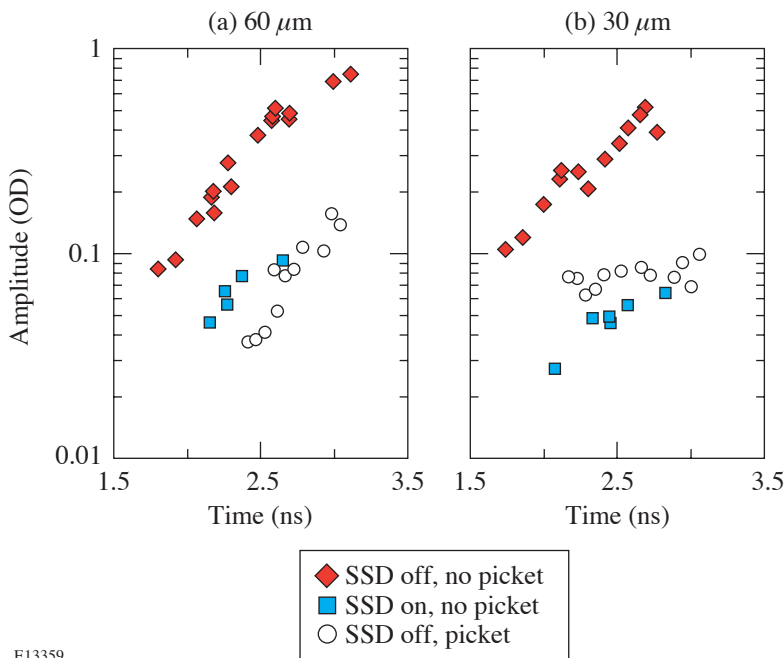


Figure 101.12
Imprinting data for 60- μm and 30- μm intensity perturbations. Data with SSD off and no picket are plotted as diamonds, data with SSD on and no picket as squares, and data with SSD off and with the picket as circles.

E13359

wavelength perturbations when the picket pulse was used. There is no difference at 120- μm -wavelength perturbations [Fig. 101.11(a)] with and without the picket. The data for a 90- μm -wavelength perturbation [Fig. 101.11(b)] with the picket pulse lie between the data without the picket and with SSD off and SSD on. The shorter-wavelength perturbations show a greater effect on optical-depth modulation for the picket pulse [Figs. 101.12(a) and 101.12(b)].

Modulation in optical-depth data shows that the amplitude of the imprint with the picket is the same as that when SSD is on and there is no picket pulse. The DPP's used to impose the intensity perturbations are refractive optics, so SSD will not affect the perturbation wavelength but will reduce the contrast and, thus, the perturbation amplitude. The picket is as effective as one-dimensional (1-D), 1.5- \AA SSD at reducing the imprint for 60- μm -wavelength [Fig. 101.12(a)] and 30- μm -wavelength [Fig. 101.12(b)] perturbations.

The temporal evolution of the optical-depth data shown in Figs. 101.11 and 101.12 shows that only the 30- μm -wavelength perturbation has its RT growth rate reduced. This is not unexpected. Previous planar growth experiments with picket pulses²⁰ have shown that the RT growth of long-wavelength perturbations ($\lambda \geq 60 \mu\text{m}$) is less affected by the picket pulse than the short-wavelength perturbations ($\lambda = 30$ and $20 \mu\text{m}$). This is a result of the k -dependence of the ablation-velocity stabilization term in the dispersion formula for the RT growth rate.

Spherical Experiments

The OMEGA²⁶ laser system imploded spherical targets with the pulse shapes shown in Fig. 101.13. Sixty beams of 351-nm radiation were incident onto the target. All beams had

polarization smoothing, 1-THz bandwidth, 2-D SSD, and DPP's with an intensity envelope given by a third-order super-Gaussian to minimize the illumination nonuniformities imposed by the laser. The targets used for these measurements are shown as the inset in Fig. 101.13. The shells were made of either 33- or 27- μm -thick polystyrene and filled with three gas-fill conditions: 15 atm of D_2 ; 3 atm of D_2 ; and a mixture of 12 atm of ^3He and 6 atm of D_2 . All targets had a 1000- \AA layer of aluminum as a gas-retention barrier. The laser pulse shapes were optimized for an outer diameter of 906 μm , and the targets had diameters that ranged from 901 to 923 μm .

Results from the fusion-product-yield measurements for three shots for each target and pulse shape are shown in Figs. 101.14(a) and 101.14(b). For the 15-atm- D_2 -filled, 33- μm -thick shell [Fig. 101.14(a)], there is a factor-of-3 increase in the number of D_2 neutrons from the target irradiated with a picket pulse than that from the target without a picket. The experiment was optimized for the 33- μm -thick shells; the improvement for the 27- μm -thick shells is only 50%. Both the 3-atm- D_2 -filled and the ^3He - D_2 -filled, 33- μm -thick shells show an improved fusion yield by a factor of 2. The ratio of the measured primary neutron yield to the neutron yield predicted by the hydrodynamics simulation [usually referred to as yield-over-clean (YOC)] is plotted in Fig. 101.14(b) and shows that the 15-atm- D_2 -filled, 33- μm -thick shells improve from 0.03 to 0.19. In all cases, the YOC can be seen to improve significantly. The results from high-adiabat implosions with 1-ns square drive pulses are also plotted in Figs. 101.14(a) and 101.14(b). The absolute fusion yield from the 1-ns square data is between yields measured without and with the picket pulse. A high-adiabat implosion will have a lower calculated yield, and therefore the YOC data for the 1-ns square implosions are higher than either the non-picket or picket YOC's.

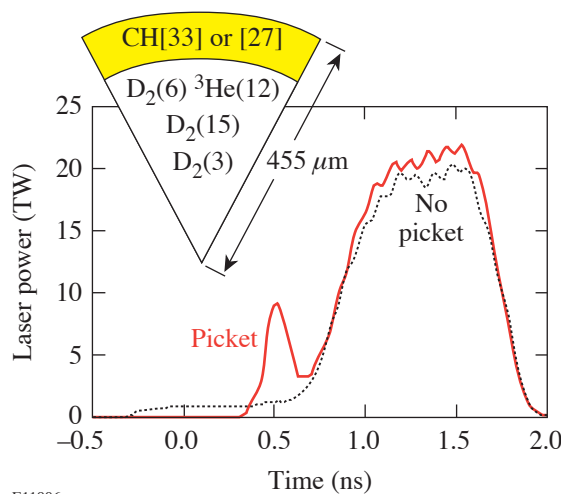
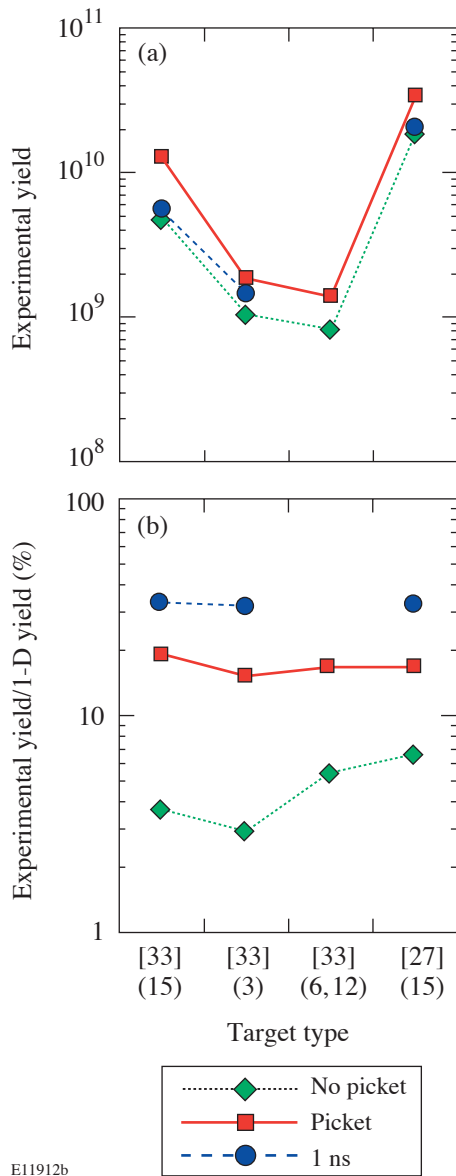


Figure 101.13 Pulse shapes used for decaying-shock-wave picket-pulse experiments. The picket drive is shown as a line and the no-picket drive as a dotted line. The targets used are shown as an inset.

E11906



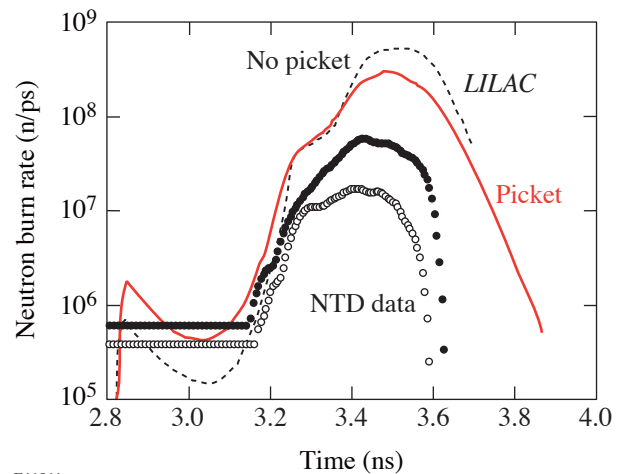
E11912b

Figure 101.14

Fusion-produced yield from the decaying-shock-wave picket implosions. The absolute yields are shown in (a) and the normalized yields in (b). The picket data are plotted as squares, non-picket data as diamonds, and 1-ns square pulse implosions as circles.

Neutron-production rates for the 15-atm- D_2 -filled, 33- μ m-thick shell, measured (symbols) and predicted (lines), are shown in Fig. 101.15. The solid curve and open circles are data from the implosion without a picket. The dashed curve and filled circle plots are from the matching implosion using a picket. The experimental data were measured with the “neutron temporal diagnostic” (NTD).²⁷ The temporal offsets needed

to compare experimental and simulation data were determined by maximizing the cross-correlation of the drive portion of the pulse as a function of a temporal shift relative to the laser pulse without a picket. This aligned the leading edges of the main drive pulse for all of the data. It is assumed that the neutron production is determined by the compression of the target by the drive pulse. Comparing the experimental data with predictions indicates that the implosions using a picket not only attain higher absolute yields than the implosions without a picket but also return, as was stated earlier, a larger fraction of the 1-D yield. This suggests more stable implosions with less mix due to RT growth. One-dimensional hydrodynamic simulations indicate that there is little if any adiabat shaping from the picket for these implosions. CH targets are affected by radiation transport that changes the shell adiabat, and this dominates the adiabat from the picket at the time of peak acceleration. Cryogenic D_2 targets will not be dominated by radiation and should show decaying shock-wave adiabat shaping.



E11911

Figure 101.15

NTD data from the decaying-shock-wave implosions. LILAC simulation results are plotted for the non-picket pulse (dashed line) and the picket pulse (solid line). Experimental data are plotted for the non-picket pulse (open circles) and the picket drive (dark circles).

The OMEGA laser system was also used to study the effect of relaxation picket target designs on imploding CH shells. A relaxation picket implosion uses a picket in front of a drive pulse that has a high foot intensity. The picket is separated from the drive pulse by a region of zero intensity during which time a rarefaction wave causes the shell to decompress. The non-picket drive is designed to implode the targets on the same adiabat ($\alpha \sim 2$) as that of the inner layer for the relaxation

picket. These pulse shapes are shown in Fig. 101.16. The picket pulse had a FWHM of ~60 ps. The targets shown schematically by the inset in Fig. 101.16 were designed for a total laser energy of 18 kJ. They are 870- μm -diam, 35- μm -thick CH shells filled with 15 atm of D_2 . A thin (1000- \AA) Al layer coated the outside of the targets and was the gas retention barrier.

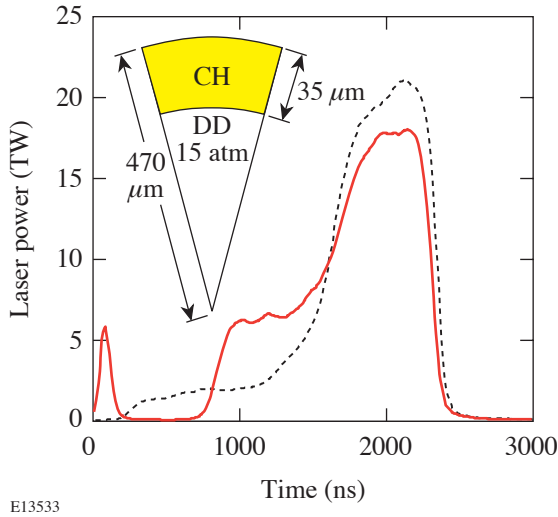


Figure 101.16 Pulse shapes used for relaxation-picket-pulse experiments. The picket drive is shown as the solid line and the non-picket drive as the dashed line. The targets used are shown as an inset.

The measured experimental yields increased when a relaxation (RX) picket pulse was used. The neutron yields shown in Table 101.I were taken for laser drives with and without SSD and with and without a picket pulse. With either SSD on or SSD off, the neutron yields are higher when a picket-pulse drive is used. The yield increases by a factor of 2.5 in the case of SSD off. The laser energy (17.3 ± 0.2 kJ) was very stable for these implosions, allowing for the direct comparison of measured yield data.

Table 101.I: Measured experimental yields increase when a relaxation picket is used.

	SSD Off	SSD On	Clean 1-D
	Yield ($\times 10^9$)	Yield ($\times 10^9$)	Yield ($\times 10^{10}$)
Picket	5.6 ± 0.2	6.8 ± 0.2	5.2 ± 0.5
No picket	2.2 ± 0.1	5.5 ± 0.5	4.0 ± 0.2

One-dimensional hydrodynamic simulations²⁸ were used to calculate the adiabat shape at the start of acceleration and at

peak acceleration shown in Fig. 101.17. LILAC simulations indicate that RX adiabat shaping in CH is effective throughout the acceleration phase. The adiabat without a picket pulse is illustrated as the “flat” case. At the start of the shell acceleration the adiabat is nearly constant at $\alpha = 2$ when no picket pulse is used. The RX drive has an adiabat of $\alpha = \sim 12$ at the ablation interface and an $\alpha = 2$ for the inner shell layer. The shape of the adiabat is still steeper for the RX drive at the time of peak acceleration, thus maintaining the effect of a high adiabat at the ablation interface while keeping a low ($\alpha = 2$) adiabat in the shell’s interior.

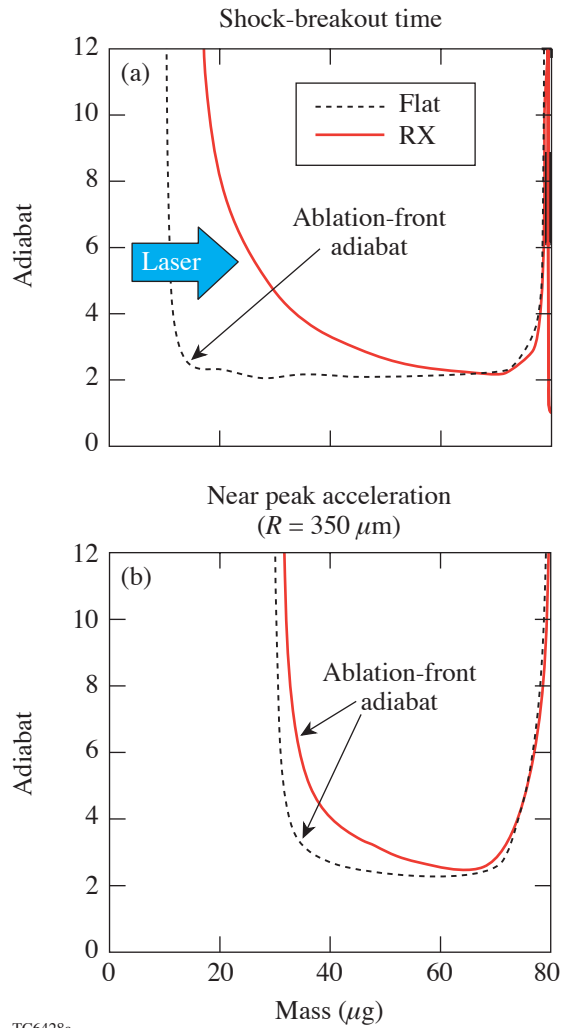


Figure 101.17 Shell adiabat shapes for the relaxation-picket-drive implosions. Shapes for the start of the acceleration are shown in (a) and those for near the peak acceleration are shown in (b). The non-picket drive is shown as a dashed line while the picket-drive profiles are shown as a solid line. The x axis is the Lagrangian mass coordinate.

Extension to Cryogenic Targets

The planar and spherical experimental data can be used to predict the expected performance of cryogenic target picket-pulse implosions. Greater shell stability is predicted for high-performance OMEGA cryogenic target designs with a picket pulse.¹⁸ The decaying-shock-wave picket pulse for a cryogenic target is shown in Fig. 101.18. An OMEGA cryogenic target is typically 860 μm in diameter with a 5-μm-or-less CH shell, with a 65-μm-or-greater DT-ice layer, and a DT-gas pressure determined by the target’s temperature. A schematic of this target is shown as the inset in Fig. 101.18. These target implosions are simulated with a drive pulse that has a peak intensity of 30 TW. A 20-TW picket is added for picket implosions. Table 101.II lists the 1-D simulation results. The simulations show that the picket does not compromise the core conditions but improves the shell’s integrity. The calculated ρR is 330 mg/cm² without the picket and 305 mg/cm² with the picket drive. Neutron yields are nearly identical at 6.5 × 10¹⁴ and 6 × 10¹⁴ without and with the picket, respectively. The shell’s stability or integrity is determined by the ratio of the bubble amplitude to the shell thickness. This ratio is greater than 100% for the non-picket implosion and only 55% for the picket implosion.

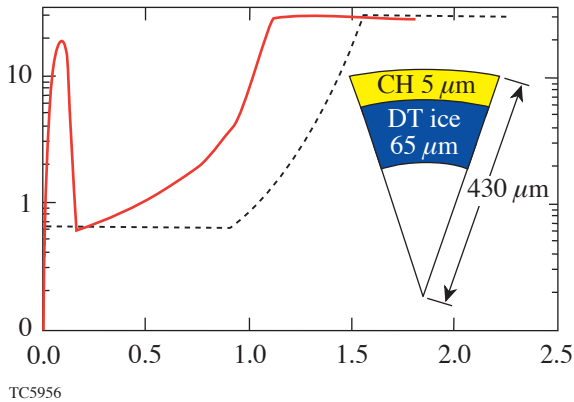


Figure 101.18 Pulse shapes used for cryogenic target simulations. The picket drive is shown as a solid line, and the non-picket drive as a dashed line. The targets used are shown as an inset.

Table 101.II: The decaying-shock-wave picket improves the stability of cryogenic target implosions.

	No Picket	Picket
ρR (mg/cm ²)	330	305
Y ($\times 10^{14}$)	6.5	6
A_{bubble}/Th (%) ¹	>100	55

Calculated adiabat and density profiles for both the decaying-shock-wave and relaxation-picket shapes are shown in Figs. 101.19(a) and 101.19(b). A decaying-shock-wave picket shapes the shell’s adiabat [Fig. 101.19(a)] for a cryogenic target at the start of acceleration. The average adiabat for the ablated mass and the inner mass can be calculated from the simulation output. The average ablated mass adiabat calculated for the adiabat shape at the start of acceleration is 8 and the average inner adiabat is 5. At the end of the acceleration phase the average shell adiabat is 5; therefore, the cryogenic target was imploded with a higher ablation interface adiabat than the interior shell adiabat. The relaxation picket shapes the adiabat of the shell at the onset of acceleration as shown in

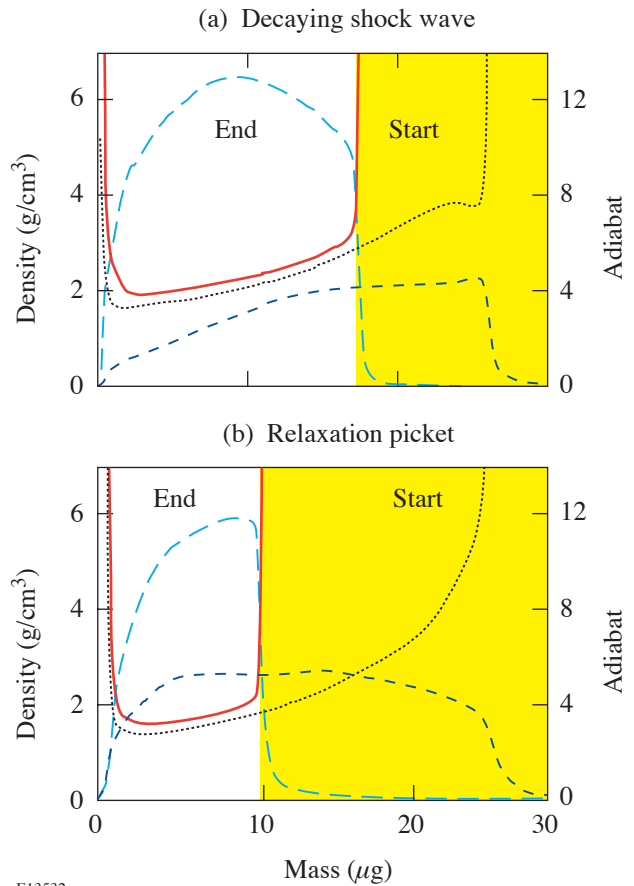


Figure 101.19 Shell adiabat and density shapes for the cryogenic target simulations. Shapes for the decaying-shock-wave picket at the start and end of shell acceleration are shown in (a) and those for the relaxation picket are shown in (b). The non-picket drive adiabat is shown as a solid line while the picket drive adiabat profiles are shown as a dotted line. The density profiles for the non-picket drive are shown as the long-dashed curves and density profiles for the picket drive are shown as the short-dashed curves. The shaded region represents the ablated mass.

Fig. 101.19(b). The RX drive simulations are also used to calculate the average adiabats for the ablated mass and the shell's interior. The shell's adiabat varies from $\alpha = 16$ at the ablation interface to $\alpha = 3$ in the shell's interior. The average adiabat for the ablated mass is 12 and for the inner shell is 3 at the start of shell acceleration. The average shell adiabat at the end of shell acceleration is 4. Both the decaying-shock-wave and the RX picket pulses shape the shell's adiabat for OMEGA cryogenic targets.

Conclusions

Picket pulses coupled to a low-adiabat drive pulse reduce both imprinting and perturbation growth. Adiabat shaping has the potential to improve target stability without significantly increasing the energy needed for compression and ignition. The ablation surface has a high adiabat to increase the ablation velocity and therefore reduce the RT growth. This is done while maintaining the inner portions of the shell on a low adiabat so that the energy needed to compress the core is minimized. The adiabat can be shaped either by launching a decaying shock wave that has a high pressure at the ablation surface and a low pressure at the inner shell surface or by using a picket pulse to produce a spatial density distribution so that a strong shock wave propagating from the ablation interface to the inner shell surface produces an adiabat that is high in the ablated material and low in the compressed material.

Planar experiments with picket pulses have reduced RT growth and imprinting, and spherical experiments with picket pulses show increased fusion yields when a picket pulse is used. With a picket-pulse intensity equal to 50% of the drive-pulse intensity, the RT growth was reduced for a 20- μm -wavelength surface perturbation and no significant RT growth was measured for a picket intensity equal to 100% of the drive pulse. Imprint experiments demonstrated that picket pulses were as effective as 1-D, 1.5- \AA SSD at the reduction of imprint for both 60- μm - and 30- μm -wavelength perturbations. Spherical target experiments were done with picket pulses that generate a decaying shock wave and a relaxed density profile. The yields of fusion products are improved both in terms of the absolute value and in terms of the comparison to 1-D hydrodynamic simulation output for the decaying-shock-wave picket, and the absolute yield increased with SSD on and SSD off when the relaxation picket was used.

One-dimensional and two-dimensional hydrodynamic simulations with cryogenic targets show that performance is expected to improve when either the decaying shock wave or the relaxation picket pulse is used. The shell's adiabat can be

shaped with either the decaying-shock-wave picket or the relaxation-picket-pulse shape. There is little difference between the core conditions with the flat-shell adiabat or the shaped-shell adiabat, but the ratio of the bubble amplitude to shell thickness is $\sim 55\%$ when the picket is added to the drive.

Results with warm CH targets and calculations with cryogenic targets indicate that picket pulses can be used for NIF direct-drive implosions. Either the decaying-shock-wave or the relaxation-picket-pulse shape can be used to improve the likelihood of achieving ignition.

ACKNOWLEDGMENT

This work was supported by the U.S. Department of Energy Office of Inertial Confinement Fusion under Cooperative Agreement No. DE-FC52-92SF19460, the University of Rochester, and the New York State Energy Research and Development Authority. The support of DOE does not constitute an endorsement by DOE of the views expressed in this article.

REFERENCES

1. J. Nuckolls *et al.*, *Nature* **239**, 139 (1972).
2. M. C. Herrmann, M. Tabak, and J. D. Lindl, *Nucl. Fusion* **41**, 99 (2001).
3. R. Betti, K. Anderson, V. N. Goncharov, R. L. McCrory, D. D. Meyerhofer, S. Skupsky, and R. P. J. Town, *Phys. Plasmas* **9**, 2277 (2002).
4. Lord Rayleigh, *Proc. London Math Soc.* **XIV**, 170 (1883).
5. G. Taylor, *Proc. R. Soc. London Ser. A* **201**, 192 (1950).
6. S. E. Bodner, *Phys. Rev. Lett.* **33**, 761 (1974).
7. J. D. Lindl, in *Inertial Confinement Fusion*, edited by A. Caruso and E. Sindoni (Editrice Compositori, Bologna, Italy, 1989), pp. 595–615.
8. H. Takabe *et al.*, *Phys. Fluids* **28**, 3676 (1985).
9. R. Betti, V. N. Goncharov, R. L. McCrory, P. Sorotokin, and C. P. Verdon, *Phys. Plasmas* **3**, 2122 (1996).
10. S. W. Haan, *Phys. Rev. A, Gen. Phys.* **39**, 5812 (1989).
11. T. J. Kessler, Y. Lin, J. J. Armstrong, and B. Velazquez, in *Laser Coherence Control: Technology and Applications*, edited by H. T. Powell and T. J. Kessler (SPIE, Bellingham, WA, 1993), Vol. 1870, pp. 95–104.
12. Y. Kato, unpublished notes from work at LLE, 1984.
13. T. R. Boehly, V. A. Smalyuk, D. D. Meyerhofer, J. P. Knauer, D. K. Bradley, R. S. Craxton, M. J. Guardalben, S. Skupsky, and T. J. Kessler, *J. Appl. Phys.* **85**, 3444 (1999).
14. S. Skupsky, R. W. Short, T. Kessler, R. S. Craxton, S. Letzring, and J. M. Soures, *J. Appl. Phys.* **66**, 3456 (1989).

15. R. H. Lehmburg and S. P. Obenschain, *Opt. Commun.* **46**, 27 (1983).
16. J. D. Lindl, *Inertial Confinement Fusion: The Quest for Ignition and Energy Gain Using Indirect Drive* (Springer-Verlag, New York, 1998), Chap. 5, p. 54.
17. J. H. Gardner, S. E. Bodner, and J. P. Dahlburg, *Phys. Fluids B* **3**, 1070 (1991).
18. V. N. Goncharov, J. P. Knauer, P. W. McKenty, P. B. Radha, T. C. Sangster, S. Skupsky, R. Betti, R. L. McCrory, and D. D. Meyerhofer, *Phys. Plasmas* **10**, 1906 (2003).
19. K. Anderson and R. Betti, *Phys. Plasmas* **10**, 4448 (2003).
20. K. Anderson and R. Betti, *Phys. Plasmas* **11**, 5 (2004).
21. J. D. Lindl and W. C. Mead, *Phys. Rev. Lett.* **34**, 1273 (1975).
22. M. Tabak, Lawrence Livermore National Laboratory, private communication (1987); R. P. J. Town and L. J. Perkins, Lawrence Livermore National Laboratory, private communication (2003).
23. T. J. B. Collins, J. P. Knauer, R. Betti, T. R. Boehly, J. A. Delettrez, V. N. Goncharov, D. D. Meyerhofer, P. W. McKenty, S. Skupsky, and R. P. J. Town, *Phys. Plasmas* **11**, 1569 (2004).
24. J. P. Knauer, R. Betti, D. K. Bradley, T. R. Boehly, T. J. B. Collins, V. N. Goncharov, P. W. McKenty, D. D. Meyerhofer, V. A. Smalyuk, C. P. Verdon, S. G. Glendinning, D. H. Kalantar, and R. G. Watt, *Phys. Plasmas* **7**, 338 (2000).
25. T. J. B. Collins and S. Skupsky, *Phys. Plasmas* **9**, 275 (2002).
26. T. R. Boehly, D. L. Brown, R. S. Craxton, R. L. Keck, J. P. Knauer, J. H. Kelly, T. J. Kessler, S. A. Kumpan, S. J. Loucks, S. A. Letzring, F. J. Marshall, R. L. McCrory, S. F. B. Morse, W. Seka, J. M. Soures, and C. P. Verdon, *Opt. Commun.* **133**, 495 (1997).
27. R. A. Lerche, D. W. Phillion, and G. L. Tietbohl, in *Ultra-high- and High-Speed Photography, Videography, and Photonics '93*, edited by P. W. Roehrenbeck (SPIE, Bellingham, WA, 1993), Vol. 2002, pp. 153–161.
28. M. C. Richardson, P. W. McKenty, F. J. Marshall, C. P. Verdon, J. M. Soures, R. L. McCrory, O. Barnouin, R. S. Craxton, J. Delettrez, R. L. Hutchison, P. A. Jaanimagi, R. Keck, T. Kessler, H. Kim, S. A. Letzring, D. M. Roback, W. Seka, S. Skupsky, B. Yaakobi, S. M. Lane, and S. Prussin, in *Laser Interaction and Related Plasma Phenomena*, edited by H. Hora and G. H. Miley (Plenum Publishing, New York, 1986), Vol. 7, pp. 421–448.

High-Spatial-Resolution Studies of UV-Laser-Damage Morphology in SiO₂ Thin Films with Artificial Defects

Introduction

The importance of conducting a quantitative, high-spatial-resolution investigation of thin-film-damage morphology is twofold. First, comparison of spatial frequencies of the damaged site with the surrounding unmodified material may indicate the presence of particular processes in the damage event. For instance, a smooth surface that is missing granular film structure usually points to melting of thin-film material. Second, experimental data on geometry (lateral size, depth, cross-sectional profiles, volume) of the modified material provide vital information for theoretical-model validation.

High-resolution studies of laser damage in thin films have generated a significant amount of information regarding morphological changes in coating materials under different conditions (wavelength and pulse length, fluence, spot size) of irradiation. The application of high-resolution methods established that nanosecond-pulse-driven damage in thin-film coatings is linked to localized absorbing defects. For lasers operating in the UV spectral range, even a few nanometer-sized defects can initiate thin-film damage in the form of craters.¹

Despite this fact, very few systematic studies link thin-film-defect parameters and local laser fluence to micron- and nanometer-scale modification of thin-film material. The most important reason for that is that size and density of defects in laser-quality coatings are extremely small,¹ thus precluding any characterization. An investigation of the role of nodular defects in multilayer 1.06- μm laser damage^{2,3} serves as one example of such studies. To assuage this challenge, SiO₂ thin films with embedded gold nanoparticles serving as artificial absorbing defects have been explored⁴⁻¹³ and have proven to be a very useful model system for unraveling damage mechanisms.

Previous experiments with this system subjected to UV, nanosecond pulses showed that during the laser pulse, absorption is not confined to the absorbing defect.⁷ Upon defect-temperature rise, modification of the surrounding matrix takes place followed by effective growth of the absorbing volume.

According to theoretical predictions by M. Feit *et al.*,^{14,15} this growth saturates when reaching a scale of the order of the excitation wavelength λ . The same theory establishes scaling relations between damage-crater diameter and particle-lodging depth at fixed laser-fluence conditions.

A detailed theoretical description of the laser-pulse-energy deposition followed by crater formation remains a challenge even for this well-characterized model system. The initial stages, including kinetics of absorption and heating in the gold particle and energy transfer processes at the particle-matrix interface, were studied by P. Grua *et al.*^{16,17} It was shown that thermionic electron emission from gold inclusion is an important mechanism of energy transfer to the surrounding matrix.

Promising results have been obtained with the one-dimensional (1-D) hydrodynamic code DELPOR (F. Bonneau *et al.*¹⁸), including electromagnetic effects, thermal conduction, radiative transfer, ionization by thermal UV radiation, and propagation of shock waves. From this code, combined with the two-dimensional (2-D) hydrodynamic code HESIONE,¹⁹ which calculates mechanical effects using brittle-fracture models, a crater-formation picture emerges for relatively large, 600-nm particles in qualitative agreement with experiment.^{8,9} Remaining difficulties here are related to the paucity of accurate data on electrical, thermal, optical, and mechanical properties of materials in the solid, liquid, vapor, and plasma states in the temperature range from ambient to $\sim 10^4$ K.

In this work, we used 18.5-nm gold nanoparticles as artificial defects embedded in a SiO₂ thin film at several well-defined distances from the film surface. Atomic force microscopy (AFM) is used to investigate the damage morphology produced by 351-nm, 0.5-ns laser pulses and dominated by submicrometer-scale craters. Variation in crater diameter, depth, and shape with laser fluence and particle-lodging depth is systematically studied and compared with phenomenological-theory^{14,15} predictions. The contributions of two major mechanisms of damage crater formation—melting/evaporation and fracture/ejection—are evaluated.

Experimental

A SiO₂ thin-film sample containing gold nanoparticles is prepared in three steps: Initially, a 240-nm SiO₂ thin film is deposited by *e*-beam evaporation onto a cleaved fused-silica (Corning 7980, 14 × 6 × 5 mm) substrate. Next, gold nanoparticles of average diameter $d = 18.5$ nm (standard deviation = 0.9 nm; data from Ted Pella, Inc.) in the form of a gold colloid are diluted in isopropanol and deposited by a micropipette onto the SiO₂-coated surface. Finally, the sample is returned to the coating chamber and coated with an additional layer of SiO₂. Five samples are prepared as described above, all coated in the same deposition run, each with a different capping-layer thickness: 30 nm, 60 nm, 110 nm, 190 nm, and 240 nm. A more detailed description of the sample preparation can be found in Ref. 7.

An Nd-doped glass laser (frequency-tripled, 351-nm, 0.5-ns pulses; 400- μ m spot size) is used for sample irradiation. Laser-beam incidence on the entrance surface was slightly off-normal ($\sim 7^\circ$) in order to prevent influence of the back-reflection ($\sim 4\%$) from the sample exit surface. No damage is observed within the bulk or at the rear surface of the cleaved fused-silica substrate at the entrance-surface fluence < 8.1 J/cm². Laser-fluence profiles are obtained from images captured by a low-noise (few electrons/pixel/s at a temperature of -40°C), high-dynamic-range, charge-coupled-device (CCD) imaging camera (Spectral Instruments, Inc.) in a sample equivalent plane. Correlation between laser-spot intensity and areal density and average size of damage craters allows attributing the peak fluence to the damage center (see Fig. 101.20). Once it is

done, laser fluence versus sample-coordinate dependence can be easily established and damage crater geometry versus fluence behavior investigated. The particular laser fluence at which the crater diameter approaches zero value is defined as the nanoscale damage threshold.

The damage morphology investigation is conducted by means of atomic force microscopy (AFM) (NanoscopeIII, Digital Inst./Veeco) operated in tapping mode. High-aspect-ratio (better than 5:1) silicon probes are used to ensure convolution-free imaging of craters with steep wall angles approaching 80° with the horizon.

Results and Discussion

1. Damage Morphology

Submicrometer-sized craters, formed exclusively at nanoparticle locations,⁷ are the main damage-morphology features. In the case of shallow particle-lodging depths (30 nm and 60 nm) and close to the crater-formation threshold, the craters are very small, with a typical lateral size of 35 to 50 nm, and randomly shaped (see Fig. 101.21). The absence of a rim elevated above the average surface level and the random shape point to a material-removal mechanism without significant melting. The portion of the film above the particle is probably ejected under pressure created in the process of particle heating. This picture holds in the fairly narrow fluence range of 0.5 to 0.8 J/cm² for a 60-nm lodging depth, and in the range of 0.6 to 4 J/cm² for a 30-nm lodging depth [detailed in the **Crater Geometry Versus Laser-Fluence Behavior** section (p. 28)]. Beyond this initial fluence range, a crater takes a

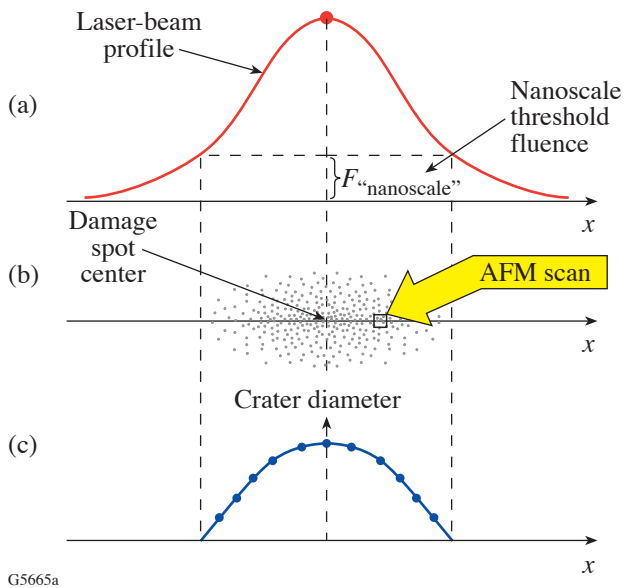


Figure 101.20

Experimental scheme of nanoscale damage threshold and crater diameter versus laser-fluence determination. (a) Laser-spot x -intensity profile; (b) damage crater areal distribution; (c) crater diameter versus x coordinate position. The nanoscale threshold value is defined as the laser fluence at which the crater diameter is approaching zero value.

conventional symmetric shape with an elevated rim, indicative of melting and resolidification (Fig. 101.22). The smooth internal surface of these craters, shown in Fig. 101.23, is missing the granular texture of the surrounding film, which is characteristic of melting and explosive vaporization. Later, this type of crater will be referred to as a *regular* crater. It is also

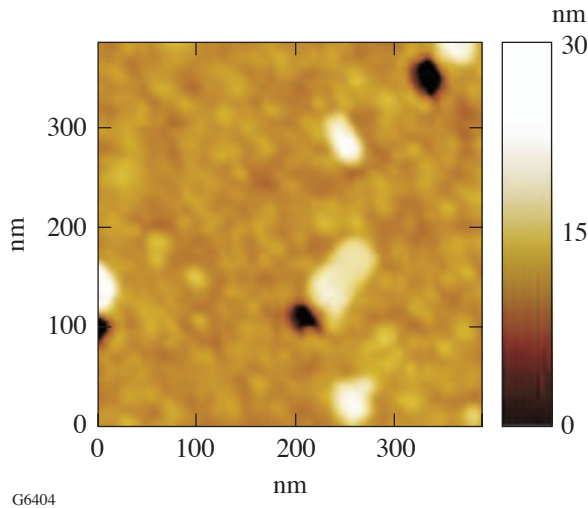


Figure 101.21
Craters originated by particles with 30-nm lodging depth at close-to-threshold conditions, $0.4\text{-}\mu\text{m} \times 0.4\text{-}\mu\text{m}$ AFM image.

useful to note here that under the term vaporization, we consider all processes transforming material from the liquid phase into the vapor phase, including fragmentation (nanocluster formation).

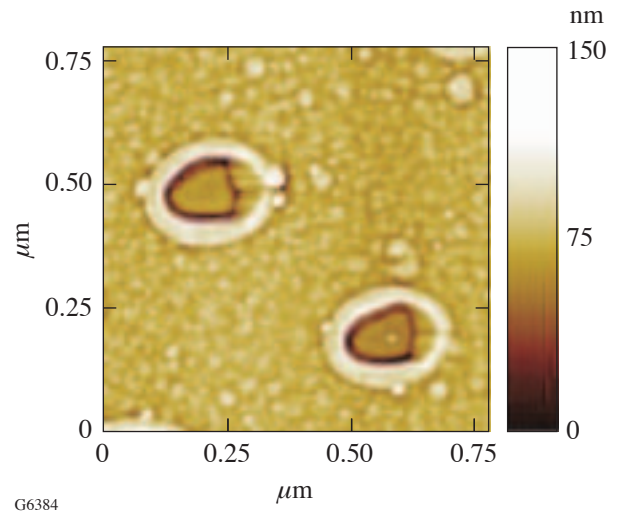


Figure 101.23
Internal walls of craters originated by particles with 60-nm lodging depth at fluences $F > 1 \text{ J/cm}^2$ are missing granular structure of the surrounding film, indicative of melting and vaporization. Contrast enhancement function is applied in order to amplify high spatial frequencies, $0.8\text{-}\mu\text{m} \times 0.8\text{-}\mu\text{m}$ AFM image.

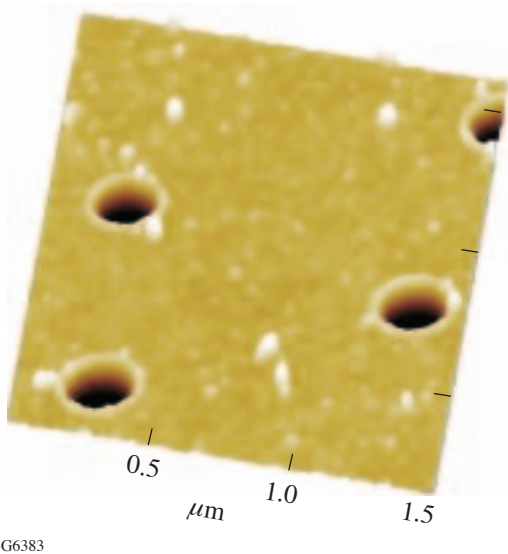


Figure 101.22
Typical craters originated by particles with 60-nm lodging depth at fluence $F = 6.2 \text{ J/cm}^2$, $1.5\text{-}\mu\text{m} \times 1.5\text{-}\mu\text{m}$ AFM scan.

Damage-crater morphology caused by particles at 190-nm and 240-nm lodging depths is very different. From this point this type of crater will be referred to as a *complex* crater. The lateral shape of these craters (depicted in Fig. 101.24) is asymmetric, most often with partial circularity and sharp corners — all pointing to hoop-stress-driven material removal. On the other hand, their internal surfaces are smooth (Fig. 101.25), indicative of the melting point having been reached. A cross-sectional profile of a typical complex crater is also depicted in Fig. 101.25. It clearly shows two parts: a narrow “channel” with vertical walls at the bottom and a wide upper part with inverse aspect ratio. Absence of the rim around the crater indicates that energy deposited in the upper part of the crater was insufficient to cause molten material flow at the outer crater boundary.

One possible scenario for the formation of this type of crater is as follows: Initially, absorption inside and around the particle causes melting and superheating of the material within the channel volume. This process is accompanied by rapid internal-pressure buildup and shock-wave generation. When the

generated hoop stress exceeds the strength of the silica material (fracture toughness $\sim 0.75 \text{ Mpa} \cdot \text{m}^{1/2}$ for bulk fused silica), fracture along the boundaries of the upper part of the crater takes place, followed by ejection of both the fractured portion and the molten material from within the channel.

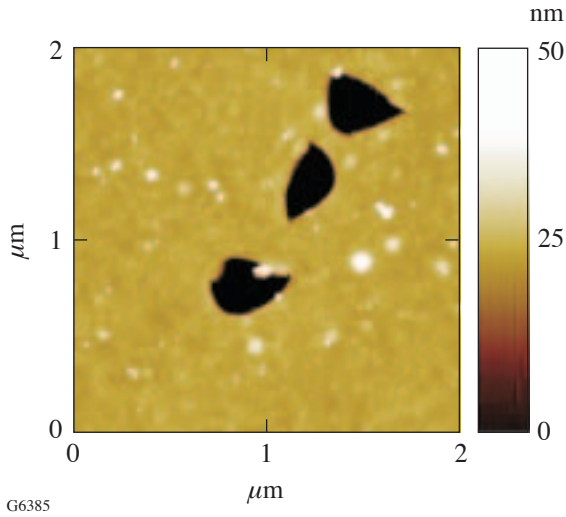


Figure 101.24
Craters originated by particles with 190-nm lodging depth. Random, partially circular shapes pointing to hoop-stress-driven material removal of the top film layer, 2- $\mu\text{m} \times 2\text{-}\mu\text{m}$ AFM scan.

Formation of such a complex crater was also reported in Refs. 9 and 10, where much larger gold particles of 600 nm were embedded in a SiO₂ film matrix. In the case of 110-nm lodging depth, both types of crater geometries characteristic for shallow and deep particle locations are present (Fig. 101.26).

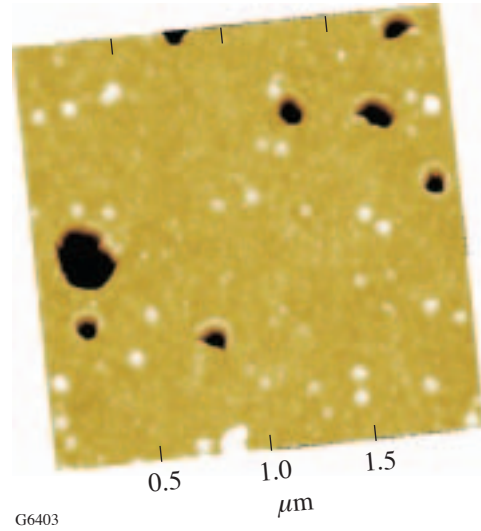


Figure 101.26
Craters formed from intermediate, 110-nm-deep particle location. Both types of craters, regular and complex, are generated simultaneously, 2- $\mu\text{m} \times 2\text{-}\mu\text{m}$ AFM scan.

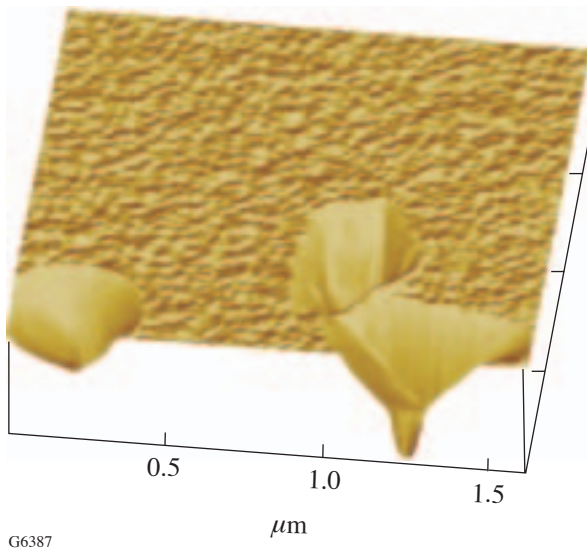


Figure 101.25
Smooth internal walls of complex craters point to the melting point having been reached. Cross-sectional crater profile reveals presence of two parts, a narrow channel on the bottom and a wide upper part removed by fracture.

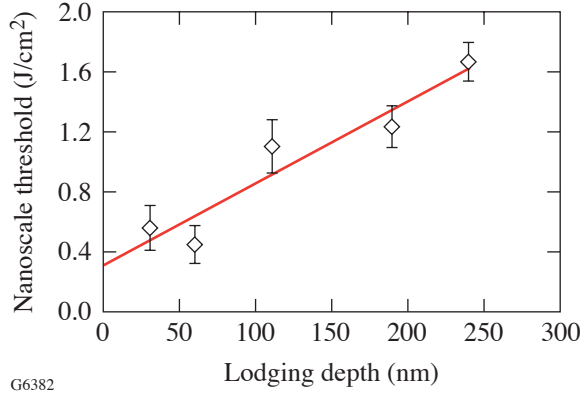
2. Nanoscale Damage Thresholds

The definition of damage threshold has always been linked to the method of detecting material modification. Consequently, type and sensitivity of the damage-detection equipment have a major impact on measured threshold values. The most commonly used optical methods are adequate for practical evaluation of optical-component survival in high-power laser systems or for studying particular trends, like pulse-length dependencies. Still, these methods are very difficult to use for meaningful comparison with the theories describing the dynamics of the damage process.

AFM investigation of crater size versus laser-fluence dependencies allows one to find the crater-formation threshold (nanoscale threshold) as that fluence at which the crater diameter approaches zero. It corresponds to a maximum fluence causing only limited localized melting without material removal. This definition is in much better agreement with theories that consider matrix melting as the onset of damage.

The results of nanoscale-threshold measurement summarized in Table 101.III and in Fig. 101.27 show a threshold

increase with increasing particle-lodging depth. An explanation comes from the fact that at near-threshold conditions, deeper particles consistently produce deeper and larger craters [see the **Crater Geometry Versus Laser-Fluence Behavior** section (p. 28)]. Consequently, larger material removal requires more energy to be absorbed for a crater to form.



G6382

Figure 101.27
Nanoscale damage thresholds as a function of particle-lodging depth.

Table 101.III: Nanoscale damage thresholds.

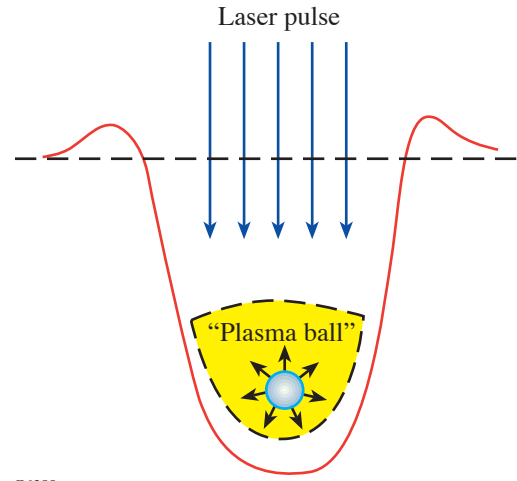
Particle Lodging Depth		Nanoscale Threshold (J/cm ²)
<i>h</i> ₀ ,nm	<i>h</i> ₀ / <i>d</i>	
30	1.6	0.56±0.15
60	3.2	0.45±0.10
110	5.9	1.11±0.21
190	10.3	1.24±0.16
240	13.0	1.67±0.14

3. Theoretical Approach to Crater Formation

As was mentioned above, numerical calculations of damage-crater-formation kinetics and final geometries are very challenging. In this work, we compare experimental results on crater lateral size behavior as a function of fluence and absorbing defect lodging depth with phenomenological-theory^{14,15} predictions.

The main assumptions and results of this theory can be formulated as follows: If the temperature around an absorbing defect exceeds a critical value, a thermal explosion²⁰ takes

place. In this process, the defect-surrounding matrix becomes absorptive and undergoes rapid heating and ionization with plasma density exceeding critical. This process is depicted schematically in Fig. 101.28.



G6389

Figure 101.28
Schematic of the plasma-ball formation around an absorbing defect.

Considering that the major part of the absorbed energy goes into ionization of the material, the ionized volume (plasma “fire ball”) radius *a* grows exponentially with laser fluence *F*:

$$a = a_0 \exp \gamma, \quad (1)$$

where the growth factor γ scales linearly with *F*.

At high laser fluences, growth of the plasma ball tends to saturate, and its diameter reaches a maximum value of the order of the absorbed-light wavelength λ . In this case absorbed energy can be estimated as

$$E = F\pi\lambda^2. \quad (2)$$

The radius *R* of a produced crater is determined by *E*, the energy deposited in the plasma-ball volume, and *h*, the lodging depth of the initiating absorber.

At fixed energy *E*, the crater radius as a function of lodging depth *h* is given by the expression

$$R^2 = h^{2/3} (h_d^{4/3} - h^{4/3}), \quad (3)$$

where h_d is the maximum lodging depth at which a crater is still formed. For this depth, energy E is the threshold energy for crater formation and corresponds to the *nanoscale damage threshold*.

The maximum crater radius R_m and corresponding lodging depth h_m are given by

$$R_m = \sqrt{2}h_m \approx 0.6h_d \text{ and } h_m \approx 0.44h_d. \quad (4)$$

At high laser fluences, when the growth of the plasma ball saturates, crater radius growth with fluence can be approximated by 1/3 power law:

$$R \sim F^{1/3}. \quad (5)$$

4. Crater Geometry Versus Laser-Fluence Behavior

a. Crater-diameter variation with fluence. Geometrical parameters measured for the two types of crater morphology are schematically presented in Fig. 101.29. Henceforth, a cross-sectional profile similar to Fig. 101.29(a) will be referred to as a regular crater, and one similar to Fig. 101.29(b) as a complex crater.

Crater diameter D is measured by means of the cross-sectional analysis of AFM images as crater opening at average surface level (see Fig. 101.29). In the case of asymmetric craters, diameter values are taken as an average of measurements taken in two orthogonal directions crossing the center of gravity of the crater opening area. Each data point in the $D(F)$

graph is obtained as an average for all craters (2 to 10) imaged within a particular AFM scan ($2 \mu\text{m} \times 2 \mu\text{m}$ or $3 \mu\text{m} \times 3 \mu\text{m}$) and correlated with one fluence value.

This averaging allows variations to be smoothed out in the crater geometry for individual particle locations caused by the inhomogeneous thin-film environment. As shown earlier (see Ref. 7), variations in the particle/thin-film interface geometry strongly affect both absorption by the particle and energy transfer to the surrounding-film matrix. This effect is more pronounced at close-to-threshold conditions, when only particles with the best contact with the matrix are producing craters. At laser fluences many times exceeding threshold, the probability of crater formation is approaching 100% and, for regular craters, variation in crater size is significantly reduced.

Crater diameter versus fluence dependence for shallow lodging depths—30 nm and 60 nm—is presented in Fig. 101.30. In the case of the 60-nm lodging depth, it can be well approximated by a linear fit. More complex behavior is observed in the 30-nm case where, after a threshold jump, stagnation of diameter growth is measured in the fluence range of 0.6 to 4 J/cm². At higher fluences, almost exponential growth sets in, and at $F > 7 \text{ J/cm}^2$, 30-nm and 60-nm curves tend to merge together.

An explanation for this behavior in the case of 30-nm lodging depth may be found in the coating geometry (see Fig. 101.31). The coating above the particle is growing like a nodule and forms a spherical bump with lateral size L for which AFM measurement (unirradiated site) gave an average value of 47 nm. This value fits well within crater diameter sizes of 35 to 50 nm measured in the fluence range of 0.6 to 4 J/cm². Together with the typical crater depth of ~30 nm this points to material removal within one nodular volume, indicated by the dashed line in Fig. 101.31. Shallow particle location and gold-silica thermal mismatch imply reduced strength of the coating within the nodular volume described above and lend support for the following explanation: Upon energy absorption from the laser pulse and particle heating, pressure applied to the portion of the coating above the particle may suffice for its ejection without melting of the surrounding matrix. With an increase in laser fluence, increased pressure leads to even faster ejection and, possibly, additional heating of the removed material, but still without reaching a critical temperature at the particle/matrix interface. Eventually, at a high-enough fluence ($>4 \text{ J/cm}^2$), coupling to the surrounding matrix takes place before material ejection, leading to dramatic growth in crater size. In the case of 60-nm lodging, a similar

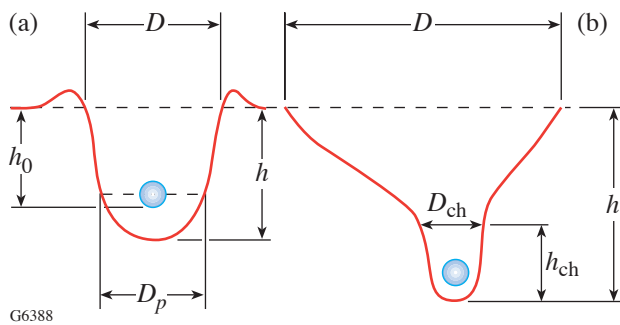
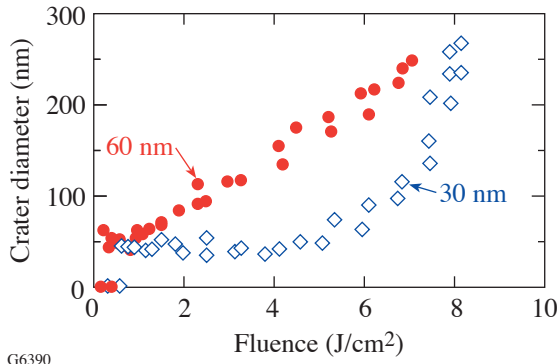


Figure 101.29

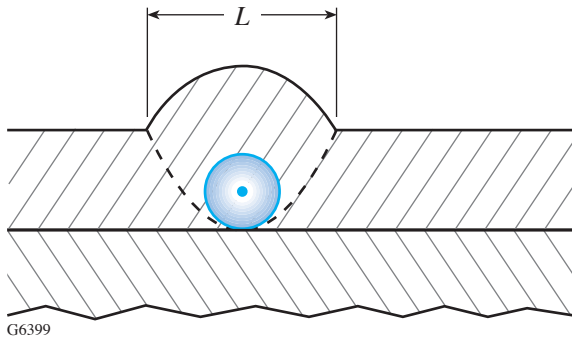
Cross-sectional profiles (not to scale) of (a) a regular crater and (b) a complex crater. Crater parameters measured by AFM: crater diameter D , crater depth h , crater channel diameter D_{ch} , channel depth h_{ch} , and crater width at particle-center position D_p .

stagnation range exists, though over a very narrow fluence range of 0.5 to 0.8 J/cm^2 . As one can notice, crater-diameter growth with fluence in the cases of 30-nm and 60-nm lodging (see Fig. 101.30) is much faster than $F^{1/3}$. This indicates that the plasma-ball saturation regime [see the **Theoretical Approach to Crater Formation** section (p. 27)] is not reached at fluences $< 8.1 \text{ J}/\text{cm}^2$.



G6390

Figure 101.30
Crater diameter versus fluence dependence for shallow particle-lodging depths, 30 nm and 60 nm.

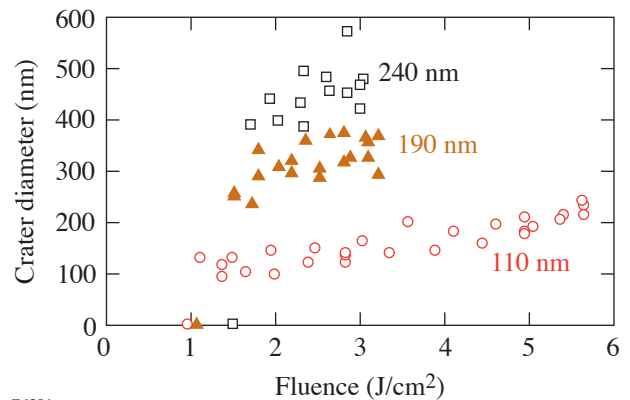


G6399

Figure 101.31
Thin-film geometry in case of 30-nm particle-lodging depth.

Crater diameter versus fluence dependence for 110-nm, 190-nm, and 240-nm lodging depths is depicted in Fig. 101.32, showing several features different from the case of shallow-lodging depth. The most notable difference is size. For instance, *at near-threshold conditions*, craters start with ~ 390 -nm diameter for 240-nm lodging compared to ~ 35 -nm diameter for 30-nm lodging. The reason goes beyond the trivial fact that at fluences just above threshold, deeper absorbers produce larger craters. More importantly, *different crater-formation*

processes come into play with increasing lodging depth. Regular craters [Fig. 101.29(a)] originate from shallow locations and are formed through the processes of melting and vaporization. Complex craters [Fig. 101.29(b)] originate from deep locations and, in addition to melting and vaporization of the material in the channel volume, have a significant amount of the top part of the material removed through a *fracture mechanism*. The process of material removal through fracture is much more favorable energetically than volumetric vaporization. In the former case, energy goes to molecular bond breaking in molecules associated only with a new surface compared to breaking bonds in the whole removed volume in the latter case. Even in the case when material removal proceeds through fragmentation (nanocluster formation), this picture holds.



G6391

Figure 101.32
Crater diameter versus fluence dependence for 110-nm, 190-nm, and 240-nm lodging depths.

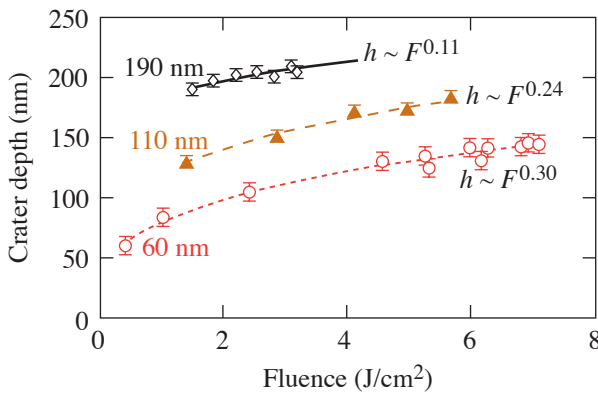
The growth of the crater diameter with fluence shows a lower growth rate for deep lodging depths, especially 190-nm and 240-nm lodgings. It can be understood considering the change in volume removed for each increment in crater diameter. At equal laser fluences, the same partial increment in the diameter will result in much larger volume removal for a large crater than for a small one. Consequently, it results in a larger fluence increment required for diameter increase and slower growth rate with fluence for larger craters.

The other feature in the $D(F)$ dependence for craters originating from deep (190-nm and 240-nm) particle locations (see Fig. 101.32) is a large variation in diameter. As was discussed earlier [see the **Damage Morphology** section (p. 24)], these craters are formed in a process involving fracture and ejection of the top portion of the coating. Due to the inhomogeneity of

the thin-film material, variation in local material strength and stress factors can significantly affect size and shape of the fracture-removed portion of the complex crater.

b. Crater-depth variation with fluence. Crater depth versus fluence behavior for 60-nm, 110-nm, and 190-nm lodging depths is presented in Fig. 101.33. At laser fluences slightly above threshold, crater-depth values are very close to the particle-lodging-depth values and deeper absorbers produce not only wider [see the **Crater-Diameter Variation with Fluence** section (p.28)] but also deeper craters. With fluence increase, however, the rate of depth growth with fluence is reduced with increasing lodging depth, which is clearly seen from power-law approximation of the $h(F)$ curves in Fig. 101.33. The explanation here is similar to the case of the $D(F)$ dependencies. Since crater volume is roughly proportional to h^3 , deep craters require a larger fluence increment to achieve the same partial depth increment compared to shallow craters.

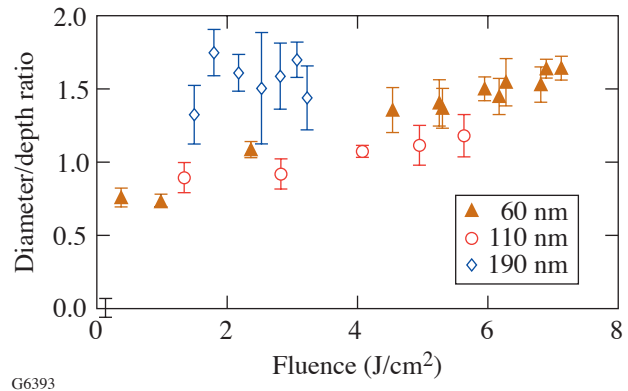
In the case of deep lodging depth (190 nm), the $h(F)$ dependence is much more deterministic than the $D(F)$ dependence, which is probably associated with the mechanism of complex-crater channel formation. The channel morphology suggests a channel-formation process very similar to the regular-crater formation involving phases of plasma-ball growth, melting, and vaporization. Comparison of channel geometry with regular crater geometry [see the **Features of Complex-Crater Channel Formation** section (p. 31)] lends strong support to this hypothesis.



G6392
Figure 101.33
Crater depth versus fluence dependence for 60-nm, 110-nm, and 190-nm lodging depths.

c. Transformation of crater aspect ratio with fluence. One of the important features of crater growth with laser fluence is the modification in aspect ratio. Changes in aspect ratio are linked to the kinetics of energy deposition and dissipation processes.

Figure 101.34 depicts crater diameter/depth ratio versus fluence for 60-nm, 110-nm, and 190-nm lodging depths. In the case of 60-nm and 110-nm lodging depths, there is clear evidence that the crater diameter grows faster than the depth, indicating that crater growth preferentially happens in the lateral dimension. For 190-nm lodging depth, large scatter in data points and a relatively narrow fluence range prevent a definitive conclusion. This trend is highlighted further by Fig. 101.35, which shows cross-sectional AFM profiles for three craters generated from the 60-nm lodging depth at three different fluences: 1 J/cm², 2.4 J/cm², and 6 J/cm². Comparison of diameter ratios to depth ratios underscores the dominance of the lateral scale in crater growth: $D_3/D_1 = 3.5$ and $h_3/h_1 = 1.7$.



G6393
Figure 101.34
Crater-diameter to crater-depth ratio as a function of fluence for 60-nm, 110-nm, and 190-nm lodging depths.

An interesting observation is that the D/h aspect ratio grows faster for more-shallow 60-nm lodging compared to 110-nm lodging. A probable explanation may be linked to the fact that instantaneous temperature distribution in the material depends on the absorber lodging depth. For a shallow initiation point, the proximity of the adiabatic boundary (silica/air interface) means that heat propagating from the absorbing volume (plasma ball) will be caught at the boundary and eventually spread laterally. Since plasma-ball growth preferentially proceeds toward the adiabatic boundary due to irradiation geometry and screening effect (see Fig. 101.28), fluence

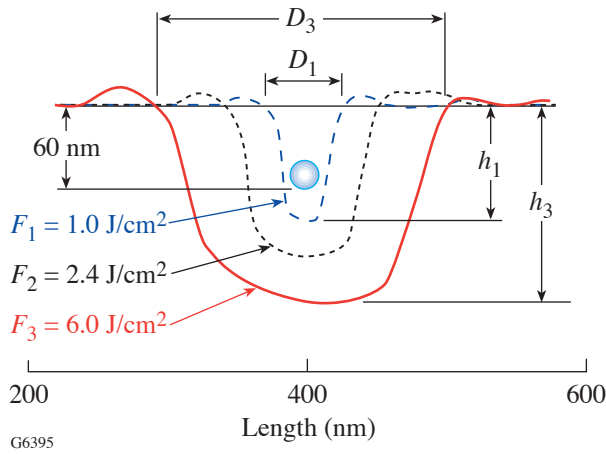


Figure 101.35
AFM-measured cross-sectional profiles for craters originated by particles with 60-nm lodging depth at fluences of 1.0 J/cm², 2.4 J/cm², and 6.0 J/cm². Crater growth with fluence is dominated by lateral scale.

increase should enhance lateral heat redistribution. For deep absorbers this effect may be less pronounced due to a more symmetric heat dissipation.

d. Features of complex-crater channel formation. To understand the mechanism of complex-crater formation, both channel diameter D_{ch} and depth h_{ch} [Fig. 101.29(b)] are measured as functions of fluence for 190-nm lodging. The results are plotted in Fig. 101.36 together with diameter and depth data (Figs. 101.30 and 101.33) for regular craters initiated by absorbers with 60-nm lodging. The striking agreement is seen for both diameter [Fig. 101.36(a)] and depth [Fig. 101.36(b)] values: channel data overlap well with regular-crater curves. This result lends support to a channel-formation mechanism through similar processes of melting and vaporization as in regular-crater formation. It also indicates that a *major part of the energy deposition in a complex crater takes place in the channel volume and goes into channel formation*. This immediately brings up a question about mechanism of the fracture generation leading to the removal of the complex crater’s upper part. The most probable candidate here is a shock wave generated during localized heating by a 0.5-ns laser pulse.

It is also useful to compare channel dynamics with the dynamics of the whole complex crater. For this purpose, D_{ch} and h_{ch} are normalized to their counterparts of the whole crater and plotted as a function of fluence in Fig. 101.37. Both dependencies show growth, which provides circumstantial evidence that plasma-ball and melt-front-propagation velocity

in the channel exceeds the fracture velocity in the studied range of fluence.

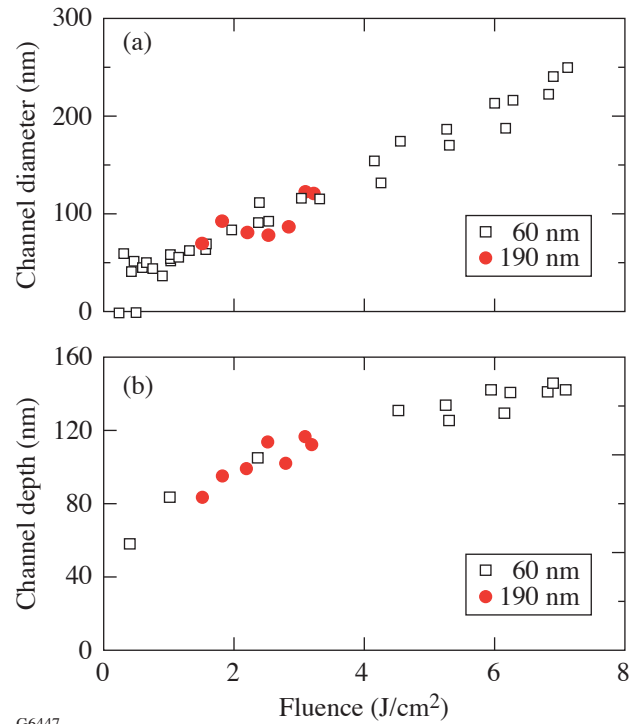


Figure 101.36
Complex-crater-channel diameter and depth variation with laser fluence: (a) channel diameter and (b) channel depth. Data for craters initiated by particles with 190-nm lodging depth are interleaved with data for regular craters originated by particles with 60-nm-deep location (see Figs. 101.30 and 101.33).

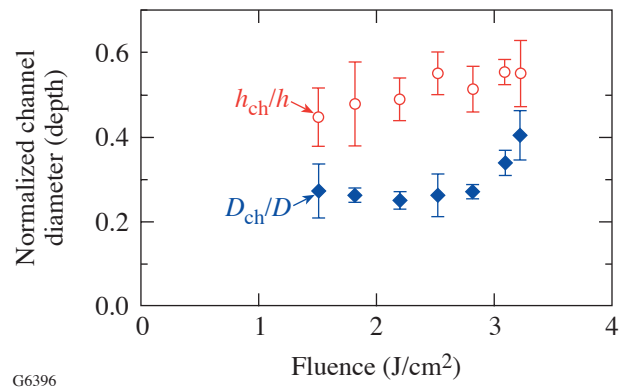
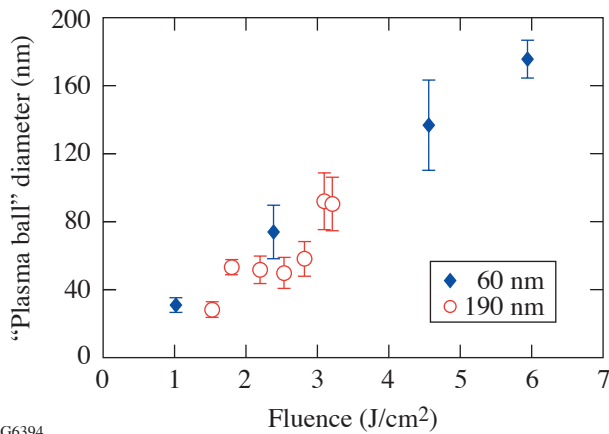


Figure 101.37
Channel diameter/crater diameter and channel depth/crater depth ratios as functions of fluence.

5. Estimates of Plasma-Ball Scale

Estimating the size of the plasma ball using only AFM data on crater geometry is not a straightforward task. Due to the dynamic nature of crater formation, the final shape of the regular crater is the result of interplay between processes of energy deposition, dissipation, hydrodynamic motion, and evaporation of the material. From this point of view, crater width at the particle-center position (see Fig. 101.28) is only remotely connected to the plasma-ball diameter. Nevertheless, with an increase in fluence and plasma-ball growth, part of the deposited energy used for crater formation will also grow due to the reduced role of dissipation processes (surface-to-volume ratio). It allows the use of crater width at the particle-center position D_p in the upper limit of fluence range as an estimate for the plasma-ball size. D_p values for 60-nm and 190-nm lodging are depicted in Fig. 101.38 as a function of fluence. In the case of 60-nm lodging, D_p shows linear growth and reaches a maximum value of ~ 180 nm at a fluence of ~ 6 J/cm² (~ 13 times threshold). According to phenomenological theory [see the **Theoretical Approach to Crater Formation** section (p. 27)], plasma-ball growth saturates upon reaching a size comparable with laser wavelength in SiO₂ film, $\lambda_f = 351/n_f \sim 250$ nm (n_f , film refractive index ≈ 1.4). Both the maximum measured value of $D_p \sim 180$ nm $\approx 3/4\lambda_f$ and the linear behavior of $D_p(F)$ suggest that plasma-ball growth is not reaching its saturation regime within the investigated fluence range.



G6394

Figure 101.38 Estimate of plasma-ball size. Crater width at the particle-center position taken as a function of fluence for the particle-lodging depths of 60 nm and 190 nm.

6. Scaling Relations

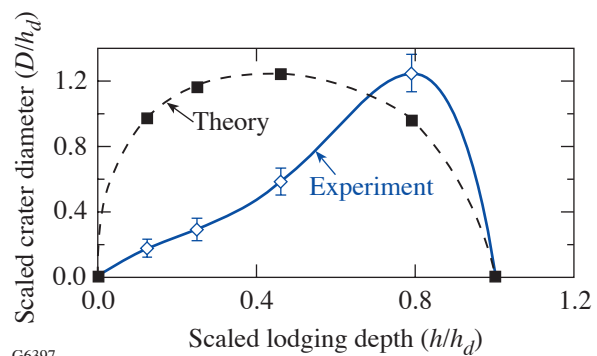
There are two lodging-depth cases where the crater is not formed: the first case is where the lodging depth is so large that the pulse energy deposited in the material is not enough to create a crater; the second case is zero depth, where the defect

can experience desorption without any modification of the film. At all intermediate locations, craters can be formed and the theory predicts a “bell”-shaped curve for crater diameter versus lodging depth dependence, in agreement with Eq. (3).

Our previous attempt to check scaling relations¹¹ with 8.4-nm particles showed qualitative agreement with theory, although only three relatively shallow lodging depths (10 nm, 30 nm, and 48 nm) were available at the time.

In this work, crater diameter was measured as a function of lodging depth at a fixed laser fluence of 1.67 J/cm²—the threshold fluence for the deepest lodging depth $h_d = 240$ nm. The results, normalized to h_d , are presented in Fig. 101.39 together with the theoretical curve predicted by Eq. (3). The departure from the theoretically predicted (“bell”-shaped) curve and shift in the peak position may be directly attributed to the change in the crater-formation mechanism with increasing lodging depth. The experimental curve shows clearly a transition taking place between 60-nm and 110-nm lodging depths and manifests the onset of the fracture-driven material removal. Significant change (4.3 times) in the diameter size for 190-nm lodging ($h/h_d = 0.79$) compared to 60-nm lodging ($h/h_d = 0.25$) points to the energetic preference of the fracture mechanism compared to melting and vaporization.

Figure 101.39 also shows surprisingly close agreement between the experimental maximum value of normalized crater size $D/h_d = 1.25$ and the theoretically predicted ≈ 1.2 value [see Fig. 101.39 and Eq. (4)]. Further investigations of scaling relations, preferably with only one dominating mechanism of crater formation, should test the strength of this result.



G6397

Figure 101.39 Scaled crater diameter versus scaled particle-lodging depth. Experimental data are taken at fluence 1.67 J/cm², corresponding to the crater-formation threshold for lodging depth $h_d = 240$ nm.

Conclusions

1. High-resolution investigation of 351-nm damage morphology in SiO₂ thin films with 18.5-nm gold nanoparticles serving as artificial, absorbing defects revealed sub-micrometer-scale craters as the main damage features.
2. Two different crater geometries are attributed to either (1) shallow absorbers and a melting/vaporization mechanism of crater formation, or (2) deep absorbers and complex-crater formation involving a combination of melting/vaporization and fracture.
3. The nanoscale thresholds (crater formation thresholds) increase with increasing particle-lodging depth, owing to the increased amount of energy required for craters to form.
4. At near-threshold conditions, craters initiated by deep absorbers are much larger than craters initiated from shallow depth mainly due to additional fracture-driven material removal from the top film layer. This mechanism is energetically much more efficient than melting and vaporization.
5. The growth of crater diameter and crater depth with laser fluence shows a higher rate for shallow absorbers compared to deep absorbers, which is explained by the difference in energy to be deposited to achieve the same partial increment in size.
6. Comparison with theoretical predictions for regular crater growth with fluence leads to the conclusion that the *saturation regime associated with the 1/3 power law is not reached* in the fluence range $< 8.1 \text{ J/cm}^2$. This conclusion is strongly supported by a plasma-ball-size estimate showing linear growth with fluence and reaching a value of $\sim 3/4$ of a wavelength for 60-nm lodging depth and an $\sim 6\text{-J/cm}^2$ fluence.
7. Analysis of crater-aspect-ratio variation with laser fluence proved that *crater growth with fluence is dominant in the lateral dimension*, especially in the case of shallow absorbers.
8. Investigation of complex-crater formation showed that the channel part of the crater is formed through melting and vaporization with geometry and size closely resembling a regular crater, provided fluence is the same. The rate of channel scale growth with fluence is exceeding the rate of growth of the complex crater as a whole, indicating that the major part of energy deposition takes place in the channel volume.
9. Scaling relations between crater diameter and absorber lodging depth are influenced by changes in crater-formation mechanism with increasing lodging depth. Good agreement with theoretical predictions is found for scaled maximum-diameter values. Further understanding of the crater-formation picture can be achieved with the help of numerical modeling (as reported in Refs. 18 and 19) with realistic temperature-dependent material parameters and absorbing-particle sizes.

ACKNOWLEDGMENT

The authors would like to thank P. A. Jaanimagi, R. Boni, and M. Millecchia for help with implementation of the CCD imaging system. This work was supported by the U.S. Department of Energy Office of Inertial Confinement Fusion under Cooperative Agreement No. DE-FC52-92SF19460, the University of Rochester, and the New York State Energy Research and Development Authority. The support of DOE does not constitute an endorsement by DOE of the views expressed in this article.

REFERENCES

1. S. Papernov and A. W. Schmid, *J. Appl. Phys.* **82**, 5422 (1997).
2. M. C. Staggs *et al.*, in *Laser-Induced Damage in Optical Materials: 1991*, edited by H. E. Bennett *et al.* (SPIE, Bellingham, WA, 1992), Vol. 1624, pp. 375–385.
3. R. J. Tench, R. Chow, and M. R. Kozlowski, in *Laser-Induced Damage in Optical Materials: 1993*, edited by H. E. Bennett *et al.* (SPIE, Bellingham, WA, 1994), Vol. 2114, pp. 415–425.
4. S. Papernov, A. W. Schmid, R. Krishnan, and L. Tsybeskov, in *Laser-Induced Damage in Optical Materials: 2000*, edited by G. J. Exarhos *et al.* (SPIE, Bellingham, WA, 2001), Vol. 4347, pp. 146–154.
5. S. Papernov, A. W. Schmid, A. L. Rigatti, and J. D. Howe, in *Laser-Induced Damage in Optical Materials: 2001*, edited by G. J. Exarhos *et al.* (SPIE, Bellingham, WA, 2002), Vol. 4679, pp. 282–292.
6. A. V. Hamza *et al.*, in *Laser-Induced Damage in Optical Materials: 2001*, edited by G. J. Exarhos *et al.* (SPIE, Bellingham, WA, 2002), Vol. 4679, pp. 96–107.
7. S. Papernov and A. W. Schmid, *J. Appl. Phys.* **92**, 5720 (2002).
8. F. Bonneau *et al.*, *Appl. Phys. B* **75**, 803 (2002).
9. H. Bercegol *et al.*, in *Laser-Induced Damage in Optical Materials: 2002*, edited by G. J. Exarhos *et al.* (SPIE, Bellingham, WA, 2003), Vol. 4932, pp. 297–308.
10. H. Bercegol *et al.*, in *High-Power Laser Ablation IV*, edited by C. R. Phipps (SPIE, Bellingham, WA, 2002), Vol. 4760, pp. 1055–1066.
11. S. Papernov and A. W. Schmid, in *Laser-Induced Damage in Optical Materials: 2002*, edited by G. J. Exarhos *et al.* (SPIE, Bellingham, WA, 2003), Vol. 4932, pp. 66–74.
12. F. Bonneau *et al.*, *Appl. Phys. Lett.* **83**, 3855 (2003).

13. A. During *et al.*, in *Laser-Induced Damage in Optical Materials: 2003*, edited by G. J. Exarhos *et al.*, (SPIE, Bellingham, WA, 2004), Vol. 5273, pp. 366–372.
14. M. D. Feit *et al.*, in *Laser-Induced Damage in Optical Materials: 1997*, edited by G. J. Exarhos *et al.* (SPIE, Bellingham, WA, 1998), Vol. 3244, pp. 350–355.
15. M. D. Feit *et al.*, in *Laser-Induced Damage in Optical Materials: 2000*, edited by G. J. Exarhos *et al.* (SPIE, Bellingham, WA, 2001), Vol. 4347, pp. 316–323.
16. P. Grua and H. Bercegol, in *Laser-Induced Damage in Optical Materials: 2000*, edited by G. J. Exarhos *et al.* (SPIE, Bellingham, WA, 2001), Vol. 4347, pp. 579–587.
17. P. Grua *et al.*, Phys. Rev. B **68**, 035424 (2003).
18. F. Bonneau *et al.*, in *Laser-Induced Damage in Optical Materials: 2000*, edited by G. J. Exarhos *et al.* (SPIE, Bellingham, WA, 2001), Vol. 4347, pp. 308–315.
19. F. Bonneau *et al.*, Appl. Phys. B **78**, 447 (2004).
20. Yu. K. Danileiko, A. A. Manenkov, and V. S. Nechitailo, Sov. J. Quantum Electron. **8**, 116 (1978).

Minimizing Artifact Formation in Magnetorheological Finishing of CVD ZnS Flats

Introduction and Motivation

The development of optics for new applications is based on the use of materials that have the appropriate mechanical and optical properties. For infrared (IR) window and dome materials that protect imaging systems against damaging conditions, three main considerations are taken into account: material strength, thermal-shock resistance, and optical characteristics, such as transmission, absorption, scattering, and emissivity. To obtain maximum transmittance, a good IR material should exhibit minimum optical scattering due to a rough surface finish. The synthetic materials that meet the requirements for IR windows could be either single crystals or polycrystalline with cubic crystallographic structure, the latter being usually tougher, which is desired.¹ Polycrystalline ZnS is an excellent candidate for these applications.

The chemical vapor deposition (CVD) process was developed in the 1970s in response to the need for increased volumes of polycrystalline ZnS with improved transparency.² The CVD process takes place in a chamber similar to an autoclave at increased temperatures (600°C to 1000°C) and at pressures below 100 Torr. Deposits of solid grains are formed on the inside walls of a graphite mandrel. The size of the grains depends on the deposition temperature and has a dramatic impact on the mechanical properties, such as the erosion rate.³

Two types of CVD ZnS are available on the market from domestic sources: regular grade and multispectral grade. The first type has a grain size of about 2 to 8 μm , is yellow-orange in color, and is used in the 3- to 5- μm -wavelength and 8- to 12- μm -wavelength regions. The “multispectral (or ‘water clear’) grade” ZnS is colorless, exhibits high transmittance over a wider range of wavelengths, and can be used in the 0.5- to 12- μm region of the spectrum. This latter material undergoes a hot isostatic pressing (HIP) process to grow the grain size to 20 to 100 μm , eliminating microscopic voids and other internal defects; however, this refining process leads to a reduction in strength and erosion resistance of the clear material.

The CVD process offers many advantages over conventional techniques for preparing infrared transmitting materials, the most significant being the purity of the material, its minimized IR absorption, and the fact that the process is not size limited. A potential disadvantage of the process is that the CVD ZnS material, though it possesses a fine grain structure, contains a micro- to macroscopic inhomogeneous “nodular” structure, referred to as “hillocks” or “pebbles.” Pebbles nucleate from dust and dust-like inclusions on the mandrel where substrate growth initiates. These then grow up from the bottom in the form of expanding “cones” through the bulk of a CVD ZnS puck.⁴ They may reach several millimeters in size on the free surface.

The process of surface finishing is of great importance since the final surface quality has an impact on optical properties of a ZnS optic. Single-point diamond turning, a common method for finishing nonspherical surfaces, is especially effective with long-wave infrared materials (LWIR = 8 to 12 μm) like ZnS, ZnSe, and Ge. Magnetorheological finishing (MRF), described elsewhere,⁵⁻⁷ is a deterministic polishing process that is now widely used in the production of high-precision optics around the world. The extension of MRF to a vast array of materials is possible because of the accommodating nature of this finishing process, which offers a wide range of removal rates required for the surface finishing of glasses, crystals, polycrystalline, and plastic materials. The objective of this work was to determine which aqueous magnetorheological (MR) fluid composition and conditions would provide the best polishing and smoothing performance on CVD ZnS flats that differed in initial surface preparation and source of supply. During this research the emergence of pebbles upon polishing with MRF was revealed. Suppression of these artifacts at the surface was accomplished by changing the composition of the MR fluid.

Experimental Details

MR fluids were prepared with a variety of magnetic and nonmagnetic ingredients. Two types of magnetic carbonyl iron (CI) particles were evaluated. Each type was spherical in shape

with an average particle size of $\sim 4 \mu\text{m}$. One type was mechanically “hard”, and the second was mechanically “soft”.⁸ Four nonmagnetic polishing abrasives were evaluated: cerium oxide, diamond, alumina, and silica. Table 101.IV lists the attributes of these abrasives. Abrasive size was difficult to ascertain. It depended on milling time during use for those abrasives that were strongly agglomerated. These abrasives were used previously in experiments on MRF of polymers.⁹

CVD ZnS from two manufacturers—“regular grade” from II-VI, Inc.,¹⁰ and “high-quality” material from the Research Institute of Synthetic Crystal, Beijing¹¹—were used in the experiments. Samples were provided in the form of 35- to 40-mm-diam pucks that were 8 to 20 mm thick. Surfaces were used as prepared by outside sources or after additional processing in-house.

Spotting and polishing experiments with uniform removal (successive dc polishing runs) were conducted on a Q22Y MRF polishing machine.¹² Peak and volumetric removal rates were calculated using interferometric data obtained on a Zygo GPI phase-shifting interferometer.¹³ Polishing performance of the various MR fluids was evaluated by measuring the removal rate, the final surface roughness (p–v and rms), and the visual appearance of the surfaces after polishing runs.

The evolution of surface morphology and texture was determined using a Zygo New View5000 White Light Optical Profilometer.¹⁴ This instrument quantifies microroughness

and reveals surface defects. Two types of objectives were used for the analysis: a 20× Mirau (with a 0.26-mm × 0.35-mm image size) and a 2.5× Michelson (with a 2.11-mm × 2.81-mm image size for 1× zoom and 5.38 mm to 7.17 mm for a 0.4× zoom) with no digital filter applied. The higher magnification allowed for the evaluation of areal rms and p–v surface roughness, while the lower magnification was useful for studying the extent and shape of pebble-like surface artifacts.

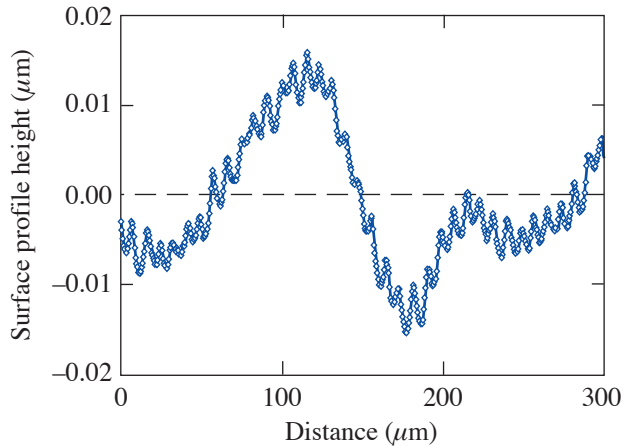
Five initial surface states were investigated: deterministically microground, single-point diamond turned, and after pitch-polishing in-house (for ZnS from II-VI); “as received” and after pitch-polishing in-house (for ZnS from China). Pitch-polished surfaces were prepared in-house in a four-step process: controlled loose-abrasive grinding (40 μm of alumina on cast iron, 20 μm of alumina on glass, and 9 μm of alumina on glass) followed by polishing on a beeswax/Gugolz73 lap (10%/90%) with a 50/50 acidic mixture of 0.3 μm of alumina/colloidal silica. Resulting surfaces were flat to better than 0.5 μm p–v, with areal surface roughnesses as good as 10 nm p–v and 0.5-nm rms.¹⁵

The deterministically microground surfaces were prepared in-house using a three-step protocol consisting of computer numerically controlled removal with three diamond ring tools: rough (220 μm in bronze), medium (15 μm in bronze), and fine (3 μm in resin). Surface-roughness levels after grinding were ~ 400 nm p–v and ~ 20 -nm rms.

Table 101.IV: Abrasive particles used in MR fluids for CVD ZnS polishing.

Dry Abrasive	pH in DI Water	Primary Particle Size ^(b)	Median Size ^(c)	Comments
CeO ₂	—	40 nm	96 nm	^(b) Provided as 20.9-wt.% solids in pH7.4 solution
Diamond ^(a)	2.5	4 nm	1.4 μm	Milling in an MRF machine increased vol % of particles <0.6 μm from 0.5 to 21 in 7 days
Al ₂ O ₃ γ phase	4.7	33 nm	93 nm	Milling in an MRF machine increased vol % of particles <225 nm from 0 to 75 in 24 h
SiO ₂	4.7	40 nm	—	^(b) Amorphous, fumed, hydrophilic
^(a) Standard MR fluid constituent; ^(b) information supplied by vendor; ^(c) powder dispersed in DI water with a surfactant and intensively sonicated prior to sizing.				

Samples of CVD ZnS from II-VI were single-point diamond turned (SPDT) by an outside vendor;¹⁶ surface-roughness levels after SPDT were 33 ± 6 nm p-v and 6.4 ± 1.0 -nm rms.¹⁵ A typical lineout of an SPDT surface is shown in Fig. 101.40. Over a distance of $300\ \mu\text{m}$ one can see the fine diamond-turning marks (spatial periodicity of $\sim 8\ \mu\text{m}$), superimposed on undulations with large amplitudes and periods of over $100\ \mu\text{m}$. Power spectral density (PSD) analyses were conducted on these surfaces before and after MRF to track the evolution of these features (described later).



COM92

Figure 101.40
The initial surface profile of an SPDT surface on CVD ZnS used in this work.

Some of the CVD ZnS parts manufactured in Beijing were used as received from China (specular surfaces with an areal surface roughness of 300 ± 155 nm p-v and 8.8 ± 0.5 -nm rms).¹⁵ Others were used after polishing in-house on pitch (areal surface roughness of 10 ± 3 nm p-v and 0.8 ± 0.0 -nm rms).¹⁵

No discussion has been found in the literature regarding the relevance of pebble-like structures on CVD ZnS used in IR applications. Since the CVD process imposes rather different growing conditions as the growth surface extends out from the mandrel, care was taken to keep track of CVD ZnS surfaces. The sides of the ZnS pucks that were in contact with the growth mandrel were designated S1 (more yellow coloration), and the sides farthest away from the mandrel were designated S2 (more orange in color).

The work described here consisted of three phases: Experiments were first conducted on the in-house pitch-polished surfaces of CVD ZnS from II-VI. The immediate goal was to identify the optimal nonmagnetic abrasive from the four types

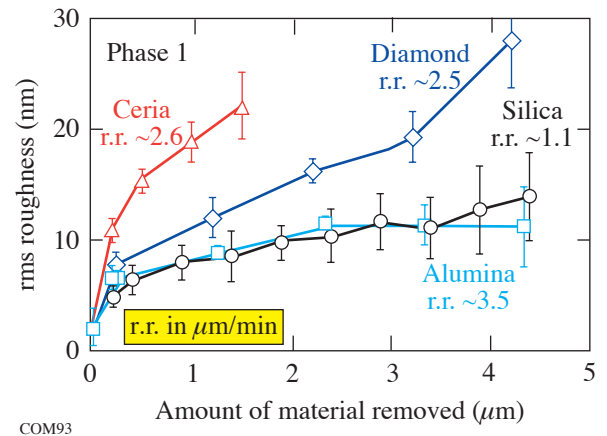
of powders in tests with hard CI. S1/S2 side-related effects were studied on 20-mm-thick flats. Secondly, magnetic-particle type and MR fluid chemistry were further altered to make additional improvements in the final surface roughness. Finally, the polishing performance of the altered fluid was evaluated on the four types of surfaces previously described, for both the domestic and foreign-made ZnS materials.

Nonmagnetic Abrasive Study (Phase 1)

MR fluids using hard CI were prepared with each of the four nano-abrasives from Table 101.IV, which differ in particle hardness (from soft silica particles to hard diamond ones), as well as in the particle surface chemistry. This latter characteristic affects fluid rheology, thus setting individual limits for the maximum abrasive content that can be used. MRF trials with each of these abrasives were conducted on the same part and surface (S2). The part was repolished on pitch before each successive trial.

The results of these experiments are presented in Figs. 101.41 and 101.42. Figure 101.41 tracks the evolution of surface microroughness as a function of material removed. Figure 101.42 shows the peak removal rate achieved for a given abrasive concentration and the level of p-v surface roughness after removing $1\ \mu\text{m}$ of material.

The highest removal rate along with the least degradation to surface roughness was provided by the hard CI-based MR fluid with >1.0 vol% of alumina; the removal rate observed for the fluid with nanodiamond was quite similar to that for



COM93

Figure 101.41
Evolution of rms surface roughness with the amount of material removed during dc polishing of pitch-polished CVD ZnS with a hard CI-based fluid prepared with each of four different abrasives.

the ceria-based MR fluid, which was almost two times higher than the removal rate provided by the silica-containing fluid. These results clearly demonstrate the dramatic difference in abrasive polishing efficiency on ZnS, independent of the abrasive concentration. (It was not possible to relate removal rates to the number of abrasive particles of a given abrasive type because of issues of aggregation and agglomeration previously discussed relative to Table 101.IV.)

The two abrasives, ceria and diamond, provided similar removal rates with drastically different surface-roughness characteristics. As shown in Fig. 101.41, rms surface roughness increased dramatically from 2.7 nm for the initially pitch-polished surface up to 11 nm after polishing out 0.2 μm of material with the ceria-based MR fluid. Roughness continued to increase after every subsequent polishing run and approached 22-nm rms with the cumulative removal of 1.5 μm . Roughness values grew slowly but steadily when using diamond abrasives, exceeding 25-nm rms after the removal of 4 μm . Silica and alumina abrasives caused less surface degradation. The silica-based MR fluid provided relatively lower roughness levels with the rms leveling out at around 11 nm after removing as much as 3.5 μm of material. However, this abrasive demonstrated a tendency for increasing roughness with further polishing. The results obtained for the alumina-based fluid were quite similar to those of the silica-based fluid, with rms not exceeding 11 nm after polishing out more than 2 μm . Root-mean-square roughness remained at this same

level after polishing out another 2.5 μm of material. Moreover, the p-v surface characteristics showed the lowest values as well. The alumina-based fluid was chosen for further experiments due to its 3.5 \times -higher removal rate than the silica, a low level of surface roughening, and its excellent rheological properties.

Pebbles were first observed on the S2 surface of the CVD ZnS puck after the first 0.5- μm dc polishing runs were made, regardless of the type of abrasive used. The emergence of pebbles on S2 became more noticeable to the eye after each subsequent polishing run; however, the quantification of these topographic features was difficult to document since they caused no increase to the surface roughness measured with either 20 \times or 2.5 \times objectives. On S1, the situation was different. Pebble-like features became noticeable to the eye only with removal of over 1.5 μm of material. As they emerged with additional polishing, the features on S1 exhibited a different shape, areal density, and intensity than those on S2.

Images of S1 and S2 on a 20-mm-thick CVD ZnS puck after 1.5 μm of material was polished out from an initially pitch-polished ZnS surfaces were obtained using a laser interferometer (40-mm aperture) and a white-light interferometer (2.5 \times : 7.2-mm \times 5.4-mm area). The images are presented in Fig. 101.43 and clearly demonstrate the pronounced difference

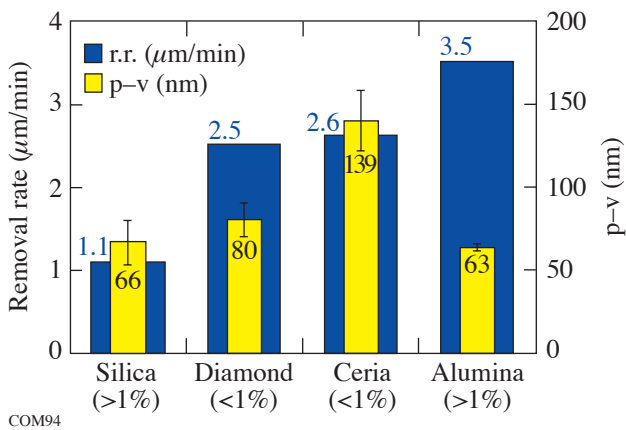


Figure 101.42
The removal rates and p-v surface-roughness values measured after polishing out 1 μm of material with hard CI-based fluids prepared with four different abrasives. Approximate abrasive concentration is indicated in volume percent.

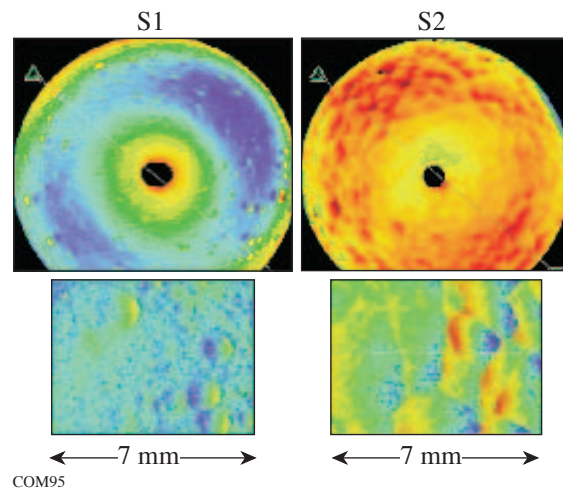


Figure 101.43
Laser interferometer images (40-mm aperture) and white-light interferometer intensity maps (2.5 \times , 7.2-mm \times 5.4-mm field) for two opposite sides of a 20-mm-thick CVD ZnS puck after polishing out 1.5 μm of material by a hard CI-based nanoalumina fluid.

in the shape and density of the artifacts. Pebbles on S1 resemble distinct, separated craters, having a circular shape with a diameter smaller than 1 mm, while the pebbles observed on S2 appear as large, overlapped petals of a flower. The features on S2 are quite different in size, with some being larger than 5 mm across. In terms of visual appearance, the S2 side showed significant decoration to the eye, whereas S1 looked nicely polished with no observable artifacts. These micro- and macrostructures fit previous descriptions and microphotographs of CVD ZnS that indicate cones of material growing up and away from S1 (mandrel/side) toward S2 (free side).⁴

Composition and Chemistry Alterations (Phase 2)

The necessity for making further improvements to surface roughness and surface visual appearance resulted in the second phase of our experiment, during which MR fluid composition and chemistry were altered employing alumina as the nonmagnetic polishing abrasive. Use of a soft type of CI improved long-term stability of the altered alumina-based fluid and provided removal rates of $\sim 1 \mu\text{m}/\text{min}$. Additional alterations of

fluid chemistry gave very beneficial results. The evolution of p-v and rms surface roughness as a function of material removed by these MR fluids with soft CI and altered chemistry are plotted in Figs. 101.44(a) and 101.44(b) for initially pitch-polished surfaces. The use of soft CI led to the noticeable improvement in the surface roughness although there was a 3 \times reduction in the removal rate from phase 1. The alteration of both CI type *and* chemistry lowered the surface roughness to below 20 nm p-v and 2-nm rms after polishing out as much as $2 \mu\text{m}$ of material from an initially pitch-polished surface. Further polishing to remove a total of $3.5 \mu\text{m}$ led to a modest increase in both roughness parameters to 25 nm p-v and 2.5-nm rms.

The other significant advantage of using the altered fluid was the fact that no pebbles were observed on either S1 or S2 [see Fig. 101.44(c)], providing good visual appearance after polishing out a total of $3.5 \mu\text{m}$. These results made the chemically altered, alumina-based, soft-CI MR fluid an advantageous choice for figure correction of prepolished CVD ZnS.

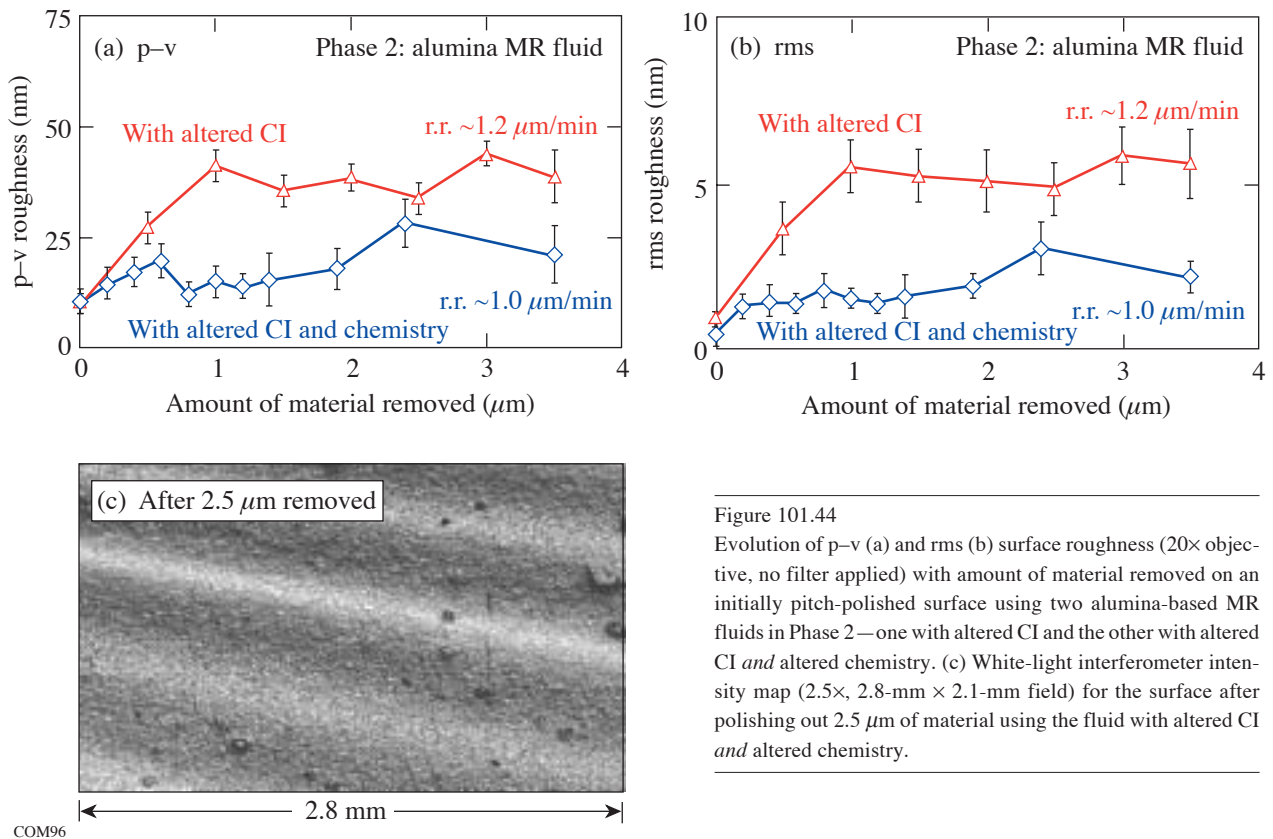


Figure 101.44 Evolution of p-v (a) and rms (b) surface roughness (20 \times objective, no filter applied) with amount of material removed on an initially pitch-polished surface using two alumina-based MR fluids in Phase 2—one with altered CI and the other with altered CI *and* altered chemistry. (c) White-light interferometer intensity map (2.5 \times , 2.8-mm \times 2.1-mm field) for the surface after polishing out $2.5 \mu\text{m}$ of material using the fluid with altered CI *and* altered chemistry.

The Effect of Initial Surface Preparation (Phase 3)

The effect of initial surface preparation on the polishing and smoothing performance of MRF was studied using the chemically altered, alumina-based, soft-CI MR fluid on five types of CVD ZnS surfaces from the two manufacturers described earlier.

The removal rate was measured to be 1.2 to 1.4 $\mu\text{m}/\text{min}$ with no significant dependence on the initial surface preparation in the tested range of initial roughness parameters. The evolution of roughness with the amount of material polished out from domestic CVD ZnS with different initial surface preparation is presented in Figs. 101.45(a) and 101.45(b). Similar roughness levels were achieved on all three tested surfaces after polishing out 2 μm of material, with the p-v falling to below 20 nm and the rms going below 2 nm. This was accomplished despite the

fact that p-v values for the initial surfaces were in a range that varied from 10 nm p-v for the pitch-polished surface to more than 400 nm p-v for the microground surface. This result is of great importance for the MRF process because it widens the range of initial surface conditions that can be processed. The other noteworthy result is that no signs of surface decoration (e.g., pebble-structure formation) were observed on any surfaces of ZnS after removing up to 4 μm of material.

The surface of an SPDT ZnS part before and after MRF polishing was examined using PSD analysis of lineouts from roughness scans. This analysis is useful for showing the evolution of various spatial frequencies in the surface. The initial surface exhibited primary peaks in power density (e.g., diamond-turning grooves) with several periodicities between 8 μm and 15 μm (spatial frequencies from $1.2 \times 10^{-4}/\text{nm}$ to $7 \times 10^{-5}/\text{nm}$), with a broad secondary peak (grooves presumably caused by misalignment or chatter) between 100 μm and 500 μm (spatial frequencies from $1 \times 10^{-5}/\text{nm}$ to $2 \times 10^{-6}/\text{nm}$).

The PSD data in Fig. 101.46 demonstrate that the primary diamond-turning grooves (8 to 15 μm) were eliminated after the removal of only 0.2 μm of material. Removal of 1 μm was sufficient to decrease the signature near 200 μm ($5 \times 10^{-6}/\text{nm}$) by over an order of magnitude. This demonstrated ability of MRF to reduce the intensity and even eliminate the periodic

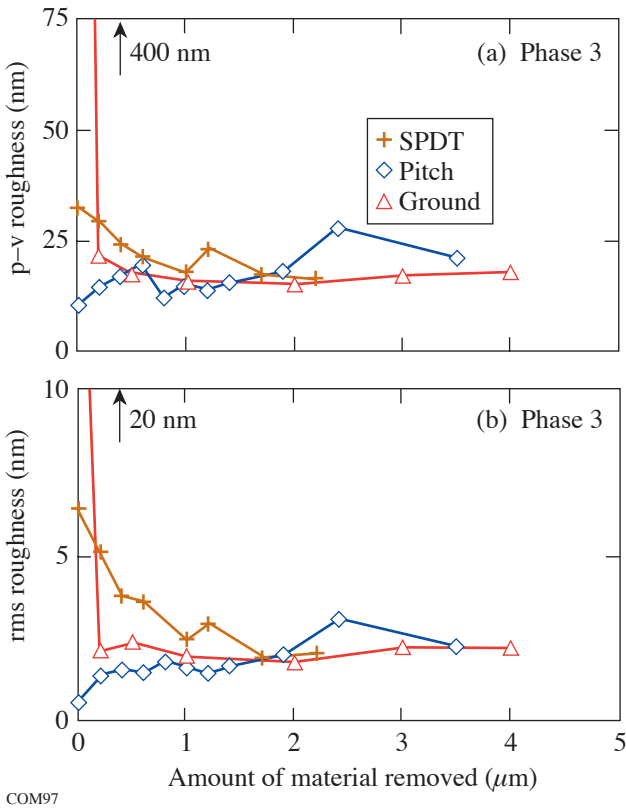


Figure 101.45 Evolution of p-v (a) and rms (b) surface roughness with the amount of material polished out for three types of initial surfaces—pitch-polished, ground, and SPDT—using the chemically altered, soft-CI MR fluid (domestic material from II-VI, Inc).

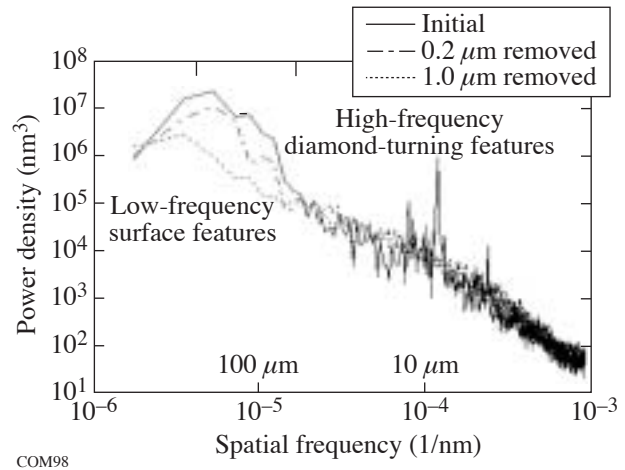


Figure 101.46 PSD plots on an SPDT ZnS surface showing the removal of high-frequency diamond-turning grooves after polishing out 0.2 μm of material. Additional polishing reduced the power density of low-frequency artifacts by 10 \times .

marks of different frequencies, accompanied by a dramatic improvement in surface roughness without introducing artifacts, makes the altered MR fluid a strong candidate for improving SPDT surfaces of CVD ZnS.

CVD ZnS manufactured in Beijing was evaluated in a series of dc polishing runs using the chemically altered, soft-CI MR fluid. Both as-received surfaces and surfaces prepolished in-house on pitch were processed with MRF without uncovering any surface artifacts. As shown in Fig. 101.47, it was impossible to improve the roughness of as-received surfaces (initial: 300 nm p-v/9-nm rms) to less than 30 to 40 nm p-v/5-nm rms. Starting from an in-house pitch prepolish, however, it was possible to bring the Chinese material to p-v and rms roughness levels comparable to those achieved for the domestic material.

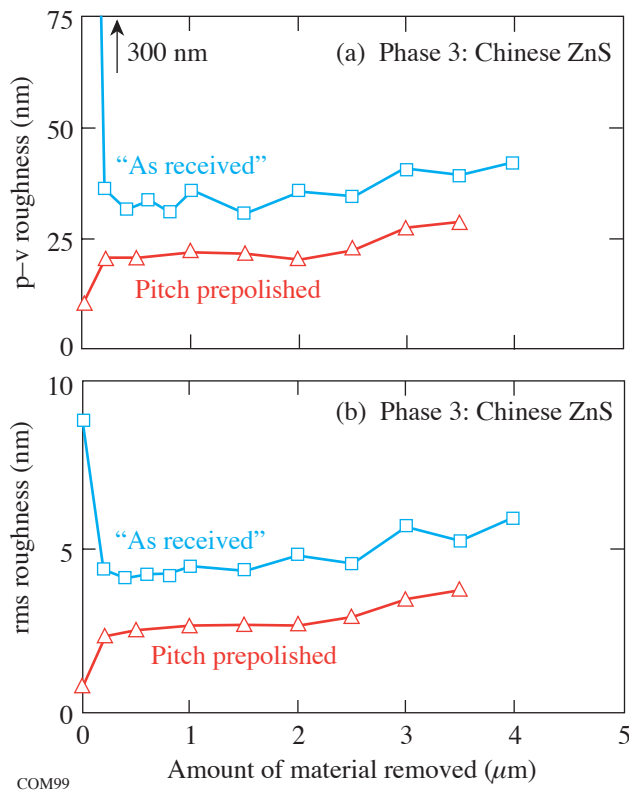


Figure 101.47

Evolution of p-v (a) and rms (b) surface roughness with the amount of material removed for CVD ZnS from China using chemically altered, soft-CI MR fluid. Two initial surfaces were used in the experiment: as received and after in-house prepolishing on pitch.

Summary

The finishing performance of magnetorheological (MR) fluids prepared with a variety of magnetic and nonmagnetic ingredients was studied on CVD ZnS flats from different manufacturers. Surfaces studied were used as received, after polishing on pitch, after single-point-diamond-turning (SPDT), and after deterministic microgrinding. MR polishing using hard CI and standard MR fluid chemistry yielded a surface with high roughness and pebble-like structures. The severity of pebble-like decoration was shown to be related to the processed side of the ZnS puck. Pebbles were more pronounced on the free surface farthest from the graphite growth mandrel. Experiments on pitch-polished surfaces showed nanoalumina abrasives to be the least detrimental of four nanoabrasives tested. These abrasives were then combined with soft CI and altered MR fluid chemistries to enable several microns of ZnS material to be removed with suppression of pebble-like decoration. Surfaces that were initially microground, diamond turned, or pitch polished were all processed with this altered MR fluid to ~ 20 nm p-v and 2-nm rms. Diamond-turning marks were eliminated.

REFERENCES

1. R. Lane and B. Battat, Advanced Materials and Processes Technology Information Analysis Center (AMPTIAC), **AMPT-18**, IIT Research Institute, Rome, NY, Contract No. SPO700-97-D-4001 (December 1999).
2. H. H. Karow, *Fabrication Methods for Precision Optics* (Wiley, New York, 1993), Chap. 2.
3. C. S. Chang, J. L. He, and Z. P. Lin, *Wear* **225**, 115 (2003).
4. K. L. Lewis, A. M. Pitt, and J. A. Savage, in *Proceedings of the Ninth International Conference on Chemical Vapor Deposition 1984*, edited by Mc. D. Robinson *et al.* (Electrochemical Society, Pennington, NJ, 1984), pp. 530–545.
5. S. D. Jacobs, S. R. Arrasmith, I. A. Kozhinova, L. L. Gregg, A. B. Shorey, H. J. Romanofsky, D. Golini, W. I. Kordonski, P. Dumas, and S. Hogan, *Am. Ceram. Soc. Bull.* **78**, 42 (1999).
6. D. Golini, in *Precision Science and Technology for Perfect Surfaces*, edited by Y. Furukawa, Y. Mori, and T. Kataoka, JSPE Publication Series No. 3 (The Japan Society for Precision Engineering, Tokyo, Japan, 1999), pp. 132–137.
7. S. D. Jacobs, S. R. Arrasmith, I. A. Kozhinova, S. R. Gorodkin, L. L. Gregg, H. J. Romanofsky, T. D. Bishop II, A. B. Shorey, and W. I. Kordonski, in *Initiatives of Precision Engineering at the Beginning of a Millennium*, edited by I. Inasaki (Kluwer Academic Publishers, Boston, 2001), pp. 501–505.

8. A. B. Shorey, S. D. Jacobs, W. I. Kordonski, and R. F. Gans, *Appl. Opt.* **40**, 20 (2001).
9. J. E. DeGroote, H. J. Romanofsky, I. A. Kozhinova, J. M. Schoen, and S. D. Jacobs, in *Manufacturing and Testing V*, edited by H. P. Stahl (SPIE, Bellingham, WA, 2004), Vol. 5180, pp. 123–134.
10. II-VI, Inc., Saxonburg, PA 16056-9499.
11. Research Institute of Synthetic Crystals State Administration of Building Materials, Industry, Beijing, Peoples Republic of China.
12. Q22Y, Commercial MRF machines manufactured by QED Technologies, LLC, Rochester, NY 14607.
13. Zygo GPIxpHR phase shifting interferometer system, Zygo Corporation, Middlefield, CT 06455.
14. Zygo New View™ 5000 White Light Optical Profilometer, Zygo Corporation, Middlefield, CT 06455.
15. New View™ 5000 setting for roughness measurements with 20× objective: scan length: 20 μm bipolar; min. mode: 5.0%; min. area size: 7; FDA: high. The reported roughness values are the average of eight to ten measurements at different sites.
16. Corning NetOptix, Diamond Turning Division, Keene, NH 03431.

A Multichannel, High-Resolution, UV Spectrometer for Laser-Fusion Applications

Introduction

The 60-beam OMEGA laser system is used for inertial confinement fusion (ICF) studies.¹ The configuration of each of the 60 beams should be exactly the same to produce the most-uniform ICF implosions.² A shaped infrared (IR) ($\lambda = 1053$ nm) pulse is generated from a single master oscillator and fed into 60 beamlines with large Nd:glass amplifiers.³ Each beamline produces approximately 800 J of IR light in a 1-ns pulse. The frequency of the IR light is tripled in a series of KDP crystals to produce UV light at 351 nm, which is used to illuminate the ICF target. An important feature of this laser system is that spectral broadening can be deliberately imposed on the emitted radiation using a technique called smoothing by spectral dispersion (SSD).⁴ This is done to produce a more-uniform, time-integrated illumination profile at the target. The imposed bandwidth has a width of 1.2 nm in the IR, which exceeds the acceptance bandwidth of the potassium dihydrogen phosphate (KDP) crystals used for frequency tripling.⁵ To overcome this problem, each beam has two tripling crystals that are angularly detuned with respect to the direction of propagation.⁶ The acceptance bandwidth of the combined crystals is large enough to efficiently convert the SSD pulses. To maintain the highest conversion efficiency, the angular detuning of the KDP crystals must be controlled to approximately $100 \mu\text{rad}$. Mistuned crystals decrease the UV conversion efficiency and change the spectra of the converted light. A procedure has been developed to tune the crystals by looking at the conversion efficiency on nine laser shots; however, the tuning can drift with time, and checks of individual beamlines have revealed that the spectra were different. Figure 101.48 illustrates the differences in spectra between two beamlines. To facilitate a more-accurate tuning procedure, a spectrometer was built to measure the UV spectra of all 60 beams on all OMEGA shots. This article describes that spectrometer.

In addition to the bandwidth imposed by the SSD system, there is an intrinsic source of bandwidth on the OMEGA system. If the intensity of a laser pulse varies rapidly in time, the nonlinear index of refraction produces a time-varying phase.⁷ The time-varying phase produces a wavelength shift.

The spectral structures associated with these intrinsic wavelength shifts have typical widths of 3 picometers (pm). The ability to understand and control this intrinsic bandwidth was a secondary motivation for building this spectrometer.

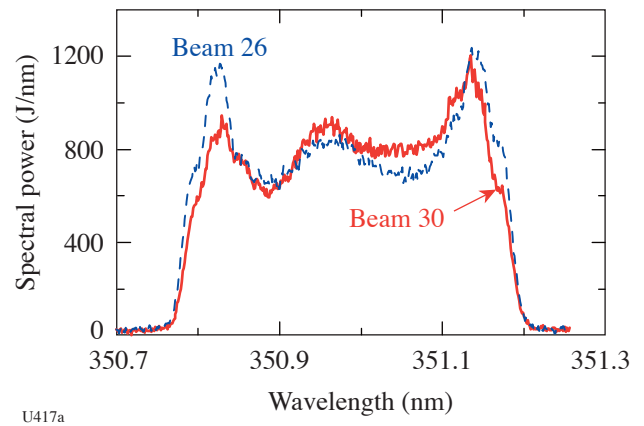


Figure 101.48

The spectra, with SSD on, vary from beam to beam on the same shot. The dashed curve is for beam 26 on shot 35711, and the solid curve is for beam 30 on the same shot.

The dual missions mentioned above determined the specifications of the spectrometer that was constructed. The spectrometer had to be able to acquire at least 60 complete spectra in a single shot. To allow for the possibility of corrupt channels and to incorporate *in-situ* wavelength calibration, an imaging spectrometer was constructed to accommodate 63 channels. Each channel must span a 0.5-nm bandwidth around $\lambda = 351.01$ nm to be capable of viewing the entire SSD-broadened spectra. With SSD turned off, the spectrometer must be able to resolve spectral features of the order of 3 pm. The light that feeds the spectrometer will come from a small fraction of the light from each beamline that is split off for diagnostic purposes (about $1 \mu\text{J}$ on a full-energy shot). The total UV energy per beamline on OMEGA can range from 10 to 500 J. The fraction of light that is split off is linearly dependent on the total beam energy, so the detection system must be able to accommodate signal levels that vary by a factor of 50.

Spectrometer Layout

The physical layout of the spectrometer is shown in Fig. 101.49. The input to the spectrometer comes from 60 fiber bundles. Each fiber bundle consists of three 300- μm , UV-transmitting, step-index fibers.⁸ The fiber bundles are attached to an integrating sphere, which is illuminated with a portion of the light from each beamline. Three fibers are used to increase the light coupled out of the integrating sphere. The fiber bundles attach to an input manifold. Within the manifold, three fibers from each bundle are realigned into a linear array and coupled into a UV-transmitting, fused-silica bar $10 \times 1.2 \times 0.4 \text{ mm}^3$, along the 1.2-mm dimension. The bar, which is aluminized on all four sides with a 10-nm edge, acts as an optical homogenizer via multiple reflections off the metallized sides. The light emerging from the fiber should be approximately spatially uniform and have a Gaussian dependence on angle. The homogenizer will cause the high-angle rays that have the lowest uniformity to undergo at least two reflections from the sides, thus increasing the uniformity of the output radiation. This assembly constitutes a single channel, which is the input to the spectrometer. Twenty-one of these channels are arranged in a line. The center channel is fed with a neon pencil lamp, which provides a wavelength fiducial for calibrating the wavelength. The entire manifold consists of three lines of 21 channels separated by 10.4 mm. In between the lines are three uniform bars that can be used to flat-field the instrument.

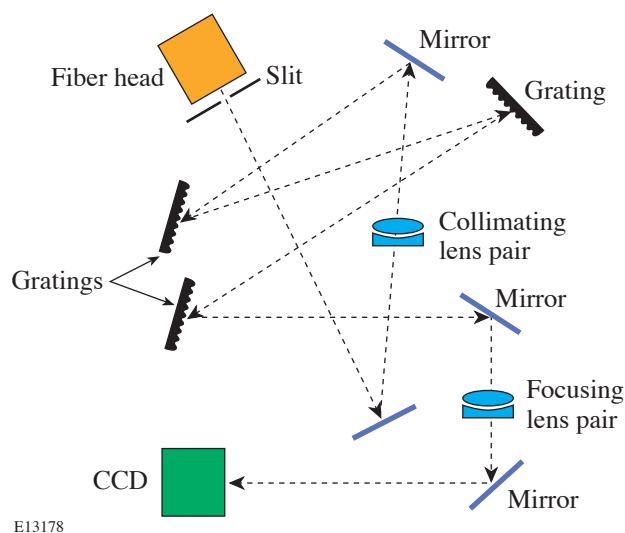


Figure 101.49

The layout of the spectrometer. The light from the fiber bundles passes through a slit array and a pair of collimating lenses before reflecting off of four mirrors and three gratings. A second pair of lenses focuses the light onto a CCD (charge-coupled device).

The resolution of the spectrometer would be limited by the 0.4-mm width of the bar unless the field of view is further limited. Unlike the adjustable slit commonly employed in spectrometers, the resolution of this instrument is selected from a fixed set of slit widths. The manifold sits behind a metallized fused-silica plate. The side of the plate facing the fiber manifold is coated with chromium. The backside is antireflection (AR) coated for UV light. The chromium was photolithographically etched with three sets of slits. Each set contained four slit openings: 10, 20, 40, and 60 μm . The plate sits on a computer-controlled linear stage that allows the selection of a single slit opening for all channels. The diffusing bars provide a uniform light source for illuminating the slit. The bars are at least six times larger than the slit width. By recording the slit opening for each shot, the response of the instrument can be photometrically calibrated.

Table 101.V gives the position and properties of each optical element in the path between the fiber manifold and the CCD (charge-coupled-device) detector. After passing through the slit, the light reflects off of a flat dielectric mirror. Four mirrors are used in the instrument to create a folded optical path. The folded path enables us to compress the instrument, with a total optical path length of greater than 5 m, onto a breadboard 1.2 m on an edge.

The optical system has a total demagnification factor of 0.87; therefore the slits at the input of the system appear smaller at the detector plane. The imaging is done with refractive optics.⁹ Four lenses are arranged in two pairs: a collimating pair and a focusing pair. The focus can be adjusted by means of a micrometer that controls the separation of each pair of lenses. Many spectrometers use reflective optics to image the light through the instruments to avoid chromatic aberrations associated with the refractive elements; however, this instrument has a limited spectral range of 0.6 nm centered about 351 nm. Over this spectral range, spectral dispersion in the fused silica can be ignored. The index of refraction changes by less than one part in 10^5 over this wavelength range. For the optical system described here, the point-spread function at the CCD detector, due to chromatic aberration, was calculated at three wavelengths (350.7 nm, 351.0 nm, and 351.3 nm) and found to be 11 μm , 6 μm , and 12 μm , respectively, on axis. This means the resolution changes across the spectral range from 1.8 pm to 1.4 pm to 1.9 pm. The advantage of using refractive optics is that the imaging can be done on axis, which allows a wider field of view (FOV) than off-axis imaging. The large FOV is needed because the spatial extent of the fiber manifold is $21 \times 25 \text{ mm}^2$. The effective width of the 21-mm dimension

expands to approximately 29 mm when wavelength dispersion of the full bandwidth is taken into account.

The spectral resolution of the system is achieved by using three $110 \times 110\text{-mm}^2$, 3600-line/mm holographic gratings. At a wavelength of 351 nm, the first-order diffraction efficiency is 38.8%. Based on a simulation of the spectrometer in OSLO,¹⁰ a combination of the three gratings produces a total dispersion at the CCD detector in wavelength units per spatial distance of $9.1 \times 10^{-2} \text{ pm}/\mu\text{m}$.

The CCD detector is a scientific-grade, 2048×2048 back-illuminated, thinned array.¹¹ The pixel pitch is $13.5 \mu\text{m}$.¹² To increase the sensitivity and eliminate any interference effects, the array has no protective window; therefore, the CCD is mounted in vacuum to protect the chip from degradation. Light enters the vacuum chamber through a window mounted at 25° to the optic axis so that any back-reflections from the CCD surface are removed from the FOV of the detector. The CCD is cooled to -30°C to reduce dark noise. The smallest slit size should image to approximately $8.7 \mu\text{m}$ at the detector plane,

Table 101.V: Specification of the optical system.

Optical Element	Position	Size (diameter for circular edge for square)	Specifications	Transmission
Slit	0.1 mm		10, 20, 40, 60 μm Cr, AR	
Mirror	801.1 mm	150 mm on edge	HR 351 23° surface roughness 2.5 nm	0.995
Plano-concave collimation lens	1001.1 mm	192-mm diam \times 30 mm thick	Radius 1 = ∞ Radius 2 = 368 mm	0.98
Convex-convex collimation lens	1105.2 mm	192-mm diam \times 40 mm thick	Radius 1 = 524 mm Radius 2 = 473 mm	0.98
Mirror	1575.2 mm	150 mm on edge	HR 351 27° surface roughness 2.5 nm	0.995
Diffraction grating	2255.2 mm	110 mm	3600 gr/mm gold @ 45.5°	0.388
Diffraction grating	3015.2 mm	110 mm	3600 gr/mm gold @ 45.5°	0.388
Diffraction grating	3795.2 mm	110 mm	3600 gr/mm gold @ 45.5°	0.388
Mirror	4625.2 mm	150 mm on edge	HR 351 37° surface roughness 2.5 nm	0.995
Convex-convex focusing lens	4715.2 mm	192-mm diam \times 40 mm thick	Radius 1 = 401 mm Radius 2 = 549 mm	0.98
Concave-plano focusing lens	4830.4 mm	192-mm diam \times 30 mm thick	Radius 1 = 357 mm Radius 2 = ∞	0.98
Mirror	5050.4 mm	150 mm on edge	HR 351 45° surface roughness 2.5 nm	0.995
Vacuum window	5666.4 mm	50.8-mm diam \times 5 mm thick	25° relative to normal incidence	0.992
CCD camera	5709.4 mm			0.17 (Q.E.)

which is less than the pixel pitch. Ideally, the image of a slit can illuminate just one pixel; however, the slit width must be convolved with the point-spread function listed above to determine the instrument resolution.

Instrument Performance

The multichannel spectrometer is now operational on the OMEGA laser system, and the instrument performance can be compared with the design specifications. Figure 101.50 shows the image of an acquired laser shot. The first operational issue is calibrating the wavelength. The middle channel of the middle column can be illuminated with the light from a neon pencil lamp.¹³ This channel is on the optical axis and has very small optical aberrations due to imperfections in the imaging system. In this configuration, four Ne I lines are visible.¹⁴ A least-squares fit to those wavelengths yields an absolute wavelength calibration for the middle column and a relative calibration for the two outside columns.¹⁵ The experimentally measured dispersion was 8.6×10^{-2} pm/ μ m, giving 1.16 pm/pixel. This is 6% lower than the modeled value listed above and indicates a slight offset in the position of lenses, which decreases the magnification. When the neon lamp illuminates the outside columns, not all of the lines are visible. To determine

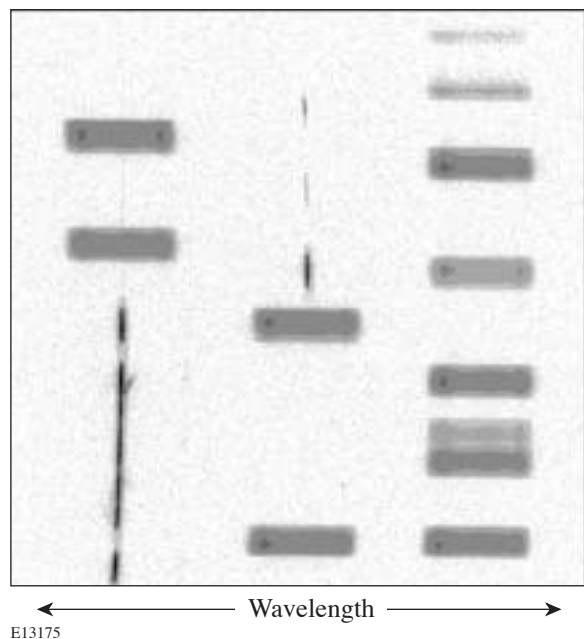


Figure 101.50

A UV-spectrometer CCD image from shot 37038 showing 23 of 60 beams with and without SSD. The density is logarithmic. The SSD beams, represented by large rectangular spectra, have approximately the same energy and 80 times the bandwidth of the narrow-linewidth beams.

the absolute calibration of the outside columns, the OMEGA laser is fired without the SSD bandwidth turned on. Under these conditions, all channels have the same narrow line spectrum. Adjusting the offset of the outside columns to match the center column gives an absolute wavelength calibration for all channels. The validity of the absolute wavelength calibration is tied to the precision to which the plate with the slit arrays can be reproducibly positioned. Since the illumination source is uniform, variations in the slit position translate to apparent shifts in the absolute wavelengths. The motorized, linear-translation stage can be reset to the same position to within 20 μ m, which implies that the wavelength calibration is accurate to approximately 2 pm after the slits are changed. To obtain the highest accuracy, the wavelength should be recalibrated every time the slit width is adjusted.

Aberrations within the imaging system of the spectrometer have been reduced to bring all channels within specifications. Channels near the optical axis exceed the performance requirements of the system. With SSD turned off, these channels will record a spectral full width at half maximum (FWHM) of 2.5 pm for laser energies that vary by a factor of 36 for 1-ns square pulses. The laser that seeds all sixty beams has a nearly transform-limited bandwidth, which has a measured UV-equivalent linewidth of less than 0.3 pm (the calculated linewidth of this laser is 4×10^{-4} pm). The independence of the spectral FWHM on laser energy implies that there is no *B*-integral broadening of the laser linewidth and the inputs to the spectrometer have the same spectral width as the seed laser; therefore, the measured linewidth is the intrinsic response of the instrument. For subnanosecond pulses, this is not the case. Figure 101.51 illustrates that the instrument performance is sufficient to observe *B*-integral broadening when it occurs. Two normalized spectra are shown: the wider spectrum is of a 100-ps pulse, the second spectrum is from a low-energy, 2-ns laser shot, which represents the instrument-limited response. As the position of the channels moves away from the optic axis, line-spread function increases. At the edges of the FOV of the CCD, the minimum FWHM is 6 pm. This resolution is sufficient for tuning the frequency-conversion crystals.

In addition to broadening, the optical system introduces curvature to the wavelength field. The straight slits in the object plane map to curves in the image plane, which deviate quadratically with distance from the center of the FOV. The maximum deviation at 14 mm from the optic axis is 300 μ m. With additional fine-tuning of the alignment, it might be possible to remove these aberrations. It was decided, however, that since the aberrations were sufficiently well characterized,

it was easier to remove them using image-processing algorithms than to realign the spectrometer.

The optical transmission through the spectrometer was measured by removing the fibers from the input to the spectrometer and recording the amount of light emerging from the fiber with a calibrated energy meter. The fiber was again connected to the spectrometer, and the total CCD analog-to-digital units (CCD_ADU) were recorded. The CCD_ADU total was converted to joules using the manufacturer's supplied quantum efficiency of the camera. A typical transmission value was $1.6 \times 10^{-5} \pm 0.5 \times 10^{-5}$, with most of the variation associated with the alignment of the fibers in the external fiber bundle with a similar internal fiber bundle that connects to the manifold. The transmission losses are dominated by the 10- μm slit aperture on the 400- μm source (transmission = 2.5%) and the mismatch between the $f/2.5$ numerical aperture of the fibers coupling into the $f/10$ of the collimating lens, which gives an effective transmission of 6%. The product of these transmissibilities is multiplied by the product of all the transmission factors listed in Table 101.V to estimate the transmission through the spectrometer as 2.1×10^{-5} . The light from a single channel that is transmitted to the CCD is very uniform in the spatial direction because of the homogenizer in the fiber manifold. There are 570 columns in each of the 63 spectra, and each of those 570 is the average of approximately 100 spatial pixels, all of which are nearly identical. The signal-to-noise

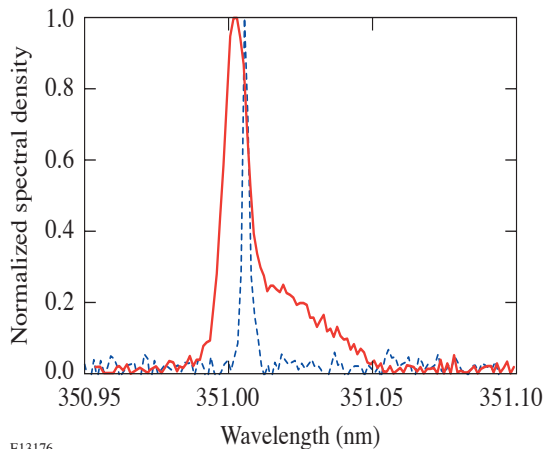


Figure 101.51
The dashed curve represents a 9-J, 2-ns pulse on beam 61 (shot 35921). Under these conditions, the spectral width is expected to be transform limited. This curve represents the instrument response to a single frequency. The solid curve shows the broadening and spectral shift associated with a 50-J, 100-ps pulse (shot 36701).

ratio (SNR) at each point (the average over the column) is just the average divided by the standard deviation times the square root of the number of points averaged.¹⁶ In a single image there are 35,910 individual measurements of the SNR. Figure 101.52 is a plot of the SNR as a function of the average signal in CCD_ADU. This data was taken with SSD on and a 20- μm slit. The peak SNR is 100 at an average signal of 300 ADU. Typical SSD spectra can be characterized as a flattop at 80% of the peak and a peak-to-valley modulation of 40% of the peak value. Over this range, most of the spectra have an SNR of 70 to 100. The SNR drops to 1 when the average pixel value is 1.4 ADU, so the dynamic range of this instrument is about 200. The solid line in Fig. 101.52 represents the SNR if the data followed Poisson statistics. At low signal counts, the SNR falls below this line due to the read noise of the CCD.

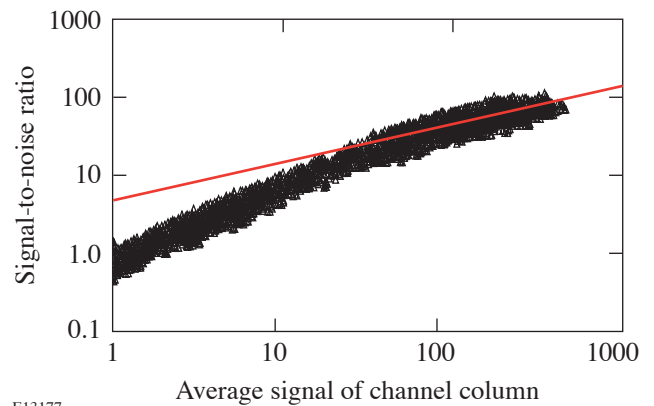


Figure 101.52
The SNR ratio for each point in the image was calculated by dividing the average CCD_ADU count in a 1-pixel-wide segment of a 100-pixel-high channel by the standard deviation of that same set of pixels times the square root of the number of pixels. These values are plotted as triangles. The solid line is the expected SNR of data following Poisson statistics.

A separate instrument records the energy of the UV light before it enters the fiber. The total CCD_ADU for each channel has been correlated with this number, and the ratio is constant to within 8.5%. This is the precision to which the photometric calibration can be trusted. The precision is limited by crosstalk between the channels. Decreasing the channel width will decrease the crosstalk at the expense of the SNR.

Preliminary measurements with this instrument have verified that SSD spectra vary from beam to beam. A protocol is being developed to remove this variation by adjusting the angular tuning of the frequency-tripling KDP crystals. In

addition, the instrument is being used to study the spectral broadening that occurs in the OMEGA laser system when the pulse duration is less than 100 ps. The spectral shifts are closely tied to the rise and fall times of the pulse.

This spectrometer can prove to be a useful diagnostic instrument on large multibeam ICF laser systems such as LLE's OMEGA laser, the National Ignition Facility at Lawrence Livermore National Laboratory,¹⁷ and the Le MegaJoule Laser in France,¹⁸ where the bandwidth is deliberately added to the laser spectrum for spatial smoothing or for suppression of nonlinear processes such as stimulated Brillouin scattering. The spectrometer's unique design employing refractive optics makes it suitable for imaging spectroscopic applications that deal with relatively narrow spectroscopic ranges such as laser line broadening or for resolving a specific atomic transition.

ACKNOWLEDGMENT

This work was supported by the U.S. Department of Energy Office of Inertial Confinement Fusion under Cooperative Agreement No. DE-FC52-92SF19460, the University of Rochester, and the New York State Energy Research and Development Authority. The support of DOE does not constitute an endorsement by DOE of the views expressed in this article.

REFERENCES

1. T. R. Boehly, D. L. Brown, R. S. Craxton, R. L. Keck, J. P. Knauer, J. H. Kelly, T. J. Kessler, S. A. Kumpan, S. J. Loucks, S. A. Letzring, F. J. Marshall, R. L. McCrory, S. F. B. Morse, W. Seka, J. M. Soures, and C. P. Verdon, *Opt. Commun.* **133**, 495 (1997).
2. F. J. Marshall, J. A. Delettrez, R. Epstein, R. Forties, R. L. Keck, J. H. Kelly, P. W. McKenty, S. P. Regan, and L. J. Waxer, *Phys. Plasmas* **11**, 251 (2004).
3. M. D. Skeldon, *Rev. Sci. Instrum.* **71**, 3559 (2000).
4. S. Skupsky, R. W. Short, T. Kessler, R. S. Craxton, S. Letzring, and J. M. Soures, *J. Appl. Phys.* **66**, 3456 (1989).
5. R. S. Craxton, *Opt. Commun.* **34**, 474 (1980).
6. A. Babushkin, R. S. Craxton, S. Oskoui, M. J. Guardalben, R. L. Keck, and W. Seka, *Opt. Lett.* **23**, 927 (1998).
7. Y. R. Shen, *The Principles of Nonlinear Optics* (Wiley, New York, 1984), pp. 324–329.
8. Polymicro Technologies, Polymicro FVP 300 330 370, 2003, <http://www.polymicro.com> (4 August 2004).
9. J. P. Knauer, E. Pasch, G. Kühner, and the W7-AS Team, *Rev. Sci. Instrum.* **74**, 1679 (2003).
10. *OSLO User's Guide*, Version 5 (Sinclair Optics, Pittsford, NY 14534, 1996) (<http://www.sinopt.com>).
11. Spectral Instruments, Tucson, AZ 85745 (see <http://www.specinst.com/files/datasheets/4204-.pdf>).
12. e2v technologies, Elmsford, NY 10523-1482 (see <http://e2vtechnologies.com>).
13. T. Han *et al.*, *Rev. Sci. Instrum.* **74**, 2973 (2003).
14. NIST Atomic Spectra Database, NIST Standard Reference Database #78, 1999, http://physics.nist.gov/cgi-bin/AtData/main_asd (4 August 2004).
15. M. Born and E. Wolf, *Principles of Optics: Electromagnetic Theory of Propagation, Interference and Diffraction of Light*, 6th ed. (Pergamon Press, Oxford, 1980), p. 436.
16. W. R. Donaldson, R. Boni, R. L. Keck, and P. A. Jaanimagi, *Rev. Sci. Instrum.* **73**, 2606 (2002).
17. E. I. Moses *et al.*, in *Optical Engineering at the Lawrence Livermore National Laboratory*, edited by T. T. Saito and M. A. Lane (SPIE, Bellingham, WA, 2003), Vol. 5001, pp. 1–15.
18. G. Thiell *et al.*, *Fusion Sci. Technol.* **43**, 478 (2003).

Quantum Efficiency and Noise-Equivalent Power of Nanostructured, NbN, Single-Photon Detectors in the Wavelength Range from Visible to Infrared

Introduction

Single-photon-detection schemes based on sensitive and ultrafast optical quantum detectors gain their dominance in various single-photonics applications. The development of superconducting single-photon detectors (SSPD's), based on ultrathin, submicron-width NbN structures has already been reported.¹⁻⁴ SSPD's are ultrafast and sensitive for ultraviolet, visible, and infrared (IR) photons. They exhibit very low dark counts and require no active or passive quenching. As recently demonstrated, SSPD's exhibit real-time counting rates of above 2 GHz and a <20-ps timing jitter.^{5,6} The SSPD operation principle has been introduced within a phenomenological hot-electron photoresponse model.^{1,7} In this article, the results of our research on the latest generation of SSPD's are presented, including their quantum efficiency (QE) and the noise-equivalent power (NEP) in the wavelength range between 0.5 and 5.6 μm , and their dependencies on an operating temperature in the 2.0- to 4.2-K range. The main emphasis is on the very low-temperature (2.0-K) performance of our SSPD's.

Device Fabrication

NbN superconducting films used for the fabrication of SSPD's had a thickness of 4.0 nm and were deposited on sapphire substrates by dc reactive magnetron sputtering in an Ar and N₂ gas mixture. The films were characterized by a surface resistance $R_S = 500 \Omega/\text{square}$, a critical temperature $T_C = 10$ to 11 K, a superconducting transition width $\Delta T_C \sim 0.3$ K, and a critical current density $j_c = 6$ to $7 \times 10^6 \text{ A}/\text{cm}^2$ at 4.2 K. During our deposition process, the sapphire substrate with *c*-cut crystalline orientation was heated up to 900°C, leading to an epitaxial growth of the NbN thin film. Our detectors had a meander-type geometry that covered a $10 \times 10\text{-}\mu\text{m}^2$ area and had a filling factor (the ratio of the area occupied by the superconducting meander to the device nominal area) of up to 0.5. The width of the superconducting stripe was typically 100 to 120 nm, but it could be as low as 80 nm. The devices were fabricated using the process based on direct electron-beam lithography and reactive ion etching.

A detailed description of our technological operations was presented in a recent publication.⁸ During the electron-beam lithography process, the areas under which the superconductor was removed were exposed in the resist. The minimal width of the superconducting stripe did not depend directly on the electron-beam diameter; rather, it was largely determined by the electron scattering in the photoresist. The resist PMMA 950 K was used and later removed from the superconductor using the reactive ion-etching process. The choice of the 80-nm resist thickness ensured a reliable protection of the superconducting film. Significant reductions of resist thickness allowed us to fabricate meanders with a filling factor of up to 0.5 and superconducting stripes as narrow as 80 nm (Fig. 101.53).

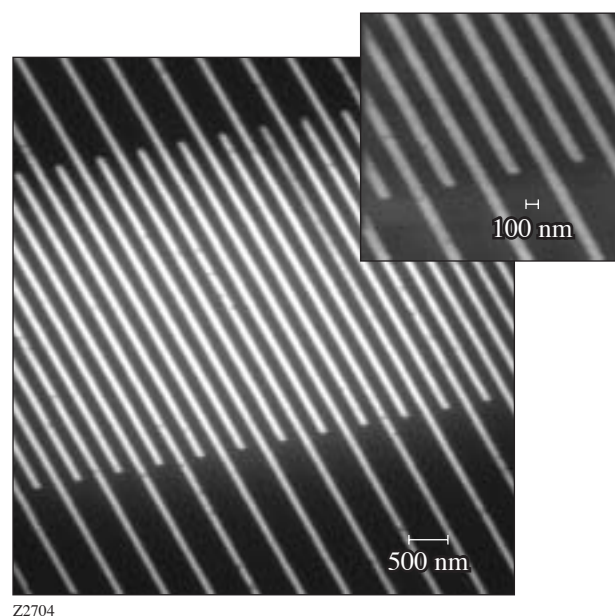


Figure 101.53 SEM (scanning electron microscope) image of an SSPD (NbN is black). The inset shows the meander structure in detail.

To test the impact of the NbN film processing on its superconducting properties, the temperature dependence of the resistance of the patterned SSPD was measured and compared to the original NbN film. The T_c and ΔT_c of the reactive ion-etched devices and the original films were practically the same within 0.1-K accuracy. This latter fact proves the optimal character of our technological process since no negative impact on the NbN SSPD was observed. In addition, it confirmed the very high quality of our initial, ultrathin NbN films.

Experimental Setup

A schematic diagram of our experimental setup is shown in Fig. 101.54. The SSPD was wire-bonded to a coplanar transmission line and then connected to a very stable, constant-voltage bias source and the output circuitry through a coaxial cryogenic bias-tee. The constant-voltage operation regime ensured a rapid return to the superconducting state after the photon detection of the SSPD and prevented self-heating of the device. The entire assembly was placed on a cold plate, inside an optical cryostat. The SSPD voltage response was amplified by a room-temperature, 40-dB-gain, 1- to 2-GHz-bandwidth amplifier and then fed to a pulse counter for statistical analysis.

Light sources consisted of a set of continuous-wave (cw) laser diodes covering the range from 0.56 μm to 1.55 μm and pulsed laser diodes delivering 40- to 60-ps-wide pulses at a repetition rate of 1 to 103 kHz at 637-nm, 845-nm, and 1554-nm wavelengths. A grating monochromator for generating IR (1- to 5.6- μm -wavelength) radiation was also used.

Photons from the lasers were delivered to the detector either by propagating in free space or by an optical fiber. In each case, the input radiation was focused and attenuated down to the picowatt power level or below. Sapphire input windows were used for measurements in the 0.6- to 3.0- μm -wavelength range and silicon windows for measurements in the 1.2- to 5.6- μm -wavelength range. Cold sapphire or silicon filters were placed inside the cryostat to cut parasitic room-temperature background radiation.

Experimental Results and Discussion

QE is defined as the ratio of the detection events registered by the counter N_{reg} to the number of incident photons N_{inc} for a given time interval per the device area:

$$QE = N_{\text{reg}} / N_{\text{inc}} \cdot \tag{1}$$

In cw measurements, the N_{inc} value was determined from the power incident on the device’s nominal active area of 100 μm^2 measured by a power meter. The power of our laser sources was always measured separately by calibrated optical attenuators. In experiments with pulsed sources, experimental QE was simply the probability of photon counting, measured at the one-photon-per-pulse level, incident upon the SSPD nominal area and expressed in percent.

Figure 101.55 shows that our most recent advances in SSPD fabrication technology led to the greatly improved stripe uniformity and resulted in significant QE enhancement.

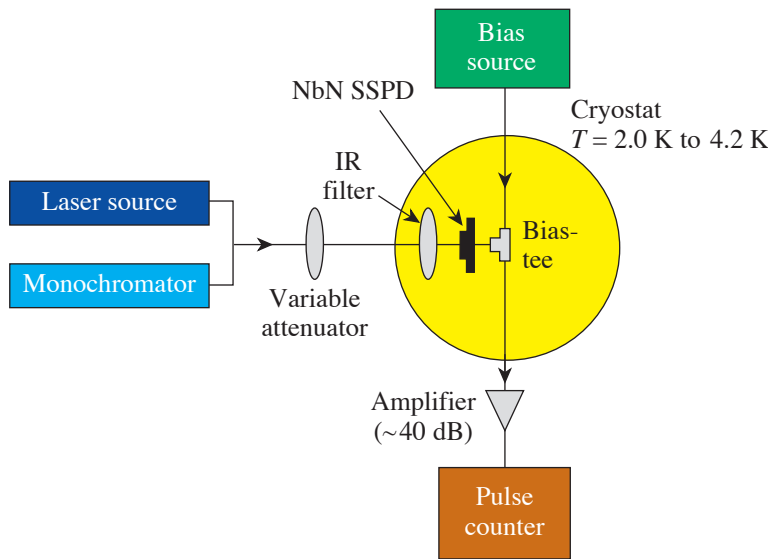


Figure 101.54
Experimental setup.

Z2582a

Figure 101.55 presents the QE's dependence on normalized bias current I_b/I_c at two different operating temperatures. At 4.2 K, QE for visible-light photons reaches an ~30% value. One can also note in Fig. 101.55 an evidence of QE saturation at the 0.56- μm wavelength at 4.2 K. The saturation-like behavior is, however, more obvious looking at the 2-K, 0.56- μm data. Furthermore, for visible light, the decrease in operating temperature below 4.2 K led to no improvement in QE; therefore, the observed saturation means that in the visible range, our SSPD detects every photon absorbed by the superconducting NbN film.

From an application point of view, the telecommunication 1.3- μm and 1.55- μm wavelengths are the most interesting. The QE at these wavelengths at 2 K is also presented in Fig. 101.55. One can see that at 1.3 μm , the QE reaches 30% saturation value, while at 1.55 μm , the maximum QE is 17%. At 4.2 K, the QE for IR light is quite far from saturation. For example, the maximum QE at 1.55 μm at 4.2 K is only 3.7% and only for I_b approaching I_c (Fig. 101.55).

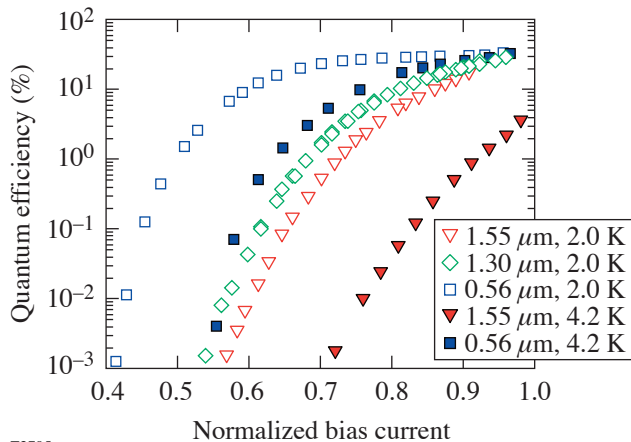


Figure 101.55
Quantum efficiency measured at different wavelengths at 4.2-K and 2.0-K operating temperatures.

Figure 101.56 presents the dark-count rate R versus I_b/I_c . R is determined as a number of spurious counts per second when the SSPD input is completely blocked by a cold metal shield inside the cryostat. Without the shield or cold filter, e.g., when the device was directly connected to the fiber, the SSPD was exposed to 300-K background radiation, which manifested itself as extrinsic dark counts. The $R(I_b)$ dependence

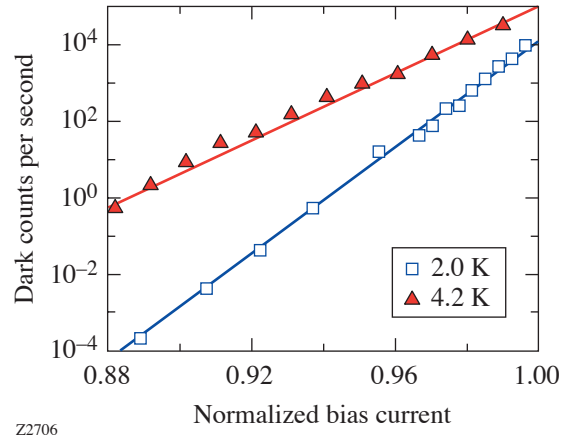


Figure 101.56
SSPD dark counts as a function of the normalized bias current measured at 4.2 K and 2.0 K.

demonstrates the activation law in the whole biasing range used in our experiments ($0.87 < I_b/I_c < 0.99$):

$$R = a \times \exp\left(b \frac{I_b}{I_c}\right), \quad (2)$$

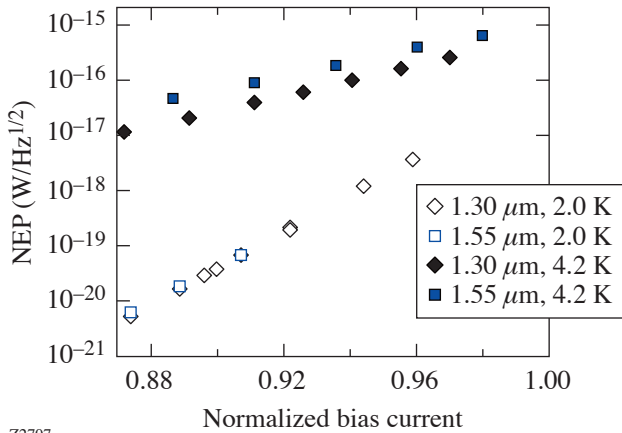
where a and b are constants. The activation-type behavior of $R(I_b)$ extends up to over seven orders of magnitude. The minimum measured R was as low as $2 \times 10^{-4} \text{ s}^{-1}$ and was limited by the duration of the experiment, i.e., accumulating several dark counts took about 8 h.

An optimal operation regime of the SSPD is a trade-off between QE and R . The maximum value of QE corresponds to rather high ($\sim 1000 \text{ s}^{-1}$ or above) R . Quantitatively this interplay between QE and R can be presented in terms of the noise-equivalent power (NEP), which can be defined for quantum detectors as

$$\text{NEP} = \frac{h\nu}{\text{QE}} \sqrt{2R}, \quad (3)$$

where $h\nu$ is photon energy. The open symbols in Fig. 101.57 show the results of the NEP calculation using Eq. (3) and experimentally measured QE (Fig. 101.55) at 1.3 μm and 1.55 μm and R (Fig. 101.56) values. Only the lowest points at 2.0 K (for $I_b/I_c < 0.88$) were calculated using extrapolated values of R .

As one can see, at 2.0 K for photons at the telecommunication wavelengths, our SSPD's exhibit QE > 10% and simultaneously reach an NEP level as low as 5×10^{-21} W/Hz^{1/2}. To our knowledge, this is the best performance for any currently available single-photon detector.



Z2707

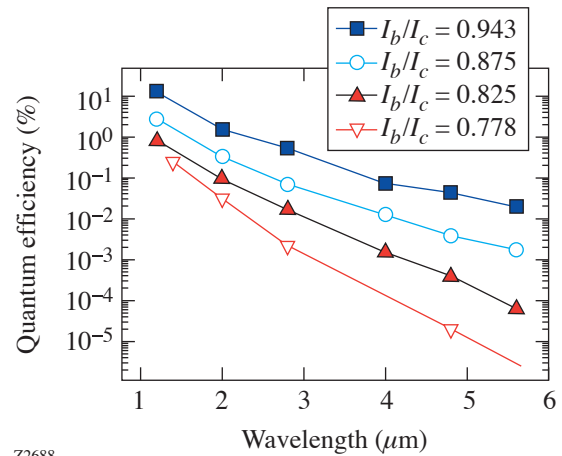
Figure 101.57

The SSPD NEP at 4.2 K (closed symbols) and 2.0 K (open symbols), calculated for 1.30 μm (diamonds) and 1.55 μm (squares) using the experimental R and QE values from Figs. 101.55 and 101.56, respectively.

The spectral characteristics of the NbN SSPD's using radiation from the monochromator (see Fig. 101.54) have been investigated in the IR 0.9- to 5.6- μm -wavelength range at different operating temperatures (2.9 to 4.3 K) and bias currents. In our best devices, single-photon counting was observed up to 5.6- μm wavelength. Figure 101.58 shows that the spectral sensitivity has exponential character and strongly depends on I_b . The highest detection probabilities are measured for I_b values very close to I_c . The decrease in operating temperature for a given I_b/I_c improves QE and also extends the SSPD's single-photon-counting capabilities farther into the IR wavelength range.

Conclusions

The performance of our latest-generation SSPD's tested at 2.0 K has been presented. The very low-temperature operation extends the single-photon-counting capabilities of our detectors to 5.6- μm IR wavelength. Simultaneously, at 2 K, the QE of our devices reached $\sim 30\%$ saturation, which corresponds to the photon absorption in a 4-nm-thick NbN film. Finally, the 2-K temperature environment resulted in a drastic (over two orders of magnitude as compared to the 4.2-K opera-



Z2688

Figure 101.58

QE spectral dependencies, measured for a NbN SSPD at 3 K at different bias currents ($I_c = 29.7$ at 3 K). Solid lines are guides for the eye.

tion) decrease in the detector dark counts. The QE increase and the R decrease led to NEP values at 2 K as low as 5×10^{-21} W/Hz^{1/2} at the IR wavelength.

The demonstrated SSPD performance at 2 K shows that in the IR range, the SSPD's significantly outperform the best semiconductor devices and photomultiplier tubes. The SSPD's have already found practical applications for the debugging of very large-scale, integrated Si complementary metal-oxide-semiconductor circuits,⁹ and they are of great interest in other areas, such as single-molecule fluorescence and high-resolution astronomy.

For applications in the areas of fiber-based and fiberless (free-space) optical quantum communications, quantum metrology, quantum key distribution, and linear optical quantum computation, it is interesting to compare the NbN SSPD with its superconducting counterparts. The other superconducting radiation detectors,¹⁰ such as superconducting tunnel junctions (STJ)¹¹ and superconducting transition edge sensors (STES),¹² exhibit a very slow (kHz-range) photoresponse speed, and their jitter in the photon-counting mode is difficult to determine. The fundamental reason for the slow speed of these detectors is that they are bolometric (thermometer-like) devices based on superconductors with very low (below 1 K) T_c , which is dictated by the desire to reach the lowest-possible intrinsic noise levels and NEP; therefore, STJ's and STES's are not optimal for very high-speed quantum communication. The

STES's, however, are photon-number-resolving devices with very high (>80%) QE values, which makes them very attractive for quantum metrology and optical quantum computations.¹³

ACKNOWLEDGMENT

This work was funded by RFBR grant 03-02-17697 (Moscow), CRDF grant RE2-2529-MO-03 (Moscow and Rochester), and US AFOSR grant FA9550-04-1-0123 (Rochester). Additional support was provided by a MIT Lincoln Laboratory grant.

REFERENCES

1. G. N. Gol'tsman, O. Okunev, G. Chulkova, A. Lipatov, A. Semenov, K. Smirnov, B. Voronov, A. Dzardanov, C. Williams, and R. Sobolewski, *Appl. Phys. Lett.* **79**, 705 (2001).
2. A. Verevkin, J. Zhang, R. Sobolewski, A. Lipatov, O. Okunev, G. Chulkova, A. Korneev, K. Smirnov, G. N. Gol'tsman, and A. Semenov, *Appl. Phys. Lett.* **80**, 4687 (2002).
3. R. Sobolewski, A. Verevkin, G. N. Gol'tsman, A. Lipatov, and K. Wilsher, *IEEE Trans. Appl. Supercond.* **13**, 1151 (2003).
4. J. Zhang, W. Slysz, A. Verevkin, O. Okunev, G. Chulkova, A. Korneev, A. Lipatov, G. N. Gol'tsman, and R. Sobolewski, *IEEE Trans. Appl. Supercond.* **13**, 180 (2003).
5. A. Verevkin, A. Pearlman, W. Slysz, J. Zhang, M. Currie, A. Korneev, G. Chulkova, O. Okunev, P. Kouminov, K. Smirnov, B. Voronov, G. N. Gol'tsman, and R. Sobolewski, *J. Mod. Opt.* **51**, 1447 (2004).
6. A. Korneev, P. Kouminov, V. Matvienko, G. Chulkova, K. Smirnov, B. Voronov, G. N. Gol'tsman, M. Currie, W. Lo, K. Wilsher, J. Zhang, W. Slysz, A. Pearlman, A. Verevkin, and R. Sobolewski, *Appl. Phys. Lett.* **84**, 5338 (2004).
7. A. D. Semenov, G. N. Gol'tsman, and A. A. Korneev, *Physica C* **351**, 349 (2001).
8. G. N. Gol'tsman, K. Smirnov, P. Kouminov, B. Voronov, N. Kaurova, V. Drakinsky, J. Zhang, A. Verevkin, and R. Sobolewski, *IEEE Trans. Appl. Supercond.* **13**, 192 (2003).
9. J. Zhang, N. Boiadjieva, G. Chulkova, H. Deslandes, G. N. Gol'tsman, A. Korneev, P. Kouminov, M. Leibowitz, W. Lo, R. Malinsky, O. Okunev, A. Pearlman, W. SByz, K. Smirnov, C. Tsao, A. Verevkin, B. Voronov, K. Wilsher, and R. Sobolewski, *Electron. Lett.* **39**, 1086 (2003).
10. A. D. Semenov, G. N. Gol'tsman, and R. Sobolewski, *Supercond. Sci. Technol.* **15**, R1 (2002).
11. J. H. J. de Bruijne *et al.*, *Opt. Eng.* **41**, 1158 (2002).
12. B. Cabrera *et al.*, *Appl. Phys. Lett.* **73**, 735 (1998).
13. A. J. Miller *et al.*, *Appl. Phys. Lett.* **83**, 791 (2003).

Measurement of Preheat due to Fast Electrons in Laser Implosions of Cryogenic Deuterium Targets

Introduction

The fraction of the incident laser energy that is deposited by energetic electrons as preheat in the cryogenic fuel of imploded spherical targets has been measured for the first time. Preheat due to fast electrons has long been identified as a contributing factor in performance degradation in laser-imploded fusion targets.¹ Fast-electron preheat reduces the fuel compressibility, thereby reducing the ignition margin. Theoretical designs for direct-drive fusion experiments on the National Ignition Facility (NIF)² use shock preheat to control the isentrope of the ablation surface and the fuel by varying the incident laser pulse shape. However, additional preheat due to fast electrons can be detrimental to the target gain. Detailed simulations have shown that the fraction of the laser energy dumped as total preheat in the cryogenic DT fuel has to be well below 0.1% for the preheat problem to have a negligible impact on target performance.³ This fraction is the key parameter in assessing the severity of preheat and is the quantity determined in this work, based on the measured hard-x-ray (HXR) continuum on the OMEGA⁴ laser system. In an earlier work,⁵ the source of the fast electrons has been identified as the two-plasmon-decay instability, but the determination of preheat level is independent of this identification. Measuring the fast-electron preheat is particularly important because the calculation of the fast-electron source is difficult and is not included in most hydrodynamic target simulations. The present measurements of preheat in cryogenic-fuel targets on the OMEGA laser system are relevant to future high-gain direct-drive implosions on the NIF since the laser irradiation, $\sim 10^{15}$ W/cm², is similar to the design irradiance for the NIF direct-drive cryogenic targets.² Although the ablation density scale length (which affects the generation of fast electrons) is shorter than that of NIF targets, earlier experiments⁵ on planar CH targets with scale lengths comparable to those on NIF-design targets have shown the preheat fraction to be about the same as in the present spherical experiments. Furthermore, using various combinations of phase plates and laser-beam configurations on planar targets, the experiments showed⁵ that the total HXR signal scaled primarily with irradiance, not with scale length or plasma tempera-

ture. Thus, the present OMEGA preheat results can be projected to future direct-drive experiments on the NIF.

To calibrate the HXR detectors, a CH-coated molybdenum solid sphere was irradiated, and the HXR continuum and absolutely calibrated Mo-K α line were measured simultaneously. Using the relationship between these two measured quantities (through the preheat) provided a calibration of the HXR detectors. Using this calibration, we determine, first, the preheat in thick imploding CH shells filled with deuterium gas and then the preheat in cryogenic-deuterium targets. In all these cases (including the cryogenic targets) the laser interaction and, thus, the production of fast electrons occur within the outer CH layer.

The preheat level is determined directly from the measured spectrum of the hard x rays. The only required parameters are the total hard-x-ray energy and the fast-electron temperature, both obtained from the measured spectrum. This determination bypasses the need to know the trajectories or dynamics of the fast electrons: for each fast electron interacting with the target, there is a direct ratio between the cross section for slowing down collisions (which constitute preheat) and the cross section to emit continuum or K α radiation. Thus, the observed radiation (of either kind) leads directly to the preheat level. These assertions are strongly supported by the transport simulation results shown below.

Preheat in Thick CH Shells

The HXR signal for a series of deuterium-gas-filled, thick CH shells as a function of laser irradiance has been published,⁵ but without a determination of the preheat level. The CH shells were 27 μm thick, 900 to 1100 μm in diameter, and filled with 20 atm of deuterium gas. They were irradiated with 60 beams at 351-nm wavelength, of 1-ns square pulse, and irradiance in the range of 6 to 9×10^{14} W/cm². The beam parameters specified here were also used for the molybdenum and the cryogenic targets described below. In the case of thick CH shells, the fast electrons interact mostly with cold CH. The

slowing down and radiation by electrons passing through the deuterium fill gas is negligible. We simulate the transport of fast electrons and emission of bremsstrahlung radiation within the CH by a multigroup transport code⁶ that assumes the initial electron energy distribution function to be Maxwellian (this assumption is based on 2-D simulations of the two-plasmon-decay instability⁷). The number of fast electrons is immaterial for the calculation of the ratio of preheat to x-ray emission. The collisions causing the slowing down are calculated from the stopping-power and range tables of the National Institute of Standards and Technology (NIST),⁸ which are based on Bethe's dE/dx formula⁹ and the density correction of Sternheimer.¹⁰ The energy loss rate due to bremsstrahlung is given by the Heitler relativistic formula.¹¹

Figure 101.59 shows the results of these calculations. The curve marked "transport" is the result of transporting the multigroup distribution of initial temperature T through the total CH shell thickness. The curve marked " dE/dx ratio" is the ratio of the energy-loss rates for slowing-down collisions and for bremsstrahlung emission of electrons of a single energy E . The major factor determining the shape of these curves (and their differences) is the fact that the slowing-down rate is approximately proportional to $1/E$. The two curves differ in two

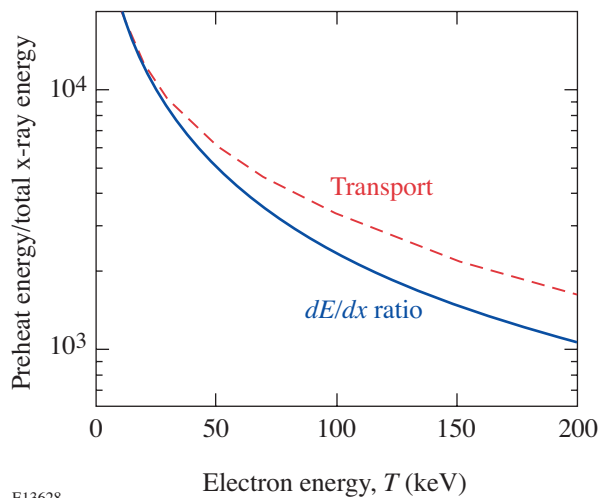


Figure 101.59
Calculated ratio of preheat energy to total hard-x-ray energy for CH shells. The curve marked "transport" is the result of multigroup fast-electron transport through the 27- μm -thick shell, for an initially Maxwellian distribution of temperature T . The curve marked " dE/dx ratio" is the ratio of the energy-loss rates for stopping-power collisions and for bremsstrahlung emission for electrons of a single energy E . The abscissa values for the two curves refer to fast-electron temperature (for the transport curve) and electron energy (for the dE/dx -ratio curve).

respects: the transport curve is the result of integration over the thickness of the target and it refers to an initially Maxwellian energy distribution, whereas the dE/dx curve refers to the local rates and to a single energy. At the limit of very high temperature, where transport is unimportant, the second factor dominates: since in a Maxwellian energy spectrum there are more electrons below the energy $E = T$ (where the slowing-down rate is higher) than above it, the preheat for the transport curve is higher than for the dE/dx -ratio curve. For lower temperatures the same effect dominates only in a thin layer below the target surface; farther in, more and more of the slow electrons lose all their energy and the distribution is left with only higher-energy electrons, for which the slowing-down rate is lower.

The purpose of comparing the two curves in Fig. 101.59 is to show that the role of scattering (which was neglected here) is relatively unimportant for the calculation of the ratio of preheat to x-ray emission. Thus, the dE/dx ratio can be viewed as the result of transport in the limit of a very thin shell for which scattering is negligible. The inclusion of scattering in the transport, by extending the electron paths, would increase both the preheat and the HXR energy by the same factor. Furthermore, varying the shell thickness leaves the ratio of preheat to total HXR energy virtually unchanged, which again supports the omission of scattering. An additional confirmation of this assertion is provided by the molybdenum results below. Thus, by relating the preheat to the observed HXR signal, we bypass all questions related to the fast-electron paths. The slowing down from the NIST tables pertains to cold material. This assumption is true for most of the CH shell throughout the duration of the laser pulse. Furthermore, using a slowing-down formula for ionized material yields only slightly different results (see below). Thus, using the NIST tables for the total CH shell is adequate. The transport curve in Fig. 101.59 is used to determine the preheat fraction for the imploding CH shells. The fast-electron temperature for each target shot was determined from the slope of the HXR spectrum;⁵ for the narrow range of laser irradiance $I \sim 6$ to 9×10^{14} W/cm², the fast-electron temperature changes in the range of 60 to 80 keV. The temperature was determined⁵ with a precision of $\pm 15\%$, which translates to a precision of about $\pm 10\%$ in the preheat fraction in this temperature range.

To determine the preheat energy, the HXR energy must be measured absolutely. To that end, we irradiated a CH-coated molybdenum solid sphere where the preheat was measured simultaneously through the HXR continuum and the (absolutely calibrated) Mo-K α line. Most of the HXR emission

(and all the $K\alpha$ emission) comes from the molybdenum. Molybdenum was chosen to minimize the contribution of thermal x rays to the excitation of the $K\alpha$ line. Previous experiments on planar targets⁶ with $K\alpha$ lines of energy around 5 keV showed that the contribution of radiation to the production of $K\alpha$ lines was comparable to that of fast electrons (in all cases the laser interacts only with the CH coating). To differentiate between the two contributions, dual-element (V and Ti) targets were used, and the $K\alpha$ lines were observed from both sides of the target. Since that solution is not available with spherical targets, we chose a much-higher- Z element. Only radiation above the Mo-K edge, at 20 keV, can contribute to the excitation of the Mo- $K\alpha$ line. At that energy, the thermal x-ray spectrum is several orders of magnitude lower than at 5 keV. Figure 101.60 shows a film lineout of the $K\alpha$ line of molybdenum from a CH-coated molybdenum sphere. The target consisted of a 1.07-mm-diam Mo sphere coated with 12 μm of CH and was irradiated at $7.7 \times 10^{14} \text{ W/cm}^2$. As expected, the continuum intensity underlying the $K\alpha$ line is too weak to measure. This confirms the assertion that the $K\alpha$ line is excited exclusively by fast electrons (neither can it be excited by the hard x rays, whose energy is found to be lower than that of the $K\alpha$ line).

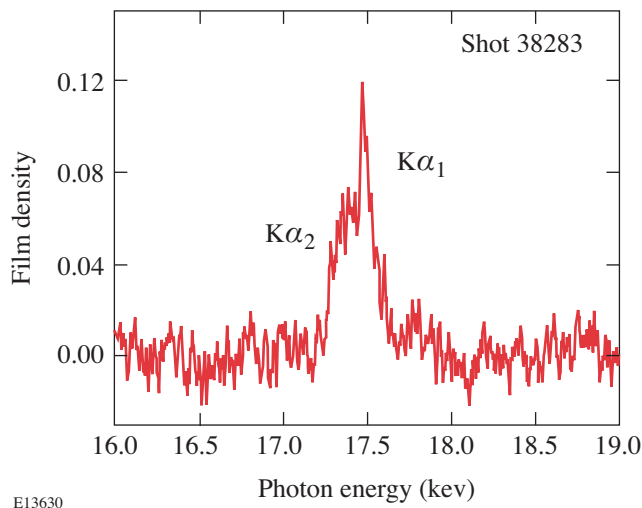


Figure 101.60
Measured $K\alpha$ line of molybdenum from CH-coated molybdenum sphere.

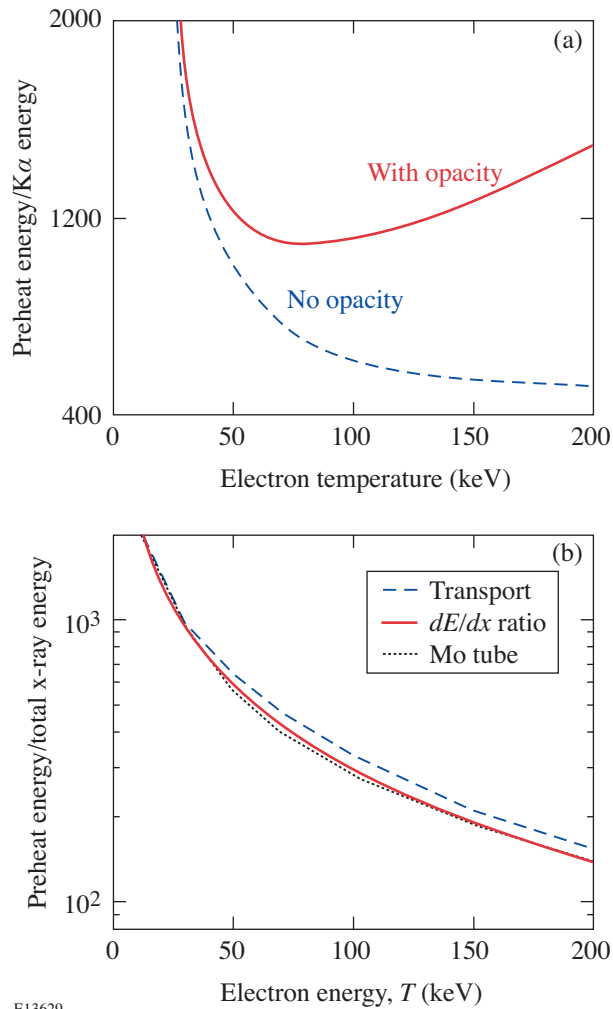
The measured $K\alpha$ line on film is converted to energy using the crystal and film calibrations. For the crystal used [polished and etched LiF (2,0,0)], our calibration¹² agrees well with the results of Toh *et al.*¹³ and Gilfrich *et al.*¹⁴ The published calibration for the Kodak direct-exposure film (DEF) was used¹⁵ with the film-processing procedure closely followed. Above the Br K edge (at 13.475 keV) the film density is almost

exactly linear with x-ray flux, which greatly simplifies the film conversion. The total energy emitted by the target in the $K\alpha$ line per unit solid angle is given by $E_l L/R$, where E_l is the energy incident on the film per unit length along the line, R is the crystal integrated reflectivity at the $K\alpha$ energy, and L is the distance from target to film along the spectral ray.

To relate the intensity of the Mo- $K\alpha$ line to the fast-electron energy, we use the multigroup code for the transport of the fast electrons with the inclusion of the rate for excitation of the $K\alpha$ line. The photoionization rate of K-shell electrons, which leads to $K\alpha$ emission, is given by the semi-empirical cross section of Powell.¹⁶ In addition, the code calculates the transport of the $K\alpha$ line emission out of the target. The results, with and without the inclusion of the $K\alpha$ opacity, are shown in Fig. 101.61(a). Using the curve marked “with opacity” and the measured $K\alpha$ emission, the preheat can be determined. The HXR emission in molybdenum is calculated in the same way as for the CH targets, and the results are shown in Fig. 101.61(b). As in Fig. 101.59, the abscissa designates electron temperature for the transport curve and electron energy for the dE/dx -ratio curve.

We can gain additional confidence in the curves of Fig. 101.61(b), and, by implication, those of Fig. 101.59, by comparing them with the known efficiency ε of an x-ray tube with a molybdenum anode. The input power that accelerates the electrons in the tube is converted mainly to heating the anode (equivalent to preheat in our case), with a small fraction converted to x rays, mostly continuum. The power P of x-ray continuum emission is given by the empirical relation¹⁷ $P = K(Z) \times Z \times I \times V^2$, where V and I are the accelerating voltage and the tube current, respectively, and K depends weakly on the atomic charge Z . Thus, the ratio of heating to radiation is $\varepsilon^{-1} = [Z \times V \times K(Z)]^{-1}$. For molybdenum, the empirical value¹⁷ of K is $\sim 0.85 \times 10^{-6} \text{ keV}^{-1}$. Plotting ε^{-1} as a function of V results in the dotted curve for the Mo tube in Fig. 101.61(b) (where the electron energy is given by V). Good agreement with the theoretical curves is seen. This provides an additional confirmation that the modeling of preheat-to-radiation ratio, in particular the neglect of scattering, is correct.

Using both Figs. 101.61(a) and 101.61(b) for the same molybdenum target shot, we derive the calibration of the HXR detector against the absolute energy of the Mo- $K\alpha$ line. The resulting calibration, in units of x-ray energy per electrical charge of the time-integrated HXR signal, is $C = 0.018 \text{ mJ/pC}$. This calibration factor depends weakly on the fast-electron temperature. To determine this dependence, we averaged the



E13629

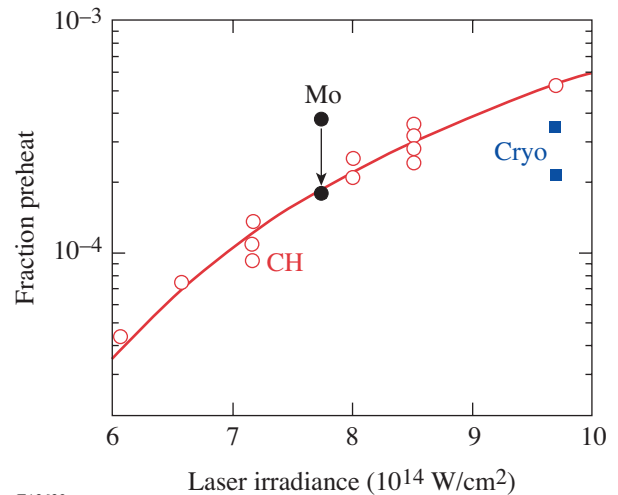
Figure 101.61

Calculations for a molybdenum target. (a) Ratio of preheat energy and emission energy in the $\text{Mo-K}\alpha$ line, calculated by a multigroup electron transport through a molybdenum sphere. The curve marked "with opacity" includes the transport of the $\text{K}\alpha$ line through the target. (b) The transport curve (dashed) and the dE/dx ratio curve (solid) are equivalent to the two curves in Fig. 101.59. The dotted curve is the inverse of the empirical x-ray efficiency of an x-ray tube with a Mo anode (the abscissa for the latter curve is given by the tube voltage).

relative detector sensitivity¹⁸ over the HXR spectrum for each temperature. The uncertainty in the calibration factor is determined by that of the $\text{K}\alpha$ energy, which is estimated to be $\pm 20\%$. This adds to the effect of temperature uncertainty discussed above to yield a total uncertainty in the preheat of $\pm 30\%$.

The final values of preheat as a fraction of the laser energy for the thick ($27\text{-}\mu\text{m}$) CH shells are shown as open circles in

Fig. 101.62. Also shown as a solid circle marked "Mo" is the preheat in the CH-coated molybdenum target. In that case, the preheat energy can be equated with the initial energy in fast electrons that travel through the target since their range is much smaller than the radius of the molybdenum sphere and almost all the incident energy is converted to preheat. This energy can also be equated with the initial energy E_{init} in fast electrons that travel through a $27\text{-}\mu\text{m}$ -thick CH shell at the same irradiance ($I_0 = 7.7 \times 10^{14} \text{ W/cm}^2$) since, in the two cases, a laser of the same irradiance and pulse shape interacts with a spherical CH layer of the same radius. For the measured fast-electron temperature at irradiance I_0 , the transport code calculates the fraction of E_{init} absorbed as preheat when an electron distribution of temperature T travels through a $27\text{-}\mu\text{m}$ -thick CH shell. The result is shown by the solid circle at the end of the arrow, and it agrees with the measured preheat for CH shells (i.e., it lies on the curve). This agreement indicates that the fast electrons traverse the shell only once, otherwise the point would lie below the curve. The possible reflection of electrons back into the target, due to a surrounding electric field, is an important factor in the study of fast-electron dynamics. The question of reflection, however, is not germane to the determination of the preheat level.



E13632

Figure 101.62

Preheat energy as a fraction of the incident laser energy deduced from the hard-x-ray measurements. Open circles: deuterium-gas-filled thick CH shells; point marked "Mo": CH-coated molybdenum sphere; solid squares: cryogenic-deuterium-filled CH shells. For the point at the end of the arrow see the text.

Preheat in Cryogenic Targets

A series of laser implosion experiments of cryogenic-deuterium targets were conducted recently and are described

in detail in Ref. 19. The preheat level for a few typical shots from this series was determined based on the HXR measured signals. The targets were $\sim 3.5\text{-}\mu\text{m}$ -thick CH shells, filled with about 1000 atm of deuterium, which upon solidification yielded $\sim 100\text{-}\mu\text{m}$ -thick solid deuterium layer on the inner surface of the CH shell. The laser energy was ~ 22.6 kJ in a 1-ns square pulse. Other details (target quality, etc.) are discussed in Ref. 19.

The determination of preheat in cryogenic targets is more involved than that for thick CH shells. First, because the cryogenic fuel is not cold, the formula for electron slowing down in a plasma rather than in a cold material must be used. Furthermore, most of the measured HXR signal is emitted by the CH layer, not the DD fuel. This is in spite of the fact that most of the electron slowing down occurs in the deuterium fuel. Therefore, to find the fraction of the HXR signal coming from the fuel, the successive transport of electrons through the CH and fuel layers is computed.

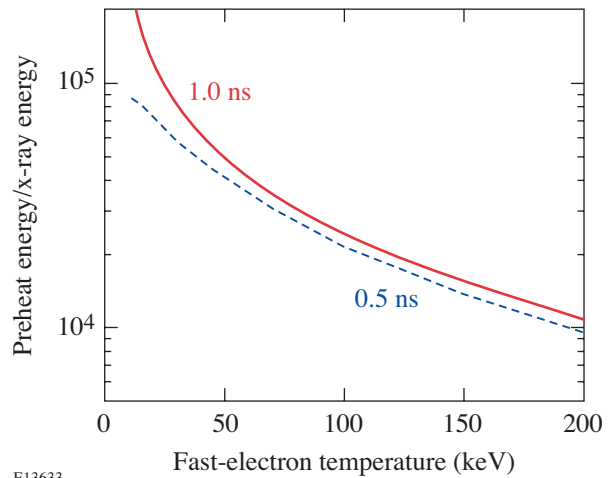
The slowing down of electrons in a plasma has two contributions: binary collisions and collective interactions (i.e., excitation of plasma waves). In the kinetic formulations of the problem, the division between the two regimes is marked by an impact parameter that is smaller or larger than the Debye length L_D . In the continuum (or dielectric) formulations of the problem, the division is marked by a density modulation wave number k that is larger or smaller than $k_D = 1/L_D$. The effect of the plasma ions is negligible for the high projectile velocities considered here.²⁰ The addition of the two electron collision terms for high projectile velocities yields²⁰

$$(-dE/dx) = (2\pi e^4 N_e / E_0) \ln(1.52 E_0 / \hbar \omega_p),$$

where the plasma frequency is given by $\omega_p = (4\pi e^2 N_e / m)^{1/2}$. The Debye length dependence has canceled out because the argument of the logarithm in the binary-collision term is $(L_D / 1.47 b_{\min})$, where b is the impact parameter, whereas in the collective-collision term it is $(1.123 V_0 / \omega_p L_D)$, where V_0 is the projectile velocity; thus, by adding the two terms, the Debye length cancels out. This is an indication that the result is independent of the degree of degeneracy, which was also shown directly by Maynard and Deutsch.²¹ The issue of using single-particle slowing-down formulas in this work was addressed in detail in the Appendix of Ref. 6; the main justification for neglecting collective effects is that the preheat is measured from HXR emission rather than deduced from the motion of the electrons that produce it. The result is very similar to the Bethe stopping-power formula⁹ with the main

difference being that the average ionization energy in the Bethe formula is replaced by $\hbar \omega_p$. For the deuterium fuel used in these experiments, the two equations yield very similar results.

The transport of electrons in these targets is calculated using the density profiles calculated by the one-dimensional (1-D) *LILAC* hydrodynamic code.²² Throughout the laser pulse, the quarter-critical density surface (the region where the fast electrons are generated) remains within the CH layer. The fraction of the total HXR signal emitted by the deuterium fuel increases slightly during the laser pulse. The time-integrated HXR emission from the fuel is $\sim 1/4$ of the total HXR signal. The transport through the fuel layer can be used to generate preheat curves similar to those of Figs. 101.59 and 101.60(b), for various assumed fast-electron temperatures. Figure 101.63 shows the energy ratio of preheat and HXR computed for two instances during the laser pulse. The ratio is seen to change very little during the laser pulse. It also changes very little if the *LILAC* density profiles are replaced by constant-density profiles of the same total mass. Thus, because the preheat and HXR depend mostly on the areal density of material traversed (in addition to the number and spectrum of the fast electrons), the results are relatively insensitive to the precision of 1-D code simulations. Finally, the resulting preheat level for two cryogenic shots is shown as solid squares in Fig. 101.62. The results for all other cryogenic targets in this series (all at about the same laser irradiance) fall within the range spanned by



E13633

Figure 101.63

Calculated ratio of preheat energy and total hard-x-ray energy in the cryogenic-deuterium fuel. The electron transport code used the electron-density profiles calculated by *LILAC*. Shown is the ratio at two instances during the 1-ns laser pulse.

these two points. The preheat in the cryogenic fuel is smaller than that in the thick CH shells mainly because the electron areal density in the former is $\sim 1/3$ smaller than that in the latter.

As seen in Fig. 101.62, the preheat fraction is well below 0.1%. This indicates that preheat in these cryogenic target implosions will have a negligible impact on target performance. Since direct-drive target designs employ some shock preheating to reduce the growth of hydrodynamic instability (by adjusting the laser pulse shape), a reduction of the designed shock heating level could compensate for the preheat due to fast electrons. As explained in the introduction, these considerations are expected to hold equally for future direct-drive experiments on the NIF.

ACKNOWLEDGMENT

This work was supported by the U.S. Department of Energy Office of Inertial Confinement Fusion under Cooperative Agreement No. DE-FC52-92SF19460, the University of Rochester, and the New York State Energy Research and Development Authority. The support of the Department of Energy (DOE) does not constitute an endorsement by DOE of the views expressed in this article.

REFERENCES

1. J. D. Lindl, *Inertial Confinement Fusion: The Quest for Ignition and Energy Gain Using Indirect Drive* (Springer-Verlag, New York, 1998), Chap. 11.
2. P. W. McKenty, V. N. Goncharov, R. P. J. Town, S. Skupsky, R. Betti, and R. L. McCrory, *Phys. Plasmas* **8**, 2315 (2001).
3. Laboratory for Laser Energetics LLE Review **79**, 121, NTIS document No. DOE/SF/19460-317 (1999). Copies may be obtained from the National Technical Information Service, Springfield, VA 22161.
4. T. R. Boehly, R. S. Craxton, T. H. Hinterman, J. H. Kelly, T. J. Kessler, S. A. Kumpan, S. A. Letzring, R. L. McCrory, S. F. B. Morse, W. Seka, S. Skupsky, J. M. Soures, and C. P. Verdon, *Rev. Sci. Instrum.* **66**, 508 (1995).
5. C. Stoeckl, R. E. Bahr, B. Yaakobi, W. Seka, S. P. Regan, R. S. Craxton, J. A. Delettrez, R. W. Short, J. Myatt, A. V. Maximov, and H. Baldis, *Phys. Rev. Lett.* **90**, 235002 (2003).
6. B. Yaakobi, C. Stoeckl, T. Boehly, D. D. Meyerhofer, and W. Seka, *Phys. Plasmas* **7**, 3714 (2000).
7. A. B. Langdon, B. F. Lasinski, and W. L. Kruer, *Phys. Rev. Lett.* **43**, 133 (1979).
8. M. J. Berger, J. S. Coursey, and M. A. Zucker, *ESTAR, PSTAR, and ASTAR: Computer Programs for Calculating Stopping-Power and Range Tables for Electrons, Protons, and Helium Ions* (version 1.2.2). [Online] Available: <http://physics.nist.gov/Star> [2005, February 25]. National Institute of Standards and Technology, Gaithersburg, MD.
9. H. Bethe, *Ann. Phys.* **5**, 325 (1930); *Z. Phys.* **76**, 293 (1932).
10. R. M. Sternheimer, *Phys. Rev.* **88**, 851 (1952).
11. W. Heitler, *The Quantum Theory of Radiation*, 2nd ed., The International Series of Monographs on Physics (Oxford University Press, London, 1947).
12. A. J. Burek and B. Yaakobi, *Final Report to the National Bureau of Standards Contract NB81NAHA2032*, Appendix A, NTIS document No. DE83015439 (1983). Copies may be ordered from the National Technical Information Service, Springfield, VA 22161.
13. K. Toh, T. Ui, and E. Asada, in *Advances in X-Ray Analysis*, edited by C. S. Barrett, P. K. Predecki, and D. E. Leyden (Plenum Press, New York, 1985), Vol. 28, pp. 119–126.
14. J. V. Gilfrich, D. B. Brown, and P. G. Burkhalter, *Appl. Spectrosc.* **29**, 322 (1975).
15. B. L. Henke, E. M. Gullikson, and J. C. Davis, *At. Data Nucl. Data Tables* **54**, 181 (1993).
16. C. J. Powell, *Rev. Mod. Phys.* **48**, 33 (1976).
17. N. A. Dyson, *X-Rays in Atomic and Nuclear Physics*, 2nd ed. (Cambridge University Press, Cambridge, England, 1990), p. 47.
18. C. Stoeckl, V. Yu. Glebov, D. D. Meyerhofer, W. Seka, B. Yaakobi, R. P. J. Town, and J. D. Zuegel, *Rev. Sci. Instrum.* **72**, 1197 (2001).
19. P. W. McKenty, T. C. Sangster, M. Alexander, R. Betti, R. S. Craxton, J. A. Delettrez, L. Elasky, R. Epstein, A. Frank, V. Yu. Glebov, V. N. Goncharov, D. R. Harding, S. Jin, J. P. Knauer, R. L. Keck, S. J. Loucks, L. D. Lund, R. L. McCrory, F. J. Marshall, D. D. Meyerhofer, S. P. Regan, P. B. Radha, S. Roberts, W. Seka, S. Skupsky, V. A. Smalyuk, J. M. Soures, K. A. Thorp, M. Wozniak, J. A. Frenje, C. K. Li, R. D. Petrasso, F. H. Séguin, K. A. Fletcher, S. Padalino, C. Freeman, N. Izumi, J. A. Koch, R. A. Lerche, M. J. Moran, T. W. Phillips, G. J. Schmid, and C. Sorce, *Phys. Plasmas* **11**, 2790 (2004).
20. J. D. Jackson, *Classical Electrodynamics* (Wiley, New York, 1962).
21. G. Maynard and C. Deutsch, *Phys. Rev. A, Gen. Phys.* **26**, 665 (1982).
22. R. Epstein, S. Skupsky, and J. Delettrez, *J. Quant. Spectrosc. Radiat. Transfer* **35**, 131 (1986).

The Saturn Target for Polar Direct Drive on the National Ignition Facility

Direct-drive illumination plays a significant role in plans to achieve ignition on the National Ignition Facility (NIF).¹ Ignition requires the uniform implosion of a fuel capsule containing a deuterium–tritium mixture with intense laser beams, using either direct laser illumination of the capsule² or indirect drive,³ in which laser beams focused into a hohlraum generate x rays to drive the capsule. The baseline NIF target chamber geometry requires that all the NIF beams be incident through 48 beam ports, known as the “indirect-drive” ports, located in rings with angles varying from 23.5° to 50° with respect to the vertical (pole). Additional beam ports near the equator, at an angle of 77.45°, allow symmetric direct-drive illumination to be accommodated at a later time by rerouting half of the beams to these ports.⁴ Considerable interest has been stimulated by the recent reconsideration^{5–8} of direct drive using the indirect-drive ports with the beams repointed toward the equator, a concept once dismissed as ineffective because of the difficulty of ensuring uniformity on the imploding critical surface⁹ and now known as polar direct drive (PDD).⁶ PDD may allow direct-drive ignition and possibly high gain to be achieved on the NIF many years earlier than would otherwise be possible.

This article reports on a new PDD target design concept that promises to improve the drive uniformity on the capsule compared with the previous (“standard PDD”) designs of Refs. 6–8. The new “Saturn” design, whose distinctive feature is a low-Z ring placed in the equatorial plane of the capsule (Fig. 102.1), is applied to the “all-DT” design of Refs. 10 and 11. The Saturn design can result in a DT shell that is imploding at the end of the laser pulse with a velocity uniform to a little over 1% (rms), close to the uniformity expected for the “symmetric” design that uses the direct-drive ports with all beams pointed to the capsule center.¹¹

The next article (“Polar Direct Drive—Proof-of-Principle Experiments on OMEGA and Prospects for Ignition on the National Ignition Facility,” which begins on p. 67) describes PDD experiments that validate both hydrodynamic PDD simulations and the Saturn concept. It also presents a simulation of the NIF Saturn design that results in high gain close to the prediction from an ideal one-dimensional calculation. These results increase the prospects of obtaining direct-drive ignition with the initial NIF configuration.

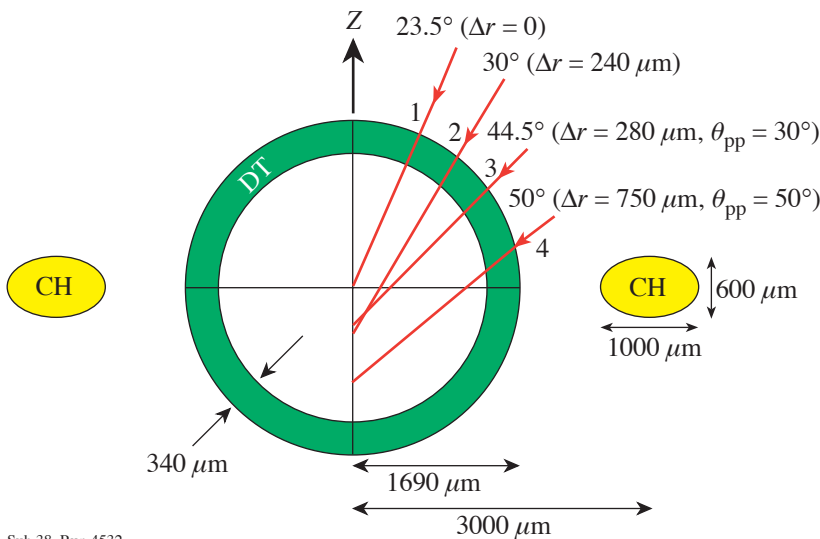


Figure 102.1
Vertical cross section of a Saturn target for direct drive on the NIF. The capsule (the “all-DT” design of Ref. 11) is a 340- μm layer of cryogenic DT supported in a thin (few- μm) plastic shell. It is irradiated using the four rings of indirect-drive ports in each hemisphere and the indicated repointings. The capsule is surrounded by a low-Z (CH) ring whose plasma provides time-dependent pointing correction for ring-4 beams.

Sub 38, Run 4532
TC6654

The primary limitation on the uniformity attainable with standard PDD arises because extra laser power needs to be focused near the equator to compensate for the oblique angle of incidence, but the radius of the critical surface (near which most absorption occurs) decreases significantly during the laser pulse. Since the NIF laser beams cannot be dynamically repointed, two methods have hitherto been proposed to minimize this effect: careful optimization of the beam pointings⁶⁻⁸ and the use of different pulse shapes for the different rings of beams.⁶ The essence of the Saturn design is that a plasma forms around the low-*Z* ring from laser rays refracted from the capsule plasma and from rays on the edges of ring-4 beams (those incident at 50° in Fig. 102.1) that clip the low-*Z* ring. The ring plasma has little impact on the capsule irradiation pattern at early times, but later expands into the path of a significant portion of ring-4 rays, deflecting them to strike the imploding critical surface near the equator. Optimum designs match the expansion of the ring plasma to the implosion of the capsule plasma.

Figure 102.1 gives the main parameters of the Saturn design. Three of the four rings of beams in each hemisphere (the lower-hemisphere beams are not shown) are repointed toward the equator with the specified distances Δr measured perpendicular to the beam axes. Rings 3 and 4 use “elliptical phase plates,” whose focal spot is shortened in the vertical direction by a factor of $\cos \theta_{pp}$. Prior to this shortening, all beams have super-Gaussian target-plane spatial shapes with the intensity proportional to $\exp-(r/r_0)^{2.5}$ with $r_0 = 1200 \mu\text{m}$. The capsule is a thick shell (340 μm) of cryogenic DT ice contained within a thin (few- μm) plastic shell of 1690- μm outer radius.¹¹ The low-*Z* ring, made of CH to minimize radiation preheat, has a major radius R_{major} of 3000 μm and an elliptical cross section. While the parameters listed in Fig. 102.1 were selected as a result of numerous two-dimensional (2-D) simulations, improvements are likely because of the large range of possible parametric variations.

The Saturn design is compared with standard PDD and symmetric designs obtained using similar optimizations and the same super-Gaussian profiles. The pointings used for standard PDD are $\Delta r = 100, 290, 380,$ and $750 \mu\text{m}$, respectively, for rings 1-4 and $\theta_{pp} = 30^\circ$ and 60° , respectively, for rings 3 and 4 (as in Ref. 8).

The target is irradiated by the incident laser temporal pulse shape taken from Ref. 11 and shown in Fig. 102.2 as the upper curve. The total incident energy is 1.53 MJ, less than the nominal total NIF energy¹ of 1.8 MJ. All beams have the same power history, maximizing the available on-target energy. The

other curves in Fig. 102.2 give the absorbed laser power for the three cases. The overall absorption for standard PDD (63%) is only slightly less than the 66% of the symmetric case because the elliptical phase plates compensate for the absorption loss of the repointed beams. The inset in Fig. 102.2 shows the elliptical 10% intensity contour (the outer ellipse) in the target plane of a ring-4 beam pointed 750 μm below the target center together with the initial and final critical surface radii. The Saturn capsule absorbs slightly more (70%), and just under half of the energy refracted from the capsule is absorbed in the CH ring (bottom curve).

The simulations reported here used the 2-D Eulerian hydrodynamics code *SAGE*, which includes fully self-consistent, 3-D laser ray tracing.¹² Each of the eight rings (four per hemisphere) is represented by a single beam whose incoming cross section is broken into a grid of ~ 1000 rays (shown schematically in the inset in Fig. 102.2). Each ray is traced through an (x,y,z) coordinate system, with z vertical, and the energy at each step is deposited by inverse bremsstrahlung onto the spherical (r,θ) simulation grid at radius $r = (x^2 + y^2)^{1/2}$. This

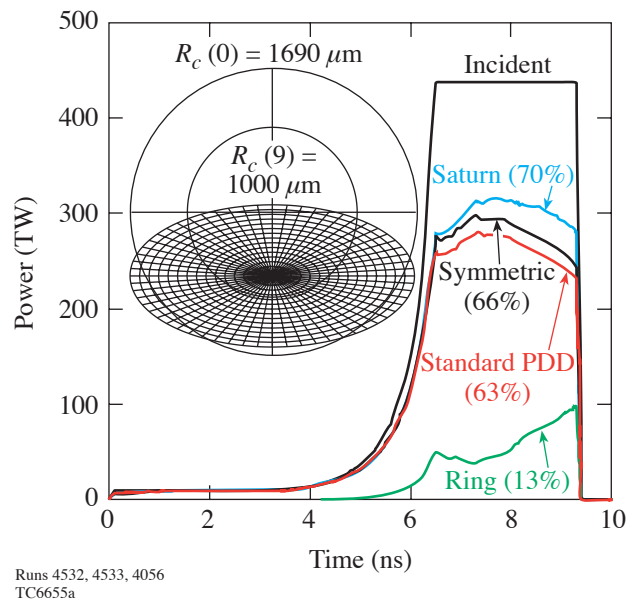


Figure 102.2 Incident and capsule-absorbed laser power as a function of time for three cases: “symmetric,” “standard PDD,” and Saturn. The bottom curve applies to the ring of the Saturn target. The time-integrated absorption fractions are given in parentheses. Inset: The critical surface of the capsule at 0 and 9 ns (radii $R_c = 1690$ and $1000 \mu\text{m}$, respectively) viewed along the axis of the ring-4 beam for the standard-PDD design, together with the elliptical far field (out to the 10% intensity contour) centered 750 μm below the target center. The grid indicates starting points for the simulation ray trace.

is equivalent to averaging the deposited energy in the azimuthal (ϕ) direction. The azimuthal variations due to the finite number of beams in each NIF ring are expected to be smaller than the variations in θ due to the PDD geometry.

Typical plots of density contours and ray trajectories [projected into the (r, θ) plane] are shown in Fig. 102.3 for the Saturn and standard-PDD cases, at 5.8 ns (close to the time that the initial shock reaches the inner DT surface) and at 9 ns

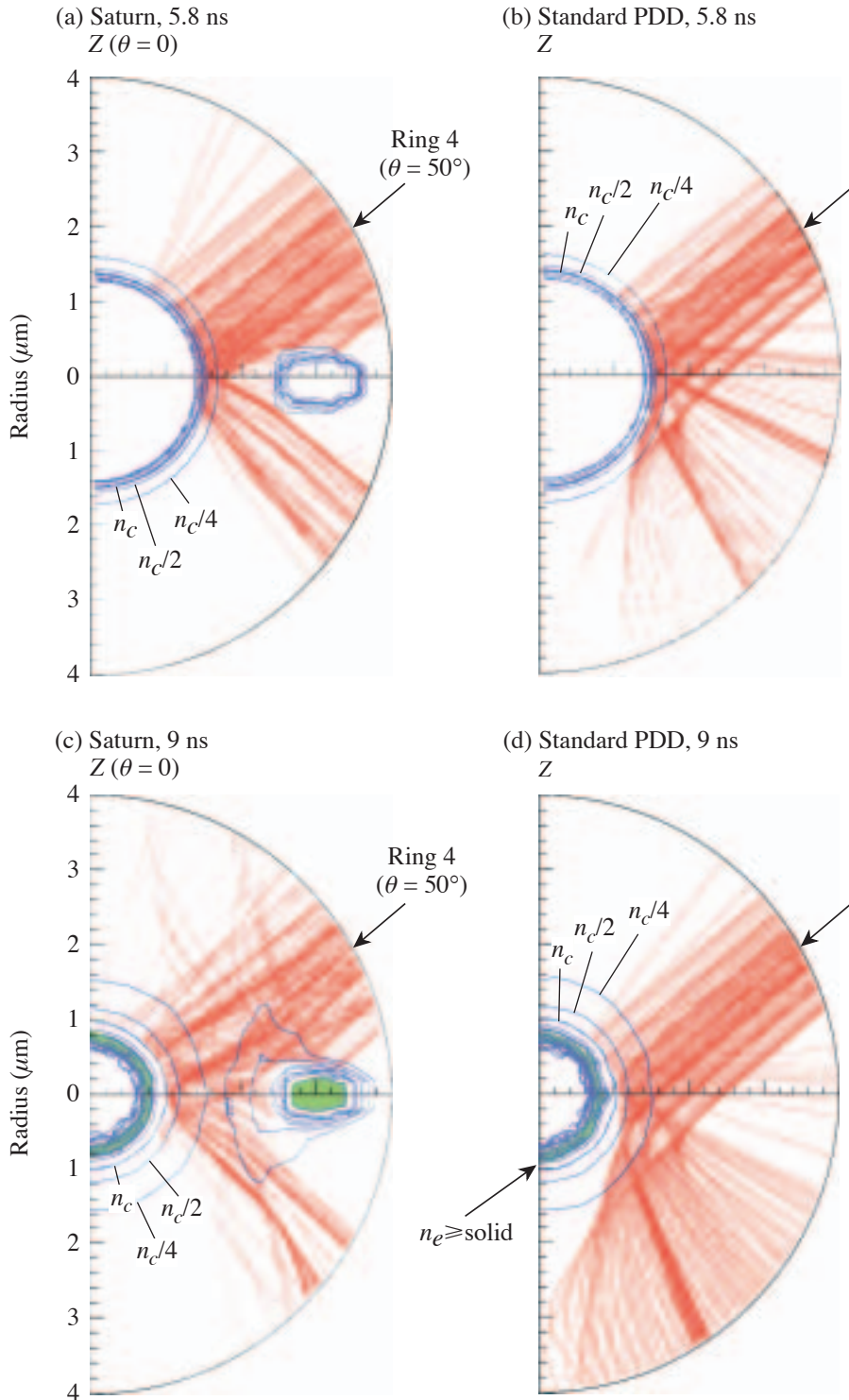


Figure 102.3
Electron-density contours (some of which are labeled as fractions of the critical electron density n_c) and a representative subset of ring-4 ray trajectories projected into the (r, z) plane for a Saturn target and a standard PDD target, at the time of shock breakout (5.8 ns) and at the end of the laser pulse (9 ns). In the Saturn design, the central group of rays refract in the ring plasma at the later time (c) toward the capsule equator. The shaded areas at 9 ns represent material above solid density.

Run 4532=4341, 4056
TC6848

(roughly the end of the laser pulse). For clarity, only a small fraction of the ring-4 rays are shown. At 5.8 ns, the plasma forming around the CH ring is not large enough to significantly deflect the central rays (marked with arrows). At 9 ns, however, significant refraction of the central group of rays toward the capsule equator is evident in the Saturn case, while these rays pass significantly below the equator in the standard-PDD case. An additional effect included in the simulations is tamping of the blowoff by the CH ring that may also enhance the pressure near the equator.

The deviations of the center-of-mass radius and radial velocity (V_r) of the imploding shell at 9 ns are shown in Fig. 102.4 for the three cases. The standard-PDD case shows significant structure, in particular a large radius and small velocity near the equator. The Saturn case reduces the rms velocity variation to 1.3%, close to the 1.0% predicted for the symmetric case. A uniform V_r is critical to a uniform implosion, and the target designs were chosen to minimize the rms of this quantity. The quoted rms values are probably upper bounds since the simulations, which should be symmetric about $\theta = 90^\circ$, include some numerical noise. The Saturn-design V_r nonuniformity is dominated by Legendre modes $\ell = 2$ and 4 (1.1% in these modes), with the other 0.2% attributable to noise. The predominantly low- ℓ content in the Saturn case provides a significant advantage compared with the standard-PDD case, as the all-DT capsule design is more tolerant of low- ℓ modes.¹¹ Figure 102.4 also shows that the DT shell in the Saturn case moves approximately the same distance and acquires the same velocity as for the symmetric target, indicating (consistently with Fig. 102.2) that there is no energy penalty associated with the Saturn design even though the laser energy, incident more obliquely, is on average absorbed farther from the critical surface.

The standard-PDD pointings provide excessive drive on the equator at early times to compensate for the reduced drive at later times. This produces increased pressure gradients and motion in the θ direction. The rms V_r is 7.2% at 5.8 ns, compared with 2.5% for Saturn, and the rms V_θ at 9 ns is 1.4×10^6 cm/s, compared with 9×10^5 cm/s ($\sim 3\%$ of V_r) for Saturn. The Saturn design thus enables slightly smaller repointings to be used for rings 1–3 to provide better early time uniformity. The simulations all used a flux limiter¹³ f of 0.06, broadly consistent with the observed absorption and drive in current OMEGA experiments.¹⁴ The parameters Δr and θ_{pp} needed to optimize the PDD designs are insensitive to f .

Some simulation results of the parametric sensitivities of the designs are shown in Fig. 102.5, which gives the rms center-of-mass radius (ΔR_{rms}) and velocity (ΔV_{rms}) variations as functions of the pointing error of the most-sensitive laser ring for all three cases and as functions of R_{major} for the Saturn design. As in Fig. 102.4, the Saturn performance is close to that of the symmetric case. The NIF single-beam pointing tolerance of $50\text{-}\mu\text{m}$ rms¹⁵ should be adequate in all cases, especially as the calculations make the pessimistic assumption that all beams in the ring are displaced in unison. Figures 102.5(c) and 102.5(d) point to an optimum R_{major} of $3100 \pm 100 \mu\text{m}$. As the ring is moved away from the capsule, ΔV_{rms} increases because fewer rays intersect the ring plasma. As the ring is moved toward the capsule, ΔV_{rms} increases dramatically due to the capsule equator becoming shadowed by the ring. Adjustment of the ring parameters provides a means for tuning the time-dependent drive symmetry of different capsule designs. Such tuning may also be required because the ring plasma, whose rate of formation depends in part on the energy near the beam edges, may evolve differently than predicted here.

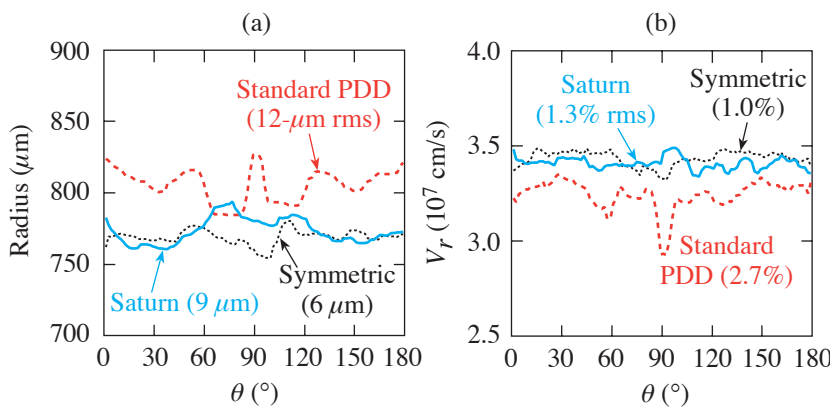


Figure 102.4
(a) Center-of-mass radius and (b) radial velocity (V_r) as a function of angle θ from the vertical for the three cases — symmetric, standard PDD, and Saturn — at the end of the laser pulse (9 ns).

Runs 4533, 4056, 4532=4341
TC6656

From other sensitivity studies, the positioning tolerances of (a) the capsule with respect to the target chamber center and (b) the CH ring with respect to the capsule in the z direction are critical: preliminary results suggest that these should each be less than $50 \mu\text{m}$, preferably by a factor of 2. Capsule-mounting schemes taking advantage of the Saturn design must provide accurate centering of the capsule within the ring.

The optimization process that led to the Saturn design started with the investigation of target-plane profiles of the form $I(r) \propto \exp-(r/r_0)^n$ for the symmetric case. Obtaining a smooth overlap of deposited energy profiles from neighboring laser rings for all critical-surface radii between the initial and final becomes hard when n increases above 2.5, as the edge of the profile steepens. For smaller n , an energy penalty results from rays near the edge of the beam missing the target. For $r_0 < 1200 \mu\text{m}$, nonuniformities result from the deposition being too localized, while for larger r_0 , the uniformity remains good but energy is lost. For the PDD designs, the same n and r_0 are used on the assumption that this will provide comparable azimuthal uniformity to the symmetric case. The values of Δr and θ_{pp} are chosen to spread the deposited laser energy as uniformly as possible around the capsule surface. The CH-ring

parameters are chosen on the basis of surveys such as shown in Fig. 102.5.

Experimental investigations of PDD on the OMEGA laser system and extended simulations of the Saturn design to examine the implosion physics beyond the end of the laser pulse are reported in the next article and in Ref. 16. Preliminary results demonstrate that the Saturn ring does indeed increase the drive on the equator. Issues for future investigation include characterization of the evolution and azimuthal symmetry of the Saturn ring plasma.

In conclusion, the Saturn concept will enable direct-drive implosions to be carried out on the NIF, using only the indirect-drive ports, with a uniformity approaching that of the symmetric configuration. A low- Z ring placed around the capsule provides time-dependent correction of critical laser ray trajectories to ensure adequate drive on the capsule equator at all times. Preliminary parameter surveys indicate that the tolerances necessary to ensure this high level of uniformity are reasonable. The prospects for an early ignition demonstration on the NIF using direct drive are thus greatly enhanced.

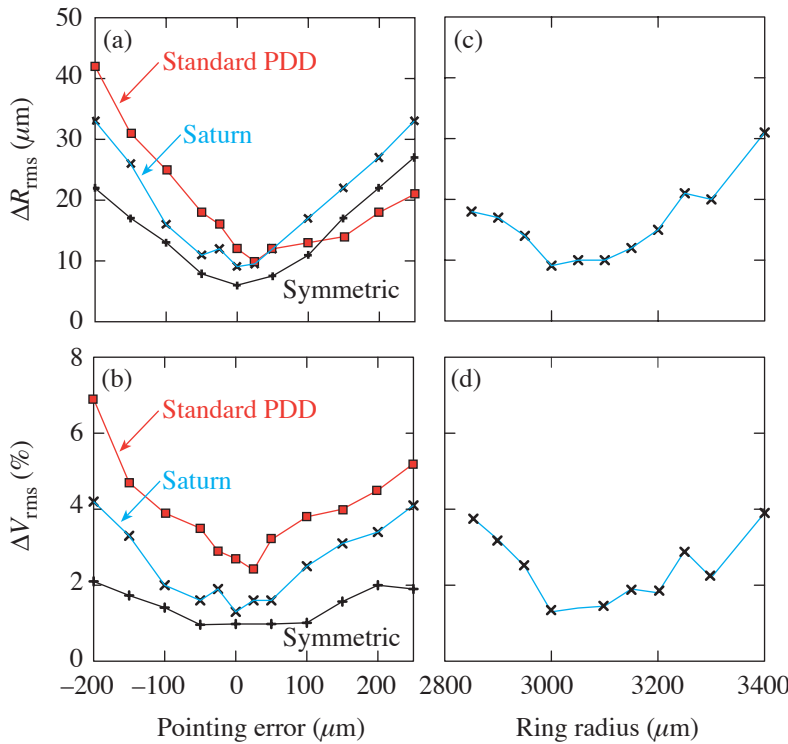


Figure 102.5
 Dependence of (a) the rms center-of-mass radius variation ΔR_{rms} and (b) the rms radial velocity variation ΔV_{rms} at 9 ns on the pointing error of the ring of beams with the greatest sensitivity (ring 2 for the symmetric case, ring 4 for the others). The same quantities are plotted against the low- Z ring's major radius in (c) and (d) for the Saturn design. Each symbol corresponds to a 2-D simulation; the thin lines serve only to guide the eye.

Sub 39
 TC6649

ACKNOWLEDGMENT

This work was supported by the U.S. Department of Energy Office of Inertial Confinement Fusion under Cooperative Agreement No. DE-FC52-92SF19460, the University of Rochester, and the New York State Energy Research and Development Authority. The support of DOE does not constitute an endorsement by DOE of the views expressed in this article.

REFERENCES

1. E. M. Campbell and W. J. Hogan, *Plasma Phys. Control. Fusion* **41**, B39 (1999).
2. J. Nuckolls *et al.*, *Nature* **239**, 139 (1972).
3. J. D. Lindl, *Inertial Confinement Fusion: The Quest for Ignition and Energy Gain Using Indirect Drive* (Springer-Verlag, New York, 1998), Chap. 6, pp. 61–82.
4. D. Eimerl, J. Rothenberg, M. Key, S. Weber, C. Verdon, S. Skupsky, J. Soures, and S. Craxton, in *First Annual International Conference on Solid State Lasers for Application to Inertial Confinement Fusion*, edited by M. André and H. T. Powell (SPIE, Bellingham, WA, 1995), Vol. 2633, pp. 170–182.
5. J. D. Kilkenny, Laboratory for Laser Energetics, private communication (2002).
6. S. Skupsky, J. A. Marozas, R. S. Craxton, R. Betti, T. J. B. Collins, J. A. Delettrez, V. N. Goncharov, P. W. McKenty, P. B. Radha, T. R. Boehly, J. P. Knauer, F. J. Marshall, D. R. Harding, J. D. Kilkenny, D. D. Meyerhofer, T. C. Sangster, and R. L. McCrory, *Phys. Plasmas* **11**, 2763 (2004).
7. R. S. Craxton, presented at the 33rd Anomalous Absorption Conference, Lake Placid, NY, 22–27 June 2003 (Paper WO3).
8. R. S. Craxton, *Bull. Am. Phys. Soc.* **48**, 56 (2003).
9. D. Eimerl, ed., Lawrence Livermore National Laboratory, Livermore, CA, UCRL-ID-120758 (1995).
10. C. P. Verdon, *Bull. Am. Phys. Soc.* **38**, 2010 (1993).
11. P. W. McKenty, V. N. Goncharov, R. P. J. Town, S. Skupsky, R. Betti, and R. L. McCrory, *Phys. Plasmas* **8**, 2315 (2001).
12. R. S. Craxton and R. L. McCrory, *J. Appl. Phys.* **56**, 108 (1984).
13. R. C. Malone, R. L. McCrory, and R. L. Morse, *Phys. Rev. Lett.* **34**, 721 (1975).
14. J. A. Delettrez, Laboratory for Laser Energetics, private communication (2004).
15. R. A. Zacharias *et al.*, in *Optical Engineering at the Lawrence Livermore National Laboratory II: The National Ignition Facility*, edited by M. A. Lane and C. R. Wuest (SPIE, Bellingham, WA, 2004), Vol. 5341, pp. 168–179.
16. R. S. Craxton, F. J. Marshall, M. Bonino, R. Epstein, P. W. McKenty, S. Skupsky, J. Delettrez, I. V. Igumenshchev, D. W. Jacobs-Perkins, J. P. Knauer, J. A. Marozas, P. B. Radha, and W. Seka, “Polar Direct Drive—Proof-of-Principle Experiments on OMEGA and Prospects for Ignition on the NIF,” to be published in *Physics of Plasmas*.

Polar Direct Drive—Proof-of-Principle Experiments on OMEGA and Prospects for Ignition on the National Ignition Facility

Introduction

This article supports the preceding article (“The Saturn Target for Polar Direct Drive on the National Ignition Facility,” p. 61) by presenting recent experimental and simulation results indicating that ignition may be feasible on the National Ignition Facility (NIF)¹ using polar direct drive (PDD).²

Since the recent suggestion³ that the PDD option be reconsidered on account of the cost and complexity of rerouting half of the NIF beams, a number of two-dimensional (2-D) hydrodynamic PDD simulations have been reported. Simulations^{4,5} of the all-DT capsule design of Refs. 6 and 7 were carried out using the hydrodynamics code *SAGE*, which includes fully self-consistent 3-D ray tracing.⁸ These simulations used sets of optimized repointings of the four rings of NIF beams and elliptical far-field focal spots for some rings to increase the drive on the capsule equator. Skupsky *et al.*² used the 2-D code *DRACO*^{9,10} to examine PDD designs for wetted-foam capsules,¹¹ which are attractive because of increased laser absorption. They concluded that PDD enhances the capability of the NIF to explore ignition conditions and found that the primary cause of gain reduction was the time-dependent drive deficit on the equator due to target compression.¹² The previous article (p. 61) describes simulations of a new “Saturn” target concept for PDD in which a low-*Z* ring is placed around the capsule in the equatorial plane. The plasma produced around the ring (by a combination of light refracted from the capsule and light directly intercepted by the ring) grows so that, at later times, laser rays that would otherwise miss the critical surface in the equatorial region of the capsule are now refracted by the ring plasma to provide stronger irradiation of this region. With appropriately chosen ring dimensions, the capsule can be driven with a uniformity (~1%) approaching that of a symmetrically driven capsule.

The success of PDD on the NIF depends, to a large extent, on the accuracy with which the drive uniformity resulting from proposed laser-beam repointings can be predicted and diagnosed. Two initial series of PDD experiments have been

carried out using the 60-beam OMEGA Laser Facility to address these issues. To approximate the NIF irradiation configuration, 40 OMEGA beams are used to irradiate the capsule, with the 20 beams near the equator omitted from the laser drive (some of these beams are used for backlighting).

The optimum repointings for the experiments were calculated on the basis of numerous 2-D *SAGE* simulations for different combinations of these parameters. In every case, the drive was found to be too low on the equator. The optimum repointings minimized the overall rms nonuniformity in the center-of-mass velocity of the imploding shell at the end of the laser pulse, producing a predicted $\ell = 4$ pattern with the drive low at both the equator and the poles. Both experimental series showed this $\ell = 4$ pattern with the predicted amplitude, confirming the simulations as well as the pointing accuracy and reproducibility of the OMEGA system.

The low drive on the equator can be understood as follows: Since the central portion of the OMEGA on-target beam profile is fairly flat, the intensity incident from a beam with the largest angle (59°) to the vertical is larger at the point on the capsule ($\theta = 59^\circ$) irradiated at normal incidence than at the equator, which sees a flux reduced by $\cos(31^\circ)$. Two other factors further reduce the equatorial drive: (a) the absorption falls off as the angle of incidence increases, and (b) once a plasma has formed around the capsule, the energy deposited from obliquely incident rays is spread over a curved path. To provide compensation for all of these factors, the beams aimed at the equator would need more tightly focused spatial profiles (as proposed for the NIF^{4,5}).

In the second series of experiments, three Saturn targets were imploded on OMEGA. For these targets, the framed x-ray backlighting results showed a clear $\ell = 2$ drive nonuniformity, with an enhanced drive at the equator that was greater than predicted. These results are very encouraging and suggest that it should be possible to move some of the beam pointings back toward the poles to remove the $\ell = 2$ mode.

This article begins with a description of the initial PDD experiments on OMEGA and their associated modeling. One novel aspect of this modeling is the use of *SAGE*-calculated velocity perturbations at the end of the laser pulse to perturb 2-D *DRACO* simulations that are symmetric until this time. This combines the *SAGE* ray-tracing capability with the burn physics and better implosion hydrodynamics in *DRACO*. These initial experiments are known as “standard-PDD” experiments to distinguish them from the Saturn experiments that are described in the following section. The combined *SAGE/DRACO* modeling is then applied to the NIF all-DT Saturn design of the previous article. When the implosion-velocity nonuniformity at the end of the laser pulse ($\sim 1\%$ rms) is imposed on a uniform *DRACO* simulation at this time, the resulting target gain is close to the gain of 45 that results from a 1-D symmetric calculation.⁷ This greatly enhances the prospects of obtaining direct-drive ignition on the NIF using the indirect-drive configuration.

Standard-PDD Experiments on OMEGA

Figure 102.6 shows an Aitoff projection of the OMEGA experimental configuration used to approximate the NIF irradiation configuration. Some of the near-equatorial beams are directed to a gold backlighter foil, viewed by an x-ray framing camera at an angle of 10.8° below the horizontal. Similar

40-beam configurations were first used by Glendinning¹³ and Kyrala¹⁴ to diagnose approximately spherical implosions with x-ray backlighting.

The pointings Δr used for the three rings of beams are shown in Fig. 102.7(a). They were verified experimentally by irradiating 4-mm-diam, gold-coated spheres with the repointed beams and comparing x-ray pinhole images with predictions. (This method, applied previously to beams pointed at target chamber center, is described in Ref. 15.) The implosion target is nominally a 20- μm -thick CH shell of 865- μm diameter filled with 15 atm of D_2 . The arrows in Fig. 102.7(a) indicate the beam axes. Optimum drive at the equator is obtained by overlapping ring 3 and its lower-hemisphere counterpart on the equator. The beam spatial profile $I(r)$ (including 2-D smoothing by spectral dispersion¹⁶ with 1-THz bandwidth and polarization smoothing¹⁷) is approximated¹⁸ as a “super-Gaussian” with $I(r) = \exp[-(r/r_0)^n]$, with $r_0 = 380 \mu\text{m}$ and $n = 3.7$ [Fig. 102.7(b)]. A significant portion of the laser energy initially misses the target. This is temporary, however, as many of these rays refract through the expanding plasma (see Fig. 102.8), propagating significant distances at densities above quarter-critical ($n_c/4$) and undergoing significant absorption. Some rays that miss the initial target surface later experience $\sim 50\%$ absorption.

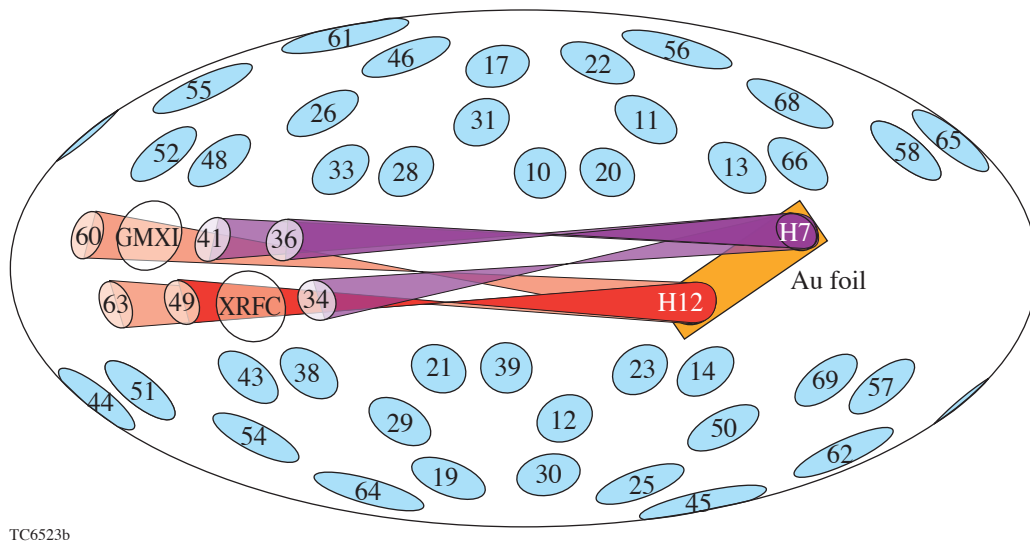
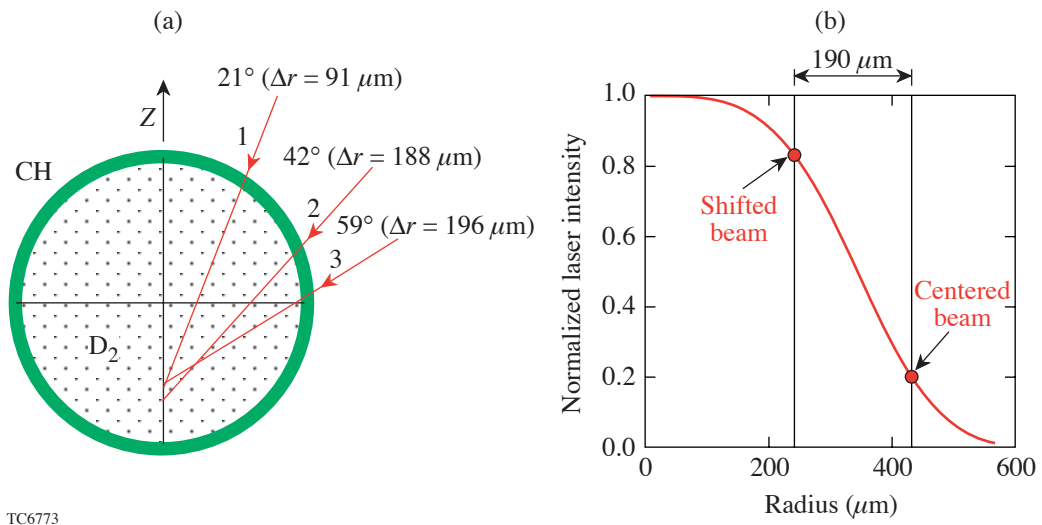


Figure 102.6

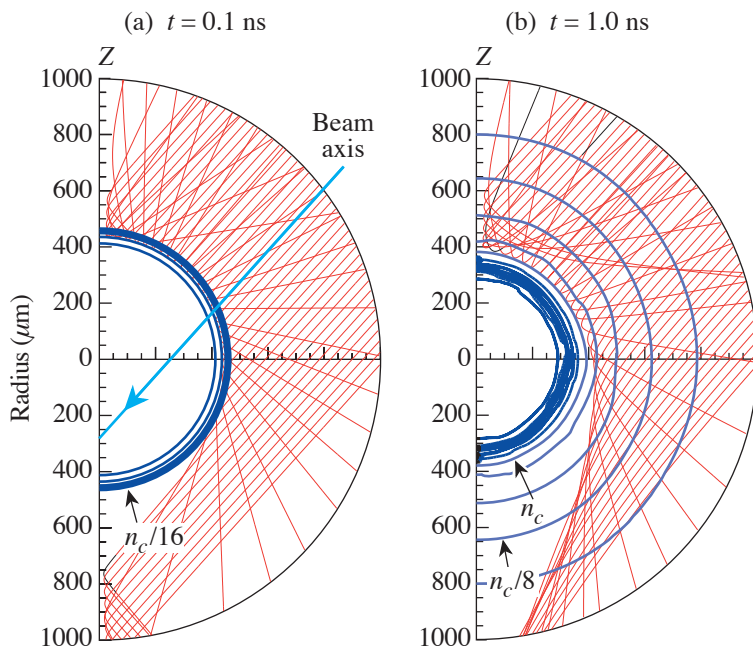
Configuration for polar-direct-drive (PDD) experiments on OMEGA. To best approximate the NIF indirect-drive configuration, the target is irradiated with 40 of the 60 OMEGA beams in rings at 21° , 42° , and 59° from the vertical axis of symmetry (top and bottom portions). Some of the other beams at $\pm 9^\circ$ from the equator (central portion) irradiate a gold backlighter foil, viewed in particular by an x-ray framing camera (XRFC).



TC6773

Figure 102.7

(a) Repointings Δr used for the three rings of OMEGA laser beams, measured perpendicular to the beam axes. The capsule is a 20- μm -thick CH shell of 865- μm diameter filled with 15 atm of D_2 . (b) Target-plane intensity distribution for an OMEGA beam. The solid circles indicate the intensities and radii of rays that can miss the initial target edge for shifted and centered beams.



Run 4187
TC6525

Figure 102.8

Electron-density contours (heavy lines) and a selection of ring-2 ray trajectories in the plane containing the laser axis and the z axis (thin lines), (a) near the start and (b) near the end of the laser pulse. The contour spacing is a factor of 2 in density. The energy loss due to PDD is less than might be expected from Fig. 102.7(b) because of absorption in the expanding plasma.

The time dependence of the predicted absorption is quantified in Fig. 102.9. The incident laser pulse is represented as a 1-ns flat pulse with a linear rise and fall, producing a nominal 16 kJ on target (400 J per beam). The absorbed power rises in time as the coronal scale length increases. The standard-PDD target is predicted to absorb 66% of the incident laser energy, compared with 75% for the 1-D (center-pointed) case. This is roughly equivalent to a 10% incident energy reduction, used when the 1-D code *LILAC* simulates the PDD implosions. The curve labeled “1-D” corresponds to this case and is quite close to the standard-PDD curve.

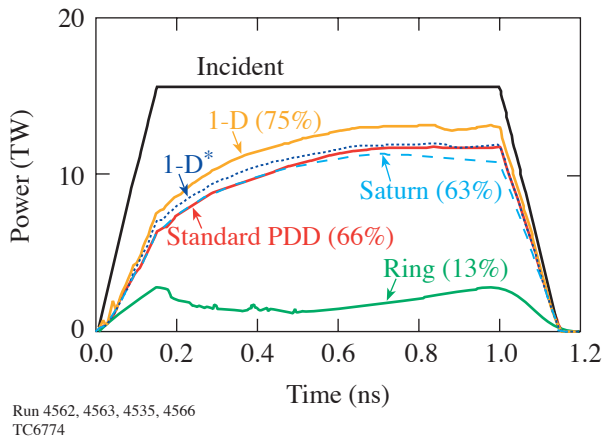


Figure 102.9

Incident and absorbed power as a function of time for several *SAGE* simulations with 16 kJ of incident laser energy, the time-integrated absorption fractions given in parentheses. The curves labeled 1-D are for symmetric irradiation, with 1-D* indicating a 10% reduction of incident energy. For the Saturn simulation, the upper and lower curves apply to the capsule and ring, respectively.

The highly anisotropic distribution of unabsorbed light predicted for PDD makes it difficult to measure the laser absorption using the small number of scattered-light calorimeters on the OMEGA target chamber, as does the material blowoff from the backlighting targets. A separate absorption experiment was carried out to test the modeling of obliquely incident beams. This was done in a symmetric way by taking advantage of the grouping of the OMEGA beams into 12 pentagonal faces of five beams each.² Each beam was repositioned so that its axis intersected a 1600- μm -diam, solid-CH target at the point where the axis of its first or second nearest neighbor would normally intersect. This is illustrated in the inset to Fig. 102.10 for a single move around the group (corresponding to $\Delta r = 335 \mu\text{m}$). Targets were also shot for a double move ($\Delta r =$

514 μm). Large targets were used for this experiment to minimize the transmission of laser energy into the opposing beam ports. The absorption fractions determined by a pair of full-aperture backscatter calorimeters, shown in Fig. 102.10, agree very closely with the *SAGE* predictions, providing confidence in the absorption modeling of obliquely incident beams.

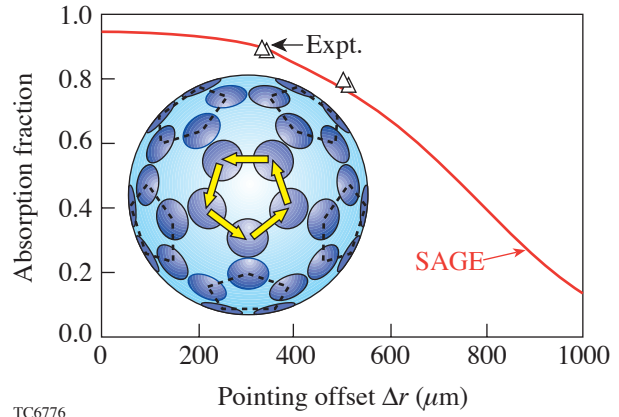


Figure 102.10

Experimental and simulated absorption as a function of pointing offset Δr on large, 1600- μm -diam solid CH targets. Each beam was repositioned either one position (as shown in the inset) or two positions around its pentagonal ring on the OMEGA target chamber to allow the effect of oblique incidence to be studied with the minimum loss of uniformity.

Framed x-ray backlighting was the primary diagnostic used for the implosion experiments. A set of four images at 250-ps intervals, integrated over 50-ps frame times, is shown in Fig. 102.11. The framing camera was timed to diagnose the implosion from the end of the laser pulse to ~ 1 ns later. The first frame, at 1.0 ns (around the end of the laser pulse), showed a ring of coronal self-emission that extended beyond the x-ray emission spot from the gold backlighter foil. This self-emission was also observed by an imaging streak camera. Each of the later images shows a ring of x-ray absorption that becomes smaller as the target implodes. The rings are almost round, indicating that the PDD drive is nearly uniform, but with some low-mode structure analyzed in detail below. The position of the ring relative to the backlighting spot varies due to parallax. Simulations show that, for the first three images, the x-ray absorption minimum is virtually independent of x-ray wavelength in the relevant 2- to 3-keV range and is located very close to the inner surface of the imploding shell, whereas the self-emission ring comes from the corona on the outside of the target. (The fourth image is harder to interpret since it depends on the profiles near stagnation.)

Experimental determinations of the average shell radius as a function of time are shown in Fig. 102.12. The imaging streak camera provided data up to the end of the laser pulse. The average radii from framing-camera images were available through most of the implosion (although not up to peak compression). The horizontal error bars on these data points indicate the timing uncertainty and the vertical error bars represent the accuracy with which the shell radius can be determined. The experimental data were simulated in 1-D by *LILAC* (postprocessed using Spect3D¹⁹) and *SAGE*, both codes using a flux limiter²⁰ f of 0.06. The lowest-order shell motion is modeled well by both codes, with a small timing difference evident with respect to the framing-camera data.

The main result of the experiment is provided by the solid points and curves of Fig. 102.13, which gives the x-ray absorption radius R_{abs} as a function of θ at two successive times during the early stages of the implosion [corresponding to Figs. 102.11(b) and 102.11(c)]. To obtain $R_{\text{abs}}(\theta)$, the positions of the absorption maximum at points around the ring were visually determined, a circle was fit through these positions,

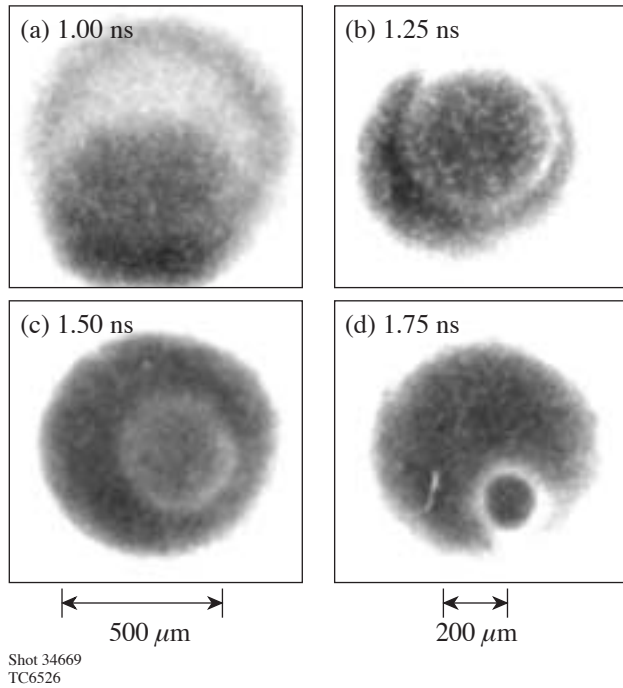


Figure 102.11
A sequence of four backlit x-ray images at successive times. The first image (at the end of the laser pulse) shows a ring due to self-emission from the corona. The following images show distinct rings of x-ray absorption, corresponding roughly to the inner edge of the imploding CH shell.

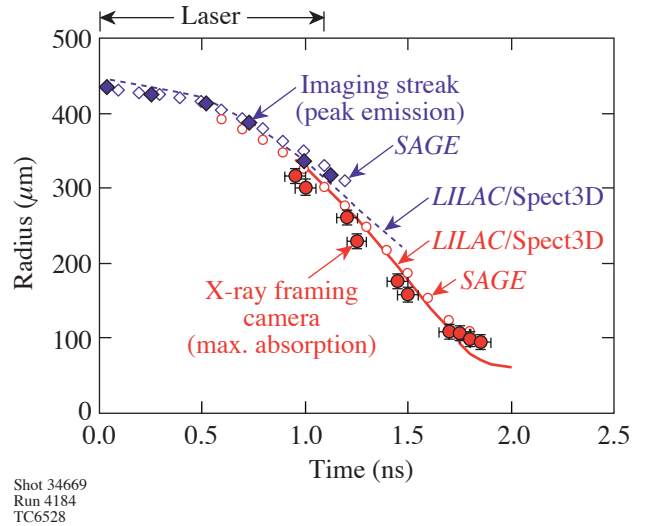


Figure 102.12
Measured and simulated trajectory of the imploding CH shell. The radius of maximum self-emission from the imaging streak camera (solid diamonds) is compared with *SAGE* predictions (open diamonds) and predictions from *LILAC* postprocessed by Spect3D (dotted line). The radius of maximum x-ray absorption (solid circles) is compared with *SAGE* (open circles) and *LILAC*/Spect3D (solid line). Both simulations assume 1-D symmetric irradiation with the incident laser energy reduced by 10%.

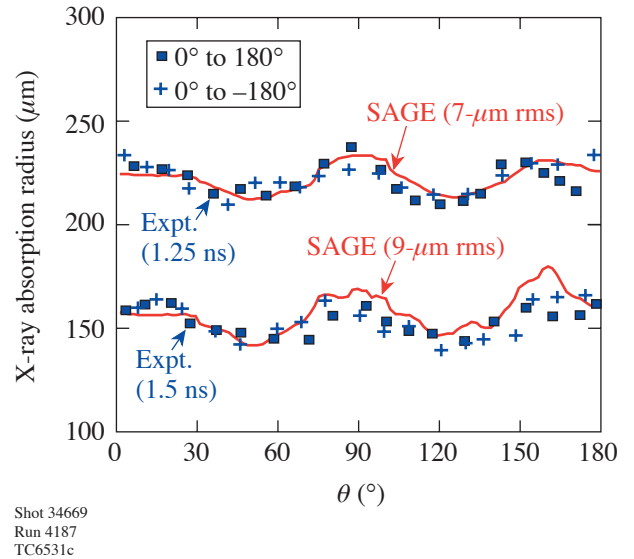


Figure 102.13
Experimental radii of maximum x-ray absorption R_{abs} obtained from the framing-camera images of Fig. 102.11 at 1.25 and 1.5 ns, plotted as a function of angle from the vertical. Squares (pluses) indicate clockwise (counterclockwise) scans from the top of the images. The solid lines are the *SAGE* predictions of R_{abs} based on the calculated center-of-mass location R_{cm} , with minor adjustments for the viewing angle and the difference between R_{cm} and R_{abs} .

and the center of this circle was used as a reference point. No corrections were made for nonuniformities in the backlighter. The different symbols in Fig. 102.13 correspond to scanning around the images from top to bottom in the two angular directions. These are equivalent for an azimuthally symmetric implosion; the good agreement is consistent with good azimuthal symmetry and also indicates that errors associated with nonuniformities in the backlighter are minimal. The calculated curves are based on the center-of-mass radius R_{cm} of the imploding shell, adjusted by estimates of the distance to the x-ray minimum ($14 \mu\text{m}$ at 1.25 ns and $24 \mu\text{m}$ at 1.5 ns). This method proved more robust than direct comparison with the calculated x-ray minimum, whose exact location was subject to some numerical noise. The calculated curves are taken at times (0.15 ns later than the nominal experimental times) that allow comparison to be made of the θ variations at the same values of the average shell radius. The 0.15-ns offset represents a combination of the experimental timing uncertainty and the observation that the agreement between simulation and experiment for the lowest-order shell motion (Fig. 102.12), while very close, is not exact. Deviations from symmetry about $\theta = 90^\circ$ in the simulations, in particular the peak at 160° at the later time, are due to numerical noise that grows at later times. The best indication of the PDD drive nonuniformity is provided at the earlier time when the noise is small.

Figure 102.13 shows that the rms perturbation amplitude increased from $7 \mu\text{m}$ to $9 \mu\text{m}$ as the shell radius decreased from $\sim 225 \mu\text{m}$ to $\sim 150 \mu\text{m}$ (compared with an initial radius of $\sim 430 \mu\text{m}$). At both times the experimental mode structure and amplitude agree well with the simulations, with the drive weak at the equator and at the poles. This agreement provides confidence that the beam pointings for optimum uniformity can be accurately predicted. This is important for the NIF, where a limited number of shots will be available for tuning the drive uniformity.

The compressed core was imaged using a time-integrating Kirkpatrick–Baez (KB) microscope with $\sim 3\text{-}\mu\text{m}$ spatial resolution, filtered to look at x rays from 3 to 7 keV.²¹ Shot 34644 (60 beams, each with $2/3$ of the nominal beam energy of 400 J pointed to target chamber center) and shot 34668 (40 PDD beams) are compared in Figs. 102.14(a) and 102.14(b). The core in the PDD case was less spherical, and the neutron yield Y_{DD} was reduced by a factor of about 3.

The evolution of the shell nonuniformity observed in Fig. 102.13 was consistent with the center-of-mass velocity nonuniformity at the end of the laser pulse (1.1 ns), shown in

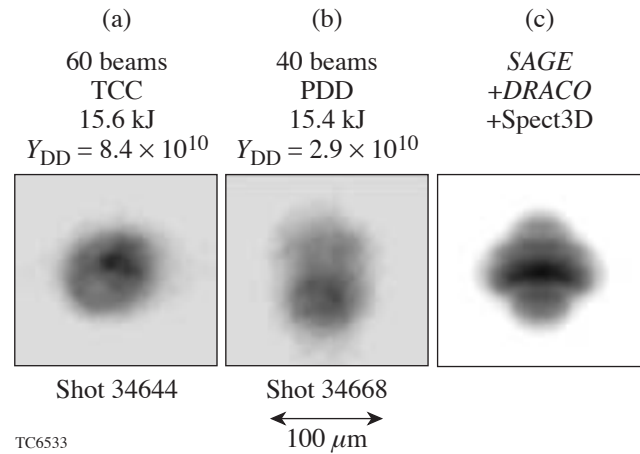


Figure 102.14

Time-integrated KB microscope images for (a) a target irradiated symmetrically with 60 beams, each with $2/3$ nominal energy, pointed at target chamber center (TCC), (b) a 40-beam PDD target, and (c) a simulation of (b). While all images share the same spatial scale, care should be exercised when comparing (b) and (c) because of the different gray scales used.

Fig. 102.15(a). The minimum at the equator (and, indeed, the falloff from $\theta = 60^\circ$ to $\theta = 90^\circ$) is found for all feasible combinations of ring pointings. The optimum overall rms nonuniformity of 3.8% is obtained by reducing the drive at the poles. The low drive pressure at the equator causes mass to flow toward the equator. Figure 102.15(b) shows the transverse velocity V_θ , positive between $\theta = 60^\circ$ and $\theta = 90^\circ$ and negative from 90° to 120° . This small velocity (whose rms is $\sim 2.5\%$ of V_r) can lead to increasing transverse mass flow toward the equator as the implosion proceeds.

To follow the implosion from the end of the laser pulse, low- ℓ fits to the *SAGE* center of mass V_r and V_θ were used to perturb a hitherto uniform *DRACO* simulation. Even values of ℓ were used for V_r and odd for V_θ (as V_θ results from gradients in the θ direction). *DRACO* contours of mass density ρ and electron temperature T_e at the time of peak neutron production are given in Figs. 102.15(c) and 102.15(d), respectively. The solid line indicates the CH/D₂ interface. The $\ell = 4$ perturbation continues throughout the implosion. The calculated neutron yield was 5.4×10^{10} , reduced from 1.3×10^{11} for a comparison unperturbed simulation by a factor of 0.42, close to the experimental reduction factor of 0.35, suggesting that the experimental reduction can be explained mainly by the imposed low- ℓ perturbations. (Similar yield reductions have been obtained in full *DRACO* simulations using its approximate ray-trace option.)

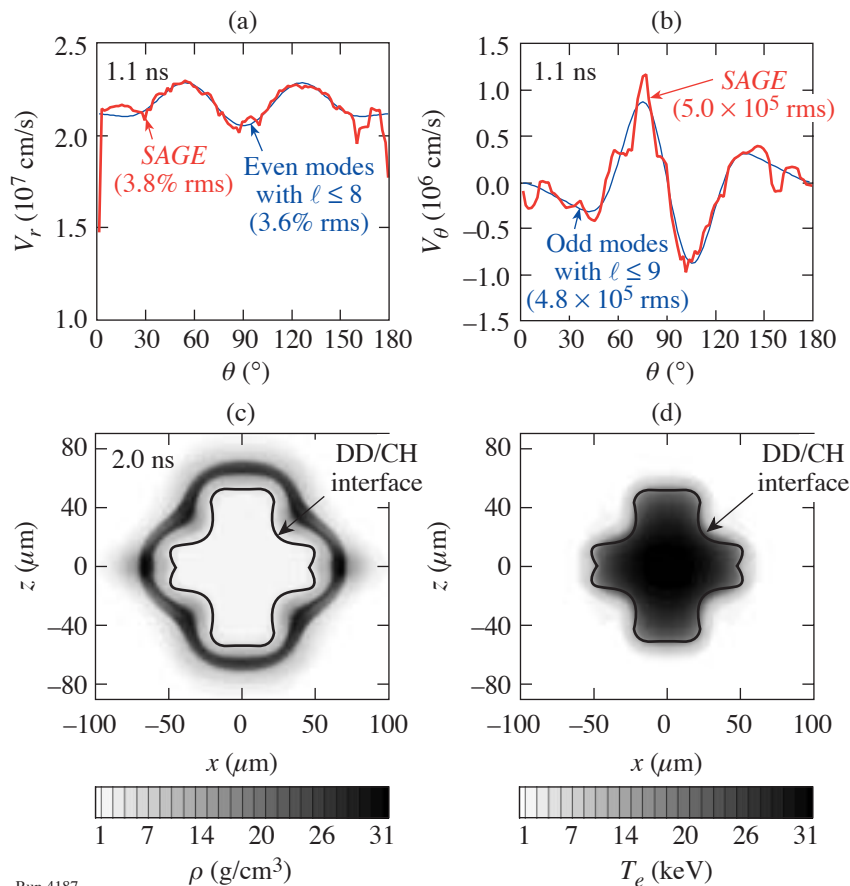


Figure 102.15

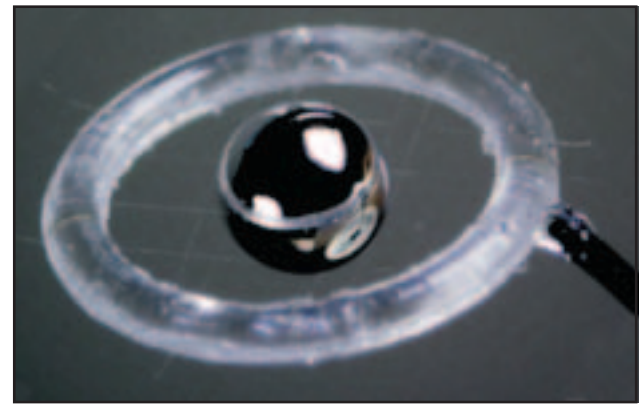
SAGE/DRACO simulation of a PDD implosion. Low- ℓ Legendre fits to (a) the center-of-mass radial velocity V_r and (b) the transverse velocity V_θ calculated by *SAGE* at the end of the laser pulse (1.1 ns) were used to perturb a hitherto symmetric *DRACO* simulation. The density ρ and electron temperature T_e contours at the time of peak neutron production are given in (c) and (d), respectively.

Run 4187
Shot 34669
TC6928

The *DRACO* profiles were postprocessed by Spect3D to form the time-integrated x-ray image shown in Fig. 102.14(c). The experimental image shows a lower intensity in the upper half as indicated in the calculated image. This is ascribed to mass that has accumulated near the equator, partially obstructing the view of the core taken from 15.6° below the equator.²²

Saturn Experiments on OMEGA

The first Saturn target implosion experiments have been performed on OMEGA. Standard OMEGA capsules (20- μm CH shells filled with 15 atm of D_2) were supported using spider silk on a CH ring of 1100- μm major radius and 150- μm minor radius (see Fig. 102.16). The capsule was centered in the ring to an accuracy usually better than 40 μm . While the calculated optimum pointing called for the ring-1 Δr to be changed from 90 μm to 30 μm , to give a stronger drive at the poles, the actual experimental pointing was unchanged to isolate the change of uniformity induced by the ring.²³ The backlighting configuration was modified from that shown in Fig. 102.6 to include a second framing camera viewing from 26.6° above the equator, to avoid obscuration by the ring.



TC6659

Figure 102.16

A Saturn target shot on OMEGA. Using eight strands of spider silk, a standard 865- μm -diam capsule is mounted on a CH ring of major radius 1100 μm and minor radius 150 μm .

The ring plasma forms mainly in the later part of the laser pulse, as in the NIF design described in the preceding article. Predicted density contours at two times are shown in Fig. 102.17. A “bow shock” is observed where the ring plasma and capsule plasma collide. The absorbed power in the capsule was almost the same as in the standard-PDD case (see Fig. 102.9) and that in the ring was fairly constant.

Figure 102.18(a) shows a time-integrated pinhole-camera image of the target, viewed 10.8° above the equator. The ring appears as a shadow obscuring some of the plasma. There is evidence of the bow shock near the inner edge of the ring. The imploded core is heavily overexposed. A better-filtered image of the core, obtained from the KB microscope and dominated by emission from the CH/D₂ interface, shows prolate core emission [Fig. 102.18(b)].

Framing-camera images of the imploding shell obtained from the 26.6° view [Figs. 102.18(c)–102.18(e)] show a clear $\ell = 2$ mode, evident from the earliest time. The x-ray absorption radii from the first two images, whose times correspond to the standard-PDD data shown in Fig. 102.13, are plotted in Fig. 102.19 along with predictions corrected for the viewing angle (i.e., around a great circle in a plane tipped 26.6° from the vertical). The predictions (solid curves) show an $\ell = 4$ pattern with slightly reduced amplitude compared with the standard-PDD case (dotted curves). The Saturn data show an $\ell = 2$ mode with the strongest drive on the equator, larger than predicted.

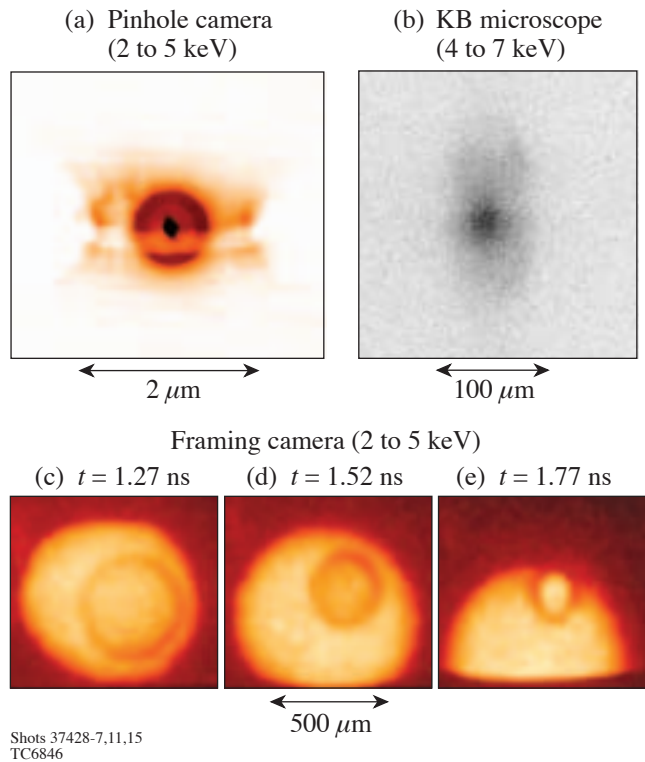


Figure 102.18 X-ray images of Saturn-target implosions. (a) Time-integrated pinhole-camera image, from 10.8° above the equator, including self-emission, the shadow of the ring, the bow shock, and a prolate core (saturated). (b) Time-integrated KB microscope image of the core. (c)–(e) Framing-camera backlit images of the imploding shell viewed 26.6° above the equator.

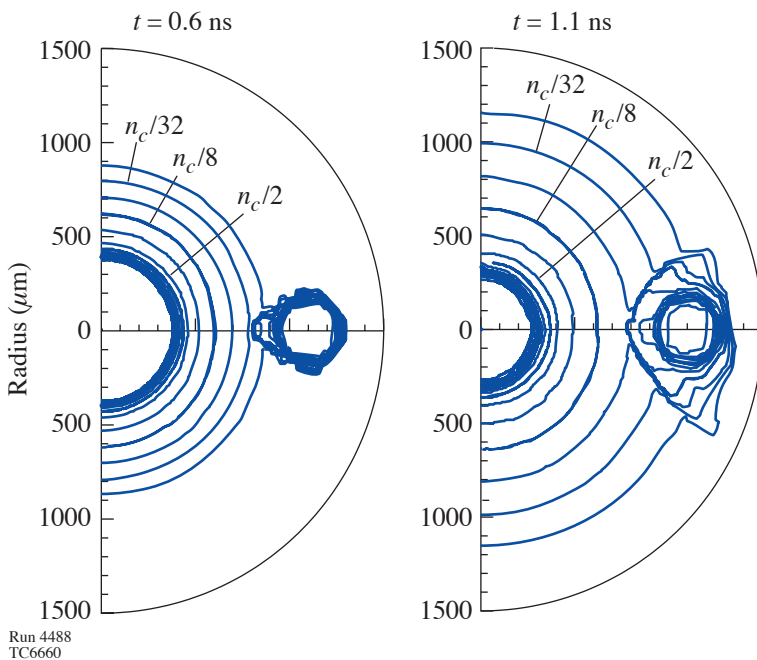


Figure 102.17 Simulated electron-density contours at 0.6 and 1.1 ns for the Saturn target. The ring plasma grows primarily in the second half of the laser pulse, forming a “bow shock” where it collides with the plasma ablating from the capsule.

The primary reason for this disagreement is believed to be radiation from the ring plasma to the capsule, not included in the simulations. In addition, it is possible that the ring plasma is not behaving as modeled. Much of the laser energy absorbed by the ring comes from rays near the edge of the beam profile, which may contain more energy than implied by the super-Gaussian fit. The ring may not be azimuthally symmetric: while it is probably irradiated uniformly by the light from all beams that is refracted from the capsule plasma, it is also irradiated directly in localized regions by the edges of the ring-3 beams. Such asymmetries would lead to a more rapid local growth of the ring plasma.

The Saturn target that came closest to design specifications yielded 1.8×10^{10} DD neutrons, slightly less than two standard-PDD targets shot immediately prior to the Saturn targets that yielded 2.1 and 2.4×10^{10} neutrons, respectively. This is consistent with the greater low- ℓ drive variations seen in Fig. 102.19, suggesting that removal of the strong $\ell = 2$ non-uniformity would improve the Saturn yield. This can be accomplished by changing some of the repointings Δr to shift some of the drive back toward the poles or by increasing the major radius (or decreasing the minor radius) of the ring.

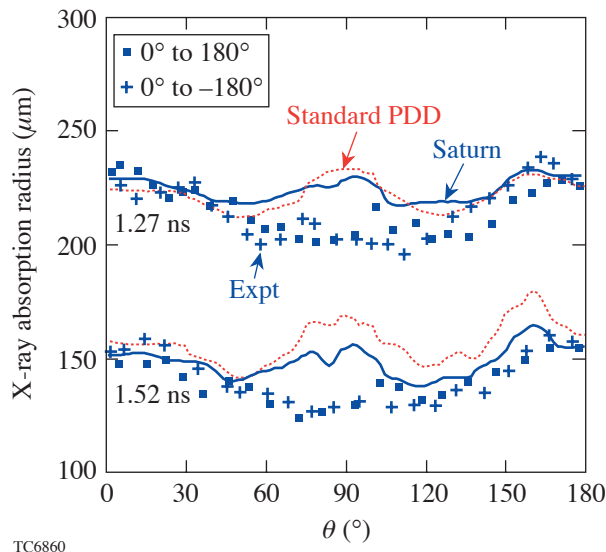


Figure 102.19
X-ray absorption radius as a function of angle θ around the image obtained from the 1.27-ns and 1.52-ns Saturn-target images in Fig. 102.18 together with *SAGE* predictions obtained as in Fig. 102.13 (solid curves). The dotted curves are taken from Fig. 102.13 for a standard-PDD target. The experimental data indicate that the increase in equatorial capsule drive is greater than predicted.

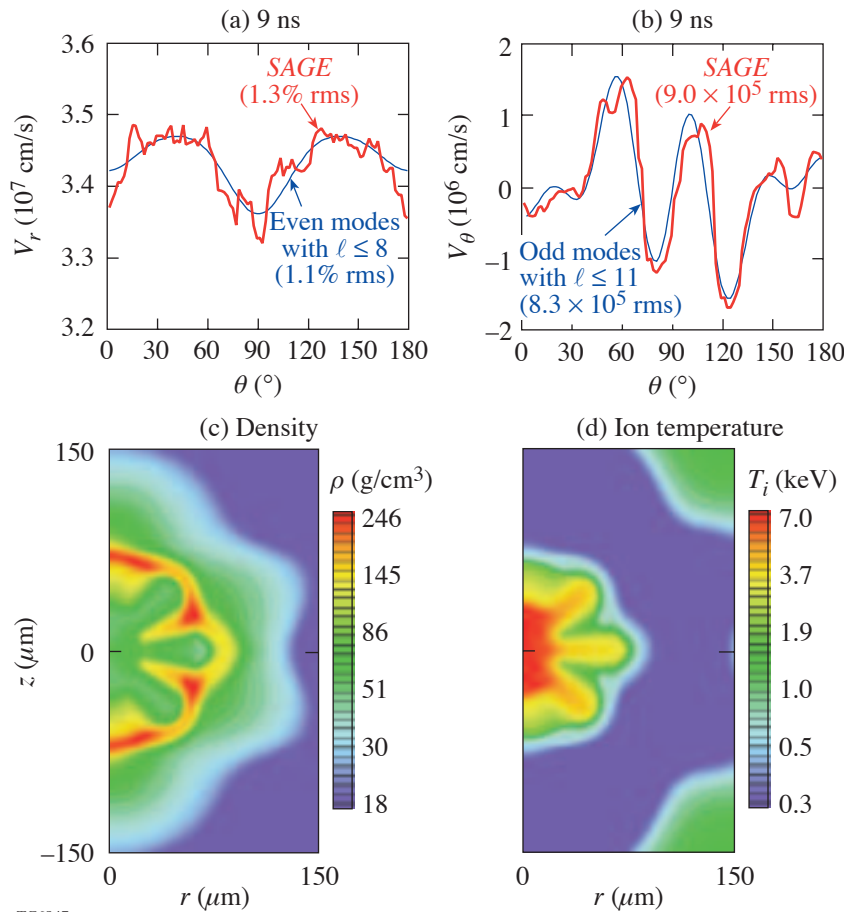
High-Gain Saturn Design for the NIF

In the preceding article, a Saturn design for the NIF was calculated up to the end of the laser pulse and optimized for minimum rms center-of-mass nonuniformity. In this section the subsequent implosion of this design is modeled using the *SAGE/DRACO* technique described above.

The Saturn ignition design adds a CH ring of 3000- μm major radius to the all-DT capsule described in Ref. 7 and repoints the beams incident at 30° , 44.5° , and 50° with $\Delta r = 240 \mu\text{m}$, $280 \mu\text{m}$, and $750 \mu\text{m}$, respectively. The 44.5° and 50° beams use “elliptical” phase plates whose target-plane profiles are reduced in the z direction by factors of $\cos(30^\circ)$ and $\cos(50^\circ)$, respectively. The center-of-mass velocity perturbations V_r and V_θ near the end of the laser pulse are shown in Figs. 102.20(a) and 102.20(b), together with low-mode Legendre fits. Of the 1.3% calculated rms V_r perturbation, 1.1% can be accounted for by modes 2 and 4 (the difference largely being due to noise in the simulation). An initially symmetric *DRACO* simulation was perturbed with the Legendre fits and was continued through the thermonuclear burn phase. (More-accurate simulations would also transfer the 9- μm -rms center-of-mass modulations in shell excursion at this time and modulations in mass per solid angle, both considered to be small.) Contours of density and ion temperature from *DRACO* are shown in Figs. 102.20(c) and 102.20(d) at the onset of ignition. The imposed ℓ -mode pattern is maintained through the coasting and deceleration stages. This nonuniformity is sufficiently small to allow ignition to occur, with little effect on the propagating burn wave. The resulting gain is 38, close to the 1-D gain of 45. This result is consistent with the work of McKenty *et al.*,⁷ who found that low- ℓ perturbations have less effect on the gain of the all-DT design than higher- ℓ perturbations ($\ell \geq 10$) of the same amplitude. Consistently, other *SAGE/DRACO* calculations with similar rms nonuniformities imposed in higher- ℓ modes (~ 8) perform less well. Inner-ice roughness and imprint, not included in the simulation presented here, are likely to result in similar ($\sim 30\%$) reductions in yield as for symmetrically driven capsules.⁷

Conclusions

Experiments on OMEGA have confirmed that reasonably symmetric implosions can be carried out using 40 of the 60 beams in a polar configuration. Further, the drive perturbations can be diagnosed with amplitudes and mode structure that are in good agreement with simulations.



TC6847

Figure 102.20

SAGE/DRACO simulation of the NIF Saturn target. Low- ℓ fits to (a) the *SAGE*-calculated center-of-mass radial velocity V_r and (b) the transverse velocity V_θ were used to perturb a symmetric *DRACO* simulation. The density ρ and ion temperature T_i contours at the time of ignition are given in (c) and (d), respectively. The gain of 38 is close to 1-D.

The Saturn implosions reported here demonstrated that a low- Z ring can be used to increase the drive on the equator. Indeed, the maximum drive was observed at the equator, which, according to calculations, cannot happen for standard-PDD targets on the OMEGA laser system. The prospects for improving the uniformity of Saturn targets are excellent, with the possibilities including changes to the beam pointings and ring dimensions. Subsequent OMEGA experiments and modeling, to be reported in a future issue of the LLE Review, have shown that the implosion symmetry and yield can be improved by readjusting the beam pointings and that radiation is indeed the primary cause of the discrepancy between experiment and simulations. Further experiments will provide a better understanding of the formation and evolution of the ring plasma and its azimuthal symmetry, and the physics of the bow shock and its contribution to x-ray emission from the ring remains to be explored. These experiments will enable more-accurate calculations to be made of Saturn targets for the NIF.

Hydrodynamic modeling of the standard-PDD experiments using a combination of *SAGE* and *DRACO* led to a yield reduction close to that observed experimentally. Similar modeling was applied to the Saturn design for the NIF and led to a predicted gain close to 1-D. This result is very encouraging since it improves the prospects of obtaining direct-drive ignition and high gain on the NIF many years before conversion of the NIF to the direct-drive configuration. This work will be published in Ref. 24.

ACKNOWLEDGMENT

The authors are grateful to Dr. David Meyerhofer for a careful review of the manuscript and many helpful suggestions. This work was supported by the U.S. Department of Energy Office of Inertial Confinement Fusion under Cooperative Agreement No. DE-FC52-92SF19460, the University of Rochester, and the New York State Energy Research and Development Authority. The support of DOE does not constitute an endorsement by DOE of the views expressed in this article.

REFERENCES

1. E. M. Campbell and W. J. Hogan, *Plasma Phys. Control. Fusion* **41**, B39 (1999).
2. S. Skupsky, J. A. Marozas, R. S. Craxton, R. Betti, T. J. B. Collins, J. A. Delettrez, V. N. Goncharov, P. W. McKenty, P. B. Radha, T. R. Boehly, J. P. Knauer, F. J. Marshall, D. R. Harding, J. D. Kilkenny, D. D. Meyerhofer, T. C. Sangster, and R. L. McCrory, *Phys. Plasmas* **11**, 2763 (2004).
3. J. D. Kilkenny, Laboratory for Laser Energetics, private communication (2002).
4. R. S. Craxton, presented at the 33rd Anomalous Absorption Conference, Lake Placid, NY, 22–27 June 2003 (Paper WO3).
5. R. S. Craxton, *Bull. Am. Phys. Soc.* **48**, 56 (2003).
6. C. P. Verdon, *Bull. Am. Phys. Soc.* **38**, 2010 (1993).
7. P. W. McKenty, V. N. Goncharov, R. P. J. Town, S. Skupsky, R. Betti, and R. L. McCrory, *Phys. Plasmas* **8**, 2315 (2001).
8. R. S. Craxton and R. L. McCrory, *J. Appl. Phys.* **56**, 108 (1984).
9. P. B. Radha, T. J. B. Collins, J. A. Delettrez, D. Keller, P. W. McKenty, and R. P. J. Town, presented at the 30th Annual Anomalous Absorption Conference, Ocean City, MD, 21–26 May 2000 (Paper 2P11).
10. P. B. Radha, V. N. Goncharov, T. J. B. Collins, J. A. Delettrez, Y. Elbaz, V. Yu. Glebov, R. L. Keck, D. E. Keller, J. P. Knauer, J. A. Marozas, F. J. Marshall, P. W. McKenty, D. D. Meyerhofer, S. P. Regan, T. C. Sangster, D. Shvarts, S. Skupsky, Y. Srebro, R. P. J. Town, and C. Stoeckl, *Phys. Plasmas* **12**, 032702 (2005).
11. S. Skupsky, R. Betti, T. J. B. Collins, V. N. Goncharov, D. R. Harding, R. L. McCrory, P. W. McKenty, D. D. Meyerhofer, and R. P. J. Town, in *Inertial Fusion Sciences and Applications 2001*, edited by K. Tanaka, D. D. Meyerhofer, and J. Meyer-ter-Vehn (Elsevier, Paris, 2002), pp. 240–245.
12. D. Eimerl, ed., Lawrence Livermore National Laboratory, Livermore, CA, UCRL-ID-120758 (1995).
13. S. G. Gledinning, Lawrence Livermore National Laboratory, private communication (2003).
14. G. A. Kyrala *et al.*, *Laser Part. Beams* **23**, 207 (2005).
15. F. J. Marshall, J. A. Delettrez, R. Epstein, R. Forties, R. L. Keck, J. H. Kelly, P. W. McKenty, S. P. Regan, and L. J. Waxer, *Phys. Plasmas* **11**, 251 (2004).
16. S. Skupsky and R. S. Craxton, *Phys. Plasmas* **6**, 2157 (1999).
17. T. R. Boehly, V. A. Smalyuk, D. D. Meyerhofer, J. P. Knauer, D. K. Bradley, R. S. Craxton, M. J. Guardalben, S. Skupsky, and T. J. Kessler, *J. Appl. Phys.* **85**, 3444 (1999).
18. F. J. Marshall, J. A. Delettrez, R. Epstein, R. Forties, V. Yu. Glebov, J. H. Kelly, T. J. Kessler, J. P. Knauer, P. W. McKenty, S. P. Regan, V. A. Smalyuk, C. Stoeckl, J. A. Frenje, C. K. Li, R. D. Petrasso, and F. H. Séguin, *Bull. Am. Phys. Soc.* **48**, 56 (2003).
19. Prism Computational Sciences, Inc., Madison, WI, Report No. PCS-R-041, Ver. 3.0 (2002). See also J. J. MacFarlane *et al.*, in *Inertial Fusion Sciences and Applications 2003*, edited by B. A. Hammel, D. D. Meyerhofer, J. Meyer-ter-Vehn, and H. Azechi (American Nuclear Society, La Grange Park, IL, 2004), pp. 457–460.
20. R. C. Malone, R. L. McCrory, and R. L. Morse, *Phys. Rev. Lett.* **34**, 721 (1975).
21. M. C. Richardson, P. W. McKenty, F. J. Marshall, C. P. Verdon, J. M. Soures, R. L. McCrory, O. Barnouin, R. S. Craxton, J. Delettrez, R. L. Hutchison, P. A. Jaanimagi, R. Keck, T. Kessler, H. Kim, S. A. Letzring, D. M. Roback, W. Seka, S. Skupsky, B. Yaakobi, S. M. Lane, and S. Prussin, in *Laser Interaction and Related Plasma Phenomena*, edited by H. Hora and G. H. Miley (Plenum Publishing, New York, 1986), Vol. 7, pp. 421–448.
21. F. J. Marshall and Q. Su, *Rev. Sci. Instrum.* **66**, 725 (1995).
22. R. Epstein, R. S. Craxton, J. A. Delettrez, F. J. Marshall, J. A. Marozas, P. W. McKenty, P. B. Radha, and V. A. Smalyuk, *Bull. Am. Phys. Soc.* **49**, 180 (2004).
23. The second series of standard-PDD experiments and the Saturn targets used $\Delta r = 90 \mu\text{m}$, $180 \mu\text{m}$, and $180 \mu\text{m}$ for rings 1–3, respectively, not significantly different from the values for the first series indicated in Fig. 102.7.
24. R. S. Craxton, F. J. Marshall, M. Bonino, R. Epstein, P. W. McKenty, S. Skupsky, J. Delettrez, I. V. Igumenshchev, D. W. Jacobs-Perkins, J. P. Knauer, J. A. Marozas, P. B. Radha, and W. Seka, “Polar Direct Drive—Proof-of-Principle Experiments on OMEGA and Prospects for Ignition on the NIF,” to be published in *Physics of Plasmas*.

Direct-Drive, Cryogenic Target Implosions on OMEGA

Introduction

Thermonuclear ignition via direct-drive, laser-driven, inertial confinement fusion¹ (ICF) will be accomplished by the near-uniform illumination of spherical cryogenic deuterium–tritium (DT) fuel-bearing capsules with high-power laser beams. Achieving thermonuclear ignition and gain will require symmetric compression of the DT-fuel hot spot to high areal densities ($\sim 0.3 \text{ g/cm}^2$) with a temperature of $\sim 10 \text{ keV}$. The baseline target consists of either a pure cryogenic DT layer formed on the inside of a thin plastic shell² or a DT-filled foam shell.³ Target imperfections and laser illumination non-uniformities lead to Rayleigh–Taylor unstable growth of fuel-layer perturbations during the implosion and must be minimized. The minimum energy required for ignition scales as $\sim \alpha^{1.8}$ (Refs. 4–6), where α is the fuel adiabat, the ratio of the local pressure to the Fermi-degenerate pressure. It has been shown that the ablation velocity, the main contributor to the stabilization of Rayleigh–Taylor unstable growth, scales as $\sim \alpha^{0.6}$ (Ref. 4). Traditionally, direct-drive ICF has had to balance target performance and stability by a careful choice of the target adiabat. This task has been made easier with the application of adiabat shaping.⁷ The ablation region is placed on a high adiabat for stability while maintaining the main fuel layer on a low adiabat, preserving compressibility for good target performance.

The experiments described in this work were performed on LLE’s 60-beam, 30-kJ UV OMEGA laser system.⁸ The three major requirements to achieve ignition-scaled conditions in the fuel have been met: (1) near-uniform cryogenic layers, (2) near-uniform laser illumination, and (3) a high-contrast pulse shape maintaining the fuel layer on a low adiabat ($\alpha \sim 4$). The resulting high fuel areal densities ($\rho R \sim 100 \text{ mg/cm}^2$), ion temperature ($kT_i \sim 2$ to 3 keV), and fusion yield [$\sim 20\%$ of predicted by one-dimensional (1-D) simulations and in agreement with two-dimensional (2-D) simulations] give increasing confidence to the direct-drive approach to ICF ignition.

This work describes recent progress in direct-drive, cryogenic target implosions on OMEGA. The following sections

(1) describe the experimental conditions and observations, (2) compare the observations with 2-D numerical simulations, and (3) present our conclusions.

Experiments

This section describes the experimental conditions, including target and laser performance, and the primary experimental observations.

1. Targets

The targets used in these experiments were D_2 -filled, deuterated, strong GDP (a high-strength, glow-discharge polymer) shells with outer diameters of $\sim 865 \mu\text{m}$, shell thicknesses of ~ 3.7 to $4.0 \mu\text{m}$, and a density of 1.09 g/cm^3 . The shells were permeation filled with $\sim 1000 \text{ atm}$ of D_2 gas in the Fill/Transfer Station (FTS)⁹ and then slowly cooled to below the triple point (18.7 K). The targets were then transported to a characterization station for layer formation and then to the OMEGA target chamber for implosion.

The formation of a near-uniform layer is accomplished in a layering sphere⁹ using an IR laser tuned to the D_2 -ice absorption band at a wavelength of $3.16 \mu\text{m}$. The residual inner-ice-surface nonuniformities, after careful layer preparation, are determined using the shadowgraphic technique described in Stoeckl *et al.*¹⁰ and shown in Fig. 102.21. This technique has been extended to map the inner surface of the ice layer in 3-D by combining layer-thickness measurements from multiple views (48 typically, consisting of 24 orthogonal pairs). In addition to the inner-ice-surface roughness, the outer-surface roughness of the CH shell is also determined. The mean inner-ice roughness for the target experiments included in this work was $5 \mu\text{m}$ (rms) with the best being $1.3 \mu\text{m}$. Three-dimensional (3-D) reconstructions of the ice layer from these multiple views were used as input to the 2-D hydrodynamic simulations described in **Comparison of Experimental Results and 2-D Simulations** (p. 82).

The standard deviation of the mean layer thickness from individual views is typically $\leq 2 \mu\text{m}$. However, there are other

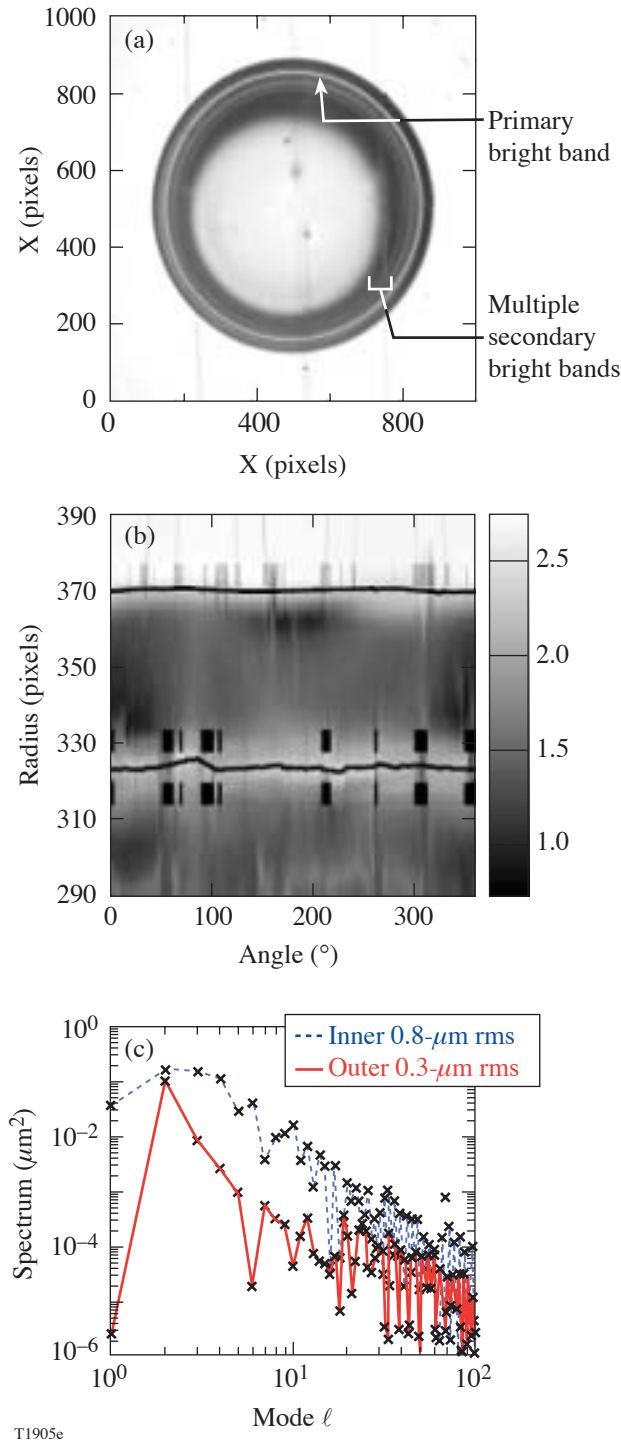


Figure 102.21
Cryogenic target layer characterization. (a) A single shadowgraph, (b) layer-thickness measurements, and (c) resultant mode spectrum.

ways to characterize the errors of the ice-layer nonuniformity. For example, the ice layer for shot 35713 had a 4.2- μm mean rms, predominately in the four lowest ℓ modes. Based on the 3-D reconstruction of the ice layer, a peak-to-valley of $\pm 10 \mu\text{m}$ existed over $\sim 1\%$ of the surface. These larger variations will likely affect target performance to a greater degree than represented by the standard deviation of the mean of the individual measurements. An effort is underway to more accurately determine the mean ice-roughness error and its impact on target performance and simulations.

2. Laser System Conditions

Cryogenic capsules were imploded with pulse shapes ranging from a high-adiabat ($\alpha \sim 25$), 23-kJ, 1-ns square pulse to a low-adiabat ($\alpha \sim 4$), 17-kJ, 2.5-ns shaped pulse. The fuel adiabat at the end of the acceleration phase is determined by using the pulse shape, as measured by a high-bandwidth streak camera,¹¹ as input to the 1-D hydrocode *LILAC*.¹² Full beam smoothing, including distributed phase plates (DPP's),¹³ polarization smoothing with distributed polarization rotators (DPR's),¹⁴ and 2-D, single-color-cycle, 1-THz smoothing by spectral dispersion (SSD),¹⁵ was used for these experiments. Recent experiments ($\alpha \sim 4$) were performed with a new set of DPP's¹⁶ with a 95% enclosed energy diameter of 865 μm and a "super-Gaussian" order $n = 3.7$. The new DPP's reduce the need to use enhanced fluence balance.¹⁷ Beam mispointing is reduced from an average of $\sim 20\text{-}\mu\text{m}$ rms to an average of $\sim 10\text{-}\mu\text{m}$ rms by active repointing requiring two pointing shots.^{16,17} These combined effects have reduced the long-wavelength nonuniformities of the laser system from $\sim 3\%$ to $\sim 1.3\%$. This condition was applied to all $\alpha \sim 4$ implosions in this work. The largest contribution to the long-wavelength nonuniformities is the location of the target with respect to the center of the target chamber (TCC offset) at shot time.

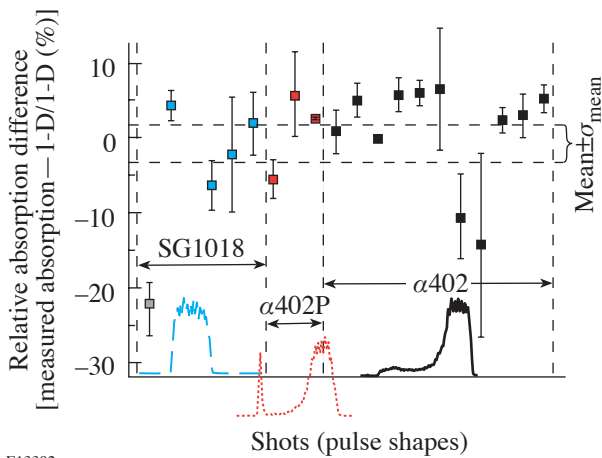
3. Absorption Measurements

The scattered light was measured by calorimeters in two full-aperture-backscatter stations (FABS's). These calorimeters sample the light backscattered through two OMEGA focusing lenses. Extensive 2-D ray-tracing simulations using 1-D hydrodynamic code predictions for the time-varying plasma density and temperature profiles have shown that the scattered light variations around the target are within $\sim 3\%$ of perfect uniformity. Spot measurements with calorimeters between the OMEGA focusing lens positions have confirmed these predictions. Nevertheless, random shot-to-shot fluctuations in the various calorimeter measurements can be as high as 7% rms per shot. These fluctuations are thought to be due to target centering and subtle beam-pointing issues. In contrast,

the shot-to-shot reproducibility of the average calorimeter reading is typically within 2% to 3%, inspiring confidence in the validity of the average scattered-light measurements. Since the long-term calibration stability of the scattered-light calorimeters between the focusing lenses is difficult to ascertain, we use only scattered-light energies measured at the two FABS's and extrapolate them to 4π . These data yield a good measure for the total absorbed energy.

Reliable measurements of absorbed energy in spherical target implosions are essential for quantitative comparison with hydrodynamic code simulations. The absorption predicted by these codes is based primarily on 2-D ray tracing and inverse bremsstrahlung absorption and depends sensitively on the electron thermal transport. The latter is typically modeled using flux-limited diffusion.^{18,19} A flux limiter $f = 0.06$ was used for all simulations in this work.

Figure 102.22 shows the fractional difference of the measured absorption from *LILAC* predictions for a series of cryogenic implosions with the pulse shapes shown as insets. Error bars represent the difference of the two FABS measurements. The agreement between the measurements and the 1-D *LILAC* predictions is excellent (horizontal dashed lines in Fig. 102.22) when averaged over all shots. We have also made time-resolved scattered-light measurements (and, consequently, time-resolved absorption measurements) that are in equally good agreement over the entire pulse shape for all of the pulse shapes.²⁰



E13392

Figure 102.22
Absorption fraction measurements shown as percent variation from 1-D predicted value.

Determination of the fuel adiabat depends on the detailed time history of the absorbed energy, requiring precision measurement of the laser pulse shape. Using P510 streak cameras¹¹ with a demonstrated bandwidth of ~ 20 GHz in the UV in selected channels, the simulations are provided with pulse shapes that include an initial low-intensity rise of ~ 40 ps/decade for all pulse shapes. These rise times were measured using 1-ns square pulses best suited for this purpose. The same pulse switching provides the initial rise for all other pulse shapes. Details of the initial rise are of importance to simulations. With these inputs, optimum zoning strategies were developed for the *LILAC* simulations that led to improved absorption calculations⁷ in the leading edge of the strongly shaped $\alpha 401$, $\alpha 402$, and $\alpha 402P$ (with picket) pulses. All of these improvements have led to better agreement between the measured and simulated time-integrated and time-resolved absorption fractions, as well as improved estimates for the fuel adiabat during the implosion phase. Thus, previously predicted $\alpha \sim 4$ pulses were found to produce slightly higher calculated adiabats ($\alpha \sim 6$). New pulse shapes, incorporating better design of the leading edge, have been incorporated into current OMEGA experiments.

4. Fusion Yield

The fusion reaction rate for these experiments is determined by the neutron temporal diagnostic (NTD),²¹ with the absolute rate obtained by normalizing with the neutron yield. Figure 102.23 shows the NTD measured and simulated neutron rate for a low-adiabat ($\alpha \sim 4$) implosion. The duration and peak time are seen to fall within the absolute measurement uncertainty (± 0.1 ns). The integrated yield for this implosion was 1.6×10^{10} , while the *LILAC* prediction was 9.1×10^{10} [yield over calculated (YOC) = 18%]. The coincidence of the measured and predicted peak burn times confirms the observations from the absorption measurements that the simulations are correctly predicting the absorption and hydrodynamic coupling in cryogenic targets.

5. Fuel Areal Density

The total fuel areal density in cryogenic D_2 implosions is inferred from the energy loss of secondary protons from the D^3He reaction. The secondary proton spectrum at birth is well defined by the kinematics of the D^3He reaction so that the average energy of the protons emerging from the dense fuel depends on the total burn-averaged areal density $\langle \rho R \rangle_n$. Wedge-range-filter spectrometers (WRF's)²² measure the secondary proton spectrum along multiple lines of sight (generally four to six). These individual measures of the ρR_n are averaged to obtain the reported $\langle \rho R \rangle_n$. The error associated with each

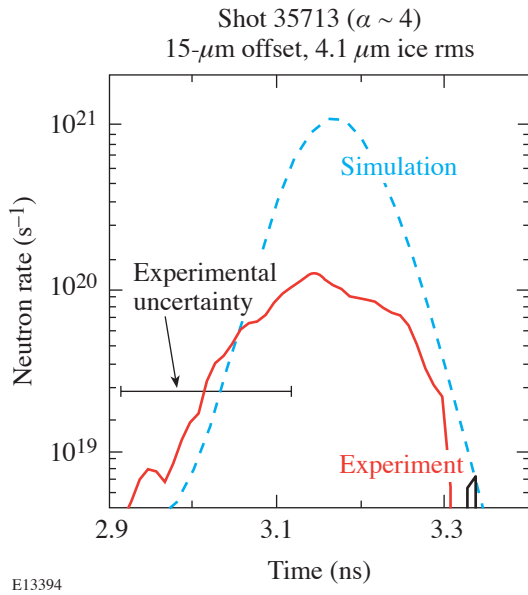


Figure 102.23
NTD measurement of the fusion reaction rate for an $\alpha \sim 4$ cryogenic target implosion (shot 35713). The 1-D simulated fusion rate is also plotted.

individual measure is approximately 5% (typically a 150-keV uncertainty out of a 3-MeV energy loss). However, the variation among the individual measurements is often quite large due to low-mode variations in the initial ice thickness and drive symmetry. The dominant factor in the drive asymmetry is the location of the capsule with respect to chamber center at shot time (the TCC offset discussed above).

Figure 102.24 shows the correlation between the experimentally inferred $\langle \rho R \rangle_n$ and the value of $\langle \rho R \rangle_n$ predicted by the 1-D hydrocode *LILAC* for all cryogenic implosions in which the offset from TCC was $< 60 \mu\text{m}$ and the inner-ice-layer rms roughness was $< 6 \mu\text{m}$. The solid circles near 50 mg/cm^2 represent high-adiabat implosions ($\alpha \sim 25$) driven by a 1-ns square pulse (see Fig. 102.22) and show near 1-D performance in the assembly of the fuel (typically, the primary neutron yields are 50% to 70% of 1-D). The open circles represent low-adiabat implosions using a high-contrast pulse shape similar to the one shown in Fig. 102.22. Although designed to put the fuel shell on an adiabat of 4, the actual shape of the drive pulse delivered to the capsules varied from shot to shot such that the calculated adiabat ranged from ~ 4 to just over 6. In a few cases, the calculated adiabat ranged between 6 and 12. Therefore, the points are labeled as “mid- α ” and “ $\alpha \sim 4$ to 6” [a subset of these implosions is discussed later in **Comparison**

of Experimental Results and 2-D Simulations (p. 82)]. The key feature to note is that as the adiabat of the fuel decreases, the deviation of the experimentally inferred $\langle \rho R \rangle_n$ from 1-D performance increases. This discrepancy is expected and discussed further in **Comparison of Experimental Results and 2-D Simulations** (p. 82).

The drive pulses for the most recent implosions (shots 37967 and 37968) were carefully tuned to obtain the desired adiabat in the fuel. These two points are labeled as “ $\alpha = 3.5$ to 3.8.” The $\langle \rho R \rangle_n$ for shot 37968 was $98 \pm 22 \text{ mg/cm}^2$. The error here represents the standard deviation of the individual measurements (seven for this shot) and suggests a significant offset from TCC at shot time (the standard deviation is typically much larger than the errors associated with the individual measurements). For this shot, the measured offset was $\sim 40 \mu\text{m}$. The error bar is considerably smaller for shot 35713 and consistent with the much smaller offset at shot time, $15 \mu\text{m}$. This confirms that the variation among the individual measurements is dominated by the offset from TCC at shot time.

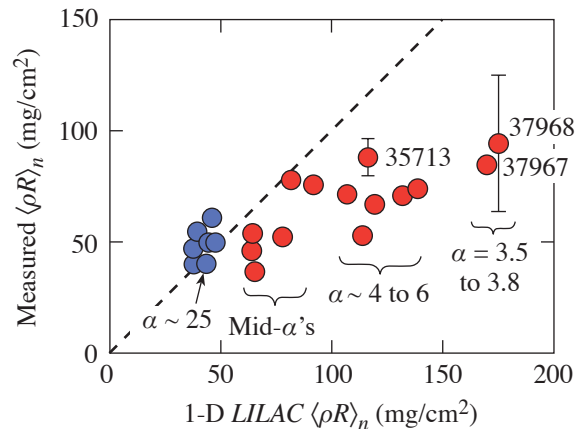


Figure 102.24
Measured $\langle \rho R \rangle_n$ as function of 1-D predicted value. The range of fuel adiabats is also indicated.

6. Stagnation

Peak density occurs in these implosions after the time of peak neutron production. Recent works^{23,24} have shown that the time history of the fuel ρR can be inferred from the combined measurements of the proton spectrum and the reaction rate history. The fuel ρR increases until final stagnation, when the bulk of the fuel is heated to a lower temperature than the hot

core. At this point, the x-ray flux increases dramatically, allowing a diagnosis of stagnation by x-ray imaging. Figure 102.25 shows a pair of quasi-monochromatic x-ray images from a grating-dispersed Kirkpatrick–Baez (KB) microscope²⁵ [Fig. 102.25(a)] and an x-ray framing camera (XRFC) filtered to be sensitive to x rays in the range of 4 to 5 keV [Fig. 102.25(b)]. The KB microscope is time integrating, has a resolution of $\sim 3 \mu\text{m}$, and is dispersed by a transmission grating that convolves space and spectrum in the spectral direction.²⁵ The stagnation-region size as a function of mean wavelength can be measured in the perpendicular direction. The radial profile of this emission at 4 keV is shown in Fig. 102.25(c) along with the azimuthal average lineout from the XRFC image (frame closest to peak x-ray emission within ± 50 ps, and within a 50-ps time window). These are compared with the simulated time-integrated emission profile from a *LILAC* postprocessor. The good agreement between both measurements and the simulated profile indicates that the fuel-stagnation core size is close to the 1-D prediction. The absolute flux and slope of the continuum determined from the grating-dispersed KB image [Fig. 102.25(d)] also show close agreement with the 1-D postprocessor prediction. The inferred stagnation electron temperature is $kT_e = 1.3$ keV (averaged over the time of the x-ray emission).

Comparison of Experimental Results and 2-D Simulations

The goal of the OMEGA cryogenic implosion program is to validate the predicted performance of low-adiabat, ignition-scaled implosions on OMEGA. The first set of experiments in this phase employs an $\alpha \sim 4$ pulse shape (shown as an inset in Fig. 102.22). Several $\alpha \leq 4$ implosions (see Fig. 102.24) were undertaken using the OMEGA laser; for brevity, only a single implosion (35713) will be described in detail.

The target was $870 \mu\text{m}$ in diameter with a $3.8\text{-}\mu\text{m}$ -thick GDP shell, a $95\text{-}\mu\text{m}$ -thick D_2 -ice layer, and an interior-ice-surface roughness of $4.2 \mu\text{m}$. The power spectrum for this surface, as shown in Fig. 102.26(a), is heavily weighted toward low-order modes. The capsule was $\sim 15 \mu\text{m}$ from target chamber center at the beginning of the implosion. The experimental neutron yield for this implosion was 1.6×10^{10} , which represents the highest-ever experimental yield obtained from a cryogenic $\alpha \sim 4$ implosion (YOC $\sim 18\%$). The ice-roughness spectrum from Fig. 102.26(a) and an initial 3.1%, $\ell = 1$ illumination nonuniformity, due to the target offset, were used in a *DRACO* 2-D hydrodynamic simulation.²⁶ Laser imprint was modeled in these calculations with modes $\ell = 2$ to 200. The simulated core can be seen in Fig. 102.26(b) to have

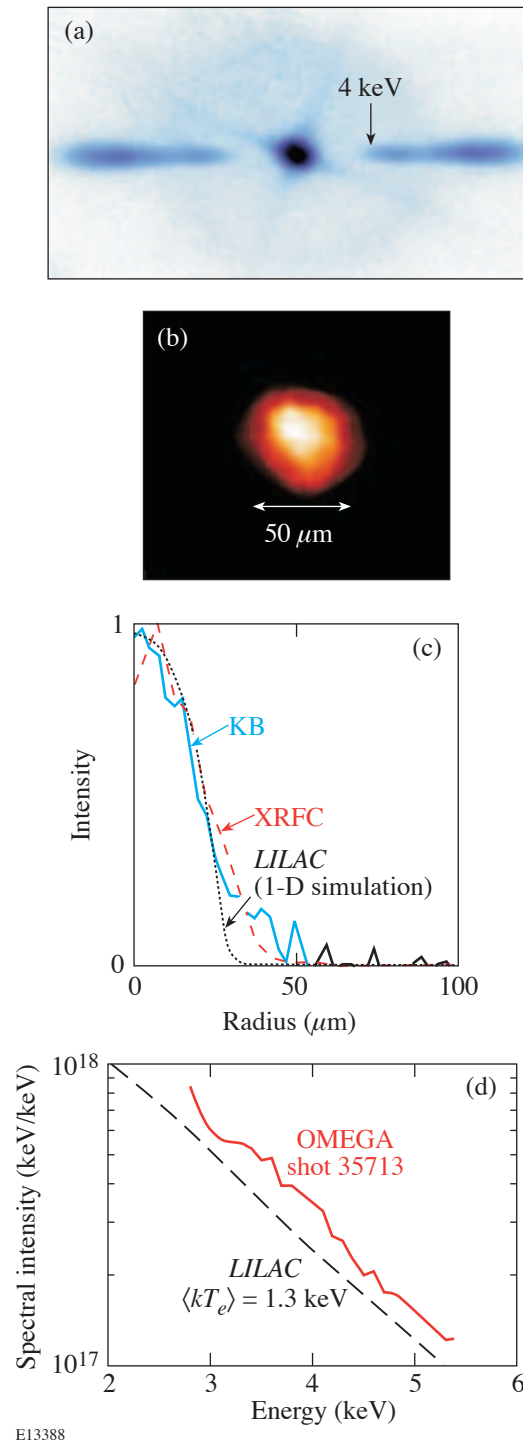


Figure 102.25

X-ray images of the fuel core at stagnation (shot 35713) from (a) a grating-dispersed KB and (b) an XRFC. (c) Radial profiles of images compared to 1-D prediction, and (d) absolute continuum x-ray spectrum (3 to 5 keV) obtained from a KB image of core emission compared to the 1-D prediction.

assembled slightly ($\sim 10 \mu\text{m}$) off-axis due to the presence of the $\ell = 1$ component of the initial inner-ice roughness and target offset, resulting in a 2-D simulated neutron yield of 1.8×10^{10} . Additional measurements and simulations are given in Fig. 102.26(c). The core performance, however, is not dominated by the $\ell = 1$ perturbation, as has been the case with previous experiments, but is dominated by the presence of growing perturbations due to modes 6 to 10 from the illumination. The performance of this implosion was also seen to be somewhat sensitive to the presence of laser imprint, due to the stability characteristics of the $\alpha \sim 4$ pulse. While the core does not appear to be influenced by the high-frequency modes, the presence of these modes is observed in the overdense regions of the shell near the corona. Simulations without laser imprint resulted in $\sim 20\%$ - to 25% -higher neutron yields. The secondary-yield comparison also shows that the *DRACO* simulation is close to the experimental result. The simulated neutron-

averaged areal density $[\langle \rho R \rangle_n (\text{DRACO}) = 101 \text{ mg/cm}^2]$ is close to the experimentally obtained value

$$[\langle \rho R \rangle_n (\text{expt.}) = 88 \pm 10 \text{ mg/cm}^2].$$

The angular variation of the simulation and the range of measured values are shown in Fig. 102.26(d).

It should be noted that the calculated and measured ion temperatures do not agree. The calculation of the ion temperature in the hydrocodes does not include the effect of the collective motion of the fuel. Furthermore, the calculation does not produce a thermally broadened neutron energy spectrum, which is what is used to experimentally infer the plasma ion temperature during the burn. This discrepancy will be addressed in the future.

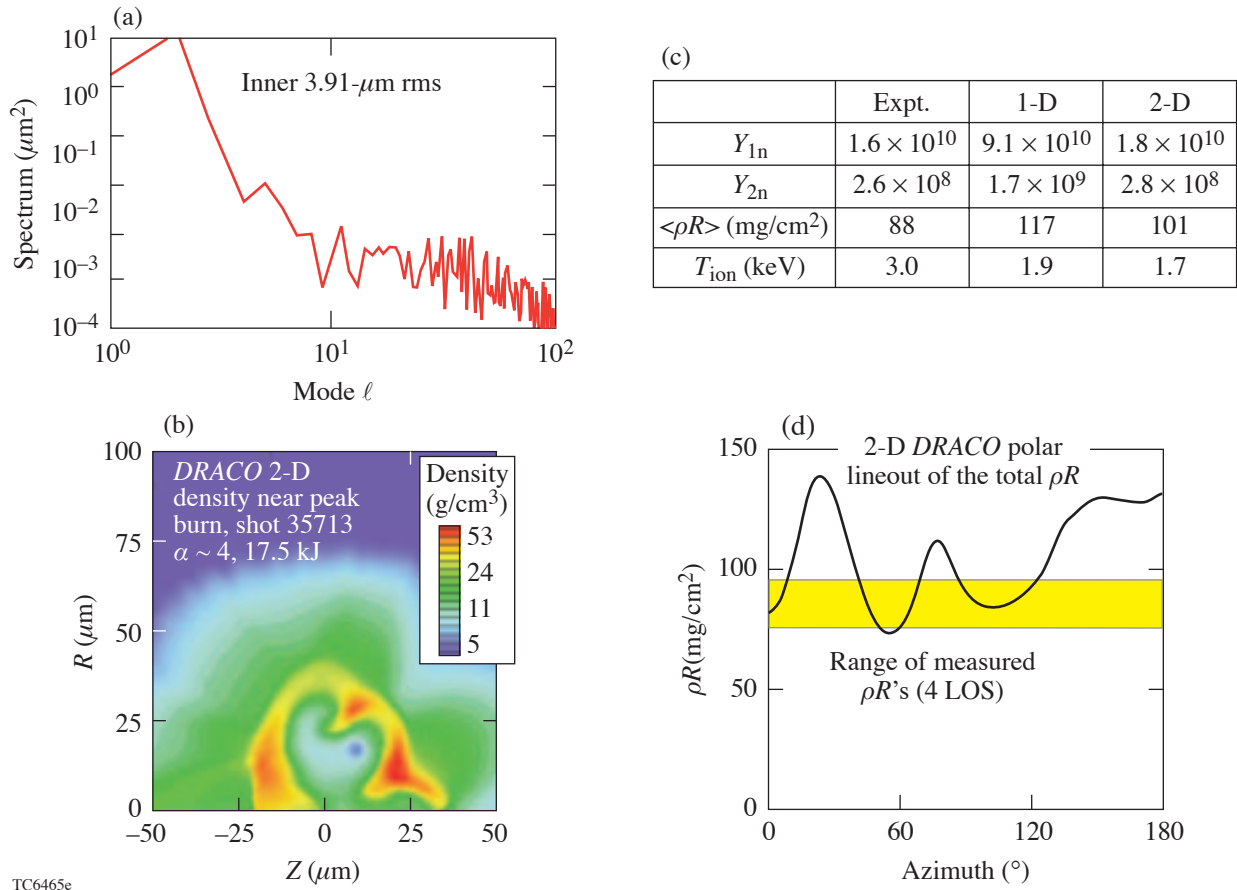


Figure 102.26

2-D *DRACO* simulation of shot 35713. (a) Spectrum of D_2 -ice-surface roughness used as input, (b) isodensity contours at time of peak neutron-production rate, (c) table of measured and predicted primary and secondary yields, $\langle \rho R \rangle_n$, and ion temperature, and (d) angular variation of areal density from *DRACO* simulation with the range of measurements indicated by the shaded region.

Low-adiabat target performance has been previously presented² as a compilation of all perturbation sources using a sum-in-quadrature representation of each source’s contribution to the roughness of the inner ice layer at the end of the acceleration phase of the implosion. The scaling parameter $\bar{\sigma}$ is defined as

$$\bar{\sigma}^2 = 0.06\sigma_{\ell(\ell < 10)}^2 + \sigma_{\ell(\ell > 10)}^2,$$

where σ_{ℓ} is the rms roughness computed over the indicated mode range. At this time in the implosion, this surface decouples from the ablation region. The effects of all major sources of perturbation leading to the initial seed of the deceleration-phase Rayleigh–Taylor (RT) instability have then been set. An example of the $\bar{\sigma}$ scaling determined from 2-D *DRACO* simulations is shown in Fig. 102.27, where a comparison is made between the NIF $\alpha = 3$ and OMEGA $\alpha = 4$ designs.

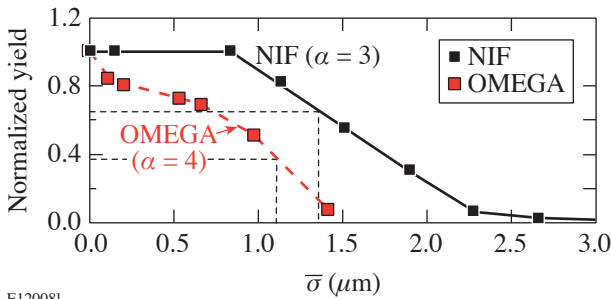


Figure 102.27 Comparison of the $\bar{\sigma}$ stability analysis for OMEGA $\alpha = 4$ and NIF $\alpha = 3$ designs. All values were determined with the hydrocode *DRACO*.

From Fig. 102.27 it can be seen that the OMEGA implosions are more sensitive to the higher values of $\bar{\sigma}$ than the NIF implosions. This is because the OMEGA targets have been energetically scaled from their NIF ignition counterparts. The physically smaller OMEGA targets are more sensitive than NIF targets when exposed to the same levels of nonuniformities. For identical values of $\bar{\sigma}$, the OMEGA implosions result in lower values of yield relative to 1-D simulations.

Using the $\bar{\sigma}$ scaling with yield allows an experimental validation of the numerical modeling of current OMEGA experiments. This lends credibility to the ability of these numerical models to predict ignition for direct-drive target designs on the NIF. Using current NIF specifications for the allowed levels of perturbations (imprint, power imbalance,

and inner- and outer-surface roughness) results in a $\bar{\sigma}$ value of ~ 1.4 for the NIF capsule with a gain of ~ 30 (see McKenty *et al.*²). The corresponding OMEGA implosion would have a $\bar{\sigma}$ value of ~ 1.1 and a performance YOC of $\sim 40\%$. These conditions are denoted as the dashed lines in Fig. 102.28, representing the performance of OMEGA implosions required for the validation of the ignition design.

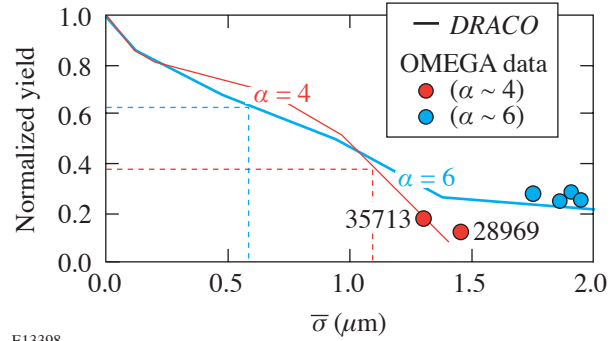


Figure 102.28 Comparison of *DRACO* predictions of yield reduction as a function of $\bar{\sigma}$ for $\alpha \sim 4$ and $\alpha \sim 6$ experiments on OMEGA.

Figure 102.28 illustrates the $\bar{\sigma}$ scaling for both the OMEGA $\alpha \sim 4$ and previous $\alpha \sim 6$ implosions. While it appears that $\bar{\sigma}$ scales the same for the $\alpha \sim 4$ and $\alpha \sim 6$ implosions, one must remember that $\bar{\sigma}$ represents the outcome of Rayleigh–Taylor growth of perturbation seeds during the acceleration phase of the implosion. Identical initial perturbations imposed during $\alpha \sim 4$ and $\alpha \sim 6$ target implosions will not result in the same $\bar{\sigma}$ value. The separate stability characteristics of the two implosions determine the final $\bar{\sigma}$ value for each target. As such, the $\alpha \sim 6$ implosions, due to their enhanced stability relative to the $\alpha \sim 4$ implosions, have resultant $\bar{\sigma}$ values that are lower than $\alpha \sim 4$ implosions with comparable initial conditions. The $\bar{\sigma}$ parameter (extracted from *DRACO* simulations) has been used to plot the experimental yield performance on the graph in Fig. 102.28 for recent OMEGA experiments. The experimental points are in good agreement with the $\bar{\sigma}$ scaling. As target-layer uniformity and OMEGA irradiation uniformity are improved, the $\alpha \sim 4$ implosion experiments are expected to approach the $\sim 40\%$ YOC goal.

Additional results obtained from all $\alpha \sim 6$ and $\alpha \sim 4$ implosions with ice quality better than $5\text{-}\mu\text{m}$ rms and target offset $< 42\ \mu\text{m}$ are shown in Fig. 102.29. The YOC for the experimen-

tal data is compared with the trends of two series of *DRACO* simulations run with varying initial ice roughness for no offset and for a 30- μm offset from target chamber center. The effects of laser imprint are included in all of the *DRACO* simulations. The *DRACO* simulations are in good agreement with the YOC values and, therefore, explain yield reduction as due principally to the ice-layer roughness and target offset.

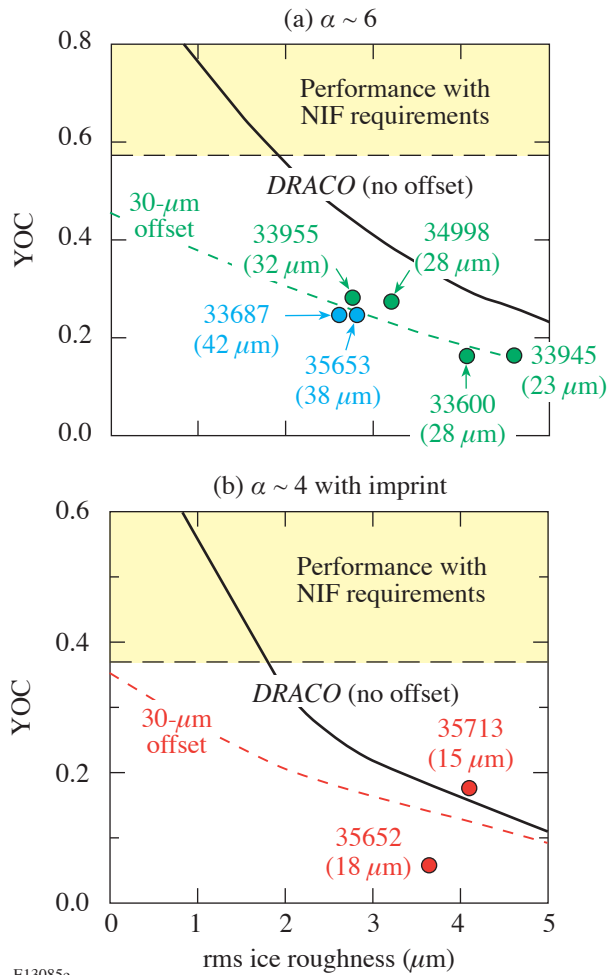


Figure 102.29 Comparison of YOC to *DRACO* predictions for (a) $\alpha \sim 6$ and (b) $\alpha \sim 4$ experiments on OMEGA as a function of ice roughness and target offset. Lower curves are *DRACO*-simulated YOC for a 30- μm target offset.

Conclusions

In summary, recent cryogenic, D_2 direct-drive implosions on the OMEGA Laser System are showing good agreement with numerical simulations. Measurement and simulation of absorption agree closely (within $\pm 2\%$), enabling the accurate

design of pulse shapes that maintain the fuel on a calculated adiabat of as low as ~ 4 . Areal densities of as high as $\sim 100 \text{ mg/cm}^2$ for temperatures of ~ 2 to 3 keV result from implosions that have low ice roughness, low target offset, and low calculated fuel adiabat. Resulting fusion yields are well explained by 2-D simulations, and the expected reduction of yield from 1-D is currently limited by the ice roughness and target offset. Extrapolation to conditions on the NIF result in high gain (≥ 30), increasing confidence in the direct-drive approach to ICF ignition.

ACKNOWLEDGMENT

The authors are extremely grateful to the staff of the Laboratory for Laser Energetics for their tireless dedication to the cryogenic implosion program and the operation of the OMEGA laser system. In particular, the authors would like to acknowledge the efforts of the Cryogenic Target Fabrication Group for the production of layered and characterized capsules on a regular schedule. This work was supported by the U. S. Department of Energy Office of Inertial Confinement Fusion under Cooperative Agreement No. DE-FC52-92SF19460, the University of Rochester, and the New York State Energy Research and Development Authority. The support of the DOE does not constitute an endorsement by the DOE of the views expressed in this article.

REFERENCES

1. J. Nuckolls *et al.*, *Nature* **239**, 139 (1972).
2. P. W. McKenty, V. N. Goncharov, R. P. J. Town, S. Skupsky, R. Betti, and R. L. McCrory, *Phys. Plasmas* **8**, 2315 (2001).
3. S. Skupsky, R. Betti, T. J. B. Collins, V. N. Goncharov, D. R. Harding, R. L. McCrory, P. W. McKenty, D. D. Meyerhofer, and R. P. J. Town, in *Inertial Fusion Sciences and Applications 2001*, edited by K. Tanaka, D. D. Meyerhofer, and J. Meyer-ter-Vehn (Elsevier, Paris, 2002), pp. 240–245.
4. R. Betti, V. N. Goncharov, R. L. McCrory, and C. P. Verdon, *Phys. Plasmas* **5**, 1446 (1998).
5. M. C. Herrmann, M. Tabak, and J. D. Lindl, *Nucl. Fusion* **41**, 99 (2001).
6. J. Meyer-ter-Vehn, *Nucl. Fusion* **22**, 561 (1982).
7. V. N. Goncharov, J. P. Knauer, P. W. McKenty, P. B. Radha, T. C. Sangster, S. Skupsky, R. Betti, R. L. McCrory, and D. D. Meyerhofer, *Phys. Plasmas* **10**, 1906 (2003).
8. T. R. Boehly, D. L. Brown, R. S. Craxton, R. L. Keck, J. P. Knauer, J. H. Kelly, T. J. Kessler, S. A. Kumpan, S. J. Loucks, S. A. Letzring, F. J. Marshall, R. L. McCrory, S. F. B. Morse, W. Seka, J. M. Soures, and C. P. Verdon, *Opt. Commun.* **133**, 495 (1997).
9. Laboratory for Laser Energetics LLE Review **81**, 6, NTIS document No. DOE/SF/19460-335 (1999). Copies may be obtained from the National Technical Information Service, Springfield, VA 22161.
10. C. Stoeckl, C. Chiritescu, J. A. Delettrez, R. Epstein, V. Yu. Glebov, D. R. Harding, R. L. Keck, S. J. Loucks, L. D. Lund, R. L. McCrory, P. W. McKenty, F. J. Marshall, D. D. Meyerhofer, S. F. B. Morse, S. P. Regan, P. B. Radha, S. Roberts, T. C. Sangster, W. Seka, S. Skupsky,

- V. A. Smalyuk, C. Sorce, J. M. Soures, R. P. J. Town, J. A. Frenje, C. K. Li, R. D. Petrasso, F. H. Séguin, K. Fletcher, S. Padalino, C. Freeman, N. Izumi, R. Lerche, and T. W. Phillips, *Phys. Plasmas* **9**, 2195 (2002).
11. W. R. Donaldson, R. Boni, R. L. Keck, and P. A. Jaanimagi, *Rev. Sci. Instrum.* **73**, 2606 (2002).
12. M. C. Richardson, P. W. McKenty, F. J. Marshall, C. P. Verdon, J. M. Soures, R. L. McCrory, O. Barnouin, R. S. Craxton, J. Delettrez, R. L. Hutchison, P. A. Jaanimagi, R. Keck, T. Kessler, H. Kim, S. A. Letzring, D. M. Roback, W. Seka, S. Skupsky, B. Yaakobi, S. M. Lane, and S. Prussin, in *Laser Interaction and Related Plasma Phenomena*, edited by H. Hora and G. H. Miley (Plenum Publishing, New York, 1986), Vol. 7, pp. 421–448.
13. T. J. Kessler, Y. Lin, J. J. Armstrong, and B. Velazquez, in *Laser Coherence Control: Technology and Applications*, edited by H. T. Powell and T. J. Kessler (SPIE, Bellingham, WA, 1993), Vol. 1870, pp. 95–104.
14. T. R. Boehly, V. A. Smalyuk, D. D. Meyerhofer, J. P. Knauer, D. K. Bradley, R. S. Craxton, M. J. Guardalben, S. Skupsky, and T. J. Kessler, *J. Appl. Phys.* **85**, 3444 (1999).
15. S. Skupsky, R. W. Short, T. Kessler, R. S. Craxton, S. Letzring, and J. M. Soures, *J. Appl. Phys.* **66**, 3456 (1989).
16. F. J. Marshall, J. A. Delettrez, R. Epstein, R. Forties, V. Yu. Glebov, J. H. Kelly, T. J. Kessler, J. P. Knauer, P. W. McKenty, S. P. Regan, V. A. Smalyuk, C. Stoeckl, J. A. Frenje, C. K. Li, R. D. Petrasso, and F. H. Séguin, *Bull. Am. Phys. Soc.* **48**, 56 (2003).
17. F. J. Marshall, J. A. Delettrez, R. Epstein, R. Forties, R. L. Keck, J. H. Kelly, P. W. McKenty, S. P. Regan, and L. J. Waxer, *Phys. Plasmas* **11**, 251 (2004).
18. R. C. Malone, R. L. McCrory, and R. L. Morse, *Phys. Rev. Lett.* **34**, 721 (1975).
19. J. Delettrez, *Can. J. Phys.* **64**, 932 (1986).
20. W. Seka, C. Stoeckl, V. N. Goncharov, R. E. Bahr, T. C. Sangster, R. S. Craxton, J. A. Delettrez, A. V. Maximov, J. Myatt, A. Simon, and R. W. Short, *Bull. Am. Phys. Soc.* **49**, 179 (2004).
21. C. Stoeckl, V. Yu. Glebov, S. Roberts, T. C. Sangster, R. A. Lerche, R. L. Griffith, and C. Sorce, *Rev. Sci. Instrum.* **74**, 1713 (2003).
22. R. D. Petrasso, J. A. Frenje, C. K. Li, F. H. Séguin, J. R. Rygg, B. E. Schwartz, S. Kurebayashi, P. B. Radha, C. Stoeckl, J. M. Soures, J. Delettrez, V. Yu. Glebov, D. D. Meyerhofer, and T. C. Sangster, *Phys. Rev. Lett.* **90**, 095002 (2003).
23. V. A. Smalyuk, P. B. Radha, J. A. Delettrez, V. Yu. Glebov, V. N. Goncharov, D. D. Meyerhofer, S. P. Regan, S. Roberts, T. C. Sangster, J. M. Soures, C. Stoeckl, J. A. Frenje, C. K. Li, R. D. Petrasso, and F. H. Séguin, *Phys. Rev. Lett.* **90**, 135002 (2003).
24. J. A. Frenje, C. K. Li, F. H. Séguin, J. Deciantis, S. Kurebayashi, J. R. Rygg, R. D. Petrasso, J. Delettrez, V. Yu. Glebov, C. Stoeckl, F. J. Marshall, D. D. Meyerhofer, T. C. Sangster, V. A. Smalyuk, and J. M. Soures, *Phys. Plasmas* **11**, 2798 (2003).
25. F. J. Marshall, J. A. Delettrez, R. Epstein, and B. Yaakobi, *Phys. Rev. E* **49**, 4381 (1994).
26. D. Keller, T. J. B. Collins, J. A. Delettrez, P. W. McKenty, P. B. Radha, B. Whitney, and G. A. Moses, *Bull. Am. Phys. Soc.* **44**, 37 (1999).

Stopping, Straggling, and Blooming of Directed Energetic Electrons in Hydrogenic Plasmas

A basic problem in plasma physics is the interaction and energy loss of energetic, charged particles in plasmas,^{1–3} including the effects of penetration, longitudinal straggling, and lateral blooming. This problem has traditionally focused on ions (i.e., protons, alphas, etc.), either in the context of heating and/or ignition in, for example, inertially confined plasmas (ICF)^{3–7} or the use of these particles for diagnosing implosion dynamics.⁸ More recently, prompted in part by the concept of fast ignition (FI) for ICF,⁹ studies have begun to consider energy deposition from relativistic fast electrons in deuterium–tritium (DT) plasmas.^{9–14} In this context, the mean penetration and stopping power for energetic electrons interacting with a uniform hydrogenic plasma of arbitrary density and temperature were recently calculated. Therein, the randomizing effect of electron scattering, which has a cumulative effect of bending the path of the electrons away from their initial direction, was linked to energy loss.¹⁴ This article presents calculations that show, for the first time, the effects of longitudinal straggling and transverse blooming and their inextricable relationship with enhanced electron energy deposition. It is demonstrated that, while the initial penetration results in approximate uniform energy deposition, the latter penetration has mutual couplings of energy loss, straggling, and blooming that lead to an extended region of enhanced, nonuniform energy deposition. This present work is important for quantitatively evaluating the energy deposition in several current problems. In the case of FI, for example, no evaluations have treated either straggling or blooming upon the energy deposition; without evaluation no confident assessment of ignition requirements can be made. Therefore, the calculations in this article form the foundation for a baseline, at the very least, or an accurate assessment, at the very most, by which to evaluate these effects upon fast ignition. In addition to FI, these calculations are, in general, sufficient to be of relevance to other current problems, such as fast-electron preheat¹⁵ in ICF, or to energy deposition of relativistic electrons in astrophysical jets.¹⁶

To delineate these processes, we calculate the different moments by analytically solving an integro-differential diffusion equation,¹⁷ thereby rigorously determining the angular and spatial distributions of the scattered electrons:

$$\frac{\partial f}{\partial s} + \mathbf{v} \cdot \nabla f = n_i \int [f(\mathbf{x}, \mathbf{v}', s) - f(\mathbf{x}, \mathbf{v}, s)] \sigma(|\mathbf{v} - \mathbf{v}'|) d\mathbf{v}', \quad (1)$$

where $f(\mathbf{x}, \mathbf{v}, s)$ is the distribution function, n_i is the number density of fully ionized plasma ions of charge Z , \mathbf{x} is the position where scattering occurs, $\sigma = \sigma_{ei} + Z\sigma_{ee}$ is the total scattering cross section with σ_{ei} the Rutherford e -ion cross section¹⁸ and σ_{ee} the Møller e - e cross section.¹⁹ We solve this equation in cylindrical coordinates with the assumption that the scattering is azimuthally symmetric. After expanding the distribution in spherical harmonics and substituting into Eq. (1), two differential equations for the longitudinal and lateral distributions are obtained. For the longitudinal distribution,

$$\frac{\partial F_{\ell m}^n(s)}{\partial s} + \kappa_{\ell}(s) F_{\ell m}^n(s) - n \left[\frac{\ell}{\sqrt{4\ell^2 - 1}} F_{\ell-1, m}^{n-1}(s) + \frac{\ell+1}{\sqrt{4(\ell+1)^2 - 1}} F_{\ell+1, m}^{n-1}(s) \right] = 0, \quad (2)$$

and for the lateral distribution,

$$\begin{aligned}
 & \frac{\partial F_{\ell m}^n(s)}{\partial s} + \kappa_\ell(s) F_{\ell m}^n(s) \\
 & - \frac{n}{2} \left[\sqrt{\frac{(\ell+m)(\ell+m-1)}{4\ell^2-1}} F_{\ell-1, m-1}^{n-1}(s) \right. \\
 & + \sqrt{\frac{(\ell+m+2)(\ell+m+1)}{4(\ell+1)^2-1}} F_{\ell+1, m+1}^{n-1}(s) \\
 & - \sqrt{\frac{(\ell-m)(\ell-m-1)}{4\ell^2-1}} F_{\ell-1, m+1}^{n-1}(s) \\
 & \left. - \sqrt{\frac{(\ell-m+2)(\ell-m+1)}{4(\ell+1)^2-1}} F_{\ell+1, m+1}^{n-1}(s) \right] = 0, \quad (3)
 \end{aligned}$$

where the moments are defined as

$$F_{\ell m}^n(s) = \int_{-\infty}^{\infty} x_j^n f_{\ell m}(\mathbf{x}, s) d\mathbf{x} \quad (4)$$

and $j=1, 2, 3$ represents x, y, z , respectively.

$$\kappa_\ell(s) = n_i \int \left(\frac{d\sigma}{d\Omega} \right) [1 - P_\ell(\cos\theta)] d\Omega, \quad (5)$$

where $P_\ell(\cos\theta)$ is the Legendre polynomial and $\kappa_\ell(s)$ is directly related to the basic transport cross section.² Equations (2) and (3) are coupled to adjacent orders in n and are solved with the boundary condition

$$F_{\ell m}^n(s) = \sqrt{\frac{2\ell+1}{4\pi}} \delta_{m0} \delta_{n0} \exp\left[-\int_0^s \kappa_\ell(s') ds'\right], \quad (6)$$

where $F_{\ell m}^n(0) = 0$ for $n \neq 0$. Solving for κ_1 and κ_2 ,

$$\kappa_1 = 4\pi n_i \left(\frac{r_0}{\gamma\beta^2} \right)^2 \left\{ Z^2 \ln \Lambda^{ei} + \frac{4(\gamma+1)^2}{\left[2\sqrt{(\gamma+1)/2} \right]^4} Z \ln \Lambda^{ee} \right\}; \quad (7)$$

and

$$\kappa_2 = 12\pi n_i \left(\frac{r_0}{\gamma\beta^2} \right)^2 \times \left\{ Z^2 \left(\ln \Lambda^{ei} - \frac{1}{2} \right) + \frac{4(\gamma+1)^2}{\left[2\sqrt{(\gamma+1)/2} \right]^4} Z \left(\ln \Lambda^{ee} - \frac{1}{2} \right) \right\}. \quad (8)$$

κ_1 is related to the slowing-down cross section,² which characterizes the loss of directed velocity in the scattering, and κ_2 is related to the deflection cross section, which represents the mean-square increment in the transverse electron velocity during the scattering process.² $\beta = v/c$ and $\gamma = (1 - \beta^2)^{-1/2}$; $r_0 = e^2/m_0c^2$ is the classical electron radius. The appropriate Coulomb logarithms are evaluated in an earlier paper.¹⁴ The angular distribution function is obtained from

$$\begin{aligned}
 f(\theta, E) &= \frac{1}{4\pi} \sum_{\ell=0}^{\infty} (2\ell+1) P_\ell(\cos\theta) \\
 &\times \exp\left[-\int_{E_0}^E \kappa_\ell(E') \left(\frac{dE'}{ds} \right)^{-1} dE' \right], \quad (9)
 \end{aligned}$$

from which $\langle P_\ell(\cos\theta) \rangle$ is calculated:

$$\langle P_\ell(\cos\theta) \rangle = \exp\left[-\int_{E_0}^E \kappa_\ell(E') \left(\frac{dE'}{ds} \right)^{-1} dE' \right], \quad (10)$$

where dE/ds is plasma stopping power taken from Ref. 14. From these results, Eqs. (2) and (3) are solved, and basic moments required for the calculation of the longitudinal and lateral distributions are evaluated:

$$\langle x \rangle = \int_{E_0}^E \langle P_1(\cos\theta) \rangle \left(\frac{dE'}{ds} \right)^{-1} dE', \quad (11)$$

which was evaluated in previous work for the case of 1-MeV electron stopping in a 300-g/cm³ DT plasma at 5 keV. This results in a penetration of 13.9 μm (Ref. 14). For astrophysical jets, however, for which $n_e \sim 10/\text{cm}^3$, the penetration is $\sim 10^4$ light years:

$$\begin{aligned} \langle x^2 \rangle &= \frac{2}{3} \int_{E_0}^E \langle P_1(\cos\theta) \rangle \left(\frac{dE'}{ds} \right)^{-1} \\ &\times \left[\int_{E_0}^{E'} \frac{1 + 2 \langle P_2(\cos\theta) \rangle}{\langle P_1(\cos\theta) \rangle} \left(\frac{dE''}{ds} \right)^{-1} dE'' \right] dE', \quad (12) \end{aligned}$$

because of azimuthal symmetry,

$$\langle y \rangle = \langle z \rangle = 0, \quad (13)$$

and

$$\begin{aligned} \langle y^2 \rangle = \langle z^2 \rangle &= \frac{2}{3} \int_{E_0}^E \langle P_1(\cos\theta) \rangle \left(\frac{dE'}{ds} \right)^{-1} \\ &\times \left[\int_{E_0}^{E'} \frac{1 - \langle P_2(\cos\theta) \rangle}{\langle P_1(\cos\theta) \rangle} \left(\frac{dE''}{ds} \right)^{-1} dE'' \right] dE'. \quad (14) \end{aligned}$$

Range or longitudinal straggling is defined by

$$\Sigma_R(E) = \sqrt{\langle x^2 \rangle - \langle x \rangle^2}. \quad (15)$$

Beam blooming is defined by

$$\Sigma_B(E) = \sqrt{\langle y^2 \rangle}. \quad (16)$$

Figure 102.30 shows the calculated straggling [Fig. 102.30(a)] and blooming [Fig. 102.30(b)] that result from the effects of scattering off electrons alone and off electrons plus ions. Energy deposition, toward the end of the penetration, is transferred to an extended region about the mean penetration of 13.8 μm , specifically $\sim \pm 3 \mu\text{m}$ longitudinally and $\sim \pm 5 \mu\text{m}$ laterally. From a different point of view, Fig. 102.31 shows the

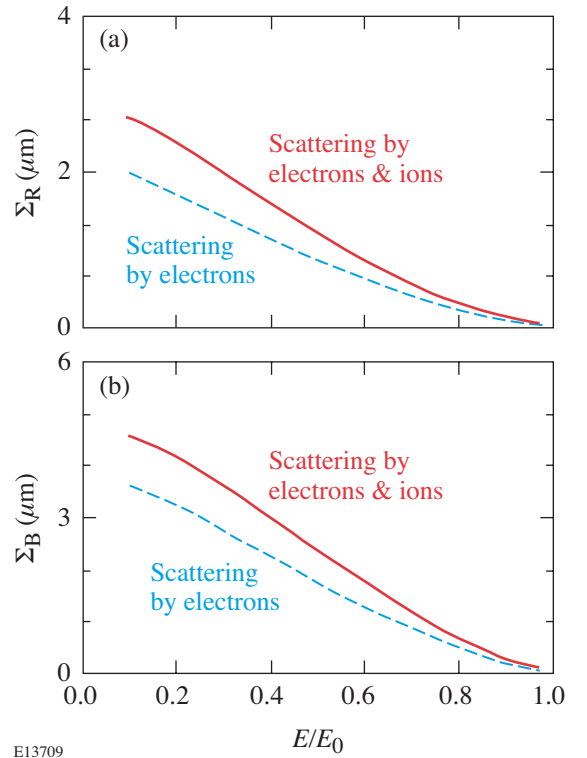


Figure 102.30
For 1-MeV electrons in a DT plasma ($\rho = 300 \text{ g/cm}^3$, $T_e = 5 \text{ keV}$): (a) The calculated range straggling $\Sigma_R(E)$ and (b) lateral blooming $\Sigma_B(E)$ are plotted as functions of electron residual energy. For this case, the penetration $\langle x \rangle$ is 13.9 μm (Ref. 14).

enhancement of the stopping power in the extended region in which longitudinal straggling is important. Including the effects of blooming would effectively increase (decrease) Σ_R for values less (greater) than the mean penetration.

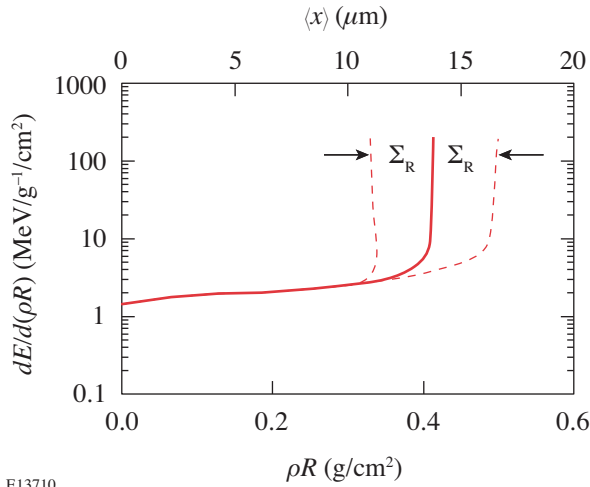


Figure 102.31
The stopping power, plotted as a function of the electron penetration. The solid line represents the mean energy loss, while the two dashed lines indicate the straggling range over which energy is effectively spread (in this plot, important contributions from blooming are not included; see text). As a result of the scattering, the energy transfer increases notably near the end of the penetration (i.e., an effective Bragg peak).

Figure 102.32 shows the effects of both straggling and blooming as a function of the square root of the penetration. Note that little straggling or blooming occurs until the 1-MeV electrons have traversed a significant portion of the final penetration (~60%, corresponding to only ~40% energy loss). Therefore, the assumption of uniform energy deposition, used in some previous calculations,¹¹ has some approximate justification for only the first ~40% of the energy loss. For energy loss greater than 40%, both straggling and blooming expand linearly with the square root of the penetration, an effect associated with the enhanced energy loss of the effective Bragg peak (Fig. 102.31). As a direct consequence of these multiple scattering effects, these results demonstrate the inextricable linkage between enhanced energy loss, straggling, and blooming.

Figure 102.33 shows a schematic representation of an FI capsule. The relativistic electrons are generated by an intense laser interacting at the critical surface. As the electrons are initially generated and transported, they are subject to Weibel-like instabilities,^{20,21} which can cause both spreading and

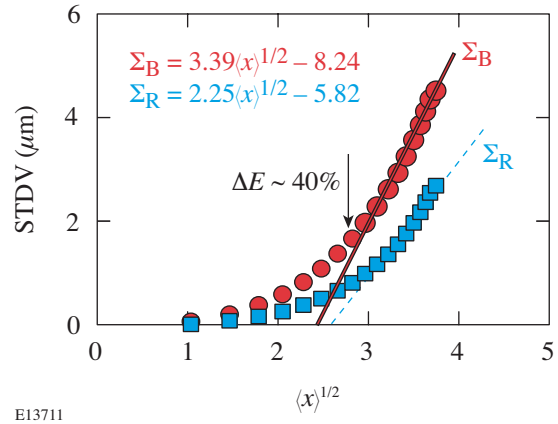


Figure 102.32
The longitudinal range straggling and lateral blooming of a 1-MeV electron beam, plotted as a function of the square root of the penetration ($\langle x \rangle$), for conditions of Fig. 102.30. Note that when the electrons have lost more than ~40% of their energy, both Σ_R and Σ_B are approximately proportional to $\sqrt{\langle x \rangle}$. Equations listed in the figure are the results of fitting only this final portion of the penetration.

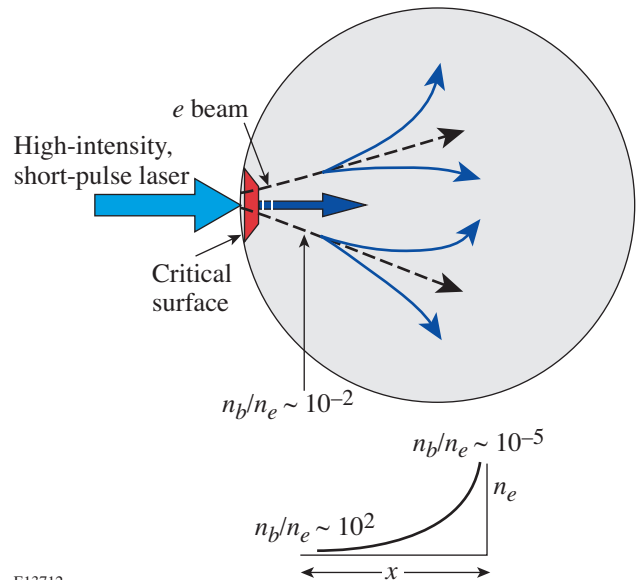


Figure 102.33
Schematic illustration of beam blooming in a precompressed FI capsule. Two distinct regions for electron transport are illustrated: first, when $n_b/n_e > 10^{-2}$, the electron transport is highly filamented due to Weibel-like instabilities that dominate energy loss and beam blooming; however, for $n_b/n_e < 10^{-2}$, which occurs as the beam penetrates farther into the denser portion of the capsule, Weibel-like instabilities are stabilized and the electrons are then subject to the multiple scattering, straggling, and blooming processes described herein. The dashed lines schematically indicate electron-beam trajectories without the effects of multiple scattering blooming and straggling (see text).

energy loss in this region. However, for electrons that transport farther into the increased-density portions of the capsule $n_b/n_e < 10^{-2}$, Weibel-like instabilities are stabilized and the electrons then become subject to the multiple scattering processes described herein. In this regime, the interaction can be envisioned as the linear superposition of individual, isolated electrons interacting with plasma. Therefore, these scattering processes, which involve energy loss, straggling, and beam blooming, become the ultimate mechanism that determines the details of energy deposition, whether in the dense core or outside, and ultimately determine the effectiveness of capsule ignition. From a different point of view, the extent of beam blooming and straggling is critical for FI target design since the finite size of the highly compressed core requires accurate understanding and control of beam divergence, which, if too severe, will preclude ignition.

In summary, from fundamental principles, the interaction of directed energetic electrons with hydrogenic plasmas is analytically modeled. For the first time, the effects of stopping, straggling, and beam blooming—a consequence of multiple scattering and energy loss—are rigorously treated from a unified approach. For fast ignition, enhanced energy deposition is found to be inextricably linked to beam blooming and straggling. We demonstrate that the mutual interaction of these effects will lead to an enhanced nonuniform region of energy deposition. Blooming and straggling effects will eventually dominate over all other sources of beam divergence and are therefore critical for evaluating the requirements of fast ignition.

ACKNOWLEDGMENT

This work was supported in part by U.S. Department of Energy Contract #DE-FG03-99SF21782, LLE subcontract #PO410025G, LLNL subcontract #B313975, and the Fusion Science Center for Extreme States of Matter and Fast Ignition Physics at University of Rochester.

REFERENCES

1. L. Spitzer, *Physics of Fully Ionized Gases*, 2nd rev. ed., Interscience Tracts on Physics and Astronomy (Interscience, New York, 1962).
2. B. A. Trubnikov, in *Reviews of Plasma Physics*, edited by M. A. Leontovich (Consultants Bureau, New York, 1965).
3. C. K. Li and R. D. Petrasso, *Phys. Rev. Lett.* **70**, 3063 (1993).
4. J. D. Lindl, *Inertial Confinement Fusion: The Quest for Ignition and Energy Gain Using Indirect Drive* (Springer-Verlag, New York, 1998).
5. J. D. Lindl, R. L. McCrory, and E. M. Campbell, *Phys. Today* **45**, 32 (1992).
6. S. Skupsky, *Phys. Rev. A* **16**, 727 (1977).
7. C. K. Li and R. D. Petrasso, *Phys. Rev. Lett.* **70**, 3059 (1993).
8. R. D. Petrasso, J. A. Frenje, C. K. Li, F. H. Séguin, J. R. Rygg, B. E. Schwartz, S. Kurebayashi, P. B. Radha, C. Stoeckl, J. M. Soures, J. Delettrez, V. Yu. Glebov, D. D. Meyerhofer, and T. C. Sangster, *Phys. Rev. Lett.* **90**, 095002 (2003); V. A. Smalyuk, P. B. Radha, J. A. Delettrez, V. Yu. Glebov, V. N. Goncharov, D. D. Meyerhofer, S. P. Regan, S. Roberts, T. C. Sangster, J. M. Soures, C. Stoeckl, J. A. Frenje, C. K. Li, R. D. Petrasso, and F. H. Séguin, *Phys. Rev. Lett.* **90**, 135002 (2003); F. H. Séguin, J. A. Frenje, C. K. Li, D. G. Hicks, S. Kurebayashi, J. R. Rygg, B.-E. Schwartz, R. D. Petrasso, S. Roberts, J. M. Soures, D. D. Meyerhofer, T. C. Sangster, J. P. Knauer, C. Sorce, V. Yu. Glebov, C. Stoeckl, T. W. Phillips, R. J. Leeper, K. Fletcher, and S. Padalino, *Rev. Sci. Instrum.* **74**, 975 (2003); J. A. Frenje, C. K. Li, and F. H. Séguin, *Phys. Plasmas* **11**, 2798 (2004).
9. M. Tabak *et al.*, *Phys. Plasmas* **1**, 1626 (1994).
10. C. Deutsch *et al.*, *Phys. Rev. Lett.* **77**, 2483 (1996); **85**, 1140 (E) (2000).
11. S. Atzeni, *Phys. Plasmas* **6**, 3316 (1999).
12. M. H. Key, M. D. Cable, T. E. Cowan, K. G. Estabrook, B. A. Hammel, S. P. Hatchett, E. A. Henry, D. E. Hinkel, J. D. Kilkenny, J. A. Koch, W. L. Kruer, A. B. Langdon, B. F. Lasinski, R. W. Lee, B. J. MacGowan, A. MacKinnon, J. D. Moody, M. J. Moran, A. A. Offenberger, D. M. Pennington, M. D. Perry, T. J. Phillips, T. C. Sangster, M. S. Singh, M. A. Stoyer, M. Tabak, G. L. Tietbohl, M. Tsukamoto, K. Wharton, and S. C. Wilks, *Phys. Plasmas* **5**, 1966 (1998).
13. C. Ren *et al.*, *Phys. Rev. Lett.* **93**, 185004 (2004).
14. C. K. Li and R. D. Petrasso, *Phys. Rev. E* **70**, 067401 (2004).
15. M. D. Rosen *et al.*, *Phys. Rev. A* **36**, 247 (1987).
16. P. A. Hughes, ed. *Beams and Jets in Astrophysics*, Cambridge Astrophysics Series (Cambridge University Press, Cambridge, England, 1991).
17. H. W. Lewis, *Phys. Rev.* **78**, 526 (1950).
18. N. F. Mott, *Proc. R. Soc. Lond. A, Math. Phys. Sci.* **A124**, 425 (1929); N. F. Mott, M. A. Gonville, and C. College, *Proc. R. Soc. Lond. A, Math. Phys. Sci.* **CXXXV**, 429 (1932).
19. Chr. Møller, *Ann. Phys.* **14**, 531 (1932).
20. E. S. Weibel, *Phys. Rev. Lett.* **2**, 83 (1959).
21. M. Honda, J. Meyer-ter-Vehn, and A. Pukhov, *Phys. Rev. Lett.* **85**, 2128 (2000).

Multidimensional Analysis of Direct-Drive, Plastic-Shell Implosions on OMEGA

Introduction

In direct-drive inertial confinement fusion (ICF),¹ nominally identical beams heat and compress a nearly spherical shell containing low-density gas. The high-density shell is unstable due to the Rayleigh–Taylor instability (RT)² at the ablation surface when the low-density blowoff plasma accelerates it. The target becomes RT unstable again, but at the inner fuel–shell interface or inner shell surface, later in the implosion when the lower-density gas decelerates the cold shell. Nonuniformities associated with the target, beam-to-beam power imbalance, and the individual beams seed this instability growth during both acceleration and deceleration phases. This compromises the uniformity of compression and degrades target performance.

Direct-drive-ignition designs require a cryogenic DT-ice layer imploded by a “shaped” pulse, with a long, low-intensity foot and a relatively slow rise to peak intensity.³ This article discusses warm, plastic-shell targets^{4,5} imploded on the OMEGA⁶ laser with a 1-ns square pulse, characterized by an initial sharp rise to peak intensity. Plastic-shell implosions are more susceptible to instability growth than cryogenic targets during both the acceleration and deceleration phases. The in-flight aspect ratio (IFAR; defined as the ratio of the shell position to the shell thickness when the shell has moved about half the total acceleration distance) of plastic shells discussed in this article is between 80 and 110, significantly larger than the ignition-design IFAR of ~60 (Ref. 3). The number of e -foldings due to RT growth increases for a larger IFAR.⁷ Consequently, plastic shells are more unstable during the acceleration phase than cryogenic shells. Plastic shells have two unstable surfaces during the deceleration phase: the gas–plastic (fuel–shell) interface whose growth dominates for all wavelengths, and the rear shell surface where short-wavelength growth is reduced due to a finite-density scale length. In contrast, during the deceleration phase, cryogenic targets are unstable only at the rear shell surface where finite density scale lengths and ablation⁸ (in the case of ignition targets) can significantly reduce growth rates of $\ell > 50$, where ℓ is the Legendre mode number. Implosions of warm plastic shells,

however, offer the advantage that complementary information of the compressed core can be obtained due to the variety of gas-fill types (D₂, DT, D³He, etc.) and fill pressures. This variety is unavailable with ignition-scaled cryogenic targets. As a result, detailed verification of the multidimensional hydrodynamics due to the presence of target and laser asymmetries can be performed with plastic shells.

Experimental results from direct-drive plastic-shell implosions have been discussed previously in the literature. Meyerhofer *et al.*⁴ first presented experimental results to infer core conditions. Radha *et al.*⁵ first pointed out the presence of small-scale mix in these implosions. Complementary diagnostics⁶ were employed to confirm this observation. However, the role of small-scale mix on target yields remained an outstanding question. Recently, 2-D simulations were employed by Radha *et al.*⁵ to understand the role of laser and target nonuniformities on implosion performance. It was determined that small-scale mix is not the primary determinant of gross target performance as measured through yields. Instead, long ($\ell \leq 10$) and intermediate ($10 \leq \ell \leq 50$) wavelengths dominated performance for the thick, stable shells, and short wavelengths ($\ell \leq 50$) determined target performance for the thin, unstable shells. In this article, this latter work has been extended to include a larger range of target types and fill pressures. In addition, a wider range of observables is compared to simulation results. This work summarizes simulations of plastic-shell implosions using the methods described in Ref. 5.

Imperfect illumination and target roughness seed the nonuniformity growth of hydrodynamic instabilities in direct-drive implosions. The incident laser irradiation on the target includes nonuniformities that result from energy and power imbalances among the beams and from nonuniformities within each beam. The former results in long-wavelength ($\ell \leq 10$, where $\ell = 2\pi R/\lambda$ is the Legendre mode number, R is the target radius, and λ is the nonuniformity wavelength) perturbations that lead to deformations of the shell. The latter are manifest in the intermediate-wavelength ($10 < \ell \leq 50$) and short-wavelength ($\ell > 50$) nonuniformities that can lead to shell breakup

during the acceleration phase due to Rayleigh–Taylor growth. All of these sources of nonuniformity can lead to a disruption of final fuel assembly. Two-dimensional simulations of plastic-shell implosions that take these effects into account using the hydrodynamic code *DRACO*⁵ are presented here. The modeling of multidimensional hydrodynamics is verified, leading to increased confidence in the predictions of direct-drive ignition³ on the National Ignition Facility.⁹ Simulation results are consistent with experimental observations.

The following sections (1) describe one-dimensional shell dynamics and laser drive, followed by nonuniformity seeding; (2) discuss the effect of short-wavelength growth on shell stability along with the effect of shell stability on experimental observables; (3) compare results from 2-D simulations to experimental results; and (4) present conclusions.

Targets, Laser Drive, and Shell Dynamics

A variety of gas-filled plastic (CH) shells, with thicknesses varying from 15 μm to 27 μm [Fig. 102.34(a)], have been imploded on OMEGA. Four target configurations are primarily discussed in this article: 20- μm -thick, 15-atm-fill; 20- μm -thick, 3-atm-fill; 27- μm -thick, 15-atm-fill; and 27- μm -thick, 3-atm-fill. A 1-ns square pulse¹⁰ [Fig. 102.34(b)] with ~ 23 kJ of energy irradiates these targets with full beam smoothing [two-dimensional smoothing by spectral dispersion¹¹ (1-THz, 2-D SSD with one color cycle) with polarization smoothing (PS)¹²]. Simulations presented here are for targets irradiated using distributed phase plates (DPP's)¹³ that have a super-Gaussian order ~ 2.26 with a spot size (defined as the diameter that is $1/e$ of peak intensity) of 616 μm (SG3 phase plates).¹⁴ More recently, phase plates on OMEGA have been upgraded to a super-Gaussian order ~ 4.12 with a spot size of 716 μm (SG4 phase plates) that primarily reduces the $\ell \leq 50$ nonuniformity.¹⁴ Comparison of observables between the SG3 and SG4 phase plates will also be presented to confirm the effect of laser nonuniformity on observables.

Plastic shells can be filled with a variety of gases at differing pressures that, during the implosion, provide a variety of nuclear and charged particles to diagnose implosion characteristics. Observables shown in this article include the primary neutron yield from the D_2 reaction, the shell areal density (ρR) inferred from both the energy loss of the protons from the D^3He reaction¹⁵ and the energy loss of the elastically scattered protons from the CH in DT-filled targets,¹⁶ the neutron-averaged ion temperatures inferred from neutron time-of-flight measurements, and ion temperatures inferred from the ratio of the DD neutron to D^3He proton yields.¹⁵ Time-resolved ob-

servations of neutron production rates¹⁷ and x-ray image self-emission¹⁸ are also routinely obtained. All of these experimental observables will be compared with results of simulations.

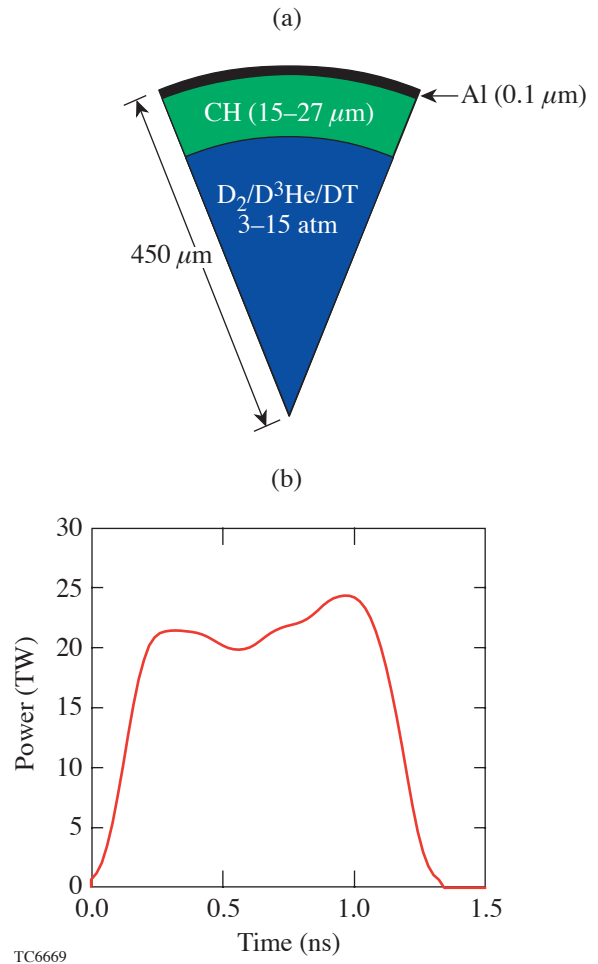


Figure 102.34

(a) Plastic-shell targets studied in this work. Two thicknesses—20 μm and 27 μm —with D_2 fills at 3 and 15 atm are considered. (b) The pulse shape (1 ns square) used to irradiate these targets sets the shell on a relatively high adiabat (~ 5).

The one-dimensional (1-D) dynamics of plastic shells can be divided into four stages: shock transit, acceleration, coasting, and deceleration. Shock dynamics simulated using the 1-D hydrodynamic code *LILAC*¹⁹ is shown in Fig. 102.35(a) as a contour plot of the gradient magnitude of the logarithm pressure, $|\partial \ln P / \partial r|$, as a function of Lagrangian coordinate and time. The target simulated in Fig. 102.35 has a shell thickness of 20 μm and encloses D_2 gas at a pressure of 15 atm. The dark lines correspond to shock trajectories. The dashed line is the trajectory of the fuel–shell interface. Since the rise

time of the laser is relatively fast (~ 200 ps), a strong shock is driven into the target. The rarefaction wave launched at the breakout of the shock (~ 0.4 ns) from the rear surface of the

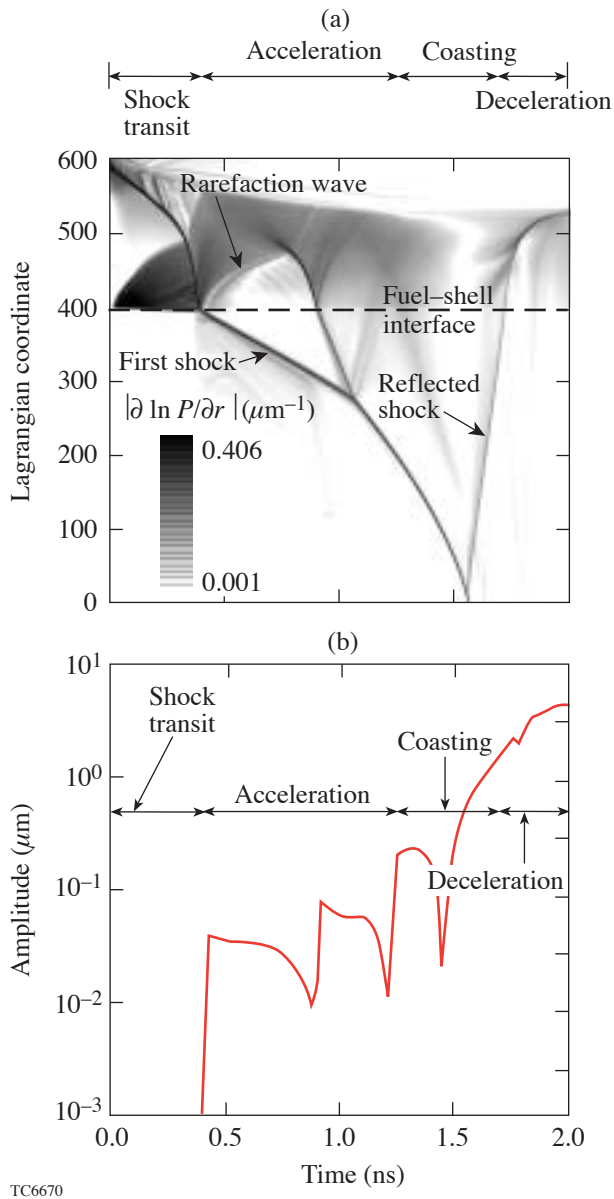


Figure 102.35

(a) Contour plot of the gradient magnitude of the natural log of the pressure for a $20\text{-}\mu\text{m}$ -thick CH shell enclosing 15 atm of D_2 gas. The y axis corresponds to the Lagrangian coordinate in the 1-D simulation. The darker contours correspond to shock trajectories. The dashed line is the fuel-shell interface. The duration of the four phases of the implosion (shock transit, acceleration, coasting, and deceleration) is also shown. (b) The growth of a single mode ($\ell = 30$) at the fuel-shell interface through the implosion. The interface is seeded primarily by the shock and grows significantly during the coasting phase.

shell reaches the ablation surface, launching a compression wave into the target. At this time, the shell accelerates inward and the ablation surface is subject to RT growth.²⁰ The compression wave travels down the decreasing density gradient and breaks out of the rear surface of the shell as a shock (at ~ 0.8 ns). The shocks meet in the gas (at ~ 1 ns) before reaching the center.

The fuel-shell interface has a non-zero Atwood number ($A_T = 0.18$ for D_2 fills)⁵ and is unstable for all wavelengths. The growth of a single mode at the fuel-shell interface simulated using the code *DRACO*⁵ is shown in Fig. 102.35(b). The interface is primarily seeded by the shock (~ 0.4 ns). The acceleration phase occurs after shock transit until ~ 1.4 ns, during which feedthrough from the RT growth at the ablation surface plays an important role in increasing the nonuniformity at the fuel-shell interface. For the mode $\ell = 30$ [shown in Fig. 102.35(b)], the negative spikes for $t < 1.4$ ns correspond to repeated shock interactions with the interface. Significant growth of the interface occurs after the acceleration phase and during the coasting phase due to Bell-Plesset²¹ growth. This persists until the shock reflects from center and returns to the shell (~ 1.75 ns). This impulsive deceleration is followed by a period of continuous deceleration, when the fuel-shell interface is RT unstable due to pressure buildup in the gas. The RT-unstable interface distorts with bubbles of the lower-density fuel rising into the high-density plastic and spikes of the high-density CH falling into the lower-density fuel. Most observables for diagnosing implosion dynamics occur during this final phase of the implosion. Comparison of simulation to observations, therefore, provides an extremely stringent test of modeling perturbation growth and multidimensional fluid flow.

Nonuniformity Seeding

The nonuniformity sources seeding the instabilities at the ablation surface and the fuel-shell interface can be divided into three wavelength ranges for the analysis of these implosions. Long-wavelength modulations ($\ell \leq 10$) result in an overall deformation of the shell, whereas the intermediate ($10 < \ell \leq 50$) and short wavelengths ($\ell > 50$) result in a mass-modulated shell that can show considerable distortions including shell breakup. The time evolution of the long-wavelength nonuniformity sources due to imbalances between the OMEGA beams is modeled by overlapping the 60 beams on a sphere.⁵ Beam mispointing ($\sim 23\text{-}\mu\text{m}$ rms²²), beam mistiming (~ 12 -ps rms is used in the calculation although ~ 9 -ps rms²³ is more typical of OMEGA), energy imbalance ($\sim 2.6\%$ ²²), and differences in the phase plates including azimuthal asymmetries are taken into account. These numbers are averaged over several

shots. The overlap is decomposed into spherical harmonics, and the amplitude of the corresponding Legendre mode is obtained by adding all the m -mode amplitudes in quadrature. The phase of the mode is chosen to be that of the $m=0$ spherical harmonic. These time-dependent amplitudes are used as the laser modulation input to the 2-D axisymmetric hydrodynamic code *DRACO*.

The amplitudes of the dominant modes at the ablation surface (defined as the outer $1/e$ point of maximum density) at the start of the acceleration phase are shown in Fig. 102.36(a). These amplitudes are seeds for RT growth during the acceleration phase. Also shown in Fig. 102.36(a) are the amplitudes due to target surface roughness²⁴ at the same time in the simulation. Figure 102.36(a) indicates that power imbalance is the larger of the two contributors to low-order nonuniformity.

Intermediate and shorter wavelengths are dominated by single-beam nonuniformity (through laser imprint²⁵). An analytical model²⁶ describing the DPP's is used to modulate the laser illumination on target. In addition, polarization smoothing reduces the amplitudes by $\sqrt{2}$ (Ref. 12), and smoothing by spectral dispersion¹¹ (1-THz, 2-D SSD with one color cycle) is also applied. These models are described in detail in Ref. 5. The resultant amplitudes at the ablation surface at the start of the acceleration phase are shown in Fig. 102.36(b). The ampli-

tudes decrease with increasing mode number. This is due to the earlier decoupling of the shorter wavelengths from the target and stabilization due to dynamic overpressure.²⁵

Effect of Shell Stability on Observables

Figure 102.37 shows density contours from multimode simulations that include only the effect of single-beam nonuniformity ($2 \leq \ell \leq 200$) for two CH-shell thicknesses [Fig. 102.37(a): 20 μm ; Fig. 102.37(b): 27 μm]. These contours are shown at the end of the acceleration phase. The 20- μm -thick shell, being less massive, has traveled a greater distance during acceleration and is considerably more distorted than the 27- μm -thick CH shell. The peak-to-valley variation in the center-of-mass radius for the 20- μm -thick shell is 6.6 μm at the end of the acceleration phase, significantly greater than the calculated 1-D shell thickness (defined as the distance between the $1/e$ points of maximum density in a spherically symmetric simulation) of $\sim 5 \mu\text{m}$, indicating shell breakup. The high-density regions are considerably distorted with portions of the shell at less than solid density. Therefore, short wavelengths play an important role in increasing the adiabat of the shell by introducing additional degrees of freedom for the fluid flow. This influences the compressibility of the shell and, therefore, quantities such as neutron yields and areal densities. In comparison, the 27- μm -thick implosion has an integral shell at the end of the acceleration phase with a

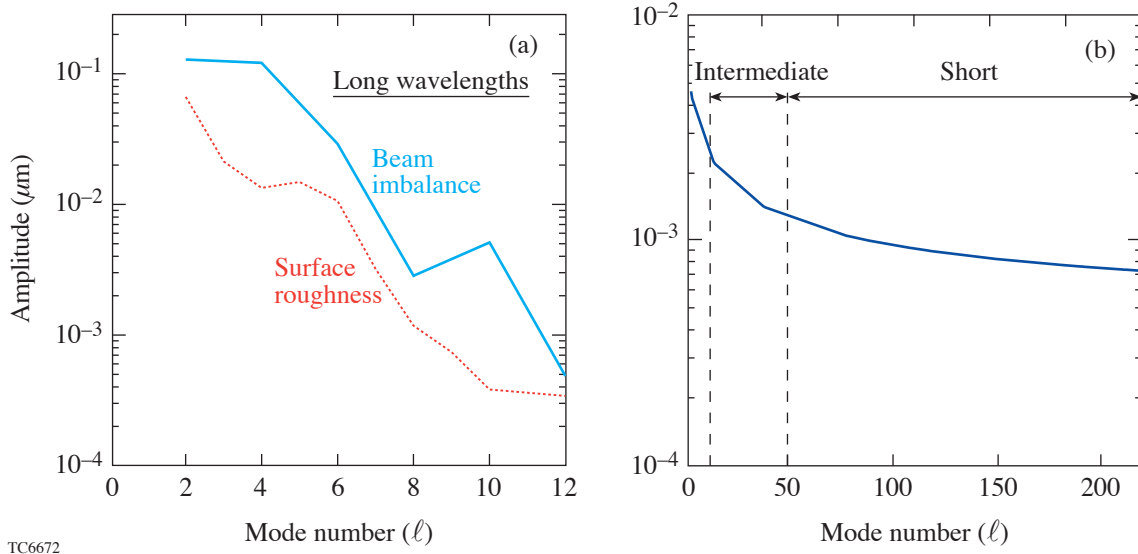


Figure 102.36 (a) Long-wavelength perturbations at the ablation surface due to beam imbalance (solid line) and surface roughness (dotted line) at the start of acceleration. Beam imbalance provides the larger contribution to long-wavelength nonuniformity seeds. (b) Imprint spectrum from single-mode simulations. Note that imprint efficiency decreases with increasing mode number.

peak-to-valley amplitude of $3.4 \mu\text{m}$ in the center-of-mass radius compared to a 1-D shell thickness of $\sim 6.8 \mu\text{m}$. To realistically model the effect of laser imprint, modes resolved up to $\ell \sim 400$ are required in the simulation.⁵ A reliable simulation of this type is numerically challenging. Instead, a stability postprocessor²⁷ to *LILAC* is used to confirm that the qualitative conclusions do not change, i.e., the integrity of the 20- μm -thick CH shell is severely compromised, whereas the 27- μm -thick CH shell is essentially intact when the full range of modes is included.

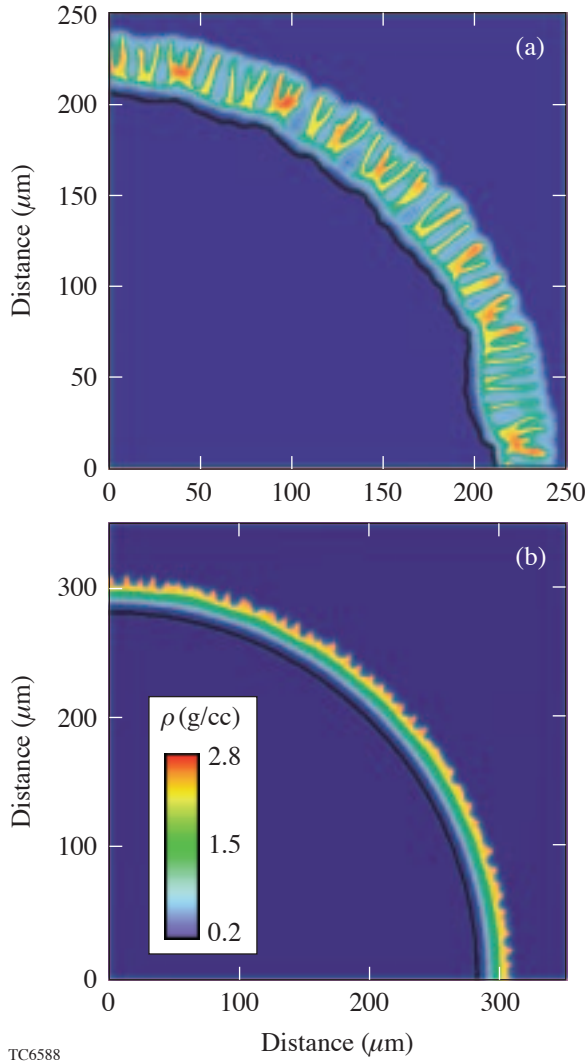


Figure 102.37 Density contours at the end of the acceleration phase for (a) a 20- μm -thick CH shell and (b) a 27- μm -thick CH shell from a multimode simulation of laser imprint. The solid lines correspond to the D_2 -CH interface. Note that the shell (indicated by the higher-density contours) is significantly more distorted for the 20- μm implosion than the 27- μm implosion.

When the severely distorted 20- μm -thick CH shell reassembles during the later stages of the implosion (around the time of the interaction of the reflected shock with the converging shell), the lower density due to shell breakup will result in a thicker shell than predicted with 1-D and a ρR that is lower than 1-D predictions. The thicker shell will influence neutron production rates as follows: Between the time of peak neutron production and peak compression (shown schematically in Fig. 102.38), the neutron rate decreases due to the falling temperature in the gas because of heat conduction and radiative losses. The subsequent decrease in the neutron-production rate occurs due to shell disassembly. If the shell is thicker due to nonuniformity growth, disassembly occurs later in the implosion. The time between the interaction of the reflected shock (which is very similar for both integral and severely distorted shells) and the shock breakout of the shell is given by $t_s = \Delta_{\text{sh}}/U_s$, where Δ_{sh} is the shell thickness and U_s is the shock speed. From Ref. 5, $U_s = \sqrt{E_{\text{kin}}/R_{\text{hs}}^2 \Delta_{\text{sh}} \rho_{\text{sh}}}$, where E_{kin} is the shell kinetic energy, R_{hs} is the radius of the hot spot, and ρ_{sh} is the shell density. Since E_{kin} is similar between the integral shell and the severely distorted shell implosion (only a small portion of the total energy goes into lateral flow in the

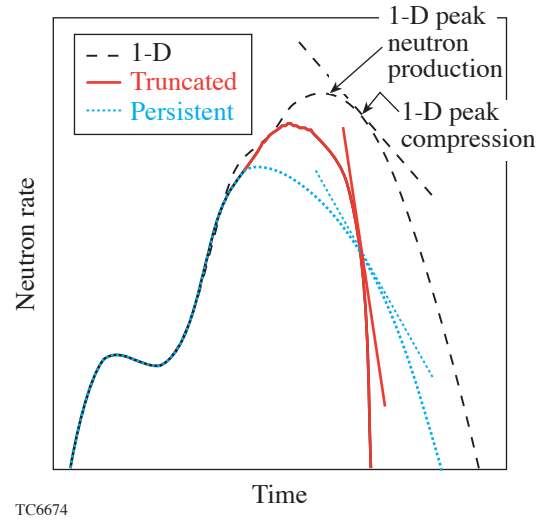


Figure 102.38 Schematics of a persistent neutron-production history and a truncated neutron-production history. In persistent neutron-production histories, burn follows 1-D (dashed) and then turns over (dotted). The rate of falloff near the peak is slower than in 1-D, as indicated by the lines drawn as tangents at peak compression. In truncated neutron-production histories, burn follows 1-D and then turns over rapidly near the peak with a distinct increase in the rate of falloff relative to 1-D (solid). The tangent line drawn at peak compression has a steeper slope compared to 1-D.

distorted shell implosion) and mass ($\propto R_{\text{hs}}^2 \Delta_{\text{sh}} \rho_{\text{sh}}$) is conserved, the shock velocity is similar in both cases; therefore, $t_s \propto \Delta_{\text{sh}}$ and is longer for the severely distorted shell, and disassembly is delayed. Consequently, neutron production falls less steeply than 1-D (Fig. 102.38, dashed line) in the implosion where shell stability is compromised (Fig. 102.38, dotted line). This is indicated in Fig. 102.38 by the decreased slope of the tangent line drawn at peak compression. For stable shells (27 μm), the shell thickness during neutron production is comparable to the 1-D thickness. In this case, the neutron-production rate will truncate (Fig. 102.38, solid line) primarily due to the RT-instability-induced mass flow into the colder bubbles near the fuel-shell interface.⁵ This is indicated by the increased slope of the tangent line drawn at peak compression.

Comparison of Simulations with Observables

The effect of the entire range of nonuniformities is modeled with two-mode simulations with mode numbers 4 and 20 used to represent the effect of long and intermediate wavelengths and three-mode simulations with modes 4, 20, and 200 used to represent all mode ranges. These simulations are performed on a 45° wedge. The initial amplitude for each mode is chosen from the amplitudes added in quadrature of a range of mode numbers (from the DPP and PS spectrum for $\ell = 20$ using modes between 15 and 40 as the mode range and using modes between 100 and 300 as the mode range for $\ell = 200$, and from the initial power balance and surface-roughness data for modes $2 < \ell \leq 10$ for mode $\ell = 4$). SSD is applied to $\ell = 200$ by reducing its initial amplitude by a factor $\sqrt{(t_c/t_D)}$, where t_c is the coherence time of mode 200 (~2 ps) and t_D is the decoupling time for this mode (~16 ps for the 1-ns square

pulse). This reduction factor is in agreement with measurements.²⁸ Density contours at peak neutron production in 2-D are shown for the two thicknesses in Fig. 102.39. The 2-D fuel-shell interface (solid black line) in both cases is significantly distorted compared to 1-D (dashed line). The peak density in the thinner shell is ~70% of the 1-D peak density compared to nearly 100% for the thick shell. This undercompression is due to shell breakup during the acceleration phase, as discussed in the previous section.

Neutron-production rates from these simulations are compared against 1-D rates (solid line) in Fig. 102.40 [Fig. 102.40(a): 20- μm -thick CH shell; Fig. 102.40(b): 27- μm -thick CH shell]. With low and intermediate modes alone (dashed line), burn truncation is evident for both shell thicknesses. In this case, the in-flight shell thickness is the same as the 1-D shell thickness. The addition of the short wavelength (dotted line) significantly influences the neutron-production rate for the 20- μm shell; the burn rate deviates from 1-D with a more gradual falloff. The short wavelength has only a marginal effect on the thicker shell. Similar trends are observed in experiments. The 1-D calculated and measured neutron-production rates are shown in Fig. 102.41 for three shell thicknesses. The 1-D neutron rates are temporally shifted to align the rise of neutron production with the rise of the measured rate curves. The required time shifts are within the uncertainties in absolute timing in the experiment. Burn truncation is evident for the thick shell case [Fig. 102.41(c)]; the tangent line has a steeper slope compared to 1-D, whereas, with decreasing shell thickness, neutron-production falls off less rapidly near the peak. Measurement and 1-D simulations from a 15- μm -thick CH implosion are

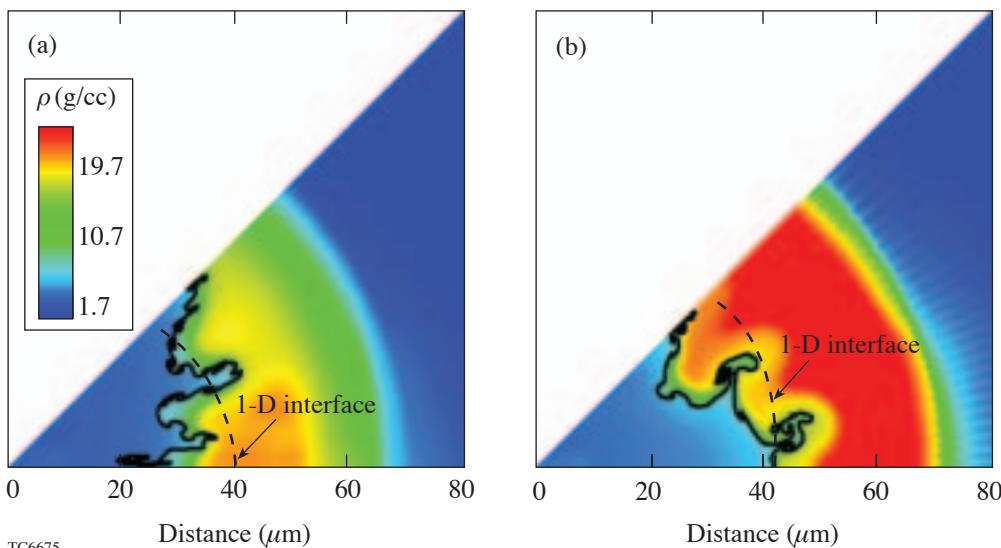


Figure 102.39 Density contours for simulations including the effect of all mode ranges at peak neutron production for (a) the 20- μm -thick CH shell and (b) the 27- μm -thick CH shell. The solid line is the fuel-shell interface. The peak density in (a) is ~70% of the 1-D peak density, whereas in (b) it is ~100% of 1-D peak density. This undercompression in the 20- μm -thick shell occurs due to shell instability during acceleration.

compared in Fig. 102.41(a). This shell should be even more compromised in its integrity than the 20- μm -thick CH shell. The measured rates show the expected trend: a more gradual falloff near the peak.

Simulated neutron-production rates for the 20- μm -thick CH shell with a 3-atm fill are shown in Fig. 102.42(a). Even though the shell is severely compromised during acceleration, burn truncation is evident in this case. Nonuniformity growth

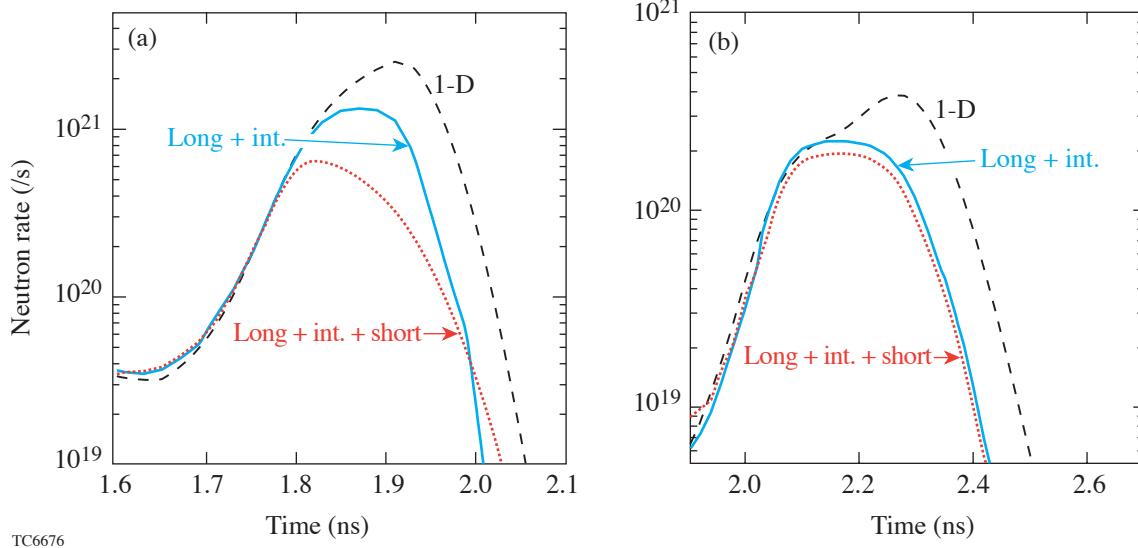


Figure 102.40 Neutron-production rates from the simulation including only low- and intermediate-mode numbers (dotted line) and the simulation including short wavelengths (solid line) compared to 1-D (dashed line) for (a) the 20- μm -thick CH shell and (b) the 27- μm -thick CH shell. Note that the inclusion of the shorter wavelengths in the simulation results in a less-steep fall of the neutron-production rate for the 20- μm implosion and retains burn truncation for the 27- μm case.

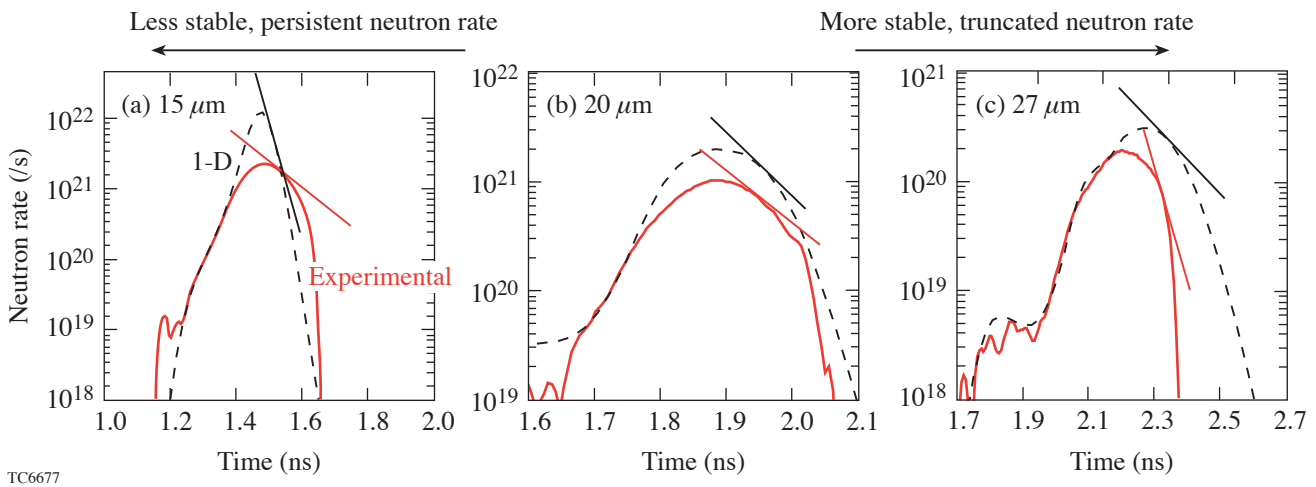


Figure 102.41 Comparison of calculated (1-D) neutron rates (dashed) with experiment (solid line) for (a) the 15- μm -thick implosion (shot 36100), (b) the 20- μm -thick implosion (shot 30628), and (c) the 27- μm -thick implosion (shot 22088). All implosions have a 15-atm fill. Burn truncation is evident for the 27- μm -thick implosion. The neutron-production rate persists and is almost as wide as 1-D for the 20- μm -thick implosion and wider than 1-D for the 15- μm -thick implosion.

at the interface compromises the core; at peak neutron production in 1-D (~1.85 ns), there is no clean core evident in the 2-D simulations, reducing the neutron rate significantly and resulting in truncation. Consistent with this simulation, burn truncation is evident in the measured neutron-production rates [Fig. 102.42(b)] when overlaid onto the 1-D simulation results.

Two-dimensional simulated primary neutron yields compare very favorably with measured values. Figure 102.43 shows the experimental yield⁴ normalized to the correspond-

ing 1-D yields (open circles) for the four target configurations: 20- μm -thick, 15-atm-fill; 20- μm -thick, 3-atm-fill; 27- μm -thick, 15-atm-fill; and 27- μm -thick, 3-atm-fill. Each point is this quantity averaged over many OMEGA shots. The error bars are the one-standard-deviation variation over these shots. All simulated values (solid symbols) compare well with observations.

Simulated neutron-averaged shell areal densities normalized to the 1-D values (solid) are shown in Fig. 102.44, comparing favorably with the experimentally inferred val-

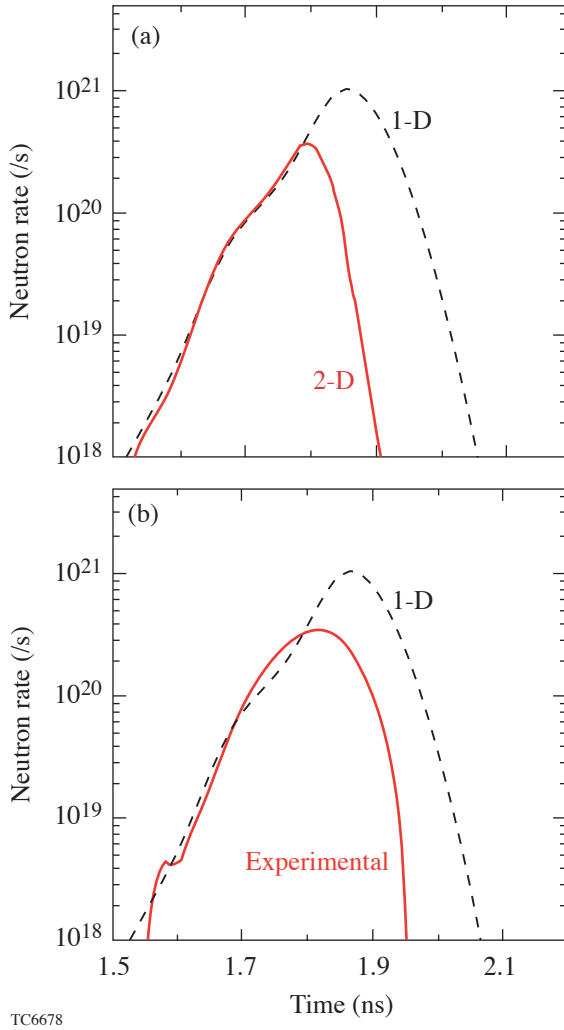


Figure 102.42 (a) Simulated neutron-production rates for the 20- μm -thick, 3-atm-fill implosion: 2-D (solid) and 1-D (dashed). Burn truncation is evident even though the shell is significantly distorted during acceleration because of the absence of a “clean” core early during deceleration. (b) Comparison of the 1-D simulation with measured neutron-production rate (shot 22864). The same trend of burn truncation is observed in experiment.

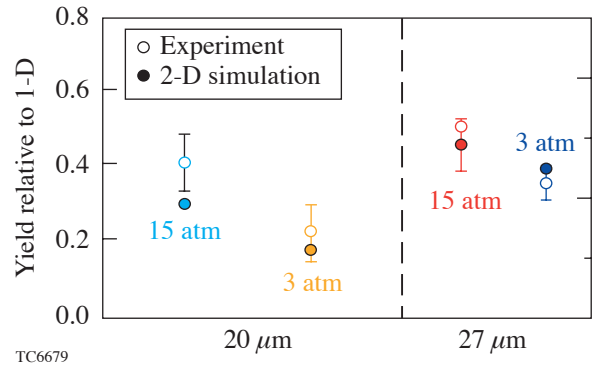


Figure 102.43 Yields relative to 1-D for four cases: 20- μm -thick, 15-atm-fill; 20- μm -thick, 3-atm-fill; 27- μm -thick, 15-atm-fill; and 27- μm -thick, 3-atm-fill (measured: open circles; 2-D: closed circles). Good agreement is obtained between experiment and simulation.

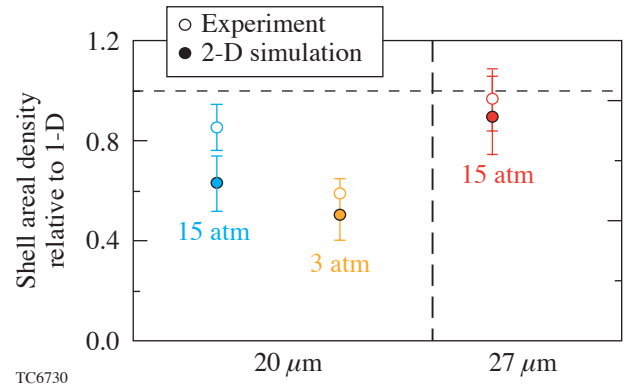


Figure 102.44 Neutron-averaged shell areal density relative to 1-D for the same four targets as in Fig. 102.43. Simulations are shown as the solid symbols. The “error bar” in the 2-D results is the one standard deviation in the variation in the polar angle areal density.

ues¹⁵ (open). The error bars associated with the simulation points are the one-standard-deviation polar-angle variation in the areal density. There is no data for the 27- μm -thick, 3-atm-fill implosion.

Experimental neutron-averaged ion temperatures⁴ inferred from neutron time of flight are shown in Fig. 102.45 (open circles). Experimentally inferred ion temperatures are systematically higher than those simulated (solid). Reasons for this systematic deviation are being investigated currently. Ion temperatures from the measured DD neutron to D³He proton yield ratios¹⁵ are also shown in Fig. 102.45 (open squares) for the cases where data are available. This temperature shows better agreement with simulation results.

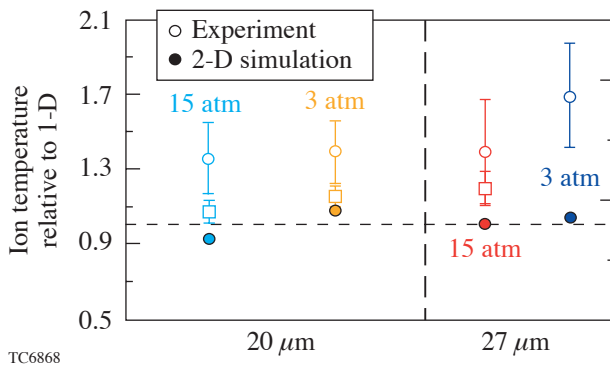


Figure 102.45

Neutron-averaged ion temperatures relative to 1-D for the four target configurations as in Fig. 102.43. Inferred ion temperatures from neutron time-of-flight (open circles) are systematically higher than simulated ion temperatures (solid circles). The ion temperatures inferred from the DD neutron to D³He proton yield ratios (open squares) are also shown.

The significant influence of low and intermediate wavelengths on thick shells is consistent with observations of neutron yields using the newer SG4 phase plates¹⁴ on the OMEGA laser beams. The improvement in the on-target laser nonuniformity between the SG3 and the SG4 phase plates has been modeled to be primarily in the low- and intermediate-mode ranges [Fig. 102.46(a)].¹⁴ The ratio of the calculated rms nonuniformity with the SG3 phase plates relative to the SG4 phase plates is shown in Fig. 102.46(a). In Fig. 102.46(b), the measured yield relative to 1-D is shown for both shell thicknesses. Significant improvement in the 27- μm -thick shell's performance is measured [Fig. 102.46(b)].

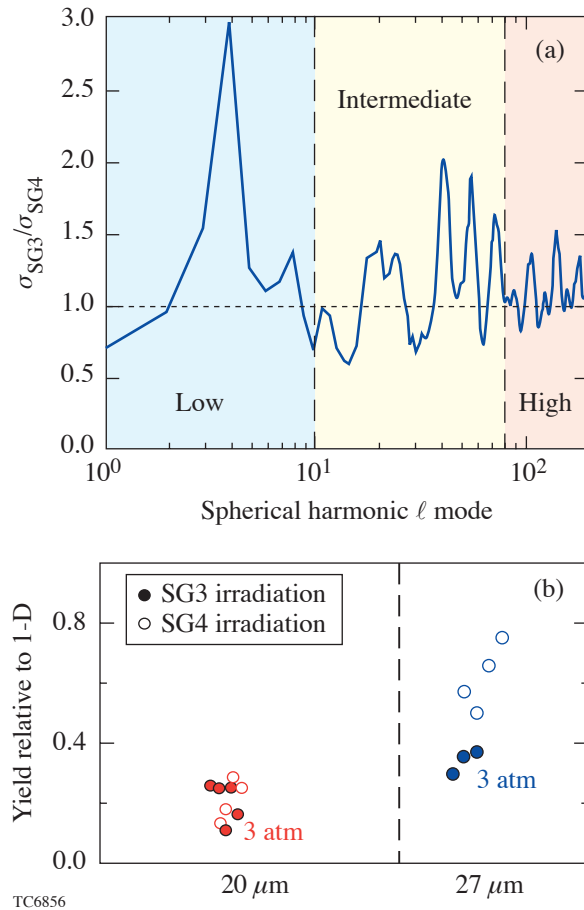


Figure 102.46

(a) Ratio of the modeled on-target laser nonuniformity due to the SG3 and SG4 phase plates (see text). Significant improvements in the uniformity of low and intermediate wavelengths have been modeled, whereas marginal improvements in the uniformity of short wavelengths are calculated. (b) Measured yields relative to 1-D for the SG3 phase plates (solid) and the SG4 phase plates (open) for 20- μm -thick and 27- μm -thick CH shells with 3-atm fills. Significant improvement is observed in target performance for the thicker shells unlike the thin shells. Thin-shell performance is dominated by the seeding of short-wavelength modes, which has marginally changed in the transition from SG3 to SG4 phase plates.

Lineouts from ~ 4.5 -keV gated x-ray pinhole camera images of the core self-emission for the 20- μm -thick CH shell are shown in Fig. 102.47. The results of Spect3D²⁹ post-processing of 2-D simulations (solid) with the 1-D results (dashed) are shown at peak neutron production [Fig. 102.47(a)] and at peak compression [Fig. 102.47(b)]. Each curve is normalized to the corresponding peak intensity. The postprocessed 1-D simulation shows a distinct limb corresponding to the fuel-shell interface position. The 2-D simulated emission in Figs. 102.47(a) and 102.47(b) is the polar angle average of the

emission from the target. The averaging process smears out the limb due to the nonuniformity of the fuel–shell interface. Further, peak simulated emission in 2-D occurs from the hot CH spikes, which are at a smaller radius than the 1-D fuel–shell interface (Fig. 102.39). As a result, the brightness profile in 2-D decreases rapidly at a smaller radius than in the 1-D emission profile. The more distorted shell also results in a more gradual decrease in the brightness compared to the 1-D profile. Comparisons of the measured azimuthally averaged curves¹⁸ normalized to peak intensity and the corresponding 1-D simulations are shown at peak neutron production [Fig. 102.47(c)] and at peak compression [Fig. 102.47(d)]. Similar trends are observed in experiments; the limb is no longer evident, the decrease in brightness occurs at a smaller radius than in 1-D, and this decrease is more gradual than in the 1-D profile.

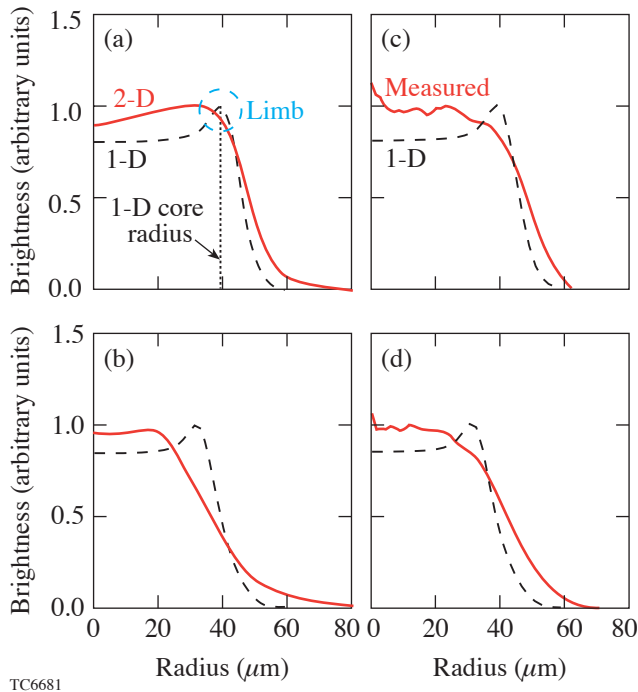


Figure 102.47

Brightness profile at ~ 4.5 keV of the core normalized to peak intensity for the 20- μm -thick CH shell. (a) Comparison of 1-D profiles (dashed) with the polar-averaged 2-D profile (solid) at peak neutron production. 1-D simulation indicates a prominent limb due to the fuel–shell interface. 2-D simulation indicates a smeared-out limb. (b) Same as (a) but at peak compression. (c) Azimuthally averaged brightness profile from measured pinhole camera images (shot 22546) at peak neutron production (solid line) compared to 1-D (dashed line). (d) Same as (c) but at peak compression. Good agreement is obtained between the 2-D profiles and the measured profiles including the absence of a significant limb and more gradual decrease in brightness relative to the 1-D profile.

In previous work, homogenous mixing of D_2 and CH^{30-33} has been inferred from experimental observables such as secondary neutron ratios,^{30,31} argon spectral lines,³² and D^3He yields in ^3He -filled CD shells.^{30,31} These observables preferentially sample the turbulently mixed region of the target and are sensitive to mix. The primary neutron yields were not directly used to determine the presence of turbulence. These neutrons are produced in the bulk of the fuel; the reduced values of the primary yields relative to 1-D are instead due to the effects discussed in **Effect of Shell Stability on Observables** (p. 95).

An order-of-magnitude estimate of the small-scale mixing length can be obtained as follows: The turbulent mixing layer grows self-similarly with a mixing thickness h , given by Ref. 34,

$$h = \alpha A_T g t^2, \quad (1)$$

where α is a dimensionless constant. Taking $A_T = 0.18$ for the D_2 –CH interface gives $\alpha = 0.05$ (Ref. 34). The expression in Ref. 34 is for planar turbulent growth due to the presence of many modes. In the cases considered in this article, convergence effects play an important role. In addition, the return shock recompresses the mixing layer. Subsequent reshocking of the mixing layer can occur in implosions; therefore, this estimate of mixing lengths should be considered as an order-of-magnitude estimate. A hydrodynamics code, such as *DRACO*, cannot follow materials into the turbulent regime. Using $\alpha = 0.05$ leads to $h = 0.9 \mu\text{m}$; therefore, if the simulated short-wavelength amplitude is considered to be a mix thickness, the value of $\sim 1 \mu\text{m}$ (Fig. 102.39) compares favorably with the estimated mix thickness. Larger mixing widths ($\sim 17 \mu\text{m}$) have been inferred based on spherically symmetric 1-D mix models.^{30,31} Since 1-D mix models do not account for the increased volume due to long-wavelength distortions, it is very likely that they overestimate the mixing length.

Conclusions

Two-dimensional simulations of imploding plastic shells are presented using the radiation hydrodynamic code *DRACO*. Shell instability through the growth of short-wavelength perturbations plays an important role in determining target performance for “thin” (≤ 20 - μm -thick) CH shells. Target performance is dominated by long and intermediate wavelengths for thicker shells. Observables such as primary neutron yields, areal densities, temporal histories of neutron production, and x-ray images of self-emission compare very well with experimental

measurements. Neutron-averaged ion temperatures inferred from neutron time of flight are significantly higher than the calculated values. The reasons for this systematic discrepancy are under investigation. Calculated ion temperatures, however, are more consistent with values inferred from the ratios of DD neutron to D³He proton yield. The good agreement with experiment for most observables indicates that the modeling of nonuniformity seeds for instability growth and multidimensional implosion dynamics due to realistic laser and target asymmetries describe realistic direct-drive inertial confinement fusion implosions reasonably well.

ACKNOWLEDGMENT

This work was supported by the U.S. Department of Energy Office of Inertial Confinement Fusion under Cooperative Agreement No. DE-FC52-92SF19460, the University of Rochester, and the New York State Energy Research and Development Authority. The support of DOE does not constitute an endorsement by DOE of the views expressed in this article.

REFERENCES

1. J. Nuckolls *et al.*, *Nature* **239**, 139 (1972).
2. Lord Rayleigh, *Proc. London Math Soc.* **XIV**, 170 (1883); G. Taylor, *Proc. R. Soc. London Ser. A* **201**, 192 (1950).
3. C. P. Verdon, *Bull. Am. Phys. Soc.* **38**, 2010 (1993); P. W. McKenty, V. N. Goncharov, R. P. J. Town, S. Skupsky, R. Betti, and R. L. McCrory, *Phys. Plasmas* **8**, 2315 (2001).
4. D. D. Meyerhofer, J. A. Delettrez, R. Epstein, V. Yu. Glebov, V. N. Goncharov, R. L. Keck, R. L. McCrory, P. W. McKenty, F. J. Marshall, P. B. Radha, S. P. Regan, S. Roberts, W. Seka, S. Skupsky, V. A. Smalyuk, C. Sorce, C. Stoeckl, J. M. Soures, R. P. J. Town, B. Yaakobi, J. D. Zuegel, J. Frenje, C. K. Li, R. D. Petrasso, D. G. Hicks, F. H. Séguin, K. Fletcher, S. Padalino, M. R. Freeman, N. Izumi, R. Lerche, T. W. Phillips, and T. C. Sangster, *Phys. Plasmas* **8**, 2251 (2001).
5. P. B. Radha, V. N. Goncharov, T. J. B. Collins, J. A. Delettrez, Y. Elbaz, V. Yu. Glebov, R. L. Keck, D. E. Keller, J. P. Knauer, J. A. Marozas, F. J. Marshall, P. W. McKenty, D. D. Meyerhofer, S. P. Regan, T. C. Sangster, D. Shvarts, S. Skupsky, Y. Srebro, R. P. J. Town, and C. Stoeckl, *Phys. Plasmas* **12**, 032702 (2005).
6. T. R. Boehly, D. L. Brown, R. S. Craxton, R. L. Keck, J. P. Knauer, J. H. Kelly, T. J. Kessler, S. A. Kumpan, S. J. Loucks, S. A. Letzring, F. J. Marshall, R. L. McCrory, S. F. B. Morse, W. Seka, J. M. Soures, and C. P. Verdon, *Opt. Commun.* **133**, 495 (1997).
7. J. D. Lindl, *Phys. Plasmas* **2**, 3933 (1995).
8. V. Lobatchev and R. Betti, *Phys. Rev. Lett.* **85**, 4522 (2000).
9. E. M. Campbell and W. J. Hogan, *Plasma Phys. Control. Fusion* **41**, B39 (1999).
10. W. R. Donaldson, R. Boni, R. L. Keck, and P. A. Jaanimagi, *Rev. Sci. Instrum.* **73**, 2606 (2002).
11. S. Skupsky, R. W. Short, T. Kessler, R. S. Craxton, S. Letzring, and J. M. Soures, *J. Appl. Phys.* **66**, 3456 (1989).
12. T. R. Boehly, V. A. Smalyuk, D. D. Meyerhofer, J. P. Knauer, D. K. Bradley, R. S. Craxton, M. J. Guardalben, S. Skupsky, and T. J. Kessler, *J. Appl. Phys.* **85**, 3444 (1999).
13. C. B. Burckhardt, *Appl. Opt.* **9**, 695 (1970); Y. Kato *et al.*, *Phys. Rev. Lett.* **53**, 1057 (1984); Laboratory for Laser Energetics LLE Review **65**, 1, NTIS document No. DOE/SF/19460-117 (1995). Copies may be obtained from the National Technical Information Service, Springfield, VA 22161.
14. S. P. Regan, J. A. Delettrez, V. Yu. Glebov, V. N. Goncharov, J. A. Marozas, F. J. Marshall, P. W. McKenty, D. D. Meyerhofer, P. B. Radha, T. C. Sangster, V. A. Smalyuk, C. Stoeckl, J. A. Frenje, C. K. Li, R. D. Petrasso, and F. H. Séguin, *Bull. Am. Phys. Soc.* **49**, 62 (2004).
15. C. K. Li, D. G. Hicks, F. H. Séguin, J. A. Frenje, R. D. Petrasso, J. M. Soures, P. B. Radha, V. Yu. Glebov, C. Stoeckl, D. R. Harding, J. P. Knauer, R. L. Kremens, F. J. Marshall, D. D. Meyerhofer, S. Skupsky, S. Roberts, C. Sorce, T. C. Sangster, T. W. Phillips, M. D. Cable, and R. J. Leeper, *Phys. Plasmas* **7**, 2578 (2000).
16. C. K. Li, F. H. Séguin, D. G. Hicks, J. A. Frenje, K. M. Green, S. Kurebayashi, R. D. Petrasso, D. D. Meyerhofer, J. M. Soures, V. Yu. Glebov, R. L. Keck, P. B. Radha, S. Roberts, W. Seka, S. Skupsky, C. Stoeckl, and T. C. Sangster, *Phys. Plasmas* **8**, 4902 (2001).
17. R. A. Lerche, D. W. Phillion, and G. L. Tietbohl, *Rev. Sci. Instrum.* **66**, 933 (1995).
18. S. P. Regan, J. A. Delettrez, R. Epstein, P. A. Jaanimagi, B. Yaakobi, V. A. Smalyuk, F. J. Marshall, D. D. Meyerhofer, W. Seka, D. A. Haynes, Jr., I. E. Golovkin, and C. F. Hooper, Jr., *Phys. Plasmas* **9**, 1357 (2002).
19. M. C. Richardson, G. G. Gregory, R. L. Keck, S. A. Letzring, R. S. Marjoribanks, F. J. Marshall, G. Pien, J. S. Wark, B. Yaakobi, P. D. Goldstone, A. Hauer, G. S. Stradling, F. Ameduri, B. L. Henke, and P. Jaanimagi, in *Laser Interaction and Related Plasma Phenomena*, edited by H. Hora and G. H. Miley (Plenum Press, New York, 1986), Vol. 7, pp. 179–211.
20. S. E. Bodner, *Phys. Rev. Lett.* **33**, 761 (1974); H. Takabe *et al.*, *Phys. Fluids* **28**, 3676 (1985); R. Betti, V. N. Goncharov, R. L. McCrory, P. Sorotokin, and C. P. Verdon, *Phys. Plasmas* **3**, 2122 (1996).
21. G. I. Bell, Los Alamos National Laboratory, Los Alamos, NM, Report LA-1321 (1951); M. S. Plesset, *J. Appl. Phys.* **25**, 96 (1954); D. L. Book and S. E. Bodner, *Phys. Fluids* **30**, 367 (1987); Laboratory for Laser Energetics LLE Review **94**, 81, NTIS document No. DOE/SF/19460-485 (2003). Copies of LLE Review **94** may be obtained from the National Technical Information Service, Springfield, VA 22161.
22. F. J. Marshall, J. A. Delettrez, R. Epstein, R. Forties, R. L. Keck, J. H. Kelly, P. W. McKenty, S. P. Regan, and L. J. Waxer, *Phys. Plasmas* **11**, 251 (2004).
23. K. A. Thorp, Laboratory for Laser Energetics, private communication (2004).

24. R. C. Cook, R. L. McEachern, and R. B. Stephens, *Fusion Technol.* **35**, 224 (1999).
25. V. N. Goncharov, S. Skupsky, T. R. Boehly, J. P. Knauer, P. McKenty, V. A. Smalyuk, R. P. J. Town, O. V. Gotchev, R. Betti, and D. D. Meyerhofer, *Phys. Plasmas* **7**, 2062 (2000).
26. R. Epstein, *J. Appl. Phys.* **82**, 2123 (1997).
27. V. N. Goncharov, P. McKenty, S. Skupsky, R. Betti, R. L. McCrory, and C. Cherfils-Clérouin, *Phys. Plasmas* **7**, 5118 (2000).
28. T. R. Boehly, V. N. Goncharov, O. Gotchev, J. P. Knauer, D. D. Meyerhofer, D. Oron, S. P. Regan, Y. Srebro, W. Seka, D. Shvarts, S. Skupsky, and V. A. Smalyuk, *Phys. Plasmas* **8**, 2331 (2001).
29. J. J. MacFarlane *et al.*, in *Inertial Fusion Sciences and Applications 2003*, edited by B. A. Hammel *et al.* (American Nuclear Society, La Grange Park, IL, 2004), pp. 457–460; Prism Computational Sciences, Inc., Madison, WI, 53711.
30. C. K. Li, F. H. Séguin, J. A. Frenje, S. Kurebayashi, R. D. Petrasso, D. D. Meyerhofer, J. M. Soures, J. A. Delettrez, V. Yu. Glebov, P. B. Radha, F. J. Marshall, S. P. Regan, S. Roberts, T. C. Sangster, and C. Stoeckl, *Phys. Rev. Lett.* **89**, 165002 (2002).
31. P. B. Radha, J. Delettrez, R. Epstein, V. Yu. Glebov, R. Keck, R. L. McCrory, P. McKenty, D. D. Meyerhofer, F. Marshall, S. P. Regan, S. Roberts, T. C. Sangster, W. Seka, S. Skupsky, V. Smalyuk, C. Sorce, C. Stoeckl, J. Soures, R. P. J. Town, B. Yaakobi, J. Frenje, C. K. Li, R. Petrasso, F. Séguin, K. Fletcher, S. Padalino, C. Freeman, N. Izumi, R. Lerche, and T. W. Phillips, *Phys. Plasmas* **9**, 2208 (2002).
32. S. P. Regan, J. A. Delettrez, V. N. Goncharov, F. J. Marshall, J. M. Soures, V. A. Smalyuk, P. B. Radha, B. Yaakobi, R. Epstein, V. Yu. Glebov, P. A. Jaanimagi, D. D. Meyerhofer, T. C. Sangster, W. Seka, S. Skupsky, C. Stoeckl, D. A. Haynes, Jr., J. A. Frenje, C. K. Li, R. D. Petrasso, and F. H. Séguin, *Phys. Rev. Lett.* **92**, 185002 (2004).
33. D. C. Wilson, C. W. Cranfill, C. Christensen, R. A. Forster, R. R. Peterson, H. M. Hoffman, G. D. Pollak, C. K. Li, F. H. Séguin, J. A. Frenje, R. D. Petrasso, P. W. McKenty, F. J. Marshall, V. Yu. Glebov, C. Stoeckl, G. J. Schmid, N. Izumi, and P. Amendt, *Phys. Plasmas* **11**, 2723 (2004).
34. G. Dimonte, *Phys. Plasmas* **6**, 2009 (1999).

Effects of Temporal Density Variation and Convergent Geometry on Nonlinear Bubble Evolution in Classical Rayleigh–Taylor Instability

Introduction

Rayleigh–Taylor (RT) instability develops in a large variety of physical systems, including an imploding shell during inertial confinement fusion experiments¹ and a supernovae explosion in astrophysics.² RT instability occurs at the interface between two fluids subject to an acceleration field pointing from the heavier to the lighter fluid.³ Analytical modeling of such an instability, as well as many other physical phenomena, is based mainly on perturbation methods. In such methods, the equations describing both the physical laws and unknown physical quantities are expanded in a series of small parameters. This allows an approximate solution to otherwise mathematically intractable problems to be obtained. When the amplitude of the interface distortion η between fluids is much smaller than the perturbation wavelength λ (linear perturbation analysis), the small parameter of the perturbation method is $k\eta$, where $k = 2\pi/\lambda$ is the wave number. The hydrodynamic equations in this case can be linearized, yielding an exponential in time perturbation growth.³ When the distortions are amplified by RT instability to amplitudes comparable to the wavelength, the perturbation series based on $k\eta$ expansion becomes divergent and the expansion breaks down. At such amplitudes a different expansion parameter is needed. It was first proposed in Ref. 4 to use a spatial variable along the fluid interface as a small parameter. The perturbation series in this case gives an approximate analytic solution to the nonlinear problem. Such a solution, however, is valid only locally at the tip of the bubble of the lighter fluid raising into the heavier fluid. Layzer's model, despite its simplicity, has been shown to work remarkably well in describing the nonlinear bubble evolution in classical RT instability.^{5–9} Recently⁹ the model was extended to arbitrary Atwood numbers $A_T = (\rho_h - \rho_l)/(\rho_h + \rho_l)$, where ρ_h and ρ_l are the densities of heavier and lighter fluids, respectively. The convergence effects have been included in Ref. 10 for cylindrical geometry and in Ref. 11 for spherical geometry in the case of self-similar flow. In addition to the Layzer's theory, other models have been successfully used to study the nonlinear RT evolution (see, for example, Refs. 12 and 13). This article presents a general scaling of the bubble evolution with the flow

parameters in planar and spherical geometries for arbitrary temporal density variations and shell trajectories.

The following sections (1) discuss the effects of the temporal density variation on the bubble evolution in the planar geometry and (2) describe the model that predicts the nonlinear perturbation evolution in a spherical geometry.

Planar Geometry: Time-Dependent Density

We consider a fluid with time-dependent uniform density $\rho(t)$ supported in a gravitational field $\mathbf{g}(t)$ by a lighter fluid with density $\rho_l \ll \rho$. The effects of the finite density of the lighter fluid will be neglected in the analysis ($A_T = 1$). The gravity is pointing in the negative z direction. The heavier fluid occupies the upper half of the space with $z > 0$. We choose the unperturbed fluid interface to lie in the (x,y) plane. The regions of the distorted interface where the lighter fluid rises into the heavier fluid are referred to as bubbles; regions where the heavier fluid protrudes into the lighter fluid are referred to as spikes. The standard Layzer's approach⁴ deals with the flow at the tip of the bubbles where the vortex motion developed at large perturbation amplitudes has a small effect. Next, introducing a velocity potential $\mathbf{v} = \nabla\Phi$, the mass conservation equation is reduced to Poisson's equation:

$$\nabla^2\Phi = \partial_x^2\Phi + \partial_y^2\Phi + \partial_z^2\Phi = -\frac{\dot{\rho}}{\rho}. \quad (1)$$

The right-hand side of Eq. (1), neglected in the original Layzer's work,⁴ is due to the temporal variation in the fluid density. Such a term, however, was retained previously in the analysis of the linear perturbation evolution.^{14,15} In the unperturbed case, Eq. (1) yields the velocity field with the uniform spatial gradient $v_z = z\dot{\rho}/\rho$. One must keep in mind that the Layzer's model deals with flow in the proximity of the fluid interface; therefore, the actual flow is not required to have a uniform velocity gradient throughout the whole region. When the fluid interface is distorted, the perturbations start to grow due to RT instability. To find the perturbation evolution, the

fluid equations and hydrodynamic functions are expanded in powers of \bar{x} near the tip of the bubble (we assume that the center of the bubble is localized at $\bar{x}=0$). Here, $\bar{x}=x$ in two-dimensional perturbed flow and $\bar{x}=r=\sqrt{x^2+y^2}$ in three-dimensional flow. The expansion of the position of the distorted interface $\eta(\bar{x},t)$ gives $\eta(\bar{x},t)=\eta_0(t)+\eta_2(t)\bar{x}^2+\dots$, where $\eta_0>0$ is the bubble amplitude, and η_2 is related to the bubble curvature R as $\eta_2=-1/(2R)$. The solution of Eq. (1) expanded up to \bar{x}^2 takes the form

$$\Phi=\frac{a(t)}{k}\left(1-\tilde{c}_g\frac{k^2\bar{x}^2}{4}\right)e^{-k(z-\eta_0)}-\frac{\dot{\rho}}{2\rho}z^2, \quad (2)$$

where k is the perturbation wave number and $\tilde{c}_g=2$ and $\tilde{c}_g=1$ for two- and three-dimensional geometries, respectively. Note that the standard Layzer's model keeps only terms up to \bar{x}^2 in the expansion of hydrodynamic functions. It is sufficient, therefore, to retain only the fundamental harmonic in solution (2) to satisfy such accuracy. For higher-accuracy models, the higher harmonics must be included in the velocity potential.⁹ The potential Φ is subject to the following jump conditions at the interface $z=\eta(\bar{x},t)$:

$$\partial_t\eta+v_{\bar{x}}\partial_{\bar{x}}\eta=v_z, \quad (3)$$

$$\partial_t\Phi+\frac{v^2}{2}+g\eta=f(t). \quad (4)$$

Equation (3) is due to mass conservation and the incompressibility condition, and Eq. (4) is the Bernoulli's equation. Here, $f(t)$ is an undetermined function of time and $v^2=v_{\bar{x}}^2+v_z^2$ is the total fluid velocity. Substituting Eq. (2) into boundary conditions (3) and (4) and expanding the latter in powers of \bar{x} yields

$$\frac{d}{dt}(\rho\eta_2)=-\frac{d}{dt}(\rho\eta_0)\frac{\tilde{c}_g k}{4}\left(k+4\frac{\tilde{c}_g+1}{\tilde{c}_g}\eta_2\right), \quad (5)$$

$$\begin{aligned} &\frac{d}{dt}\left[\frac{1}{\rho}\frac{d}{dt}(\rho\eta_0)\right]+\frac{\tilde{c}_g k}{2\rho^2}\left[\frac{d}{dt}(\rho\eta_0)\right]^2 \\ &+\frac{4}{k\tilde{c}_g}(g+\ddot{\eta}_0)\eta_2=0. \end{aligned} \quad (6)$$

In the limit of a small perturbation amplitude when $k\eta_0\ll 1$, the nonlinear terms are negligible (linear regime) and Eqs. (5) and (6) reduce to a well-known limit,^{14,15} $\eta_2^{\text{lin}}=-\tilde{c}_g k^2\eta_0^{\text{lin}}/4$ and

$$\frac{d}{dt}\left[\frac{1}{\rho}\frac{d}{dt}(\rho\eta_0^{\text{lin}})\right]-\gamma^2\eta_0^{\text{lin}}=0, \quad (7)$$

where $\gamma(t)=\sqrt{kg(t)}$ is the growth rate and the superscript "lin" denotes perturbed quantities in the linear regime. An approximate solution of Eq. (7) can be found in the limit $\dot{\rho}/\rho\ll\gamma$ using the Wentzel-Kramers-Brillouin (WKB) method.¹⁶ According to such a method, the solution is sought in the form $\eta_0^{\text{lin}}=e^{\tilde{S}(t)/\epsilon}$, where

$$\epsilon\sim\max\left[(\gamma t_\rho)^{-1},(\gamma t_\gamma)^{-1}\right]\ll 1$$

is a small parameter and $t_\rho=\rho/\dot{\rho}$ and $t_\gamma=\gamma/\dot{\gamma}$ are characteristic time scales of the density and growth-rate variation. Then, up to the first order in ϵ , Eq. (7) has the solution

$$\frac{\tilde{S}(t)}{\epsilon}=\pm\gamma-\frac{1}{2}\left(\frac{\dot{\rho}}{\rho}+\frac{\dot{\gamma}}{\gamma}\right). \quad (8)$$

Using Eq. (8), the physical optics approximation of η_0 becomes

$$\eta_0^{\text{lin}}=\sqrt{\frac{\rho(0)\gamma(0)}{\rho(t)\gamma(t)}}\left[c_1e^{\int_0^t\gamma(t')dt'}+c_2e^{-\int_0^t\gamma(t')dt'}\right], \quad (9)$$

where integration constants c_1 and c_2 depend on the initial amplitude $\eta_0(0)$ and the initial bubble velocity $\dot{\eta}_0(0)$:

$$c_1=\frac{\eta_0(0)}{2}\left[1+\frac{1}{2\gamma}\left(\frac{\dot{\rho}}{\rho}+\frac{\dot{\gamma}}{\gamma}\right)\right]_{t=0}+\frac{\dot{\eta}_0(0)}{2\gamma(0)},$$

$$c_2=\frac{\eta_0(0)}{2}\left[1-\frac{1}{2\gamma}\left(\frac{\dot{\rho}}{\rho}+\frac{\dot{\gamma}}{\gamma}\right)\right]_{t=0}-\frac{\dot{\eta}_0(0)}{2\gamma(0)}.$$

When the perturbation amplitude becomes large enough, $k\eta_0 > 1$, the bubble growth slows down from the exponential [Eq. (9)] to a power-law dependence. At such amplitudes, the nonlinear terms cannot be neglected (nonlinear regime), and Eqs. (5) and (6) can be solved in the limit $|\dot{\rho}|/\rho \ll \sqrt{kg}$ and $|\dot{\eta}_0/\eta_0| \gg \dot{\rho}/\rho$. The leading-order solution of Eq. (5) becomes $\eta_2^{\text{nl}} = -\tilde{c}_g k/4(1+\tilde{c}_g)$, where the superscript “nl” denotes the perturbations in the nonlinear regime. Substituting η_2^{nl} into Eq. (6) gives

$$\begin{aligned} & -\frac{2}{\tilde{c}_g+1}\dot{a}+ka^2-\frac{2}{\tilde{c}_g(1+\tilde{c}_g)}\left(\frac{\dot{\rho}}{\rho}a+g\right) \\ & =-\frac{2\rho\eta_0}{\tilde{c}_g(1+\tilde{c}_g)}\frac{d}{dt}\left(\frac{\dot{\rho}}{\rho^2}\right), \end{aligned} \quad (10)$$

where $a(t) = -d_t(\rho\eta_0)/\rho$ is the amplitude of the velocity potential defined in Eq. (2). The perturbation growth in the nonlinear regime changes from the exponential to a power law; therefore, $ka^2 \gg \dot{a}$ and the first term in Eq. (10) can be neglected. Then, keeping the terms up to order t_ρ^{-1} in Eq. (10) yields

$$\frac{d(\rho\eta_0^{\text{nl}})}{dt} = -\frac{\dot{\rho}}{2kC_g} + \frac{\rho\gamma(t)}{\sqrt{C_g k}}, \quad (11)$$

where $C_g = \tilde{c}_g(1+\tilde{c}_g)/2$. Integrating Eq. (11) leads to

$$\begin{aligned} \eta_0^{\text{nl}}(t) & = \frac{1}{\sqrt{C_g k \rho(t)}} \int_{t_s}^t \rho(t') \gamma(t') dt' \\ & + \eta_S \frac{\rho_s}{\rho(t)} + \frac{\rho_s/\rho(t)-1}{2C_g k}, \end{aligned} \quad (12)$$

where t_s is the saturation time, $\rho_s = \rho(t_s)$, and $\eta_S = \eta_0(t_s)$ is the bubble amplitude at the saturation time (saturation amplitude). Following Ref. 4, the saturation amplitude can be estimated by equating the bubble velocities $\dot{\eta}_0$ calculated in the linear and nonlinear regimes using Eqs. (9) and (11), respectively. The result takes the form

$$\eta_S = \frac{1}{\sqrt{C_g k}} \left\{ 1 + \frac{1}{2\gamma} \left[\frac{\dot{\gamma}}{\gamma} - \frac{\dot{\rho}}{\rho} \left(1 + \frac{1}{\sqrt{C_g}} \right) \right] \right\}_{t=t_s}. \quad (13)$$

Thus, to the lowest order, $\eta_S = 1/\sqrt{C_g k}$ and Eq. (12) becomes

$$\begin{aligned} \eta_0^{\text{nl}}(t) & = \eta_S \frac{\rho_s}{\rho(t)} \left\{ \int_{t_s}^t \frac{\rho(t')}{\rho_s} \gamma(t') dt' \right. \\ & \left. + 1 + \frac{1}{2\sqrt{C_g}} \left[1 - \frac{\rho(t)}{\rho_s} \right] \right\} \\ & = \frac{1}{\rho(t)} \int_{t_s}^t \rho(t') U_L(t') dt' \\ & + \eta_S \left\{ \frac{\rho_s}{\rho(t)} + \frac{1}{2\sqrt{C_g}} \left[\frac{\rho_s}{\rho(t)} - 1 \right] \right\}, \end{aligned} \quad (14)$$

where

$$U_L(t) = \sqrt{\frac{g(t)}{C_g k}} \quad (15)$$

is the Layzer velocity. It is convenient in many applications to express the nonlinear bubble evolution in terms of the linear perturbation growth.¹⁷ For the large linear growth factors $[\eta_0 \gg \eta_0(0)]$, Eq. (9) can be rewritten as

$$\eta_0^{\text{lin}}(t) = \eta_S \sqrt{\frac{\rho_s \gamma(t_s)}{\rho(t) \gamma(t)}} e^{\int_{t_s}^t \gamma(t') dt'}. \quad (16)$$

Taking the logarithm of both sides in the last equation yields

$$\int_{t_s}^t \gamma(t') dt' = \ln \frac{\eta_0^{\text{lin}}(t)}{\eta_S} + \frac{1}{2} \ln \frac{\rho(t) \gamma(t)}{\rho_s \gamma(t_s)}. \quad (17)$$

The second term in the right-hand side of Eq. (17) is logarithmically small at large times with respect to the first term and can be neglected without a significant loss in accuracy. With the help of Eq. (17), the nonlinear bubble amplitude (14) can be rewritten in terms of the linear perturbation growth:

$$\eta_0^{\text{nl}} = \eta_S \left\{ \ln \frac{\eta_0^{\text{lin}}(t)}{\eta_S} - \int_{t_s}^t \ln \left[\frac{\eta_0^{\text{lin}}(t')}{\eta_S} \right] \frac{\dot{\rho}(t')}{\rho(t')} dt' + \frac{\rho_s}{\rho(t)} + \frac{1}{2\sqrt{C_g}} \left[\frac{\rho_s}{\rho(t)} - 1 \right] \right\}. \quad (18)$$

The saturation time t_s is easily obtained using Eq. (9):⁷

$$\int_0^{t_s} \gamma(t') dt' - \frac{1}{2} \ln \left[\frac{\gamma(t_s) \rho_s}{\rho(0) \gamma(0)} \right] = \ln(\eta_S / c_1). \quad (19)$$

The second term in the left-hand side of Eq. (19) has a weak logarithmic time dependence and can therefore be neglected. Substituting $c_1 \approx \eta_0(0)/2$, Eq. (19) reduces to

$$\int_0^{t_s} \gamma(t') dt' \approx \ln \frac{2\eta_S}{\eta_0(0)}. \quad (20)$$

Equation (20) defines the saturation time t_s in terms of the initial amplitude $\eta_0(0)$.

Equation (11) shows that the temporal density variation modifies the asymptotic bubble velocity U_b :

$$U_b \equiv \dot{\eta}_0 \rightarrow U_L - \frac{\dot{\rho}}{\rho} \left(\eta_0 + \frac{1}{2C_g k} \right). \quad (21)$$

In the case of the decompression flow when the density decreases in time ($\dot{\rho} < 0$), the bubble grows faster, and, in the case of compression ($\dot{\rho} > 0$), the bubble grows slower than the classical Layzer velocity $U_L = \sqrt{g/kC_g}$.

Next, to validate the results of the analysis, we compare the bubble evolution in the three-dimensional geometry ($\tilde{c}_g = 1$)

calculated using the system (5)–(6) and the results of asymptotic analysis [Eqs. (9) and (14)]. The gravitational field is assumed in the form $g = g_0 / [1 + (t/t_g)^{s_g}]$. The fluid density changes in time as (a) $\rho(t) = \rho_0 [1 + C_\rho (t/t_0)^{s_\rho}]$ and (b) $\rho(t) = \rho_0 (1 + D_\rho \cos \Omega t)$, where s_g and s_ρ are the power indexes for acceleration and fluid density, respectively, and C_ρ , D_ρ , t_0 , and Ω are the normalization constants. Figure 102.48 shows a plot of the bubble amplitude calculated for case (a) with $g_0 = 10 \lambda/t_0^2$, $t_g = t_0$, $s_g = 1$, $s_\rho = 2$, $C_\rho = 0.25$ (solid line), $C_\rho = 0$ (dashed line), and $C_\rho = -0.15$ (dotted line). The initial conditions are $\eta_0(0) = \lambda/200$ and $\dot{\eta}_0(0) = \lambda/(200 t_0)$. Thick lines represent the exact solutions of Eqs. (5) and (6); thin lines show the WKB solution for $t < t_s$ and the asymptotic solution (14) after $t = t_s$. Note the larger amplification factor of the bubble amplitude in the decompression flow. Figure 102.49 plots the linear (thin lines) and nonlinear (thick lines) perturbation growth. Observe that the value of η_S calculated using

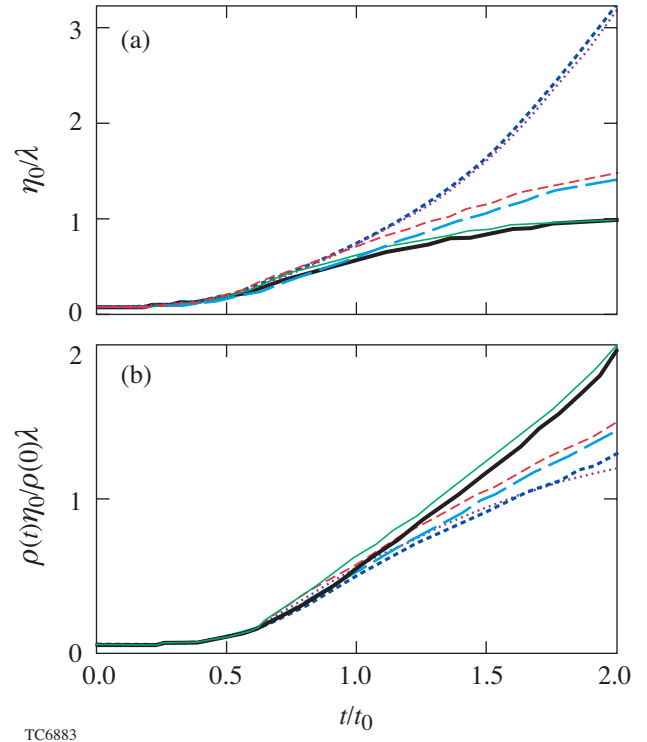


Figure 102.48

Plot of normalized bubble amplitude calculated using the exact numerical solution of Eqs. (5) and (6) (thick lines) and analytical solutions (9) and (14) (thin lines). The solid lines correspond to the fluid compression with $C_\rho = 0.25$, the dashed lines represent the constant density case (classical Layzer's model⁴), and the dotted lines are obtained for the decompression flow with $C_\rho = -0.15$.

Eq. (13) represents a good approximation to the saturation amplitude. The bubble evolution in case (b) is plotted in Fig. 102.50 for $D_\rho = 0.3$ (solid line) and $D_\rho = -0.3$ (dashed line). The initial conditions for this case are $\eta_0 = \lambda/2 \times 10^{-3}$ and $\dot{\eta}_0 = \Omega\lambda/2 \times 10^{-3}$ and $t_g = 1/\Omega$. A good agreement between the exact solution and the asymptotic formulas validates the accuracy of the performed analysis.

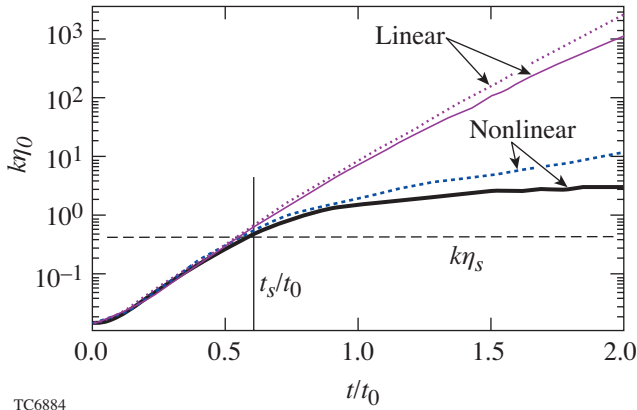


Figure 102.49
Plot of normalized bubble amplitude calculated using the exact numerical solution of Eqs. (5) and (6) with (thick lines) and without (thin lines) nonlinear terms. The solid and dotted lines correspond to $C_\rho = 0.25$ and -0.15 , respectively. The dashed line shows the saturation amplitude defined in Eq. (44).

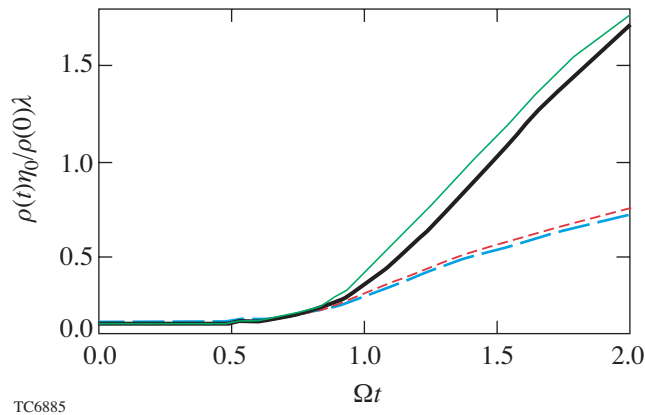


Figure 102.50
Plot of normalized bubble amplitude calculated using the exact numerical solution of Eqs. (5) and (6) (thick lines) and analytical solutions (9) and (14) (thin lines). The solid and dashed lines correspond to $D_\rho = 0.3$ and -0.3 , respectively.

To comment on the effects of temporal density variation on the asymptotic behavior of the Richtmyer–Meshkov (RM) instability, such an instability occurs when a shock passes through a corrugated interface between two fluids. As opposed to RT instability, the instability drive in this case has a finite duration (of the order of the sound-wave propagation across the perturbation wavelength). Thus, the asymptotic evolution of the bubble amplitude can be found using Eq. (10) with $g = 0$. When the fluid density does not change with time ($\dot{\rho} = 0$), the sum of the first two terms in Eq. (10) must be zero. This yields a decay in time velocity^{5,7}

$$\dot{\eta}_0^{\text{RM}} \rightarrow U_L^{\text{RM}} = 2/[(\tilde{c}_g + 1)kt]$$

and logarithmically growing bubble amplitude $\eta_0^{\text{RM}} \sim \ln t$. For a finite density derivative, one can attempt to generalize Eq. (14) to RM instability by replacing U_L with U_L^{RM} :

$$\eta_0^{\text{RM}} \rightarrow \frac{2}{k(\tilde{c}_g + 1)\rho(t)} \int^t \frac{\rho(t')}{t'} dt'. \quad (22)$$

Equation (22) is the result of balancing the first two terms in Eq. (10) and neglecting its right-hand side. It is easy to show, however, that, opposed to the RT instability, the right-hand side of Eq. (10) cannot be considered small in the RM instability at all times, regardless of the value of $\dot{\rho}/\rho$. Indeed, substituting the constant-density solution into Eq. (10) shows that the first two terms decrease in time ($\sim 1/t^2$), while the right-hand side has a factor of $\ln t$. Thus, even a small density variation can significantly change the asymptotic behavior of the bubble velocity in the RM instability. Although Eq. (22) predicts correctly the trend of the effect, the accuracy of such a scaling is inadequate. To illustrate a strong dependence on the density variation, Fig. 102.51 plots the bubble velocity calculated for densities $\rho = \rho_0$ (dashed line) and $\rho = \rho_0 [1 - \epsilon(t/t_0)^2]$ (solid line), where $\epsilon = 5 \times 10^{-4}$. The velocities are plotted up to the time when the density difference between two cases is only 10%. The bubble velocity, however, is twice as large with the time-dependent density. The approximate solution (22), shown by the dotted line, gives only half of the decompression effect. For a more accurate estimate, the right-hand side of Eq. (10) must be retained. The solution in this case, however, cannot be written in a closed analytical form for an arbitrary density variation.

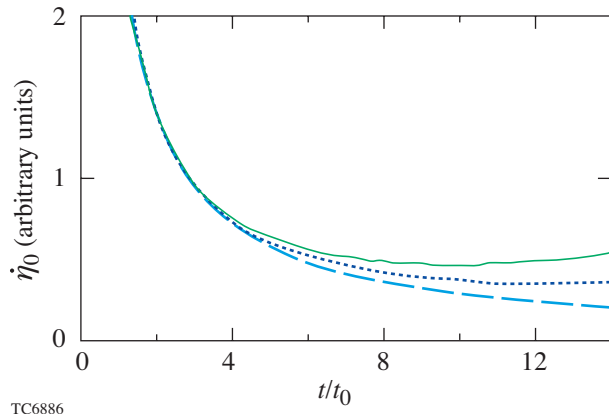


Figure 102.51

The asymptotic bubble velocity for RM instability. The dashed line represents the constant-density solution ($\sim 1/t$), the solid line is the result of the exact solution of Eqs. (5) and (6) with time-dependent density $\rho = \rho_0 [1 - 5 \times 10^{-4} (t/t_0)^2]$, and the dotted line shows scaling defined in Eq. (22).

Bubble Growth in Spherical Geometry

In a spherical shell of uniform density ρ with an outer radius r_0 and inner radius r_1 , the fluid density outside the shell is assumed to be much smaller than ρ ($A_T = 1$). The shell interfaces are distorted with a single-mode perturbation of the mode number ℓ . To simplify the analysis, a short-wavelength limit was used when the perturbation wavelength was much smaller than the shell thickness $\ell(r_0 - r_1)/r_0 \gg 1$ or $\ell \gg 1$. The perturbations at the inner and outer surfaces in such an approximation are decoupled and can be treated separately. One must keep in mind, however, that even though only a single interface is considered, the product ρr_0^3 is not a constant. If the outer shell boundary is considered, the points where the shell interface has the maximum radii correspond to the perturbation spikes and the points of the minimum radii correspond to the perturbation bubbles. Following Layzer's approach, only the bubble evolution is described. In addition, similar to the analysis in the previous section, the effects due to the surface tension and thermal conduction are neglected.

A bubble is assumed to be symmetric with respect to the polar angle ϕ . The axis of symmetry is along z direction. Solution of the Poisson's equation

$$\nabla^2 \Phi = \frac{1}{r^2} \frac{\partial}{\partial r} \left(r^2 \frac{\partial \Phi}{\partial r} \right) + \frac{1}{r^2 \sin \theta} \frac{\partial}{\partial \theta} \left(\sin \theta \frac{\partial \Phi}{\partial \theta} \right) = -\frac{\dot{\rho}}{\rho} \quad (23)$$

can be written in the form

$$\Phi = \frac{r_0}{\ell} \left[a(t) \left(\frac{r}{r_0} \right)^\ell + b(t) \left(\frac{r_0}{r} \right)^{\ell+1} \right] P_\ell(\cos \theta) - \frac{c(t)}{r} - \frac{\dot{\rho} r^2}{\rho 6}, \quad (24)$$

where P_ℓ is the Legendre polynomial, θ is the azimuthal angle, $a(t)$ and $b(t)$ are undetermined functions of time, and function $c(t)$ is defined by the unperturbed flow condition $\partial_r \Phi(r_0) = \dot{r}_0$,

$$c(t) = r_0^2 \left(\dot{r}_0 + \frac{r_0 \dot{\rho}}{3 \rho} \right). \quad (25)$$

Here, \dot{r}_0 is the velocity of the outer shell boundary. Since terms up to θ^2 are retained in the analysis, only the fundamental harmonic is kept in Eq. (24). In what follows an imploding shell with the unstable outer interface is considered. Thus, $b(t) = 0$ must satisfy the boundary condition at $(r/r_0)^\ell \rightarrow 0$. The case of the expanding shell ($a = 0$) can be treated in a similar fashion and will not be described in detail in this article. Solution (24) must satisfy the boundary condition at $r = r_0 + \eta(t, \theta)$, where η is the interface distortion. The first condition is easily derived from the mass conservation equation

$$\dot{\eta} + \frac{v_\theta}{r_0 + \eta} \partial_\theta \eta = v_r - \dot{r}_0. \quad (26)$$

Then, assuming a uniform density inside the shell, the momentum equation is integrated to yield Bernoulli's equation

$$-\frac{p}{\rho} = \partial_t \Phi + \frac{1}{2} v^2 - f(t), \quad (27)$$

where p is the pressure, $v^2 = v_r^2 + v_\theta^2$ is the total velocity, and $f(t)$ is an undetermined function of time. Pressure must be continuous across the boundary; therefore, Eq. (27) reduces to

$$\partial_t \Phi + \frac{1}{2} v^2 = \tilde{f}(t), \quad (28)$$

where $\tilde{f}(t) = f(t) - p_a(t)/\rho$ and $p_a(t)$ is the drive pressure. To find the distortion amplitude η , the boundary conditions

(26) and (28) and the potential (24) are expanded near the tip of the bubble in series of azimuthal angle θ :

$$\begin{aligned}\eta(t, \theta) &= \eta_0 + \eta_2 \theta^2 + O(\theta^4), \\ P_\ell(\cos \theta) &= 1 - \frac{\ell(\ell+1)}{4} \theta^2 + O(\theta^4).\end{aligned}\quad (29)$$

Note that $\eta_0 < 0$ at the bubble. The resulting system of differential equations takes the form

$$\begin{aligned}3 \frac{d}{dt} (\rho r_0^2 \eta_2) - \frac{2\eta_2}{r_0} \frac{d(\rho r_0^3)}{dt} \left[1 - \left(\frac{r_0}{r_0 + \eta_0} \right)^3 \right] \\ = \left(\frac{r_0}{r_0 + \eta_0} \right)^2 \frac{d}{dt} \rho \left[(r_0 + \eta_0)^3 - r_0^3 \right] \\ \times \left[\frac{2\ell}{r_0 + \eta_0} \eta_2 - \frac{\ell(\ell+1)}{4} \right],\end{aligned}\quad (30)$$

$$\begin{aligned}\frac{d}{dt} \left\{ \frac{1}{3\rho(r_0 + \eta_0)} \frac{d}{dt} \rho \left[(r_0 + \eta_0)^3 - r_0^3 \right] \right\} \left(\frac{\eta_2}{r_0 + \eta_0} - \frac{\ell+1}{4} \right) \\ + \frac{1}{3\rho(r_0 + \eta_0)^2} \frac{d}{dt} \rho \left[(r_0 + \eta_0)^3 - r_0^3 \right] \\ \times \left\{ \frac{1}{3\rho(r_0 + \eta_0)^2} \frac{d}{dt} \rho \left[(r_0 + \eta_0)^3 - r_0^3 \right] \right. \\ \times \left[\frac{(\ell+1)^2}{8} - \frac{\eta_2}{r_0 + \eta_0} \right] - \frac{\eta_2}{\rho(r_0 + \eta_0)^3} \frac{d(\rho r_0^3)}{dt} \left. \right\} \\ + \frac{\eta_2}{(r_0 + \eta_0)^2} \left\{ r_0^2 \ddot{\eta}_0 + \left[(r_0 + \eta_0)^3 - r_0^3 \right] \right. \\ \times \left. \left[\frac{2r_0^3}{9(r_0 + \eta_0)^3} \left(\frac{d_t \rho r_0^3}{\rho r_0^3} \right)^2 + \frac{4}{9} \left(\frac{\dot{\rho}}{\rho} \right)^2 - \frac{\ddot{\rho}}{3\rho} \right] \right\} = 0.\end{aligned}\quad (31)$$

Although the system (30)–(31) can be easily integrated numerically for a given trajectory $r_0(t)$ and shell density $\rho(t)$, it is difficult to get a physical insight on the convergence effects from this rather cumbersome system. To obtain a scaling of the asymptotic nonlinear bubble amplitude with the flow parameters, the equations can be significantly simplified by assuming that the bubble amplitude is much smaller than the shell radius $|\eta_0| \ll r_0$ (a combination $\ell|\eta_0|/r_0$, however, can be arbitrarily large since $\ell \gg 1$). Simple calculations reduce Eqs. (30) and (31) in this case to

$$\frac{d}{dt} (\rho r_0^2 \eta_2) = -\frac{\ell(\ell+1)}{4} \frac{d}{dt} (\rho r_0^2 \eta_0) \left(1 - \frac{8}{\ell+1} \frac{\eta_2}{r_0} \right), \quad (32)$$

$$\begin{aligned}\frac{d}{dt} \left[\frac{d_t (\rho r_0^2 \eta_0)}{\rho r_0} \right] - \frac{\ell+1}{2} \left[\frac{d_t (\rho r_0^2 \eta_0)}{\rho r_0^2} \right]^2 - \frac{4\eta_2}{\ell+1} (\ddot{\eta}_0 + \ddot{\eta}_0) \\ = -(\ell+1) \frac{\eta_0^2}{r_0^2} \frac{d_t (\rho r_0^2 \eta_0)}{\rho r_0} \frac{d_t (\rho r_0^3)}{\rho r_0^3}.\end{aligned}\quad (33)$$

The term in the right-hand side of Eq. (33) is retained for the high-convergence-ratio implosions.

When $\ell|\eta_0|/r_0 \ll 1$, the nonlinear terms can be neglected, leading to $\eta_2^{\text{lin}} = -\eta_0^{\text{lin}} \ell(\ell+1)/4$. Equation (33) recovers, in this limit, the results of Refs. 15, 18, and 19,

$$\frac{d}{dt} \left(\frac{r_0^2 \xi_0^{\text{lin}}}{m} \right) + \ell \frac{\ddot{\eta}_0 r_0}{m} \xi_0^{\text{lin}} = 0, \quad (34)$$

where $\xi_0 = \rho(t) r_0^2(t) \eta_0$, $m(t) = \rho(t) r_0^3(t)$, and the dot denotes the time derivative. The new function ξ_0 can be related to a very important parameter characterizing the shell stability. In comparing performances of different implosions with respect to the shell breakup, it is not the bubble amplitude itself, but the ratio of the amplitude η_0 to the in-flight shell thickness Δ that must be considered. The parameter $\Upsilon = |\eta_0|/\Delta$ is referred to as an instability factor. Multiplying the denominator and numerator in Υ by ρr_0^2 , we obtain $\Upsilon = 4\pi |\xi_0|/M_{\text{sh}}$, where $M_{\text{sh}} = 4\pi \rho r_0^2 \Delta$ is the shell mass. Thus, divided by the shell mass, $|\xi_0|$ shows how close the imploding shell is to

breaking up. If $|\xi_0|/M_{\text{sh}} \simeq (4\pi)^{-1}$, the shell integrity is compromised by the instability growth.

An approximate solution of Eq. (34) can be found in the limit $\ell \gg 1$ using the WKB method. Writing the solution as $\xi_0^{\text{lin}} = e^{S/\epsilon}$ ($\epsilon \ll 1$ is a small parameter), Eq. (34) becomes

$$\dot{S}^2 + \epsilon \left[\ddot{S} + \left(2 \frac{\dot{r}_0}{r_0} - \frac{\dot{m}}{m} \right) \dot{S} \right] + \epsilon^2 \ell \frac{\ddot{r}_0}{r_0} = 0. \quad (35)$$

To satisfy Eq. (35) we must require $\epsilon = 1/\sqrt{\ell}$. Then, expanding S in powers of ϵ , the solution up to the first order in ϵ takes the form

$$S = \pm \int^t \sqrt{-\frac{\ddot{r}_0(t')}{r_0(t')}} dt' + \frac{\epsilon}{2} \ln \left(\frac{m}{r_0^2} \sqrt{-\frac{r_0}{\ddot{r}_0}} \right). \quad (36)$$

The WKB solution (36) is valid if the shell acceleration \ddot{r}_0 does not go to zero during the implosion. With the help of Eq. (36), ξ_0^{lin} becomes

$$\xi_0^{\text{lin}} = \frac{\sqrt{m(t)m(0)}}{r_0(t)} \sqrt{\frac{\Gamma(0)}{\Gamma(t)}} \times \left[C_1 e^{\int_0^t \Gamma(t') dt'} + C_2 e^{-\int_0^t \Gamma(t') dt'} \right], \quad (37)$$

where

$$\Gamma(t) = \sqrt{-\ell \frac{\ddot{r}_0(t)}{r_0(t)}},$$

and the integration constants C_1 and C_2 depend on the initial bubble amplitude $\eta_0(0)$ and bubble velocity $\dot{\eta}_0(0)$,

$$C_1 = \frac{\eta_0(0)}{2} \left\{ 1 + \frac{1}{2\Gamma(0)} \left[\frac{\dot{m}(0)}{m(0)} + \frac{\dot{\Gamma}(0)}{\Gamma(0)} \right] \right\} + \frac{\dot{\eta}_0(0)}{2\Gamma(0)},$$

$$C_2 = \frac{\eta_0(0)}{2} \left\{ 1 - \frac{1}{2\Gamma(0)} \left[\frac{\dot{m}(0)}{m(0)} + \frac{\dot{\Gamma}(0)}{\Gamma(0)} \right] \right\} - \frac{\dot{\eta}_0(0)}{2\Gamma(0)}.$$

In the limit of $\ell \gg 1$, coefficients C_1 and C_2 in the leading order reduce to $C_1 = C_2 \simeq \eta_0(0)/2$. The perturbations grow according to Eq. (37) until the nonlinear effects become important and the bubble growth slows down (nonlinear saturation). To find the perturbation amplitude η_S at which the transition from linear to nonlinear growth occurs, we must first determine the bubble evolution in the nonlinear regime. Then, equating the linear and nonlinear bubble velocities will define an approximate saturation amplitude.⁴

We begin the nonlinear analysis with Eq. (32), which can be rewritten in the limit $\ell \gg 1$ as

$$\dot{\xi}_0 \left(1 - 8\epsilon^2 \frac{\eta_2}{r_0} \right) = -4\epsilon^4 \frac{d}{dt} (\rho r_0^2 \eta_2), \quad (38)$$

where $\epsilon = 1/\sqrt{\ell}$. The left-hand side of Eq. (38) is of the order of $\epsilon^0 \xi_0$; the right-hand side is of the order of $\epsilon^4 \eta_2$. It can be shown that to satisfy Eq. (38), we must order $\eta_2^{\text{nl}}/r_0 \sim \epsilon^{-2}$. Here, the superscript “nl” denotes the functions in the nonlinear regime. To the lowest order in ϵ , the latter ordering gives $\eta_2^{\text{nl}}/r_0 = \ell/8$. Keeping the higher-order terms in η_2^{nl} yields

$$\frac{\eta_2^{\text{nl}}}{r_0} = \frac{\ell}{8} + \frac{\dot{m}(t)}{16 \dot{\xi}_0^{\text{nl}}}. \quad (39)$$

For a decreasing $m(t)$ (which is almost always the case in a converging shell), η_2 reaches an asymptotic value that is slightly larger than $r_0 \ell/8$ (keep in mind that the bubble amplitude η_0 is negative). The difference between η_2/r_0 and $\ell/8$ decays in time in the case of growing $|\xi_0|$. When the ratio η_0/r_0 cannot be neglected compared to unity, the solution (39), according to Eq. (30), is multiplied by a factor $(1 + \eta_0^{\text{nl}}/r_0)$:

$$\frac{\eta_2^{\text{nl}}}{r_0} = \left[\frac{\ell}{8} + \frac{\dot{m}(t)}{16 \dot{\xi}_0^{\text{nl}}} \right] \left(1 - \frac{|\eta_0^{\text{nl}}|}{r_0} \right). \quad (40)$$

Such a factor further reduces the asymptotic value of η_2^{nl} at the large bubble amplitudes. A detailed comparison with the

exact numerical solution of Eqs. (30) and (31) shows that η_2^{nl} can be replaced by $r_0\ell/8$ in Eq. (33) without significant loss in accuracy. This yields

$$\begin{aligned} & \ell \left(\dot{\xi}_0^{\text{nl}} \right)^2 - \dot{\xi}_0^{\text{nl}} \dot{m} \left[1 + 2\ell \left(\frac{\xi_0^{\text{nl}}}{m} \right)^2 \right] + 2m\dot{\xi}_0^{\text{nl}} \frac{\dot{r}_0}{r_0} + \frac{\ddot{r}_0}{r_0} m^2 \\ &= \frac{m^2}{r_0^2} \frac{d}{dt} \left(\frac{\dot{\xi}_0^{\text{nl}}}{\rho r_0} \right) + \xi_0^{\text{nl}} \frac{m^2}{r_0} \frac{d}{dt} \left(\frac{\dot{\rho}}{\rho^2 r_0^2} \right). \end{aligned} \quad (41)$$

As in the planar geometry case, $\dot{a}(t)$ can be neglected with respect to $\ell a^2(t)$ in the nonlinear regime, where $a = \dot{\xi}_0 / \rho r_0^2$ is the amplitude in the velocity potential defined in Eq. (24). Furthermore, we also drop the second term in the right-hand side of Eq. (41). This term is identically zero at a constant density; if $\dot{m} = 0$ (solid sphere implosion), the term is equal to $-3m^2(\ddot{r}_0/r_0)(\eta_0^{\text{nl}}/r_0)$, which is smaller by a factor η_0^{nl}/r_0 compared to the last term in the left-hand side of Eq. (41). Next, solving the second-order algebraic equation for $\dot{\xi}_0^{\text{nl}}$ yields

$$\begin{aligned} \dot{\xi}_0^{\text{nl}} &= \dot{m} \left[\frac{1}{2\ell} + \left(\frac{\xi_0^{\text{nl}}}{m} \right)^2 \right] \\ &= \sqrt{\dot{m}^2 \left[\frac{1}{2\ell} + \left(\frac{\xi_0^{\text{nl}}}{m} \right)^2 \right]^2 - \frac{2\dot{m}\dot{r}_0}{\ell r_0} \xi_0^{\text{nl}} - \frac{\ddot{r}_0}{r_0} \frac{m^2}{\ell}}. \end{aligned} \quad (42)$$

As mentioned earlier, the approximate value of the saturation amplitude η_S can be obtained by equating $\dot{\xi}_0$ in the linear and nonlinear regimes. In the linear case, using the WKB solution (37), we write $\dot{\xi}_0 = \sqrt{\ell} \dot{S}(t) \xi_0$. This gives

$$\dot{\xi}_0 = \xi_0 \left[\Gamma(t) + \frac{1}{2} \left(\frac{\dot{m}}{m} - 2 \frac{\dot{r}_0}{r_0} - \frac{\dot{\Gamma}}{\Gamma} \right) \right]. \quad (43)$$

Substituting Eq. (43) into Eq. (42) and neglecting terms with ξ_0^2 (shell convergence ratio is assumed to be not very large at the time of the bubble saturation, so the terms with ξ_0^2 are

small) yields the saturation amplitude

$$\frac{|\eta_S|}{r_0(t_s)} = \frac{|\xi_S|}{m_s} = \frac{1}{\ell} \left[1 + \frac{1}{\Gamma} \left(\frac{\dot{\Gamma}}{2\Gamma} + \frac{\dot{r}_0}{r_0} - \frac{\dot{m}}{m} \right) \right]_{t=t_s}, \quad (44)$$

where t_s is the saturation time, $m_s = m(t_s)$, $\eta_S = \eta_0(t_s)$, and $\xi_S = \xi_0(t_s)$. Since $\Gamma \sim \sqrt{\ell}$, the bubble saturation amplitude, to the lowest order in ℓ^{-1} , is $|\eta_S| \sim r_0(t_s)/\ell$. To find the bubble evolution after the saturation, we solve Eq. (42) in the limit of $\ell \gg 1$, expanding the solution $\xi_0^{\text{nl}} = \xi_{00} + \xi_{01} + \dots$, where $\xi_{00}/\xi_{01} \sim \sqrt{\ell} \gg 1$. Keeping the lowest-order terms in Eq. (42) gives

$$\xi_{00} = -\frac{1}{\ell} \int_{t_s}^t \Gamma(t') m(t') dt' + c_0, \quad (45)$$

where c_0 is an integration constant. Substituting ξ_{00} back into Eq. (42) and retaining the terms of the order $1/\ell$ yields ξ_{01} . Combining ξ_{00} and ξ_{01} and using the saturation condition $\xi_0(t_s) = -m_s/\ell$ leads to

$$\begin{aligned} \xi_0^{\text{nl}} &= -m(t) I(t) + \frac{m(t) - 3m_s}{2\ell} \\ &+ \int_{t_s}^t \dot{m} \left[I(t')^2 - I(t') \frac{\dot{r}_0}{r_0 \Gamma} \right] dt', \end{aligned} \quad (46)$$

where

$$\begin{aligned} I(t) &= \frac{1}{\ell m(t)} \int_{t_s}^t \Gamma(t') m(t') dt' \\ &= \frac{1}{m(t)} \int_{t_s}^t U_L^{\text{sp}}(t') \frac{m(t')}{r_0(t')} dt' \end{aligned}$$

and

$$U_L^{\text{sp}} = \sqrt{-\frac{\ddot{r}_0(t) r_0(t)}{\ell}}.$$

Equation (46) can be further simplified by taking the integral by parts,

$$\begin{aligned} & \int_{t_s}^t \dot{m} \left[I(t')^2 - I(t') \frac{\dot{r}_0}{r_0 \Gamma} \right] dt' \\ &= m(t) \ln \left[\frac{m(t)}{m_s} \right] \left(I^2 - I \frac{\dot{r}_0}{\Gamma r_0} \right) \\ & \quad - \int_{t_s}^t \ln \frac{m(t')}{m_s} \frac{d}{dt'} \left[m(t') \left(I^2 - I \frac{\dot{r}_0}{\Gamma r_0} \right) \right] dt', \end{aligned} \quad (47)$$

and neglecting the second integral in the right-hand side of Eq. (47). This gives a relatively simple scaling with $\sim 20\%$ error. Substituting Eq. (47) into Eq. (46) and replacing

$$1 + \left(\frac{\dot{r}_0}{r_0 \Gamma} - I \right) \ln \frac{m(t)}{m_s} \approx \left[\frac{m(t)}{m_s} \right]^{\dot{r}_0 / r_0 \Gamma - I}$$

yields

$$\begin{aligned} \xi_0^{\text{nl}} & \approx -m(t) I(t) \left[\frac{m(t)}{m_s} \right]^{\dot{r}_0 / (r_0 \Gamma) - I} + \frac{m(t) - 3m_s}{2\ell} \\ & \approx \xi_s \left\{ \left[\frac{m(t)}{m_s} \right]^{\dot{r}_0 / (r_0 \Gamma) - I} \int_{t_s}^t \Gamma(t') \frac{m(t')}{m_s} dt' \right. \\ & \quad \left. + \frac{3 - m(t)/m_s}{2} \right\} \\ & = - \left[\frac{m(t)}{m_s} \right]^{\dot{r}_0 / (r_0 \Gamma) - I} \int_{t_s}^t U_L^{\text{sp}}(t') \rho(t') r_0^2(t') dt' \\ & \quad + \xi_s \frac{3 - m(t)/m_s}{2}. \end{aligned} \quad (48)$$

To use Eq. (48), one must specify the saturation time t_s . The latter can be easily obtained with the help of Eq. (37). At the time of bubble saturation, the following equality must be satisfied:

$$\frac{m_s}{\ell} \approx |C_1| \frac{\sqrt{m_s m(0)}}{r_0(t_s)} \sqrt{\frac{\Gamma(0)}{\Gamma(t_s)}} e^{\int_0^{t_s} \Gamma(t') dt'}, \quad (49)$$

which leads to

$$\int_0^{t_s} \Gamma(t') dt' \approx \ln \left[\frac{r_0(t_s)}{\ell |C_1|} \sqrt{\frac{m_s \Gamma(t_s)}{m(0) \Gamma(0)}} \right]. \quad (50)$$

It is sufficient in many cases to keep only the lowest-order terms in Eq. (50). This gives

$$\int_0^{t_s} \Gamma(t') dt' \approx \ln \left[\frac{r_0(0)}{\ell |C_1|} \right] \approx \ln \left[\frac{2r_0(0)}{\ell |\eta_0(0)|} \right]. \quad (51)$$

To obtain a more accurate value of t_s , one must solve Eq. (50).

It is interesting to note that the perturbation growth factors are smaller in a “compact” shell with a larger density than in a decompressed, lower-density shell [$\eta_0 \sim 1/\sqrt{m}$ before and $\eta_0 \sim m^{-I - \dot{r}_0 / (\Gamma r_0)}$ after the saturation]. The shell thickness Δ , however, is inversely proportional to m ; therefore, the ratio $\Upsilon = |\eta_0|/\Delta$ is larger in the higher-density shell [$\Upsilon \sim \xi_0 \sim \sqrt{m(t)}$ in the linear regime and $\Upsilon \sim m(t)$ in the nonlinear regime]. Thus, for the same shell trajectory, the thinner shell is more unstable.

As a next step, the nonlinear bubble evolution is expressed in terms of the linear perturbation growth. The linear growth can be calculated, for example, using the stability postprocessor described in Ref. 15. When the perturbation amplitude is much larger than the initial amplitude $\eta_0(0)$, Eq. (37) can be rewritten as

$$\eta_0^{\text{lin}} \approx \eta_s \sqrt{\frac{m_s \Gamma(t_s)}{m(t) \Gamma(t)}} e^{\Psi(t)}, \quad \Psi(t) = \int_{t_s}^t \Gamma(t') dt', \quad (52)$$

where $\eta_S \approx -r_0(t_s)/\ell$ is the saturation amplitude. Then,

$$\Psi(t) = \ln \frac{\eta_0^{\text{lin}}}{\eta_S} + \frac{1}{2} \ln \left[\frac{\Gamma(t)m(t)}{\Gamma(t_s)m_s} \right]. \quad (53)$$

The linear RT growth is exponential; thus, assuming that $\Gamma(t)$ and $m(t)$ grow slower than η_0^{lin} , the second logarithm in the right-hand side of Eq. (53) can be neglected. Function $I(t)$ in Eq. (48) can be rewritten in terms of the function $\Psi(t)$:

$$\ell I(t) = \Psi(t) - \frac{1}{m(t)} \int_{t_s}^t \Psi(t') \dot{m}(t') dt'.$$

With the help of the latter relation and substituting $\ell \approx -r_0(t_s)/\eta_S$, Eq. (48) becomes

$$\begin{aligned} \eta_0^{\text{nl}}(t) = \eta_S \frac{r_0(t)}{r_0(t_s)} & \left\{ \left[\ln \frac{\eta_0^{\text{lin}}(t)}{\eta_S} \right. \right. \\ & \left. \left. - \frac{1}{m(t)} \int_{t_s}^t \ln \frac{\eta_0^{\text{lin}}(t')}{\eta_S} \dot{m}(t') dt' \right] \left[\frac{m_s}{m(t)} \right]^{\alpha_m(t)} \right. \\ & \left. + \frac{3}{2} \frac{m_s}{m(t)} - \frac{1}{2} \right\}, \end{aligned} \quad (54)$$

where

$$\begin{aligned} \alpha_m(t) = & -\frac{\dot{r}_0 \eta_0^{\text{lin}}(t)}{r_0 \dot{\eta}_0^{\text{lin}}} \\ & + \frac{|\eta_S|}{r_0(t_s)} \left[\ln \frac{\eta_0^{\text{lin}}(t)}{\eta_S} - \frac{1}{m(t)} \int_{t_s}^t \ln \frac{\eta_0^{\text{lin}}(t')}{\eta_S} \dot{m}(t') dt' \right]. \end{aligned}$$

Equation (54) is especially simple in the case of a solid-sphere implosion when $m = \rho r_0^3 = \text{const}$,

$$\eta_0^{\text{nl}}(t) \Big|_{\rho r_0^3 = \text{const}} = \eta_S \frac{r_0(t)}{r_0(t_s)} \left[\ln \frac{\eta_0^{\text{lin}}(t)}{\eta_S} + 1 \right]. \quad (55)$$

Except for the factor $r_0(t)/r_0(t_s)$, Eq. (55) reproduces the asymptotic formula proposed in Ref. 17.

To validate the accuracy of the derived results, we compare the bubble evolution calculated using the exact system [Eqs. (30) and (31)] with the analytical scaling [Eqs. (37) and (48)]. Figure 102.52(a) plots the bubble amplitude for mode numbers $\ell = 100$ and $\ell = 200$. The outer shell radius changes according to a power law $r_0 = R_0(1-t/t_0)^{1/3}$, where $0 \leq t < t_0$. The density is inversely proportional to the trajectory,

$$\rho(t) = \rho_0 [R_0/r_0(t)].$$

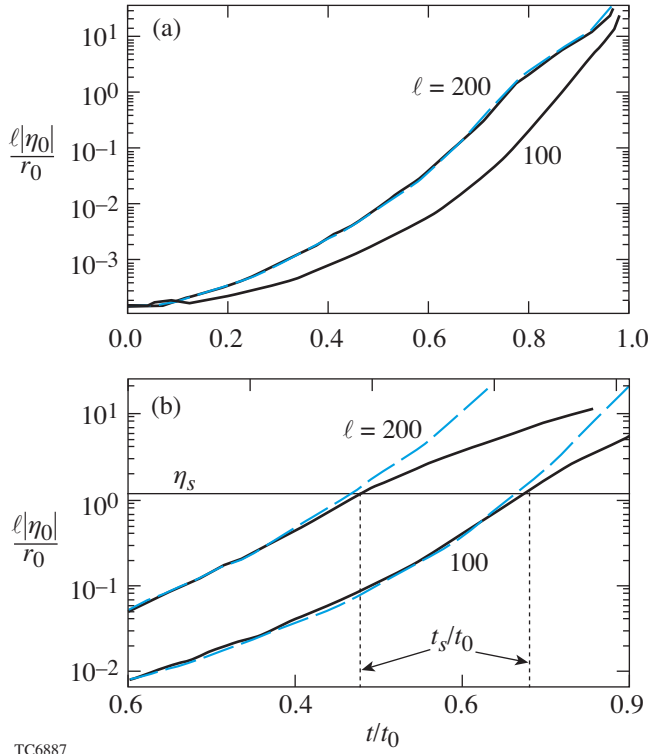
The initial conditions are

$$\eta_0 = -2 \times 10^{-4} R_0 / \ell$$

and

$$\dot{\eta}_0 = 2 \times 10^{-4} R_0 / \ell t_0.$$

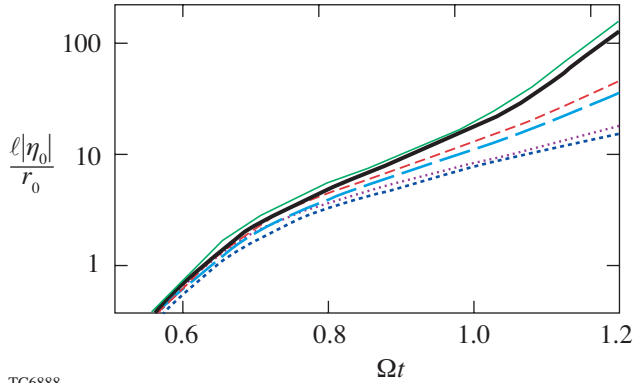
The solid lines represent the exact solution of Eqs. (30) and (31), and dashed lines are obtained using Eq. (37) for $t < t_s$ and Eq. (48) for $t > t_s$. The saturation time t_s is defined as the time of intersection of the linear amplitude [Eq. (37)] with the saturation amplitude [Eq. (44)]. Figure 102.52(b) plots the normalized amplitudes with (solid curves) and without (dashed curves) the nonlinear effects. Observe that the saturation value defined by Eq. (44) reproduces very well the bubble amplitude at which the growth slows down and becomes nonlinear. Figure 102.53 plots the bubble evolution for the shell with $r_0 = R_0 \cos \Omega t$ ($0 \leq \Omega t < \pi/2$) and mode number $\ell = 200$. The initial conditions for the perturbations are the same as in the previous case ($\Omega = 1/t_0$). The density is assumed to follow a power law of the radius, $\rho(t) = \rho(0) [R_0/r_0(t)]^s$. The thick lines represent the exact numerical solution of Eqs. (30) and (31), and the thin lines are the results of the asymptotic analysis. The solid, dashed, and dotted lines in Fig. 102.53



TC6887

Figure 102.52

(a) Plot of normalized bubble amplitude calculated using the exact numerical solution of Eqs. (30) and (31) (solid lines) and analytical solutions (37) and (48) (dashed lines). (b) Plot of the normalized bubble amplitude with (solid lines) and without (dashed lines) nonlinear terms.



TC6888

Figure 102.53

Bubble amplitude calculated using the exact numerical solution of Eqs. (30) and (31) (thick lines) and analytical solutions (37) and (48) (thin lines) for $\rho = \text{const}$ (solid lines), $\rho \sim 1/r_0$ (dashed lines), and $\rho \sim 1/r_0^2$ (dotted lines).

correspond to $s_\rho = 0, 1,$ and $2,$ respectively. Note that the bubble growth factors decrease with increasing density. Good agreement between the exact solution and the analytic scaling confirms the accuracy of the asymptotic analysis.

In summary, Layzer's model to study the nonlinear bubble evolution in classical RT instability has been extended to include the temporal density variation and spherical convergence effects. The bubble amplitude in planar geometry with the time-dependent density $\rho(t)$ was shown to asymptote to $\int^t U_L(t') \rho(t') dt' / \rho(t)$, where $U_L = \sqrt{g/C_g k}$ and $C_g = 3$ and $C_g = 1$ for two- and three-dimensional geometries, respectively. The model applied to the spherical geometry predicted the nonlinear bubble amplitude

$$\eta \sim \bar{\eta}(t) [m(t)/m_s]^{-|r_0|/\ell U_L^{\text{SP}} - \bar{\eta}/r_0},$$

where r_0 is the outer shell radius,

$$\bar{\eta}(t) = \int^t U_L^{\text{SP}}(t') \rho(t') r_0^2(t') dt' / \rho(t) r_0^2(t),$$

$$U_L^{\text{SP}}(t) = \sqrt{-\ddot{r}_0(t) r_0(t) / \ell},$$

$$m(t) = \rho(t) r_0^3(t),$$

$$m_s = m(t_s),$$

t_s is the saturation time, and ℓ is the mode number.

ACKNOWLEDGMENT

This work was supported by the U.S. Department of Energy Office of Inertial Confinement Fusion under Cooperative Agreement No. DE-FC52-92SF19460, the University of Rochester, and the New York State Energy Research and Development Authority. The support of DOE does not constitute an endorsement by DOE of the views expressed in this article.

REFERENCES

1. J. D. Lindl, *Inertial Confinement Fusion: The Quest for Ignition and Energy Gain Using Indirect Drive* (Springer-Verlag, New York, 1998); S. Atzeni and J. Meyer-ter-Vehn, *The Physics of Inertial Fusion: Beam Plasma Interaction, Hydrodynamics, Hot Dense Matter*, International Series of Monographs on Physics (Clarendon Press, Oxford, 2004).
2. B. A. Remington *et al.*, Phys. Plasmas **7**, 1641 (2000).

3. Lord Rayleigh, in *Scientific Papers* (Cambridge University Press, Cambridge, England, 1900), Vol. II, pp. 200–207.
4. D. Layzer, *Astrophys. J.* **122**, 1 (1955).
5. D. Oron *et al.*, *Phys. Plasmas* **8**, 2883 (2001); U. Alon *et al.*, *Phys. Rev. Lett.* **74**, 534 (1995); G. Dimonte, *Phys. Plasmas* **7**, 2255 (2000); G. Dimonte and M. Schneider *et al.*, *Phys. Fluids* **12**, 304 (2000).
6. G. Dimonte, *Phys. Rev. E* **69**, 056305 (2004); G. Dimonte *et al.*, *Phys. Fluids* **16**, 1668 (2004).
7. K. O. Mikaelian, *Phys. Rev. Lett.* **80**, 508 (1998); K. O. Mikaelian, *Phys. Rev. E* **67**, 026319 (2003).
8. Q. Zhang, *Phys. Rev. Lett.* **81**, 3391 (1998).
9. V. N. Goncharov, *Phys. Rev. Lett.* **88**, 134502 (2002).
10. Y. Yedwab *et al.*, presented at the 6th International Workshop on the Physics of Compressible Turbulent Mixing, Marseille, France, 18–21 June 1997, pp. 528–533.
11. D. Clark and M. Tabak, *Bull. Am. Phys. Soc* **49**, 281 (2004).
12. N. A. Inogamov and S. I. Abarzhi, *Physica D* **87**, 339 (1995); S. I. Abarzhi, *Phys. Rev. E* **59**, 1729 (1999).
13. G. Hazak, *Phys. Rev. Lett.* **76**, 4167 (1996); A. L. Velikovich and G. Dimonte, *Phys. Rev. Lett.* **76**, 3112 (1996).
14. G. I. Bell, Los Alamos National Laboratory, Los Alamos, NM, Report LA-1321 (1951).
15. V. N. Goncharov, P. McKenty, S. Skupsky, R. Betti, R. L. McCrory, and C. Cherfils-Clérouin, *Phys. Plasmas* **7**, 5118 (2000).
16. C. M. Bender and S. A. Orszag, *Advanced Mathematical Methods for Scientists and Engineers* (McGraw-Hill, New York, 1978), p. 484.
17. S. W. Haan, *Phys. Rev. A, Gen. Phys.* **39**, 5812 (1989).
18. R. Epstein, *Phys. Plasmas* **11**, 5114 (2004).
19. P. Amendt *et al.*, *Phys. Plasmas* **10**, 820 (2003).

High Density and High ρR Fuel Assembly for Fast-Ignition Inertial Confinement Fusion

Introduction

In direct-drive inertial confinement fusion,¹ a cryogenic shell of deuterium and tritium (DT) filled with DT gas is accelerated inward by direct laser irradiation (direct drive). The energy gain G is defined as the ratio between the thermonuclear energy yield and the laser energy on target. The gain is directly related to the capsule implosion velocity $G = (1/V_I^2)\eta_h \theta E_f/m_i$, where V_I is the implosion velocity, $\eta_h = E_K/E_L$ is the hydrodynamic efficiency representing the ratio between the shell kinetic energy and the laser energy on target, $E_f = 17.6$ MeV is the energy of the fusion products for a DT fusion reaction, and $m_i = 2.5 m_H$ is the average ion mass. The function θ represents the fraction of burned fuel depending on the fuel areal density $\rho R \equiv \int_0^R \rho dr$. The function $\theta = \theta(\rho R)$ is commonly approximated¹ by $\theta \simeq (1 + 7/\rho R)^{-1}$, where ρR is given in g/cm². If the driver energy is kept constant, higher implosion velocities require lower masses. In this case, the effect on the ρR of a lower mass balances the effect of higher velocity, thus making ρR independent of velocity. The hydrodynamic efficiency¹ depends on the ratio between the initial M_0 and final mass M_1 of the capsule; $\eta_h \propto (M_1/M_0)(\ln M_1/M_0)^2/(1 - M_1/M_0)$. The difference $M_a = M_0 - M_1$ is the ablated mass, and the approximation $\eta_h \propto (M_a/M_0)^{0.87}$ can be used for $M_a < 0.7 M_0$. The ablated mass is proportional to the ablation velocity V_a , the in-flight shell density ρ_{if} , the implosion time t_b , and the ablation surface area $\sim R^2$; $[M_a \sim \rho_{if} V_a R^2 t_b]$. By setting $M_0 \sim \rho_{if} R^2 \Delta_{if}$ (Δ_{if} is the in-flight thickness) and by using the well-known scaling relation¹ $V_a \sim \alpha_{if}^{3/5} I_L^{-1/5}$, where α_{if} is the in-flight adiabat and I_L is the laser intensity, one can easily rewrite $(M_a/M_0) \sim \alpha_{if}^{3/5} A_{if}/V_I I_L^{1/15}$, where A_{if} is the in-flight aspect ratio and the relation $t_b \sim R/V_I$ has been used. Since the aspect ratio¹ scales as $A_{if} \sim M_{if}^2$ (where M_{if} is the in-flight Mach number), the final scaling of the hydro-efficiency can be easily derived by substituting $\rho_{if} \sim (p_{if}/\alpha_{if})^{3/5}$ into the Mach number, and¹ $p_{if} \sim P_L \sim I_L^{2/3}$, where P_L is the laser-driven ablation pressure. A straightforward manipulation yields $\eta_h \sim V_I^{0.87} I_L^{-0.29}$, which compares favorably with a numerical fit obtained from 1-D hydrodynamic simulations

$$\eta_h^{\text{fit}} \approx \frac{0.049}{I_{15}^{0.25}} \left[\frac{V_I (\text{cm/s})}{3 \times 10^7} \right]^{0.75}, \quad (1)$$

where I_{15} is the laser intensity in 10^{15} W/cm². The simulations are for ten direct-drive cryogenic targets with laser energies varying from 25 kJ to 1.5 MJ and are carried out using the 1-D code *LILAC*.² The targets used in the simulations are either all DT ice or wetted-foam CH(DT)₆ capsules with a 2- μ m CH overcoat. Substituting the hydro-efficiency into the gain formula yields a thermonuclear gain that increases for the lower implosion velocities

$$G \approx \frac{73}{I_{15}^{0.25}} \left[\frac{3 \times 10^7}{V_I (\text{cm/s})} \right]^{1.25} \left(\frac{\theta}{0.2} \right). \quad (2)$$

Equation (2) shows that, if ignited, slow targets yield high gains. The energy required for ignition from a central hot spot, however, increases rapidly as the velocity decreases³ ($E_{\text{ign}}^{\text{hot-spot}} \sim V_I^{-6}$). This is because the hot-spot temperature increases with the velocity. Since the fusion cross section is a strong function of the temperature, slow targets have a relatively cold hot spot and therefore require greater energy for ignition. If the implosion velocity is below 2×10^7 cm/s, the hot spot cannot be ignited regardless of the shell energy since the radiation losses dominate the hot-spot energy balance. However, such slow targets can be optimal for fast ignition (FI) since the hot-spot size and energy decreases with the implosion velocity.

In fast ignition,⁴ a relatively cold, high-density, and high-areal-density assembly of thermonuclear fuel is ignited by the external heating of a small volume of the dense fuel. The external heating is provided by fast electrons accelerated by the interaction of an ultra-intense petawatt ($= 10^{15}$ W) laser pulse with either the coronal plasma or a solid target. The fast electrons slow down in the cold, dense fuel and release their kinetic energy through collisions with the electrons.

The electron range is measured in terms of the fuel areal density that, for a 1-MeV electron beam,⁵ is about 0.4 to 0.6 g/cm². The igniter beam energy required for fast ignition increases inversely to the fuel density.⁶ According to Ref. 6, the 1-MeV e-beam ignition energy follows the simple formula $E_{\text{ign}}^{\text{fast}} = 11(400/\rho_f)^{1.85}$, where ρ_f is the dense fuel density in g/cc. In order to keep the petawatt laser energy in the range of a few tens of kilojoules, the thermonuclear fuel density needs to exceed the value of about 300 g/cc. However, higher densities require higher beam intensities and a smaller beam radius;⁶ $r_b(\mu\text{m}) \simeq 15(400/\rho_f)$. Because of the difficulties in focusing the electron beam at radii less than 10 μm , fuel densities within the 300 to 500 g/cc range are desirable. In addition to the density range, fast ignition requires that the volume of the hot spot be much smaller than the dense core volume to reduce the thermal energy of the hot spot in favor of the internal energy of the compressed fuel. Furthermore, a small-size hot spot limits the detrimental effects of the central low-density plasma on the burn wave propagation that starts in the dense volume. Other fuel-assembly requirements come from the specific applications of FI. For inertial fusion energy (IFE) applications, the thermonuclear gain must be greater than 100 and the areal density must be at least 2.5 to 3 g/cm². Here we show that a fuel assembly meeting all these requirements can be produced with a direct-drive laser facility in the 700 kJ range, about half the size of the National Ignition Facility⁷ and significantly smaller than the multimegajoule drivers required for direct-drive IFE based on hot-spot ignition.

Scaling Laws for Density, Areal Density, and Stagnation Aspect Ratio

We start our analysis by deriving a scaling law for the shell density, areal density, and hot-spot size as a function of characteristic implosion parameters such as shell energy, implosion velocity, and in-flight adiabat. By indicating with Δ_s the stagnating shell thickness, with R_h the hot-spot radius and M_s the shell mass, the compressed shell areal density scales as

$$\rho_s \Delta_s \sim M_s / R_h^2 \Sigma(A_s) \sim E_K / R_h^2 V_I^2 \Sigma(A_s),$$

where E_K is the shell kinetic energy at the end of the acceleration phase, $A_s = R_h / \Delta_s$ is the stagnation aspect ratio, and $\Sigma(x) = 1 + 1/x + 1/3x^2$ is a volume factor. The hot-spot radius R_h can be derived by setting the total shell internal energy at stagnation equal to the shell kinetic energy $E_K \sim p_s (R_h + \Delta_s)^3$, where the stagnation pressure p_s has been assumed to be approximately uniform through the hot spot and shell. This energy conversion condition (from kinetic to internal) can be rewritten by setting $p_s \sim \alpha_s \rho_s^{5/3}$, where α_s is

the stagnation adiabat that is related⁸ to the in-flight adiabat α_{if} through the in-flight Mach number $\alpha_s \sim \alpha_{\text{if}} M_{\text{if}}^{2/3}$, leading to $\alpha_s \sim \alpha_{\text{if}}^{0.8} V_I^{0.67} / P_L^{0.13}$. It follows that the shell density and the shell areal density can be rewritten as

$$\rho_s \Delta_s \sim \Phi(A_s) E_K^{0.33} V_I^{0.67} I_L^{0.09} \alpha_{\text{if}}^{-0.8} \quad (3)$$

and

$$\rho_s \sim \Psi(A_s) V_I^{0.13} I_L^{0.13} \alpha_{\text{if}}^{-1.2}, \quad (4)$$

where

$$\Phi(x) \equiv (x^2 + x + 1/3)^{2/3} / (1+x)^3$$

and

$$\Psi(x) = [\Phi(x)(1+x)]^{9/4}.$$

Though the stagnation aspect ratio is of order unity, it is important to accurately determine its functional dependency on the implosion parameters. For reasonable values of the stagnation aspect ratio ranging between $1 < A_s < 4$, Φ and Ψ can be approximated with a power law as $\Phi(A_s) \sim 1/A_s^{0.92}$ and $\Psi(A_s) \sim 1/A_s^{0.62}$. A_s grows with the implosion velocity since the mass decreases for a fixed energy leading to smaller Δ_s , while R_h depends mostly on energy. In order to determine an accurate dependence on the velocity, we fit the results of the simulations where R_h is defined as the point of maximum shell density, and Δ_s is the distance between R_h and the return shock at the time of peak areal density. The simulations show a clear dependence on the velocity and almost no dependence on energy and adiabat leading to

$$A_s^{\text{fit}} \approx 2.1 \left[\frac{V_I (\text{cm/s})}{3 \times 10^7} \right]^{0.96}, \quad (5)$$

as shown in Fig. 103.1. Substituting Eq. (5) into (3) and (4) yields scaling laws for the density and areal density

$$\rho_s \Delta_s \sim E_L^{0.33} V_I^{0.03} \alpha_{\text{if}}^{-0.8}, \quad \rho_s \sim V_I^{1.4} I_L^{0.13} \alpha_{\text{if}}^{-1.2}, \quad (6)$$

where the hydro-efficiency from Eq. (1) has been used. These semi-analytical scaling laws compare favorably with the numerical fits of the peak values of the densities and areal densities

$$(\rho R)_{\max}^{\text{fit}} \approx \frac{1.3}{\alpha_{\text{if}}^{0.55}} \left[\frac{E_L \text{ (kJ)}}{100} \right]^{0.33} \left[\frac{V_I \text{ (cm/s)}}{3 \times 10^7} \right]^{0.06} \quad (7)$$

and

$$\rho_{\max}^{\text{fit}} \approx \frac{788}{\alpha_{\text{if}}} I_{15}^{0.13} \left[\frac{V_I \text{ (cm/s)}}{3 \times 10^7} \right], \quad (8)$$

where the subscript max indicates the maximum values during the implosion and ρR and ρ_{\max} are in g/cm^2 and g/cc , respectively. The laser-intensity scaling in (8) is analytical from (6) since the intensity varies only within a $\pm 15\%$ range in the simulation, and it does not represent a good scaling parameter. Note the density scaling is somewhat different from the indirect-drive scaling shown in Ref. 9. The areal density in Eq. (7) includes the inner portion of the shell that has been compressed by the return shock as well as the surrounding portion that has not been shocked. Typically, the unshocked portion has significantly lower density and lower ρR with respect to the shocked portion (see Fig. 103.4 on p. 121). In a $\rho R \sim 3 \text{ g/cm}^2$ implosion, however, a 20% fraction of unshocked ρR can stop energetic electrons at lower densities (with $\rho < 300 \text{ g/cc}$), preventing them from reaching the dense shocked core. The presence of the unshocked areal density has important consequences on the choice of the fast-ignition time. If the fast electrons have 1-MeV energy, then the fast-ignition time is when the unshocked areal

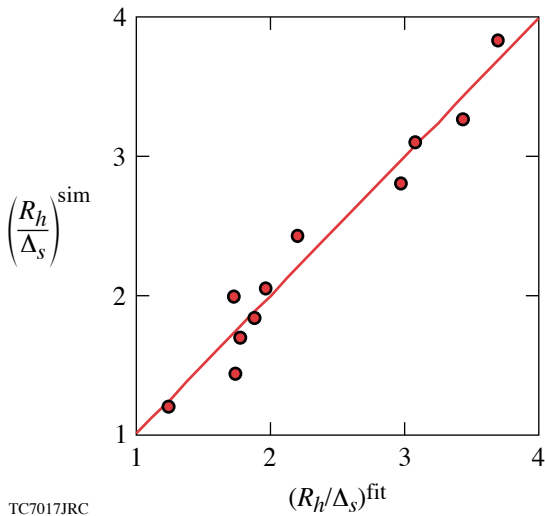
ρR is significantly less than 0.6 g/cm^2 , which occurs after the time of peak ρR . This constraint is relaxed as the fast-electron energy exceeds 1 MeV. Note that Eq. (8) represents the maximum density. The time of peak ρR occurs after the time of peak density, and the average density at the time of peak ρR is slightly below 80% of Eq. (8). If fast ignition is triggered at or soon after the time of peak ρR , the corresponding average density is significantly below its maximum value.

Laser Pulse Shaping

Other important considerations in optimizing fast-ignition targets concern the pulse length and laser power contrast ratio. It is clear from Eqs. (7) and (8) that low adiabat implosions lead to high densities and areal densities. However, very low adiabat implosions require long pulse lengths and careful pulse shaping. The long pulse length is because of the slow velocity of the low-adiabat shocks, and the careful shaping is required to prevent spurious shocks from changing the desired adiabat. Furthermore, the ratio between the peak power and the power in the foot of the laser pulse (i.e., the power contrast ratio) increases as the adiabat decreases thus leading to difficult technical issues in calibrating the pulse shape. These constraints on the pulse shape are relaxed by using the relaxation (RX) laser pulse technique.¹⁰ The relaxation pulse consists of a prepulse followed by an interval of laser shutoff and the main pulse. The RX pulse induces an adiabat profile that is monotonically decreasing from the ablation surface to the inner shell surface. In addition to improving the hydrodynamic stability of the implosions, the RX main pulse is shorter and requires a lower contrast ratio than the equivalent flat adiabat pulse with the same inner surface adiabat.

High-Gain Fast-Ignition Capsule Design

By using the results in Eqs. (5), (7), and (8), a high-gain fast-ignition capsule can be designed. We start by setting a low value for the inner-surface adiabat $\alpha_{\text{if}}^{\text{min}} \approx 0.7$. An adiabat below unity implies that, at shock breakout, the inner portion of the shell is not fully ionized. In order to achieve a $\rho R \approx 3 \text{ g/cm}^2$, Eq. (7) yields a laser energy $E_L \approx 750 \text{ kJ}$ [the velocity term in Eq. (7) has been ignored because of the low power index]. Equation (8) is then used to determine the velocity required to obtain a peak density of 640 g/cc that corresponds to an average density of the shocked shell at the time of peak ρR of $\langle \rho \rangle \approx 0.8 \rho_{\max} \approx 500 \text{ g/cc}$. The corresponding velocity from (8) is $V_I = 1.7 \times 10^7 \text{ cm/s}$, leading to a hot-spot aspect ratio [Eq. (5)] of $A_s \sim 1$. Since the required laser energy of 750 kJ is approximately half the NIF energy, we use a reference driver with half the energy and half the power of the NIF. For a peak power of 220 TW, the outer shell radius is chosen to keep the



TC7017JRC

Figure 103.1
Hot-spot aspect ratio from simulation compared with numerical fit (9).

peak intensity at 10^{15} W/cm², thus leading to $R_{\text{out}} \approx 1.3$ mm. The target mass at stagnation is derived from the kinetic energy $M_s \approx 2E_K/V_I^2$, with $E_K \approx \eta_h E_L$. Using Eq. (1) for η_h and $E_L = 750$ kJ, $V_I \approx 1.7 \times 10^7$ cm/s yields a stagnation mass of $M_s \approx 1.7$ mg. Assuming that $\sim 20\%$ of the mass is ablated leads to an initial mass of about $M_0 \approx 2$ mg. In order to improve the laser energy absorption, we consider a wetted-foam target with an inner ice layer, an outer wetted-foam CH(DT)₆ layer, and a 2- μm CH overcoat. Given the low density of the foam and the small thickness of the overcoat, we can assume that the average density is the same as DT ice, $\rho_0 \approx 0.25$ g/cc, and determine the inner-shell radius from the volume $\sim M_0/\rho_0$ and the outer radius leading to $R_{\text{inn}} \approx 660$ μm . Figure 103.2 shows the FI target with a foam layer thickness that is large enough to reabsorb the coronal radiation and reduce the radiation heating of the inner ice layer. It is important to notice that the large shell thickness combined with the slow implosion velocity makes the target performance insensitive to the hydrodynamic instabilities and 1-D codes suitable for realistic simulations of the implosion. The 750-kJ RX pulse is shown in Fig. 103.3. The main foot-pulse length is about 22 ns, and the power contrast ratio is about 150. Those pulse characteristics are not far from the NIF indirect-drive pulse requirements with a pulse length of ~ 18 ns and a contrast ratio of ~ 100 . A LILAC simulation of the 750-kJ implosion yields the exact desired implosion parameters. Sub-

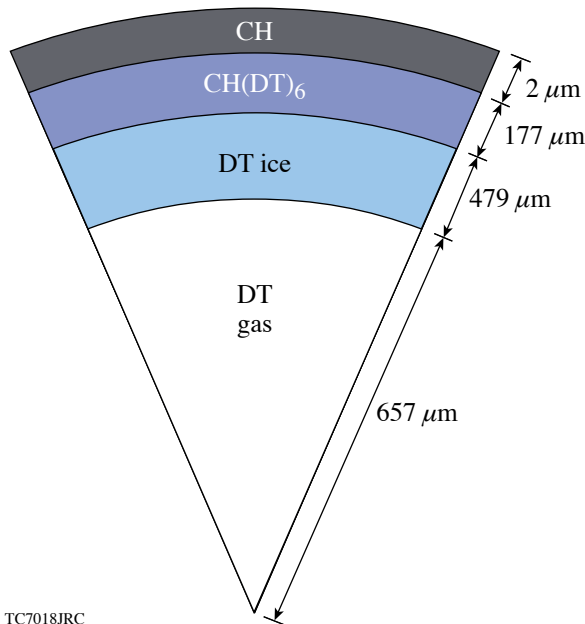


Figure 103.2
 Fast-ignition IFE target.

stituting the implosion parameters into the gain formula (1) yields a thermonuclear gain of about $G = 220/(1 + E_{\text{PW}}/750)$, where E_{PW} is the petawatt laser energy required for ignition in kilojoules. This is probably an optimistic assessment since it assumes that the peak value of the areal density is available at the time of ignition. Figure 103.4 shows the density profiles versus the areal density at different times about the peak ρR time. The sharp drops in density shown in Fig. 103.4 correspond to the return shock traveling outward from the center. Notice that the density varies significantly while the total ρR remains above 2.5 g/cm². Ignition can therefore be triggered at an average density varying from 300 to 550 g/cc without significant changes to the target gain. It is important to observe that the areal density of the low-density unshocked portion of the shell is significant and decreases with time from 0.9 g/cm² at time of $\rho R = 3$ g/cm² to 0.3 g/cm² at the time $\rho R = 2.5$ g/cm². This implies that the electron energy in the fast-ignitor beam needs to exceed 1 MeV to allow the electron penetration into the high-density core. The density versus volume plots in Fig. 103.5 indicate that the hot-spot volume is less than 10% of dense core during hundreds of picoseconds about the time of peak ρR . Notice that at 27.5 ns, the density is about 300 g/cc, and its profile is approximately uniform. The “hot-spot” volume is small, and values below $\rho < 300$ g/cc are confined within a tiny region occupying only 6%–7% of the core.

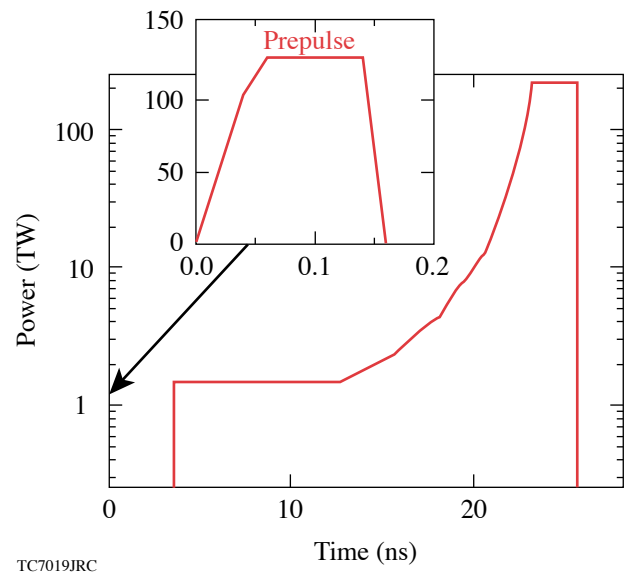
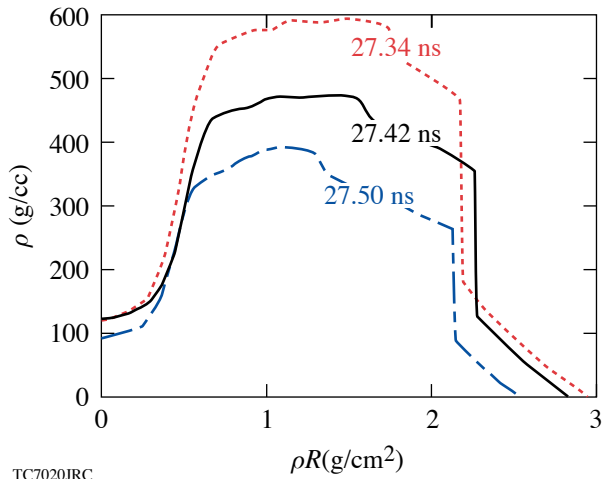
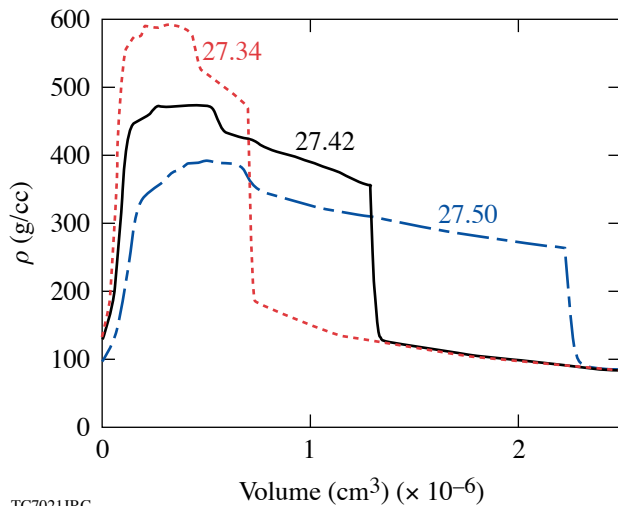


Figure 103.3
 750 kJ, $\alpha = 0.7$ relaxation laser pulse.



TC7020JRC

Figure 103.4
Density profiles versus areal density at three times about the time of peak areal density.



TC7021JRC

Figure 103.5
Density profiles versus volume at three times about the time of peak areal density.

ACKNOWLEDGMENT

This work has been supported by the US Department of Energy under Cooperative Agreement DE-FC02-04-ER54789 and DE-FC52-92SF19460, the University of Rochester, and the New York State Energy Research and Development Authority. The support of DOE does not constitute an endorsement by DOE of the views expressed in this article.

REFERENCES

1. S. Atzeni and J. Mer-ter-Vehn, *The Physics of Inertial Fusion: Beam Plasma Interaction, Hydrodynamics, Hot Dense Matter*, International Series of Monographs on Physics (Clarendon Press, Oxford, 2004); J. D. Lindl, *Inertial Confinement Fusion: The Quest for Ignition and Energy Gain Using Indirect Drive* (Springer-Verlag, New York, 1998).
2. J. Delettrez and E. B. Goldman, Laboratory for Laser Energetics Report No. 36, University of Rochester (1976).
3. M. C. Herrmann, M. Tabak, and J. D. Lindl, *Nucl. Fusion* **41**, 99 (2001).
4. M. Tabak *et al.*, *Phys. Plasmas* **1**, 1626 (1994).
5. C. Deutsch *et al.*, *Phys. Rev. Lett.* **77**, 2483 (1996); **85**, 1140(E) (2000); C. K. Li and R. D. Petrasso, *Phys. Rev. E* **70**, 067401 (2004).
6. S. Atzeni, *Phys. Plasmas* **6**, 3316 (1999).
7. E. M. Campbell and W. J. Hogan, *Plasma Phys. Control. Fusion* **41**, B39 (1999).
8. R. Betti, K. Anderson, V. N. Goncharov, R. L. McCrory, D. D. Meyerhofer, S. Skupsky, and R. P. J. Town, *Phys. Plasmas* **9**, 2277 (2002).
9. S. A. Slutz and M. C. Herrmann, *Phys. Plasmas* **10**, 234 (2003).
10. R. Betti, K. Anderson, J. Knauer, T. J. B. Collins, R. L. McCrory, P. W. McKenty, and S. Skupsky, *Phys. Plasmas* **12**, 042703 (2005).

Direct-Drive Fuel-Assembly Experiments with Gas-Filled, Cone-in-Shell, Fast-Ignition Targets on the OMEGA Laser

Introduction

The fast-ignition concept for inertial confinement fusion^{1,2} has the potential for higher gains and lower driver energies than central hot-spot ignition.³ The fast-ignition concept separates the fuel assembly and heating by using an ultrafast laser. The ultrafast laser produces relativistic electrons with high efficiency (up to 50% has been reported⁴) that heat the fuel, significantly easing the requirements on the compression driver.^{2,5} Laser or heavy-ion beam-heated hohlraums or direct-drive laser are options for the compression driver.

The biggest challenge of the fast-ignition concept is the transport of the relativistic electrons from the critical-density region ($n_e \sim 10^{21} \text{ cm}^{-3}$ for a typical 1- μm laser), where the ultrafast laser is absorbed and converted into electrons, to the compressed fuel—a distance that can be hundreds of microns in an ignition-scale target. For an electron beam divergence of $>20^\circ$, the overlap between the electron beam originating from a small focal spot ($\sim 10\text{-}\mu\text{m}$ radius) and the dense core with a diameter of $<50 \mu\text{m}$ would be very small.^{6,7} Most of the energy in the electron beam would be wasted. Two solutions have been proposed to minimize this standoff distance: a channeling beam to bore a hole in the plasma atmosphere around the core^{2,8} that allows the ultrafast laser to be absorbed closer to the core and a re-entrant cone to keep the path of the ultrafast laser free of plasma and bring it as close as possible to the dense core.^{9–11}

A few experiments have been performed to assess the potential of the re-entrant-cone concept. Integrated experiments at ILE-Osaka examined the coupling between the electron beam and the compressed core and found a 20%–30% energy transfer.^{11,12} A thousand-fold increase in neutron yield from 10^4 to 10^7 was observed by coupling a 0.5-PW, short-pulse laser into an empty CD target imploded by 2.5 kJ of laser light at a wavelength of 0.53 μm . A first series of hydro experiments¹³ with re-entrant cone targets in indirect-drive geometry on OMEGA studied the fuel assembly with 1 kJ of x-ray energy coupled to the capsule. Significant mixing between the gold cone and plastic shell material was observed. Mixing gold

into the dense fuel/shell material substantially increases the required ignition energy. Stephens *et al.* predicted that using direct drive would minimize the mixing between the gold cone and the fuel/shell material.¹³ Plasma filling the inside of the cone where the ultrafast laser has to propagate is another issue for cone targets. The high-pressure core plasma sends a shock wave through the gold cone that creates a plasma inside the cone when it breaks out, significantly increasing the electron propagation distance.

Fuel-assembly experiments with gas-filled, direct-drive, re-entrant cone-in-shell targets were performed on the OMEGA Laser System¹⁴ to study whether the cone-in-shell design is scalable to higher-energy densities and in preparation for future integrated experiments on the OMEGA EP laser,^{15,16} which will be operational in 2007. The experimental setup is described in the next section, which includes the laser configuration and imaging diagnostic arrangement. **Fuel Assembly in 35° and 70° Cone Targets** (p. 123) discusses backlighting of the fuel assembly of 35° and 70° cone targets. **Mixing of Au Cone and Core Material** (p. 124) reports an analysis of the mixing of cone and shell material, and **Compressed Core Areal Density Measurements** (p. 125) describes areal-density measurements using nuclear diagnostic methods. **Cone Filling** (p. 125) shows measurements of the shock breakout into the inside of the cone. Conclusions are presented in the last section, which also describes prospects for integrated experiments using the OMEGA EP laser.

Experimental Setup

Several different laser configurations were used for the direct-drive, cone-in-shell experiments on the 60-beam OMEGA laser. The targets were illuminated at a wavelength of 351 nm with a 1-ns square pulse and an energy of ~ 400 J per beam using two-dimensional smoothing by spectral dispersion (SSD)¹⁷ with 1-THz bandwidth in the UV and polarization smoothing (PS).¹⁸ The beams driving the shell used distributed phase plates (DPP).¹⁹ For the backlighting experiments, 15 beams ($\sim 6\text{-kJ}$ energy) were diverted to a backlighter foil of either vanadium (V) or iron (Fe) and focused to a spot size of

600 μm without DPP's. To provide a nearly uniform illumination of the shell, 15 beams were run at half energy and 20 beams at full energy, a total of ~ 11 kJ of laser energy driving the implosion. The nuclear diagnostics experiments used 55 beams, with ~ 21 kJ of total energy. The cone-filling experiments used 48 beams for the 70° cones or 54 beams for the 35° cones to avoid the laser hitting the inside of the cones.

The targets consist of gas-tight, $\sim 870\text{-}\mu\text{m}$ outer diameter, $24\text{-}\mu\text{m}$ -thick CH shells with a hollow gold cone with an opening angle of 35° or 70° inserted through a hole in the shell (see Fig. 103.6). The distance between the cone tip and the center of the shell, typically $30 \pm 10 \mu\text{m}$, is defined by a shelf on the cone that provides a gas-tight interface for the assembly. Both the 70° and 35° gold cones had a thickness of roughly $100 \mu\text{m}$ outside the shell, approximately $10 \mu\text{m}$ inside the shell, and end in a hyperbolic-shaped tip with its asymptotes intersecting $12 \mu\text{m}$ from the target center resulting in an Au thickness of $\sim 30 \mu\text{m}$ at the tip of the cone. Time-resolved x-ray framing cameras²⁰ recorded both backlit and self-emission images. The backlighter framing camera had an exposure time of ~ 40 ps and the self-emission camera ~ 80 ps. The framing cameras acquired 16 images with an ~ 60 ps temporal separation between exposures. Both cameras used a pinhole imager with a spatial resolution of $\sim 10 \mu\text{m}$ in the target plane. The self-emission camera was filtered with $\sim 200 \mu\text{m}$ of beryllium, with a lower cutoff at 50% transmission of ~ 3 keV. The backlighter camera used either a $25\text{-}\mu\text{m}$ -thick V filter to pass the predominantly He_α line

emission of the V backlighter at 4.95 keV or a $25\text{-}\mu\text{m}$ -thick Fe filter for the He_α line emission of a Fe backlighter at 6.7 keV. These filters suppress the thermal radiation from the implosion, improving the contrast of the backlit images.

Fuel Assembly in 35° and 70° Cone Targets

A comparison of the fuel assembly between 35° and 70° cone targets is shown in Fig. 103.7. Backlit images from unfilled 35° [Fig. 103.7(a)] and 70° [Fig. 103.7(b)] targets were recorded using a Fe backlighter. Three images spaced ~ 250 ps apart

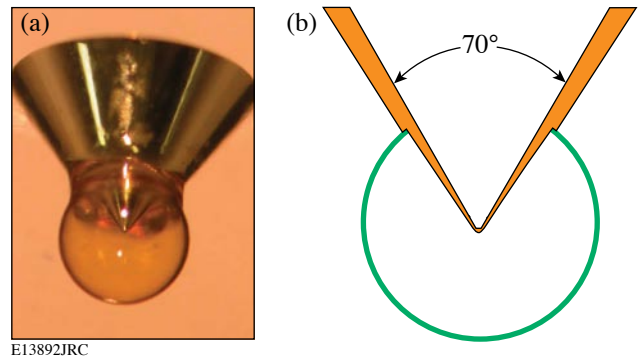


Figure 103.6
Picture of a gas-tight, fast-ignition cone target (a) and a schematic of its cross section (b). A gold cone with an opening angle of 70° is inserted through a hole in a $24\text{-}\mu\text{m}$ -thick CH shell of $\sim 870\text{-}\mu\text{m}$ outer diameter.

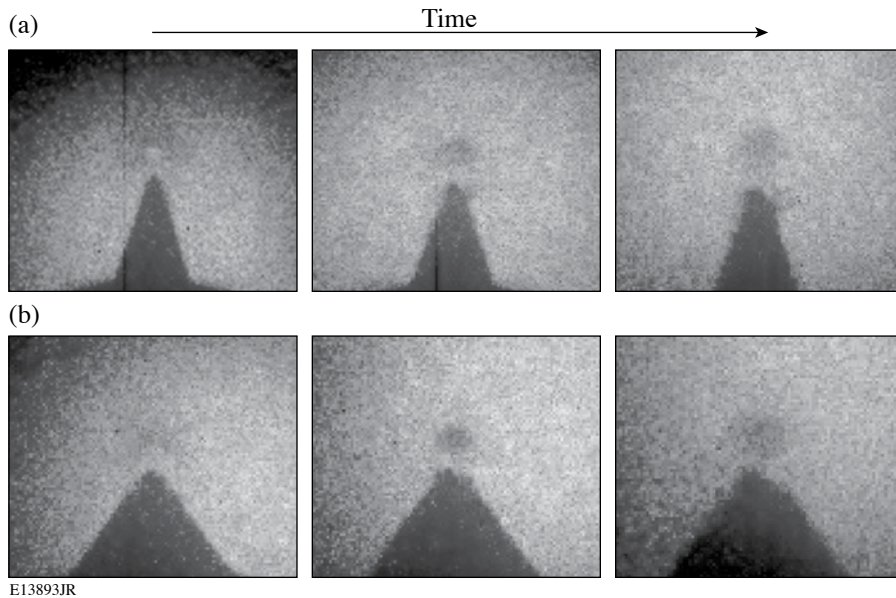


Figure 103.7
Backlit framing camera images from a 35° cone target (a) and a 70° target (b) using a Fe backlighter. Three images spaced ~ 250 ps apart show the assembly of the core and the erosion of the cone, with the central image close to the time of peak compression.

show the assembly of the core, with the central image close to the time of peak compression. The core assembly is similar in both cases, particularly the evolution of the core size. At early times, a horseshoe-shaped dense area is observed, with the opening toward the cone as expected. At peak compression, the core looks quite round and symmetric, with no influence of the cone visible. After peak compression, the core expands in an almost symmetric fashion. Both targets exhaust plasma toward the tip of the cone, eroding the tip at later times. The 35° targets shows less backlighter absorption in the core than the 70° cone targets, possibly due to the incomplete suppression of the core self-emission since the narrow cones are expected to disturb the implosion less and lead to higher core temperatures. The images also show that the plasma flow is directed from the core toward the tip of the cone, an indication that mixing gold and core material is not significant in these implosions.

Mixing of Au Cone and Core Material

Unfilled capsules were used to evaluate the mixing of the gold cone with the CH shell material to compare with previous indirect-drive experiments.¹³ Figure 103.8 shows a backlit image using a V backlighter (a) and a self-emission image (b) taken at the time of peak compression. The backlit image shows absorption outside the original extent of the cone, as indicated by the dashed lines, showing that an expanding plasma is created on the surface of the cone. A gap between the cone tip and core assembly is seen in both images, unlike the data obtained using indirect drive.¹³ The indirect-drive data were interpreted as a 0.04% mass density gold contamination in the compressed shell material. No signatures of mixing were observed in direct drive data; therefore, only an estimate of the minimum detectable gold contamination can be obtained from the analysis of the self-emission images. Figure 103.8(c) shows a lineout through the center of the self-emission image. A Gaussian fit of the core emission shows a symmetric core, with no indication of extra emission because of Au mixing into the core from the cone. At high temperatures (>1 keV) and moderate densities (<1 g/cm³), the plasma conditions expected in the gap, the CH emissivity at 2 to 4 keV is roughly 2,000× smaller than the Au opacity. Consequently, a gold contamination of the order of 0.01% of the mass density in the gap would be visible as an ~10% enhancement of the emission, the estimated error of the symmetry of the emission profile. The x-ray emission from shell plasma in the gap between cone and core reduces the absorption minimum seen in the backlit image. This can be corrected using the self-emission images that show that the emission intensity in the gap is about 1/3 of the emission at the center of the collapsed shell. An analysis of corrected backlit images analogous to the self-emission images using the cold Au

and the hot CH opacities shows no indication of gold plasma streaming into the core with a detection threshold of roughly 0.01% of the mass density.

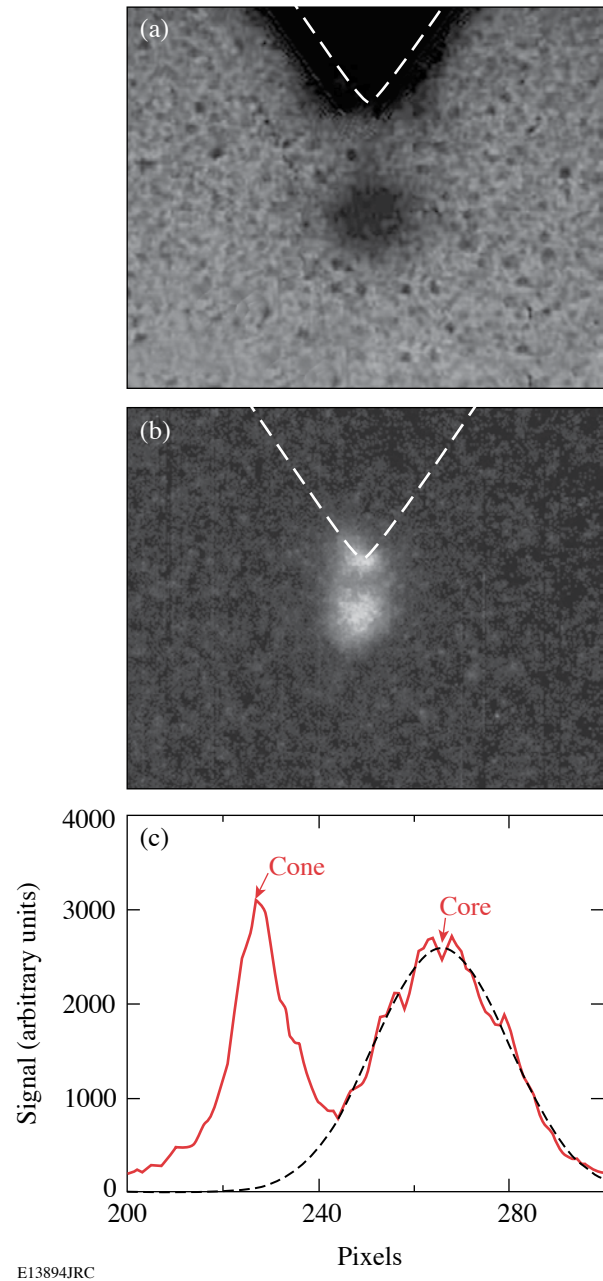


Figure 103.8

(a) Backlit and (b) self-emission x-ray framing camera images of unfilled cone targets obtained using pinhole imaging taken at peak compression. The extent of the cone before the laser shot is indicated with dashed lines. A lineout through the self-emission image is shown in (c).

Compressed Core Areal Density Measurements

The areal density of the assembled core was determined from experiments with targets filled with D^3He gas using nuclear diagnostics. Because of the strong He x-ray emission, the size and location of the hot-fuel region can be inferred from x-ray images of D^3He -filled targets. Figure 103.9(a) shows a backlit x-ray image of a 70° cone target filled with 10-atm D^3He at the time of peak proton production using a Fe backlighter at 6.7 keV. Wedged-range-filter spectrometers²¹ are used to infer the areal density of the compressed shell^{22,23} from the energy loss of the 14.7-MeV primary fusion protons. The proton spectrometers are deployed in two different directions

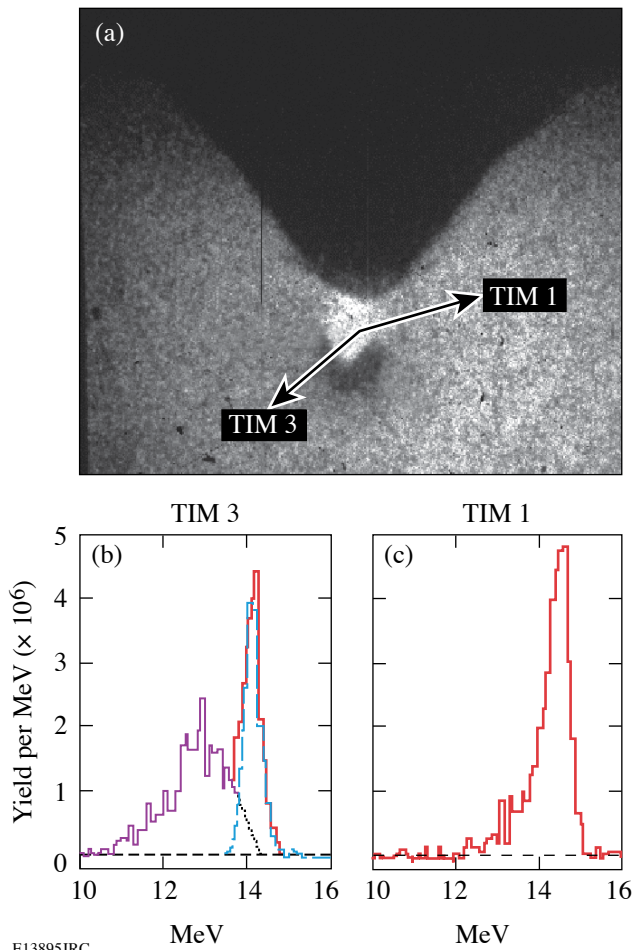


Figure 103.9 Backlit image (a) of a 10-atm, D^3He -filled cone target at time of peak proton production using a Fe backlighter. Significant self-emission from the hot D^3He gas is seen in the image. The directions of the proton spectrometers used to determine the core areal density are indicated as TIM1 and TIM3. D^3He proton spectra taken along two different lines of sight: TIM3 (b) and TIM1 (c).

~15 cm from the target. Figure 103.9(a) shows the line of sight of the two proton spectrometers (labeled TIM1 and TIM3). Figure 103.9 also shows the proton spectra from three 35° cone targets imploded with 55 beams at 21 kJ with a total a proton yield ($\sim 3 \times 10^6$) integrated onto the wedged-range filters in TIM3 (b) and TIM1 (c). Two peaks are observed in the TIM3 spectrum, because the protons detected in TIM3 pass through the dense core (see Fig. 103.9). The narrow peak at ~ 14 MeV is attributed to the shock coalescence phase of the implosion, when the assembled areal density is low.²³ The second, broader peak at ~ 12 MeV is due to protons passing through the dense core close to peak compression.²³ An areal density of $\sim 70 \pm 5$ mg/cm² is inferred from the average energy downshift of ~ 2 MeV (Ref. 21). The protons detected on the TIM2 detector from both the shock and compression phases experience little energy loss and produce only a single narrow peak. The proton yields from the 70° cone targets were about a factor of 2 lower than the yields recorded from the 35° cone targets and showed marginally lower areal densities of $\sim 60 \pm 10$ mg/cm². A fuel ion temperature of 1.2 ± 0.4 keV was inferred from the ratio of the D^3He proton and the DD neutron yields.²²

The experimental areal density values were compared to simulations of full-sphere (no cone) implosions using the 1-D hydrocode *LILAC*.²⁴ *LILAC* predicts a total areal density (shell and fuel) of ~ 90 mg/cm² at the time of peak proton emission for a $24\text{-}\mu\text{m}$ -thick full spherical shell with an average ion temperature of 2.3 keV and a total proton yield of 3×10^8 . The experimental areal density values are more than 66% of the predicted values in both cases. The measured ion temperature is much lower and the measured proton yield is almost three orders of magnitude lower than the simulation yield, showing that the presence of the cone reduces the central hot-spot temperature. Breaking the spherical symmetry by introducing a cone in the shell affects the ion temperature and consequently the proton yield much more than the fuel assembly and the core areal density. Reducing the cone angle from 70° to 35° has a small effect on the areal density. It improves the yield by a factor of 2, though it is still very far from the 1-D predictions.

Cone Filling

The filling of the inside of the cones was investigated using a streaked optical pyrometer (SOP)²⁵ (see Fig. 103.10). The SOP optical system images the inside of the tip of the cone onto the slit of the streak camera with an $\sim 10\text{-}\mu\text{m}$ spatial resolution and a $500\text{-}\mu\text{m}$ field of view. The camera is filtered to record in a wavelength band centered at 660 nm with a 140-nm FWHM to minimize the background from scattered 3ω , 2ω , and 1ω laser light. The breakout of the shock produces a short burst of light.

Its timing relative to peak compression can be determined from the absolute temporal calibration of the SOP with an uncertainty of 50 ps. The shock temperature is inferred from the observed light signal using the absolute calibration of the SOP in intensity with an uncertainty of 10% above ~1 eV (Ref. 26). The number of laser beams used to drive the target is limited to prevent laser light from hitting the inside of the cone and produce a high background signal on the SOP. Figure 103.11(a) shows the SOP streak signal from a 70° cone target irradiated by 48 OMEGA beams with a total energy of ~18 kJ in a 1-ns square pulse. The time axis zero represents the start of the laser pulse. A very clean shock-breakout signal can be seen starting at the tip of the cone and becoming less intense and moving away from the tip as time progresses. Figure 103.11(b) shows a lineout through the center of the SOP trace in comparison with 1-D hydrocode simulations from *LILAC* of the total areal density of the compressed core for a spherical target. The 70° cone targets show a clean shock-breakout signal, similar to data seen in planar shock experiments.²⁷ The shock signal starts well after the time of peak compression (~500 ps) as calculated by *LILAC*, showing that the inside of the cone is free of plasma at the time when the short-pulse laser would propagate. An estimated shock temperature of ~10 eV is obtained using the absolute intensity calibration of SOP.

Conclusions

Fuel-assembly experiments with laser-irradiated, cone-in-shell targets performed on OMEGA indicate that this fast-ignition concept is likely to be scalable to higher energy cryogenic targets. No significant mixing of the gold from the cone with the fuel/shell material was observed, unlike the earlier results seen in the indirect-drive experiments. The core assembly is not severely affected by the presence of the cone, and more than 66% of the expected areal density is inferred from the experiments. Shock-breakout plasma does not begin filling the inside of the cone before peak compression when the ultrafast laser propagates.

In a cryogenic DT ignition capsule, the final core density will be higher, but the core pressure will be similar because of the lower average ionization of the DT compared to CH and the lower-drive adiabat.²⁸ This limits the strength and speed of the shock that causes the inside of the cone to fill with plasma and the erosion of the cone by the core plasma. The thin plastic shell containing the cryogenic fuel radiates much less in cryogenic implosions, reducing the heating and expansion of the gold cone at early times, which minimizes the amount of Au that can mix with the fuel.

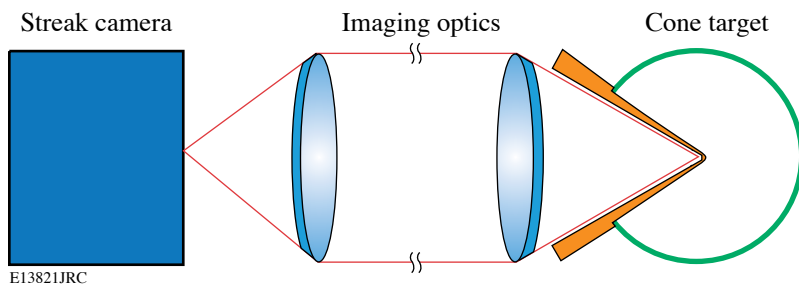


Figure 103.10 Streaked optical pyrometry (SOP) setup used to investigate the filling of the inside of the cone.

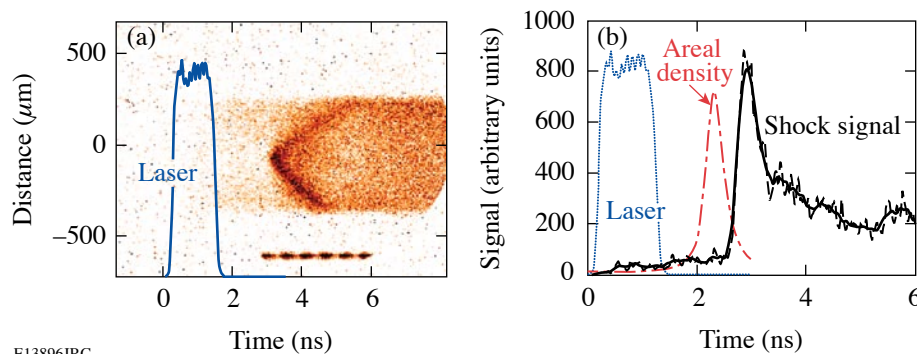


Figure 103.11 Streaked SOP signal from a 70° cone target (a) and lineout through the center of the signal (b) showing a clean shock breakout.

ACKNOWLEDGMENT

The authors are indebted to the Target Fabrication Groups at GA and LLE, especially Mark Bonino, Abbas Nikroo, and Joe Smith. This work was supported by the U.S. Department of Energy Office of Inertial Confinement Fusion under Cooperative Agreement No. DE-FC52-92SF19460, the University of Rochester, and the New York State Energy Research and Development Authority and with corporate support from General Atomics. The support of DOE does not constitute an endorsement by DOE of the views expressed in this article.

REFERENCES

1. N. G. Basov, S. Yu. Gus'kov, and L. P. Feokistov, *J. Sov. Laser Res.* **13**, 396 (1992).
2. M. Tabak *et al.*, *Phys. Plasmas* **1**, 1626 (1994).
3. J. D. Lindl, R. L. McCrory, and E. M. Campbell, *Phys. Today* **45**, 32 (1992).
4. K. Yasuike *et al.*, *Rev. Sci. Instrum.* **72**, 1236 (2001).
5. S. Atzeni, *Phys. Plasmas* **6**, 3316 (1999).
6. Y. T. Li *et al.*, *Phys. Rev. E* **69**, 036405 (2004).
7. R. B. Stephens *et al.*, *Phys. Rev. E* **69**, 066414 (2004).
8. Y. Kitagawa *et al.*, *Phys. Plasmas* **9**, 2202 (2002).
9. M. Tabak *et al.*, Lawrence Livermore National Laboratory Patent Disclosure, IL-8826B, Lawrence Livermore National Laboratory, Livermore, CA (1997).
10. P. A. Norreys *et al.*, *Phys. Plasmas* **7**, 3721 (2000).
11. R. Kodama *et al.*, *Nature* **412**, 798 (2001).
12. R. Kodama *et al.*, *Nature* **418**, 933 (2002).
13. R. B. Stephens *et al.*, *Phys. Rev. Lett.* **91**, 185001 (2003).
14. T. R. Boehly, D. L. Brown, R. S. Craxton, R. L. Keck, J. P. Knauer, J. H. Kelly, T. J. Kessler, S. A. Kumpan, S. J. Loucks, S. A. Letzring, F. J. Marshall, R. L. McCrory, S. F. B. Morse, W. Seka, J. M. Soures, and C. P. Verdon, *Opt. Commun.* **133**, 495 (1997).
15. C. Stoeckl, J. A. Delettrez, J. A. Kelly, T. J. Kessler, B. E. Kruschwitz, S. J. Loucks, R. L. McCrory, D. D. Meyerhofer, D. N. Maywar, S. F. B. Morse, J. Myatt, A. Rigatti, L. J. Waxer, J. D. Zuegel, and R. B. Stephens "High-Energy Petawatt Project at the University of Rochester's Laboratory for Laser Energetics," submitted to *Fusion Science and Technology*.
16. L. J. Waxer, D. N. Maywar, J. H. Kelly, T. J. Kessler, B. E. Kruschwitz, S. J. Loucks, R. L. McCrory, D. D. Meyerhofer, S. F. B. Morse, C. Stoeckl, and J. D. Zuegel, *Opt. Photonics News* **16**, 30 (2005).
17. S. Skupsky and R. S. Craxton, *Phys. Plasmas* **6**, 2157 (1999).
18. T. R. Boehly, V. A. Smalyuk, D. D. Meyerhofer, J. P. Knauer, D. K. Bradley, R. S. Craxton, M. J. Guardalben, S. Skupsky, and T. J. Kessler, *J. Appl. Phys.* **85**, 3444 (1999).
19. Y. Lin, T. J. Kessler, and G. N. Lawrence, *Opt. Lett.* **21**, 1703 (1996).
20. D. K. Bradley *et al.*, *Rev. Sci. Instrum.* **66**, 716 (1995).
21. F. H. Séguin, J. A. Frenje, C. K. Li, D. G. Hicks, S. Kurebayashi, J. R. Rygg, B.-E. Schwartz, R. D. Petrasso, S. Roberts, J. M. Soures, D. D. Meyerhofer, T. C. Sangster, J. P. Knauer, C. Sorce, V. Yu. Glebov, C. Stoeckl, T. W. Phillips, R. J. Leeper, K. Fletcher, and S. Padalino, *Rev. Sci. Instrum.* **74**, 975 (2003).
22. C. K. Li, D. G. Hicks, F. H. Séguin, J. A. Frenje, R. D. Petrasso, J. M. Soures, P. B. Radha, V. Yu. Glebov, C. Stoeckl, D. R. Harding, J. P. Knauer, R. L. Kremens, F. J. Marshall, D. D. Meyerhofer, S. Skupsky, S. Roberts, C. Sorce, T. C. Sangster, T. W. Phillips, M. D. Cable, and R. J. Leeper, *Phys. Plasmas* **7**, 2578 (2000).
23. R. D. Petrasso, J. A. Frenje, C. K. Li, F. H. Séguin, J. R. Rygg, B. E. Schwartz, S. Kurebayashi, P. B. Radha, C. Stoeckl, J. M. Soures, J. Delettrez, V. Yu. Glebov, D. D. Meyerhofer, and T. C. Sangster, *Phys. Rev. Lett.* **90**, 095002 (2003).
24. J. Delettrez, R. Epstein, M. C. Richardson, P. A. Jaanimagi, and B. L. Henke, *Phys. Rev. A, Gen. Phys.* **36**, 3926 (1987).
25. J. A. Oertel *et al.*, *Rev. Sci. Instrum.* **70**, 803 (1999).
26. J. Miller, *Bull. Am. Phys. Soc* **49**, 181 (2004).
27. R. E. Olson *et al.*, *Phys. Rev. Lett.* **91**, 235002 (2003).
28. C. Stoeckl, C. Chiritescu, J. A. Delettrez, R. Epstein, V. Yu. Glebov, D. R. Harding, R. L. Keck, S. J. Loucks, L. D. Lund, R. L. McCrory, P. W. McKenty, F. J. Marshall, D. D. Meyerhofer, S. F. B. Morse, S. P. Regan, P. B. Radha, S. Roberts, T. C. Sangster, W. Seka, S. Skupsky, V. A. Smalyuk, C. Sorce, J. M. Soures, R. P. J. Town, J. A. Frenje, C. K. Li, R. D. Petrasso, F. H. Séguin, K. Fletcher, S. Padalino, C. Freeman, N. Izumi, R. Lerche, and T. W. Phillips, *Phys. Plasmas* **9**, 2195 (2002).
29. T. C. Sangster, J. A. Delettrez, R. Epstein, V. Yu. Glebov, V. N. Goncharov, D. R. Harding, J. P. Knauer, R. L. Keck, J. D. Kilkenny, S. J. Loucks, L. D. Lund, R. L. McCrory, P. W. McKenty, F. J. Marshall, D. D. Meyerhofer, S. F. B. Morse, S. P. Regan, P. B. Radha, S. Roberts, W. Seka, S. Skupsky, V. A. Smalyuk, C. Sorce, J. M. Soures, C. Stoeckl, K. Thorp, J. A. Frenje, C. K. Li, R. D. Petrasso, F. H. Séguin, K. A. Fletcher, S. Padalino, C. Freeman, N. Izumi, J. A. Koch, R. A. Lerche, M. J. Moran, T. W. Phillips, and G. J. Schmid, *Phys. Plasmas* **10**, 1937 (2003).
30. J. A. Delettrez, J. Myatt, P. B. Radha, C. Stoeckl, S. Skupsky, and D. D. Meyerhofer, "Hydrodynamic Simulations of Integrated Experiments Planned for OMEGA/OMEGA EP Laser Systems," submitted to *Plasma Physics and Controlled Fusion*.

Planar Cryogenic Target Handling Capability for the OMEGA Laser-Fusion Facility

Introduction

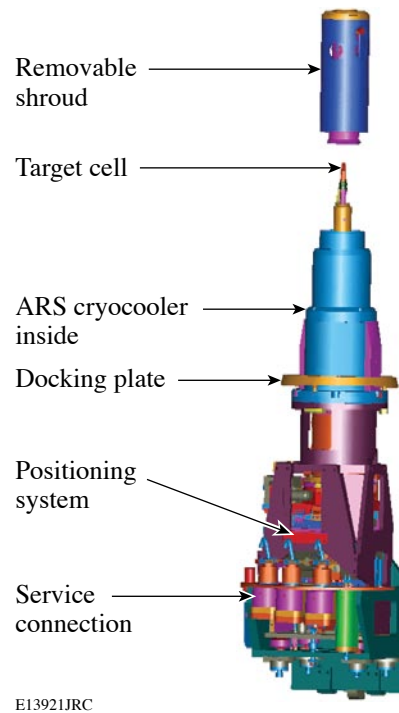
A high-performance “planar” Cryogenic Target Handling System has been added to LLE’s OMEGA Laser-Fusion Facility.¹ Initially designed for equation of state measurements of liquefied D₂, its versatility enables studies of Rayleigh–Taylor instabilities, shock timing, and cryogenic hohlraum performance. The system has demonstrated a shot-to-shot cycle interval of less than two hours and has fielded more than 125 experiments using several distinct target types. This article provides an overview of the cryogenic capabilities at LLE and compares the operational requirements of LLE’s spherical and planar cryogenic systems. The unique features of the planar cryogenic system are described, and applications of this technology within the ICF community are discussed.

Direct-drive inertial confinement fusion (ICF)² implosion targets are susceptible to shell distortion because of Rayleigh–Taylor instability.³ During the ablation phase, shock waves are launched into the capsule, resulting in compression of the fuel and gas core. Drive nonuniformities can be mitigated by rapidly heating the ablative surface of a fuel-containing capsule. Models used to predict how shock waves propagate in an ICF target and the resulting target performance depend on an accurate knowledge of the equation of state (EOS) of hydrogen isotopes at pressures exceeding 1000 GPa. Numerous experiments have been conducted in this regime using several different techniques with differing measured compressibility.⁴

LLE’s planar Cryogenic Target Handling System [CTHS (Fig. 103.12)] is a versatile experimental platform used to study the EOS of D₂ using laser-driven shock waves. This apparatus was developed to obtain a better understanding of the discrepancies in prior experimental results. The planar CTHS leverages the technical expertise and infrastructure developed for direct-drive spherical cryogenic target experiments at LLE.^{5–8} This system produces very repeatable experimental conditions with a short (~2 h) cycle time between target experiments and has been adapted to many different target and diagnostic configurations. Because of its versatile design, it is well suited to

other applications like testing cryogenic sensors and evaluating tube-filled spherical ICF targets.

This article presents an overview of LLE’s cryogenic target capabilities followed by a discussion of the operational differences between spherical and planar cryogenic experiments. Details of the planar CTHS hardware implementation and target construction are presented. Finally, performance of the planar cryogenic system is discussed.



E13921JRC

Figure 103.12

This moving cryostat (MC) was developed for cryogenic equation of state experiments. It occupies the same space envelope as a spherical MC. An MC module can be installed in approximately 4 h.

Overview

Since 1999, LLE has had the unique capability of diffusion-filling, freezing, layering, characterizing, and imploding thin-walled spherical cryogenic targets on the OMEGA Laser System.^{5,6} This system requires an extensive infrastructure to support each stage of the process, as described in Refs. 7 and 8. The Planar and Spherical Cryogenic Target Handling Systems have much in common. In contrast, planar targets are filled through a tube from a self-contained reservoir, making the process much simpler than the diffusion-filling process used for spherical targets.

LLE's diffusion-filling apparatus for spherical ICF targets is located remotely from the OMEGA target chamber. Consequently, a self-contained transport system, known as the Moving Cryostat Transfer Cart (MCTC), was developed so that filled targets could be maintained at cryogenic temperatures indefinitely and transported between the filling and characterization stations and to the target chamber. The MCTC payload, known as the moving cryostat (MC), has several functions that include

- precisely controlling the thermal environment surrounding the target until moments before an implosion experiment,
- transporting targets ~6 m vertically into the target chamber, and
- providing fine-position control for the target once it is at target chamber center (TCC).

Cooling power for the MC is provided by a closed-cycle Gifford–McMahon helium refrigeration system.⁹ A helium compressor is mounted on the MCTC, and a two-stage cryocooler is housed within the MC. The first stage of the cryocooler operates near 50 K, and the second stage operates between 10 and 20 K. Services for the MC, which include high-pressure helium lines, electrical conductors used for sensors and actuators, optical fibers, and exchange gas lines, are provided by an umbilical that extends and retracts with the MC.

Each MC assembly includes a multilayer removable shroud; its outer wall is at room temperature, whereas the inner walls are cooled. Once an MC is raised and secured at TCC, a four-axis positioner (X, Y, Z, rotation about Z) within the MC is used to position the target as it is viewed through windows in the shroud. A linear induction motor (LIM) then lowers a gripping mechanism that mates to the thermal shroud. Immediately before the laser is fired, the LIM rapidly pulls the shroud clear of all laser beams. The hardware supporting

the target is designed so that it does not interfere with laser beam propagation.

The entire process is controlled by a combination of hardware and software interlocks, automated control systems, and operating procedures. Five MCTC's have been deployed. Currently, four are dedicated to spherical ICF experiments and one is configured for planar cryogenic target experiments. In all, more than two hundred cryogenic target experiments have been fielded on OMEGA.

Distinguishing Differences Between Spherical and Planar Moving Cryostats

The planar and spherical CTHS's are required to field (up to) 15 and 8 targets per 36-h shot week, respectively.^(a) A major distinction between these systems is that a single planar MC can satisfy this requirement, whereas four spherical MC's are required. In addition, planar targets are hand-loaded into a warm MC, while spherical targets are transferred into a cold (~18 K) MC. The cycle time for planar targets includes cool down and warm up of the MC, whereas a spherical MC is not generally warmed between shots. As a result, the cycle time for planar targets is governed by the planar MC's thermal time constant and evacuation/vent times, while for spherical targets cycle times are dictated by the ice layering process.⁸ Table 103.I summarizes some of the key requirements of, and differences between, the planar and spherical MC's.

The cooldown time (time to reach 18 K) for a spherical MC exceeds 3 h. Many MCTC's would have been required to satisfy the goal of 15 planar shots/week if the same MC were adapted for the planar experiments. Instead, a new planar MC having a short thermal time constant (τ_{th}) was developed. The required shot rate is satisfied using a single MCTC. The reduction of τ_{th} was possible because of the different operating requirements of the two systems, as discussed below.

Spherical cryogenic targets are cooled indirectly using helium "exchange" gas to conduct heat from the target to the surrounding cold copper "layering" sphere [Fig. 103.13(a)].⁸ This design minimizes thermal gradients surrounding the capsule so that uniformly smooth ice layers form on the interior of the target shell. Exchange gas also allows the target support hardware to be mechanically decoupled from the cryocooler. The layering sphere is contained in the upper half

^(a)Eight spherical target implosions have been carried out in a single week, but campaigns are currently planned assuming ≤ 4 shots/week to allow sufficient time to develop an ice layer and characterize it.

Table 103.I: Key differences and requirements for planar and spherical moving cryostats.

	Planar MC	Spherical MC
Target cooling method	Conduction through copper	Conduction through ~80 mTorr He exchange gas
Target temperature	13 to 30 K±50 mK (achieves <±10 mK)	17 to 21 K±10 mK
Target filling method	“Crypumping” from integral reservoir through fill tube while target is in the MC	Diffusion filled in dedicated filling station, then frozen before transferring to the MC
Target installation method	Loaded by hand into the warm MC (open to atmosphere)	Mechanical manipulator transfers target at cryogenic temperature
Required shot rate	Up to 15 shots/week using ≤2 MCTC’s	Up to 8 shots/week using 4 MCTC’s
Laser beams required for target shots	Selected from all beams with $\theta < 155^\circ$ (55 possible)*	All 60 beams
Target rotation	±5°	360°, continuous
Target heat source	Resistance heater	OPO IR laser, $\lambda = 3.16 \mu\text{m}$

* θ is the angle measured relative to the vertical axis of the chamber. $\theta = 0^\circ =$ top of chamber.

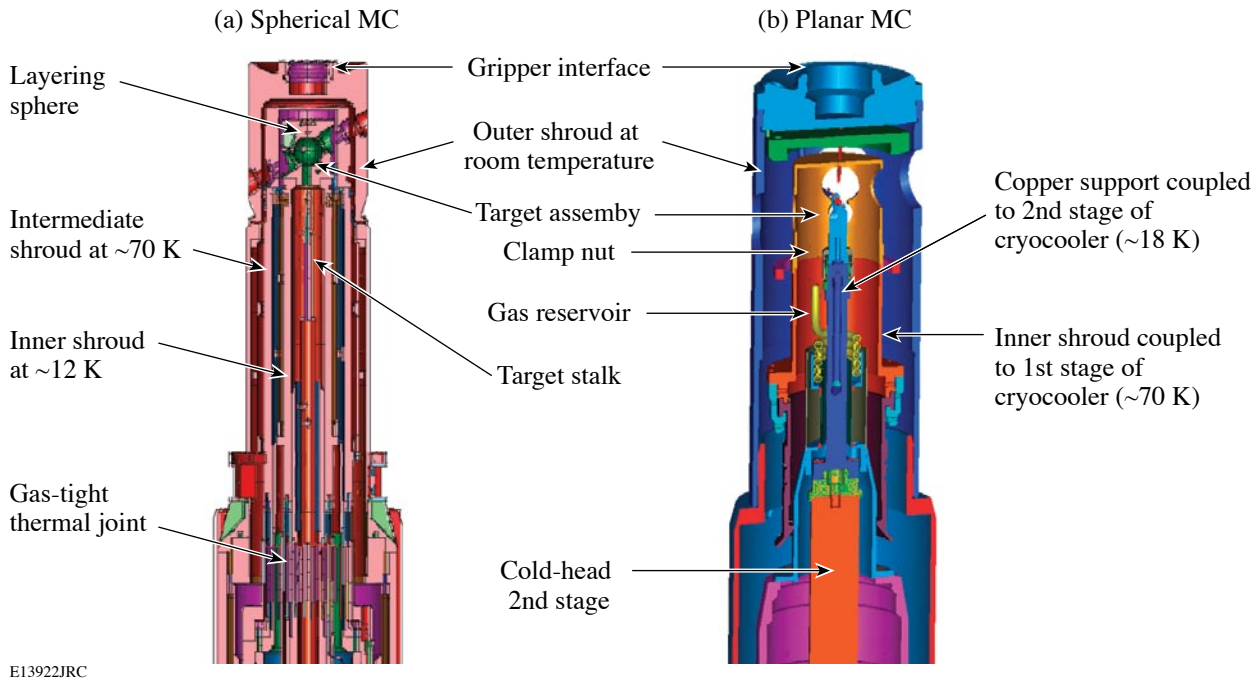


Figure 103.13

Exploded views of (a) a spherical MC and (b) a planar MC. The spherical system cools targets using a helium exchange gas; the planar system uses direct conduction through copper. These cross sections do not show the four-axis target positioners or the cold heads. The planar cold head is attached directly to the positioner; the spherical cold head is mechanically and thermally decoupled from the positioner.

of the shroud and is thermally connected to the second stage of the cryocooler.

The entire MC is inside the target chamber (maintained below 1×10^{-5} Torr); therefore, exchange-gas leakage from the spherical MC must be minimized. This constraint is satisfied by enclosing the (room temperature) fine-motion target positioner in a sealed box that mates to the upper shroud using complex, gas-tight, thermal joints. The room-temperature positioner is mechanically coupled to, but thermally isolated from, the target by means of a long slender “stalk.” This stalk is supported near its midpoint by a compliant joint that provides the necessary degrees of freedom to position a target, including the full 360° rotation needed to characterize the ice layer.^{10,11} The design chosen to satisfy these requirements separates the layering sphere from the cryocooler’s second stage by nearly 0.6 m. Approximately 8 kg of material must be cooled to an average temperature of 14 K in order to freeze the D_2 fuel in a spherical target.

The layering sphere in a spherical MC has an optical fiber to transmit radiation heat from an optical parametric oscillator (OPO) IR laser source ($\lambda = 3.16 \mu\text{m}$, matched to an absorption band of D_2) to heat the ice during the layering process.⁸ This requires spherical shrouds to be equipped with optical fiber connectors as well as temperature sensors and a cryogenic photodetector to provide feedback for closed-loop control of the OPO. The planar system has no requirements for sensors in the shroud.

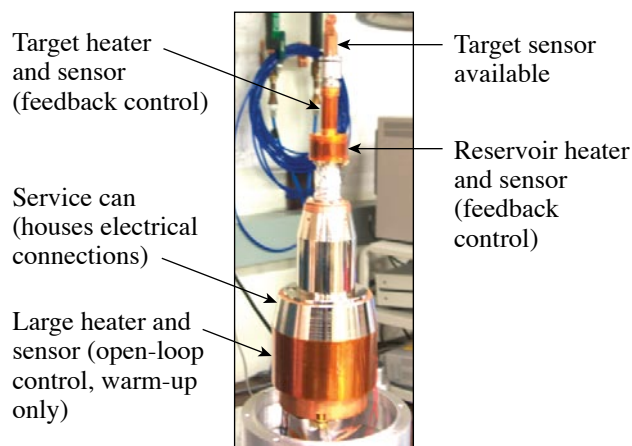
Vibration is a critical issue for the spherical MC.⁶ Spherical target assemblies are delicate, supported by a slender stalk (and its compliant joint), and are susceptible to vibration sources that couple to the MC. Many hardware improvements have been made to mitigate vibration susceptibility, with more pending.

Planar Cryogenic Target Handling System

The planar MC was designed to be interchangeable with a spherical MC and to use a common control system. The planar MC module [Fig. 103.13(b)] can be interchanged with a spherical MC in approximately 4 h, giving a high degree of flexibility when planning experimental campaigns. Since its first use on OMEGA, one planar MCTC has been used for over 125 target shots with up to 5 shots per day. OMEGA typically has three shot days per week; one planar MC can meet the 15 shot per week requirement. Target fabrication, diagnostic setup, and personnel availability are often the rate-limiting factors in the shot cycle. Typically, ambient temperature shots are inter-

leaved with planar cryo shots to take advantage of OMEGA’s 1-h repetition rate.

The planar system was not required to use exchange gas and was required to have only $\pm 5^\circ$ of rotation, since coarse rotational alignment can be established by target design. These requirements were satisfied by mounting an ARS (Advanced Research Systems, Inc.)¹² cryocooler directly onto the planar MC’s fine-motion positioner. The target is attached to the cryocooler’s second stage using a high-thermal-conductivity copper support [Fig. 103.13(b)]. The resulting cold mass in the planar MC is less than 0.5 kg; therefore, the time constant τ_c is dramatically shorter than a spherical MC. This design is mechanically very stable and eliminates the exchange gas and complex thermal joints used on a spherical MC. Figure 103.14 shows the structure of the planar MC without a shroud.



E13923JR

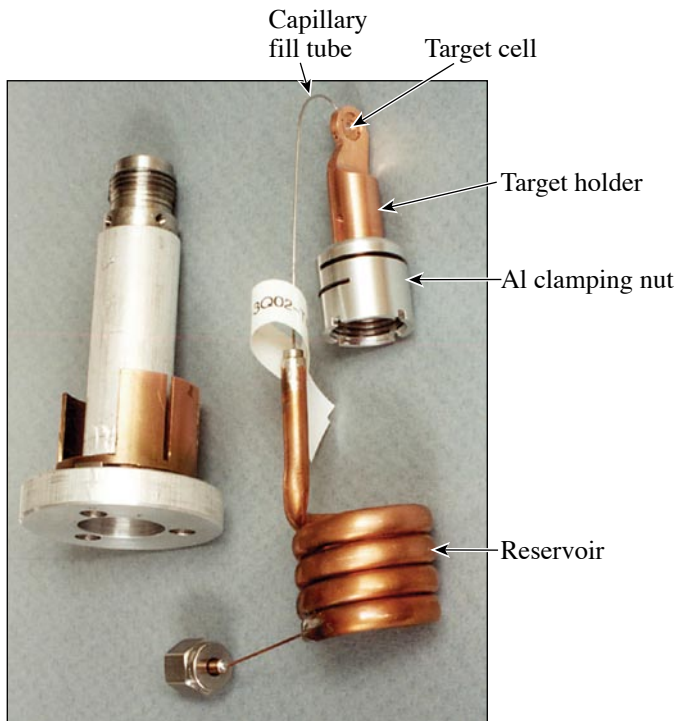
Figure 103.14
The internal structure of the planar MC (target is shown without reservoir).

Planar cryogenic experiments typically use a subset of OMEGA’s 60 laser beams that are located no more than 65° below the equator, however, spherical targets with fill tubes could be fielded on the planar MC using all 60 beams.

1. Planar Cryogenic Target Design

The primary requirement for planar cryogenic targets is to contain liquid or solid D_2 in a cell having a 1-mm inside diameter and a 0.5-mm depth. Diffusion filling was deemed impractical; therefore, targets are filled through a tube from a local reservoir. Various options were considered, including supplying the fill gas through the umbilical and using valves and pressure sensors to meter the gas. This would have required a vent line in the umbilical to purge contaminants from the

target cell and fill lines. A much simpler approach was adopted; a sealed gas reservoir is connected to each target cell by a stainless steel capillary fill tube (Fig. 103.15). The reservoir (approximately 4-cc capacity at STP) is an accurately formed spiral copper tubing coil that is filled to a known initial temperature and pressure.



E13924JRC

Figure 103.15

A typical planar cryogenic target assembly (right) is shown beside an assembly fixture (left). The split aluminum nut maintains joint preload when cooled. The gas reservoir is connected to the target cell by a capillary tube.

Planar targets are filled off-line at room temperature. Purge gas is circulated through the reservoir/cell assembly and exits through vent tube attached to the cell. Blocked tubes are detected if the purge gas is not discharged through the vent tube. After purging, the vent tube is crimped to form a gas-tight seal, and the assembly is filled to the desired pressure (typically <math><2\text{ atm}</math>). After reaching the desired pressure, the valve on the fill source is closed, and the reservoir pressure is monitored.^(b) If the pressure decay is within acceptable limits, the fill line is crimped and the target is ready for use.

This design allows great flexibility in the choice of fill gas with no chance of cross-contamination between experiments. It

^(b)The pressure sensor is part of the filling apparatus, not the target.

minimizes the volume of gas released into the target chamber and limits the total gas inventory for each target in the event that DT targets are fielded using this system.

When conducting equation of state experiments, the MC maintains the gas reservoir at about 250 K. Once the cell reaches 20 K, gas begins to condense in the cell, creating a pressure gradient between the cell and reservoir. Condensation is monitored with cameras that view the target through the shroud windows, and the process continues until the cell is full. Given that the fill volume of a target cell is approximately 0.2 mm^3 , it is not practical to install sensors in the cell. Instead, a temperature sensor is permanently installed in the copper adapter, immediately below the target holder.

Liquid D_2 density decreases at a rate of $-1.3\%/K$ from 20 to 24 K (Ref. 13). Targets that can withstand ice formation are cooled through the triple point (18.63 K) during shot preparation. The temperature at which an operator first observes ice formation in the cell is recorded. This calibrates the sensor with the accuracy needed to determine the initial state. Variations in observed triple-point measurements give a clear indication of the quality of the thermal joint formed between the target and the copper support [Fig. 103.13(b)]. Targets that cannot withstand ice formation are equipped with temperature and pressure sensors on the gas reservoir. These sensors are connected to the umbilical for readout by signal conditioning hardware external to the MCTC.

Thermal joints require preload to maintain intimate contact between mating surfaces. The thermal conductivity of a joint degrades if this preload decreases when it is cooled. The planar MC overcomes this difficulty by using a novel aluminum nut to clamp the copper target to the copper cryocooler adapter (Fig. 103.15). Spiral grooves on the nut's perimeter form bending-beam spring elements. Joint preload increases in a deterministic manner as the target assembly is cooled because of differential contraction of the aluminum and copper components. An optimized nut design results from properly choosing the cross section and length of the bending element. When a small amount of thermal grease is applied between the mating copper surfaces that have roughness $\leq 16\text{ }\mu\text{in rms}$, the temperature drop across the joint is less than 1 mK, even when the nut is initially only finger-tight.

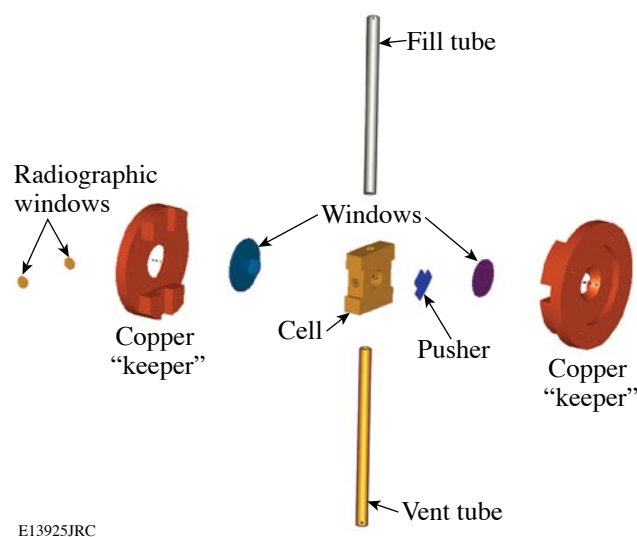
The gas reservoir rests inside a copper cup that is weakly coupled to the first stage of the cryocooler. The perimeter of the cup is split axially, forming a series of spring "fingers" similar to the assembly fixture in Fig. 103.15. A resistive foil heater

on a Kapton substrate¹⁴ is wrapped around the cup to heat the reservoir. This joint also employs differential contraction to increase preload between the cup and reservoir as the heater's Kapton substrate cools and contracts. It is possible to operate with a differential up to 250 K between the reservoir and cell and still freeze D₂ in the cell.

Controlling the thermal gradient between the reservoir and target has several benefits. It permits control of gas transfer into the cell, prevents ice from obstructing the fill tube, and provides a heat source that controls the rate of ice formation in the cell. Void-free ice layers have been produced. Heat transfer through the fill tube is very low because it is made of low thermal conductivity stainless steel. The thermal conductivity of this path can be altered as needed by adding a thermal shunt or by altering the tubing's cross section, length, or material.

2. Target Cell Construction

A typical target cell is shown in Fig. 103.16; it consists of stacked components that are bonded together and then inserted into a copper holder. This modular design allows users to select from various windows, "pushers," cell sizes, and radiographic windows without altering the basic geometry. Copper holders are reused 2 to 3 times or until laser-induced damage is too severe. Reservoirs can be reused many times after replacing the fill and vent tubes.



E13925JRC

Figure 103.16

A target cell assembly consists of several elements that enclose a gas-tight volume of approximately 1-mm diameter and 500- μ m deep. Fill and vent tubes are soldered to the cell. Some cells have radiographic windows (far left) that permit the driven shock to be imaged using an x-ray camera.

The outermost rings, referred to as "keepers," clamp the assembly into the holder. Safety wires are wrapped through holes in the keepers and holder to minimize debris ejection into the target chamber. The tension in these safety wires is critical to their effectiveness. Two opposing wires are tightly twisted, and the remaining two are relatively loose. The tight pair suffers from the initial impact and generally fail. The remaining pair of safety wires generally survive, allowing the entire assembly to be retrieved.

Although this modular target design is robust, fabrication is time consuming and requires highly skilled technicians to achieve satisfactory results. Some early targets failed because of gas leakage or blockage of the fill tube. These and other problems have been virtually eliminated with the processes that have been developed and the quality-control measures employed.

3. Shroud Construction

The spherical MC shrouds use a complex design, primarily because of the exchange-gas requirement. The heat capacity of the planar system allows it to be operated without a shroud and still freeze the fill gas. When practical, a shroud is used to minimize the possibility of condensate formation on the target and other cold components in the MC. The inner shield of the shroud [Fig. 103.17(a)] is cooled by the cryocooler's first stage to below 70 K. Thin-film Kapton windows permit the target to be observed while the shroud is in place using the OMEGA target viewing system and the video camera on the active shock breakout diagnostic.¹⁵ The upper-shroud thermal joint consists of a set of spring-loaded fingers [Fig. 103.17(b)] that maintain thermal conductivity with the lower half of the MC while accommodating large radial positioning errors. The shroud can accommodate targets of up to 50 mm in diameter. The planar MC shroud weighs 70% less than the spherical shroud (3.6 kg versus 12.7 kg), is far less costly to manufacture, and is robust. These shrouds require no maintenance.

4. Performance Results

The planar MC has a cooldown time of 50 min. It is a very robust and stable mechanical platform that can support a wide variety of targets. Figure 103.18 shows a flow chart of the shot process, including approximate times, based on the most rapid shot cycles achieved to date. Several processes are performed concurrently, such as diagnostic alignment and cooling. During warm-up, all heaters in the MC are run at maximum output. Once the MC reaches 70 K and it is isolated from the target chamber, heated dry nitrogen is used to vent the MCTC to ambient pressure. This prevents moisture from condensing in the multilayer insulation used in the MC that, in turn, reduces

the time required to achieve high vacuum for the next shot cycle. Variations in the shot cycle time are generally attrib-

able to diagnostic preparation. Table 103.II summarizes performance achievements with planar and spherical MC's.

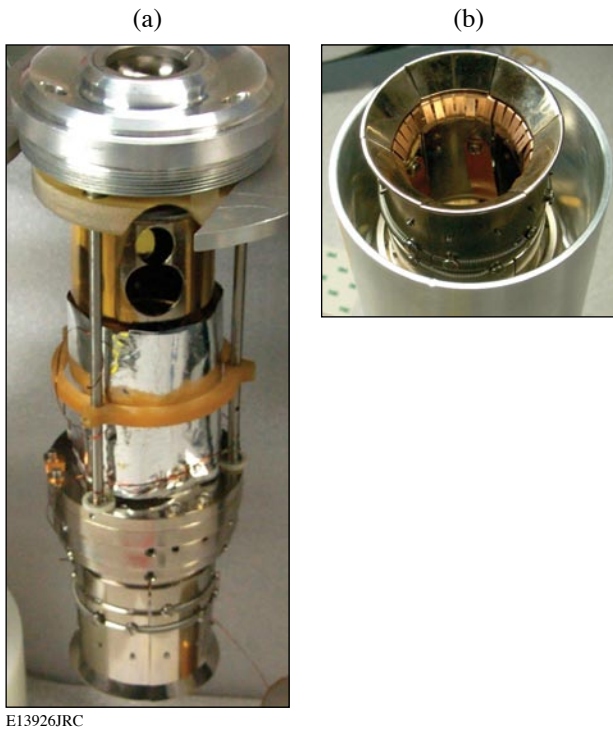


Figure 103.17
 (a) The inner shroud of the planar MC operates at ~70 K during a target shot. Windows in the shroud permit the target to be imaged by the OMEGA target viewing system and the active shock breakout diagnostic. Window openings on the inner shroud are covered with Kapton film. (b) A compliant thermal joint connects the inner shroud to the cryocooler's first stage.

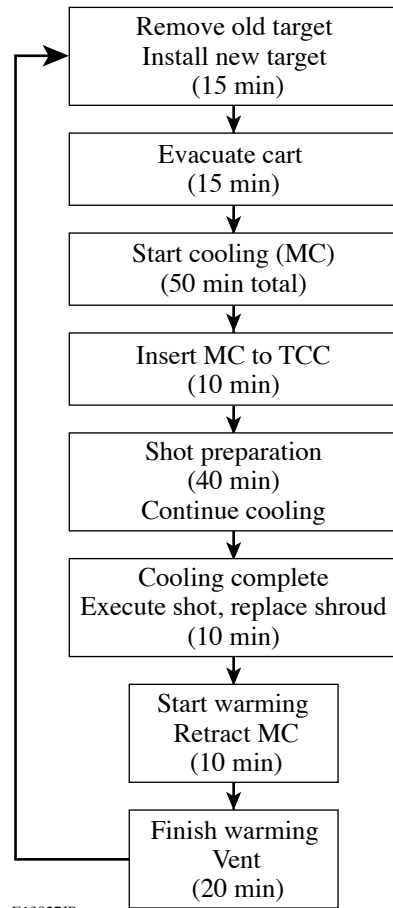


Figure 108.18
 The shot cycle flow chart depicts how 2-h cycle times have been achieved.

Table 103.II: Cryocoolers used and resulting performance comparison between planar and spherical MC's.

	Planar MC	Spherical MC
Cryocooler model	ARS Displex DE204 60 Hz	Sumitomo RDK408S 60 Hz
Cryocooler load capacity	1 W at 10 K, 6 W at 16 K	1.8 W at 10 K, 9 W at 16 K
Target operating procedure	15 to 30 K	17 to 22 K
Mass cooled <50 K	<0.5 kg	8 kg
Maximum number of target shots/day	5, using single MCTC	4, using 4 MCTC's
Actual shot cycle using one MCTC (h)	<2	72 minimum
Cooldown time (min)	<50	>180

Future Applications

Many of the design features developed for, and proven on, LLE's planar Cryogenic Target Handling System are well-suited to other cryogenic applications within the ICF community and elsewhere. LLE may use the planar cryogenic system to evaluate the feasibility of filling spherical targets with a fill tube. Targets such as this may be used for cryogenic campaigns at the National Ignition Facility.¹⁶

The exceptional stability of the planar moving cryostat allows it to be used as a target chamber center alignment reference on OMEGA, both at vacuum and at ambient pressure. The planar MC serves as a "transfer standard" so that the target chamber center can be accurately established throughout the cryogenic system infrastructure, including the characterization stations used for layering spherical cryogenic targets.

Conclusion

This article has described a high-performance planar cryogenic target positioner for use on the OMEGA Laser System. Although initially designed for equation of state studies of cryogenic hydrogen isotopes, it is a versatile platform, readily adapted to suit a wide range of experimental designs. Through careful attention to experimental and operational requirements, this design has achieved shot-to-shot cycle times below two hours. Novel thermal joints employ differential contraction of dissimilar materials to maintain joint preload at all temperatures. The target has an integrated gas reservoir, permitting users wide latitude in designing experiments with different gasses. Modularity permits flexibility in designing each target. Many of these concepts are directly applicable to cryogenic devices being developed for the ICF community and elsewhere.

ACKNOWLEDGMENT

The authors would like to thank the entire LLE cryogenic support staff for their contributions in the development and operation of the P-CTHS. This work was supported by the U.S. Department of Energy Office of Inertial Confinement Fusion under Cooperative Agreement No. DE-FC52-92SF19460 and the University of Rochester. The support of DOE does not constitute an endorsement by DOE of the views expressed in this article.

REFERENCES

1. T. R. Boehly, D. L. Brown, R. S. Craxton, R. L. Keck, J. P. Knauer, J. H. Kelly, T. J. Kessler, S. A. Kumpan, S. J. Loucks, S. A. Letzring, F. J. Marshall, R. L. McCrory, S. F. B. Morse, W. Seka, J. M. Soures, and C. P. Verdon, *Opt. Commun.* **133**, 495 (1997).
2. J. D. Lindl, *Phys. Plasmas* **2**, 3933 (1995).
3. V. N. Goncharov, S. Skupsky, T. R. Boehly, J. P. Knauer, P. McKenty, V. A. Smalyuk, R. P. J. Town, O. V. Gotchev, R. Betti, and D. D. Meyerhofer, *Phys. Plasmas* **7**, 2062 (2000).
4. T. R. Boehly, D. G. Hicks, P. M. Celliers, T. J. B. Collins, R. Earley, J. H. Eggert, D. Jacobs-Perkins, S. J. Moon, E. Vianello, D. D. Meyerhofer, and G. W. Collins, *Phys. Plasmas* **11**, L49 (2004).
5. T. C. Sangster, J. A. Delettrez, R. Epstein, V. Yu. Glebov, V. N. Goncharov, D. R. Harding, J. P. Knauer, R. L. Keck, J. D. Kilkenny, S. J. Loucks, L. D. Lund, R. L. McCrory, P. W. McKenty, F. J. Marshall, D. D. Meyerhofer, S. F. B. Morse, S. P. Regan, P. B. Radha, S. Roberts, W. Seka, S. Skupsky, V. A. Smalyuk, C. Sorce, J. M. Soures, C. Stoeckl, K. Thorp, J. A. Frenje, C. K. Li, R. D. Petrasso, F. H. Séguin, K. A. Fletcher, S. Padalino, C. Freeman, N. Izumi, J. A. Koch, R. A. Lerche, M. J. Moran, T. W. Phillips, and G. J. Schmid, *Phys. Plasmas* **10**, 1937 (2003).
6. P. W. McKenty, T. C. Sangster, M. Alexander, R. Betti, R. S. Craxton, J. A. Delettrez, L. Elasky, R. Epstein, A. Frank, V. Yu. Glebov, V. N. Goncharov, D. R. Harding, S. Jin, J. P. Knauer, R. L. Keck, S. J. Loucks, L. D. Lund, R. L. McCrory, F. J. Marshall, D. D. Meyerhofer, S. P. Regan, P. B. Radha, S. Roberts, W. Seka, S. Skupsky, V. A. Smalyuk, J. M. Soures, K. A. Thorp, M. Wozniak, J. A. Frenje, C. K. Li, R. D.

- Petrasso, F. H. Séguin, K. A. Fletcher, S. Padalino, C. Freeman, N. Izumi, J. A. Koch, R. A. Lerche, M. J. Moran, T. W. Phillips, G. J. Schmid, and C. Sorce, *Phys. Plasmas* **11**, 2790 (2004).
7. Laboratory for Laser Energetics LLE Review **81**, 21, NTIS document No. DOE/SF/19460-335 (1999). Copies may be obtained from the National Technical Information Service, Springfield, VA 22161.
 8. D. R. Harding, T. C. Sangster, D. D. Meyerhofer, P. W. McKenty, L. D. Lund, and T. H. Hinterman, "Producing Cryogenic Deuterium Targets for Experiments on OMEGA," to be published in *Fusion Science and Technology*.
 9. SHI-APD Cryogenics, Inc., A Subsidiary of Sumitomo Heavy Industries Ltd., Allentown, PA 18103-4783.
 10. D. D. Meyerhofer, R. S. Craxton, L. M. Elasky, D. R. Harding, R. L. Keck, M. Pandina, W. Seka, M. D. Wittman, A. Warrick, and T. G. Brown, *Bull. Am. Phys. Soc.* **48**, 55 (2003).
 11. D. H. Edgell, W. Seka, R. S. Craxton, L. M. Elasky, D. R. Harding, R. L. Keck, and M. D. Wittman, "Analysis of Cryogenic Target Shadowgraphs at LLE," to be published in *Fusion Science and Technology*.
 12. Advanced Research Systems, Inc., Macungie, PA 18062.
 13. P. C. Souers, *Hydrogen Properties for Fusion Energy* (University of California Press, Berkeley, 1986).
 14. e.g., Minco, Minneapolis, MN 55432-3177.
 15. R. J. Leeper, G. A. Chandler, G. W. Cooper, M. S. Derzon, D. L. Fehl, D. L. Hebron, A. R. Moats, D. D. Noack, J. L. Porter, L. E. Ruggles, J. A. Torres, M. D. Cable, P. M. Bell, C. A. Clower, B. A. Hammel, D. H. Kalantar, V. P. Karpenko, R. L. Kauffman, J. D. Kilkeny, F. D. Lee, R. A. Lerche, B. J. MacGowan, M. J. Moran, M. B. Nelson, W. Olson, T. J. Orzechowski, T. W. Phillips, D. Ress, G. L. Tietbohl, J. E. Trebes, R. J. Bartlett, R. Berggren, S. E. Caldwell, R. E. Chrien, B. H. Failor, J. C. Fernández, A. Hauer, G. Idzorek, R. G. Hockaday, T. J. Murphy, J. Oertel, R. Watt, M. Wilke, D. K. Bradley, J. Knauer, R. D. Petrasso, and C. K. Li, *Rev. Sci. Instrum.* **68**, 868 (1997).
 16. J. Edwards *et al.*, *Phys. Plasmas* **12**, 056318 (2005).

Fourier-Space, Nonlinear Rayleigh–Taylor Growth Measurements of 3-D Laser-Imprinted Modulations in Planar Targets

Introduction

The unstable growth of target nonuniformities is the most important factor that limits target performance in inertial confinement fusion (ICF)¹ and is crucial in understanding many astrophysics phenomena.² In ICF, the target is driven either directly with laser beams (direct drive)³ or indirectly by x rays, in which the laser drive is converted into x rays in a high-Z enclosure (hohlraum).⁴ When laser light is incident on the target in a direct-drive configuration, the pressure created by the target ablation launches a shock wave that compresses the target. Any target modulations, either existing surface imperfections or modulations created by laser nonuniformities through laser imprinting, grow because of shock-driven Richtmyer–Meshkov (RM) instability as a shock wave propagates toward the rear surface of the target.^{5–8} When the shock front reaches the rear surface of the target, it sends a rarefaction wave back toward the ablation surface; when it arrives, the target begins to accelerate. During the acceleration phase, the ablation-surface modulations grow exponentially because of Rayleigh–Taylor (RT) instability.^{9–19} RT instability has been extensively studied in both ablative^{12–19} and classical^{9–11} (with no ablative stabilization) regimes. RT growth rates were studied in the linear regime of the instability with both direct^{14–17} and indirect^{12,13} drive. The highly nonlinear, turbulent regime of RT instability was studied mostly in the classical regime.^{8–11} Weakly nonlinear features, such as harmonic generation and mode coupling to longer wavelengths, were measured in experiments using indirect drive^{12,19} coupled to targets with preimposed, single-mode, and multimode initial perturbations. The saturation amplitudes of 3-D broadband nonuniformities were measured using laser-imprinted modulations as initial seeds for RT growth (conditions most relevant to direct-drive ICF).¹⁸ In those experiments, the finite target thickness limited unstable hydrodynamic growth, which did not allow accurate measurements of the nonlinear velocities.²⁰ The experiments in this article present the first measurements of nonlinear saturation velocities, allowing a direct comparison with the Haan nonlinear-growth model²¹ near saturation levels. The transition from linear to nonlinear growth of 3-D broadband modulations presented in this article is among the key factors required to

understand nonlinear RT instability. This experimental study is critical to the success of ICF because most ICF ignition designs rely on the accuracy of Haan’s predictions.

Experimental Details

In the experiments, initially smooth, 1-mm-diam, 20- and 50- μm -thick CH targets were driven with 12-ns square pulses at a laser intensity of $\sim 5 \times 10^{13}$ W/cm² on the OMEGA Laser System.²² The modulation growth was measured with through-foil, x-ray radiography²⁰ using x rays from three different backlighters: an ~ 1.3 -keV uranium backlighter for 20- μm -thick targets and an ~ 2.0 -keV dysprosium and an ~ 2.5 -keV tantalum for 50- μm -thick targets. Harder x rays were used at later times when target modulations reached larger amplitudes. The backlighter x rays were imaged by an 8- μm pinhole array onto a framing camera, allowing for up to eight images with a temporal resolution of ~ 80 ps and a spatial resolution of ~ 10 μm to be captured at different times in each shot.²⁰ The initial target modulations, used for RT growth measurements, were imprinted by laser-intensity nonuniformities of the imprint beam, which arrived ~ 200 ps before all other drive beams, used for target acceleration.^{18,20} The process of laser imprinting takes ~ 200 ps. During this time, a plasma develops (from laser ablation) between the laser absorption (near the critical surface) and ablation surfaces, which decouples laser beams from the target, thereby stopping the imprinting process.^{23,24} Two different initial target modulations were created by a laser beam with either a standard distributed phase plate²⁵ (SG8 DPP) or a laser beam with no DPP, defocused to an ~ 1 -mm spot. Figure 103.19 shows measured central, 333- μm -sq parts of laser equivalent-target-plane images with an SG8 DPP [Fig. 103.19(a)] and with no DPP [Fig. 103.19(b)]. The laser-modulation Fourier spectra of these laser images are shown in Fig. 103.19(c). The beam with a DPP (solid curve) has broadband modulations with spatial frequencies up to ~ 320 mm⁻¹, corresponding to the smallest spatial size of ~ 3 μm and an intensity modulation σ_{rms} of $\sim 94\%$. The beam with no DPP (dashed curve) has modulations with spatial frequencies up to ~ 50 mm⁻¹, corresponding to the smallest spatial size of ~ 20 μm , and an intensity modulation σ_{rms} of $\sim 51\%$.

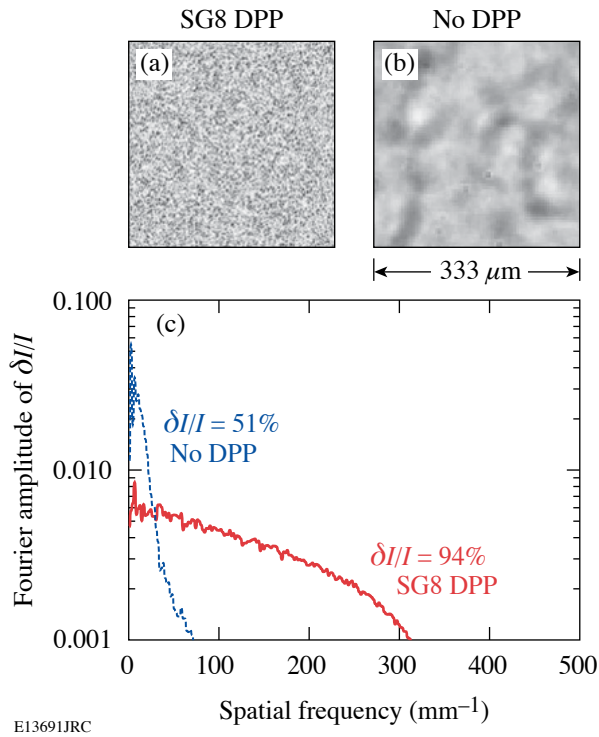


Figure 103.19 Central, 333- μm -sq parts of the measured equivalent-target-plane images of laser beams with (a) a regular SG8 DPP and (b) with no DPP used to produce initial 3-D broadband modulations for RT growth. (c) Fourier amplitudes of relative laser intensity as a function of a spatial frequency of these laser-beam images with a SG8 DPP (solid line) and with no DPP (dashed line).

Experimental Results

The optical-depth (OD) images (obtained by taking the natural logarithm of intensity-converted, framing-camera images) of x-ray radiographs are shown in Figs. 103.20(a), 103.20(b), and 103.20(c) for SG8 DPP initial conditions and in Figs. 103.20(d), 103.20(e), and 103.20(f) for no-DPP initial conditions. The early-time images (a) and (d) were obtained using a uranium backlighter, while later-time images (b) and (e) were obtained with a dysprosium backlighter and images (c) and (f) with a tantalum backlighter. A Wiener filter (based on measured system resolution and noise) was applied to these images to remove noise and deconvolve the system's modulation transfer function to recover target OD modulations.²⁰ The measured target OD variations are proportional to the variations of target areal density $\delta[\rho R]$, $\delta[\text{OD}(t)] = \mu_{\text{CH}}(E)\delta[\rho R(t)]$, where $\mu_{\text{CH}}(E)$ is the CH target mass absorption rate at the x-ray energy E used for backlighting and t is the time of the measurement. The measured (in undriven targets) mass absorption rates were $950 \pm 100 \text{ cm}^2/\text{g}$, $320 \pm 30 \text{ cm}^2/\text{g}$, and $240 \pm 20 \text{ cm}^2/\text{g}$ for uranium, dysprosium, and tantalum backlighters, respectively. The

areal-density modulations were obtained by dividing measured OD modulations by the target mass absorption rates. Harder x rays were used to measure higher-amplitude modulations at late times because softer x rays are completely absorbed in large modulation spikes, compromising the measurements. Measurement timings of 20- μm -thick targets were converted to those of 50- μm -thick targets according to the calculated (by 1-D hydrocode *LILAC*²⁶) target distance traveled.

During the acceleration phase, the target's laser-imprinted modulations grow because of RT instability. During this growth, the modulations shift to longer wavelengths, with initial small structures growing into large bubbles (the dark regions in x-ray radiographs shown in Fig. 103.20) and narrow spikes (light areas in the radiographs). Figure 103.21 shows the evolution of modulation areal-density Fourier amplitudes (for shots with DPP initial seeds). The dotted line is the Haan saturation level²⁰ $S_k = 2/Lk^2$, where $L = 333 \mu\text{m}$ is the box size of the x-ray image, k is the spatial wave number of modulations, $k = 2\pi f$, and f is the spatial frequency. The saturation level S_k was converted to areal density by multiplying it by the *LILAC*-calculated foil density of $\sim 1.7 \text{ g/cc}$, which was predicted to be constant (within about 10%) for the duration of the experiment. In the Haan model,²¹ the spectral amplitudes grow exponentially with the RT growth rate $\gamma(k)$ until they reach the saturation levels S_k ; at this point they grow

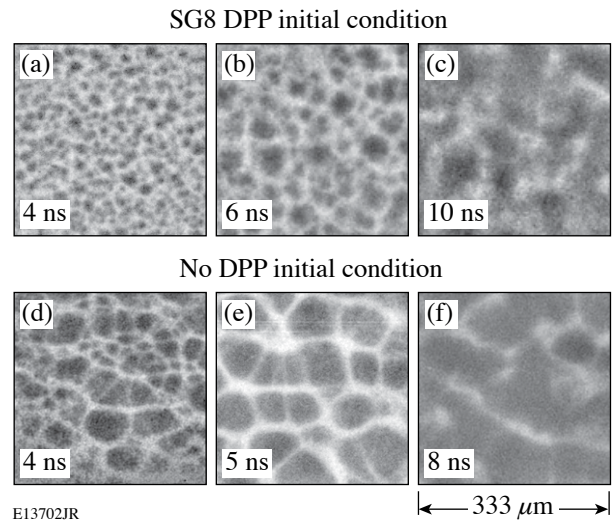


Figure 103.20 X-ray radiographs of the 3-D broadband modulations initially produced by the imprinting of the laser beam with a SG8 DPP and measured at 4, 6, and 10 ns [images (a), (b), and (c), respectively] and with the laser beam with no DPP and measured at 4, 5, and 8 ns [images (d), (e), and (f), respectively].

linearly in time with saturation velocities $V_s(k) = S_k \gamma(k)$. The RT growth rate is determined by the Betti-Goncharov dispersion relation²⁷ $\gamma(k) = 0.94 [kg/1 + kL_m]^{0.5} - 1.5kV_a$, where $g = 10 \mu\text{m}/\text{ns}^2$ is the target acceleration, $V_a = 0.65 \mu\text{m}/\text{ns}$ is the ablation velocity, and $L_m = 0.1 \mu\text{m}$ is the density scale length (all three parameters were calculated by *LILAC*). The shorter-wavelength modes grow most rapidly and quickly saturate at levels S_k while the longer-wavelength modes grow more slowly. As a result, the mid-wavelength modes have the largest growth factors, producing a peak in the spectrum. As the evolution continues, this peak moves to longer wavelengths, as shown in Fig. 103.21. Because the effects of finite target thickness, which compromised the evolution of the thin, 20- μm -thick targets in previous experiments,²⁰ were detected only after ~ 7 ns in the present experiments with 50- μm -thick targets, the analysis was limited to data taken up to ~ 6 ns.

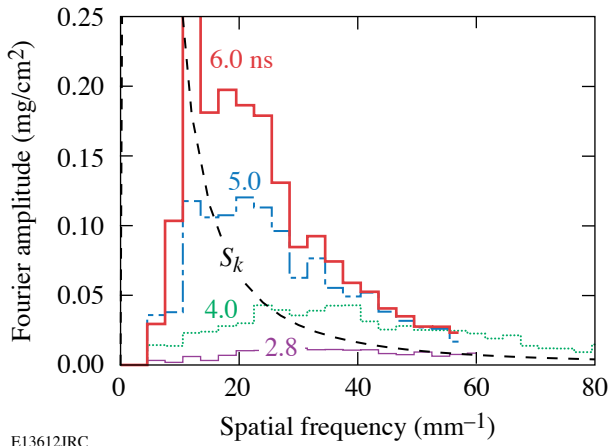


Figure 103.21
 Fourier amplitudes of the target areal-density modulations as a function of spatial frequency initially produced by the imprinting of the laser beam with SG8 DPP and measured at 2.8 (thin solid), 4.0 (dotted), 5.0 (dotted-dashed), and 6.0 ns (thick solid curve). The dashed curve corresponds to the saturation amplitude predicted by Haan.²⁰

Figure 103.22 shows the temporal evolution of the areal-density Fourier amplitudes at four spatial wavelengths of 20, 30, 60, and 120 μm for shots with DPP initial conditions. The amplitudes of the 120- μm spatial wavelength [see Fig. 103.22(a)] are below their saturation levels S_k . They are growing exponentially in the linear regime. The solid lines in Figs. 103.22(a) and 103.22(b) are the exponential fits to the data, from which the growth rate is determined. The amplitudes of the 60- μm -wavelength modulations [see Fig. 103.22(b)] undergo a transition from exponential growth to linear temporal growth. The solid lines represent the exponential fit to the data below the saturation level S_k , while the dashed lines represent

the linear fit above the saturation level. The dotted lines in Figs. 103.22(c) and 103.22(d) are the linear fits to the 30- and 20- μm -wavelength data above their saturation levels. Similar fits were performed to the data with no DPP initial conditions. Figure 103.23 summarizes the growth results. The dashed line in Fig. 103.23(a) shows the growth rate $\gamma(k)$ (defined in the previous paragraph) as a function of spatial frequency. The diamonds correspond to the measured growth rates of 120- and 60- μm -wavelength modulations (corresponding to the spatial frequencies of 8 and 16 mm^{-1} , respectively) from all shots (with initial conditions including both SG8 DPP and no DPP). The dashed line in Fig. 103.23(b) shows the saturation velocity $V_s(k) = S_k \gamma(k)$ as a function of the spatial frequency, as defined by the Haan model.²¹ The diamonds correspond to the measured saturation velocities of the 120-, 60-, 30-, and 20- μm -wavelength modulations (corresponding to spatial frequencies of 8, 16, 33, and 50 mm^{-1} , respectively). The measured saturation velocities are in excellent agreement with Haan-model²¹ predictions. Once the modulations enter the nonlinear regime, the velocities no longer depend on initial conditions. The measured growth rates of long-wavelength modulations are higher (by about a factor of 2) than the Haan-model predictions (given by the Betti-Goncharov formula). Previous studies^{28,29} have predicted enhanced growth (with respect to the Haan model) of long-wavelength modes in the classical RT instability (without

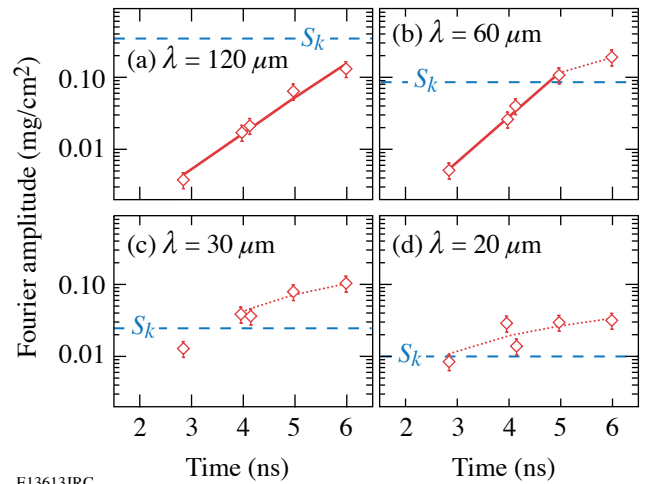
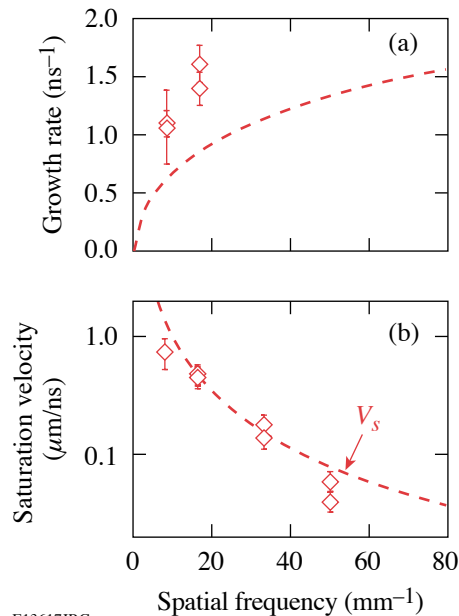


Figure 103.22
 Temporal evolution of the target areal-density modulations measured at spatial wavelengths of 120, 60, 30, and 20 μm [(a), (b), (c), and (d), respectively]. The solid and dotted lines represent exponential and linear-in-time fits to the experimental data, respectively, initially produced by the imprinting of the laser beam with an SG8 DPP. The horizontal dashed lines show the saturation amplitudes predicted by Haan.²⁰

ablation stabilization) because of enhanced mode-coupling of higher-amplitude, faster-growing, shorter-wavelength modes. The same studies,^{28,29} however, predicted no significant contribution of mode coupling for the ablative RT growth (relevant to our experiments). A recent study³⁰ by Sanz *et al.* predicted enhanced mode coupling to longer-wavelength modes in the ablative RT instability, compared to the classical RT case. The present experiments are consistent with this new study³⁰ rather than with the previous predictions.^{28,29} This correction to the Haan model has a small effect on the overall growth of the total rms modulation level because the longer wavelengths (120 μm and 60 μm) have smaller amplitudes than the shorter-wavelength modes (as shown in Fig. 103.21) and shorter modes grow with the velocities that are in agreement with Haan model. Therefore, the average modulation levels (rms amplitudes) grow very close to Haan-model predictions.²¹ We find it remarkable that this simple model predicts so accurately such a complicated phenomenon as the nonlinear saturation of the RT instability.



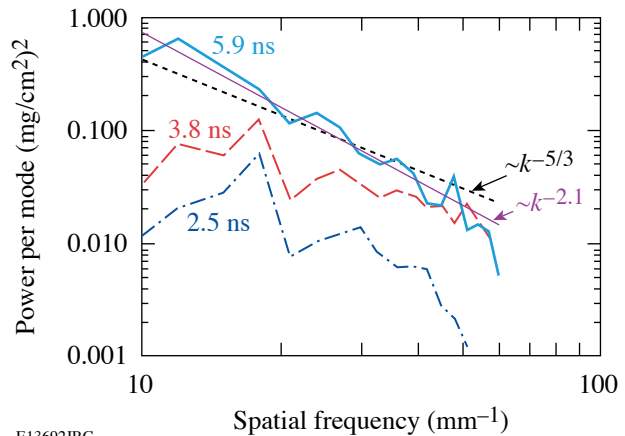
E13617JRC

Figure 103.23

(a) Modulation RT growth rates as a function of spatial frequency measured (diamonds) and predicted by the Betti–Goncharov dispersion relation (dashed curve). (b) Modulation nonlinear saturation velocities as a function of spatial frequency measured (diamonds) and predicted by the Haan model (dashed curve).

Figure 103.24 shows the evolution of power spectra at three different times (with no DPP initial conditions). In the highly nonlinear, turbulent regime, it has been determined that the power spectra follow the “ $-5/3$ ” Kolmogorov power-law scaling.¹⁰ In the present experiments, the modulations undergo the

transition from linear to nonlinear growth near the saturation levels. At a later time (~ 5.9 ns), a large part of the modulation spectrum is in the nonlinear regime, while modulations at 2.5 and 3.8 ns approach the saturation levels. The thin, solid line presents the power-law fit to the 5.9-ns data showing the power-law slope of ~ -2.1 . This slope is steeper than Kolmogorov’s slope of $-5/3 = -1.67$, shown by a dotted line. Once the modulations enter the highly nonlinear, turbulent regime of RT instability, the slope is expected to approach $-5/3$, as was shown in earlier classical RT experiments.¹¹



E13692JRC

Figure 103.24

Measured power per mode of areal-density modulations at 2.5, 3.8, and 5.9 ns. The thin and dashed curves represent the lines with power-law slopes of -2.1 and -1.67 (or $-5/3$), respectively.

Conclusions

In conclusion, the unstable RT growth of 3-D broadband modulations was measured near nonlinear saturation levels in planar plastic targets directly accelerated by laser light. The nonlinear saturation velocities were measured for the first time and are in excellent agreement with the Haan model.²¹ Once modulations enter the nonlinear regime, the measured growth does not depend on the initial modulation spectrum. The measured growth of low-amplitude, long-wavelength modes is consistent with the generation of enhanced nonlinear long wavelengths in ablatively driven targets, predicted³⁰ by Sanz *et al.* This experimental study is critical to the success of ICF because most ICF ignition designs rely on Haan’s predictions.

ACKNOWLEDGMENT

The authors thank Prof. D. Shvarts, Prof. R. Betti, and Dr. B. A. Remington for helpful discussions. This work was supported by the U.S. Department of Energy Office of Inertial Confinement Fusion under Cooperative Agreement No. DE-FC52-92SF19460, the University of Rochester, and the New York State Energy Research and Development Authority. The support

of DOE does not constitute an endorsement by DOE of the views expressed in this article.

REFERENCES

1. J. Nuckolls *et al.*, *Nature* **239**, 139 (1972).
2. B. A. Remington *et al.*, *Phys. Plasmas* **4**, 1994 (1997).
3. S. E. Bodner, D. G. Colombant, J. H. Gardner, R. H. Lehmborg, S. P. Obenschain, L. Phillips, A. J. Schmitt, J. D. Sethian, R. L. McCrory, W. Seka, C. P. Verdon, J. P. Knauer, B. B. Afeyan, and H. T. Powell, *Phys. Plasmas* **5**, 1901 (1998).
4. J. D. Lindl, *Phys. Plasmas* **2**, 3933 (1995).
5. G. Dimonte and B. Remington, *Phys. Rev. Lett.* **70**, 1806 (1993).
6. Y. Aglitskiy *et al.*, *Phys. Plasmas* **9**, 2264 (2002).
7. J. W. Jacobs and V. V. Krivets, *Phys. Fluids* **17**, 034105 (2005).
8. O. Sadot *et al.*, *Phys. Rev. Lett.* **80**, 1654 (1998).
9. K. I. Read, *Physica* **12D**, 45 (1984).
10. M. B. Schneider, G. Dimonte, and B. Remington, *Phys. Rev. Lett.* **80**, 3507 (1998).
11. G. Dimonte *et al.*, *Phys. Fluids* **16**, 1668 (2004).
12. B. A. Remington *et al.*, *Phys. Fluids B* **5**, 2589 (1993).
13. K. S. Budil *et al.*, *Phys. Rev. Lett.* **76**, 4536 (1996).
14. K. Shigemori *et al.*, *Phys. Rev. Lett.* **78**, 250 (1997).
15. C. J. Pawley *et al.*, *Phys. Plasmas* **4**, 1969 (1997).
16. J. P. Knauer, R. Betti, D. K. Bradley, T. R. Boehly, T. J. B. Collins, V. N. Goncharov, P. W. McKenty, D. D. Meyerhofer, V. A. Smalyuk, C. P. Verdon, S. G. Glendinning, D. H. Kalantar, and R. G. Watt, *Phys. Plasmas* **7**, 338 (2000).
17. T. Sakaiya *et al.*, *Phys. Rev. Lett.* **88**, 145003 (2002).
18. V. A. Smalyuk, T. R. Boehly, D. K. Bradley, V. N. Goncharov, J. A. Delettrez, J. P. Knauer, D. D. Meyerhofer, D. Oron, and D. Shvarts, *Phys. Rev. Lett.* **81**, 5342 (1998).
19. M. M. Marinak *et al.*, *Phys. Rev. Lett.* **80**, 4426 (1998).
20. V. A. Smalyuk, T. R. Boehly, D. K. Bradley, V. N. Goncharov, J. A. Delettrez, J. P. Knauer, D. D. Meyerhofer, D. Oron, D. Shvarts, Y. Srebro, and R. P. J. Town, *Phys. Plasmas* **6**, 4022 (1999).
21. S. W. Haan, *Phys. Rev. A, Gen. Phys.* **39**, 5812 (1989).
22. T. R. Boehly, D. L. Brown, R. S. Craxton, R. L. Keck, J. P. Knauer, J. H. Kelly, T. J. Kessler, S. A. Kumpan, S. J. Loucks, S. A. Letzring, F. J. Marshall, R. L. McCrory, S. F. B. Morse, W. Seka, J. M. Soures, and C. P. Verdon, *Opt. Commun.* **133**, 495 (1997).
23. S. E. Bodner, *J. Fusion Energy* **1**, 221 (1981).
24. V. N. Goncharov, S. Skupsky, T. R. Boehly, J. P. Knauer, P. McKenty, V. A. Smalyuk, R. P. J. Town, O. V. Gotchev, R. Betti, and D. D. Meyerhofer, *Phys. Plasmas* **7**, 2062 (2000).
25. Y. Lin, T. J. Kessler, and G. N. Lawrence, *Opt. Lett.* **20**, 764 (1995).
26. J. Delettrez, R. Epstein, M. C. Richardson, P. A. Jaanimagi, and B. L. Henke, *Phys. Rev. A, Gen. Phys.* **36**, 3926 (1987).
27. R. Betti, V. N. Goncharov, R. L. McCrory, and C. P. Verdon, *Phys. Plasmas* **5**, 1446 (1998).
28. S. W. Haan, *Phys. Fluids B* **3**, 2349 (1991).
29. D. Ofer, U. Alon, D. Shvarts, R. L. McCrory, and C. P. Verdon, *Phys. Plasmas* **3**, 3073 (1996).
30. J. Sanz, J. Ramírez, R. Ramis, R. Betti, and R. P. J. Town, *Phys. Rev. Lett.* **89**, 195002 (2002).

Technologies for Mitigating Tritium Releases to the Environment

Historical Background

The University of Rochester's Laboratory for Laser Energetics is preparing to fabricate and implode targets containing DT ice. To minimize risk to the environment and personnel, a tritium-handling infrastructure has been installed within the laboratory. The infrastructure strives to intercept tritium emissions from the process loops and to reduce emissions arising from contaminated surfaces.

Historically, in the 1950s through the late 1960s, tritium-handling systems were housed in air-ventilated enclosures. Room air was drawn over the equipment, directed to a stack, and discharged. Tritium that escaped through leaks in the plumbing, desorbed from contaminated internal surfaces exposed to air, or was collected by vacuum systems would be entrained in the airflow and directed to the stack. There was no effort to extract the tritium species from the effluent stream. This practice was attractive because it was the least costly to implement, offered flexibility during upgrades and maintenance, and imposed the least number of constraints during routine operations. The facilities needed to be remote from populated areas, however, because the emissions imposed a significant impact on the environment surrounding the plants. While this approach offered short-term relief from tritium releases, over the longer term, the environment surrounding the facilities became severely contaminated. As a consequence, contamination levels within the facilities gradually rose and chronic worker dose increased. By the time the United States Atomic Energy Commission issued a directive (in 1969) to all tritium facilities to reduce effluents to levels "as low as practical," most large-scale tritium-handling facilities had already started to implement containment technologies.

To be successful and economically viable, the trapping and removal technologies had to be installed as near the point of origin as possible before any excessive dilution with air had occurred. In most cases, gaseous effluents were converted to water and collected on molecular sieves. The system throughputs, which were determined to first order by the sizes of the

oxidation reactors and the driers, varied from a few liters/h to 2000 liters/min (LPM).

In the mid to late 1970s, efforts to replace air in the containment boxes with inert gas were met with limited success. In this approach, tritium gas could be captured directly without conversion to tritium oxide by reacting with a titanium sponge. However, water vapor in the atmosphere would permeate into the boxes and passivate the sponge by forming an impenetrable oxide layer on the titanium. Systems containing fresh charges of titanium sponge would scavenge tritium from the inert gas for brief periods, but the performance would gradually degrade as the thickness of the oxide coating grew on the titanium. As a result, cleanup systems that collected tritium gas directly were reserved for special applications in which large quantities of tritium gas were at risk and needed to be recovered without conversion to tritium oxide. More common, however, containment systems using either air or inert gas relied on the oxidation of all tritium species and the collection of the tritiated water vapor with driers. Periodically, the driers could be regenerated to recover their effectiveness. The highly active condensate would be solidified and land disposed. In effect, tritium discharges that would have contaminated the environment around a processing facility were collected on disposable beds and stored at burial sites in leak-tight containers.

The advent of new alloys comprising a mixture of iron and zirconium (Zr-Fe) dramatically broadened the options for tritium effluent treatment.¹ The Zr-Fe alloy offered stability against passivation when exposed to impurity fluxes far superior to that demonstrated by titanium sponge and, simultaneously, offered the potential for recovering the captured tritium gas.² Facilities that handled significant quantities of gas could recover and re-use tritium originally destined for the stack, and, as such, recoup some of their investment in the tritium while simultaneously reducing the cost of land-disposing solidified tritiated effluent. In the 1980s and 1990s, this alloy found utility not only in glovebox applications, but also in treating vacuum effluents.³ The acceptance of the alloy as a tritium-capture

device has spread across the tritium community over the past two decades.⁴

Currently, an array of devices including Zr-Fe scavenger beds,⁵ uranium scavenger beds,⁶ molecular sieve driers, and nickel catalyst beds⁷ offers the potential to treat both inert gas and air streams.⁸ Both glovebox atmospheres and vacuum effluent streams can be processed. These systems can be scaled over a broad range of throughputs and capacities, but, nevertheless, economic drivers continue to favor tritium recovery before any significant dilution with air occurs.^{9,10}

By the mid-1970s, tritium became the dominant isotope for the radioluminescent industry, replacing both radium-226 and strontium-90. Tritium was viewed as radiologically safer and more environmentally acceptable by comparison to the other two isotopes. The industry appeared to be on the threshold of an unprecedented expansion with self-powered backlighting for digital watches leading a host of other ubiquitous applications. However, this optimistic growth was quickly tempered. The general tightening of environmental and safety regulations being applied to the nuclear industry spread to the radioluminescent industry. In part, this movement was driven by the Three Mile Island accident and the discovery of small amounts of tritium in a public school food-preparation facility across the street from a tritium light-manufacturing plant in Tucson, Arizona. By the 1980s the industry had stabilized, focusing on applications where absolute reliability was needed, such as in hospitals, mines, multilevel buildings, and aircraft exit markings. A number of military applications in which the benefit clearly outweighed the perceived risk have been identified and exploited.

Just as the optimism in the radioluminescent industry abated, fusion fuel needs for the magnetic confinement program spawned an intense, worldwide effort to identify materials suitable for tritium handling, techniques to purify and measure tritium, and technologies to extract tritium from effluent streams. Significant advances were made in tritium-handling systems during the 1980s and 1990s.

This article reviews the technologies that minimize tritium releases from systems and discusses the strengths and weaknesses of those options. To this end, the components and systems that apply are reviewed, the optimal applications for those components and systems are identified, and their applicability to air and inert gas streams discussed.

The section entitled **Guiding Principles** (p. 143) reviews the guiding principles to consider when designing and operating process and capture systems. Ignoring these principles could convert the capture equipment into emission sources. In **Options for Tritium Capture** (p. 144), capture options for both air-bearing and inert carrier streams are presented. Component selection and the rationale for selecting the order of the components are also discussed. **Typical Tritium-Capture Schemes** (p. 146) provides examples to illustrate the application of the guiding principles. **Description of Components Used for Tritium Capture** (p. 148) provides the salient performance features of the components discussed in the previous sections. Component throughputs are discussed in **Throughput and Construction Guidelines** (p. 153).

Guiding Principles

Several principles apply to the effective handling and capture of tritium. These include

- understanding the global requirement for tritium trapping,
- defense in depth,
- interception close to the emission source,
- circulation,
- tailoring the capture system to the application,
- monitoring all effluent streams, and
- minimizing process volumes.

Each of these principles is discussed in the following paragraphs.

Many of the devices discussed in this article have demonstrated long-term effectiveness in mitigating tritium releases. However, these devices do not represent “magic bullets.” Their effectiveness depends heavily on the manner in which they are implemented and integrated into the process loops. To simply view these devices solely as “bolt-on” components will severely restrict their utility, reduce their effectiveness, or, in some cases, increase the potential for significant tritium releases. A holistic approach to trapping and containment is required. Careful evaluation of the intended application, the operating regime, and the composition of the effluent is required if the trapping and containment of the tritium in the effluent is to be effective and robust.

The defense-in-depth concept provides robustness. Layering trapping technologies provide the opportunity for staged tritium recovery. Should the first barrier fail or perform below

design expectations, the second barrier can reduce the impact of the impending release.

Intercepting tritium emissions as close to their sources as possible continues to be the preferred option. The approach holds several advantages.

- The scale of the equipment and, consequently, its cost can be greatly reduced.
- Emissions in one subsystem do not impact the operation of other subsystems.
- Equipment can be tailored with greater precision to address specific potential release scenarios.
- Component selection options increase significantly if trapping occurs before mixing with air.
- The degree of secondary contamination is usually greatly reduced.

Circulating systems are preferred over once-through systems. These systems provide more time to process tritiated effluent, increase the effective decontamination factor (DF) through the use of multiple passes, and permit monitoring of the efficiency of the trapping process. Operators can increase the processing time should the treated-gas activity remain unacceptably high. Additionally, they can temporarily stop the process to repair a defective component and then continue the treatment before releasing the gas to the environment.

Trapping and removal technology is most effective when designed for specific tasks. Additionally, technology effectiveness is enhanced when coupled with certain operating techniques. For example, lines and equipment should be evacuated repeatedly or flushed with inert gas or air and the effluent directed to the trapping system before proceeding with any dismantling. If feasible, air flushes should follow inert gas flushes to encourage the release of loosely bound tritium. Work should proceed in environments that are drier than the flush gas to minimize the moisture-stimulated release of tritium from surfaces. Plastic tents or temporary enclosures should be built around the equipment that will be maintained. The atmosphere from the tents or enclosures should be purged through the trapping system. Where routine maintenance is expected, separate maintenance gloveboxes with supporting trapping technology should be used to dismantle and decontaminate equipment. Materials, such as elastomeric O rings, have a high solubility for tritium and will release large quantities of tritium when removed from service. These items should be stored in small purged containers until they are packaged for land disposal.

Effluent from these containers may contain sufficient tritium to collect with trapping technologies.

All process exhausts should be monitored and, if necessary, treated before release to the stack. Typically, process exhausts represent the highest activity streams and make up the majority of the tritium chronically vented to the stack. The need for redundant isolation valves, or combinations of valves that are actuated by inline tritium monitors, should be reviewed. Where the potential for release is high, automated isolation valves should be installed.

Process loop volumes should be minimized, particularly in regions where tritium gas is susceptible to accidental release. Similarly, loop volumes that require frequent dismantling should be minimized. To achieve this, microwelding is preferred to demountable fittings; smaller-diameter tubing is preferred over 1/2-in. tubing; and 1/4-in. bellows sealed valves are preferred over 1/2-in. valves. The use of close-fitted enclosures over vulnerable components is preferred over the use of larger, more conventional gloveboxes to reduce the amount of atmosphere that need to be processed. Such designs, in turn, reduce the scale of the trapping technology required. In high specific activity applications, inert gas is preferred over air as a purge gas. Tritium gas can be captured without conversion to oxide and recovered for re-use.

Options for Tritium Capture

The tritium-capture technologies available for scrubbing tritium from gaseous effluents fall into two categories: (1) those used to treat air or inert gas containing air, and (2) those used to treat inert gas streams. The devices used to process these gaseous effluent streams and their relative placement in the treatment train are illustrated in Figs. 103.25 and 103.26.

1. Air Detritiation

Elemental tritium can be readily converted to oxide with hot copper oxide (CuO), Hopcalite,^(a) or a precious metal catalyst (Pd, Pt, etc.). Tritiated organic vapors are more difficult to oxidize than elemental tritium. CuO reactors need to operate at 750°C to promote hydrocarbon oxidation efficiencies greater than 50% with a gas residence time^(b) in the reactor exceeding 2 s. Hopcalite should be operated at 700°C to achieve complete oxidation of hydrocarbons at similar residence times. Palladium catalysts are more effective and achieve complete oxidation at 400°C. Occasionally, combinations of catalysts are used in the

^(a)Hopcalite is a commercially available mixture of MnO₂ and CuO.

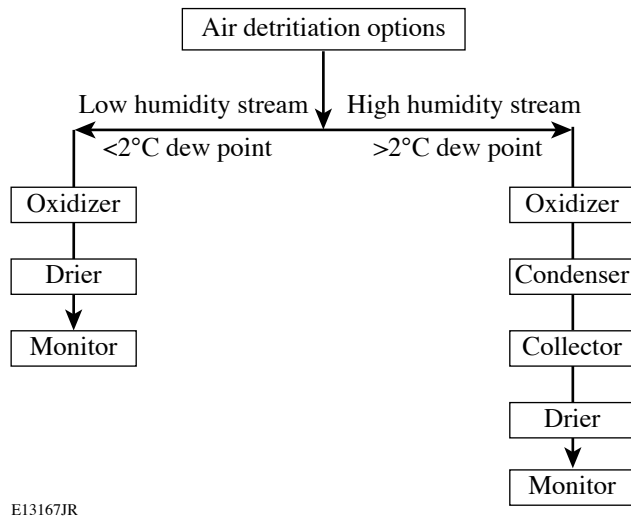
^(b)Gas residence time is the time required for a slug of gas to transverse the hot region of a reactor.

same oxidation system to ensure complete oxidation of tritiated hydrocarbon species. Additionally, the efficiency of oxidation decreases as the absolute concentration of hydrogen decreases. Hydrogen (protium) can be added in low concentrations to the effluent stream to raise the total hydrogen content in the stream and improve the oxidation efficiency.

In low-humidity applications and at low flow rates, the stream containing elemental tritium that has been oxidized

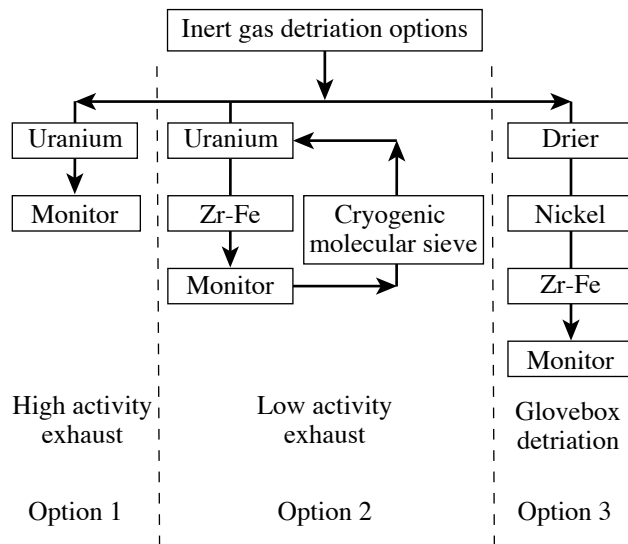
to tritiated water (HTO)^(c) enters the drier directly. The gas temperature leaving the oxidizer has sufficient time to return to room temperature. As the flow rate increases, however, the oxidizer effluent must be cooled with an air-to-air heat exchanger to prevent heating the molecular sieve above room temperature. Drier capacity and performance degrades with increasing temperature. In high-humidity applications, a condenser should be used to remove the bulk of the water vapor before directing the effluent stream to the drier. Drier capacity and performance also degrades with increasing water content in the drier.

Driers adsorb^(d) tritiated water vapor on the molecular sieve. Approximately 7% water by weight can be loaded on the driers^(e) before HTO breakthrough is observed. Dual-column drier systems permit continuous operation; while one drier is in service, the second can be regenerated.^(f) Purging the drier during regeneration in the flow direction opposite to that used during the normal operation improves the performance of the drier because the exit end of the drier is never exposed to the high concentrations of HTO that are present at the drier inlet. Smaller systems may use a disposable drying column to eliminate the need for regeneration and packaging the desorbed water for land disposal. These driers can be outfitted with high-integrity, quick-disconnect fittings to minimize effluent releases during replacement.



E13167JR

Figure 103.25
Devices used in air detritiation schemes.



E13168JR

Figure 103.26
Inert gas detritiation options depend on the target activity of the effluent and the intended application.

The detritiation schemes for the high- and low-humidity effluent streams are illustrated in Fig. 103.25. A dew point of 2°C typically distinguishes the boundary between the two humidity regimes. When the water vapor concentration in the effluent exceeds 2°C (of the order of 0.7% water content by volume in the carrier), water can be condensed out of the effluent stream on a chilled surface and collected in a tank. The attractiveness of the condensation step increases as the humidity in the effluent increases because the drier operating time between regenerations can be optimized by capping the dew point of the effluent entering the drier at or near 2°C.

^(c)In this document, tritiated water implies a mixture of H₂O and HTO. In HTO, one proton has been replaced with a triton.

^(d)Adsorption is a physical process by which water molecules bond to the surface of the molecular sieve without decomposing. During absorption, molecules decompose into their constituents and are incorporated into the bulk of the sorbing material.

^(e)A drier containing 5 kg of molecular sieve will collect approximately 350 ml of water before any tritiated water is observed at the outlet of the drier.

^(f)Regeneration is the process of removing adsorbed water by heating the molecular sieve and purging the drier with a very dry stream until the humidity of the purge gas at the drier exhaust drops below a target value, typically of the order of -80°C.

2. Inert Gas Detritiation

The options for detritiating inert gas streams are shown in Fig. 103.26. These options rely on the ability of elemental tritium to bind chemically with preactivated metal powder. The tritium concentration leaving one of these hydride-forming materials depends on the metal. In general, uranium finds utility within circulating process loops where exhaust concentrations up to 10 mCi/m³ can be tolerated. Zr-Fe alloy, on the other hand, is more suited to polishing effluent streams and has the ability to reduce effluent concentrations below ~50 μCi/m³.

Streams containing less than a few tens of parts per million (ppm) water vapor and/or organic species can be processed directly via option 1 or 2 without the need to dry or precondition the streams. Uranium will crack the incoming water vapor and modest quantities of hydrocarbons to form a uranium hydride/tritide, uranium oxides, and uranium carbides. The hydrogen can be released from the uranium metal thermally. However, the uranium oxide and carbides become irreversibly bound to the metal and represent a loss of hydrogen storage capacity and, ultimately, a reduction in the decontamination factor.^(g) Water vapor will also react readily with the Zr-Fe alloy to form oxides. Hydrocarbons, however, tend to pass through the Zr-Fe alloy without reacting,⁸ unless gas residence times exceed 10 s.

As the impurity content increases above a few ppm in the effluent stream, the oxides are more likely to passivate the reactive metal, making it incapable of capturing elemental hydrogen. In such cases, a nickel catalyst can be introduced upstream of the uranium and/or Zr-Fe beds to crack the hydrocarbons and the water vapor to form nickel carbides and oxides, respectively.⁷ The hydrogen/tritium produced by the decomposition of the hydrocarbons or the water vapor passes through the nickel bed and is collected by the Zr-Fe alloy. Streams with larger water vapor loads, such as glovebox atmospheres, may require driers upstream of the nickel catalyst to remove the majority of the water first. In these applications, the nickel bed polishes the discharge from the drier to further decrease the stream humidity and reduces the load on the downstream hydrogen getter.

A cryogenic molecular sieve bed^(h) can be added to the uranium/Zr-Fe circuit to facilitate *in-situ* regeneration of the

^(g)The decontamination factor is the ratio formed by dividing the inlet activity concentration by the outlet activity concentration.

^(h)Elemental tritium can be adsorbed on a molecular sieve at 77 K (-196°C), provided all traces of water vapor are removed from the surface of the molecular sieve.

Zr-Fe alloy. The regeneration entails transferring the tritium inventory from the Zr-Fe alloy to the cryogenic molecular sieve bed in a closed-loop operation and subsequently releasing the gas from the molecular sieve bed as a slug to the uranium. The intermediate step of transferring to the cryogenic molecular sieve bed is required to increase the elemental tritium partial pressure so that the uranium can absorb the gas.

Finally, the selection of one technological approach to trapping over another requires a considered evaluation by the end user, taking into account economic factors, intended end goals, and application. Although trapping technology for air applications tends to be somewhat more robust in that it is less likely to release its tritium inventory and less likely to be irreversibly damaged, that technology requires a significant investment in ancillary infrastructure if the tritium is to be reclaimed for re-use. Additional process loops are required to regenerate the drier and to collect and handle highly active water for either land disposal or for tritium recovery. In the latter case, the water must be decomposed in an electrolysis facility and the hydrogen transferred to an isotopic separation station for enrichment. On the other hand, metal beds are restricted to operate in inert gas streams. They can be destroyed with an unintentional ingress of air and release the entire resident tritium inventory during the accident. However, these metal beds capture elemental tritium directly and permit easy recovery of the gas for re-use. Metal beds avoid all issues related to water handling. Tritium enrichment, if required, can proceed directly after unloading the metal beds. In general, direct gas-capture systems are preferred over oxidation approaches in applications that

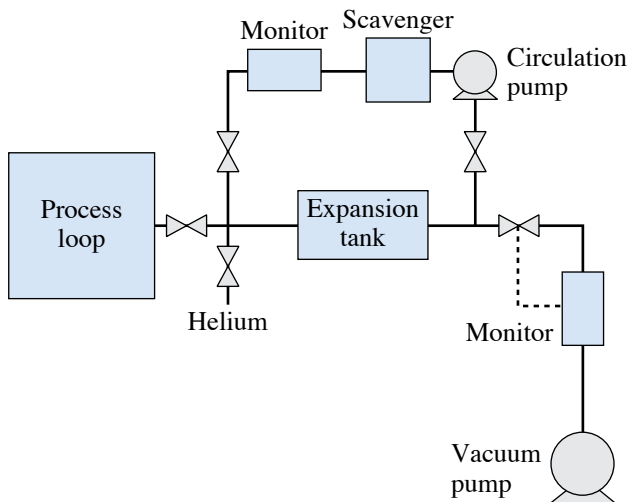
- require the recovery and re-use of elemental gas or
- lead to the production of high (>10 Ci/liter) specific activity water.

Direct gas-capture approaches can reduce gaseous emissions while simultaneously reducing the production of tritiated solid wastes that must be land disposed. Direct inert gas-capturing approaches simplify tritium recycling because these approaches eliminate the need to convert tritiated water to elemental hydrogen.

Typical Tritium-Capture Schemes

A configuration commonly used to reduce emissions from process loops is illustrated in Fig. 103.27. In this example, the tritium recovery subsystem comprising a tank, monitor, scavenger bed (or a train of scavenger beds if the makeup of the effluent dictates a more aggressive treatment), and isolation valves is installed between the process loop and the dry vacuum

pump.⁽ⁱ⁾ Instead of evacuating the process loop directly to stack or via a single scavenger bed in a once-through operation, the contents of the process loop are expanded into the pre-evacuated tank for treatment. The process loop is then isolated from the tritium recovery system. Helium gas pressurizes the tritium recovery system to raise the system pressure to one atmosphere. The contents of the expansion tank are circulated through the scavenger bed and the progress of detritiating the stream is monitored with an inline tritium process monitor. At a prescribed concentration, the contents of the subsystem are then evacuated to the stack, or flushed from the subsystem with clean helium and the tank subsequently evacuated in preparation for the next operating cycle. Purging the lines with helium is recommended because the inert gas flush reduces the potential of residual tritium lingering in the plumbing between the tritium recovery system and the stack. An accumulation in this plumbing can unexpectedly trip alarms during subsequent operations and mask the actual cause of the emission.



E13169JRC

Figure 103.27

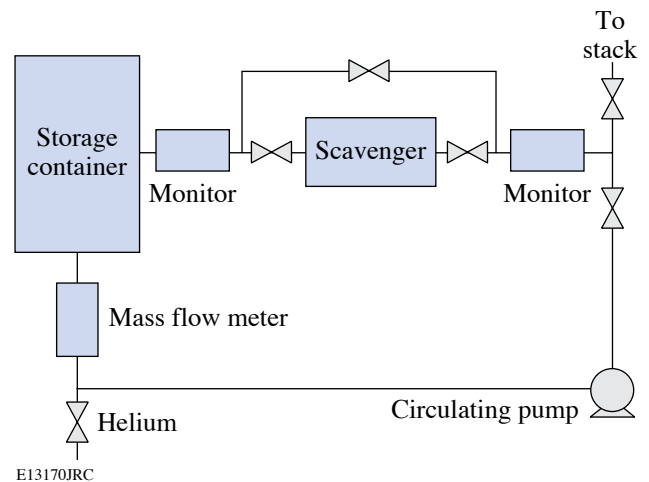
Incorporation of a simple cleanup subsystem into the exhaust of a process loop.

The second in-line tritium monitor between the vacuum pump and the treatment system is electronically coupled to the valve just upstream of the monitor. It automatically actuates the valve should the effluent activity exceed a predetermined level. Once the process loop has been isolated from the stack, an operator can intervene to rectify the fault, review the need

⁽ⁱ⁾Dry vacuum pump development in recent years has permitted the replacement of mechanical oil vacuum pumps. Pump characteristics of these dry pumps rival those attainable with oil pumps without the attendant problems of handling and containing tritiated oil.

for continued processing and, when ready, release the treated effluent to the stack. In effect, this monitor buys the operator time to make an informed decision.

Outgassing from tritiated components and tritium leaks from components represent common emission sources. Figure 103.28 illustrates an approach to capture the escaping tritium. This assembly comprises a container, a tritium scavenger bed, two in-line tritium monitors, a mass flow meter, a circulating pump, and a helium purge line. In this example, the leaky component is stored in the container. Tritium monitors track the effectiveness of the scavenger to capture the tritium. A low-throughput pump is ideal for this application. Although not shown, a nickel catalyst can be installed upstream of the Zr-Fe scavenger bed to protect the alloy from the trace water and modest amounts of air ingress. The nickel bed dramatically extends the life expectancy of the Zr-Fe alloy.



E13170JRC

Figure 103.28

Tritium reclamation subsystem for leaky components.

A typical scheme for capturing tritium from an air stream is illustrated in Fig. 103.29. This subsystem comprises an oxidizer, an air-to-air heat exchanger, a drier, and an in-line tritium monitor. Elemental tritium entrained in the stream is converted to oxide and collected in the drier. Although air can be used as a purge gas, it should be predried to reduce the inactive water load delivered to the drier and extend the operating time between regenerations. Drying the air purge also reduces the isotopic dilution of the tritiated water should tritium recovery for re-use be planned.

This configuration can be readily modified to accommodate the high-humidity (HH) streams described in Fig. 103.25 by

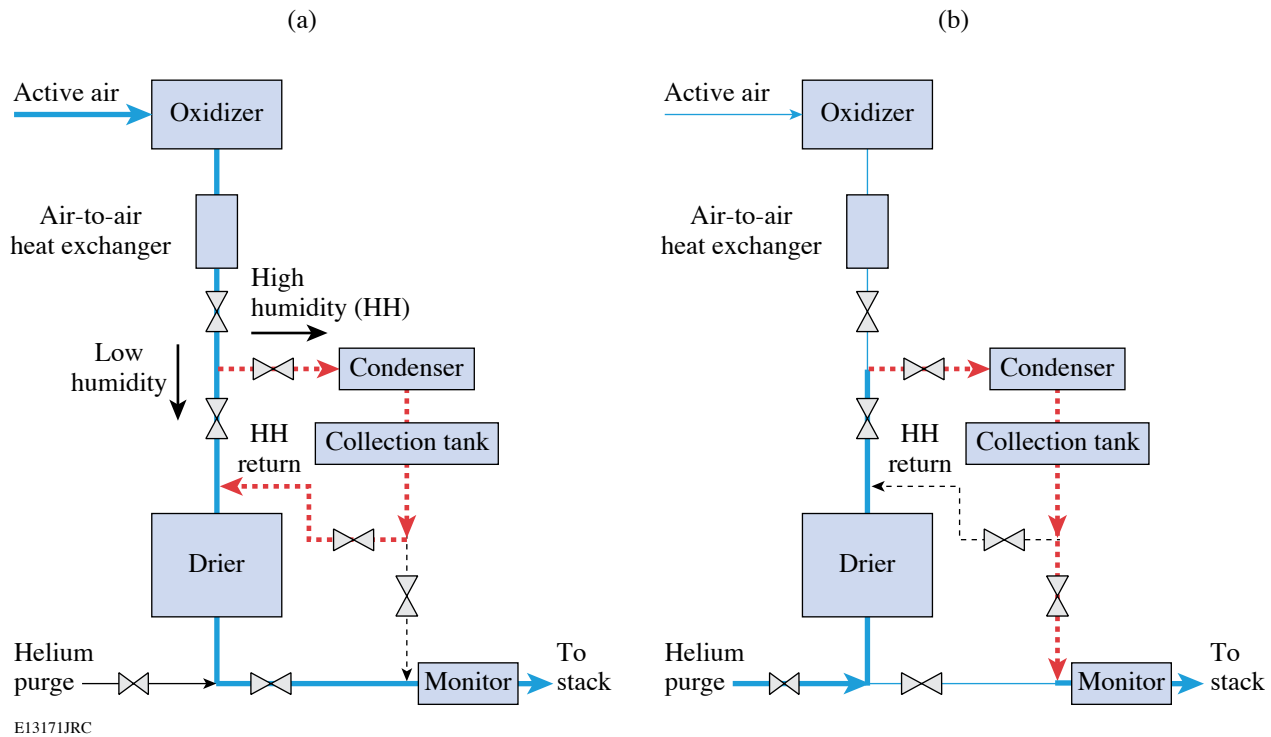


Figure 103.29
Simple air detritiation subsystem.

plumbing the system so that a condenser is used for both precipitating water vapor from the effluent stream [as shown in Fig. 103.29(a)] and for *in-situ* regeneration.

During regeneration, the helium^(j) purge would enter the exhaust end of the drier and flow through the condenser and the collection tank to the stack, as shown in Fig. 103.29(b).^(k) A second (polishing) drier could be installed downstream of the collection tank (not shown in the figure) to suppress any emissions from regeneration. System designers have the option of operating the regeneration circuit in the “once-through” mode, as shown in Fig. 103.29, or in a circulation mode by redirecting the helium flow back to the drier being regenerated.

The condensate can easily exceed several Ci/liter and requires caution when handling. The condensate can be immobilized for land disposal or packaged for shipment to a facility for tritium recovery.

^(j)Nitrogen or dry air can replace helium as a purge gas in this application.

^(k)The regenerating gas flow should be counter to the normal direction of operation so that HTO buildup near the driver exhaust is prevented.

Description of the Components used for Tritium Capture

Devices used for extracting tritium from flowing gas streams and their general integration in process loops have been described in the previous sections. This section discusses the strengths and weaknesses of the devices.

1. Uranium Scavenger Beds

Depleted uranium has a long-standing history in tritium service. This metal is used to store tritium, transport tritium gas, and, in special applications, selectively remove tritium from flowing gas streams. Designs that provide access into the uranium via a single line are the safest. They prevent the uranium from releasing its tritium inventory, even when accidentally exposed to air.^{11,12} Additionally, only a fraction of the uranium will be oxidized during the air ingress. However, helium-3 produced by tritium decay will interfere with the ability of uranium to store tritium. “Flow-through” designs are commonly used in process loops to mitigate the “helium-blanketing” effect even though these designs pose a greater risk to releasing tritium during an accidental air ingress.

Uranium offers a very high storage capacity; 120 standard cubic centimeters (scc) of gas per gram of uranium can be

easily accommodated without compromising the reaction kinetics.^{13–15} It is well-suited to removing tritium from clean inert gas streams containing high tritium concentrations and offers uniform reaction kinetics over a very broad range of tritium-to-uranium (T/U) atom ratios.¹⁶ It is possible to charge uranium with tritium up to an atom ratio of nearly three tritium atoms per uranium atom although the operating range is usually restricted to a ratio of 1.5 so that sufficient tritium storage capacity remains for unforeseen events.

Tritium gas reacts with the uranium to form a uranium tritide. This chemical compound is stable at room temperature. Heating the uranium tritide will release the tritium as a gas. The reaction is fully reversible. The pressure-composition isotherms for the uranium–tritium system are very simple.¹⁷ In the range of primary interest, i.e., at operating pressures below approximately 1.5 atm and at temperatures between 20°C and 450°C, the initiation of the tritide phase begins at T/U ~ 0.1 and is complete at T/U ~ 2.93. The plateau region between these two extremes is essentially flat. As a result, the temperature of the uranium tritide uniquely specifies the tritium gas pressure above the uranium powder. At 430°C, for example, the tritium gas pressure over uranium powder will be 1 atm. Caution is required when increasing the temperature much beyond 425°C; the pressure increases rapidly and can overpressurize the device containing the uranium. The equation

$$P = 10^{(-4590/T + 9.39)} \text{ (Torr)} \quad (1)$$

prescribes the pressure over the temperature range of 150°C to 600°C. In this equation, the pressure (P) is in Torr and the temperature (T) is in Kelvin.

The reaction rate to form tritide is dramatically enhanced by preconditioning the uranium. The uranium metal is charged to capacity with hydrogen gas to form UH_3 and subsequently unloaded by heating the UH_3 to 425°C in a vacuum. The hydrogen loading/unloading cycle should be repeated seven times to break down the uranium metal to its optimum size. This process, known as decrepitation, increases the surface area of the uranium by breaking down the bulk uranium metal into a fine powder with a particle distribution in the range of 0.1 to 10 μm . Following the last unloading, any residual hydrogen can be removed from the uranium by repeating the loading/unloading one additional time using isotopically downgraded tritium.

Uranium scavenger beds differ from storage devices in three ways. First, they require the carrier stream to flow through the container. Second, they operate at T/U ratios below 1 to

enhance the detritiation factor (DF). Third, they are typically constructed from larger diameter containers to reduce the carrier molar flux⁽¹⁾ in the container. The equation¹⁸

$$G^{1/2} \log(\text{DF}) = 0.019 - 0.006 (T/U) \quad (2)$$

relates the DF to the T/U for T/U ratios up to 2.5 and carrier molar fluxes (G) up to 2.5 mol/m²/s. This equation assumes an impurity-free carrier and a uranium operating temperature of 22°C.

Two conditions can deteriorate the performance of these devices. Impurities will coat the uranium powder surface and reduce the amount of uranium available for removing tritium from the carrier. Secondly, increasing the uranium temperature will increase the tritium partial pressure over the uranium and lower the DF.

Figure 103.30 illustrates the lowest tritium concentration attainable over uranium as a function of temperature. Inspection of this figure is instructive for two reasons: it demonstrates how rapidly the DF will deteriorate with increasing temperature, and it illustrates that the lowest attainable tritium concentration in a carrier stream possible at room temperature with a uranium scavenger bed will be in the 10 mCi/m³ range.

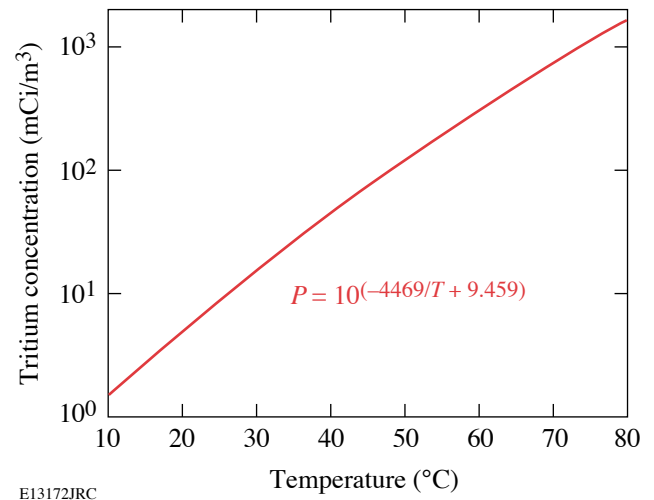


Figure 103.30
Tritium concentration dependence on uranium powder temperature.

⁽¹⁾The molar flux of the carrier is the number of moles of carrier flow per unit time and per unit cross sectional area of container perpendicular to the flow direction. It is usually expressed as mol/m²/s.

Increasing the uranium temperature twofold, from 20°C to 40°C, decreases the DF tenfold. Operating a uranium scavenger bed at 25°C precludes reducing the tritium activity of a carrier below 10 mCi/m³.

Unconfined uranium powder oxidizes spontaneously when exposed to air. Undoubtedly, the term “pyrophors,” used in the radioluminescent industry when referring to uranium storage beds, reflects some historic incident related to the propensity of the powder to ignite. Confined uranium powder, however, has a limited reaction with air, particularly if the container uses a low-porosity stainless steel filter to prevent uranium powder from migrating out of the device. In general, these devices will lose approximately 30% of their storage capacity and will not release their tritium inventory during an air ingress accident. Uranium tritide is the most secure tritium storage vehicle available to the tritium community, including any accident scenario involving air ingress not involving a flow-through configuration, i.e., a construction that permits air to enter via one port only and then becomes “dead-headed.”

Flow-through devices, both for storage and scavenging applications, are used to preclude helium blanketing. Blanketing occurs when decay-helium interferes with the bulk flow of tritium gas to the uranium powder. During blanketing, the rate of gas transfer from a vessel to the uranium powder stalls before all the tritium has had an opportunity to transform into a tritide. The balance of the tritium in the process system volume, however, can be captured on the uranium powder by circulating the remaining gas over the powder to dislodge the helium cover. Any air ingress during circulation will completely and rapidly oxidize and nitride the uranium with a concomitant release of the entire resident tritium inventory to the carrier downstream of the device. Flow-through operations represent the single most likely action that can precipitate a significant tritium release. Extreme care must be exercised during flow-through operations. Housing the process equipment in an inert environment is a very effective way of preventing the accidental ingress of air during circulation.

2. Zr-Fe Scavenger Beds

A Zr-Fe alloy developed by SAES Getters under the trade name ST198 can also be used to scavenge tritium from gas streams.¹ The alloy can be used in conjunction with noble gas carriers and nitrogen gas streams, albeit there is a gradual loss of capacity with time as the elements of the alloy nitride.⁵ As with uranium metal, the alloy spontaneously forms a tritide when exposed to elemental tritium; the reaction is reversible. The alloy must be heated to 550°C for the tritium recovery

and has a moderate storage capacity for tritium, typically of the order of 0.8 scc of gas per gram of alloy.

The nominal operating temperature for ST198 is 350°C. Decreasing the operating temperature increases the storage capacity for tritium gas. Decreasing the operating temperature also decreases the tritium partial pressure over the alloy, thereby improving the DF. However, the reaction kinetics and the tolerance of the alloy to any impurities entrained in the carrier also decrease with decreasing temperature. Additionally, the modest ability of the alloy to crack organic volatile species decreases. Operating above 300°C strikes a reasonable balance between the various competing factors. At 350°C, excellent tritium scavenging properties are exhibited by ST198 in noble gas streams, provided the gas residence time in the reactor exceeds 3 s.

Scavenging tritium from a nitrogen environment requires special attention. The alloy exhibits good scavenging properties in nitrogen at 350°C. The reaction kinetics between the alloy and nitrogen are slow at this temperature; however, the rate of nitriding increases noticeably at alloy temperatures above 400°C. The alloy is unusable at 500°C in the presence of nitrogen. Operating conditions that momentarily spike the alloy above 500°C can lead to a runaway nitriding condition. The alloy will react vigorously with the nitrogen cover gas to release approximately 600 kJ per mole of gas consumed. This energy will heat the alloy to very high temperatures and desorb the entire tritium inventory from the alloy. For example, a sudden ingress of 20-scc air into the nitrogen carrier stream could precipitate such a runaway condition unless the alloy temperature is monitored and the flow stopped whenever the alloy temperature exceeds 400°C in nitrogen. Nitriding ST198 is irreversible and will decrease the capacity of the bed.

The pressure-composition isotherm for the Zr-Fe alloy/hydrogen system is considerably more complex than the uranium/hydrogen system. A single tritide phase does not exist for the Zr-Fe alloy/hydrogen system. The elemental gas pressure over the alloy depends on both the resident tritium inventory of the alloy and the operating alloy temperature. The relationship between tritium pressure P in Torr, the resident inventory Q in Torr-liters/g, and the alloy temperature T in Kelvin is given by the equation

$$P = Q^2 * 10^{(-6220/T + 5.03)}. \quad (3)$$

Inspection of Fig. 103.31 reveals that operating at 350°C will reduce the activity of a carrier below 20 μ Ci/m³, provided

the resident inventory remains below approximately 100 mCi/g of alloy. In practice, this target is difficult to attain except for the first few operating cycles of the alloy. Typically, this alloy is used to reduce carrier stream activities below 400 to 500 $\mu\text{Ci}/\text{m}^3$, suggesting that the resident inventory of the ZrFe reaches approximately 500 mCi/g.

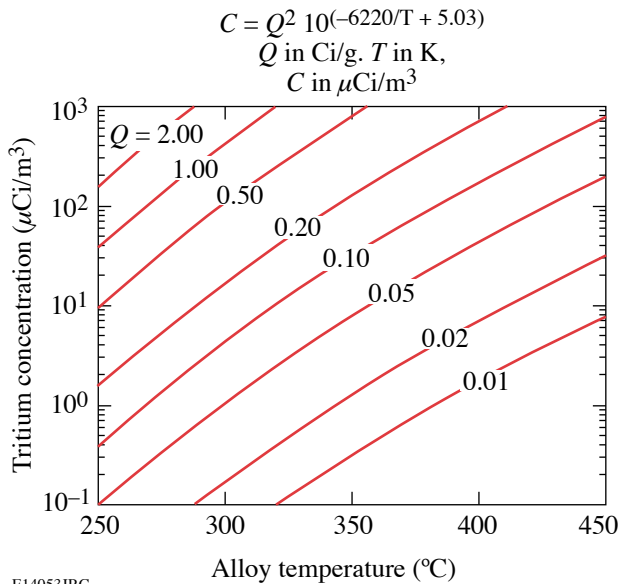


Figure 103.31
Tritium concentration dependence on resident inventory and ST198 alloy temperature.

The alloy is suitable for treating effluent streams that will be discharged to the stack. Examples include treating effluents evacuated from process loops, polishing effluent streams that have passed through uranium scavenger beds, and tritium recovery from gloveboxes using nitrogen or helium cover gases.

Impurities are decomposed at the alloy surface to form tritides, hydrides, oxides, and carbides. The latter two compounds represent an irreversible chemical reaction with the alloy that reduces its capacity for tritium storage. If the impurity flux to the alloy exceeds the impurity-clearing rate^(m) from the alloy surface, the scavenging performance of the alloy will degrade with time. To recover the tritium-capture efficiency, either the incoming impurity flux needs to be reduced or the operating temperature of the alloy must be increased so that the oxides and carbides can diffuse into the alloy bulk more quickly. In

^(m)Impurities bind chemically to the alloy surface as oxides or carbides of iron or zirconium. Gradually, the oxygen and carbon molecules diffuse into the alloy bulk where they continue to remain bound as oxides or carbides. In the process, the surface reactivates itself and can adsorb elemental hydrogen once again.

both cases, however, the alloy will be consumed at an accelerated rate.

Preconditioning the effluent stream reduces or eliminates alloy consumption. Water vapor can be removed with driers; hydrocarbons can be decomposed on nickel powder. The alloy, drier, and nickel reactor can be regenerated and re-used. ST198 scavenger beds protected by driers and nickel beds in high impurity load applications, such as glovebox atmosphere clean-up service, have demonstrated continued long-term service at LLE without noticeable deterioration in performance over several years.

3. Molecular Sieve Driers

Many aspects of these driers have been discussed throughout this document. The following description highlights some of the salient features of these driers.

Driers based on zeolites, particularly 4A and 5A molecular sieves, are widely used in the tritium community to remove moisture from both noble-gas and air-bearing carrier streams. Typically, these devices operate at room temperature and provide upwards of seven weight-percent storage capacities without exceeding an exhaust dew point of -40°C . Water vapor is adsorbed on the zeolite; hydrogen and organic volatile species tend not to condense in significant amounts on the zeolite. The usefulness of the driers in removing tritiated water vapor from air streams has been discussed in **Options for Tritium Capture** (p. 144) and **Typical Tritium-Capture Schemes** (p. 146).

Water vapor from the atmosphere represents a considerable impurity burden on the hydride-forming materials. For example, water vapor from the atmosphere permeating through gloves into a two cubic meter glovebox with eight standard glove ports can easily accumulate 100 ml of water per month. Without drying the stream, an entire reactor containing 5 kg of Zr-Fe alloy would be oxidized within one year.

As previously discussed, driers should be regenerated in counter-flow, that is, in the opposite direction to normal use. Tritiated water vapor that migrated through the drier to the exhaust end during normal usage is pushed back toward the entrance side of the drier during the counter-flow regeneration. This regeneration philosophy improves the detritiation efficiency of the drier during normal service.

Typically, molecular sieve driers are regenerated between 300°C and 350°C . Progress in regenerating a drier can be

monitored by measuring the temperature of the purge gas leaving the drier. During the early phase of a regeneration cycle, the gas temperature leaving the drier will remain at, or close to, room temperature, even though the drier shell is fixed at 350°C. Most of the energy delivered to the molecular sieve by external band heaters clamped to the drier shell or by heated purge gas is used to desorb the water from the molecular sieve. Once the majority of the water has been released and purged from the drier, the temperature of the exhaust gas will gradually increase to the regeneration temperature. To thoroughly void the drier, the regeneration cycle should continue an additional 5000 volume exchanges of the drier, while the exhaust gas is at the regeneration temperature.

4. Cryogenic Molecular Sieve

The earliest application of cryogenic molecular sieves⁽ⁿ⁾ was to separate hydrogen isotopes by gas–solid chromatography for the purpose of analyzing isotopic mixtures of elemental hydrogen.¹⁹ Since that time, a variety of isotopic separation systems have been developed to selectively recover tritium from the other hydrogen isotopes.²⁰

As temporary storage devices, however, cryogenic molecular sieves have found limited general utility in the tritium community. Nevertheless, these devices offer unique service in specialized applications, namely as short-term traps to capture tritium gas from a carrier and as tritium gas concentrators. For example, without the concentration step provided by the cryogenic molecular sieve, tritium could not be transferred to uranium from Zr-Fe except at high tritium partial pressures. At a concentration of 1 mCi/m³, elemental tritium will pass through the uranium powder without reacting. At 77 K, the molecular sieve can condense hydrogen on its surfaces to reduce the hydrogen partial pressures in the carrier into the 10⁻⁶ to 10⁻⁵ torr range and release the hydrogen at a partial pressure of several mTorr when heated to 150 K. As a consequence, tritium can be released from a Zr-Fe reactor at an activity of 1 mCi/m³, accumulated on a cryogenic molecular sieve, and released as a slug of gas at concentrations exceeding 1 Ci/m³ at 150 K.

Figure 103.32 illustrates the transfer of tritium gas from ST198 alloy to a cryogenic molecular sieve. Helium gas exits from hot ST198 alloy, flows through a cryogenic molecular sieve, and returns to the ST198 alloy. In this example, the carrier activities at the ST198 exhaust and the cryogenic exhaust are monitored as a function of time. The activity at the ST198

exhaust varies with the temperature of the alloy and is seen to increase as high as 810 mCi/m³. The activity of the helium gas leaving the cryogenic molecular sieve remains below 50 μCi/m³, the sensitivity level of the in-line ionization chamber. At 88 min into the operation, tritium breaks through the molecular sieve and the activity of the gas leaving the cryogenic molecular sieve increases rapidly, albeit in the low mCi/m³ range. The hydrogen content leaving the ST198 was not measured in this test. These tests demonstrate the excellent performance of the cryogenic molecular sieve trap to decontaminate the carrier stream, attaining DF's up to (750/0.5) 1500 in a single pass. This figure of merit is conservative since the presence of hydrogen was not included in the estimate.

At 77 K, tritium gas is resident on the cryogenic molecular sieve for a finite time and will slowly migrate toward the exhaust end of the bed. The transport rate from bed entrance to exhaust depends on the carrier flow rate, resident tritium inventory, resident hydrogen inventory, and the quantity of polar impurities adsorbed on the zeolite. Capacities of the order of 100 scc of elemental gas per gram of molecular sieve can be achieved on conditioned molecular sieve.

In a second example, a cryogenic molecular sieve can be used to capture the accidental release of elemental tritium from a process loop. In this case, the majority of the tritium may be held up on a cryogenic molecular sieve for 1 or 2 h before migrating through the bed. During this time, an operator can rectify the problem and return the gas directly to a storage bed.

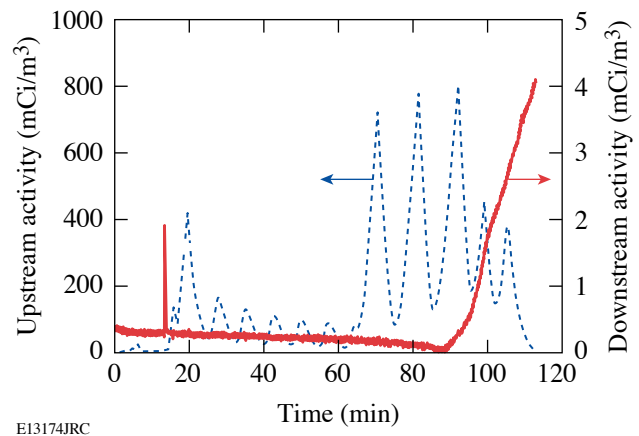


Figure 103.32

Comparison of tritium activities upstream and downstream of a cryogenic molecular sieve bed during the regeneration of a Zr-Fe bed. Helium carrier flow rate is 28 sLPM.

⁽ⁿ⁾Cryogenic molecular sieves operate at 77 K.

Cryogenic molecular sieve beds can be regenerated in steps to release different tritiated species. By raising the molecular sieve temperature from 77 K to 150 K, the elemental tritium gas will be released. Increasing the temperature further to 350°C will release all other bound impurities. Elemental tritium can be directed to one treatment process while impurities can be directed to a second treatment process.

These devices have several limitations. They are restricted to operate in helium purge streams, and the residence time on the molecular sieve is limited. Cryogenic molecular sieve beds behave more like capacitors than storage devices. They are not passively safe in that liquid nitrogen is needed to hold the tritium gas in place. There is limited experience with these devices in the tritium community for the applications discussed. Despite these limitations, however, cryogenic molecular sieve beds will fill a unique application in tritium-handling systems in the coming years.

Throughput and Construction Guidelines

The capture technology discussed in this article is intended for small-scale operations, typically required to operate between 10 standard liters/min (sLPM) to 60 sLPM with a focus on treating the emission as close to the source as feasible. Flow rates in the 10-sLPM range are suitable to a variety of process loops. Flow rates in the 60-sLPM range are more suited to glovebox cleanup applications. Table 103.III lists the approximate size of each capture device for these two throughput extremes and for three applications.

All heated devices must be rated to withstand elevated pressures, that is, they must be rated as pressure fittings. These devices must be constructed in shops qualified to build pres-

sure vessels. The vessels must be helium leak-tight to 1×10^{-9} atm-cc/s when exposed to 1 atm of helium. The valves should be bellows-sealed and use a copper or stellite stem tip. Where valve actuation will be automated, VESPEL^{®(o)} stem tips can be used, although these will require routine replacement. Stainless-steel frits should be integrated into device designs to prevent particulate transport into the process loop or the exhaust line.

Double containment can be used for devices that are expected to operate at an elevated temperature, such as uranium storage beds, where tritium permeation can be problematic. Doubly contained devices provide a secondary shell around the primary vessel. Heaters and thermocouples are attached to the primary vessel, and vacuum feed-throughs are used to access the heaters and thermocouples. The annular region between the primary and secondary vessels is evacuated and maintained under vacuum during operation. Periodically, the region is pumped to recover any tritium that has permeated into the interspace. Doubly contained devices release less tritium by permeation and consequently reduce the spread of surface contamination in the vicinity of the device. Additionally, these devices reduce heat loads in confined spaces such as gloveboxes. However, double-containment devices can easily cost twice that of single-containment device.

Uranium scavenger beds require manufacturing shops knowledgeable in handling and conditioning uranium. These facilities must be licensed to receive and handle bulk uranium metal. Manufacturing Zr-Fe and nickel beds requires caution to ensure the getter material is not accidentally oxidized during the manufacturing process.

Table 103.III: Size of the devices (in kilograms) used for three different detritiation applications.

Device	Application		
	Effluent treatment system without air ^(a)	Glovebox cleanup system using helium ^(b)	Detritiation system for high-humidity air streams ^(b)
Oxidizer	Not used	Not used	1
Drier	Not used	3	5
Nickel bed	1 ^(c)	1.5	Not used
Uranium bed	1	Not used	Not used
Zr-Fe bed	3	5	Not used

^(a)A volumetric flow rate below 10 sLPM is assumed.

^(b)A volumetric flow rate of 60 sLPM is assumed.

^(c)The quantity of material used in each device reflects the overall size of the capture devices.

^(o)VESPEL[®] is a polyimide with good stability under radiation exposure.

Conclusion

Significant developments in tritium-capture technology for both air and inert gas streams have occurred over the past two decades. Tritium removal from air streams requires the oxidation of elemental tritium and the collection of the tritiated water on driers; recovery from inert streams can also use the oxidation. Alternately, metal getter technology can be used to detritiate inert gas streams by collecting elemental tritium directly without the oxidation step.

Direct elemental tritium recovery offers several advantages. Elemental tritium is significantly less hazardous to handle than tritium oxide. In some cases, the elemental tritium can be returned to the original storage device for re-use. Oxidation technology tends to be more robust; however, unless special infrastructure is installed, oxidized tritium is a waste stream destined for land disposal. Each tritium-capture application should be carefully evaluated to assess the merits and drawbacks of oxidation against direct elemental recovery before selecting a capture technology.

Capture technology does not provide magical “bolt-on” solutions to process systems that suffer from chronic or repeated accidental releases. Rather, this technology must be integrated with the operation of the process systems. Both the process systems and the capture technology need to be configured for reliable, fail-safe operation. For example, circulating closed-loop capture subsystems are preferred to once-through subsystems. Process loop exhaust lines to the stack should be monitored for activity and interlocked with valves that automatically isolate the system from discharging tritium to the stack above predetermined limits.

Economics favors small-scale systems. Emissions should be treated as close to the source as possible, certainly before any significant dilution with air or inert gas occurs, as the first step in reducing the size of the capture equipment. Distributed capture subsystems are preferred to one large clean-up system attached to the stack; the former costs significantly less. Additionally, releases in one process do not impact the operation of other processes.

ACKNOWLEDGMENT

This work was supported by the U.S. Department of Energy Office of Inertial Confinement Fusion under Cooperative Agreement No. DE-FC52-92SF19460, the University of Rochester, and the New York State Energy Research and Development Authority. The support of DOE does not constitute an endorsement by DOE of the views expressed in this article.

REFERENCES

1. C. Boffito *et al.*, *J. Vac. Sci. Technol.* **18**, 1117 (1981).
2. C. Boffito, F. Doni, and L. Rosai, *J. Less-Common Met.* **104**, 149 (1984).
3. P. Manini *et al.*, *Vuoto Sci. Tecnol.* **XX**, 299 (1990).
4. W. T. Shmayda, N. P. Kherani, B. Wallace, and F. Mazza, *Fusion Technol.* **21**, 616 (1992).
5. K. J. Maynard, N. P. Kherani, and W. T. Shmayda, *Fusion Technol.* **28**, 1546 (1995).
6. W. T. Shmayda and N. P. Kherani, *Fusion Eng. Des.* **10**, 359 (1989).
7. A. B. Antoniazzi and W. T. Shmayda, *Fusion Technol.* **30**, 879 (1996).
8. W. T. Shmayda, in *Safety in Tritium Handling Technology*, edited by F. Mannone, Nuclear Science and Technology, Vol. 1 (Kluwer Academic Publishers, Dordrecht, The Netherlands, 1993), pp. 23–52.
9. H. Brunnader, W. T. Shmayda, D. R. Harding, L. D. Lund, and R. Janezic, *Fusion Sci. Technol.* **41**, 840 (2002).
10. A. Nobile, H. Reichert, R. T. Janezic, D. R. Harding, L. D. Lund, and W. T. Shmayda, *Fusion Sci. Technol.* **43**, 522 (2003).
11. G. R. Longhurst, A. G. Heics, and W. T. Shmayda, *Fusion Technol.* **21**, 1017 (1992).
12. G. R. Longhurst and W. T. Shmayda, *Fusion Eng. Des.* **2**, 812 (1989).
13. W. T. Shmayda and P. Mayer, *J. Less-Common Met.* **104**, 239 (1984).
14. N. P. Kherani and W. T. Shmayda, in *Proceedings of the Seventh Annual Conference* (Canadian Nuclear Society, Toronto, Ontario, Canada, 1986), pp. 232–236.
15. N. P. Kherani, W. T. Shmayda, and A. G. Heics, *Z. Phys. Chem.* **164**, 1421 (1988).
16. W. T. Shmayda, N. P. Kherani, and A. G. Heics, *J. Vac. Sci. Technol. A* **6**, 1259 (1988).
17. W. M. Mueller, J. P. Blackledge, and G. G. Libowitz, *Metal Hydrides* (Academic Press, New York, 1968).
18. W. T. Shmayda and N. P. Kherani, *Fusion Eng. Des.* **10**, 359 (1989).
19. P. L. Gant and K. Yang, *Science* **129**, 1548 (1959).
20. C. H. Cheh, *J. Chromatography A* **658**, 283 (1994).

All-Solid-State, Diode-Pumped, Multiharmonic Laser System for Timing Fiducial

Introduction

Laser timing fiducial signals are required as a timing reference for numerous laser and target diagnostics for inertial confinement fusion experiments. On OMEGA, infrared as well as visible and ultraviolet timing fiducial signals are needed to match the wavelength sensitivity of various diagnostics. Currently, a flash-lamp-pumped Nd:YLF/Nd:glass laser system operating at 1053 nm with frequency conversion to the second and fourth harmonics (527 and 264 nm) is used.¹ The system consists of a Nd:YLF master oscillator; a pulse-shaping system; a flash-lamp-pumped Nd:YLF regenerative amplifier; a Nd:glass, large-aperture ring amplifier; and frequency-conversion crystals. This fiducial laser system has a complicated design, a low repetition rate, low harmonic conversion efficiency, high maintenance because of flash-lamp pumping, and occupies a 5×14 -ft optical table and a rack of electronics. We present an all-solid-state, diode-pumped, compact laser fiducial system that satisfies all OMEGA requirements, reduces the system complexity, and improves reliability while significantly reducing the space requirements.

Fiducial Laser System Requirements

The OMEGA fiducial laser system must produce a 3.5-ns comb of 200-ps FWHM optical pulses separated by 0.5 ns at IR, green, and UV wavelengths. A Nd:YLF laser system with second and fourth harmonic generators is used to produce IR, green, and UV fiducial signals. The amplitude variation of each pulse in the comb must not exceed 50% of the maximum. The required IR/green comb energy is 1 mJ. The most critical requirements for the fiducial system are 10-mJ energy at UV (4ω) fiducial and a stable time delay (~ 165 ns) between the IR/green and UV fiducials.

High-UV fiducial energy is required because of low photocathode sensitivity for the x-ray streak cameras employed as important OMEGA target diagnostics. A UV multimode fiber delivery system is used to couple fiducial combs into the diagnostics. The required UV energy is 10 μ J at the output of a fiber launcher. OMEGA needs up to 19 channels of UV

fiducial; therefore, a 19-fiber bundle is used to launch the UV comb into the delivery fibers. To provide equal energy distribution and misalignment insensitivity for the fiber-bundle launcher, a UV fiducial beam must significantly overlap the 19-fiber bundle, bringing the total UV comb energy required to 10 mJ. Frequency-conversion efficiencies of 50%–75% for both second and fourth harmonic generation have been demonstrated;² therefore, the required IR energy should be in the 20- to 40-mJ range.

The relatively long delay between UV and IR/green fiducials is dictated by the physical location of various OMEGA diagnostics. IR/green fiducials must be generated ~ 165 ns before the UV comb to provide the simultaneous arrival of the fiducials to all OMEGA diagnostics. A 165-ns delay line is required between the IR/green and UV fiducial fiber launchers.

Laser System Description

A block diagram of the proposed system is shown in Fig. 103.33. The system is seeded by a shaped comb produced by a pulse-shaping system.³ A single-frequency, diode-pumped Nd:YLF OMEGA master oscillator (OMO)⁴ produces a 20-ns square pulse for shaping. The first integrated optics modulator is driven by the 24th harmonic of the 38-MHz OMEGA master-timing RF source. The second modulator is driven with a gate pulse that is precompensated for pulse-shape distortion caused by gain saturation in the amplifiers and gates an eight-pulse fiducial comb. A Nd:YLF OMEGA diode-pumped regenerative amplifier (ODR)⁵ boosts the comb energy from tens of picojoules to ~ 4 mJ, the main portion of which is used as an IR fiducial and for generating a green fiducial.

An additional ODR is added to the system to provide the required 165-ns delay with a small footprint and without beam degradation. At the same time, it produces the additional gain required to achieve the UV energy specification. A portion of the ODR output is used to seed the second regenerative amplifier designated ODR+. A double-pass, diode-pumped amplifier provides additional gain and is discussed further in **Two-Pass**,

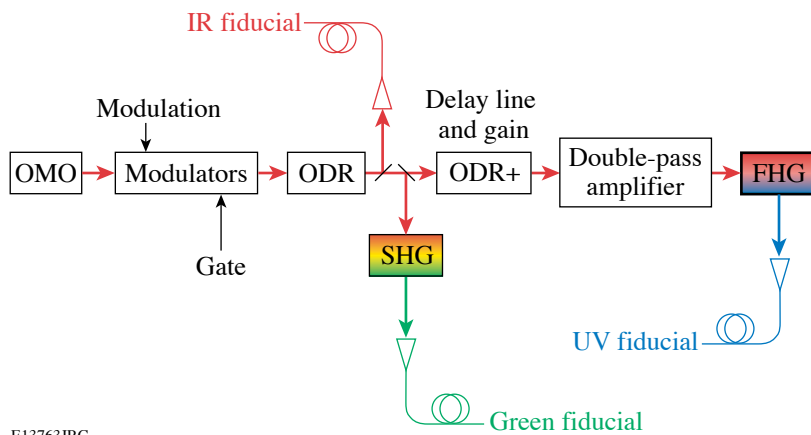


Figure 103.33

A block diagram of the proposed OMEGA fiducial laser system. OMO is the OMEGA master oscillator, ODR is the OMEGA diode-pumped regenerative amplifier, SHG and FHG are the second and fourth harmonic generators. The ODR, seeded by a pre-compensated fiducial comb, produces IR and green fiducial signals. ODR+ provides the necessary delay between IR/green and UV fiducials.

E13763JRC

Diode-Pumped Nd:YLF Amplifier. Second-harmonic generation (SHG) and fourth-harmonic generation (FHG) are realized with BBO (beta-barium borate) crystals.

The ultraviolet pulses are launched into a bundle of 19 UV fibers to distribute UV fiducials to various OMEGA diagnostics.

Two-Pass, Diode-Pumped Nd:YLF Amplifier

The double-pass amplifier must produce 20 to 40 mJ of output energy in IR. Amplifier efficiency has to be estimated for the appropriate pump power choice. Amplifier efficiency includes (a) pump energy to active-element upper-state energy-conversion efficiency and (b) upper-state energy to amplifier output conversion efficiency.⁶ Typical efficiencies for a Nd:YLF amplifier pumped by a fiber-coupled diode array through a dichroic mirror are

- Pump re-imaging optics transmission: 0.94
- Dichroic mirror transmission: 0.93
- Pump absorption: 0.8
- Quantum efficiency: 0.72

Pump energy to upper-state energy-conversion efficiency: 0.5.

Storage efficiency is calculated as follows:

$$\eta_s = \left[1 - \exp(-t_p/t_f) \right] / (t_p/t_f),$$

where t_p is the pump-pulse width and t_f is the active medium fluorescence lifetime. In the case of diode pumping, when the pump-pulse shape and wavelength do not change with the pulse duration increase, it is beneficial to make the pump pulse longer to increase the total stored energy. For Nd:YLF with $t_f = 0.5$ ms, a 1-ms pump pulse is used.

- Storage efficiency: 0.43
- Beam overlap efficiency: 0.75
- ASE loss: 0.05
- Gain extraction efficiency: 0.95

Upper-state energy to amplifier output conversion efficiency: 0.29

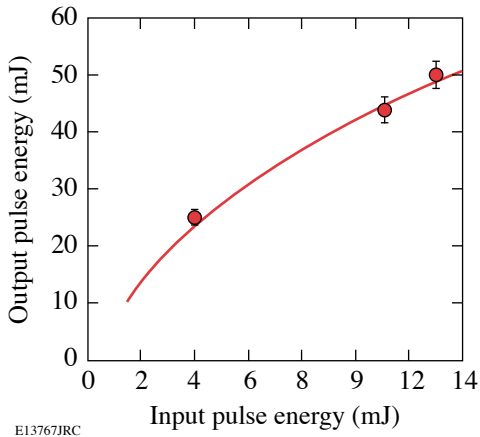
Total diode-pumped, Nd:YLF amplifier optical-to-optical efficiency: <0.15

Achieving 40 mJ of amplifier output energy requires 270 mJ of pump energy or 270 W of quasi-continuous wave power from a fiber-coupled diode array. To produce a uniformly pumped volume, an active element is pumped from both sides by 150-W, fiber-coupled diode packages from Apollo Instruments (Irvine, CA). The delivery fiber has a 1-mm core diameter. To avoid optical damage of the active element, the fluence is kept below 5 J/cm², and the delivery fiber is re-imaged into an active element with 2× magnification. Using the Frantz–Nodvik equation,⁷ the output energy of an amplifier was calculated (Fig. 103.34). Achieving a >40-mJ amplifier output requires >10-mJ input energy.

An ODR produces ~4 mJ of energy when pumped with two 25-W fiber-coupled diodes, which yields an amplifier output of only 25 mJ. In order to increase amplifier input energy, the ODR+ is pumped with one 150-W fiber-coupled diode array (Apollo Instruments). The ODR+ output energy is >13 mJ at the maximum pump energy (Fig. 103.35). With this input, the amplifier produces ~50 mJ of IR, meeting the energy requirement.

The double-pass, all-solid-state, diode-pumped Nd:YLF amplifier shown in Fig. 103.36(a) is built as a generic platform for use in a variety of applications, including a laser system for OMEGA frequency-conversion crystal tuning.⁸ An input

telescope can accommodate input beams with diameters in the range of 1 to 8 mm. The output telescope resizes and collimates the beam for efficient frequency conversion. A built-in fiber pickoff allows monitoring of the amplified pulse shape with a fast photodetector and oscilloscope. The amplifier output beam profile shown in Fig. 103.36(b) is excellent.

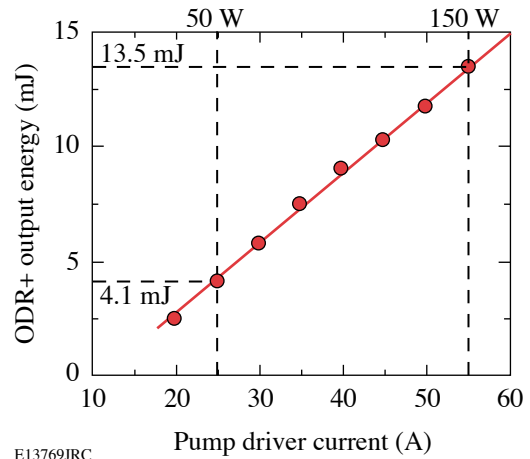


E13767JRC

Figure 103.34

The output energies of a double-pass Nd:YLF amplifier calculated using the Frantz–Nodvik equation (solid line) and measured (open circles) are in good agreement.

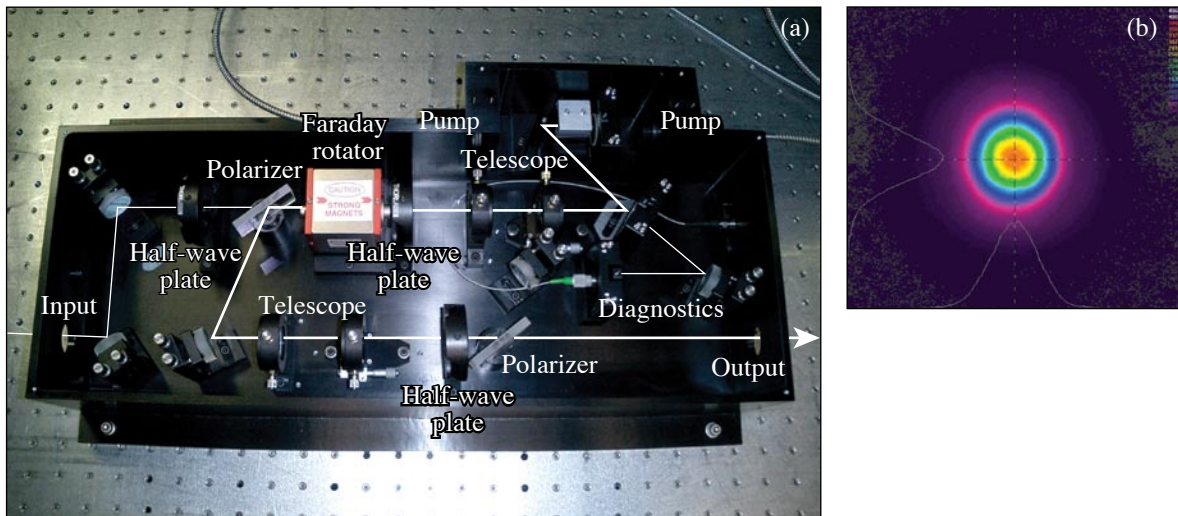
A block diagram of the frequency conversion setup is shown in Fig. 103.37. BBO crystals are utilized for frequency conversion to the fourth harmonic. An 11-mm-long type-I crystal is employed for SHG, followed by a 6-mm-long type-I crystal for FHG. A fused-silica Pellin–Broca prism is used to spatially separate the UV fiducial beam, and a telescope matches the beam size to efficiently launch the UV pulses into a multimode fiber bundle.



E13769JRC

Figure 103.35

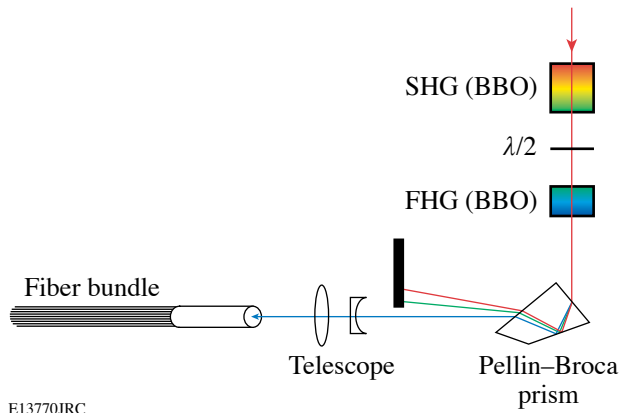
ODR+ is able to produce sufficient energy for efficient double-pass amplifier energy extraction.



E13766JRC

Figure 103.36

(a) All-solid-state, diode-pumped, double-pass Nd:YLF amplifier. (b) The output beam profile is excellent.



E13770JRC

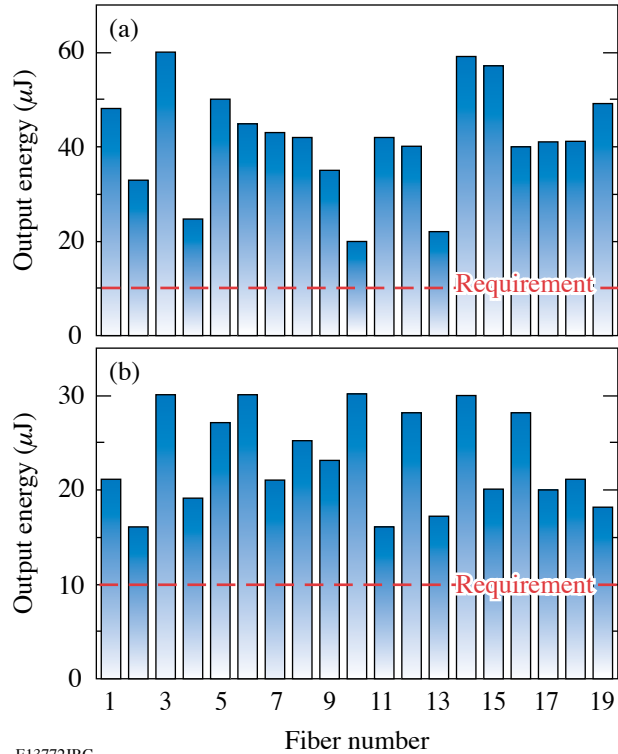
Figure 103.37
A block diagram of UV frequency conversion setup and fiber bundle launching.

Experimental Results

The double-pass amplifier must be heavily saturated in order to achieve high efficiency. To compensate for gain saturation, the ODR+ timing is set such that a switch-in Pockels cell shapes the first three to four pulses of the injected comb, decreasing their amplitudes. Even with this precompensation, the best pulse shape achieved [Fig. 103.38(a)] does not meet the requirements. After FHG, the first pulse in the comb shows significant reconversion into the fundamental wavelength, which results in two peaks instead of one [Fig. 103.38(b)], making the UV fiducial comb useless.

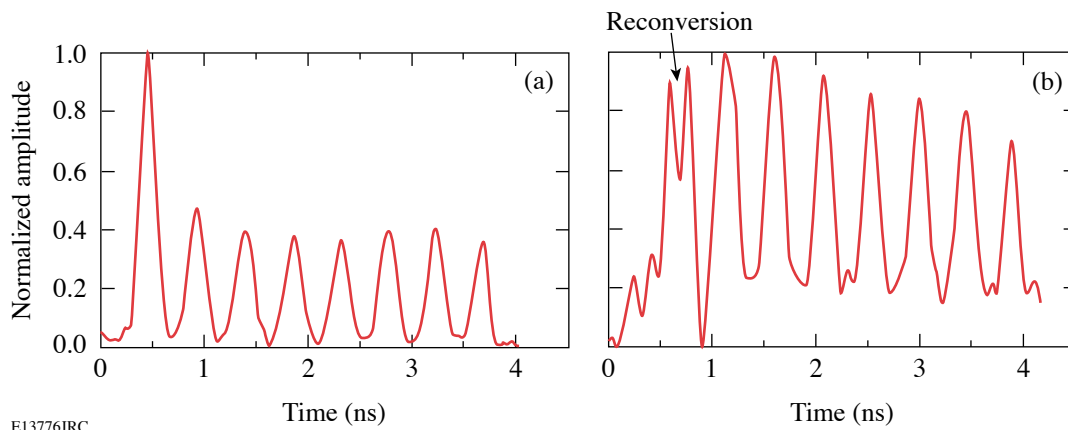
The ultraviolet comb energy has been measured in each fiber of the 19-fiber bundle [Fig. 103.39(a)]. On average, it is 4× higher than the requirement; therefore, the gain of the system can be reduced to avoid comb envelope distortion. With the

two-pass amplifier off and the IR beam resized for efficient FHG, the energy requirement has been met [Fig. 103.39(b)]. Fourth-harmonic generation efficiency of over 30% has been observed without any sign of reconversion.



E13772JRC

Figure 103.39
The double-pass amplifier produces, on average, 4× more energy than required at the fiber-bundle output (a). ODR+ delivers enough energy to meet the requirement (b).



E13776JRC

Figure 103.38
Double-pass amplifier IR output (a) and UV comb (b) pulse shapes. The first pulse in the UV comb shows significant reconversion of UV energy.

The fiducial comb injected into the ODR [Fig. 103.40(a)] has been precompensated such that both the green [Fig. 103.40(b)] and UV fiducials [Fig. 103.40(c)] meet the amplitude requirement. Fiducial laser system performance parameters have been

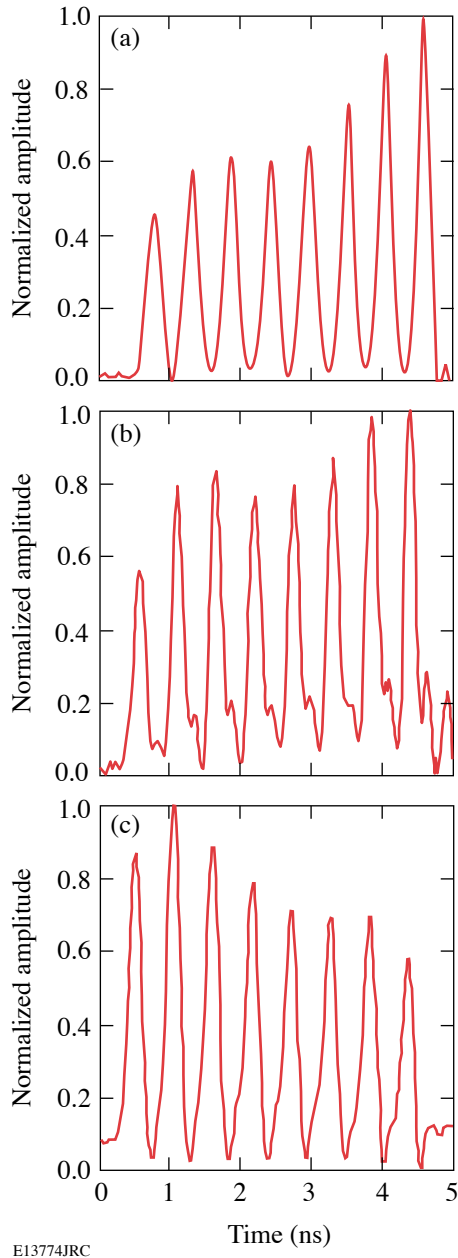


Figure 103.40
The ODR injection fiducial comb (a) is precompensated such that the green (b) and UV (c) fiducials satisfy the requirements.

measured over three days of operation. Figure 103.41 shows the stability of a UV fiducial comb in one of the fibers over three days; the peak pulse shape stability is $\sim 2\%$ rms. The UV energy stability is 1.5% rms over the same period of time.

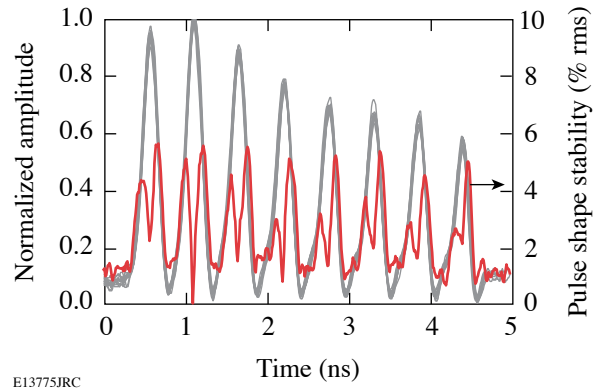


Figure 103.41
The UV fiducial peak pulse-shape stability is $\sim 2\%$ rms, and the energy stability is 1.5% rms over three days of operation.

Conclusion

An efficient, all-solid-state, diode-pumped fiducial laser system that produces IR, green, and UV fiducial combs for the OMEGA diagnostics timing reference has been developed, built, tested, and optimized. All requirements have been met. Excellent beam profile, high energy, and pulse-shape stability have been demonstrated. The turn-key system improves reliability compared to the existing flash-lamp-pumped system and has a smaller footprint of 4×5 ft.

ACKNOWLEDGMENT

This work was supported by the U.S. Department of Energy Office of Inertial Confinement Fusion under Cooperative Agreement No. DE-FC52-92SF19460, the University of Rochester, and the New York State Energy Research and Development Authority. The support of DOE does not constitute an endorsement by DOE of the views expressed in this article.

REFERENCES

1. A. Babushkin, W. Seka, S. A. Letzring, W. Bittle, M. Labuzeta, M. Miller, and R. Roides, in *22nd International Congress on High-Speed Photography and Photonics*, edited by D. L. Paisley and A. M. Frank (SPIE, Bellingham, WA, 1997), Vol. 2869, pp. 540–544.
2. C. Chen *et al.*, in *Laser and Nonlinear Optical Materials*, edited by L. G. DeShazer (SPIE, Bellingham, WA, 1986), Vol. 681, pp. 12–17.
3. M. D. Skeldon, *Rev. Sci. Instrum.* **71**, 3559 (2000).

4. A. V. Okishev, M. D. Skeldon, and W. Seka, in *Advanced Solid-State Lasers*, edited by M. M. Fejer, H. Injeyan, and U. Keller, OSA TOPS, Vol. 26 (Optical Society of America, Washington, DC, 1999), pp. 228–235.
5. A. V. Okishev and J. D. Zuegel, *Appl. Opt.* **43**, 6180 (2004).
6. W. Koechner, *Solid-State Laser Engineering*, 4th rev. ed., Springer Series in Optical Sciences, Vol. 1 (Springer, Berlin, 1996).
7. L. M. Frantz and J. S. Nodvik, *J. Appl. Phys.* **34**, 2346 (1963).
8. A. Babushkin, R. S. Craxton, S. Oskoui, M. J. Guardalben, R. L. Keck, and W. Seka, *Opt. Lett.* **23**, 927 (1998).

EXAFS Measurement of Iron bcc-to-hcp Phase Transformation in Nanosecond-Laser Shocks

Introduction

The dynamics of material response to shock loading has been extensively studied in the past.¹ The goal of those studies was to understand the shock-induced deformation and structural changes at the microscopic level. Laser-generated shocks have been recently employed² to broaden these studies to higher pressures (~ 100 GPa) and strain rates ($\sim 10^7$ to 10^8 s^{-1}). The use of *in-situ* EXAFS for characterizing nanosecond laser-shocked vanadium and titanium has been recently demonstrated.³ Additionally, the observed fast decay of the EXAFS modulations in titanium shocked to ~ 40 GPa was shown³ to be due to the α -Ti to ω -Ti phase transformation. We show that EXAFS can likewise be used to demonstrate the bcc-to-hcp phase transformation in iron. The great interest in this transformation stems from the fact that a significant part of the earth's core is thought to consist of hcp iron.⁴ Initially, Bancroft *et al.*⁵ showed that the multiple fronts propagating within shocked iron indicated a phase transformation at around 13 GPa. Subsequently, Jamieson and Lawson have shown,⁶ by diffraction in a diamond anvil cell, that a bcc-to-hcp phase transformation indeed occurs at around 13 GPa. The historical importance of this transition is that it was first observed under shocked, rather than static, compression. It also established the reliability of shocks for obtaining pressure-compression relations. The transformation has been extensively studied in gas-gun shock experiments^{7,8} using the velocity history of the back surface of the target, where a long (>10 ns) characteristic time for the transformation was deduced. This contrasts with the subnanosecond time derived in the present experiment. The longer times deduced from velocity measurements⁷ have been explained⁸ in terms of the pressure dependence of the characteristic time. Using Fig. 5 of Ref. 8, we can estimate a characteristic time for iron at a pressure of 35 GPa of ~ 5 ns. Much shorter times have been inferred from the residual microstructure that is quenched after the passage of nanosecond and even subnanosecond shocks.⁹ This observation of the transformation in nanosecond laser shocks confirms the latter finding. Unlike the evidence⁹ derived from the examination of residual microstructure after the experiment, the measurements here are *in-situ*.

The EXAFS spectrum of iron is markedly different in the bcc (or α -Fe) phase as compared with the hcp (or ϵ -Fe) phase;¹⁰ this provides a signature for identifying the transformation in laser-shock experiments. Transient phase-transformation experiments require methods for characterizing the crystal conditions (e.g., the pressure) during the transformation to substantiate the occurrence of the transformation. In static compression experiments, the temperature and pressure are independently controlled and measured. We show that the temperature and compression (and, hence, the pressure) can be deduced from the EXAFS record itself in addition to providing evidence of the phase transformation.

Experimental Setup

K-edge EXAFS measurements were performed on iron shocked to ~ 35 GPa with a 3-ns laser pulse, provided by 3 of the 60 beams of the OMEGA laser.¹¹ The radiation source for the EXAFS measurement was obtained by imploding a spherical target using the remaining 57 OMEGA beams. In a previous paper,¹² we showed that a CH shell imploded by a multibeam laser system emits intense and spectrally smooth radiation, lasting ~ 120 ps, and is suitable for EXAFS measurements on nanosecond time scales.

Figure 103.42 shows a schematic of the experimental configuration used to measure K-edge EXAFS absorption spectra in laser-shocked iron targets. Two cross-calibrated, flat-crystal spectrometers equipped with a Ge (1,1,1) crystal were used for measuring the incident and transmitted spectra on a single laser shot. The three shock-generating laser beams were stacked to form a 3-ns square pulse focused to an irradiance of 0.4 to 0.5 TW/cm². The delay time of the three-stacked beams, with respect to the remaining beams, was adjusted so that peak implosion (and emission) of the spherical target occurred just when the shock wave exited the metal layer. The planar target consisted of 8- μ m-thick polycrystalline iron foil (purity of 99.85%) coated on both sides with a 17- μ m-thick CH layer; thus, the iron layer is directly affected by the shock but not by the laser absorption and heating. A heat shield (1-mm-thick CH foil) minimizes the heating of the metal layer by the soft

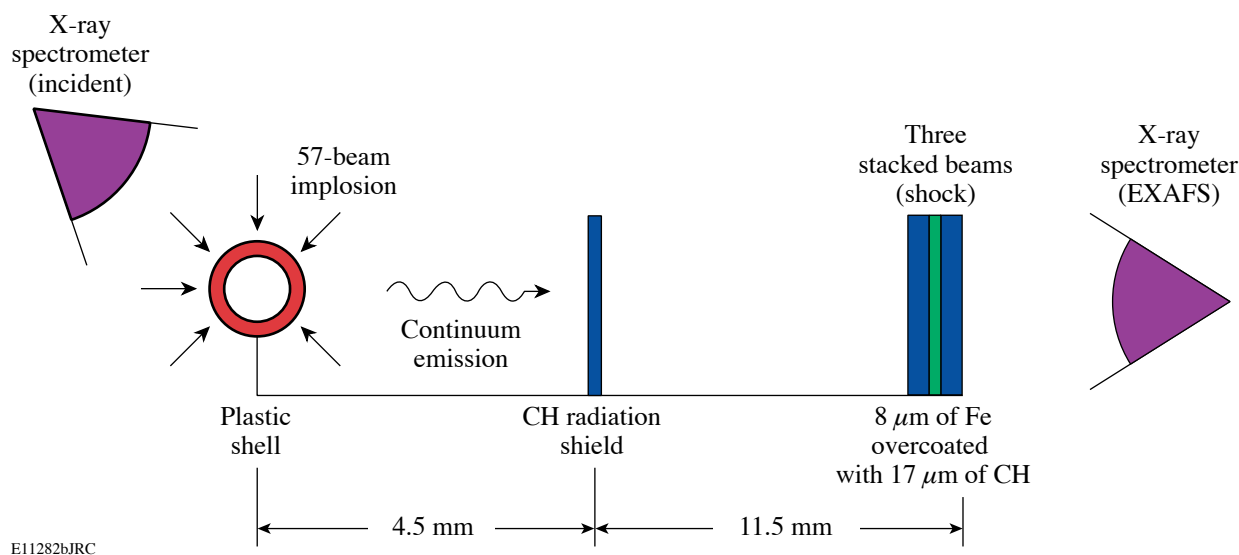


Figure 103.42

Schematic of the experimental configuration. The spherical target, imploded by 57 laser beams, serves as a radiation source for EXAFS measurements. The three-stacked beams launch a shock through the iron layer.

radiation from the imploding spherical target. The iron thickness is the largest that can still yield significant transmitted x-ray intensity. Although the spectrometers used in the EXAFS measurement are time integrated, a meaningful shock diagnosis can be obtained without streaking the spectrum in time because the x-ray pulse width is only ~ 120 ps,¹² much shorter than the shock transit time through the metal (~ 2 ns).

Theory

The expected shock strength and the properties of the shocked iron were determined using 1-D simulations with the hydrodynamic code *LASNEX*.¹³ The tabular equation of state incorporated into the code includes the α -Fe to ϵ -Fe phase transformation. Figure 103.43 shows the computed profiles just as the shock exits the iron layer. The volume-averaged values are a pressure of 36 GPa, a temperature of 645 K, and a compression of 1.2 (or 20%).

The measured spectra were analyzed with the FEFF8 *ab initio* EXAFS software package.¹⁴ The basic theory of EXAFS¹⁵ yields an expression for the relative absorption $\chi(k) = \mu(k)/\mu_0k - 1$, where $\mu(k)$ is the absorption coefficient and $\mu_0(k)$ is the absorption of the isolated atom. The wave number k of the ejected photoelectron is given by the de Broglie relation $\hbar^2 k^2 / 2m = E - E_K$, where E is the absorbed photon energy and E_K is the energy of the K edge. The FEFF8 package uses the scattering potential to calculate the amplitude and phase shift of the photoelectron waves scattered from several

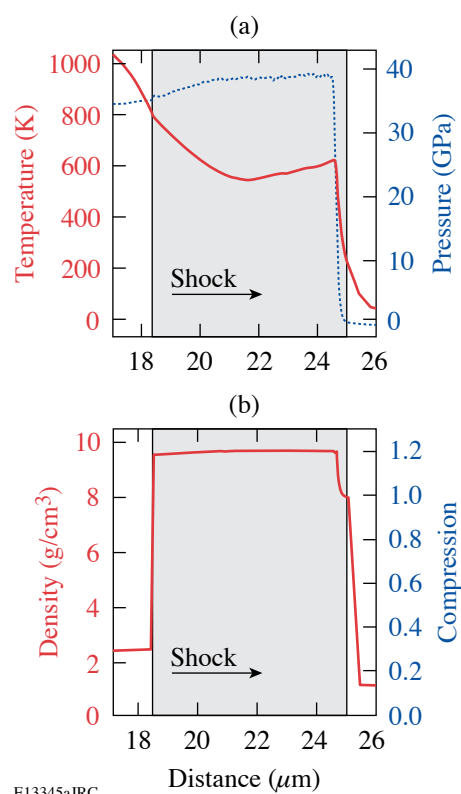
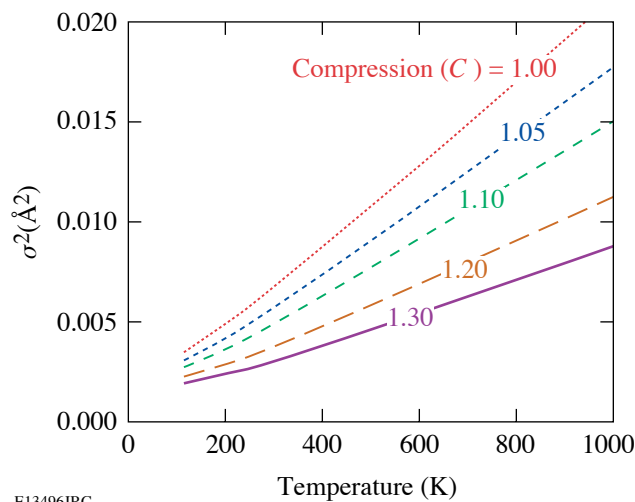


Figure 103.43

Profiles of (a) target pressure and temperature and (b) density calculated by *LASNEX* (the iron layer, enclosed within CH layers, is highlighted). The laser propagates toward the right.

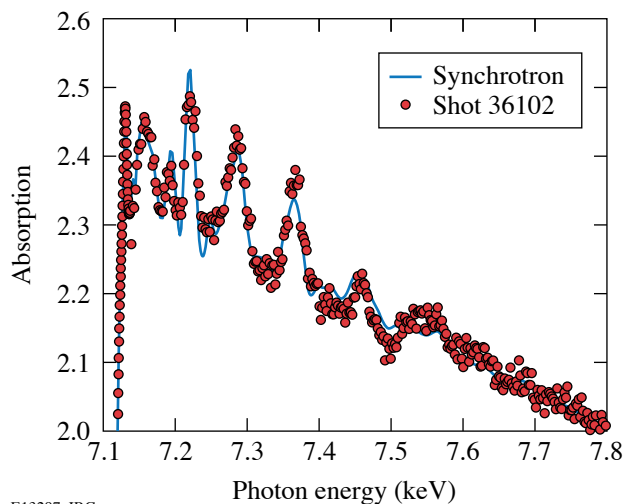
shells of neighboring atoms, including multiple-scattering paths. The main fitting parameters are the nearest-neighbor distance R and the vibration amplitude σ^2 appearing in the Debye–Waller term.¹⁵ The distance R yields the density or compression; σ^2 as a function of temperature was calculated using the Debye model¹⁶ for the phonon density of states, including correlation, and it also depends on the density through the



E13496JRC

Figure 103.44

Debye–Waller factor (σ^2) of ϵ -Fe, calculated from the correlated model of Sevillano *et al.*¹⁶ and the measured dependence of the ϵ -Fe Debye temperature on compression.¹⁷



E13297aJRC

Figure 103.45

Comparison of the measured absorption of unshocked iron on OMEGA and a standard iron EXAFS measured at the Stanford Synchrotron Radiation Laboratory.

Debye temperature. The density dependence of the Debye temperature for Fe- ϵ was taken from published measurements.¹⁷ The results (shown in Fig. 103.44) can be approximated by $\sigma^2(\text{\AA}^2) = 0.001 + 2 \times 10^{-5} T(K)/C^3$,⁵⁸ where $C = (\rho/\rho_0)$ is the compression ratio. Using this dependence and the result for σ^2 from FEFF8 fitting, the temperature can be derived.

Experimental Results and Analysis

To assess the reliability of our Fe EXAFS measurements, we obtained the EXAFS spectrum for unshocked iron using the configuration described above but without firing the shock-launching beams. Figure 103.45 shows a comparison between the resulting absorption and a standard iron absorption spectrum measured at the Stanford Synchrotron Radiation Laboratory (SSRL). The agreement is seen to be good.

EXAFS provides a very distinct, qualitative signature for the bcc-to-hcp phase transformation in iron.¹⁰ This is demonstrated by Fig. 103.46, showing (a) the EXAFS spectrum for the two phases calculated by the FEFF8 code and (b) the EXAFS spectrum measured on OMEGA for unshocked and shocked iron. Anticipating the fitting results described below, a compression of 20% (with respect to the initial bcc density) and a temperature of 700 K were assumed in Fig. 103.46(a) for the hcp phase. The bcc calculation is for room-temperature and ambient-pressure conditions. The main signature of the phase transformation is seen to be the disappearance of the peak marked “W.” When the calculations for the bcc phase are repeated for a wide range of compressions, the feature W remains intact. Thus, its disappearance can only be because of the phase transformation, not because of the shock compression (we later show that this is true—even in the case of 1-D compression). The effect of compression on the EXAFS spectrum is to increase the period of oscillation (in k space), and the effect of the heating is to cause the oscillations to decay faster with increasing k ; both are evident in Fig. 103.46(a).

The experimental results shown in Fig. 103.46(b) mirror the changes seen in Fig. 103.46(a). Compression and heating are evident, and the disappearance of the W feature indicates a bcc-to-hcp phase transformation. The complete disappearance of that feature indicates that the transformation is complete, hence that its time constant must be shorter than ~ 1 ns. Additionally, the predicted enhancement in the peak around $k \sim 3 \text{\AA}^{-1}$ is also observed in Fig. 103.46(b). These results were consistently observed on repeated experiments under the same conditions. These conclusions are borne out by the more precise fitting analysis below.

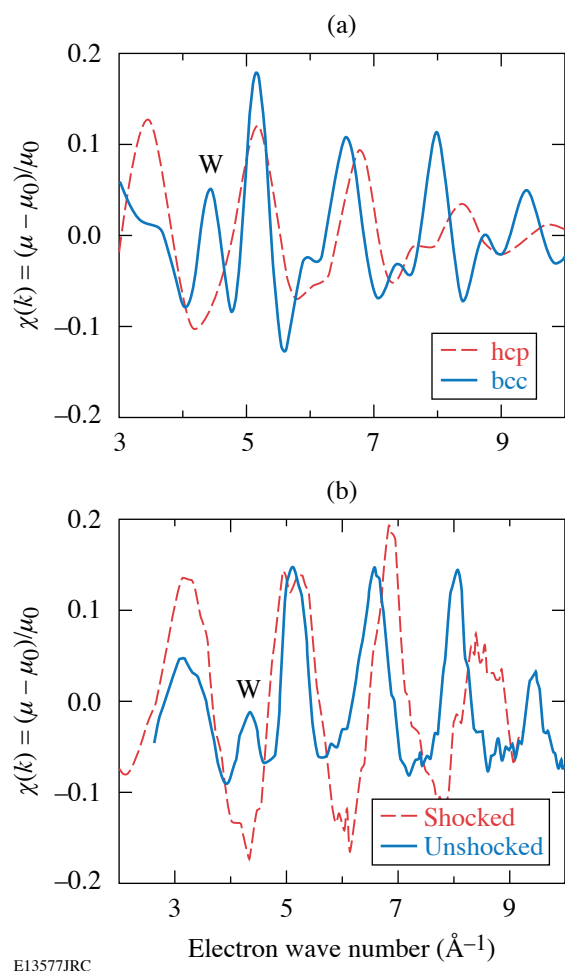


Figure 103.46

(a) FEFF8 code calculation of the EXAFS spectrum for unshocked α -Fe (bcc) and ϵ -Fe (hcp), the latter compressed by 20% with respect to the initial bcc iron. (b) Experimental results for unshocked and shocked iron. In the shocked case (at a deduced pressure of ~ 35 GPa), the peak marked W is seen to disappear, indicating a bcc-to-hcp phase transformation. Also, the period of oscillation is seen to increase, indicating compression. Finally, the damping rate increases, indicating heating.

To understand the origin of the W feature, we show the major components of the full EXAFS spectra calculated by the FEFF8 code for the bcc and hcp crystals in Fig. 103.47. The contributions from the first several shells of nearest neighbors, including several multiple scattering paths, are shown. Both crystals were assumed to be compressed by 20% and to have a temperature of 700 K. The calculation of a bcc crystal compression by 20% may seem unwarranted because the bcc phase is known to transform into the hcp phase at compressions above $\sim 6\%$. However, because of the much higher strain rate in this experiment, the phase transformation cannot be assumed *a priori* to take place. The origin of the W feature is seen to be a coincidence in the

waves scattered from the $n = 3$ and $n = 4$ shells occurring (for this compression) at $k \sim 4.7 \text{ \AA}^{-1}$. No such coincidence occurs for the hcp crystal. As mentioned before, the W feature is seen to remain intact even under compression. Thus, the disappearance of the W feature upon shocking in this experiment is not due to compression, but rather by phase transformation.

We now turn to FEFF fitting to the experimental EXAFS spectra. As Fig. 103.46 shows, we cannot fit the data with bcc EXAFS spectra; the two are qualitatively different. Conversely,

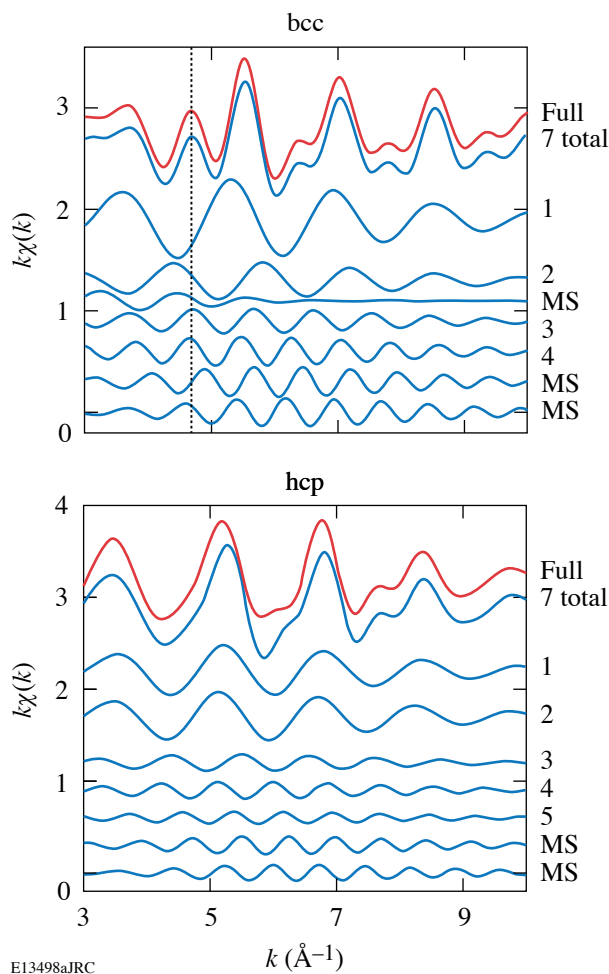
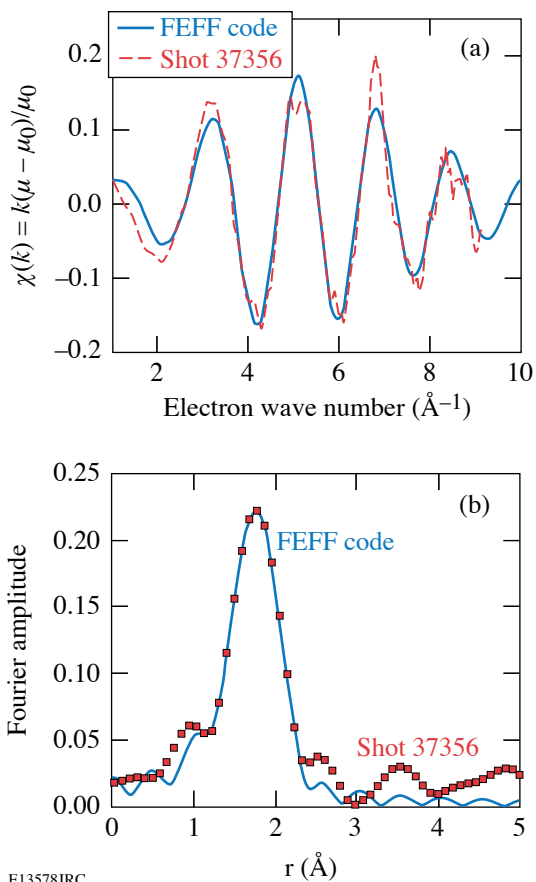


Figure 103.47

The major components of the FEFF-calculated EXAFS spectra due to scattering from the various shells of neighbors around the absorbing atom. The contributions of significant multiple scatterings are also shown ("7 total" is the sum of only the components shown in the figure). The peak marked W in Fig. 103.46 is marked here by a dotted vertical line. It is seen to arise from a coincidence in the scattering from the third and fourth shells at $k \sim 4.7 \text{ \AA}^{-1}$. Both crystals are assumed to be compressed by 20% and to be heated to 700 K.

hcp-calculated EXAFS agrees well with the experimental EXAFS data. Figure 103.48 shows the best fit, in wave number (k) space and in distance (r) space. The fit in r space (where the spectrum shows the spatial charge distribution around the absorbing atom) is obtained by inverse Fourier transforming the experimental, as well as the theoretical, curves in k space.¹⁵ The dimensions a and c of the hcp unit cell are known as a function of hydrostatic compression¹⁸ (for all compressions $c/a \sim 1.6$), and thus, the bond length (or nearest-neighbor distance) R is simply related to the compression under such conditions (we discuss the implications of finite shear strength below). Note that the value of R corresponding to the best fit is larger than the position of the peak in Fig. 103.48(b) because of the phase factors in the wave scattering. The fitting yields $R = (2.39 \pm 0.013) \text{ \AA}$, which corresponds to a compression of

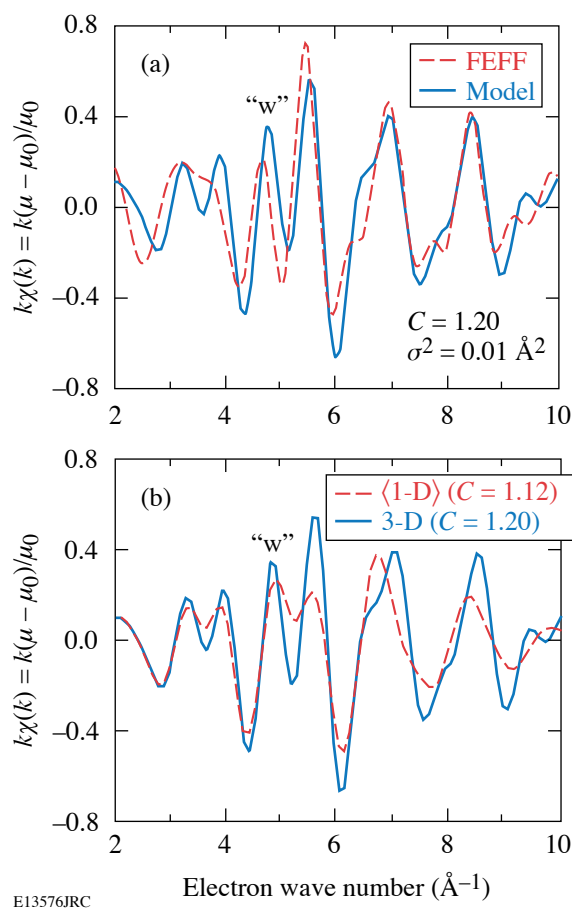


E13578JRC

Figure 103.48

FEFF code fitting to the experimental results (a) in the k space and (b) in the r space. The simulations assume the hcp phase. The best fit corresponds to a bond length of $R = (2.39 \pm 0.013) \text{ \AA}$ and $\sigma^2 = (0.0078 \pm 0.0030) \text{ \AA}^2$. These values correspond to a 20% volume compression and a temperature of 670 K.

1.22 ± 0.023 . This value agrees well with the average compression of 1.2 predicted by *LASNEX* [see Fig. 103.43(b)]. Turning now to the estimate of temperature, the FEFF best fit to the data [Fig. 103.49(a)] corresponds to $\sigma^2 = 0.0078 \pm 0.0030 \text{ \AA}^2$. From Fig. 103.44, this value of σ^2 corresponds to a temperature of $670 \pm 170 \text{ K}$, thus agreeing well with the average temperature of 645 K predicted by *LASNEX* [Fig. 103.43(a)]. Using the equation of state of iron and the measured temperature and compression values leads to an estimate of the pressure as $\sim 35 \text{ GPa}$. *LASNEX* uses the equation of state of iron, which includes the α to ϵ phase transformation (but not its kinetics). These values also agree with the equation of state calculated for the Hugoniot of iron.¹⁹ The deduced pressure is well above



E13576JRC

Figure 103.49

Simplified EXAFS calculations for 1-D and 3-D-compressed bcc iron. (a) Comparison of the simplified results and a full FEFF8 calculation for 3-D-compressed iron [$C = (\rho/\rho_0) = 1.2$, $T = 700 \text{ K}$]. (b) Two simplified EXAFS calculations: 3-D compression of $C = 1.2$ and 1-D compression of $C = 1.12$ (averaged over all directions). The compression in each case is adjusted to yield the measured EXAFS modulation frequency.

the pressure of slower shocks in iron, where a bcc-to-hcp phase transformation takes place.¹⁸ Also, the derived values of pressure and temperature correspond to a point on the phase diagram of iron⁵ that is well within the Fe- ϵ (hcp) region.

Velocity interferometric measurements (VISAR)²⁰ were performed on iron targets identical to those used for the EXAFS measurements, except that the CH coating was placed only on the side facing the laser. In this way, the velocity of the iron-free back surface could be measured. From the surface velocity, the particle velocity could be determined by dividing by 2. This relationship has been shown²¹ to hold for iron shocked to pressures of up to ~ 150 GPa. Because of the relatively high pressure and the small foil thickness in this experiment, the velocity waves^{7,8} indicative of a transition to plastic flow and of a phase transformation were not resolved; thus, the VISAR results cannot confirm either transition. However, the deduced particle velocity can be used with the known Hugoniot curve of iron to determine the compression. For the measured rear-surface velocity of 1.5×10^5 cm/s, the resulting compression is $C = 1.17$, in agreement with the values predicted by *LASNEX* and with the values measured by EXAFS (using the FEFF8-code fitting).

Elastic-to-Plastic Transition

The analysis above has assumed that the compression of the hcp crystal, but not necessarily that of the bcc crystal, is hydrostatic. The dynamic yield stress in polycrystalline iron has been found to be lower than 1 GPa,²² using millimeter-scale specimen thicknesses and strain rates of order of 10^5 s⁻¹. Because the dynamic yield stress in iron increases with strain rate as well as with decreasing specimen thickness,²² we cannot assume plastic compression of the bcc crystal prior to the phase transformation; in thin iron samples, the Hugoniot elastic limit can even be higher than the pressure for phase transformation.²³ However, the transformation involves atomic motions in various mutually perpendicular directions in the bcc phase,^{10,24} and thus, also in a direction perpendicular to the shock direction; this should lead to relaxation of the shear stress. In the hcp phase, the first shell of nearest neighbors, whose distance is given by the unit-cell parameter a , has a major contribution to the EXAFS spectrum; thus, the analysis primarily determines a , whereas the unit-cell parameter c is primarily needed for the calculation of volume compression. Therefore, values of c/a somewhat different from the static values used here cannot be excluded. However, such values would still imply a compression consistent within experimental error with the compression obtained by VISAR measurements and by hydrodynamic simulations.

Since the possibility of elastic compression of the bcc crystal cannot be discounted, the following question arises: Can the observed EXAFS be explained by a 1-D compression of the bcc crystal *with no* phase transformation? In other words: Would the W peak disappear because of 1-D compression where no phase transformation takes place? To answer this question, we calculated the EXAFS spectrum assuming that atomic coordinates in the bcc crystal are reduced only in the shock direction. Since the grains are oriented randomly in a polycrystalline sample, the angles between the crystal axes and the shock direction assume all possible values. Therefore, the result was averaged over all these angles. For simplicity, only single scattering from the first four nearest-neighbor shells was considered, using the scattering amplitudes and phase shifts from the tables of Teo and Lee.²⁵ To check the reliability of this model, Fig. 103.49(a) shows a comparison between the simplified and the full FEFF8 calculation for 20% isotropic compression of bcc iron at $T = 700$ K. Fair agreement between the two calculations is seen, and, in particular, the W feature appears in both. The W feature in both cases arises from the same coincidence of $n = 3$ and $n = 4$ scatterings. Figure 103.49(b) shows a comparison between the results for the cases of 3-D and 1-D compressions. The 3-D compression is 20%, as above. The 1-D compression was varied to match the experimental frequency of modulation, resulting in 12% compression (in slower shocks, the transformation starts to occur at a compression of $\sim 6\%$). This is larger than the reduction in distances in the 3-D case (which is $1.2^{1/3} \sim 1.06$) because in 1-D compression distances not in the direction of compression are reduced by a smaller factor. Since the W feature has not disappeared upon 1-D compression (nor has the first peak increased in intensity), the measured EXAFS spectra cannot be explained as resulting from a 1-D compression without a phase transformation. Thus, only the analysis assuming the hcp phase agrees with the measurement. As shown above, this conclusion agrees with VISAR measurements and *LASNEX* predictions.

ACKNOWLEDGMENT

This work was supported by the U.S. Department of Energy Office of Inertial Confinement Fusion under Cooperative Agreement No. DE-FC52-92SF19460, the University of Rochester, and the New York State Energy Research and Development Authority. The support of DOE does not constitute an endorsement by DOE of the views expressed in this article. Portions of this research were carried out at the Stanford Synchrotron Radiation Laboratory, a national user facility operated by Stanford University on behalf of the U.S. Department of Energy, Office of Basic Energy Sciences. Portions of this work were performed under the auspices of the U. S. Department of Energy by the University of California, Lawrence Livermore National Laboratory (LLNL) under Contract No. W-7405-Eng-48. Additional support was provided by LDRD project 04-ERD-071 at LLNL.

REFERENCES

1. J. E. Dorn and S. Rajnak, *Trans. Metall. Soc. AIME* **230**, 1052 (1964); U. F. Kocks, A. S. Argon, and M. F. Ashby, *Thermodynamics and Kinetics of Slip*, 1st ed., Progress in Materials Science, Vol. 19 (Pergamon Press, Oxford, 1975); M. A. Meyers and L. E. Murr, eds. *Shock Waves and High-Strain-Rate Phenomena in Metals: Concepts and Applications* (Plenum Press, New York, 1981).
2. B. A. Remington, G. Bazan, J. Belak, E. Bringa, M. Caturla, J. D. Colvin, M. J. Edwards, S. G. Glendinning, D. S. Ivanov, B. Kad, D. H. Kalantar, M. Kumar, B. F. Lasinski, K. T. Lorenz, J. M. McNaney, D. D. Meyerhofer, M. A. Meyers, S. M. Pollaine, D. Rowley, M. Schneider, J. S. Stölken, J. S. Wark, S. V. Weber, W. G. Wolfer, B. Yaakobi, and L. V. Zhigilei, *Metall. Mater. Trans. A* **35A**, 2587 (2004).
3. B. Yaakobi, D. D. Meyerhofer, T. R. Boehly, J. J. Rehr, B. A. Remington, P. G. Allen, S. M. Pollaine, and R. C. Albers, *Phys. Rev. Lett.* **92**, 095504 (2004); B. Yaakobi, D. D. Meyerhofer, T. R. Boehly, J. J. Rehr, B. A. Remington, P. G. Allen, S. M. Pollaine, and R. C. Albers, *Phys. Plasmas* **11**, 2688 (2004).
4. G. Steinle-Neumann *et al.* *Nature* **413**, 57 (2001).
5. D. Bancroft, E. L. Peterson, and S. Minshall, *J. Appl. Phys.* **27**, 291 (1956).
6. J. C. Jamieson and A. W. Lawson, *J. Appl. Phys.* **33**, 776 (1962).
7. L. M. Barker and R. E. Hollenbach, *J. Appl. Phys.* **45**, 4872 (1974).
8. J. C. Boettger and D. C. Wallace, *Phys. Rev. B* **55**, 2840 (1997).
9. C. S. Smith, *Trans. Am. Inst. Min. Pet. Eng.* **212**, 574 (1958); T. Sano *et al.*, *Appl. Phys. Lett.* **83**, 3498 (2003).
10. F. M. Wang and R. Ingalls, *Phys. Rev. B* **57**, 5647 (1998).
11. T. R. Boehly, R. S. Craxton, T. H. Hinterman, J. H. Kelly, T. J. Kessler, S. A. Kumpan, S. A. Letzring, R. L. McCrory, S. F. B. Morse, W. Seka, S. Skupsky, J. M. Soures, and C. P. Verdon, *Rev. Sci. Instrum.* **66**, 508 (1995).
12. B. Yaakobi, F. J. Marshall, T. R. Boehly, R. P. J. Town, and D. D. Meyerhofer, *J. Opt. Soc. Am. B* **20**, 238 (2003).
13. G. B. Zimmerman and W. L. Kruer, *Comments Plasma Phys. Control. Fusion* **2**, 51 (1975).
14. J. J. Rehr, R. C. Albers, and S. I. Zabinsky, *Phys. Rev. Lett.* **69**, 3397 (1992).
15. P. A. Lee *et al.*, *Rev. Mod. Phys.* **53**, 769 (1981).
16. E. Sevillano, H. Meuth, and J. J. Rehr, *Phys. Rev. B, Condens. Matter* **20**, 4908 (1979).
17. L. S. Dubrovinsky *et al.*, *Am. Mineral.* **85**, 386 (2000).
18. A. P. Jephcoat, H. K. Mao, and P. M. Bell, *J. Geophys. Res.* **91**, 4677 (1986).
19. R. G. McQueen *et al.*, in *High-Velocity Impact Phenomena*, edited by R. Kinslow (Academic Press, New York, 1970), Chap. VII, pp. 293–417.
20. P. M. Celliers *et al.*, *Appl. Phys. Lett.* **73**, 1320 (1998).
21. L. V. Al'tshuler *et al.*, *Sov. Phys.-JETP* **11**, 573 (1960).
22. R. W. Rohde, *Acta Metall.* **17**, 353 (1969).
23. G. E. Duvall, P. M. Bellamy, and R. J. Livak, in *Shock Waves and High-Strain-Rate Phenomena in Metals: Concepts and Applications*, edited by M. A. Meyers and L. E. Murr (Plenum Press, New York, 1981), Chap. 40, pp. 717–732.
24. V. P. Dmitriev, Y. M. Gufan, and P. Toledano, *Phys. Rev. B* **44**, 7248 (1991).
25. B.-K. Teo and P. A. Lee, *J. Am. Chem. Soc.* **101**, 2815 (1979).

Three-Dimensional Characterization of Cryogenic Target Ice Layers Using Multiple Shadowgraph Views

Introduction

The 60-beam, 30-kJ OMEGA Laser System¹ studies the laser-driven direct-drive ignition approach to inertial confinement fusion (ICF) in which many individual high-power laser beams directly illuminate a spherical target to create a spherically symmetric implosion. Current designs for high-gain ICF targets include a layer of condensed hydrogen fuel that adheres to the inner surface of a thin spherical shell ablator. Laser energy delivered to the target ablates its outer surface and the ablation pressure drives the fuel layer inward, compressing both it and the gaseous fuel at the target's center. The drive pressure is varied in time such that the fuel density is compressed by a factor of as much as 4000 while remaining relatively cold. However, shock waves resulting from the drive-pressure variations, along with compressive work, heat the gaseous core "hot spot" to the high temperatures needed to initiate burning the fuel.

"Hot-spot" ignition is a common feature of all standard ignition experiments. This requires spherically symmetric implosions to limit the effects of hydrodynamic instabilities that can reduce fusion yield or prevent ignition by causing cold fuel to mix into the hot spot or target breakup. Asymmetry-induced hydrodynamics reduce the performance of most ICF targets well below that predicted by 1-D modeling.² The symmetry requirement imposes strong constraints on the uniformity of the laser illumination and on the sphericity of the target.³ LLE has made great strides in reducing illumination asymmetries² due to drive imbalance between different beams and laser imprint. Efforts are also under way at LLE to reduce the asymmetries inherent in the target ice layer.⁴

The quality of a fuel-ice layer depends on the method used to form it. Extremely slow cooling (~1 mK/min) is required to avoid the formation of multiple crystals of different orientations.⁵ Volumetric heating, in the form of infrared heating,⁶ improves the sphericity of ice layers by driving ice mass from thicker sections of the layer to thinner areas via vapor pressure and sublimation. Ice surfaces in OMEGA cryogenic targets are beginning to approach the 1- μ m root-mean-square (rms) deviation requirement³ for successful ignition on the NIF.⁷

The degrading effect of surface roughness on implosion performance depends on the perturbation's mode number, which is the ratio of the capsule's circumference to the wavelength of the perturbation. The surface roughness is characterized in terms of a mode spectrum analogous to Fourier analysis. Since the target geometry is spherical, however, spherical harmonics

$$Y_{\ell m}(\theta, \phi) \equiv \left[\frac{(2\ell + 1)(\ell - m)!}{4\pi(\ell + m)!} \right]^{1/2} P_{\ell m}(\cos \theta) e^{im\phi} \\ -\ell \leq m \leq \ell, \quad (1)$$

where $P_{\ell m}$ are the associated Legendre functions, form the base functions used for the mode spectrum. Accurate surface characterization of ice layers requires reliable measurement of the layer's surface with submicron resolution at many points distributed over the surface of a target. Hydrodynamic codes then calculate capsule implosion performance using the measured surface mode power spectrum. The benchmarking of calculated target performance with experimental results is essential for designing ignition-scale targets and specifying their allowable surface roughness with confidence.

This article describes the optical backlit shadowgraphic characterization of cryogenic target ice layers with submicron resolution at LLE. A novel feature of this work is the ability to image the target from many different views. The analyses of multiple images of the target from different views are combined to construct a 3-D representation of the ice layer and an ice-roughness power spectrum in terms of spherical harmonics. There are many advantages to using a full 3-D representation over a single view or even over a few orthogonal views.

- The probability of missing significant local defects in the ice layer is greatly reduced.
- A 2-D surface-roughness spectrum suitable for input into a hydrodynamic code can be directly calculated. A single view provides only a 1-D Fourier roughness spectrum.

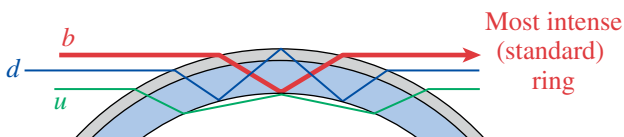
- Future detailed comparison of experimental implosions and 3-D simulations will require full surface ice characterization.
- Discrimination is possible between bumps/divots and ridges/troughs that could appear similar in a single view.
- Discrimination is possible between some outer-surface perturbation effects on the bright ring and actual ice layer defects.

Shadowgraphic Characterization of Ice Layers (p. 170) briefly describes the principles and equipment used to record a cryogenic target shadowgraph at LLE and is followed by details of the analysis of an individual shadowgraph in **Analysis of Individual Shadowgraphs** (p. 171). The 3-D ice layer reconstruction and determination of the global surface roughness power spectrum from multiple target views are reported in **Three-Dimensional Ice Layer Reconstruction Using Multiple Shadowgraph Views** (p. 175).

Shadowgraphic Characterization of Ice Layers

Optical backlit shadowgraphy is a primary diagnostic for ICF target ice layer roughness measurements.^{6,8-12} A shadowgraph records the image of light rays passing through a backlit target. The rays are reflected and refracted at the shell wall and ice layer surfaces; some rays are focused into characteristic rings. Ray-trace modeling has identified specific reflections/refractions responsible for the brightest rings (see Fig. 104.1). The most prominent or “bright” ring is the result of total internal reflection off the inner solid–vapor interface of the ice layer. The position of the bright ring in the shadowgraph is directly correlated with the position of the inner surface of the ice layer and thus allows characterization of the nonuniformity of the inner surface.

A high-magnification, high-fidelity backlit optical shadowgraphy system (Fig. 104.2) is used to diagnose the ice layer quality while a target is in one of two characterization stations. A 612-nm red LED provides backlighting, and a 0.1- to 30-ms pulse drives the LED that is coupled to a 450- μm multimode fiber used to illuminate ($\sim f/23$) the target. An $f/6$ imaging optic

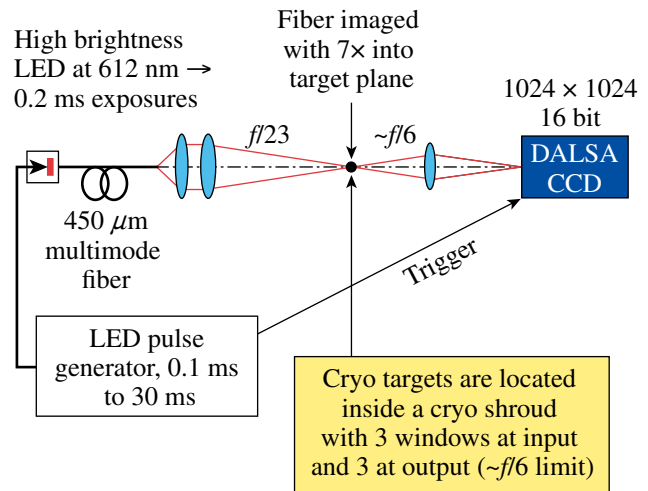


E13435JRC

Figure 104.1 Ray-trace modeling of a cryogenic target has identified the sources of the most intense rings. The bright ring *b* is by far the most intense.

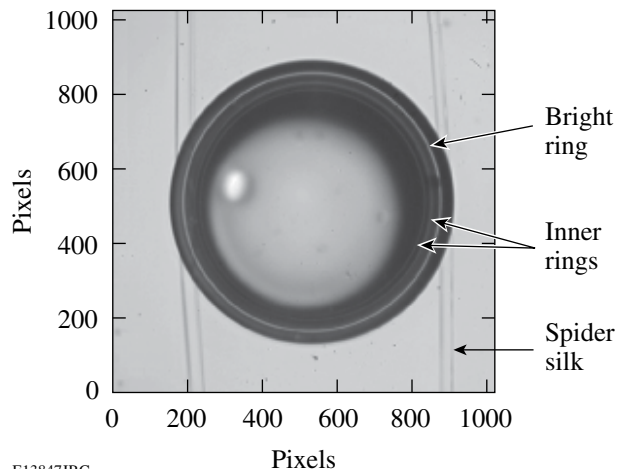
magnifies the target on a Dalsa CCD camera (12 bit, 1024 × 1024) (Ref. 13) such that the camera typically images about 1.2 μm per pixel. The camera is triggered by and integrates over the same pulse that drives the LED.

A sample shadowgraph of a LLE cryogenic target suspended from a beryllium “c mount” by four threads of spider silk (a polymerized scleroprotein)¹⁴ is shown in Fig. 104.3. The strong, unbroken bright ring and mostly featureless central spot are indicative of the high quality of this ice layer. Two inner rings are also clearly visible.



E13424JRC

Figure 104.2 The LLE cryogenic target characterization stations are based on a diffuse $f/23$ source and $f/6$ imaging optics.



E13847JRC

Figure 104.3 Shadowgraph of a cryogenic target in a logarithmic scale. The fainter inner rings are clearly visible in the image.

Analysis of Individual Shadowgraphs

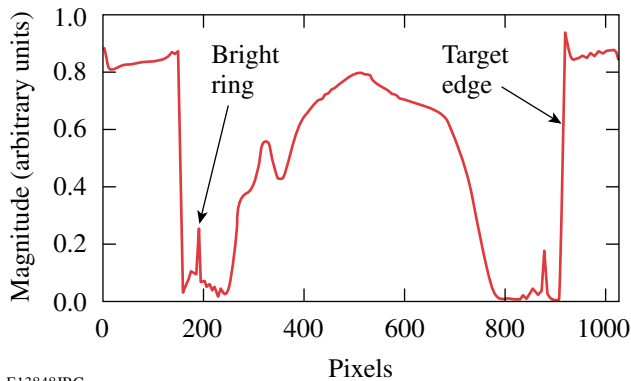
The shadowgraph analysis is performed by a MATLAB¹⁵ routine, *viewcryo*, that uses several automated steps that include:

1. Rough estimation of the target radius and center
2. Unwrapping the image in polar coordinates
3. Identification of spider webs
4. Refinement of the target edge and center estimate
5. Repetition of steps 2–4 until the target center coordinates change by less than $\sim 0.005 \mu\text{m}$
6. Identification of the bright ring using Gaussian fitting routines
7. Determination of the ice layer thickness
8. Fourier analysis of the ice layer

Details regarding each step are given below.

1. Rough Estimation of the Target Radius and Center

The target image is roughly centered in the CCD image by design and alignment. A first rough estimate of the target center location is obtained from horizontal and vertical lineouts (e.g., Fig. 104.4) averaged over several (~ 10) pixels. Taking the midpoints between the clearly visible target edges yields target center coordinates that are typically within one pixel of the more accurate center-finding routines discussed below.



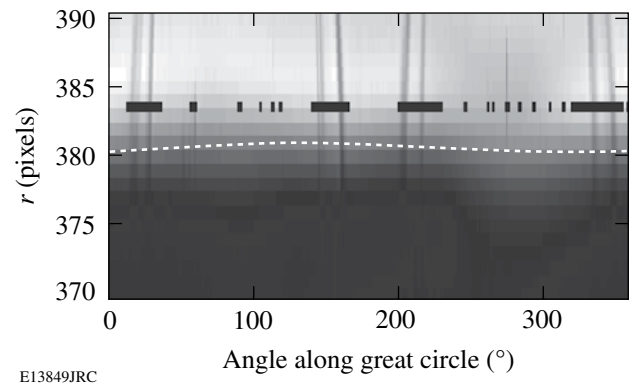
E13848JRC

Figure 104.4
Horizontal lineout through the center of the image shown in Fig. 104.3 and averaged over ~ 10 pixels.

2. Unwrapping the Image in Polar Coordinates

With an estimate of the target center, the image can be mapped to (θ, r) polar coordinates by determining the image intensity along radial lines at fixed angular intervals. A super-Gaussian interpolation function unwraps the target image to an evenly spaced grid in (θ, r) , and the interpolation function has separate Gaussian widths optimized for the angular and

radial dimensions.¹⁶ The separation of interpolation parameters allows subpixel resolution in the radial direction necessary to determine the roughness of the rather smooth outer-target surface and inner-ice layer. Pixel smoothing in the angular dimension is possible while allowing resolution of high mode numbers in the Fourier analysis of the target surfaces. Figure 104.5 shows the unwrapped image of the target edge using the initial rough estimate of the target center for the shadowgraph shown in Fig. 104.3. The unwrapped target edge shows a large $n = 1$ Fourier component, indicating an offset in the actual target center from the initial estimate. This $n = 1$ component is used below to correct the target center coordinates and, after several iterations, the center coordinates converge to a $\leq 0.005\text{-}\mu\text{m}$ variation from iteration to iteration.



E13849JRC

Figure 104.5
Close-up of the step in intensity at the target edge for the initial unwrapping of the shadowgraph shown in Fig. 104.3. The black bars indicate gaps where the edge data is *not* used to determine the target center due to the influence of spider webs and other image features outside the target. The white dotted line shows the position of the target edge (midpoint of the intensity step). The $n = 1$ component in the target edge results from an offset in the estimated target center that has not yet been removed.

3. Identification of Spider Webs

The four spider webs used to support the cryogenic targets appear in every shadowgraphic image of the target. Absorption/reflection/diffraction of light by the webs distorts the CCD image of the target's outer surface where the web images cross. These corrupted portions of the outer edge images are not used in the target-edge and center-finding routines discussed below.

The *viewcryo* code identifies where the web traces intersect the target edge by examining the region of the unwrapped image just outside the edge and isolating sections where pixel values differ significantly from a local median value. The local median is calculated for a section broad enough that it is not

located on a web. The results of the spider web identification for an initial image unwrapping are shown in Fig. 104.5.

4. Refinement of the Target Edge and Center Estimates

The target center position in the image is accurately determined by removing the $n = 1$ Fourier component of the target edge measurements in the unwrapped image. This component corresponds to a linear offset in the determination of the target center. The target edge is determined by examining the radial variation in intensity at each angular position in the unwrapped image (e.g., the data points in Fig. 104.6). While the edge corresponds to a step in intensity, no single smooth-step function (e.g., an error function) would be a good match to the data mainly because of the “overshoot” at the top of the step. A least-squares fit of the data to a set of many smooth step functions produces a good fit to the features of the measured step along with essentially flat regions on either side of the step as shown by the solid line in Fig. 104.6. The step function set consists of many (~35) error-function traces of varying widths and centers covering a range appropriate for the target edge. Negative fitting coefficients enable the fit to replicate the “overshoot” and other nonmonotonic features. Least-squares fitting via a matrix inversion results in a very fast fit. The target-edge position is defined as the radial point where the fit height is halfway between the heights of the flat regions on either side of the edge step. The radial location of this halfway point can be resolved to 0.1 pixel as is shown in **Shadowgraph Resolution** (p. 174). The data points in Fig. 104.7 show the angular variation in target’s outer-edge position along a great circle.

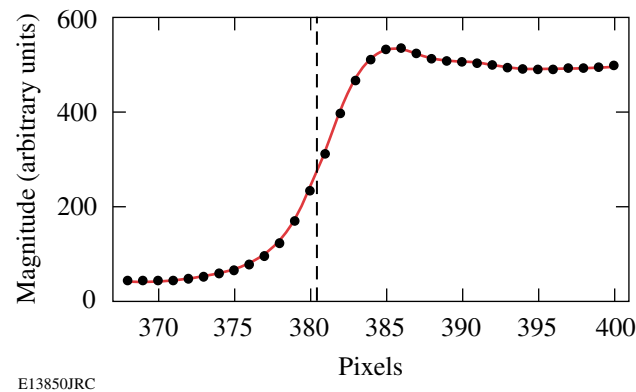


Figure 104.6 Radial variation of intensity at a specific angular position in an unwrapped image (circles) and the result of a least-squares fit to a set of error functions (solid line). The edge location (dashed line) is taken to be the radial point where the fit height is half way between the heights of the flat regions on either side of the edge step.

The variation in target-edge position with angular position is decomposed into its low-mode number (up to $n = 6$) Fourier components to remove the $n = 1$ component. These modes are sufficient to determine the large amplitude variations in the target-edge position as shown by the reconstruction (solid line) in Fig. 104.7. As mentioned previously, angular regions previously identified by the spider web finding routine are excluded from the Fourier decomposition. The routine also automatically excludes outliers from the target center finding Fourier decomposition. Outliers are identified by their deviation from the Fourier reconstruction as compared to the standard deviation and determined in terms of deviation in fitted step height, width, and radial position. The Fourier decomposition is performed iteratively with outliers excluded to ensure a self-consistent result is found. Outliers automatically identified in this way typically result from additional corruption of the edge image by spider webs, dust, and other image defects.

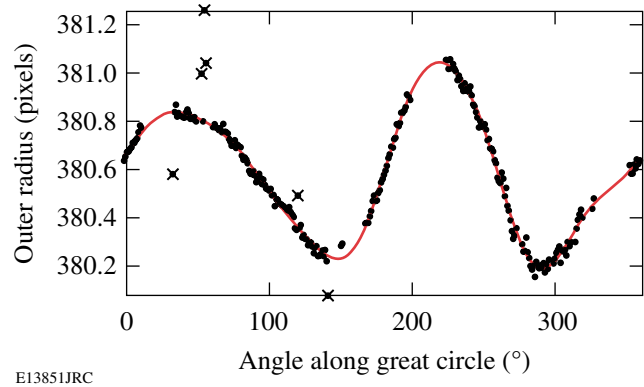
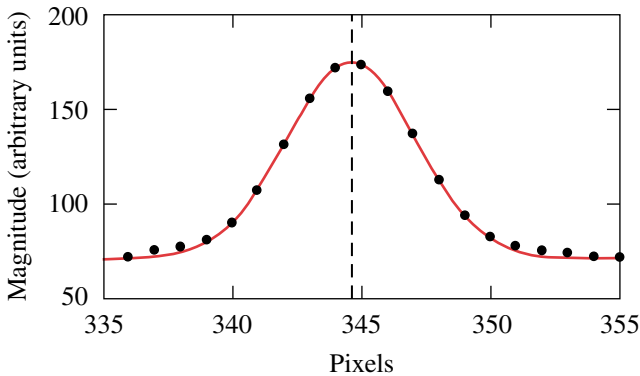


Figure 104.7 Angular variation in target edge radius as determined by the analysis of the image in Fig. 104.3 (dots) along with the fit to low mode number (up to $n = 6$) Fourier components (line). The x’s indicate data points automatically excluded from the Fourier decomposition as outliers. The large angular gaps in the data indicate regions excluded from the decomposition by the spider web finding routine.

The estimated target center position is now adjusted to eliminate the $n = 1$ Fourier component of the target’s outer edge found by the decomposition that corresponds to a linear target offset. The unwrapping, spider web finding, and target edge determination are repeated iteratively until the $n = 1$ target offset is reduced to some arbitrarily small number, typically $< 0.005 \mu\text{m}$.

5. Identification of the Bright Ring and Determination of the Ice Surface Radius

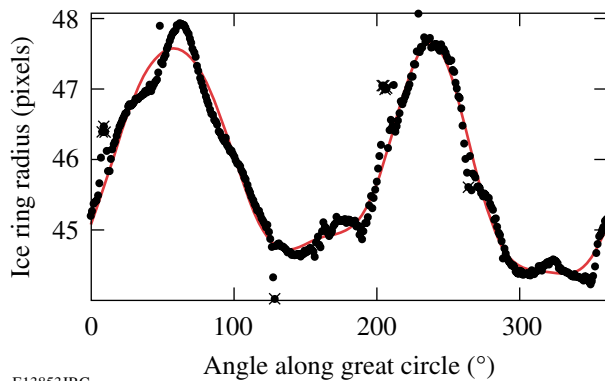
The bright ring location is identified by fitting a Gaussian peak to the radial intensity profile in the vicinity of the ring at each angular position of the unwrapped image (Fig. 104.8). The data points in Fig. 104.9 show the angular variation in bright ring position around the target. The bright ring intensity is well fit by a Gaussian peak, provided the image is focused on that ring. Ray-trace modeling of a typical cryogenic target using the PEGASUS code¹⁷ has not only identified the sources of the prominent shadowgraph rings, but also how the ring positions vary with the target parameters such as shell outer radius, shell



E13852JRC

Figure 104.8

The radial location of the bright ring (dashed line) is determined by the center of a Gaussian fit (solid line) to the radial variation in intensity across the ring (dots).



E13853JRC

Figure 104.9

Typical angular variation in bright ring radius as determined by the analysis (dots) along with the fit to low-mode number (up to $n = 9$) Fourier components (line). The x's indicate data points automatically excluded from the Fourier decomposition as outliers.

thickness, D_2 ice thickness, shell index of refraction, and the D_2 index of refraction. The PEGASUS code is 2-D and assumes spherical symmetry in the target. A linearized formula derived from this modeling is used to determine the inner-ice-surface radius from the position of the bright ring for given target parameters. Efforts are currently under way to extend the ray-trace modeling to 3-D and to explore the effects of ice-surface roughness on the bright ring in detail.

6. Fourier Analysis of the Ice Layer

The roughness and asymmetry of the inner-ice surface can degrade the performance of a cryogenic target on implosion. The Fourier power spectrum of the ice layer roughness around a great circle of the target is calculated directly from the variation in ice layer thickness or inner-ice-surface position $R(\theta)$ as determined from the bright ring analysis. We use the convenient series

$$R(\theta) = a_0 + \sqrt{2} \sum_{n=1}^{\infty} [a_n \cos(n\theta) + b_n \sin(n\theta)] (\mu\text{m}) \quad (2)$$

for Fourier decomposition. The $\sqrt{2}$ factor results in a total variance and a 1-D Fourier power spectrum of

$$\sigma_{\text{rms}}^2 = \frac{1}{2\pi} \int_{-\pi}^{\pi} [R(\theta) - \bar{R}]^2 = \sum_{n=1}^{\infty} P_n (\mu\text{m}) \quad (3)$$

and

$$P_n = a_n^2 + b_n^2 (\mu\text{m}^2), \quad (4)$$

respectively. The 1-D power spectrum of the cryogenic ice layer from the shadowgraph of Fig. 104.3 is shown in Fig. 104.10. The total 1-D rms of this layer is $1.36 \mu\text{m}$. The majority of this roughness is due to the large $n = 2$ component. The total 1-D rms of all modes except $n = 2$ is less than $0.2 \mu\text{m}$.

The 1-D Fourier power spectrum derived from a great circle ice layer measurement is a useful gauge of target quality. However, a computer simulation of implosions including instability growth and implosion performance requires a true spherical harmonic surface representation of the ice layer roughness. In **Three-Dimensional Ice Layer Reconstruction Using Multiple Shadowgraph Views** (p. 175), we will discuss using multiple shadowgraphs of different views to determine the surface asymmetry and ice roughness in terms of spherical harmonics.

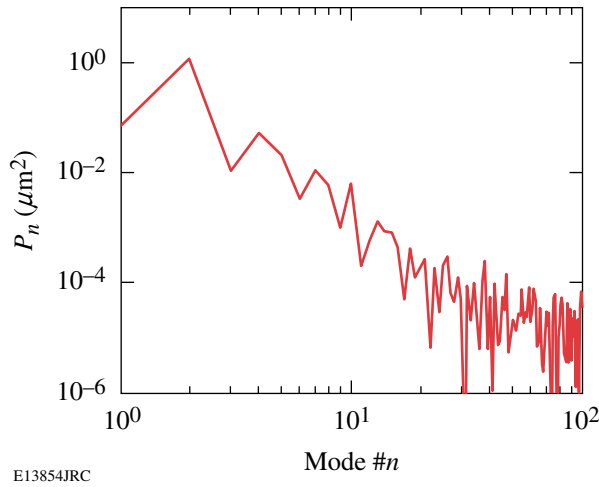


Figure 104.10
Fourier power spectrum of the ice layer from analysis of the shadowgraph shown in Fig. 104.3.

The modal analysis can be complicated by gaps in the bright ring due to ice or other defects. Direct Fourier decomposition of only the good points between the gaps is limited to relatively low mode numbers whose exact limit depends on the size of the gaps. This method prevents estimation of the high-mode ice roughness and aliases the high-mode information into errors in the low-mode determinations. Interpolation is used to bridge the gaps before the Fourier analysis. As the interpolation over small gaps preserves low-mode structure, the error due to the interpolation tends to be concentrated in higher modes, typically increasing the estimate of the higher-mode ice roughness along with an accurate determination of the low-mode ice asymmetries despite the gaps. Ice surface defects that cause gaps should ideally be included in the surface roughness analysis; however, determining the true nature of the defects is difficult. Efforts are under way to identify ice defects using nonbright ring rays from multiple views.¹⁸

7. Shadowgraph Resolution

The resolution of the shadowgraphic analysis has been examined using a sapphire sphere surrogate target for the outer-edge determination and a cryogenic target with a melted layer for the bright ring measurements. Figure 104.11 shows the scatter in outer-edge analysis from several images of a sapphire sphere at the same rotated position scaled to the nominal outer radius of 395 μm. Small vibrations varied the target’s position by a few microns between the various images ensuring that the edge crossed the CCD pixel array pattern (~1 pixel/μm) at different locations in each image. Both large- and small-scale features in the edge analysis are highly repeatable. The stan-

dard deviation between the analyses is of the order 0.01 μm at all angles. The peak-to-peak variation in edge radius is comparable to that measured for the sphere by an atomic force microscope¹⁹ along different great circles.

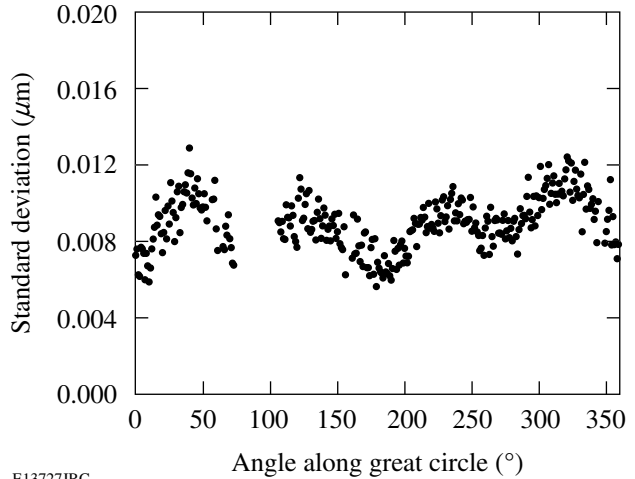


Figure 104.11
Standard deviation between outer-edge measurements of 17 different shadowgraphs viewing a sapphire sphere at slightly different positions due to vibrations of the order of a pixel. The target-mounting stalk is at 90° and causes the gap in the data at that angle.

The resolution of the bright ring measurements has been studied by analyzing the bright ring from targets whose ice layer has partially or fully melted (for an example see Fig. 104.12). In both cases, the bright ring from the very smooth liquid hydrogen surface shows an rms roughness of about 0.1 pixel (~0.12 μm).

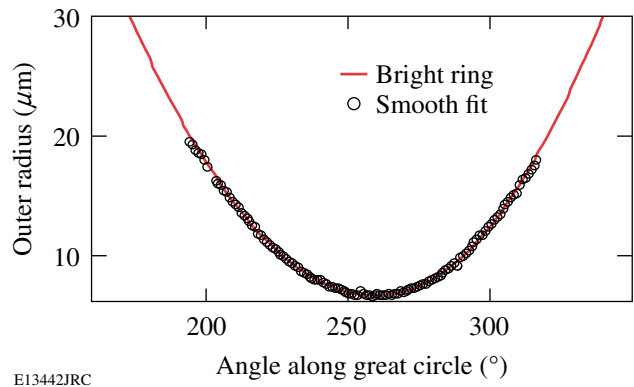


Figure 104.12
Bright ring measurements for the liquid portion of a partially melted target show a 0.1-pixel (~12-μm) rms roughness versus a smooth fit using Fourier modes 0, 1, and 2.

An error analysis of the shadowgraphic target characterization using a fully atomic-force-microscope-characterized sapphire sphere surrogate target and precision planar pattern targets is under way and will be reported in a future publication.

Three-Dimensional Ice Layer Reconstruction Using Multiple Shadowgraph Views

An important feature of LLE’s cryogenic target shadowgraph system is the use of multiple views of the target to fully characterize the ice layer. Multiple views allow a far more complete layer characterization than is possible from a single view. In fact, even with three mutually orthogonal views, it can be shown that there is only a small chance of detecting many local ice defects.¹⁹ The targets are rotated in the cryogenic target characterization stations, providing a large number of different views for a single camera. The maximum number of views is limited only by the rotation stepper motor step size of a few tenths of a degree.

Shadowgraphs are typically recorded at 15° intervals, producing a total of 48 independent views between two cameras in each station. It takes less than a minute to rotate the target to each image view. After an image is taken, the target is rotated back to its “home” position for a short rest. This procedure prevents significant changes in the ice layer due to the changing target position with respect to the geometry of the isotherms in the layering sphere. The time constant for an ice layer to change because of target rotation is of the order of 15 to 25 min, much longer than the typical time required to obtain an image at any view using this procedure. Figure 104.13 shows a target inner-ice surface reconstructed from 48 separate views. Very different low-mode asymmetries are observed for any given great circle. For this data set, the ice surface 1-D rms roughness of the individual great circle observations varies from 0.72 to 2.9 μm with an average value of 1.7 μm.

The two cameras in each characterization station have approximately orthogonal views. One camera views the target center from an angle of 26.56° above the equator. The second camera is located 109.96° azimuthally from the first and views from 12.72° above the equator. These view angles are determined by the locations of the layering sphere windows that are aligned with the OMEGA target chamber viewing ports used to center the target at shot time. Unfortunately, these views are not optimum for target characterization. An off-the-equator viewing angle always results in regions surrounding the rotation poles that cannot be observed. These unviewable “polar caps” are apparent in Fig. 104.13.

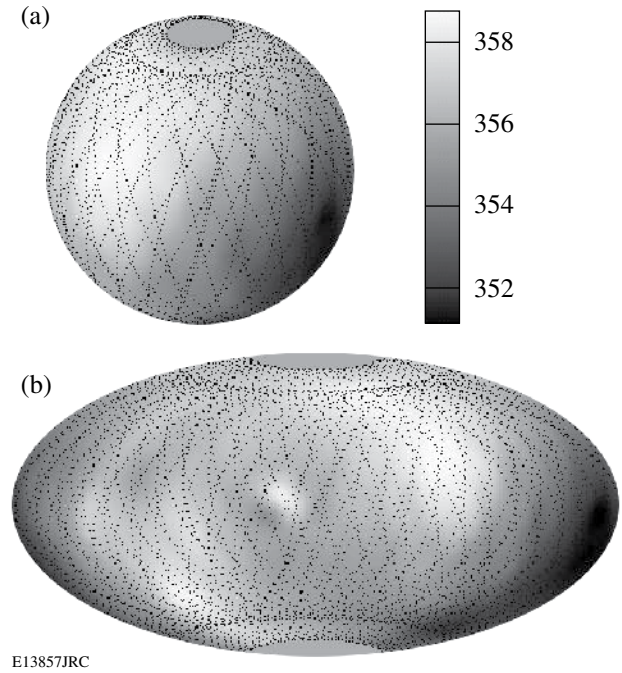


Figure 104.13 Three-dimensional representation of a cryogenic inner-ice surface (μm) displayed (a) on a spherical surface and (b) using the Aitoff projection. These displays are constructed by interpolating all the individual data from the many great circle observations to an evenly spaced (θ,φ) surface grid. The dotted lines show the location of the actual great circles observed in the individual shadowgraphs. The polar caps not crossed by the great circle observations are clearly visible. Typical surface structures are much more apparent in false color than in the gray scale representation required for publication.

As mentioned earlier, computer modeling of a spherical implosion including instability growth requires an ice roughness spectrum described in terms of spherical harmonics basis functions $Y_{\ell m}(\theta, \phi)$ on the ice surface.

$$R(\theta, \phi) = \sum_{\ell=0}^{\infty} \sum_{m=-\ell}^{\ell} A_{\ell m} Y_{\ell m}(\theta, \phi) \quad (\mu m). \quad (5)$$

This description gives a power spectrum and total surface variance of

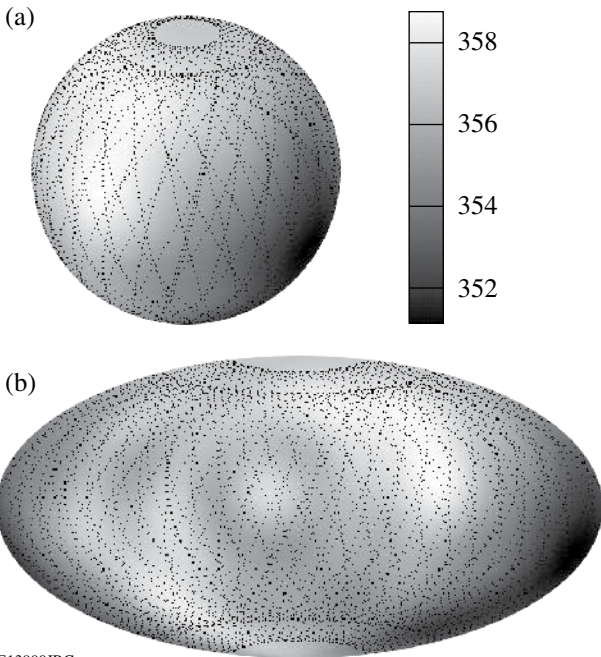
$$P_{\ell} = \frac{1}{4\pi} \sum_{m=-\ell}^{\ell} |A_{\ell m}|^2 \quad (\mu m^2) \quad (6)$$

and

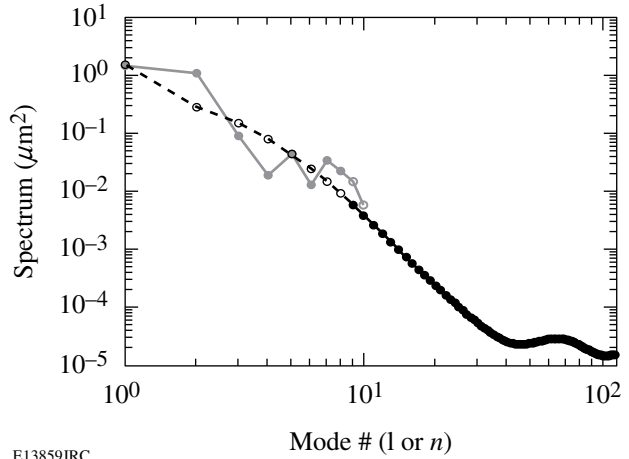
$$\sigma_{\text{rms}}^2 = \sum_{\ell=1}^{\infty} P_{\ell} \quad (\mu m^2), \quad (7)$$

respectively. The Legendre mode spectrum P_ℓ represents a sum over all azimuthal modes m . Multiple views allow the inner-ice surface to be directly fit to the $Y_{\ell m}(\theta, \phi)$'s. This fit has an upper limit on the mode number ℓ_{\max} determined by the largest space between sampled points on the surface. For typical LLE targets, the largest gap in the surface data occurs at the unviewable polar cap of the target. The many smaller surface gaps between great circle measurements, noise in the data, and uneven surface weighting (sections crossed by several great circles are more heavily weighted) also reduce the maximum mode number that can be reliably fit. These effects typically limit the direct surface fit to mode numbers to about $\ell_{\max} = 8$ to 10. The exact limit varies with each data set.

The results of a direct $Y_{\ell m}(\theta, \phi)$ fit are shown in Figs. 104.14 and 104.15. The surface reconstruction in Fig. 104.14 based on the low-mode number fit is a very good match to the data shown in Fig. 104.13. The Legendre power spectrum P_ℓ corresponding to this fit is displayed in Fig. 104.15.



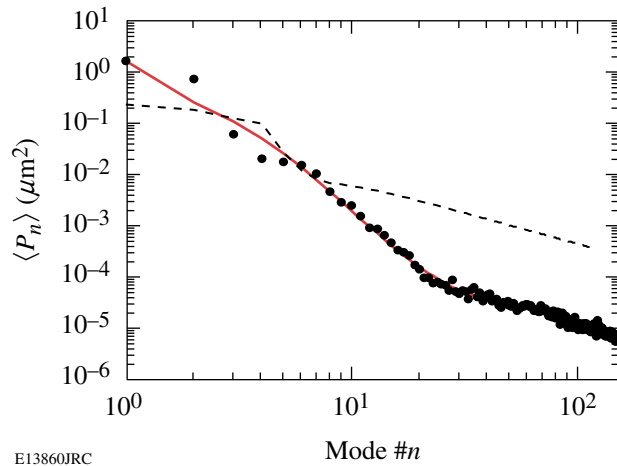
E13900JRC
 Figure 104.14
 Three-dimensional reconstruction of a cryogenic inner-ice surface (μm) based on a direct $Y_{\ell m}(\theta, \phi)$ fit to the measured data. A comparison with Fig. 104.13 shows that the low-mode features are well matched by the fit. Although the actual great circle data are used in the fitting, the results are mapped to an evenly spaced (θ, ϕ) surface grid using the $Y_{\ell m}$ coefficients for better display.



E13859JRC
 Figure 104.15
 Legendre-mode power spectrum P_ℓ of the ice surface. The gray data correspond to the low-mode-number direct fit. The black data are the result from mapping the average Fourier mode spectrum (see Fig. 104.16) of the many great circles.

Mode numbers higher than ℓ_{\max} cannot be directly fit, but can be inferred from the Fourier mode spectra of the many great circles observed. If one assumes that the surface perturbations are randomly distributed, the great circle 1-D Fourier-mode power spectrum averaged over many great circles can be mapped²⁰ to an equivalent Legendre-mode power spectrum. The assumption of randomly distributed perturbations limits the applicability of the mapping to higher mode numbers. Mode numbers up to about $\ell_{\max} = 8$ to 10 are directly fit to spherical harmonics, while higher mode numbers are determined by this mapping of the average Fourier power spectrum. Figure 104.16 shows the Fourier-mode spectrum $\langle P_n \rangle$ averaged over the many great circle views. $\langle P_n \rangle$ is first smoothed, then mapped to the equivalent high-mode-number Legendre-mode power spectrum P_ℓ shown in Fig. 104.15. The smoothing improves the behavior of the mapping.

The recently updated²¹ NIF indirect-drive specification for ice surface roughness is also plotted in Fig. 104.16. For this target, the ice layer roughness is well below the NIF specification for most mode numbers. Only modes $n = 1$ and 2 significantly exceed the specification. The bulk of the surface-roughness rms of $1.7 \mu\text{m}$ is in these two modes. Efforts are currently under way at LLE to understand and correct the sources of the low-mode asymmetries in the layering-sphere isotherms.⁴



E13860JRC

Figure 104.16

Average Fourier-mode spectrum $\langle P_n \rangle$ for the many great circle measurements of the ice surface used in the 3-D layer characterization. The dots are the actual average power for each mode number. The solid line is a smooth fit to the data used for the mapping to a Legendre-mode spectrum. The dashed line shows the recently updated NIF specification for indirect-drive ice layer roughness.

Summary

Analysis of the bright ring in backlit optical shadowgraphs of cryogenic targets is the primary diagnostic for ice layer quality at LLE. The bright ring radius is typically measured with a resolution of about $0.12 \mu\text{m}$ and is directly correlated to the position of the inner-ice surface. Two approximately orthogonal cameras and *in-situ* rotation of the target produce multiple shadowgraphs and, after analysis, the inner-ice surface radius for many different great circles on the target surface. A 3-D reconstruction of the inner-ice surface from these many views allows a direct fit of the surface roughness in terms of spherical harmonics for mode numbers up to $\ell_{\text{max}} = 8$ to 10. The surface-roughness Legendre-mode spectrum for higher mode numbers is determined by mapping the 1-D Fourier-mode spectrum averaged over all of the great circles. The final Legendre-mode spectrum for the surface roughness is suitable for input to implosion modeling codes.

ACKNOWLEDGMENTS

This work was supported by the U.S. Department of Energy Office of Inertial Confinement Fusion under Cooperative Agreement No. DE-FC52-92SF19460, the University of Rochester, and the New York State Energy Research and Development Authority. The support of DOE does not constitute an endorsement by DOE of the views expressed in this article.

REFERENCES

1. T. R. Boehly, D. L. Brown, R. S. Craxton, R. L. Keck, J. P. Knauer, J. H. Kelly, T. J. Kessler, S. A. Kumpan, S. J. Loucks, S. A. Letzring, F. J. Marshall, R. L. McCrory, S. F. B. Morse, W. Seka, J. M. Soares, and C. P. Verdon, *Opt. Commun.* **133**, 495 (1997).
2. D. D. Meyerhofer, J. A. Delettrez, R. Epstein, V. Yu. Glebov, V. N. Goncharov, R. L. Keck, R. L. McCrory, P. W. McKenty, F. J. Marshall, P. B. Radha, S. P. Regan, S. Roberts, W. Seka, S. Skupsky, V. A. Smalyuk, C. Sorce, C. Stoeckl, J. M. Soares, R. P. J. Town, B. Yaakobi, J. D. Zuegel, J. Frenje, C. K. Li, R. D. Petrasso, D. G. Hicks, F. H. Séguin, K. Fletcher, S. Padalino, M. R. Freeman, N. Izumi, R. Lerche, T. W. Phillips, and T. C. Sangster, *Phys. Plasmas* **8**, 2251 (2001).
3. P. W. McKenty, V. N. Goncharov, R. P. J. Town, S. Skupsky, R. Betti, and R. L. McCrory, *Phys. Plasmas* **8**, 2315 (2001).
4. *LLE Review Quarterly Report* **99**, 160, Laboratory for Laser Energetics, University of Rochester, Rochester, NY, LLE Document No. DOE/SF/19460-555 (2004).
5. J. Sater *et al.*, *Fusion Technol.* **35**, 229 (1999).
6. D. N. Bittner *et al.*, *Fusion Technol.* **35**, 244 (1999).
7. W. J. Hogan, E. I. Moses, B. E. Warner, M. S. Sorem, and J. M. Soares, *Nucl. Fusion* **41**, 567 (2001).
8. J. K. Hoffer *et al.*, *Fusion Technol.* **30**, 529 (1996).
9. J. D. Sheliak *et al.*, *Fusion Technol.* **30**, 83 (1996).
10. B. J. Koziolowski *et al.*, in *Inertial Fusion Sciences and Applications 2003*, edited by B. A. Hammel *et al.* (American Nuclear Society, La Grange Park, IL, 2004), pp. 762–765.
11. J. A. Koch *et al.*, *Fusion Technol.* **38**, 123 (2000).
12. J. A. Koch *et al.*, *Fusion Sci. Technol.* **43**, 55 (2003).
13. DALSA, Waterloo, Ontario, Canada, N2V 2E9 (see <http://www.dalsa.com>).
14. M. J. Bonino, “Material Properties of Spider Silk,” M.S. Thesis, University of Rochester, 2003.
15. G. J. Borse, *Numerical Methods with MATLAB:® A Resource for Scientists and Engineers* (PWS Publishing, Boston, 1997).
16. This algorithm was developed by one of the authors, A. Warrick, while on leave of absence at LLE.
17. S. Jin, 2002 Summer Research Program for High School Juniors at the University of Rochester’s Laboratory for Laser Energetics, Rochester, NY, LLE Report No. 329, LLE Document No. DOE/SF/19460-479 (2003).
18. R. B. Stephens *et al.*, *Fusion Sci. Technol.* **45**, 210 (2004).
19. S. Pollaine and S. Hatchett, *Nucl. Fusion* **44**, 117 (2004).
20. J. D. Moody, Lawrence Livermore National Laboratory, private communication (2005).

Shock-Timing Experiments Using Double-Pulse Laser Irradiation

Introduction

Direct-drive inertial confinement fusion (ICF) targets use temporally shaped drive pulses to optimize the target performance while controlling the Rayleigh–Taylor instability.^{1–3} The portion of the pulse preceding the main compression drive is used to create shocks that modify the target adiabat and thereby determine the compressibility and stability of the imploding shell. After the passage of the first shock, the compressed material at the ablation front relaxes to densities below solid, thereby increasing the ablation velocity produced by the main drive providing ablative stabilization.^{4–6} Adiabat shaping⁷ is a refinement that uses a short pulse (~100 ps) preceding the main pulse to produce an initial shock that is not supported and therefore decays as it propagates through the target shell. Ideally, this decaying shock produces a larger adiabat in the outer portion of the shell (where the shock is stronger) than the inner portion, simultaneously improving target stability and maintaining high compressibility of the main fuel.

An optimized direct-drive ICF implosion requires that the main compression wave overtake the first shock just as that shock reaches the inner surface of the cryogenic fuel layer.⁸ (Ideally, the main drive should compress and implode the capsule isentropically. In ICF, this compression is so rapid and steep that it is sometimes referred to as a shock wave.) If the compression wave is too late, the first shock enters the fuel, prematurely compressing and heating it. If it is too early, the inner portion of the target is placed on too high an adiabat, reducing its compressibility. For direct-drive ignition target designs, the compression wave must overtake the first shock to within ± 150 ps of the design specification.⁹

Indirect-drive ICF implosions are less susceptible to Rayleigh–Taylor instabilities and are therefore designed to implode along lower adiabats. Ignition designs for indirect drive use three shocks to moderately compress the target shell with a minimal increase to the adiabat before arrival of the compression wave (sometimes referred to as the fourth shock). Indirect-drive ignition target designs specify that the timing of the first three shocks be controlled to ± 50 ps and the fourth shock be timed to ± 100 ps.

In both of these cases, the target compression requires multiple shock waves to achieve optimal performance. The timing of those shocks is critical to that performance. It is therefore important that the simulation codes used to design ignition targets be validated with experiments that provide information on how multiple shocks propagate in laser-driven targets and provide the timing of those shocks. Experiments at the OMEGA¹⁰ laser are conducted to develop the experimental techniques to do this and to validate direct-drive designs. Eventually, those techniques will be used on the National Ignition Facility (NIF)¹¹ to evaluate whether a given pulse shape meets the shock-timing specification.

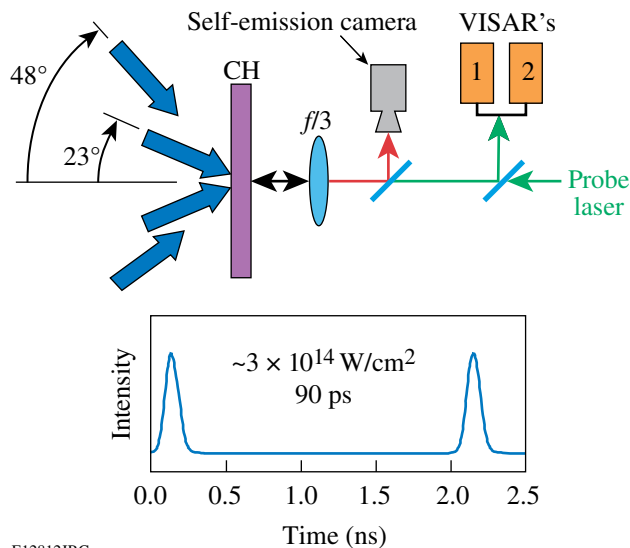
We report on a series of experiments at the OMEGA Laser Facility that study the propagation and timing of multiple shocks in planar targets. In a direct-drive implosion, shock coalescence occurs before significant target motion, making the planar approximation valid. Planar targets are ideally suited to shock-wave experiments because they afford diagnostic access and because shocks can readily be produced at conditions that are relevant to ICF. These experiments demonstrate our ability to observe shock-velocity profiles and discern shock coalescence (timing) with the precision required for ignition targets. Hydrodynamic simulations of these experiments model the time history of the shock velocities and the observed coalescence times to the accuracies required for direct-drive ignition targets.

Experiments

The experiments were performed using planar 125- μm -thick polystyrene ($\rho = 1.05$ g/cc) targets that were directly irradiated with two 90-ps pulses separated by 1 to 2 ns with 12 OMEGA laser beams.¹⁰ The shocks created by these pulses were observed using a velocity interferometer system for any reflector (VISAR)^{12,13} that records the shock velocity as a function of time. The time-resolved optical emission from the shocks was simultaneously recorded. The experimental configuration shown in Fig. 104.17 where two rings of beams (six in each) are shown at their angles of incidence (23° and 48°). Each beam has a phase plate (DPP)¹⁴ that produces a super-Gaussian intensity profile in space described by

$I(r) = I_0 \exp\left[-(r/412 \mu\text{m})^{4.7}\right]$, with I_0 being $1\text{--}5 \times 10^{14} \text{ W/cm}^2$. Obliquity causes the 48° beams to produce a spot on the target that is elongated 40% more than the 23° beams. The rear side of the target is observed with an optical system that also conveys to the target a 532-nm probe beam for the VISAR. In the reverse direction, the reflected probe beam and the self-emission from the target are imaged onto streak cameras.

The experiments were performed with 90-ps pulses, approximately Gaussian in time, in two groups of six beams.



E12812JRC

Figure 104.17

Experimental configuration with two short pulses, typically 1 to 2 ns apart. Beams arranged in two rings (having up to six beams each) at 23° and 48° irradiate solid polystyrene targets. A probe laser is image relayed by a $f/3$ telescope to the rear side of the target and reflected off a shock within the target into two VISAR diagnostics. The same telescope images the optical emission from the shock onto a streak camera.

Each group had the same angle of incidence (either 23° or 48°) and was timed so that one group arrived 1 to 2 ns later than the other. These produced two shock waves in the target that are initially separated by the beam delay. The strength and timing of the second drive pulse was arranged so the second shock overtook the first in the target, providing an observable shock-coalescence event. Experiments were performed with either the 23° beams or the 48° beams arriving first, and the relative energies of the two groups were varied. This article presents detailed results from six shots representative of many shock-timing experiments. The laser conditions for these shots are detailed in Table 104.I, which defines the energy and angle of incidence for the two groups of beams (six in each) for each shot number. The first group arrives at $t = 0$, and the arrival time of the second group is shown in the table. Each group comprises six beams oriented in hexagonal symmetry, so that for oblique angles of incidence, there is no directional bias. It should be noted that the laser spots (at normal incidence) were the same size for both sets of beams. As a result of obliquity, the 48° beams produce spots that are more elongated and therefore have, for similar energies, intensities that are 73% of the 23° beams. To accommodate this, the shots with the 48° beams first have the second group delayed an extra 0.5 ns to ensure that the coalescence signal could be observed after the blank out by the second pulse.

These drive intensities produce $\sim 10\text{-Mb}$ shocks that are hot (5,000–50,000 K), dense (2–4 times solid), and have steep gradients. At optical frequencies they are bright and reflective (30%–80%). VISAR has been demonstrated to be a very precise method for measuring shock velocities. It uses interferometry to measure the Doppler shift of a probe beam reflected off the shock front as it traverses the target.¹² A few percent precision in velocity with a time resolution of ~ 25 ps is routinely obtained.¹³

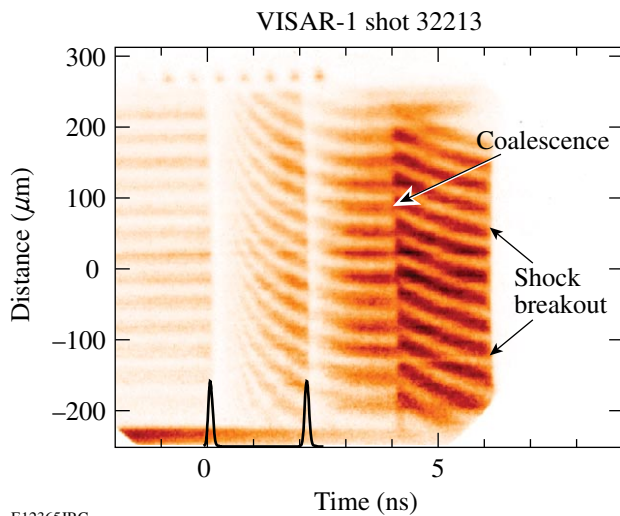
Table 104.I: Summary of beam-configuration information for shock-timing shots.

Shot #	1st group energy (J)	1st group angle ($^\circ$)	2nd group delay (ns)	2nd group energy (J)	2nd group angle ($^\circ$)
32208	120	23	1.5	258	48
32213	252	48	2.0	111	23
32214	111	48	2.0	240	23
32215	73	23	1.5	250	48
32216	119	23	1.5	258	48
32217	236	48	2.0	229	23

VISAR Experiments

VISAR is extensively used in laser-driven equation of state experiments^{15–17} where aluminum “pushers” convey the shock into the sample. These pushers act as a standard reference and shield the samples from x rays from the coronal plasma that drives the shock. In contrast, ICF capsules usually contain only low-Z materials, so x rays from the corona readily propagate through the shell and fuel. The optical diagnostics used in shock-timing experiments performed with low-Z materials can be compromised by x rays that photoionize the target material ahead of the shock. This causes the material to become opaque to the VISAR probe laser, thus “blinding” the VISAR diagnostic during the laser pulse. After the drive ends, the ionized electrons recombine, the target transparency is restored, and the shock can again be observed. With short pulses, the diagnostic record is interrupted for only a few hundred picoseconds during each laser pulse and a nearly complete shock-velocity record is obtained.

Figure 104.18 shows the VISAR record for shot 32213 having 240 J in the first group of beams incident at 48° and 111 J in the second (at 23°) that arrived 2 ns later. This figure is a



E12365JRC
Figure 104.18

Temporally resolved VISAR record from shot 32213 (see text). The fringes are initially horizontal (zero velocity) until they disappear at $t=0$ because of x-ray ionization in the target bulk. Upon reappearance, they have a curvature that results from the decreasing velocity of an unsupported first shock wave that decays as it propagates through the target. At 2 ns, the second laser pulse produces another burst of ionization, blanking the signal again. At ~4 ns, the second shock overtakes the first and the VISAR fringes have a discontinuous jump in position, brightness, and curvature. This coalesced shock also decays and finally reaches the rear surface (breakout) at ~6.2 ns, at which time the VISAR signal ceases.

streak-camera record of the VISAR fringes as a function of time with the vertical dimension corresponding to the spatial direction transverse to the drive laser (and shock) propagation direction. The fringes are deliberately superposed on the image of the target and serve as a phase reference, i.e., zero velocity. (In this case, the early signal results from reflection off the front surface of the transparent target; the rear surface has an antireflection coating). For $t < 0$, the fringes are horizontal (constant phase) because the target is not moving. At $t = 0$, the first pulse irradiates the target, forming a coronal plasma on the front side of the target and producing a shock that propagates into the target. The data record shows, that during the laser pulse, x-ray photoionization causes absorption attenuation of the VISAR laser light to below the detection threshold. After the pulse, by $t \sim 0.5$ ns, the target transmissivity rises and the VISAR signal (fringes) are again detected. During this time, a rapidly changing fringe pattern is observed. The fringe position is proportional to the velocity of the reflecting surface (the shock), so the curvature of the fringes represents the decay of the shock velocity as it propagates through the target.

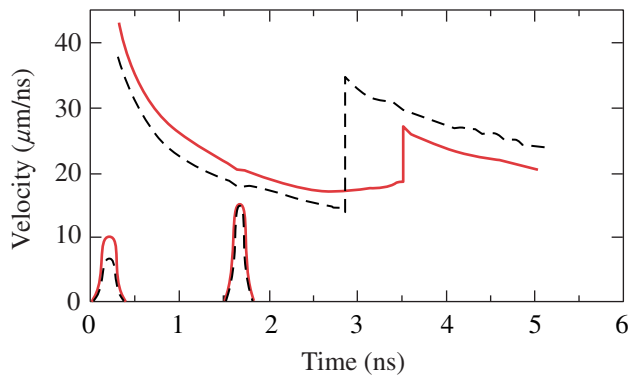
At 2 ns, the second pulse irradiates the target. X rays produced by that pulse blind the diagnostic again and the fringes disappear. When the target recovers from the second pulse (at ~3 ns) the fringe record is still due to reflection off the first shock because the first shock is still ahead of the second shock and nearer to the VISAR. (Note the continuity in the slope of the fringes before and after arrival of the second pulse at 2 ns.) The first shock ionizes the CH above the critical density of the probe beam, ensuring that the probe is reflected and preventing the second shock from being “seen” through the first.

The record from ~0.5 ns to 4.0 ns shows the expected monotonic decay¹⁸ of an unsupported shock traversing the target. At 4 ns, the second shock catches up to the first shock, forming a single coalesced shock that is stronger, and therefore faster, than the first shock. This event is recorded as a discontinuous jump in the fringe position (an increase in velocity) and an increase in the VISAR signal that is due to a concomitant jump in reflectivity for the stronger shock. The coalesced shock is also unsupported; it decays as shown by the curvature in the fringe pattern after 4 ns. The fringes from the coalesced shock persist until that shock reaches the rear surface of the target. At this point the shock “breaks out” and the rear surface releases into vacuum. These shocks produce temperatures and pressures sufficient to melt the CH, so as it releases, the material vaporizes, forming a density profile that quickly absorbs the probe laser and the VISAR signal disappears.

In this experiment, the second shock overtook the first shock despite being driven by half the energy of the first. This is the result of the increased sound speed and the particle velocity in the shock material. In the laboratory frame, one must add the particle velocity to the second shock velocity. Shock waves are supersonic relative to the unshocked material but subsonic relative to the shocked material. This is why rarefaction waves, which travel at the sound speed in the shocked material, can overtake shock waves.

Another interesting feature is the temporal rise of the signal intensity, as seen, for example, in Fig. 104.18 from 0.5 ns to 2 ns. The intensity of the VISAR fringes depends on the amount of reflection from the shock; typically, stronger shocks produce more free electrons and therefore have higher reflectivity. The gradual rise noted in Fig. 104.18 results not from increased reflectivity at the shock front because its reflectivity diminishes with decreasing velocity. Instead, the increase results from a decreased path length of the probe beam through the attenuating material as the shock moves toward the rear of the target.

Figure 104.19 shows the velocity profiles derived from the VISAR data recorded during two similar experiments. The solid line is the velocity profile from a two-pulse experi-



Shots: 32215 & 32216
E12534JRC

Figure 104.19

The shock-velocity history derived from the VISAR data for shots 32216 (solid) and 32215 (dashed). In both cases the target was irradiated by six beams at 23° and 1.5 ns later, by six beams at 48°. For shot 32166, the first group contained 119 J and the second 258 J. Shot 32215 had 73 J and 250 J, respectively. For shot 32216, the VISAR records the velocity of only the first shock until ~3.5 ns when the second shock overtakes the first. After the shocks coalesce, the velocity recorded by VISAR jumps. In the dashed curve, the catch-up occurs earlier because the initial shock is slower (lower first-pulse energy) and the jump is higher because the second shock has had less time to decay.

ment (#32216) having 119 J in the first pulse (from beams at 23°) and, 1.5 ns later, 258 J (from beams at 48°). The initial shock is observed starting at ~0.3 ns and can be seen to decay continuously until 3.5 ns, when the velocity jumps because the second shock has overtaken it. That coalesced shock then decays and eventually reaches the end of the target at 5 ns. The dashed curve in Fig. 104.19 is the velocity profile for an identical experiment (shot 32215) except that the first pulse has only 75 J. The initial shock (0.3 to ~3 ns) has a lower velocity and, as a result, the second shock overtakes it earlier (at 2.9 ns). Note also that the coalesced shock is stronger (higher velocity) than the coalesced shock in shot 32216 because the second shock overtakes the first shock sooner (earlier in the decay of the shock).

When the driving pressure behind a shock relaxes, the shock wave will begin to decay. This occurs because the material behind the shock (that is both heated and compressed) begins to rarefy. In a laser-driven shock that rarefaction begins at the coronal and propagates toward the shock at the local sound speed that is higher than the shock speed. When the rarefaction wave reaches the shock it causes the shock strength to decay at a rate that is proportional to the rarefaction rate. Note that in both experiments shown in Fig. 104.19, the first shock decays more rapidly than the coalesced shock. This is because the first shock traversed less material and hence the rarefaction rate is faster than for the second and coalesced shocks that encountered more material.

In another experiment, the timing of the pulses was reversed (i.e., 48° beams first). Figure 104.20 shows a comparison of the velocity profiles for the two cases. The solid curve is shot 32216 that has the 23° beams first (see solid curve in Fig. 104.19 and its description), and the dashed curve is shot 32214 with 111 J in the 48° beams first and 240 J in the 23° beams second. For the latter, the interbeam timing was lengthened to 2 ns so that the coalescence occurs after the blank out caused by the second pulse. It can be seen that the 48° beams produce a first shock that has 70% of the velocity of that produced by the 23° beams. This is because the 48° beams produce lower intensity and couple less efficiently to the target. In the dashed curve, the slower first-shock velocity reduces the coalescence time despite having the second pulse delayed by 0.5 ns with respect to the other case. The second shock (here produced by the 23° beams) creates a larger jump in velocity for the coalesced shock. This occurs because the 23° beams have a higher intensity and couple more efficiently, thus producing a stronger (and faster) shock.

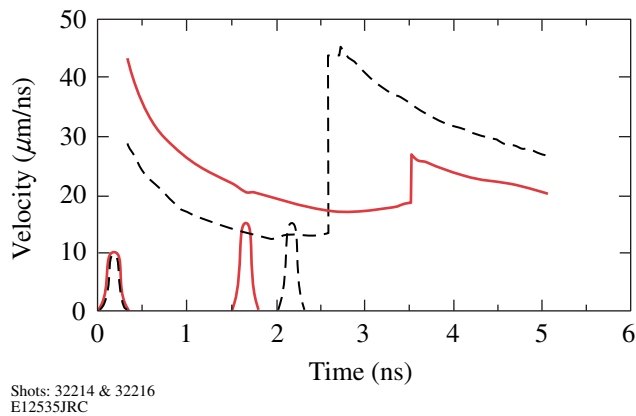


Figure 104.20

Velocity profiles from shot 32216 with 23° then 48° beams (solid) and 32214 (dashed) where the beam timing is reversed (48° beams first). Note that for similar drive energies, the first shock velocity is lower in the latter case. This is because the 48° beams couple less efficiently than the 23° beams. The velocity jump at coalescence is higher because the 23° beams produce a stronger shock.

To obtain the velocity records, the fringe position (phase) as a function of time must be determined. The sensitivity of fringe displacement to velocity is set by the length of the delay etalon in the VISAR interferometer and by the refractive index of the target material (polystyrene $n = 1.59$). VISAR can produce velocity measurements with accuracies of $\sim 1\%$ based on the ability to detect shifts of about 1/20 of a fringe and because the actual shifts are 3 to 5 fringes. We found that ionization has negligible effect on VISAR sensitivity. We estimated the ionized (or free) electron density using the loss of the VISAR signal as a measure of the absorption coefficient model to infer changes to the refractive index. Ionization fractions of ~ 0.02 would cause 100 times attenuation of the signal yet result in only a few percent change in the refractive index. Recent experiments have confirmed that severe ionization blanking occurred in polystyrene with only negligible changes in the index of refraction.²⁰ Preliminary studies of x-ray-induced ionization blanking indicate that, in addition to absorption by free electrons, valance-band vacancies play a role in the absorption of the probe beam. In Figs. 104.19 and 104.20, the experimental velocity profiles for the first shock show negligible change in the slope across the interruption caused by second pulse. Thus, despite large changes in signal level, the inferred velocity profile is negligibly changed.

Self-Emission Measurements

Simultaneous with the VISAR measurements, temporal records of the self-emission (600–1000 nm) from the shocks were acquired using an imaging streak camera with an S20 pho-

tocathode.²¹ Figure 104.21(a) shows the VISAR record for shot 32208 with the corresponding record of the spatially and temporally resolved self-emission intensity shown in Fig. 104.21(b). This shot has 120 J in first pulse at 23° and 260 J 1.5 ns later at 48°. The spatial resolution of VISAR and the self-emission monitor are along the same direction (vertical on target). The distinct shock coalescence and breakout features discussed above are readily evident in both images. In Fig. 104.21(b), the onset of emission from the shock occurs at ~ 0.7 ns as an intense planar feature whose intensity decays nearly to the background level at ~ 3 ns. At about 3.2 ns, the emission suddenly reappears when the second shock overtakes the first and the coalesced shock produces a stronger emission. The abrupt temporal

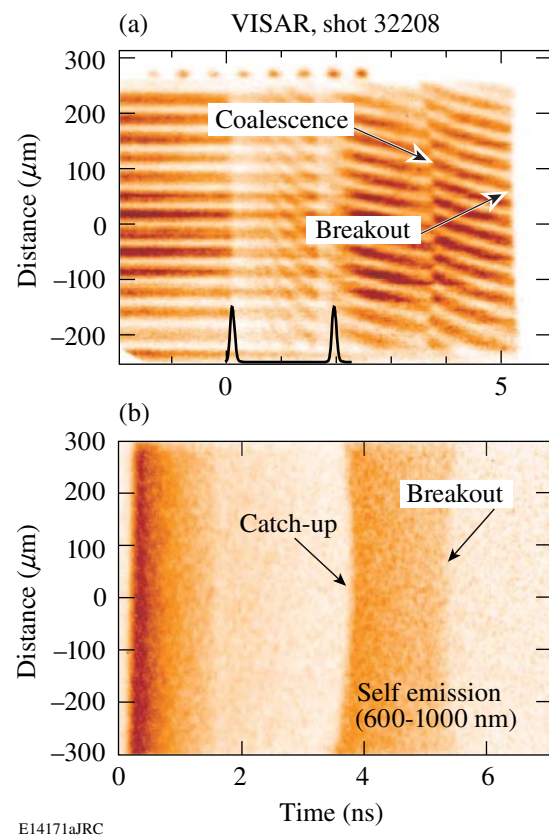


Figure 104.21

(a) The VISAR record and (b) the time-resolved optical self-emission profile for shot 32208. The velocity, catch-up, and breakout features that are seen in the VISAR record are also seen in the self-emission. At about 0.3 ns, the emission from the first shock is visible first, then it decays as the shock velocity decays. At catch-up (~ 4 ns) the coalesced shocks produce an emission that is again bright. This decays until breakout where emission ceases. The curvature of the catch-up and breakout features is related to the spatial shapes of the shock fronts.

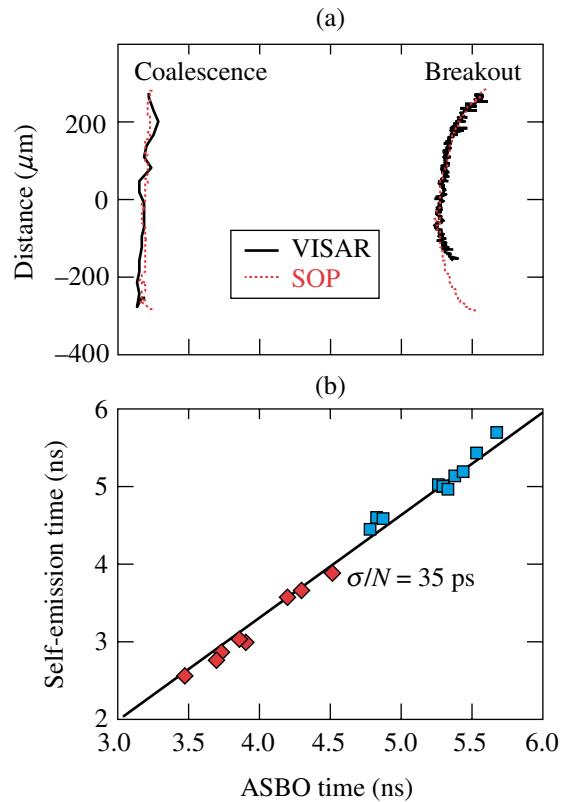
onset of the emission from the coalesced shock indicates that the second (brighter) shock cannot be “seen” through the first shock. Again, this is because the first shock produces material that is overdense for these wavelengths.

For shock velocities of 15 to 40 $\mu\text{m}/\text{ns}$ in polystyrene, the shock temperature ranges from 1 to 8 eV and depends quadratically on shock velocity. This dependence causes the self-emission intensity to drop rapidly. It falls below the detection threshold of the device for a portion of the record. These self-emission profiles corroborate the features seen in the velocity profiles. The shock catch-up and breakout times measured by each of the diagnostics agree, and the velocity profiles can be confirmed using the intensity profile as a reference.

In Figs. 104.21(a) and 104.21(b) (and Fig. 104.18 as well), the catch-up and breakout are curved; this curvature provides insight into the two-dimensional behavior of these experiments. The shock-breakout feature in these experiments is curved; the center breaks out before the edges. The curvature is a result of edge effects and velocity dispersion as the shock propagates to the rear of the target. At its edges, the shock has lower pressure because the laser is less intense, and lateral rarefaction waves move into the shock front. As a result, the shock front becomes curved as it propagates. The slower edges take longer to reach the rear surface of the target with respect to the more intense center. The result is the curved breakout signal.

In contrast, note that the coalescence signal in Fig. 104.21 has a curvature opposite of that at breakout. This is a result of the relative planarity of the two shocks. For shot 32208, the first shock was produced by the 23° beams that have a slightly smaller spot and therefore produce a shock with more curvature than that created by the larger spot because of the 48° beams. At coalescence, the flatter second shock overtakes the curved first shock, first at the edges and last at the center. The result is a catch-up signature that is curved opposite of the breakout, as in Figs. 104.21(a) and 104.21(b). In the cases where the 48° beams were first, the catch-up signal was observed to be flat or curved the other way.

Figure 104.22(a) shows the correlation of coalescence and breakout features as measured from the VISAR and self-emission records for shot 32217. The solid lines are the space-time locations of the coalescence and breakout features measured with VISAR, and the dotted lines are those determined from the self-emission record. Figure 104.22(b) is a comparison of the coalescence and breakout times derived from VISAR and self-emission for several shots over a range of detection times.



E14171bJRC

Figure 104.22

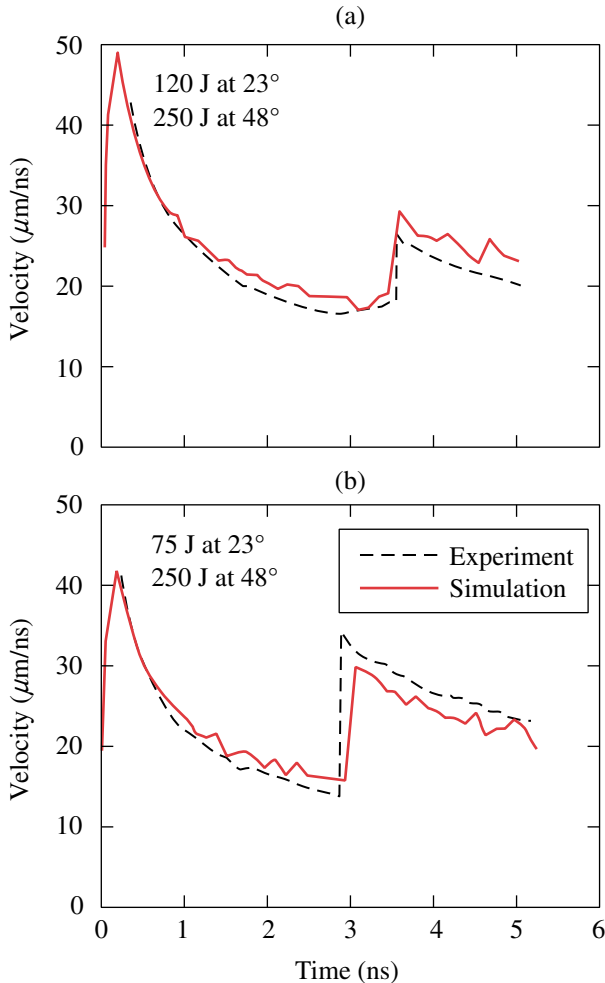
(a) Correlation of coalescence and breakout features in VISAR and self-emission data. (b) Correlation of the coalescence and breakout times as measured by VISAR and self-emission. These times agree to about the precision of the shock measurement.

Note that the correlation (± 35 ps) is of the order of the accuracy of the VISAR measurements (± 25 ps).

Simulations

Simulations of these experiments were performed using the one-dimensional hydrodynamics code *LILAC*.²² Experimental conditions for the laser and target were inputs and the *SESAME*²³ equation of state was used for the polystyrene. The shock trajectories were found by tracking the shock position defined as the steepest gradient in the pressure. Figure 104.23 shows the velocity profiles from the simulations compared to the velocity profiles measured with VISAR. Figure 104.23(a) shows shot 32215 and Fig. 104.23(b) shows shot 32216. Note that the overall profiles are well modeled, as are the catch-up and breakout times. The simulations used a flux limiter of $f = 0.06$.²⁴ The effect of the different incident angles uses an algorithm that analytically treats ray tracing in density gradients to provide path length and absorption information to the one-dimensional code.²⁵ For six such shots, the simulations

were able to predict the shock coalescence and breakout times to better than ± 150 ps, the required precision needed for the timing of the shock in direct-drive ignition targets.



E12536JRC

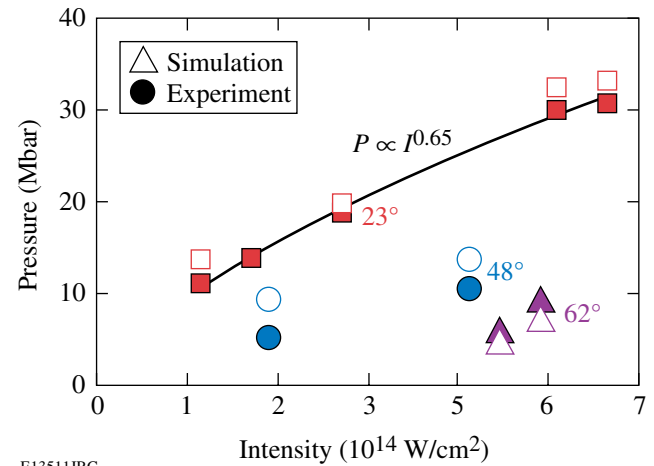
Figure 104.23

Comparison of measured (solid) and simulated (dashed) velocity profiles for (a) shot 32215 and (b) shot 32216. The measured velocities are well modeled, including the catch-up times where the shocks coalesce and the breakout times where the shocks reach the rear surface of the target.

Angle of Incidence

In a similar series of experiments, the effect of the incident angle was studied by inferring the peak shock pressure produced by beams at various angles. The velocity profiles of decaying shocks produced by beams at 23°, 48°, and 62° were compared. The velocity profiles of the decaying shocks were fit to models for unsupported shock waves,^{7,18} and the results were used to infer the peak pressure produced by these pulses. The single-drive pulses were 90 ps in duration and the energy or numbers of beams were changed to vary the incident intensity.

Figure 104.24 shows a plot of the inferred peak pressure versus the incident laser intensity. The experimental results for the three angles are shown as solid figures and the simulations of those experiments as open figures. The experiments for 23° produce a larger range of pressures because they have smaller spots and couple more efficiently. The solid line is a power-law fit to the pressure where $P \propto I^{0.65}$, in agreement with established intensity scaling of $P \propto I^{2/3}$ (Ref. 26). Note that the simulations predict the effect of the incident angle quite well.



E13511JRC

Figure 104.24

Peak shock pressure versus incident laser intensity for beams at incident angles of 23°, 48°, and 62°. The experimental peak pressure (solid points) was inferred from the measured velocity profile using a model for the decay of an unsupported shock wave. The simulated peak pressures are shown as open points. The solid line is a simple power-law scaling for the intensity dependence of pressure.

Conclusions

The velocity profiles of multiple shocks in planar targets irradiated by two short pulses have been measured using VISAR and self-emission data. The deduced velocity profiles show the shocks propagating through the targets and exhibit clear evidence of the time that the second shock overtakes the first. The coalescence times and the arrival of the coalesced shocks at the rear side of the targets are clearly observed and corroborated by the self-emission data. Shock timing and breakout were measured with accuracies of better than ± 50 ps. The spatial shape of the catch-up and breakout signals exhibit features that are attributed to two-dimensional effects caused largely by the finite size of the drive pulses.

The velocity profiles and shock timing are well modeled by one-dimensional hydrodynamics codes that include ray tracing to account for oblique incidence. The simulations predict shock

timing and breakout to better than ± 150 ps, the required precision for direct-drive ignition targets. These results demonstrate our ability to measure and model the behavior of multiple laser-driven shocks propagating in planar targets irradiated by double laser pulses and provide confidence in the hydrodynamic codes used for to design inertial confinement fusion targets.

These double-pulse experiments will be extended to cryogenic deuterium targets and continuous laser pulses. Similarly, experiments will also be performed with indirect-drive ICF to study the behavior and timing of three shocks driven by hohlraums. These experiments on OMEGA will be used to develop techniques that ultimately will be used to fine-tune targets and pulse shapes for ignition experiments on the NIF.

ACKNOWLEDGMENTS

This work was supported by the U.S. Department of Energy Office of Inertial Confinement Fusion under Cooperative Agreement No. DE-FC03-92SF19460, the University of Rochester, and the New York State Energy Research and Development Authority. The support of DOE does not constitute an endorsement by DOE of the views expressed in this article.

REFERENCES

1. J. D. Lindl, *Phys. Plasmas* **2**, 3933 (1995).
2. S. E. Bodner, D. G. Colombant, J. H. Gardner, R. H. Lehmburg, S. P. Obenschain, L. Phillips, A. J. Schmitt, J. D. Sethian, R. L. McCrory, W. Seka, C. P. Verdon, J. P. Knauer, B. B. Afeyan, and H. T. Powell, *Phys. Plasmas* **5**, 1901 (1998).
3. J. D. Kilkenny, S. G. Glendinning, S. W. Haan, B. A. Hammel, J. D. Lindl, D. Munro, B. A. Remington, S. V. Weber, J. P. Knauer, and C. P. Verdon, *Phys. Plasmas* **1**, 1379 (1994).
4. H. Takabe, L. Montieth, and R. L. Morse, *Phys. Fluids* **26**, 2299 (1983).
5. R. Betti, V. N. Goncharov, R. L. McCrory, P. Sorotokin, and C. P. Verdon, *Phys. Plasmas* **3**, 2122 (1996).
6. S. E. Bodner, *Phys. Rev. Lett.* **33**, 761 (1974).
7. K. Anderson and R. Betti, *Phys. Plasmas* **10**, 4448 (2003).
8. P. W. McKenty, V. N. Goncharov, R. P. J. Town, S. Skupsky, R. Betti, and R. L. McCrory, *Phys. Plasmas* **8**, 2315 (2001).
9. *Proposal for Renewal Award for Cooperative Agreement DE-FC03-92SF-19460*, Between the U.S. Department of Energy and the Laboratory for Laser Energetics of the University of Rochester, Addendum: Response to Reviewers' Questions (Rochester, NY, 2001).
10. T. R. Boehly, D. L. Brown, R. S. Craxton, R. L. Keck, J. P. Knauer, J. H. Kelly, T. J. Kessler, S. A. Kumpan, S. J. Loucks, S. A. Letzring, F. J. Marshall, R. L. McCrory, S. F. B. Morse, W. Seka, J. M. Soures, and C. P. Verdon, *Opt. Commun.* **133**, 495 (1997).
11. J. D. Lindl *et al.*, *Phys. Plasmas* **11**, 339 (2004).
12. L. M. Barker and R. E. Hollenbach, *J. Appl. Phys.* **43**, 4669 (1972).
13. P. M. Celliers, D. K. Bradley, G. W. Collins, D. G. Hicks, T. R. Boehly, and W. J. Armstrong, *Rev. Sci. Instrum.* **75**, 4916 (2004).
14. Y. Lin, T. J. Kessler, and G. N. Lawrence, *Opt. Lett.* **20**, 764 (1995).
15. G. W. Collins *et al.*, *Science* **281**, 1178 (1998).
16. M. Koenig, E. Henry, G. Huser, A. Benuzzi-Mounaix, B. Faral, E. Martinolli, S. Lepape, T. Vinci, D. Batani, M. Tomasini, B. Telaro, P. Loubeyre, T. Hall, P. Celliers, G. Collins, L. DaSilva, R. Cauble, D. Hicks, D. Bradley, A. MacKinnon, P. Patel, J. Eggert, J. Pasley, O. Willi, D. Neely, M. Notley, C. Danson, M. Borghesi, L. Romagnani, T. Boehly, and K. Lee, *Nucl. Fusion* **44**, S208 (2004).
17. T. R. Boehly, D. G. Hicks, P. M. Celliers, T. J. B. Collins, R. Earley, J. H. Eggert, D. Jacobs-Perkins, S. J. Moon, E. Vianello, D. D. Meyerhofer, and G. W. Collins, *Phys. Plasmas* **11**, L49 (2004).
18. R. J. Trainor and Y. T. Lee, *Phys. Fluids* **25**, 1898 (1982).
19. P. Drude, *Ann. Phys.* **1**, 566 (1900); N. W. Ashcroft and N. D. Mermin, *Solid State Physics*, College ed. (W.B. Saunders, Philadelphia, 1976).
20. W. Theobald, J. E. Miller, T. R. Boehly, E. Vianello, I. V. Igumenshchev, V. N. Goncharov, A. V. Maximov, and T. C. Sangster, *Bull. Am. Phys. Soc.* **50**, 347 (2005).
21. J. A. Oertel *et al.*, *Rev. Sci. Instrum.* **70**, 803 (1999).
22. J. Delettrez, R. Epstein, M. C. Richardson, P. A. Jaanimagi, and B. L. Henke, *Phys. Rev. A* **36**, 3926 (1987).
23. G. I. Kerley, *J. Chem. Phys.* **73**, 469 (1980).
24. R. C. Malone, R. L. McCrory, and R. L. Morse, *Phys. Rev. Lett.* **34**, 721 (1975).
25. M. Born and E. Wolf, *Principles of Optics: Electromagnetic Theory of Propagation, Interference and Diffraction of Light*, 5th ed. (Pergamon Press, Oxford, 1975).
26. J. D. Lindl, *Inertial Confinement Fusion: The Quest for Ignition and Energy Gain Using Indirect Drive* (Springer-Verlag, New York, 1998), Chap. 5, p. 54.

Polar Direct Drive—Ignition at 1 MJ

Polar direct drive (PDD) is a new and viable option for achieving ignition on the NIF using direct drive while the beams are in the x-ray drive configuration. This allows both x-ray-drive and direct-drive ignition experiments to be performed using the same beam configuration, saving the time and expense that would be incurred from switching beams to different ports. Although PDD target drive will not be as uniform as standard direct drive, computer simulations indicated that moderate to high target gains in the range of 10 to 30 can be achieved (compared to gains of 40 or higher in the symmetric illumination configuration) at the 1-MJ level.

PDD intentionally increases the irradiation intensity at the target equator relative to the pole to compensate for the reduced laser coupling and reduced hydrodynamic efficiency characteristic of oblique irradiation. This is done by a combination of beam pointing, beam focal-spot shaping, and increased laser power of the “equatorial” beams. The beam pointing strategy currently employed is illustrated in Fig. 104.25(a) and the pulse shapes are in Fig. 104.25(b). The beam focal-spot shapes for the polar and midlatitude beams are all circular, with the intensity varying as $\exp[-3(R/R_{\text{target}})^4]$. The equatorial beams use the same circular beam, but with a 5:1 ellipse superposed on them to concentrate a little additional laser intensity at the equator (as discussed in Ref. 1). Also, a wetted-foam target similar to that described in Ref. 1 was used, but scaled down to 1 MJ.

The optimal irradiation pattern is found by varying the pointing, spot shapes, and pulse shapes of the beams. Multi-dimensional hydrodynamic simulations of the implosion are required to evaluate time-dependent variations in the irradiation pattern caused by the beam axes not pointing toward the target center. A parameter search for the optimal irradiation configuration was done using LLE’s 2-D hydrocode *DRACO*. The *DRACO* simulations included a 3-D ray trace to model the laser irradiation and Monte Carlo alpha-particle transport to model the thermonuclear burn.

The pulse shapes were the same for the polar and midlatitude beams. The equatorial beams used a two-parameter

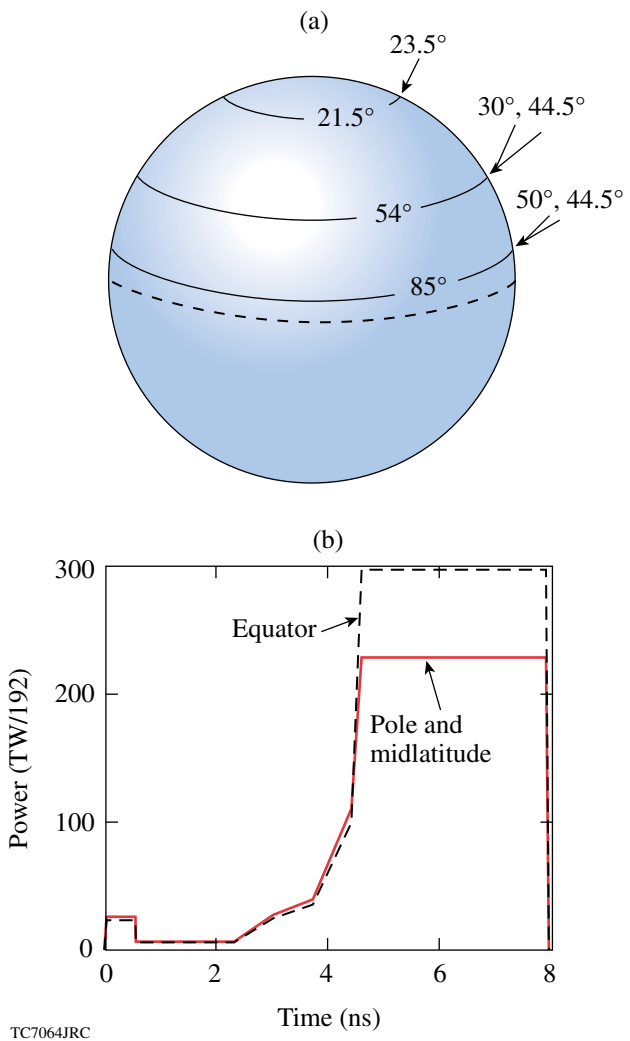


Figure 104.25
(a) Beam pointing strategy for polar direct drive. (b) Pulse shapes.

modification of this shape to allow for early-time shock timing and later-time target drive. The division occurred at 4.6 ns, at the start of the peak of the pulse. At that time, the peak power of the equatorial beams was increased by 30% to compensate for the reduced laser coupling for the oblique irradiation during

the target drive. At earlier times, the power was decreased by 10% to achieve good shock timing.

Target conditions near peak compression are shown in Fig. 104.26. Density contours and the ion-temperature contour lines of 10 and 15 keV are plotted. At this point in the simulation ignition has already occurred, and the thermonuclear burn wave is starting to propagate outward. This simulation results in a target gain of 35. This target gain is maintained over a range of laser conditions. Figure 104.27 shows how the gain varies as the pointing of the three rings changes. High performance is maintained over a spread of $40\ \mu\text{m}$ in pointing, which is well within the capability of the NIF.

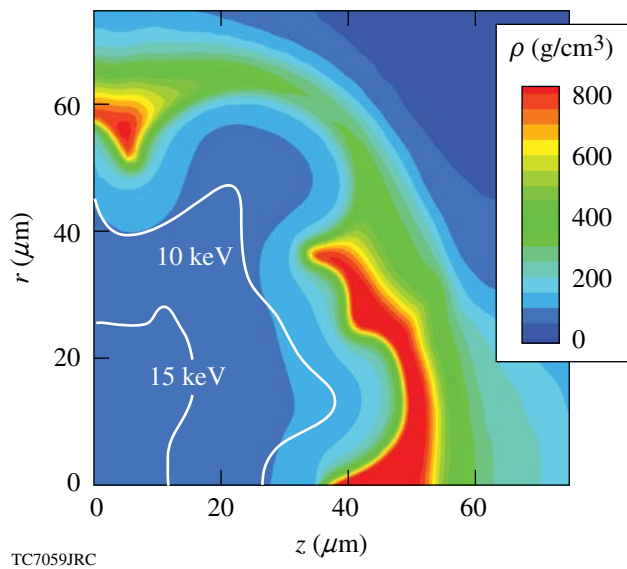


Figure 104.26
Density and temperature contours of the target near peak compression. At this point, the target has ignited and the burn has started to propagate.

Similarly, the sensitivity of target gain to variations in pulse shapes was examined. Three variations were considered: (1) variations in the length of the low-power foot of the pulse, (2) variations in the peak power, and (3) variations in the ratio of peak powers between the equatorial beams and the polar beams (and midlatitude beams). Over a reasonable range, the high gain is maintained.

Finally, the effect of inner surface roughness was considered (Fig. 104.28). Nonuniformity modes 2–10 were used in the simulations, with a spectrum similar to that obtained in current cryogenic experiments on the OMEGA laser. Most of the nonuniformity was concentrated in mode 2. The sensitiv-

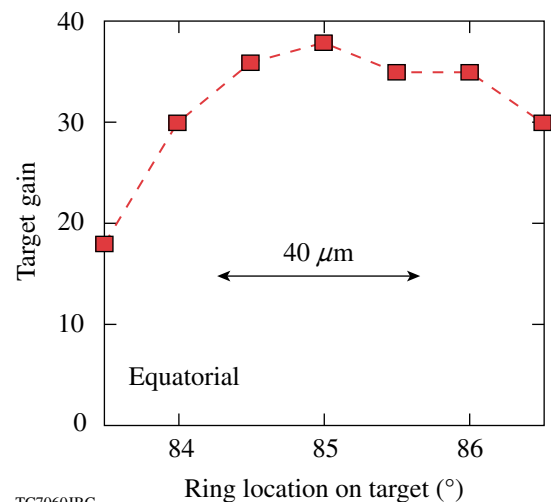
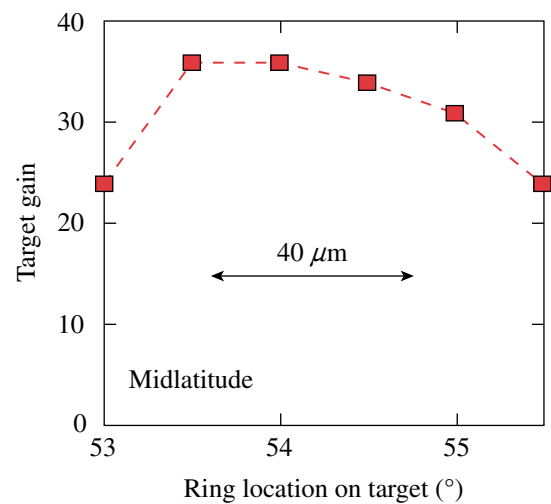
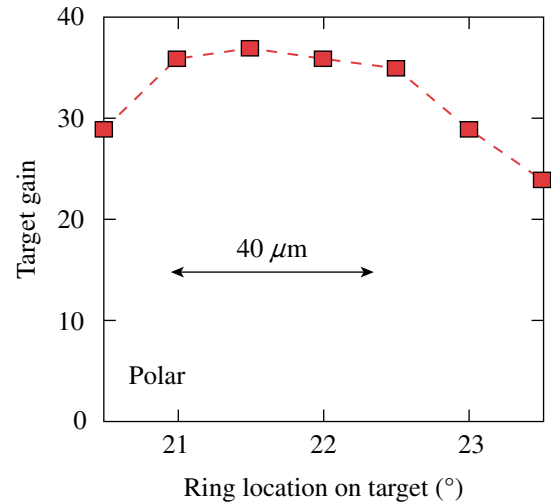
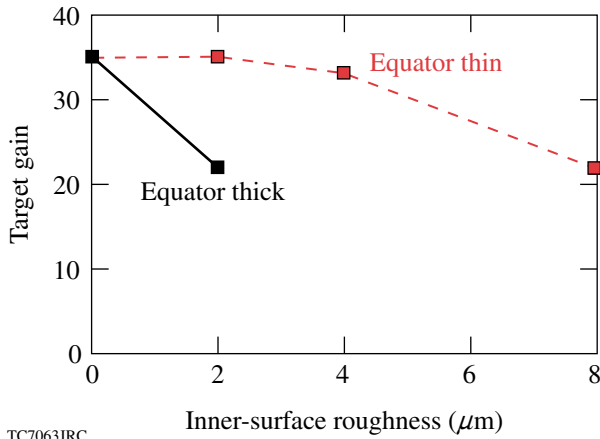


Figure 104.27
Sensitivity of target gain to beam pointing.



TC7063JRC

Figure 104.28
Sensitivity of target gain to inner-surface ice roughness.

ity of target gain to this form of nonuniformity depends on how the phases of the modes add up. When the phases result in a thinning of the equator (and a corresponding thickening of the pole) the target can survive a relatively large amount of nonuniformity. The target is much more sensitive to a thickening of the equator. This suggests that PDD might benefit from “shimming” the ice layer to make the equator intentionally thinner. For a shimmed target, a different beam-pointing strategy might be more optimal.

Further work is in progress to validate these results. This includes simulations with higher resolution, and examination of sensitivity to alternate numerical techniques.

ACKNOWLEDGMENTS

This work was supported by the U.S. Department of Energy Office of Inertial Confinement Fusion under Cooperative Agreement No. DE-FC52-92SF19460, the University of Rochester, and the New York State Energy Research and Development Authority. The support of DOE does not constitute an endorsement by DOE of the views expressed in this article.

REFERENCES

1. S. Skupsky, J. A. Marozas, R. S. Craxton, R. Betti, T. J. B. Collins, J. A. Delettrez, V. N. Goncharov, P. W. McKenty, P. B. Radha, T. R. Boehly, J. P. Knauer, F. J. Marshall, D. R. Harding, J. D. Kilkenny, D. D. Meyerhofer, T. C. Sangster, and R. L. McCrory, *Phys. Plasmas* **11**, 2763 (2004).

Hydrodynamic Simulations of Integrated Experiments Planned for the OMEGA/OMEGA EP Laser Systems

Introduction

The fast-ignitor concept^{1,2} separates the fuel assembly and fuel heating by using a laser pulse to compress the fuel to a high density and an ultrafast, high-intensity laser to heat the fuel. The ultrafast laser produces relativistic electrons with high efficiency (up to 50% has been reported³) that heat the fuel, significantly easing the requirements on the compression driver.^{2,4} Several options for the compression driver have been considered, including using a laser-heated or heavy-ion-beam-heated hohlraum or a direct-drive laser.

The Laboratory for Laser Energetics is building the OMEGA EP Laser System⁵ that will consist of two short-pulse (1 to 10 ps), high-intensity ($>10^{19}$ W/cm²) laser beams, each capable of delivering 2.6 kJ of energy to the 60-beam OMEGA⁶ target chamber. OMEGA EP is designed to act as a backlighter source for imploded high-areal-density cryogenic targets and as a tool to study high-intensity interaction physics and the transport of the relativistic electrons in imploded cryogenic targets. Integrated implosions on the combined OMEGA/OMEGA EP Laser Systems, starting in 2008, will validate the models used for the source and the transport of the relativistic electrons used in the simulation of hydrodynamic codes.

In this article, we present results of simulations of the interaction of relativistic electrons with cryogenic targets that are imploded with a pulse designed to achieve areal densities near 0.5 g/cm². The article is organized as follows: **Transport Model and Target Design** (p. 189) describes the models used in the source and transport of the relativistic electrons and the target and laser pulse designed to reach the required areal densities; **Simulation Results for Symmetric Implosions** (p. 191) presents the results of simulations carried out for uniform conditions; **Effect of Nonuniformity** (p. 193) describes the results for nonuniform implosions (power balance and ice roughness); and **Conclusions** (p. 194).

Transport Model and Target Design

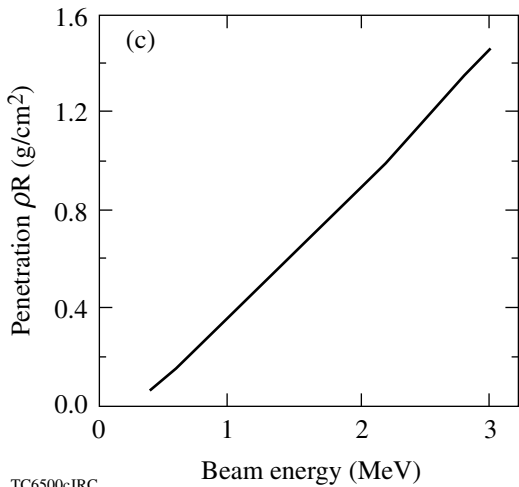
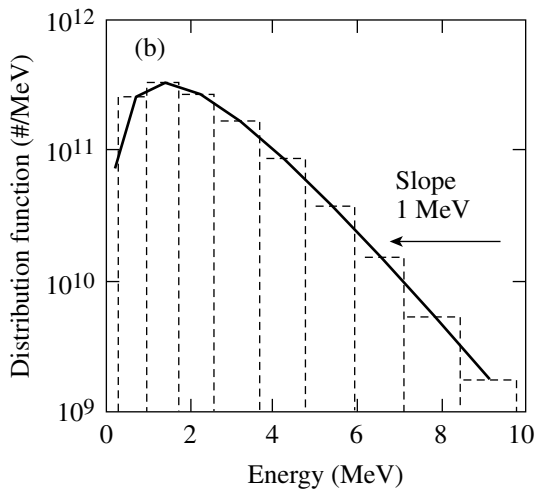
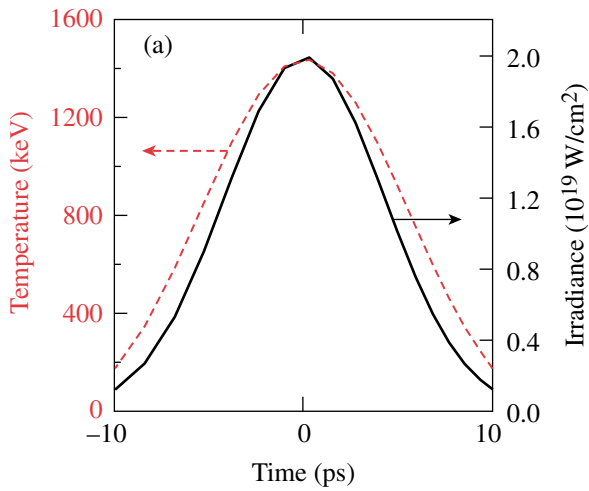
The simulation of the effects of the relativistic electron beam produced by the OMEGA EP laser requires the modeling of

the electron source and the transport of relativistic electrons in high-density materials. The characteristics of the electron source—the conversion efficiency, the spectrum (temperature) of the source, and the divergence of the electrons—are not well known because they are obtained from experiments and simulations that are carried out under conditions that are significantly different from those in an imploding target. Conditions at the end of a laser-produced channel or at the apex of a gold cone near the imploded core are that of a warm plasma (~200 eV) at near-solid density or slightly lower. Particle-in-cell (PIC) simulations are carried out for sharply rising pulses interacting with hot (several keV), low-*Z* targets.⁷ In experiments, short-pulse lasers ≤ 1 ps are focused on solid, mid-*Z* targets (usually Al) and the electron source characteristics are measured indirectly, mostly from K_{α} x-ray emission.⁸ For the simulations reported here, the source electrons are assumed to be Maxwellian with the semi-empirical temperature scaling given by⁷

$$T = 511 \times \left[\left(1 + I / 1.37 \times 10^{18} \right)^{0.5} - 1 \right] (\text{keV}), \quad (1)$$

where I is the laser intensity in W/cm². The electron source temperature, spectrum, and range are shown in Fig. 104.29 for a 2.5-kJ, 20- μm -radius laser pulse. A Gaussian laser pulse is assumed with 10-ps full width at half maximum (FWHM). The peak laser intensity and source temperature are 2×10^{19} W/cm² and 1.4 MeV, respectively.

The physics of the transport of the electrons is very complex. PIC code and hybrid PIC code results show complicated magnetic and electric field structures near the electron source and filamentary structures that depend on the background electron density.⁹ A simple straight-line transport model has been chosen since such high-energy electrons are not scattered much in low-*Z* plasmas. In this model, the electrons lose energy because of collisions with thermal electrons and ions and to collective oscillations according to a formulation that takes into account multiple scattering.¹⁰ The model does not include electric or magnetic fields and Joule heating by the return current. Figure 104.29(c) shows the penetration depth as a function of electron energy in 300-g/cm³, 5-keV DT. A total areal density

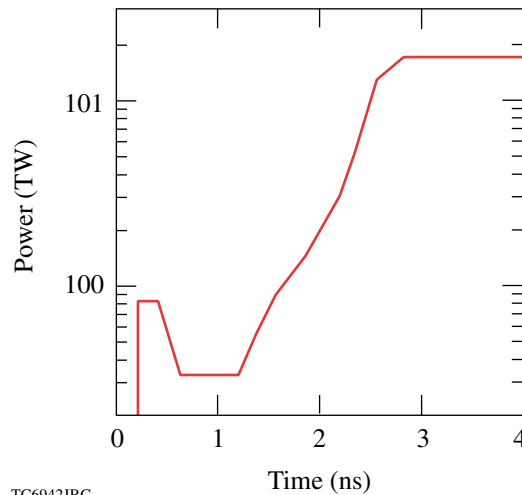
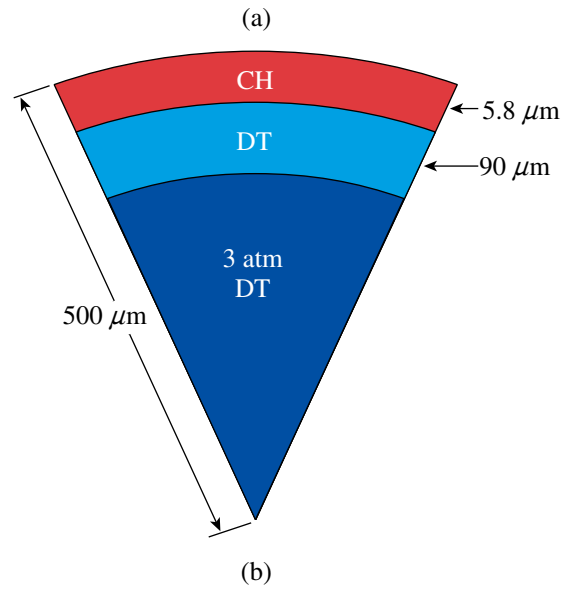


TC6500cJRC

Figure 104.29
 Details of the electron source: (a) temporal evolution of the laser intensity (dashed line) and source temperature (solid line) from Ref 7, (b) distribution function for a 1-MeV temperature and grouping, and (c) penetration depth of electrons in a 5-keV, 300-g/cm³ DT plasma.

of about 1 g/cm² is required to stop the 2-MeV electrons in the 1-MeV distribution in Fig. 104.29(b).

A cryogenic target has been designed to achieve the required core areal densities near 0.5 g/cm² that will stop electrons up to 2 MeV (total areal density of 1.0 g/cm² for a traversing electron). The target, shown in Fig. 104.30(a), is nearly identical to capsules currently being imploded on the OMEGA laser. The pulse shape in Fig. 104.30(b) was designed to provide 25 kJ at 351 nm while keeping the minimum isentrope during the



TC6942JRC

Figure 104.30
 Target design for uniform implosion: (a) target details and (b) shaped pulse producing $\alpha = P_e/P_{TF} < 2$. Nearly identical targets are being imploded on the OMEGA laser.

implosion to $\alpha = P_e/P_{TF} < 2$, where P_e is the electron pressure and P_{TF} is the Fermi pressure at $T_e = 0$. This isentrope is lower than that of present cryogenic implosions.¹¹ The maximum density and total areal density from a 1-D simulation with the hydrodynamic code *LILAC*¹² reach 500 g/cm^3 and 0.5 g/cm^2 , respectively. At peak areal density (3.96 ns) the residual gas inside the target is heated to several kilovolts, whereas the high-density shell is kept below 200 eV.

Simulation Results for Symmetric Implosions

Simulations to study the hydrodynamic response of the target to the energy deposited by the electrons were carried out for a uniform implosion with the 2-D hydrodynamic code *DRACO*.¹³ Uniform implosions can be simulated quickly and therefore permit the investigation of a larger parameter space than perturbed implosions. The electrons were produced at the pole as a cylindrical source directed parallel to the z -axis with radii varying from 5 to $30 \mu\text{m}$. The source was injected where the background electron density is $2 \times 10^{21} \text{ cm}^3$. The results are insensitive to the position of the source because the simulated electron beam has no divergence and the electrons are not effectively slowed until they reach much higher densities. The temporal Gaussian laser pulse produces 2.5 kJ of $1\text{-}\mu\text{m}$ light with the pulse duration varying from 1 to 30 ps FWHM. Two conversion efficiencies from the laser energy to the electron beam were assumed: 20% and 50%. The timing of the electron pulse with respect to the stagnation time was varied between -60 ps to 40 ps in intervals of 20 ps in order to study the sensitivity of the neutron yield to the timing.

The effect of the electron heating on the neutron production rate is illustrated in Fig. 104.31, where contours of neutron production rate per unit volume are shown at the time of peak neutron production. The mass density is shown in black contours. In Fig. 104.31(a), the neutron production in the case when the electron beam is not introduced is limited to the hot spot formed by the residual gas and a small layer inside the high-density shell. In Fig. 104.31(b), the neutron production extends over the path of the $20\text{-}\mu\text{m}$ -radius electron beam and has a greater spatial extent inside the shell than in Fig. 104.31(a). The peak neutron production occurs in a circular region in the hot core where a blast wave was created by the explosion of the shell from the heating by the relativistic electrons.

The temporal response of the stagnated core to the electron heating is shown in Fig. 104.32, where lineouts taken across the target $4 \mu\text{m}$ above the x axis in Fig. 104.31(b) of the neutron rate per volume, the ion temperature, and the mass density are plotted at four times with respect to the peak of the Gaussian high-intensity laser. The electron beam enters from the right. At the peak of the pulse [Fig. 104.32(a)], the shell has already been heated to about 2 keV as compared to the 200 eV shown in Fig. 104.30(c) without the heating beam. The shell starts to explode and decompresses and sends a blast wave into the core, which can be seen as a small jump in the ion temperature. Neutrons are produced in the high-density shell as well as in the core. The conditions in the shell are not uniform because more energy from the electron beam is deposited on the side nearer to the source (right-hand side) than on the far side. Since the

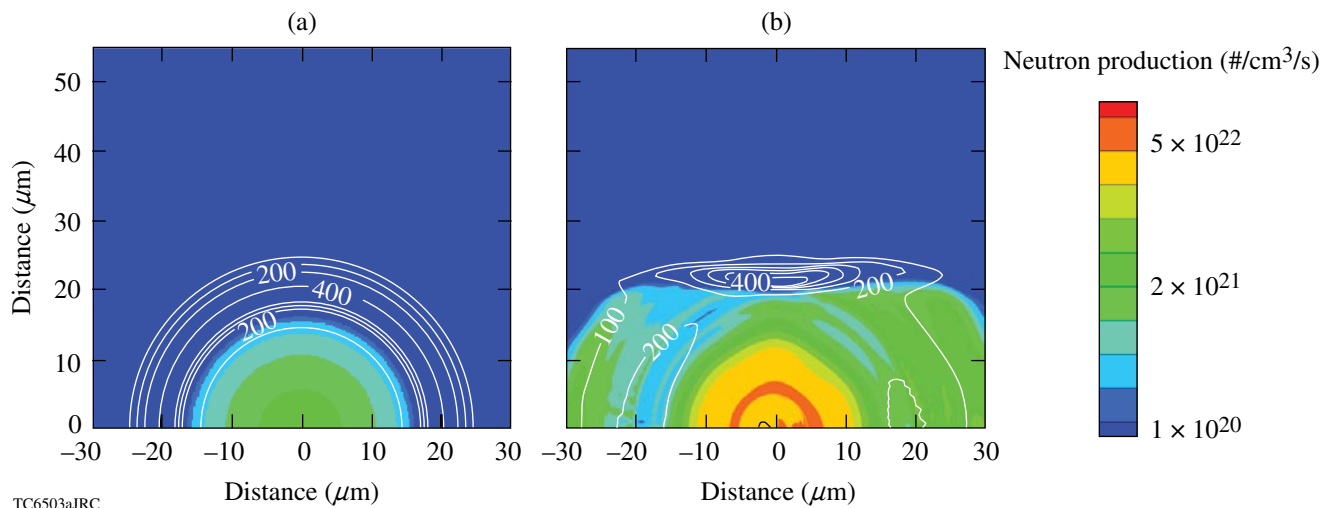
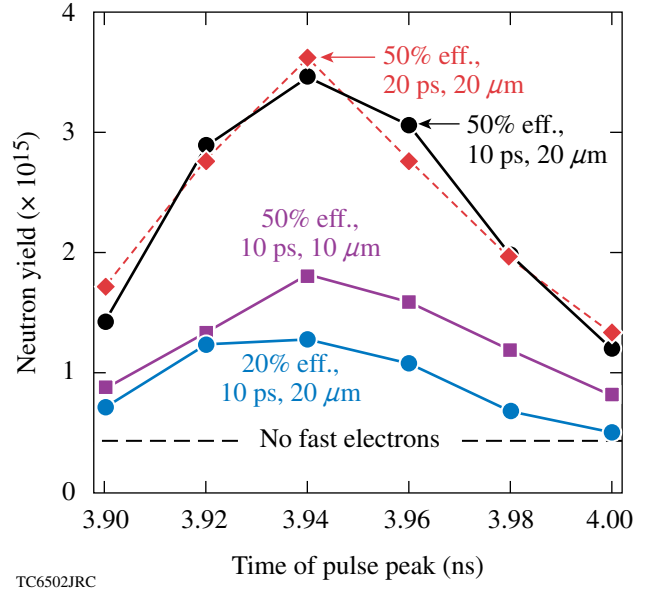


Figure 104.31

Contours of the neutron production rate per unit volume and mass density (black contours) at the time of peak neutron production in the case without an electron beam (3.95 ns) (a) and no electron beam. (b) 2.5-kJ, 50% conversion efficiency, 10-ps FWHM, and $20\text{-}\mu\text{m}$ -radius electron beam peaked at 3.94 ns.

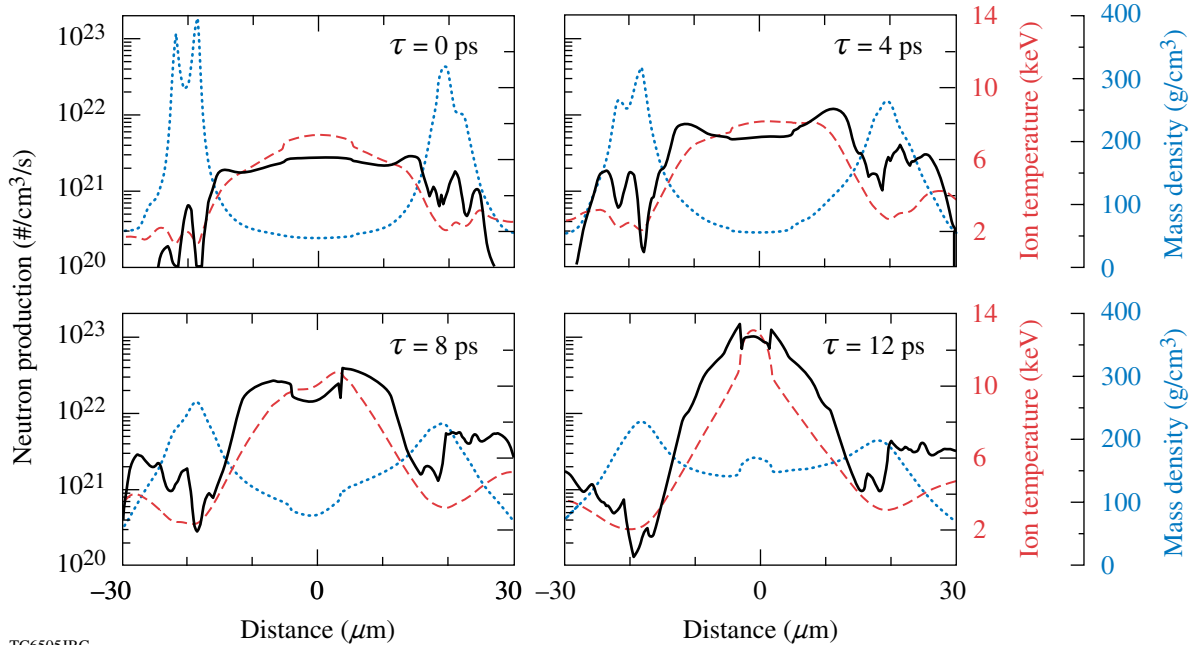
electrons are produced over a range of energies, the less-energetic electrons deposit most of their energy in the shell nearer the source, while the more-energetic electrons deposit their energy uniformly in both sides of the shell. In Fig. 104.32(b), 4 ps after the peak, the blast wave can be seen as small steps in both the ion temperature and the mass density. The neutron production rate is enhanced behind the blast wave. At 8 ps after the peak of the electron pulse [Fig. 104.32(c)], the shell density has decreased to about half its peak uniform value and the blast wave has almost reached the center of the core, heating it to about 10 keV. Neutrons are still being produced in the high-density shell where the ion temperature reaches almost 4 keV. In Fig. 104.32(d), 12 ps after the peak of the electron pulse, the blast wave has reflected from the target center, creating ion temperatures reaching 13 keV and a large neutron production rate, although the actual number of neutrons produced in that region is small because of its small volume. Large neutron rates still occur in the shell, though it is beginning to cool.

The sensitivity of the neutron yield to the timing of the high-intensity pulse for several laser conditions is shown in Fig. 104.33. In all cases, the peak yield occurs when the peak of the pulse is timed about 20 ps before peak stagnation (3.96 ps);



TC6502JRC

Figure 104.33
Sensitivity of the neutron yield to the laser pulse timing and characteristics. Peak areal density occurs at 3.96 ns.



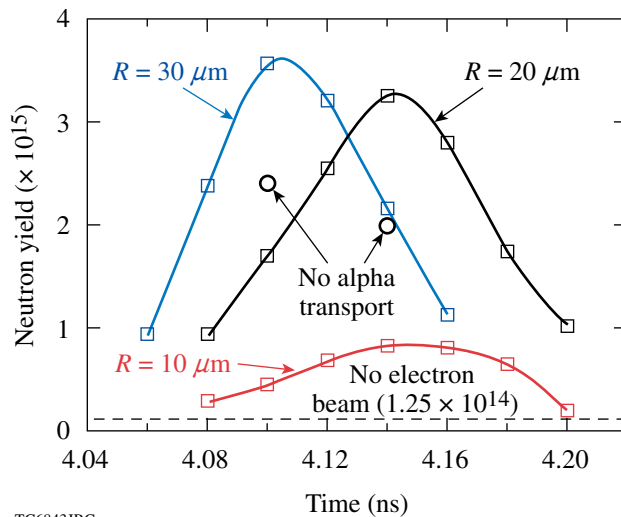
TC6505JRC

Figure 104.32
Lineouts 4 micrometers above the x-axis of the neutron production rate (solid curve), the ion temperature (dashed curve) and the mass density (dotted curve); times are with respect to the peak of the 10-ps Gaussian electron pulse timed at 3.94 ns. The electron beam enters from the right.

the highest yield is about a factor of 8 higher than the yield from the implosion without electrons. The yield remains within a factor of 2 of the peak yield within a 100-ps range for the pulse timing. The 20-ps requirement on the timing specification for the OMEGA EP beams is well within this range. For the 50% conversion efficiency, the yields were the same for the 20-ps and the 10-ps beam FWHM and a 20- μm -beam radius. The higher source temperature from the shorter pulse's higher intensity is compensated by the deposition of more electron energy early in time before the shell has decompressed. Reducing the beam radius reduces the yield by about a factor of 2 because of two effects: the higher intensity leads to a higher source-electron temperature that produces more electrons that escape the core, and the beam only partially covers the core radius, heating less of the high-density shell. Reducing the efficiency to 20% reduces the neutron yield by about a factor of 3.

Effect of Nonuniformity

A series of simulations was carried out with the power-balance nonuniformity caused by the OMEGA 60-beam geometry; they also included alpha-particle transport during neutron production. A modified target design reached a slightly lower areal density than the previous one, 0.45 g/cm², and a lower peak density, 360 g/cm³, because the beam delivered 18 kJ instead of 25 kJ in the previous series of simulations. The high-intensity laser configuration and electron source are the same as in the previous series. Figure 104.34 shows the



TC6843JRC

Figure 104.34

Sensitivity of the neutron yield to the laser pulse timing and characteristics for implosions that include the illumination nonuniformity due to OMEGA beam geometry. The pulse is 2.5 kJ, 10-ps FWHM with a 50% conversion efficiency. Open circles show the results of turning off the alpha transport.

sensitivity of the neutron yield on the timing of the ignitor pulse for three beam radii (10, 20, and 30 μm) from a 2.5-kJ, 10-ps FWHM laser with 50% conversion efficiency to electrons. The implosions without the electron beam produce a yield of 1.25×10^{14} . Introducing the electron beam increased the yield by about a factor of 25. A radius of 10 μm results in a lower yield because the laser intensity and the resulting electron source temperature are too high. The implosions with the larger electron-beam radii yield about the same maximum number of neutrons but at different beam timings. This is because the 30- μm beam produces a lower temperature electron source than that of the 20- μm beam, which is more efficient in heating the core uniformly earlier in time when the areal density of the shell is lower. The higher-temperature electrons from the 20- μm beam are more efficient later, near peak areal density. The timing sensitivity for producing more than half the peak yield is about 80 ps. The yields increased by about 50% when the alpha transport was included, showing the early phase of bootstrap heating.

Another series of simulations was carried out with the same target design and relativistic electron conditions as above but included two levels of inner-ice layer roughness, 2 and 4 μm σ_{rms} , which are larger than the expected values for these implosions.¹⁴ Figure 104.35(a) shows the perturbation cosine spectrum applied to the inner-ice surface with a random phase of $0, \pi$. The resultant core at the time of peak areal density (3.76 ns) in Fig. 104.35(b) shows nonuniform shell densities varying from 200 to 700 g/cm³. A 2.5 kJ, 10-ps FWHM laser pulse with a 20- μm radius was timed 40 ps before shell stagnation. The yields for the simulations with and without the electron beam are shown in Fig. 104.36(a) as a function of the inner-ice roughness σ_{rms} . As expected, the yield decreases in the absence of the electron beam because of the core distortions caused by the ice roughness,¹⁴ as shown in Fig. 104.35(b), down to about a factor of 6 from the uniform case at 4 μm of ice roughness. The neutron yield with the electron beam is almost a constant 10^{15} over the range of nonuniformity; in the case of 4 μm of ice roughness, the yield has improved by about a factor of 120 from that with no electron beams.

The neutron yield remains constant with increasing ice roughness when the electron beam is included because the radius of the high-density shell, whether distorted or not, is less than 20 μm [Fig. 104.35(b)], smaller than the 20- μm electron beam used in these simulations. Thus the electron beam heats the entire shell and raises the same amount of core material to the same temperatures in all cases of ice roughness, shown in Fig. 104.36(b). In the 4- μm - σ_{rms} case, the blast wave does not

converge uniformly as in the zero ice roughness case because of the nonuniform pressure in the distorted shell where it is generated. This leads to lower ion temperatures than in the uniform case, causing the small decrease in the yield observed in Fig. 104.36(a) for the electron beam case.

Conclusions

Two-dimensional hydrodynamic simulations were carried out to model the response of a cryogenic target imploded on the 60-beam OMEGA laser to the relativistic electron beam created by an OMEGA EP ultrafast laser beam. Targets were designed to produce areal densities near 0.5 g/cm^2 at stagna-

tion. A study with uniform implosion showed that the shell, heated by the electron beam, explodes and sends a blast wave into the low-density core. The neutron yield reached a factor of 8 higher than that of the case without the electron beam because of production in the heated ($\sim 2 \text{ keV}$) dense shell and increased

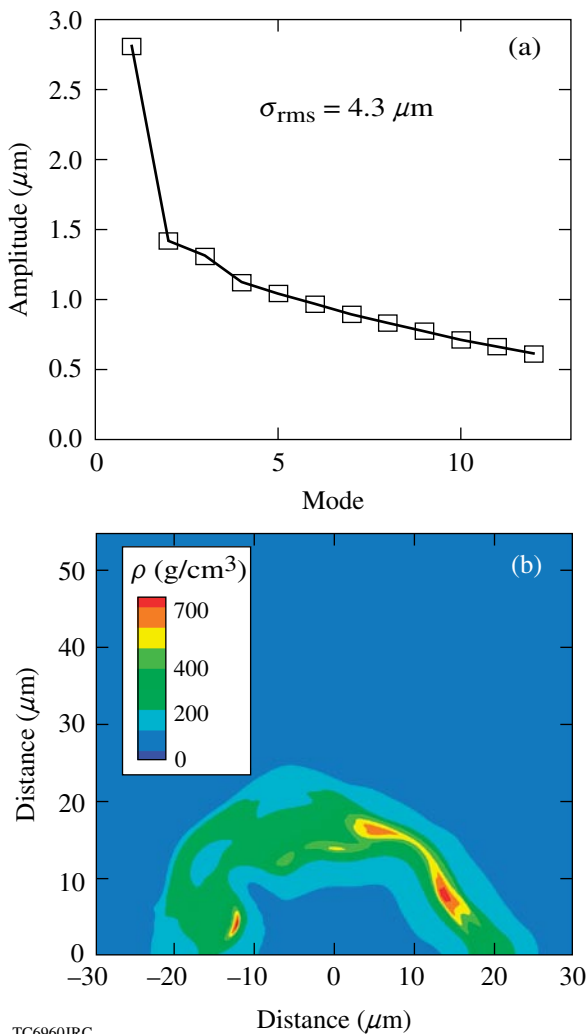


Figure 104.35 (a) Spectrum of the inner-ice roughness for $4\text{-}\mu\text{m}$ σ_{rms} and (b) core condition at stagnation.

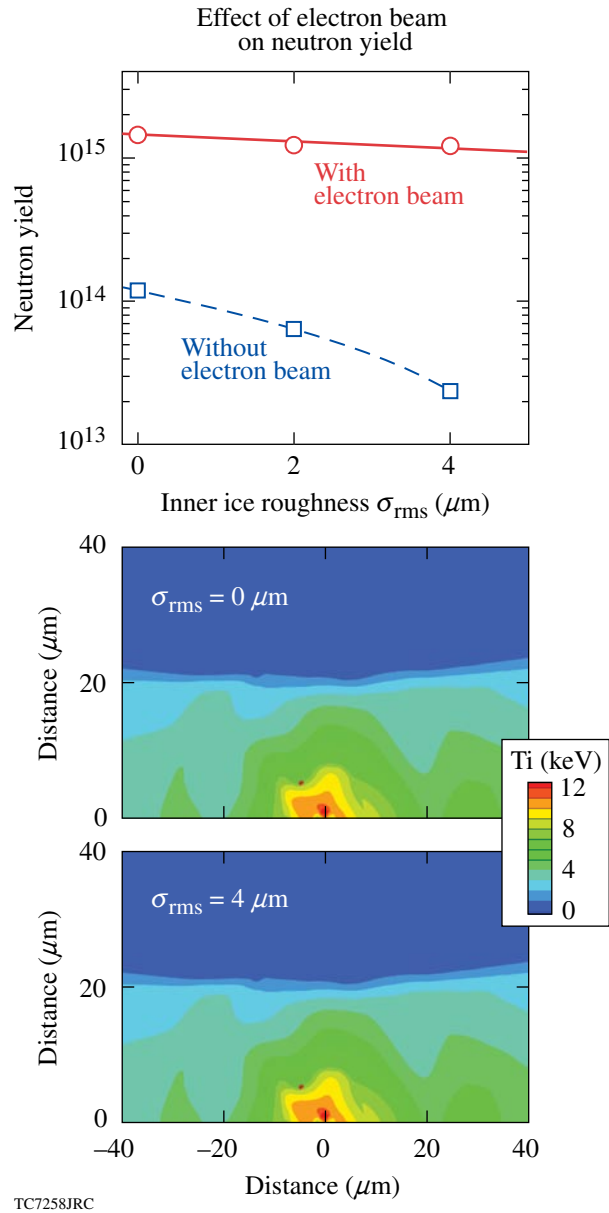


Figure 104.36 (a) Effect of the inner-ice roughness on the neutron yields—with the electron beam, the yield is constant for all levels of nonuniformity. (b) Ion temperature contours near time of peak neutron production for two ice roughness cases, $\sigma_{\text{rms}} = 0 \mu\text{m}$ and $4 \mu\text{m}$, showing that the same amount of shell material is heated by the $20\text{-}\mu\text{m}$ electron beam.

production in the low-density core heated by the blast wave. The highest yields—about 3.5×10^{15} and about a factor of 8 above the yield without the electron beam—were obtained for a 20- μm -radius beam with pulse durations of 10 and 20 ps timed 20 ps before stagnation. Yields within a factor of 2 of the peak yield were produced within a 100-ps timing window centered at stagnation. In a second study carried out with the illumination nonuniformity due to the OMEGA beam geometry, the highest yields (about 3.5×10^{15}) were produced at different beam timings for the 20- and 30- μm radii. These yields are about a factor of 25 larger than those without the electron beam. The inclusion of the alpha transport during neutron production increased the yield by about 50%. The final series of simulations were carried out with two levels of inner-ice nonuniformity, which produced a stagnating shell with nonuniform mass densities ranging from 200 to 700 g/cm^3 . A 10-ps FWHM, 20- μm -radius laser beam timed 40 ps before peak areal density increased the neutron yields by a factor of 120 from that without the electron beam for the largest level of ice roughness. The OMEGA EP beam is expected to produce neutron yields in excess of 10^{15} for all levels of inner-ice nonuniformity and to show the effects of bootstrap heating.

ACKNOWLEDGMENT

This work was supported by the U.S. Department of Energy Office of Inertial Confinement Fusion under Cooperative Agreement No. DE-FC52-92SF19460, the University of Rochester, and the New York State Energy Research and Development Authority. The support of DOE does not constitute an endorsement by DOE of the views expressed in this article.

REFERENCES

1. N. G. Basov, S. Yu. Gus'kov, and L. P. Feokistov, *J. Sov. Laser Res.* **13**, 396 (1992).
2. M. Tabak *et al.*, *Phys. Plasmas* **1**, 1626 (1994).
3. K. Yasuike *et al.*, *Rev. Sci. Instrum.* **72**, 1236 (2001).
4. S. Atzeni, *Phys. Plasmas* **6**, 3316 (1999).
5. J. D. Zuegel, S. Borneis, C. Barty, B. LeGarrec, C. Danson, N. Miyanaga, P. K. Rambo, T. J. Kessler, A. W. Schmid, L. J. Waxer, B. E. Kruschwitz, R. Jungquist, N. Blanchot, E. Moses, J. Britten, C. LeBlanc, F. Amiranoff, J. L. Porter, J. Schwarz, M. Geissel, I. C. Smith, I. Jovanovic, and J. Dawson, "Laser Challenges for Fast Ignition," submitted to *Fusion Science and Technology*; L. J. Waxer, D. N. Maywar, J. H. Kelly, T. J. Kessler, B. E. Kruschwitz, S. J. Loucks, R. L. McCrory, D. D. Meyerhofer, S. F. B. Morse, C. Stoeckl, and J. D. Zuegel, *Opt. Photonics News* **16**, 30 (2005).
6. T. R. Boehly, D. L. Brown, R. S. Craxton, R. L. Keck, J. P. Knauer, J. H. Kelly, T. J. Kessler, S. A. Kumpan, S. J. Loucks, S. A. Letzring, F. J. Marshall, R. L. McCrory, S. F. B. Morse, W. Seka, J. M. Soures, and C. P. Verdon, *Opt. Commun.* **133**, 495 (1997).
7. S. C. Wilks *et al.*, *Phys. Rev. Lett.* **69**, 1383 (1992).
8. K. B. Wharton *et al.*, *Phys. Rev. Lett.* **81**, 822 (1998).
9. L. Gremillet, G. Bonnaud, and F. Amiranoff, *Phys. Plasmas* **9**, 941 (2002).
10. C. K. Li and R. D. Petrasso, *Phys. Rev. E* **70**, 067401 (2004).
11. T. C. Sangster, J. A. Delettrez, R. Epstein, V. Yu. Glebov, V. N. Goncharov, D. R. Harding, J. P. Knauer, R. L. Keck, J. D. Kilkenny, S. J. Loucks, L. D. Lund, R. L. McCrory, P. W. McKenty, F. J. Marshall, D. D. Meyerhofer, S. F. B. Morse, S. P. Regan, P. B. Radha, S. Roberts, W. Seka, S. Skupsky, V. A. Smalyuk, C. Sorce, J. M. Soures, C. Stoeckl, K. Thorp, J. A. Frenje, C. K. Li, R. D. Petrasso, F. H. Séguin, K. A. Fletcher, S. Padalino, C. Freeman, N. Izumi, J. A. Koch, R. A. Lerche, M. J. Moran, T. W. Phillips, and G. J. Schmid, *Phys. Plasmas* **10**, 1937 (2003).
12. J. Delettrez, R. Epstein, M. C. Richardson, P. A. Jaanimagi, and B. L. Henke, *Phys. Rev. A* **36**, 3926 (1987).
13. P. B. Radha, T. J. B. Collins, J. A. Delettrez, Y. Elbaz, R. Epstein, V. Yu. Glebov, V. N. Goncharov, R. L. Keck, J. P. Knauer, J. A. Marozas, F. J. Marshall, R. L. McCrory, P. W. McKenty, D. D. Meyerhofer, S. P. Regan, T. C. Sangster, W. Seka, D. Shvarts, S. Skupsky, Y. Srebro, and C. Stoeckl, *Phys. Plasmas* **12**, 056307 (2005).
14. P. W. McKenty, V. N. Goncharov, R. P. J. Town, S. Skupsky, R. Betti, and R. L. McCrory, *Phys. Plasmas* **8**, 2315 (2001).

Proton Core Imaging of the Nuclear Burn in Inertial Confinement Fusion Implosions

Introduction

Images of the nuclear burn region in inertial confinement fusion (ICF)^{1,2} experiments can provide critical information about the complex dynamics of fuel capsule implosions, showing the spatial distributions of nuclear reactions that result from the cumulative effects of drive and compression including fuel–shell mix, implosion asymmetries, and radiation and heat transport. Such image data provide exacting tests for simulations. Burn images of deuterium–tritium-filled capsules have previously been envisioned³ and made using 14.1-MeV neutrons,^{4–7} 3-MeV protons,^{8–10} or 3.5-MeV alpha particles¹⁰ (see other papers cited in Ref. 11).

This article is the second in a series that discusses another burn imaging method based on the energetic 14.7-MeV protons from reactions in fuel with deuterium (D) and 3-helium (³He) ions. This method, utilizing multiple proton-emission cameras, allows us to study the sizes and asymmetries of burn regions in a wide range of imploded thick plastic-shell capsules that are not amenable to imaging with lower-energy charged particles (which cannot penetrate the shell) and with more angular views than have been obtained so far with neutron imaging. The first article¹¹ described the general method, presented mathematical algorithms used, and evaluated the spatial resolution and signal-to-noise issues. Here we describe details of the imaging hardware, a sample analysis of a radial burn profile measurement, and experiments and calculations that have been performed to test the accuracy of the measurements. In future articles we will show more details about analysis algorithms,¹² systematic studies of the effects of capsule and drive conditions on burn region size for a large number of nominally symmetric implosions,^{12,13} and the effects of drive asymmetry and capsule-shell asymmetry on implosion asymmetry.¹⁴

The proton-emission imaging cameras generate penumbral images of the burn region that are deconvolved using techniques described in Refs. 11 and 12. Two separate approaches are utilized; one generates a 2-D surface-brightness image of the burn, while the other generates a radial burn profile (reactions

per unit volume) for nominally symmetric implosions. The work described here uses only the second approach.

The structure of this paper is as follows. **Hardware and Design Features** (p. 196) describes the camera hardware, which consists primarily of an imaging aperture and a detector pack utilizing CR-39 solid-state nuclear track detectors. **Sample Data From a Capsule With a Plastic Shell** (p. 199) shows sample raw experimental data obtained from an implosion along with the corresponding deconvolved radial profile of emissivity in the imploded capsule. **Demonstration That Possible Sources of Image Broadening are Unimportant** (p. 200) investigates four possible sources of image degradation, all of which are shown to be unimportant. **Fidelity of the Measured Burn Region Sizes** (p. 204) discusses several experimental demonstrations of the fidelity of the reconstructed images, and **Discussion** (p. 205) summarizes the main results.

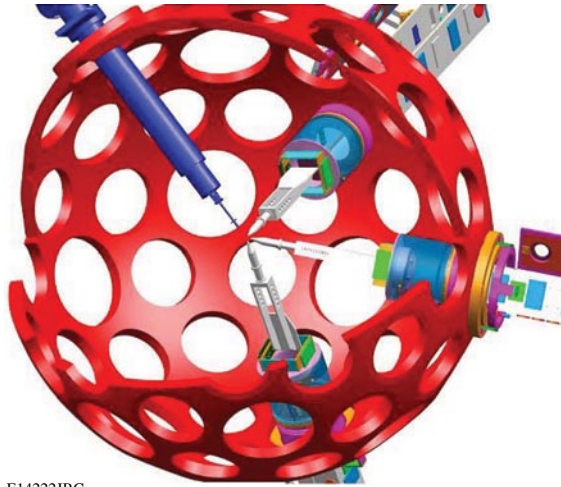
Hardware and Design Features

Three identical proton core imaging system (PCIS) cameras have been fabricated and used simultaneously for imaging D³He burn from three (nearly) orthogonal directions at the OMEGA Laser Facility.¹⁵ Design criteria for individual cameras included flexibility in imaging geometry and detector filter assignments for imaging of various implosion types, modularized design for simplified installation and minimization of turn-around time between successive experiments, and a redundant “dual detection” scheme for verifying results and backup in case of defective detectors.

The integrated system has proven very effective and practical for obtaining burn images at OMEGA. Figure 104.37 shows a schematic of three proton-emission imaging cameras mounted on the OMEGA target chamber, where each camera is positioned by a special diagnostic shuttle system. The simultaneous use of three cameras makes possible studies of burn symmetry^{11,14} and camera consistency [see **Fidelity of the Measured Burn Region Sizes** (p. 204)]. The structure of an individual camera is shown in Fig. 104.38.

After leaving an imploded capsule, protons pass through a round aperture before striking a detector pack. The aperture is typically a 2000- μm -diam hole machined into a 500- μm -thick tantalum (Ta) substrate, although diameters as small as 500 μm have occasionally been used. An accurate, clean, and burr-free

edge for the aperture wall is obtained using electrodischarge machining. Each aperture is inspected and quantitatively characterized on both sides using a microscope with a calibrated X-Y stage and a high-resolution camera to determine that deviations from roundness are small; going around the circumference, the rms deviation from constant radius is not allowed to exceed 3 μm and is usually considerably smaller.

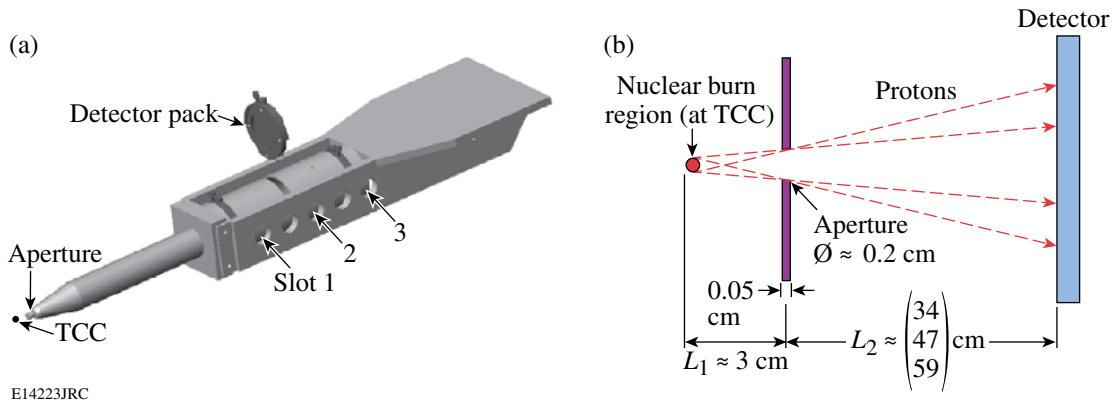


E14222JRC

Figure 104.37 Schematic of the OMEGA target chamber with three cameras for imaging a capsule implosion. The capsule is positioned at target chamber center by the positioning system located at 11 o'clock. The three structures at 1, 4, and 5 o'clock are the PCIS cameras, located approximately orthogonal to each other. This orthogonality is especially important for probing asymmetric burn.

The distance of the aperture from the imploded capsule, which is located at target chamber center (TCC), is usually as small as possible (~3 cm) to maximize counting statistics;¹¹ closer placement is not possible without interfering with laser beams. The region between the aperture and the detector is enclosed within a conductive housing [Fig. 104.38(a)]. This enclosure prevents stray charged particles from reaching the detectors and shields signal protons from possible electric and magnetic fields.

The detector pack consists of a layered assembly of metallic foils and CR-39 detectors¹⁶ held in an aluminum (Al) support. The metallic foils act as ranging filters for reducing the energy of incoming protons to the energy range 0.5 to 8 MeV, where CR-39 proton detection efficiency is essentially 100%. After exposure, each detector is etched in NaOH and scanned on an automated microscope system that locates the track of each incident proton to submicron accuracy. The distribution of proton track density on the detector forms the penumbral image referred to above.



E14223JRC

Figure 104.38 (a) Illustration of the proton-emission imaging hardware. The capsule implosion is located at target chamber center (TCC), which is about 3 cm from the imaging aperture. A detector pack may be positioned in one of three available slots (34, 47, and 59 cm from the aperture), providing geometric magnification of the capsule structure ($M \equiv L_2/L_1$) of 12.5, 16, or 20. The aperture consists of a 0.2-cm hole in a 500- μm -thick tantalum substrate. The total length of the instrument is 93 cm. (b) A line diagram illustrates the dimensions.

The choice of filters depends on the expected proton spectrum, which can be different for different types of capsule implosions. Figure 104.39 shows spectra for a 20- μm -thick plastic-shell capsule and a 2- μm -thick glass-shell capsule, which had mean proton energies of 13 MeV and 14.5 MeV, respectively. The plastic-shell implosion might be imaged using a single 800- μm -thick Al filter, while the glass-shell implosion might require a 1000- μm filter. Rather than a single filter, a

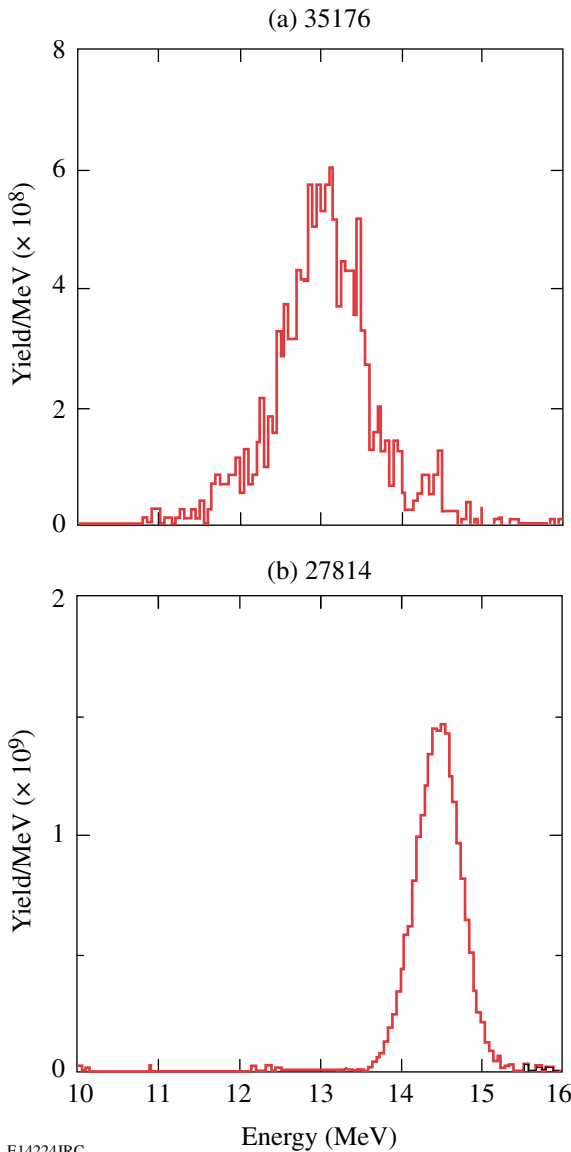


Figure 104.39 For proton-emission imaging, filters are used to reduce the incident proton energies to the range 0.5–8 MeV, where the CR-39 detectors are 100% efficient. Different implosion types result in somewhat different proton energies, as shown here, and filters must be chosen accordingly. (a) A 20- μm -thick CH capsule (shot 35176). (b) A 2.3- μm glass capsule (shot 27814).

series of filters and sheets of CR-39 are usually stacked to provide two redundant images from a single camera. As illustrated in Fig. 104.40(a), two images of the D^3He burn are obtained when a thick filter is placed in front of two back-to-back sheets of CR-39. The filter and first sheet of CR-39 range down the energetic D^3He protons for optimal detection on the back of the first sheet and again on the front of the second sheet. The redundant data are occasionally useful if one CR-39 detector has any defects (such as anomalous intrinsic noise¹⁶). Figure 104.40(b) illustrates another filter configuration that can be used for redundant data. This one places a thin filter between the two pieces of CR-39 so that the proton energy is slightly different at the two detector surfaces. This can be useful if there is a significant uncertainty in what the proton energy will be or if the proton spectrum is particularly wide; if the spectrum at the first sheet is not optimum for detection, the spectrum at the other sheet may be better.

The distance from the aperture to the detector pack can be varied by positioning the detector in any of three designated slots [shown in Fig. 104.38(a)]. The first slot provides a nominal 12.5 \times geometric magnification M (the ratio L_2/L_1), the second

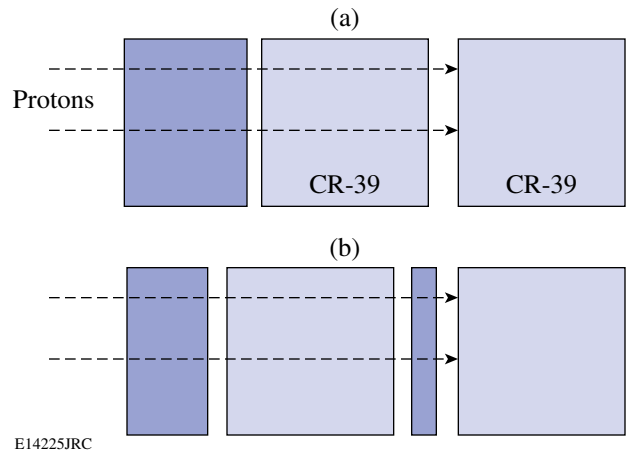


Figure 104.40 Two examples of how CR-39 detectors and filters can be stacked for redundant “front-back” particle detection. (a) Protons lose enough energy while passing through the filter and the first piece of CR-39 so that their energies are in the range of 100% detection efficiency and they leave tracks on both the back side of the first piece and the front side of the second piece. This provides protection against the possibility that either detector has a defect. (b) Protons lose enough energy while passing through the first filter and the first piece of CR-39 so that they leave tracks on the back side of the first piece. They lose slightly more energy while passing through another thin filter, leaving tracks on the front side of the second piece. This provides some protection against the possibility that the proton energy was too low at the second piece; the higher energy at the back of the first piece may then be optimal.

provides $16\times$, and the third provides $20\times$. The position is usually chosen to optimize the density of proton tracks on the detectors, which begin to saturate if the incident proton density exceeds $\sim 10^6$ protons/cm². The third slot makes possible the formation of images for D³He yields up to $\sim 5 \times 10^{10}$.

Each camera is secured to a ten-inch manipulator (TIM) on the OMEGA target chamber by way of the large, flat structure at the back end of the system (Fig. 104.38). The TIM's are diagnostic shuttle systems used to position diagnostics near the implosion. There are six TIM's on the OMEGA target chamber, allowing for the use of multiple PCIS cameras. The TIM's facilitate the installation, positioning, and removal of the cameras. Ease of access is essential since the aperture and detector pack of each camera must be replaced between every laser shot. Modularized aperture and detector packs have been implemented to ensure that the replacement time does not exceed the typical shot-to-shot time interval of the OMEGA laser.

Sample Data From a Capsule With a Plastic Shell

The proton-emission imaging cameras have been used to examine many implosions at the OMEGA Laser System; the majority of these involved direct illumination of warm plastic-shell capsules filled with a D³He gas mixture. These capsules were usually driven by 60 beams of frequency-tripled ($0.35\text{-}\mu\text{m}$) UV light, with total laser energy of 23 kJ delivered in a 1-ns square pulse.¹⁷ Individual beams underwent 1.0-THz 2-D smoothing by spectral dispersion and polarization smoothing applied through the use of birefringent wedges.¹⁸

Structural information about the source of protons in an experiment is obtained by deconvolving a penumbral-camera image using the method described in Ref. 11 and expanded in Ref. 12, which gives the time-integrated radial burn profile (reactions per μm^3) in the implosion. First the azimuthally averaged proton density $N(R)$ in the penumbral image is used to calculate the radial derivative dN/dR , as illustrated in Fig. 104.41. An example using real data is shown in Fig. 104.42(a) (from OMEGA implosion 36730, with 18-atm D³He in a $17\text{-}\mu\text{m}$ -thick plastic shell). This derivative is then fit with a family of functions of varying shapes that are analytically or numerically related to functions describing the radial profile $S_{\text{burn}}(r)$ of proton emissivity per unit volume. The result is a determination of the shape and the characteristic size of the burn region itself. The size can be quantified in different ways, but the radius R_{burn} containing 1/2 of the total local emission seems quite independent of the emission profile shape (as discussed in Ref. 12) and will be used here. For local emission profile shapes we can use the family of super-Gaussians

$$S_{\text{burn}}(r) = S_0 \exp\left[-(r/r_0)^{2/p}\right], \quad (1)$$

where p is a ‘‘peakedness’’ shape parameter and $r_0 = r_0(R_{\text{burn}}, p)$ is a radius. Numerically converting $S_{\text{burn}}(r)$ to functions for comparison with dN/dR , we find the best fit illustrated in Fig. 104.42(a); the corresponding radial profile of emissivity in the capsule is shown in Fig. 104.42(b) and has $R_{\text{burn}} = 32\ \mu\text{m}$. To give an idea of statistical errors, Fig. 104.42(b) shows inferred local emission profiles corresponding to alternative fits to the raw data with total χ^2 value higher than the minimum by one. The uncertainty in the shape is significant, but the uncertainty in R_{burn} is only about $1.6\ \mu\text{m}$ (see Ref. 12 for discussion). Note that the analysis produces absolutely normalized emissivity values.

The D³He burn data from many nominally symmetric implosions have been characterized in this way. A range of R_{burn} values from 20 to $80\ \mu\text{m}$ has been measured in other experiments, demonstrating the applicability of this imaging technique to widely different implosion types. The dependence of R_{burn} on implosion type is discussed in Ref. 12.

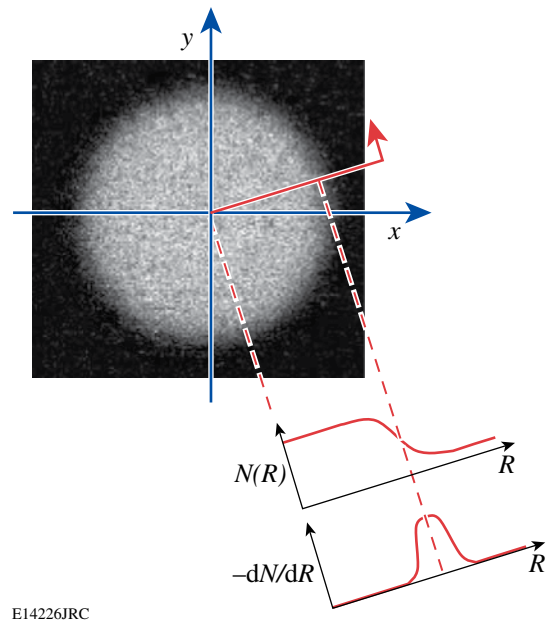
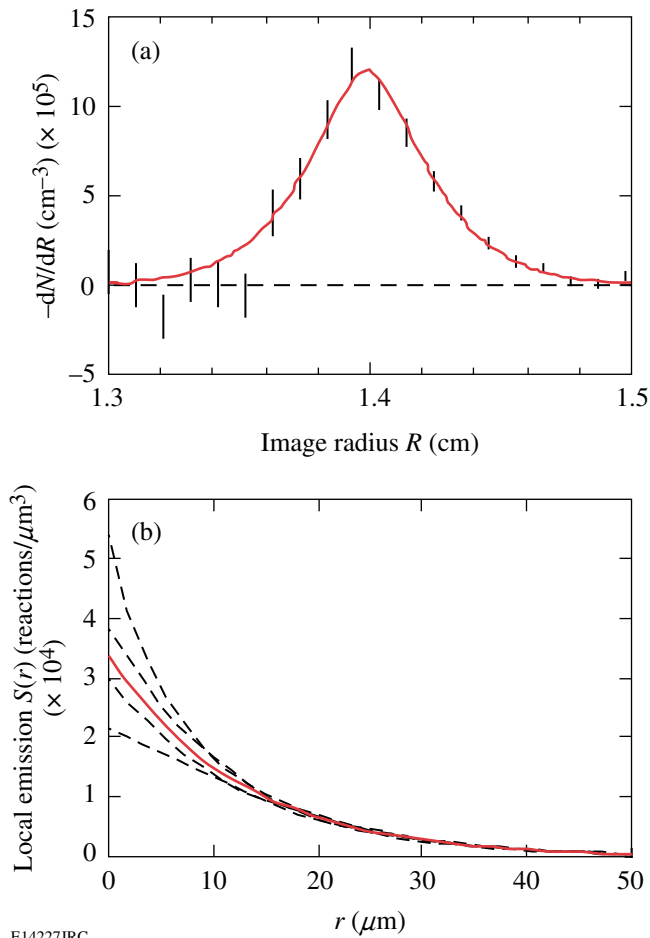


Figure 104.41
Illustration of the relationship between a raw penumbral image (brightness is proportional to the number of protons N per unit area on the detector) and its radial derivative. In the method implemented here, only the azimuthal average of this derivative is used. In the more general case, where asymmetric burn regions are studied, the angular variation of the radial derivative is used.¹¹



E14227JRC

Figure 104.42

(a) The radial derivative of the azimuthally averaged detected proton density (dN/dR) as a function of detector radius for OMEGA implosion 36730. The data were obtained with one of three proton-emission imaging cameras, and the implosion involved a 17- μm plastic shell with an 18-atm D^3He -gas fill. The statistical error bars are larger (smaller) toward the left (right) of the peak where dN/dR represents a small difference between two large (small) numbers. The solid line, representing the best fit to the data, corresponds to the radial burn profile (D^3He reactions per unit volume) shown in (b) with $R_{\text{burn}} = 32 \mu\text{m}$. The error envelope shown by the dashed lines in (b) was generated by using alternate fits to the raw data with χ^2 values exceeding χ^2_{min} by 1. Although the uncertainty in the shape is significant, the uncertainty in R_{burn} is only $\pm 1.6 \mu\text{m}$.

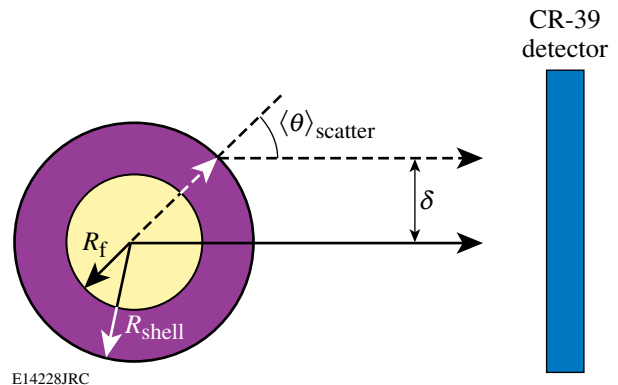
Demonstration that Possible Sources of Image Broadening are Unimportant

As illustrated in **Sample Data From a Capsule With a Plastic Shell** (p. 199), statistical errors in the measurement of burn region size are typically a few microns. In this section we investigate other possible sources of error. The protons that generate a penumbral image may experience trajectory shifts while traversing electric and magnetic fields and while interacting with different materials such as the capsule shell, aperture

substrate, and ranging filters. If these trajectory shifts are severe enough, the spatial structure in the penumbral image may be artificially broadened; the structure in deconvolved burn images or radial burn profiles will therefore also be broadened. The azimuthal average of the penumbra can also be broadened if the aperture is not round, and errors in analysis can occur from use of incorrect geometric parameters. If broadening with a characteristic length l occurs in the penumbral image, the deconvolved image of a point source (the point response function prf) will have a characteristic size l/M , where M is the geometric magnification of the camera (the value 12.5 is used in the following calculations). The effects of trajectory shifts are discussed in order of occurrence, beginning at the location of D^3He proton production and ending at the detector, and are followed by a consideration of errors in system geometry.

1. Scattering in the Compressed Capsule

The first significant materials encountered by the protons are the remnants of the shell that surround and compress the heated fuel region (see Fig. 104.43). Since the majority of implosions imaged with PCIS involved 20- μm -thick CH-plastic shells, this type of capsule will be examined. At the time of peak proton production, the shell material remaining after the ablation phase consists of a highly dense ($\sim 20 \text{ g/cc}$), low-temperature ($\sim 500\text{-eV}$) plasma.^{19,20} Spectral analysis



E14228JRC

Figure 104.43

illustration of the assumed geometry for estimating the degree of proton scattering in shell material. The radius of the fuel region R_f was taken to be $45 \mu\text{m}$; the outer radius of the shell R_{shell} was $80 \mu\text{m}$. Two proton paths originating from a point source are illustrated. The solid line represents the path taken by unscattered protons; the dashed line represents the worst-case path of scattered protons. The average scattering angle $\langle \theta \rangle_{\text{scatter}}$ was estimated both for cold CH and for a fully ionized CH plasma shell. The results were $\sim 1^\circ$ and 2° , respectively, producing corresponding source broadening δ of $\sim 1 \mu\text{m}$ and $3 \mu\text{m}$. Both are negligible compared to typical measured burn radii of $\sim 30 \mu\text{m}$.

of D^3He fusion protons has shown that the shell material, with a corresponding ρR of $\sim 60 \text{ mg/cm}^2$, is responsible for a downshift of a couple mega-electron volts from the 14.7-MeV birth energy [Fig. 104.39(a)].^{21,22} Although proton slowing down is associated with drag of the background electrons, a small amount of scattering will occur off background ions. To estimate the amount of this scattering and its effect on the broadening of the *prf* of the imaging system, two separate calculations were performed.

In the first calculation, the shell material was treated as a cold, dense solid. The Monte Carlo code TRIM²³ was used to simulate the slowing down and scatter of 14.7-MeV protons in the cold-shell material. The shell was treated as a 50/50 atomic mixture of carbon and hydrogen with a density of 20 g/cc and a thickness of 35 μm (a ρR of 70 mg/cm^2). The calculated average transmitted energy was 12.2 MeV, in reasonable agreement with experimental observations [Fig. 104.39(a)]. The average scattering angle was found to be 0.9° . Assuming the fuel-shell interface is at a radius of 45 μm and all scattering occurs on the outside edge of the shell, a worst-case amount of apparent source broadening was estimated to be $\sim 1 \mu\text{m}$ (see Fig. 104.43).

In the second, more realistic calculation, the compressed shell material was treated as hot plasma at a temperature of 500 eV.^{19,20} At this temperature and density, the shell atoms are fully ionized.²⁴ With minor modifications to Rutherford's scattering formula,²⁵ the mean squared angle of the scattered particles is given by

$$\langle \theta^2 \rangle \cong 2\pi N_i (2zeZe/pv)^2 (\ln \Lambda)t, \quad (2)$$

where N_i is the ion species density in the background plasma; t is the shell thickness; Ze is the charge of the scattering material; ze is the charge of the incident particle, with momentum p , and speed v ; and $\ln \Lambda$ is the Coulomb logarithm. The mean scattering angle was calculated for 12-MeV protons passing through 35 μm of a 500-eV, 20-g/cc CH plasma with a Coulomb logarithm of approximately 13.^{19,20} (An initial energy of 12 MeV and a ρR of 70 mg/cm^2 were selected to overestimate the effect.) The calculations gave an average scatter angle of $\sim 2^\circ$, corresponding to a broadening of the *prf* by $\sim 3 \mu\text{m}$. (A similar calculation was performed for scattering in the fuel region, but the effect was much smaller.)

2. Trajectory Shifts Due to Electric Fields

During the laser pulse of a direct-drive implosion, hot electrons are blown off the capsule and may redeposit themselves

on surrounding structures, temporarily establishing electric fields. The purpose of this section is to examine the effect a potential difference between the capsule and the aperture could have on proton trajectories and ultimately on the *prf* of the instrument. Although the effect is complicated by the structure of the OMEGA target chamber and the dynamics of the implosion, these calculations look at simplified geometries to produce an order of magnitude estimate of the effect.

A program was developed for tracking the trajectories of 14.7-MeV protons emitted from a point source as they pass through a negatively charged aperture substrate and on to the CR-39 detector plane. A diagram of the geometry is shown in Fig. 104.44(a). The aperture was positioned 3.3 cm from the

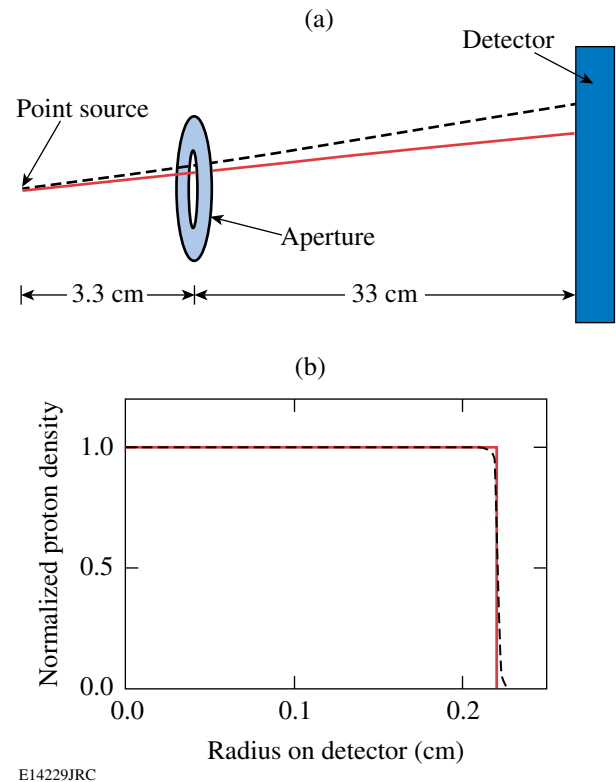


Figure 104.44

(a) Illustration of the effect of electric fields on proton trajectories. The dashed line schematically represents the proton path when a 200- μm -radius aperture carries a potential of 1 MV relative to the source (an overestimate of realistic conditions), while the solid line represents the proton path when no potential is present. Calculations were performed to estimate the image broadening of a point source. (b) The simulated proton density striking the detector for the case of no potential (solid line) and 1-MV potential (dashed line). The result was a slight outward shift of the image and a broadening of the point source by $\sim 1 \mu\text{m}$. This broadening is small compared to a typical burn radius of $\sim 30 \mu\text{m}$.

source, and the detector plane was positioned an additional 33 cm past the aperture. The figure illustrates one possible effect of a charged aperture where a proton path is indicated for two scenarios: for the case of a charged aperture (dashed line) and the case of an uncharged aperture (solid line).

The aperture substrate was modeled by a 1-cm-radius disk carrying a uniform negative charge corresponding to a potential between the source and this disk of 1 MV. The magnitude of the potential was chosen to overestimate the experimental values expected. Experiments indicate that the capsule itself may carry a charge of approximately 1 MV during the laser pulse, but that the potential quickly dissipates once the laser pulse is terminated.^{26,27} For the PCIS experiments, the proton production occurs several hundred picoseconds after laser pulse is terminated, providing a significant period of time in which the potential is known to have substantially decayed.

Calculations were performed for a 200- μm -radius aperture located in the center of the 1-cm-radius disk. Protons were launched through the aperture in all allowable directions. The code calculated particle forces and trajectories on a time scale corresponding to a 5- μm step in the linear dimension using a standard integration for the velocity and a second-order Runge–Kutta integration for the radial position. Simulations were performed with the electric field symmetric on both sides of the aperture as well as with the field turned off between the aperture and the detector, modeling the limit of a perfectly conductive cavity enclosing the instrument. Particle trajectories were individually tracked and particle-particle interactions were not included, as the particle density in the experiments is small. The simulated proton density striking the detector is shown in Fig. 104.44(b) for the case of symmetric fields. The solid line represents the proton density when no net potential exists between the source and the aperture, and the dashed line represents the proton density for a 1-MV potential.

The purpose of this study was to estimate the effect of a potential difference between the aperture and the capsule on the *prf* of the camera. For both symmetric and asymmetric fields, the *prf* was found to be broadened by only $\sim 1 \mu\text{m}$. (Additional simulations were also performed for a 500- μm -radius aperture, as well as for a 0.1-MV potential. None of the studies produced a significant broadening of the image.)

3. Scattering in Aperture Walls

One advantage of proton-emission imaging is that a thin aperture substrate is sufficient to stop D^3He protons, providing a well-defined aperture edge. The apertures commonly used

consist of a 2000- μm -diam cylindrical hole in a 500- μm -thick Ta substrate. The 14.7-MeV protons would be completely stopped by $\sim 400 \mu\text{m}$ of Ta. Protons that travel through less Ta may be stopped in the ranging filters located in the detector pack. Ideally, no detected protons would have scattered in the Ta. Since no aperture is perfectly tapered to match the trajectories of incoming protons, however, some protons will strike the inner walls of the aperture and scatter through a thinner section of Ta, as illustrated in Fig. 104.45(a). If the

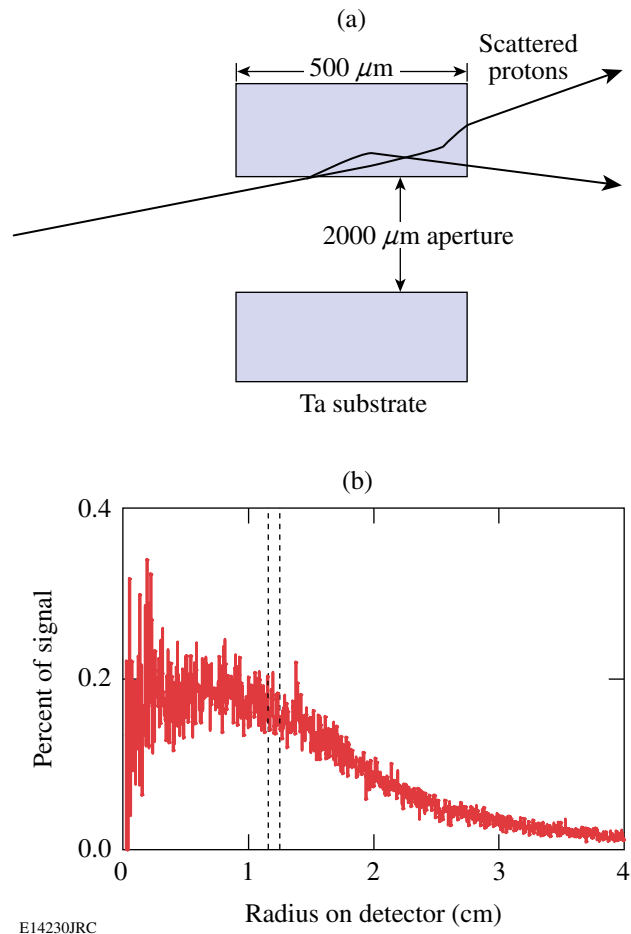


Figure 104.45

(a) Illustration of a cross sectional view of an aperture, defined as a 2000- μm -diam hole in a 500- μm -thick tantalum substrate. Not shown are the source and the detector, located 3 cm to the left and 33 cm to the right, respectively. As seen in the figure, the geometry dictates that protons may encounter less than 500 μm of Ta. If the amount of Ta encountered is sufficiently small, the protons will exit the tantalum and may broaden the image. (b) The simulated ratio of scattered proton density to unscattered signal proton density on the detector. The dotted lines represent the approximate location of an image penumbra from an $\sim 30\text{-}\mu\text{m}$ source. The calculated broadening of the point source was $\ll 1 \mu\text{m}$.

section is thin enough, protons may exit the opposite side, travel to the detector pack, pass through the ranging filters, and be detected on the CR-39. The result would be a slight broadening of the penumbra.

Simulations were performed to estimate the degradation of the camera *prf* by proton scattering in the Ta substrate utilizing the Monte Carlo program TRIM²³ to evaluate the slowing down and scatter of charged particles in matter. The source was treated as a 12-MeV monoenergetic point source of protons, chosen to approximate the observed mean energy of D³He protons after escaping an imploded 20- μ m CH-shell capsule. TRIM was used to determine the amount of scatter produced by discrete thicknesses of Ta; since the aperture wall presents a continuous range of thicknesses to protons, some assumptions were made to transform the 1-D TRIM output into the 2-D geometry of the aperture. Instead of modeling the continuous range of thicknesses, a series of seven discrete thickness steps was used. Depending on where the proton entered the aperture wall, the encountered material was approximated by one of seven Ta sheets, ranging in thickness from 10 μ m to 150 μ m. (Any proton passing through more than 150 μ m of Ta would be stopped by the ranging filters.) Several million protons were tracked through each discrete thickness. Upon exiting the Ta material, the energy and trajectory of each proton was recorded.

These trajectories, along with the system geometry, were used to predict whether scattered protons would strike the detector plane. The system geometry mimicked the actual experimental hardware; modeling of the three main components, the source, the aperture, and the detector was included. The geometry was similar to that seen in Fig. 104.38(b), where the distance from TCC to the aperture was taken to be 3 cm and the distance from the aperture to the detector was 33 cm. The aperture was modeled by a 2000- μ m-diam hole centered in a 500- μ m-thick Ta disk. Based on this geometry and the recorded trajectories from TRIM, the scattered protons that reached the detector pack were isolated from those that did not.

Each proton deflected toward the detector pack then encountered additional filtering before reaching the detector. The filtering, placed directly in front of the detector, was assumed to be 20 μ m of Al followed by 1000 μ m of Mylar and an additional 100 μ m of Al. (Mylar has chemical composition and stopping properties similar to those of CR-39). The proton was assumed detected if the energy was great enough to allow passage through these additional filters.

Thus, a record of the detection locations of all the scattered protons with an appropriate trajectory and energy was created. The ratio of the scattered proton density to unscattered signal proton density as a function of the detector radius is shown in Fig. 104.45(b); the dotted lines indicate the approximate location of the image penumbra from an \sim 30- μ m source. The simulations showed that the scattered protons represent less than 0.3% of the detected protons in the penumbral region and that the radial profile of scattered protons is fairly flat. Since the radial derivative of the proton density ultimately determines the size and shape of the source,¹¹ the small-amplitude slowly varying background would have little effect. Broadening of the *prf* was found to be \ll 1 μ m.

4. Scattering in Filters

Upon reaching the detector pack, protons pass through several ranging filters that are designed to reduce the incident proton energy for optimal detection efficiency. Along with the desired loss of energy, the protons will experience some lateral straggling, another possible source of spatial broadening. To estimate the magnitude of this effect, the Monte Carlo code TRIM was used to track 12-MeV protons from a point source through 20 μ m of Al, 1000 μ m of Mylar, and a final 100 μ m of Al. The lateral positions for protons exiting the filters were recorded and fit by a Gaussian distribution with an *e*-folding radius at the detector of \sim 30 μ m. This translates to a broadening in the camera *prf* of \sim 30 μ m/*M* \sim 3 μ m.

5. Geometric Error

Accuracy in the inference of burn profiles from penumbral images requires accurate knowledge of imaging system dimensions. Of primary importance is the radius of the aperture projection on the detector, which may not be exactly as expected if either the capsule–aperture distance or the aperture–detector distance has any uncertainty. But the radius is actually determined from the data as an integral part of the analysis [see Refs. 11 and 12 and Fig. 104.42(a)], so this is not a source of error beyond the statistical fit error. If the aperture itself is not perfectly round and has deviations from its average radius with the rms value $\delta R_{\text{aperture}}$, the rms deviation from round at the detector will be $(M+1) \delta R_{\text{aperture}}$; this will cause a broadening of the system *prf* by $[(M+1)/M] \delta R_{\text{aperture}} \approx \delta R_{\text{aperture}}$. If the deviation from roundness is due to ellipticity, either from bad fabrication or from the aperture not being exactly perpendicular to the capsule–detector direction, this effect is identified in the data processing and corrected. Other types of deviation from roundness can sometimes be identi-

fied in the data, but in the worst case, uncorrected deviations should have $\delta R_{\text{aperture}} < 3 \mu\text{m}$ as discussed in **Hardware and Design Features** (p. 196).

Another source of error would come from an inaccurate value of the magnification M (see Fig. 104.38 and its caption), which could be different from the expected value if L_1 or L_2 were not measured accurately. Since M represents the ratio of structure size at the detector to structure size in the burn region, any error in M would not cause a broadening of the prf but would cause a multiplicative error in the inferred burn region size. But since the radius of the aperture itself, R_{aperture} , is measured in advance to better than 0.1%, and since the radius of its projection on the detector, $(M+1)R_{\text{aperture}}$, is determined as part of the data analysis, a self-consistent value of M is determined from the data and is not subject to measurement error.

6. Net Broadening

The net result of these broadening effects can be estimated for the data shown in Fig. 104.42 where the measured R_{burn} was found to be $32 \mu\text{m}$ with a statistical error of $\pm 1.6 \mu\text{m}$. If we assume that the five sources of error discussed in the previous subsections are independent and that each generates a distortion in the system prf that is approximately Gaussian, then the net system prf would be a Gaussian whose radius r_{prf} is the sum (in quadrature) of the individual radii. In this case, taking the upper limit for geometric error,

$$r_{prf} \approx \sqrt{3^2 + 1^2 + 0^2 + 3^2 + 3^2} \mu\text{m} \approx 5 \mu\text{m}.$$

The measured burn radius would then be the true burn radius added in quadrature with r_{prf} . The error would be

$$\begin{aligned} \delta R_{\text{burn}} &= R_{\text{burn,measured}} - R_{\text{burn,true}} \\ &\approx 32 \mu\text{m} - \sqrt{32^2 - 5^2} \mu\text{m} \approx 0.4 \mu\text{m}, \end{aligned} \quad (3)$$

which is small compared to the statistical uncertainty of $\pm 1.6 \mu\text{m}$.

Fidelity of the Measured Burn Region Sizes

The following subsections describe experimental tests that demonstrate the repeatability and fidelity of the measured burn region sizes. In **Consistency of the Measured Burn Profiles** (p. 204), measurement consistency is experimentally demon-

strated when six independent measurements of R_{burn} made during the same symmetrically driven implosion are compatible. **Lack of Dependence on Imaging Geometry** (p. 204) shows that the reconstructed burn profiles are independent of changes in the system magnification and the aperture size. **Lack of Distortion by Ambient Fields** (p. 205) presents data suggesting that ambient fields do not affect the system response.

1. Consistency of the Measured Burn Profiles

Figure 104.42(a) shows six separate measurements of R_{burn} made during the same symmetrically driven implosion (OMEGA shot 36730, a capsule with a $17\text{-}\mu\text{m}$ -thick plastic shell filled with a mixture of 6 atm of D_2 and 12 atm of ^3He gas). The implosion was imaged with three separate PCIS cameras, fielded in TIM's 2, 3, and 4. (TIM-3 is located 109° from TIM-2, and TIM-4 is 101° from TIM-2 and 79° from TIM-3.) Each camera produced two measurements of R_{burn} using the redundant detector method described in **Hardware and Design Features**. The error bars in the figure represent statistical uncertainties, as discussed in **Sample Data From a Capsule With a Plastic Shell** (p. 199), and the set of six measurements is self-consistent.

2. Lack of Dependence on Imaging Geometry

A measurement of R_{burn} should be independent of any changes in the geometric parameters of the camera, and this is demonstrated by data plotted in Fig. 104.46. Lack of dependence on aperture diameter is illustrated in Fig. 104.46(b), which shows results from five successive implosions of capsules with $19\text{-}\mu\text{m}$ -thick plastic shells filled with 10.5-atm D_2 and 6-atm ^3He . For each implosion, one TIM was equipped with a PCIS camera. The diameter of the aperture used for the first two and last two implosions was $2000 \mu\text{m}$, while the diameter used for the third implosion was $600 \mu\text{m}$. All results were statistically consistent with the mean value of $30 \mu\text{m}$. Lack of dependence on the geometric magnification was demonstrated by simultaneous use of cameras with different M on each of two implosions. In Fig. 104.46(a), data were taken with $M = 12.5$ and $M = 20$, while in Fig. 104.46(c) $M = 6$ and $M = 9$ were used. In each case the two different values of M resulted in the same measured R_{burn} .

3. Lack of Distortion by Ambient Fields

Several plastic-shell implosions were used to look for possible systematic errors associated with stray fields. The two cameras used for shot 35004 were set up identically except that $L_1 = 5.4 \text{ cm}$ for TIM-3 and $L_1 = 3.7 \text{ cm}$ for TIM-4. If fields were significantly influencing protons in the region between the capsule and the aperture, we would expect to see a difference

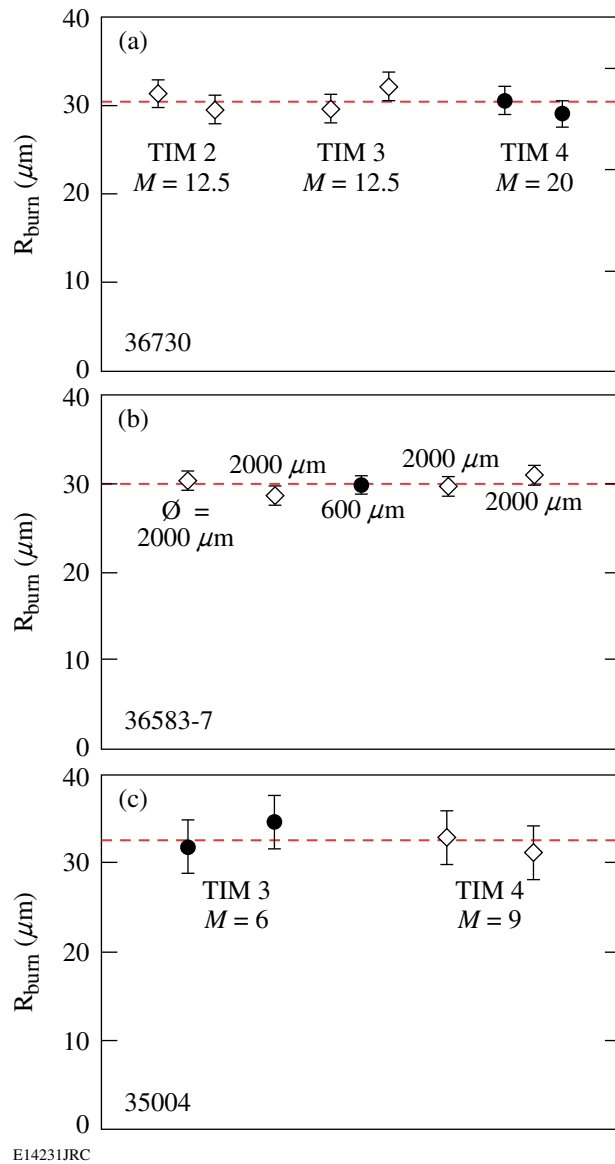


Figure 104.46

R_{burn} data are shown with the average measurement value (dashed line) for a series of implosions. (a) A 17- μm -thick plastic shell with 18-atm D^3He gas fill (OMEGA implosion 36730) was imaged by three nearly orthogonal imaging cameras with different aperture-to-detector distances, located in TIM's 2, 3, and 4. The redundant-detector method was used to generate two data sets for each camera. The geometric magnification (M) of each camera is listed. The data show that different cameras and different aperture-to-detector distances give the same result. (b) A single camera imaged a series of 19- μm -thick plastic shells filled with 10.5 atm D_2 and 6 atm ^3He . The aperture diameter (\emptyset) used for each camera is indicated; R_{burn} was unaffected by the change in aperture size. (c) A 20- μm -thick plastic shell with 18-atm D^3He gas fill was imaged by two cameras having different capsule-to-aperture distances, placed in TIM's 3 and 4. The separately inferred values of R_{burn} were statistically compatible. Note that the error bars in all plots are statistical errors.

in the measured R_{burn} from these two cameras. The results shown in Fig. 104.46(c) report essentially the same R_{burn} for both cameras, suggesting that there were no serious field effects in the region before the aperture.

The three cameras used for shot 36730 were set up identically except that $L_2 = 36.6$ cm for TIM-2 and TIM-3 while $L_2 = 58.6$ cm for TIM-4. If fields were affecting the protons between the aperture and the detector (a region surrounded by a conductor), we would expect to see differences in the measured values of R_{burn} . Figure 104.46(a) shows that all R_{burn} results were consistent, suggesting that there were no serious field effects in the region behind the aperture.

Another recent experiment²⁸ also provides evidence that fields do not dramatically alter the trajectory of D^3He protons in the region past the aperture. In this test, a steel mesh (50- μm -diam wires with 100 wires per inch) was placed directly in front of the imaging aperture. Examination of the proton-emission image revealed no distortions in the mesh-induced pattern, suggesting that fields are not significantly altering the trajectories of 14.7-MeV D^3He protons.

Discussion

Three proton core imaging cameras have been built and installed at OMEGA using the design discussed here, and they have now been used to study the spatial distributions of nuclear burn in a range of different implosion types using algorithms described elsewhere.^{11,12} An example of the analysis of the radial burn profile of a symmetric implosion was shown in **Sample Data From a Capsule With a Plastic Shell** (p. 199) with a 32- μm burn radius. In another article,¹² other types of implosions are studied and are shown to have burn radii ranging from 20 to 80 μm ; clear correlations are shown between the burn radius and implosion parameters (capsule shell material and thickness, fill gas pressure, and laser energy). In addition, 2-D reconstruction techniques have been used together with three nearly orthogonal imaging cameras to study asymmetric burn regions and to show clear relationships between laser drive asymmetry and burn asymmetry.¹⁴ In Ref. 11 the issues of spatial resolution and statistical noise were studied theoretically. A range of calculations and measurements, described in **Demonstration that Possible Sources of Image Broadening are Unimportant** (p. 200) and **Fidelity of the Measured Burn Region Sizes** (p. 204), investigated other possible sources of error in measured burn region sizes. So far there is no evidence of any other errors that are as important as the statistical errors; more calculations and measurements as well as comparisons with x-ray and neutron images will be pursued in the future for

further verification. In the meantime, proton emission imaging is providing interesting and useful data bearing on the understanding of capsule implosion dynamics and performance. A particularly nice feature of this imaging mode, which will be utilized in future studies, is the fact that the same reaction product studied here (the D^3He proton) is also utilized by other diagnostics. Proton spectrometers¹⁶ measure the proton energy at different angles around a capsule, determining the areal density of the compressed shell from the energy loss, while the proton temporal diagnostic^{29,30} measures the time evolution of the burn. The spatial distribution of D^3He burn can therefore be combined with the angular distribution of areal density in the colder shell material and the time evolution of burn, as well as other types of diagnostic measurements, for a more complete picture of implosion dynamics.

ACKNOWLEDGEMENTS

The authors express their gratitude to the OMEGA engineers and operations crew who supported these experiments. In addition, we would like to personally thank Candice Culligan, and Jocelyn Schaeffer for their continuous help. This work has been supported in part by LLE (Subcontract No. P0410025G) and LLNL (Subcontract No. B313975), and by the U.S. Department of Energy Office of Inertial Confinement Fusion (Grant No. DE-FG03-99DP00300) and under Cooperative Agreement No. DE-FC03-92SF19460, the University of Rochester, and New York State Energy Research and Development Authority.

REFERENCES

1. J. Nuckolls *et al.*, *Nature* **239**, 139 (1972).
2. S. E. Bodner, D. G. Colombant, J. H. Gardner, R. H. Lehmborg, S. P. Obenschain, L. Phillips, A. J. Schmitt, J. D. Sethian, R. L. McCrory, W. Seka, C. P. Verdon, J. P. Knauer, B. B. Afeyan, and H. T. Powell, *Phys. Plasmas* **5**, 1901 (1998).
3. K. A. Nugent and B. Luther-Davies, *J. Appl. Phys.* **58**, 2508 (1985).
4. D. Ress *et al.*, *Rev. Sci. Instrum.* **59**, 1694 (1988).
5. R. A. Lerche *et al.*, *Laser Part. Beams* **9**, 99 (1991).
6. C. R. Christensen, D. C. Wilson, C. W. Barnes, G. P. Grim, G. L. Morgan, M. D. Wilke, F. J. Marshall, V. Yu. Glebov, and C. Stoeckl, *Phys. Plasmas* **11**, 2771 (2004).
7. L. Disdier, R. A. Lerche, J. L. Bourgade, and V. Yu. Glebov, *Rev. Sci. Instrum.* **75**, 2134 (2004).
8. Y.-W. Chen *et al.*, *Opt. Commun.* **73**, 337 (1989).
9. M. Nakai *et al.*, *Rev. Sci. Instrum.* **61**, 3235 (1990).
10. A. P. Fews *et al.*, *Phys. Rev. Lett.* **73**, 1801 (1994).
11. F. H. Séguin, J. L. DeCiantis, J. A. Frenje, S. Kurebayashi, C. K. Li, J. R. Rygg, C. Chen, V. Berube, B. E. Schwartz, R. D. Petrasso, V. A. Smalyuk, F. J. Marshall, J. P. Knauer, J. A. Delettrez, P. W. McKenty, D. D. Meyerhofer, S. Roberts, T. C. Sangster, K. Mikaelian, and H. S. Park, *Rev. Sci. Instrum.* **75**, 3520 (2004).
12. F. H. Séguin, J. L. DeCiantis, J. A. Frenje, C. K. Li, J. R. Rygg, C. D. Chen, R. D. Petrasso, J. A. Delettrez, S. P. Regan, V. A. Smalyuk, V. Yu. Glebov, J. P. Knauer, F. J. Marshall, D. D. Meyerhofer, S. Roberts, T. C. Sangster, C. Stoeckl, K. Mikaelian, H. S. Park, H. F. Robey, and R. E. Tipton, "Measured Dependence of Nuclear Burn Region Size on Implosion Parameters in Inertial Confinement Fusion Experiments," submitted to *Physics of Plasmas*.
13. J. L. DeCiantis, "Proton Emission Imaging of the Nuclear Burn in Inertial Confinement Fusion Experiments," M.S. thesis, Massachusetts Institute of Technology (2005).
14. F. H. Séguin, J. L. DeCiantis, J. A. Frenje, C. K. Li, J. R. Rygg, C. D. Chen, R. D. Petrasso, V. A. Smalyuk, F. J. Marshall, J. A. Delettrez, J. P. Knauer, P. W. McKenty, D. D. Meyerhofer, S. Roberts, T. C. Sangster, H. S. Mikaelian, and H. S. Park, *Bull. Am. Phys. Soc.* **49**, 63 (2004); F. H. Séguin, J. DeCiantis, C. K. Li, J. A. Frenje, J. R. Rygg, R. D. Petrasso, S. Regan, J. A. Delettrez, J. P. Knauer, F. J. Marshall, D. D. Meyerhofer, S. Roberts, T. C. Sangster, V. A. Smalyuk, H. S. Mikaelian, H. S. Park, H. Robey, and R. Tipton, *Bull. Am. Phys. Soc.* **50**, 114 (2005); *ibid.*, "Measured Effects of Drive Asymmetry and Shell Asymmetry on Nuclear Burn Region Symmetry in Direct-Drive ICF Implosions," to be submitted to *Physics of Plasmas*.
15. T. R. Boehly, D. L. Brown, R. S. Craxton, R. L. Keck, J. P. Knauer, J. H. Kelly, T. J. Kessler, S. A. Kumpan, S. J. Loucks, S. A. Letzring, F. J. Marshall, R. L. McCrory, S. F. B. Morse, W. Seka, J. M. Soures, and C. P. Verdon, *Opt. Commun.* **133**, 495 (1997).
16. F. H. Séguin, J. A. Frenje, C. K. Li, D. G. Hicks, S. Kurebayashi, J. R. Rygg, B.-E. Schwartz, R. D. Petrasso, S. Roberts, J. M. Soures, D. D. Meyerhofer, T. C. Sangster, J. P. Knauer, C. Sorce, V. Yu. Glebov, C. Stoeckl, T. W. Phillips, R. J. Leeper, K. Fletcher, and S. Padalino, *Rev. Sci. Instrum.* **74**, 975 (2003).
17. A series of burn images have been obtained from thin glass implosions involving less than 23 kJ of laser energy,¹² several thick plastic-shell implosions involving 18 kJ and 30 kJ of laser energy,^{12,14} and a few implosions involving different shaped laser pulses.¹³
18. T. R. Boehly, V. A. Smalyuk, D. D. Meyerhofer, J. P. Knauer, D. K. Bradley, R. S. Craxton, M. J. Guardalben, S. Skupsky, and T. J. Kessler, *J. Appl. Phys.* **85**, 3444 (1999).
19. C. Li and R. D. Petrasso, *Phys. Plasmas* **2**, 2460 (1995).
20. C. K. Li and R. D. Petrasso, *Phys. Rev. Lett.* **70**, 3059 (1993).
21. C. K. Li, D. G. Hicks, F. H. Séguin, J. A. Frenje, R. D. Petrasso, J. M. Soures, P. B. Radha, V. Yu. Glebov, C. Stoeckl, D. R. Harding, J. P. Knauer, R. L. Kremens, F. J. Marshall, D. D. Meyerhofer, S. Skupsky, S. Roberts, C. Sorce, T. C. Sangster, T. W. Phillips, M. D. Cable, and R. J. Leeper, *Phys. Plasmas* **7**, 2578 (2000).

22. F. H. Séguin, C. K. Li, J. A. Frenje, S. Kurebayashi, R. D. Petrasso, F. J. Marshall, D. D. Meyerhofer, J. M. Soures, T. C. Sangster, C. Stoeckl, J. A. Delettrez, P. B. Radha, V. A. Smalyuk, and S. Roberts, *Phys. Plasmas* **9**, 3558 (2002).
23. *SRIM*, a code for calculations of *The Stopping and Range of Ions in Matter*, J. F. Ziegler and J. P. Biersack, Version 2000.39 (2000).
24. D. E. Post *et al.*, *At. Data Nucl. Data Tables* **20**, 397 (1977).
25. J. D. Jackson, *Classical Electrodynamics*, 3rd ed. (Wiley, New York, 1999).
26. D. G. Hicks, C. K. Li, F. H. Séguin, J. D. Schnittman, A. K. Ram, J. A. Frenje, R. D. Petrasso, J. M. Soures, D. D. Meyerhofer, S. Roberts, C. Sorce, C. Stoeckl, T. C. Sangster, and T. W. Phillips, *Phys. Plasmas* **8**, 606 (2001).
27. D. G. Hicks, C. K. Li, F. H. Séguin, A. K. Ram, J. A. Frenje, R. D. Petrasso, J. M. Soures, V. Yu. Glebov, D. D. Meyerhofer, S. Roberts, C. Sorce, C. Stöckl, T. C. Sangster, and T. W. Phillips, *Phys. Plasmas* **7**, 5106 (2000).
28. C. K. Li, F. H. Séguin, J. R. Rygg, J. A. Frenje, R. D. Petrasso, T. C. Sangster, V. A. Smalyuk, J. A. Delettrez, J. P. Knauer, S. P. Regan, J. Soures, F. J. Marshall, P. W. McKenty, D. D. Meyerhofer, C. Stoeckl, R. P. J. Town, P. Patel, A. J. MacKinnion, P. Amendt, N. Izumi, and O. Landen, *Bull. Am. Phys. Soc.* **50**, 266 (2005).
29. J. A. Frenje, C. K. Li, F. H. Séguin, J. Deciantis, S. Kurebayashi, J. R. Rygg, R. D. Petrasso, J. Delettrez, V. Yu. Glebov, C. Stoeckl, F. J. Marshall, D. D. Meyerhofer, T. C. Sangster, V. A. Smalyuk, and J. M. Soures, *Phys. Plasmas* **11**, 2798 (2003).
30. V. Yu. Glebov, C. Stoeckl, S. Roberts, T. C. Sangster, J. A. Frenje, R. D. Petrasso, R. A. Lerche, and R. L. Griffith, "Proton Temporal Diagnostics for ICF Experiments on OMEGA," submitted to Review of Scientific Instruments.

Hot Surface Ionic Line Emission and Cold K-Inner-Shell Emission From Petawatt-Laser-Irradiated Cu Foil Targets

Introduction

There is much interest in both experimental and theoretical studies of laser–solid target interactions with picosecond laser beams at relativistic intensities because of their relevance to fast ignition in laser fusion¹ and backlighter development.^{2,3} High-intensity, ultrashort laser pulses impinging onto solid or gaseous targets produce large quantities of suprathermal electrons ranging from ~100 keV up to several MeV with conversion efficiencies of several tens of a percent from the incident laser energy into electron energy.^{4–7} A precise physical understanding of the MeV electron production and transport in dense plasma is crucial for the success of the fast-ignition concept. This has triggered vigorous research efforts in both experimental^{8–12} and theoretical studies.^{13–16}

Strong self-generated magnetic and electric fields influence the transport of relativistic electrons in high-energy-density plasmas.^{12,15,17} Inhibited heat flux in insulators due to strong longitudinal electrical fields has recently been predicted at subrelativistic intensities with a one-dimensional Monte Carlo collisional particle-in-cell (PIC) code.¹⁸ Depending on the experimental conditions, the fields might collimate the electron beam or compromise the effectiveness of electron penetration because of flux inhibition.^{17,19,20} The guiding of electrons with MeV energy in a plasma fiber over a distance of ~1 mm is attributed to strong laser-generated fields.²¹ Many plasma processes influence the heating of solid matter by laser-generated relativistic electrons and their return currents. One example is an observed annular heating pattern that is attributed to a strong Weibel instability growth because of sharp transverse gradients in the input electron-beam current.¹¹

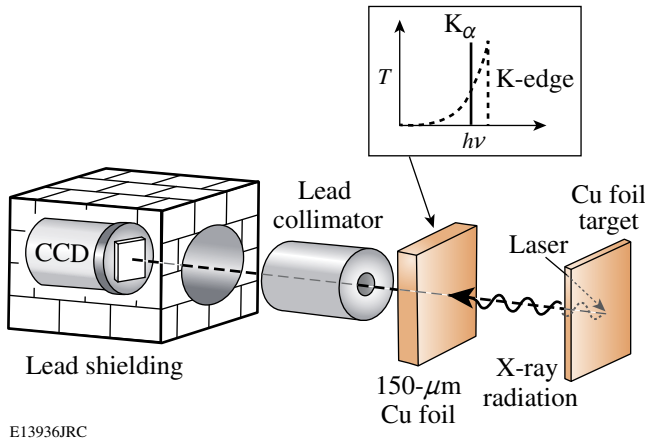
Hard x-ray bremsstrahlung and characteristic inner-shell line emissions, predominantly from the K shell, are produced when energetic electrons propagate into the bulk of a solid target. The measurement of inner-shell emission lines is a valuable diagnostic to characterize the suprathermal electron distribution.^{4,6,7,22–24} Measurements of electron temperatures and temperature gradients provide important guidance for simulations to study energy transport in relativistic laser–solid

density plasmas. The standard method used to infer electron density and temperature in laser-produced plasmas is x-ray line spectroscopy;²⁵ this method has been applied to petawatt laser–plasma experiments, e.g., Koch *et al.*, using aluminum K-shell spectra.¹¹ The dense and hot plasma environment shifts and broadens the spectral lines because of the interactions of the charged-particle plasma constituents. The comparison of measured line shapes and line ratios with calculations then allows the plasma parameters to be inferred.

In this work, measurements of the surface electron temperatures for petawatt-laser-produced copper plasmas are presented. Measurements of the scaling of the Cu K-shell emission with laser intensity and target thickness are shown and analyzed. The following three sections will present the **Experimental Setup** (p. 208), **Experimental Results** (p. 209), and **Analysis and Discussion** (p. 213). The third section contains two subsections: Resonance-Line Emission From Hot Plasmas (p. 213) and Inner-Shell Emission (p. 216), which compares the measured K_{α} laser-intensity scaling to a model calculation. **Summary and Conclusions** (p. 218) are presented in the last section.

Experimental Setup

A schematic of the experimental setup is shown in Fig. 104.47. Laser pulses from either the Rutherford Appleton Laboratory Petawatt (PW)²⁶ or the 100-TW²⁷ facilities were focused with $f/3$ off-axis parabolas to a spot size of the order of ~10 μm in diameter.²⁸ The fraction of the nominal laser energy transported onto the target through the compressor and subsequent optics of the PW and the 100-TW laser systems is 75% and 60% respectively. About half of this energy is contained in the main focal spot while the remainder is distributed over a larger area.^{28,29} The laser energy was measured for each shot before the beam entered the compressor. The maximum achievable intensities on target were $4(\pm 2) \times 10^{20}$ W/cm² and $4(\pm 2) \times 10^{19}$ W/cm² with the PW and the 100-TW lasers, respectively. The relatively large uncertainty in intensity on target is mainly due to changes in the focal-spot pattern on a shot-to-shot basis.



E13936JRC

Figure 104.47

Experimental setup. The petawatt laser is focused onto a thin copper foil target. A single-hit CCD camera measures the x-ray emission from the target's front side. Lead collimators and lead shielding provide the necessary suppression of unwanted background radiation. A 150- μm copper foil provides bandpass filtering of the Cu K-shell emission while suppressing the background radiation. The inset shows qualitatively the foil transmission versus photon energy and the position of the K_{α} line.

Preplasma formation was measured side-on with a frequency-doubled, 1-ps probe beam and a Wollaston prism interferometer, which showed that the plasma surface with an electron density of 10^{19} cm^{-3} expands at most by 40 μm from the original target surface at 100 ps prior to the main pulse interaction. Higher electron densities are not accessible by this diagnostic because of probe-light refraction out of the f number of the collecting lens in the probe line. Prepulse measurements show an amplified spontaneous emission (ASE) pulse starting at 1.5 ns ahead of the main pulse with an intensity of 5×10^{-8} of the main pulse intensity. The overall intensity contrast is better than 10^5 in a time window between 10 ns and 50 ps before the main pulse.²⁸ The p -polarized light was focused at a 30° angle of incidence onto thin ($<30 \mu\text{m}$) copper foil targets with an area of $<2000 \times 2000 \mu\text{m}^2$. The targets were mounted as flags on 6- μm -diam carbon fibers.

A single-photon-counting, x-ray back-illuminated, charge-coupled-device (CCD) camera (SI 800-145, Spectral Instruments-Photonics, Tucson AZ) measured the plasma emission from the laser irradiation side ("target front side") at a viewing angle of 16° with respect to the target normal. Radiation shielding of the CCD camera with a lead housing and lead collimators was crucial in obtaining good signal-to-noise spectra by suppressing the hard x-ray background generated by the petawatt laser.³⁰ In addition, a 150- μm -thick Cu foil filter in front of the CCD was used to adjust the signal level of the

K-shell emission to the single-photon-counting regime and to improve the signal-to-noise ratio. The experimental setup with the 100-TW facility was similar to that described above. The CCD detector was located closer to the plasma source in that case, 1.4 m instead of 3.8 m, leading to an increased solid angle by a factor of ~ 7 .

When an x-ray photon is absorbed in the material of the CCD, a certain number of free-charge carriers proportional to the x-ray photon energy are created. A significant number of x-ray events are split between adjacent pixels. Adding the value of the pixels surrounding the event centroid might be used to reconstruct the total charge collected from an event. This is useful at very low photon fluxes, especially in astronomical applications. The single pixel analysis, as used here, ignores the spread of the absorbed x-ray energy over several pixels and typically takes only $\sim 20\%$ of the absorbed 8 to 9 keV photons into account.³¹ Single pixel analysis has a slightly higher spectral resolution than summed pixel analysis.^{31,32} A CCD quantum efficiency of $\sim 10\%$ with single pixel analysis is reported in the 8 to 9 keV range for an x-ray imaging spectrometer used in the x-ray astronomical satellite Astro-E.³¹ A quantum-efficiency measurement of a SI-800 camera at 8 keV revealed a value of $\sim 5\%$ with single-pixel analysis.³³ The same kind of chip (CCD42-40 chip, e2v technologies, Chelmsford UK) was used in the two SI cameras, one for calibration and one in this experiment. The quantum efficiency is a factor 2 lower compared to the Astro-E CCD, which is probably due to a smaller pixel size and a thinner depletion layer of the SI-800 chip.

Experimental Results

Figure 104.48 shows a copper K-shell spectrum from the target's front side for laser shot 0311271. Laser pulses with an energy of 447 J and a pulse duration ~ 0.7 ps were focused to an intensity of $\sim 3 \times 10^{20} \text{ W/cm}^2$ onto a 20- μm -thick Cu foil target. The continuum x-ray background is subtracted while the filter transmission of the 150- μm Cu foil has not yet been taken into account. The measured spectrum (dashed curve) consists of four overlapping lines. The other curves denote a fit of Gaussian line shapes to the measurement, indicating a full width at half maximum of ~ 220 eV for each line. The four peaks are identified as the lines of the Cu K_{α} (8.04 keV), He_{α} (8.35 keV), Ly_{α} (8.69 keV), and K_{β} (8.91 keV) transitions.^{34,35} The He_{α} line dominates the spectrum. The observation of He_{α} and Ly_{α} is distinctly different from Cu K-shell spectra observed previously with ultrashort laser pulses at lower laser intensities.²⁴ The appearance and intensity of the He_{α} and Ly_{α} lines depend strongly on the laser intensity, as shown in Fig. 104.49. The K-shell emission was measured with 0.7 ps pulses for

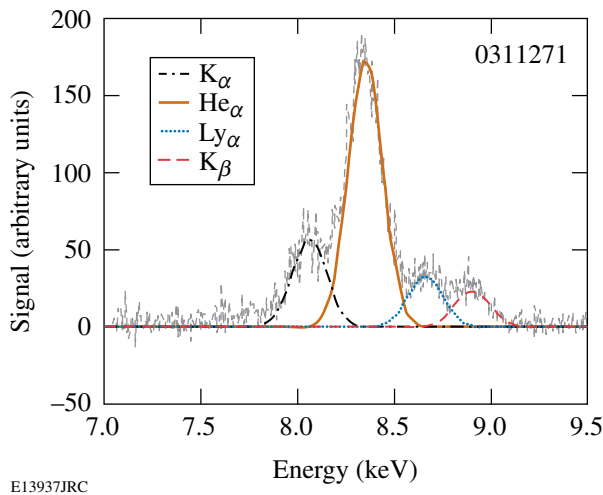


Figure 104.48
Copper K-shell spectrum from the target's front side for a laser intensity of 3×10^{20} W/cm² and a pulse duration of 0.7 ps and $E_L = 447$ J. The gray curve denotes the measurement while the other curves are Gaussian fits to the various emission lines. The He $_{\alpha}$ resonance line of helium-like copper ion dominates the spectrum.

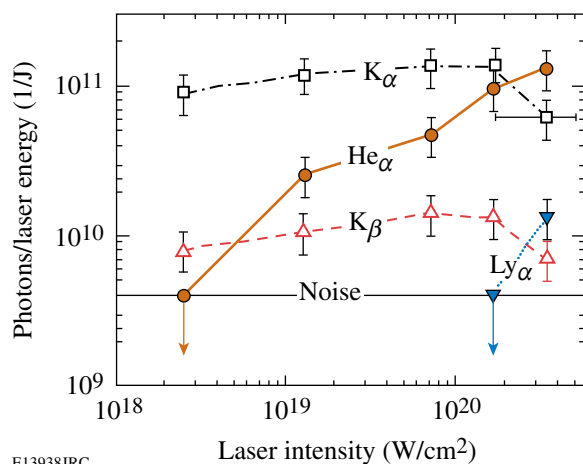


Figure 104.49
Integral x-ray photon number normalized to the laser energy contained in the central laser spot as a function of the laser intensity for Cu K $_{\alpha}$ (open squares), He $_{\alpha}$ (solid dots), K $_{\beta}$ (open triangles), and Ly $_{\alpha}$ (solid inverted triangles). Square Cu foils with thicknesses of 20 μ m and 30 μ m and areas ranging from $500 \times 500 \mu\text{m}^2$ through $2000 \times 2000 \mu\text{m}^2$ were used. The intensity was varied by the focal spot (10 to 100 μ m) and the beam energy (\sim 200 to \sim 500 J) while keeping the pulse duration constant at 0.7 ps. The apparent threshold of Ly $_{\alpha}$ is 3×10^{20} W/cm², while only K $_{\alpha}$ and K $_{\beta}$ are observed at 2.5×10^{18} W/cm². A representative error bar of the laser intensity is shown for one K $_{\alpha}$ data point.

various laser intensities between $\sim 2 \times 10^{18}$ W/cm² and $\sim 3 \times 10^{20}$ W/cm² by varying the spot size within 10 to 100 μ m and the beam energy in the range from \sim 200 J to \sim 500 J. The Ly $_{\alpha}$ line of hydrogen-like copper disappears below 3×10^{20} W/cm², while He $_{\alpha}$ is observed down to 1×10^{19} W/cm², and only K $_{\alpha}$ and K $_{\beta}$ are measured at 2.5×10^{18} W/cm². No measurements with 0.7-ps pulses are available between 2.5×10^{18} W/cm² and 1×10^{19} W/cm². Additional measurements in this intensity range with longer pulses (5 to 14 ps) show the He $_{\alpha}$ signal down to $\sim 6 \times 10^{17}$ W/cm². For 0.7-ps pulses, the noise level prevents the detection of He $_{\alpha}$ below 3×10^{18} W/cm², while for higher intensities it is always measured and steadily increases with laser intensity. In contrast, K $_{\alpha}$ and K $_{\beta}$ stay about constant between 2×10^{18} W/cm² and 1×10^{20} W/cm² and slightly decrease for intensities above 10^{20} W/cm².

The absolute number of x-ray photons in each line normalized to the laser energy contained in the central laser spot was calculated by integrating the number of hits and by taking the solid angle, filter transmission, and quantum efficiency of the CCD in single-pixel analysis mode into account. An isotropic emission into a 4π steradians solid angle is assumed. Reabsorption of the radiation inside the foil target has not been taken into account. The relative error bars are estimated to be \sim 30% based on the standard deviation of several measurements at the same intensity. The absolute error is estimated to be a factor of 2 based on an estimated uncertainty in the CCD quantum efficiency for single-pixel analysis.

The Cu K-shell spectrum was studied as a function of the foil thickness with the 100-TW laser facility for low-mass, small-area targets. Figure 104.50 shows the measured K $_{\alpha}$, He $_{\alpha}$, and K $_{\beta}$ lines for Cu foils of various thicknesses. Laser pulses with 14 ps (a) and 10 ps [(b)–(d)] durations and beam energies of \sim 100 J were focused to an \sim 10- μ m spot size, providing an intensity of $\sim 3 \times 10^{18}$ W/cm². The thickness is indicated in each figure. The foil area was $500 \times 500 \mu\text{m}^2$ in (a) while it was $100 \times 100 \mu\text{m}^2$ in (b), (c), and (d). The ratio of K $_{\alpha}$ to He $_{\alpha}$ emission changes with thickness, and the relative helium-like emission becomes larger with thinner foils for the smaller areas. Only a limited number of spectra were sampled, however, and shot-to-shot fluctuations especially influence the He $_{\alpha}$ signal. The resulting x-ray photon number per laser energy is plotted semilogarithmically as a function of the foil thickness in Fig. 104.51. The cold inner-shell emission that is created mainly by suprathermal electrons traversing the foil behaves differently than the ionic line emission. The K $_{\alpha}$ signal is relatively independent of foil thickness. A significant decrease is observed only below 3 μ m, which might be due to

several effects: (1) an increased volumetric heating might lead to a depletion of cold material and (2) an increased transfer of hot-electron energy into channels other than K_{α} emission for very low volume targets, notably ion acceleration,^{36,37} might quench the inner-shell signal. The K_{β} intensity drops by a factor of ~ 4 from $30\ \mu\text{m}$ to $20\ \mu\text{m}$, and then stays about constant with smaller thicknesses and decreases again below $3\ \mu\text{m}$. The strong decrease from $30\ \mu\text{m}$ to $20\ \mu\text{m}$ is probably due to the larger foil area, which is further discussed in **Resonance-Line**

Emission From Hot Plasmas (p. 213). While the inner-shell x-ray photon number decreases with thinner foils, the ionic line emission seems to show an opposite trend for large thicknesses. The He_{α} signal first increases with diminishing thickness, peaks at $5\ \mu\text{m}$, and then decreases to its initial value at $1\ \mu\text{m}$. The relatively large scattering of the values is probably due to shot-to-shot fluctuations in the laser conditions and the focus position on the small target.

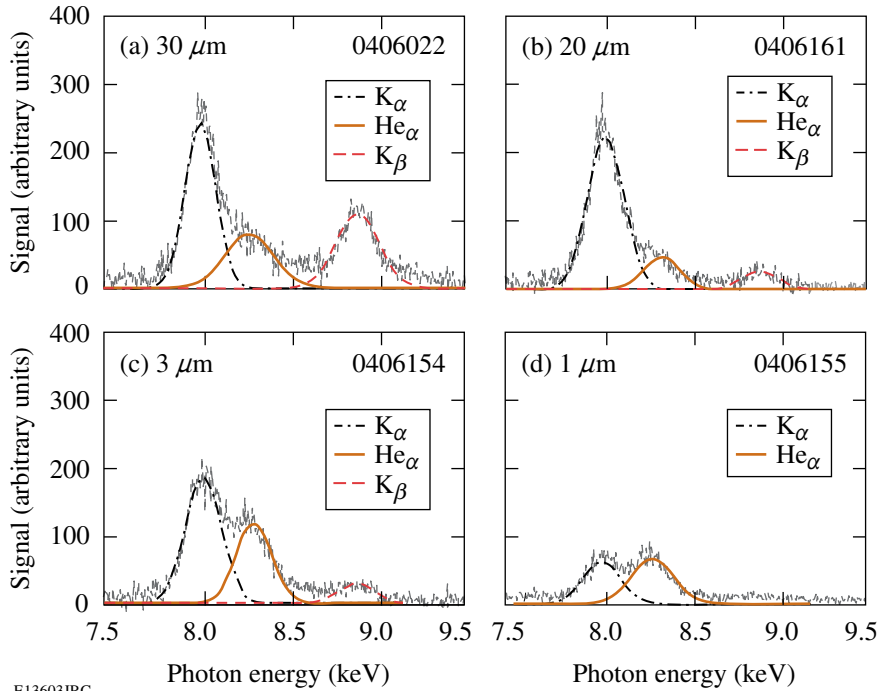


Figure 104.50

K-shell spectra showing the K_{α} , He_{α} , and K_{β} lines for various Cu foil thicknesses as is indicated in each figure. The foil areas were $500 \times 500\ \mu\text{m}^2$ (a) and $100 \times 100\ \mu\text{m}^2$ for the measurements in (b)–(d). The laser energies in (a)–(d) were 102 J, 118 J, 116 J, and 97 J, respectively. Laser pulses with 14-ps (a) and 10-ps (b)–(d) durations were focused to an $\sim 10\ \mu\text{m}$ spot, providing intensities of $\sim 3 \times 10^{18}\ \text{W}/\text{cm}^2$.

E13603JRC

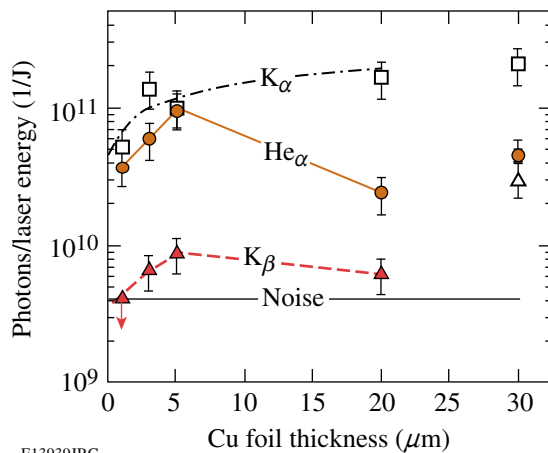


Figure 104.51

X-ray photon number per laser energy in the central laser spot versus foil thickness determined from the measured cold K_{α} , K_{β} , and the hot He_{α} emission. The experimental conditions are the same as in Fig. 104.50. The dash-dotted curve is a guide for the eye. The foil volume diminished from $30\ \mu\text{m}$ to $20\ \mu\text{m}$ by a factor of ~ 40 because of the smaller area. An increased volume heating probably depletes the copper M-shell population, yielding a decreased K_{β} signal while the K_{α} is not significantly affected.⁵⁵

E13939JRC

Evidence that the ionic emission originates from front-surface plasmas was obtained from measurements of Cu-foil targets covered with a thin layer of a different material. Figures 104.52(a)–104.52(c) show spectra at an intensity of 1.5×10^{20} W/cm² on copper-foil targets without a cover layer (a), with a 1- μ m-thick aluminum layer (b), and with a 0.5- μ m-thick tantalum layer (c). The comparison of (a) and (b) shows that the He α emission is significantly reduced by a factor of ~ 5 , while K α and K β are diminished by a factor of ~ 2 . The data suggest that, with the Al coating, the hot plasma is created mainly in the aluminum with relatively little heating of the copper. The reduction in K α and K β may indicate stopping of hot electrons in the Al layer. The Ly α is not observed at this laser intensity. An additional experiment, Fig. 104.52(c), at the same intensity with a 0.5- μ m Ta overcoat on 20- μ m Cu foil gives further evidence that the Cu He α line emission originates from a thin layer on the target's front side. Beside the Cu K α and a strong L-shell emission from tantalum peaking at 8.75 keV, no Cu He α line at 8.35 keV is measured. The mass densities of solid tantalum and aluminum are 16.7 g/cm³ and 2.7 g/cm³, respectively. The factor of 6 higher mass density explains why Ta is more efficient in blocking energy transport through the surface despite half of the film thickness, leading to plasma temperature at the Ta–Cu boundary that is not sufficient to generate He-like Cu ions.

It is interesting to compare the result from copper ($Z = 29$) to the K-shell emission of a target material with a much

higher atomic number. Figure 104.53 shows the result of an experiment with a 50- μ m-thick silver foil target ($Z = 47$) at $\sim 2 \times 10^{20}$ W/cm². Only the inner-shell emission (but no He α and Ly α lines) is observed for the higher- Z target. This indicates that the temperature is not high enough to create He- and H-like silver ions, which require estimated electron temperatures above ~ 50 keV.³⁸

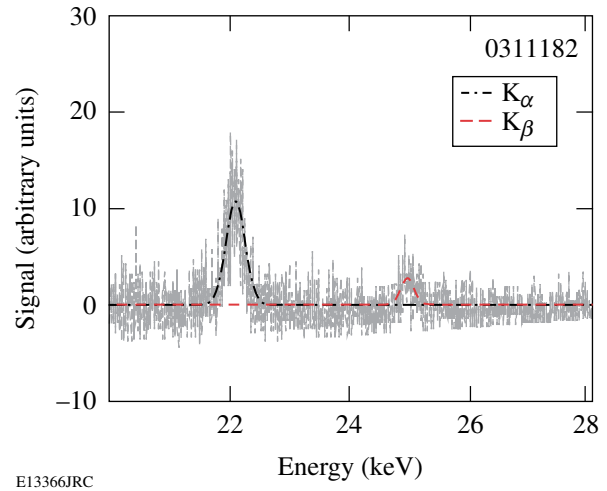


Figure 104.53

Measurement of the silver K-shell emission from a 50- μ m-thick Ag-foil target. The laser energy, pulse duration, and intensity were 275 J, 0.7 ps, and $\sim 2 \times 10^{20}$ W/cm², respectively. Only K α and K β inner-shell emission lines are measured, but not the ionic line emission.

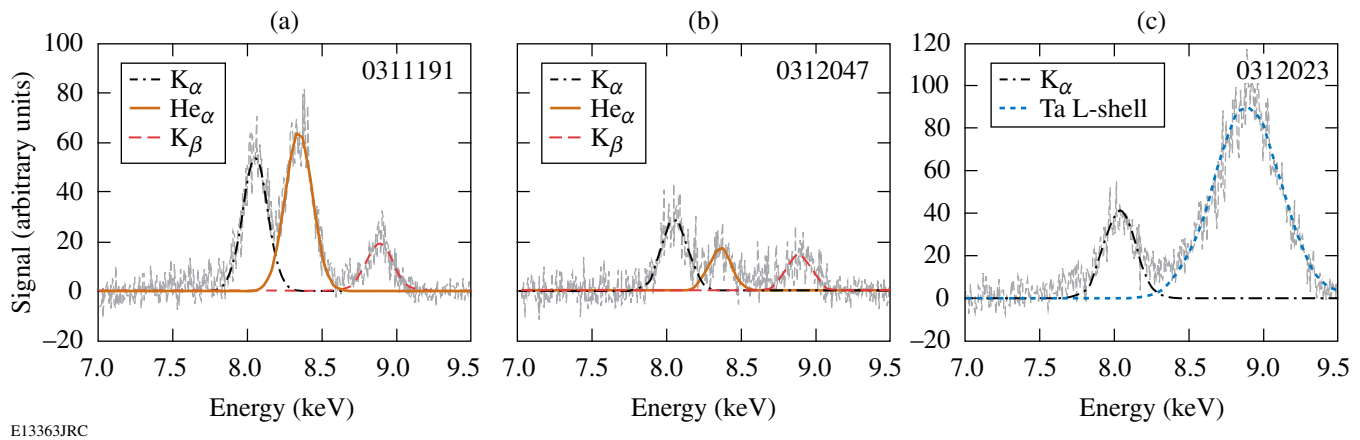


Figure 104.52

Copper K-shell spectra with the target's front side covered with a thin layer of different materials that leads to a suppression of the ionic line emission. (a) is without a cover layer, while (b) and (c) denote the results with a 1- μ m-thick aluminum and with a 0.5- μ m-thick tantalum layer, respectively. The He α line emission is strongly reduced (b) and even absent (c) compared to the no cover layer (a), indicating that the hot plasma is generated in a thin layer on the target's front side. The laser energies, pulse duration, and intensity were 254 J (a), 227 J (b), 227 J (c), 0.7 ps, and $\sim 1.5 \times 10^{20}$ W/cm².

Analysis and Discussion

Two emission processes occur in these experiments: inner-shell emission and resonance-line emission. The K_α and K_β lines are emitted by inner-shell transitions when an L- or M-shell electron fills a vacancy in the K-shell, and the corresponding excess energy is radiated away by a photon in competition with Auger decay. X rays and energetic electrons may both produce inner-shell vacancies, assuming that the radiation has sufficient energy to excite above the K-edge (for Cu $h\nu > 9$ keV). Indirect inner-shell emission due to absorption of continuous x-ray radiation that is produced while suprathermal electrons decelerate in the target is, however, relatively negligible for elements with an atomic number < 30 .³⁹ Energetic electrons are the main contribution to K_α and K_β production in a high-intensity, ultrashort, laser–solid interactions with low- and mid-Z materials.^{22,24} In contrast, the He_α and Ly_α lines are electronic transitions from the first excited to the ground level in the helium-like and hydrogen-like ions. Sufficient thermal plasma temperatures are required to generate these highly stripped ions. While the inner-shell radiation originates from the cold bulk material, the ionic lines are produced in hot plasmas, which is depicted in a schematic in Fig. 104.54. Resonance-line emission originates from a hot plasma on the laser target side while fast electrons generated by the laser–plasma interaction propagate into the cold bulk and produce the inner-shell emission.

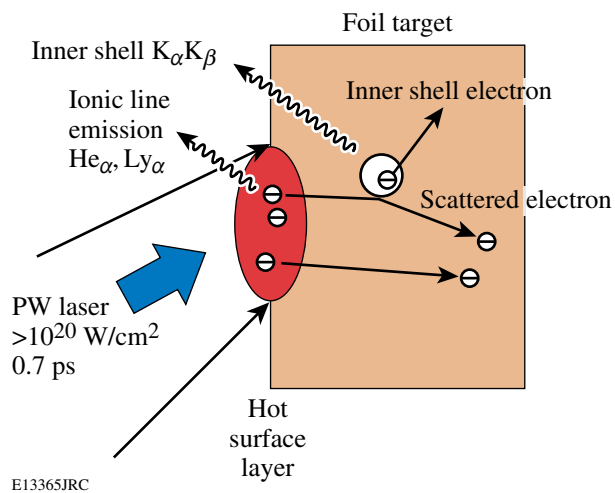


Figure 104.54
Schematic representation of the resonance and inner-shell emission generation process. The ionic lines stem from a hot surface layer while fast electrons produce the inner-shell emission.

1. Resonance-Line Emission From Hot Plasmas

Calculations with the commercially available *PrismSPECT* program⁴⁰ were performed to estimate the plasma conditions that lead to the ionic resonance-line emission from the hot plasma. *PrismSPECT* is a collisional-radiative code that takes all the necessary details of the excitation and de-excitation paths, opacity, and atomic physics into account. The plasmas are assumed to be in steady state, in nonlocal thermodynamic equilibrium conditions in slab geometry with a specified thickness, and have a homogeneous density and electron temperature. Time-dependent collisional-radiative calculations of the ionization dynamics of solid-density aluminum plasmas at $T_e = 1$ keV show that steady-state conditions are established within ~ 0.5 ps.⁴¹ Similar time-dependent calculations performed for $T_e = 1$ keV and $n_e = 10^{23}$ cm⁻³ show the Cu plasma reaching steady state within ~ 1 ps.⁴² Steady state is therefore a reasonable assumption for near-solid-density plasmas in our experiment. Suprathermal electrons were not included in the calculation. This assumption is supported by calculations of the charge-state distribution of a 1-keV, 10^{23} cm⁻³ Cu plasma including the ionization effect of a hot-electron component. The charge-state distribution is essentially given by the thermal plasma, and up to a fraction of 10% of hot electrons with an average energy of 3 MeV has no significant influence.⁴² The overcoat measurements (Fig. 104.52) show that the hot plasma is formed from a layer that has initially $t \approx 1$ - μ m thickness at solid density. Figure 104.55(a) shows a comparison for the experimentally measured ionic K-shell emission for shot 0311271 (solid square symbols) to calculations for an electron density of $n_e = 2.3 \times 10^{24}$ cm⁻³, $t = 1$ μ m, and various electron temperatures between 1 keV and 3 keV. The electron density corresponds to a solid density of $n_{\text{ion}} = 8.5 \times 10^{22}$ cm⁻³ and an average degree of ionization of 27. The K_α and K_β lines are suppressed to allow a better comparison of the resonance-line emission to the calculations. The filter transmission of the 150- μ m Cu foil was taken into account, and the calculated spectra were convolved with an instrumental resolution of 200 eV. The *PrismSPECT* calculation reveals that the measured He_α peak is a complicated array of lines including the He_α line, the intercombination line, dipole forbidden lines, and lithium-like ion satellite lines that merge together. The effective line width of this feature is ~ 90 eV at solid density and explains the slightly larger measured spectral width of ~ 220 eV for He_α . The ratio of the He_α and Ly_α lines is sensitive to the temperature and a good agreement is obtained for an electron temperature of 1.8 keV.

The ASE laser pulse pedestal causes some ablation of the front layer before the main laser pulse impinges on the target.

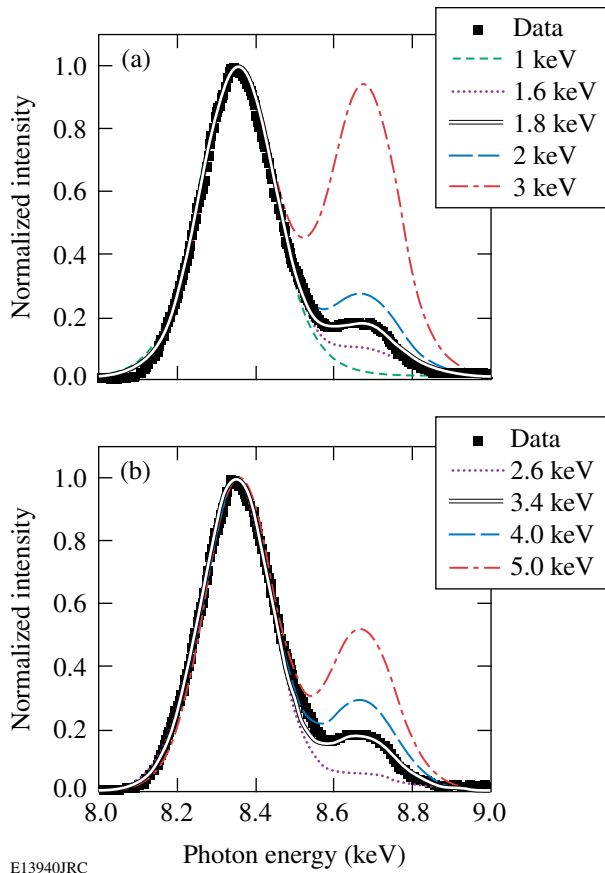


Figure 104.55

Comparison of the experimentally measured ionic K-shell emission (solid square symbols) to calculations with the computer program *PrismSPECT*⁴⁰ for (a) solid-density ($n_e \approx 2.3 \times 10^{24} \text{ cm}^{-3}$) 1- μm -thick plasma slab, and various electron temperatures between 1 keV and 3 keV. Figure (b) shows a comparison for an electron density of $2.3 \times 10^{23} \text{ cm}^{-3}$, plasma slab thickness of 1 μm , and various electron temperatures between 2.6 keV and 5 keV.

The main pulse then interacts with less than solid density plasma and an increased density scale length. The density profile depends on the laser contrast, pulse profile, and hydrodynamic expansion of the preplasma. To model the density profile generated by the ASE pulse, a two-dimensional hydrodynamic simulation of the expansion and structure of the preplasma was performed using the Eulerian code POLLUX.⁴³ A $2.5 \times 10^{13} \text{ W/cm}^2$ Gaussian temporal pulse shape was assumed with a 1.5-ns pulse duration. In the radial direction, a Gaussian-shaped intensity profile with a FWHM of 7 μm was used for the simulation. Figure 104.56 shows a lineout of the calculated electron-density profile along the target normal at the peak of the interaction pulse. The critical density expanded $\sim 2 \mu\text{m}$ from the original surface. The interaction of the main pulse with relativistic intensities and the corresponding electron mass increase

leads to a higher critical density than in the nonrelativistic case. A distance of $\sim 1 \mu\text{m}$ is then calculated for the relativistic corrected critical density. The distance from the original target surface to the 10^{19} cm^{-3} contour is $\sim 45 \mu\text{m}$, which agrees well with the shadowgraph measurements. Preplasma formation on the Vulcan 100-TW laser has been previously experimentally and theoretically investigated.^{37,44} Density scale lengths of $\sim 3 \mu\text{m}$ and $\sim 10 \mu\text{m}$ were determined at the critical density and at one-tenth of the critical density, respectively.

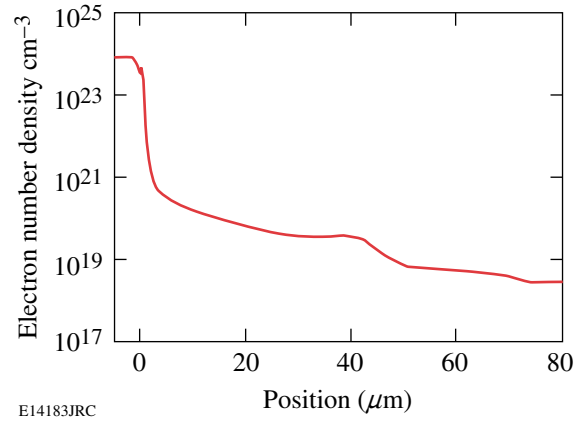


Figure 104.56

Calculated electron density profile along the target normal that is generated by an ASE prepulse; see text for details. The 2-D Eulerian code POLLUX⁴³ was used for the simulation.

The density profile shows that the ablated mass below critical density is a factor of ~ 10 smaller compared to the 1- μm layer from critical density up to solid density. Accordingly, the number of ionic line emitters in the ablation plume is negligible compared to the emitter number above critical density where most of the absorbed laser energy is deposited. Thermal energy transport into the target is estimated to be several microns deep with close to solid density based on the overcoating experiments. Figure 104.55(b) shows a comparison of measured and calculated spectra for $n_e = 2.3 \times 10^{23} \text{ cm}^{-3}$, $t = 1 \mu\text{m}$, and various temperatures with the best agreement at $T_e = 3.4 \text{ keV}$. Not shown is the comparison for $n_e = 2.3 \times 10^{23} \text{ cm}^{-3}$ and $t = 10 \mu\text{m}$, yielding $T_e = 2.6 \text{ keV}$, which has roughly the same emitter number as the solid density, $t = 1 \mu\text{m}$ calculation. Opacity effects in the blowoff plasma are negligible because of the low concentration of He- and H-like ions. The electron temperature is thus estimated to be in the range of 2 to 3 keV for a close-to-solid-density plasma and slab thickness between 1 and 10 μm . The number is in agreement with highly resolved Cu K-shell spectral measurements performed at similar experimental conditions yielding a front side electron temperature of $\sim 2 \text{ keV}$.⁴⁵

Two-dimensional opacity effects and heating of the underdense plasma by the short interaction pulse were not considered. Optical-field-ionized He- and H-like ion generation in the underdense plasma along the laser channel is negligible. Using a simple over-the-barrier suppression calculation for electric field ionization,⁴⁶ estimated saturation intensities of 2×10^{20} W/cm² and 7×10^{22} W/cm² are required to produce helium- and hydrogen-like copper ions with an ionization probability close to unity. The creation of He-like Cu ions by field ionization is therefore possible only at the highest accessible laser intensity. Ponderomotively accelerated electrons and ions in a radial direction³⁷ that might modify the charge-state distribution of the plasma as well as velocity gradients because of the tight-focusing condition and the resulting spherical expansion geometry that might affect the opacity⁴⁷ were not included in the analysis.

A precise comparison between the measured absolute He _{α} and Ly _{α} photon numbers and the predicted numbers by *PrismSPECT* are not straightforward and out of the scope of this article. A detailed knowledge of the angular emission characteristic, source area, and temporal emission characteristic is required. Laser plasmas are highly transient with strong spatial gradients in density and temperature, and a comparison to the measurement requires detailed multidimensional hydrodynamic simulations coupled to a multidimensional, time-dependent radiation transport model. An estimate of the source area may be obtained from measurements of Cu K _{α} images, typically yielding an area of 50 to 100 μ m FWHM in diameter,^{12,24} and from Ni Ly _{α} imaging measurements with ~ 30 μ m spots that were obtained under similar experimental conditions.⁴⁸ Town *et al.*, recently reported on simulations to calculate K _{α} images under similar experimental conditions and obtained agreement with measured K _{α} spot sizes.⁴⁹ Assuming an isotropic He _{α} and Ly _{α} emission and neglecting multidimensional and time-dependent opacity effects, the comparison of measured photon numbers and steady-state calculations for a solid-density, $t = 1$ μ m surface layer plasma suggests average emission times of several picoseconds.

The increase in He _{α} emission with a laser intensity above 10^{18} W/cm² shown in Fig. 104.49 shows an energy transport growing with intensity into the solid-density plasma where electron-ion collisions create the ions in the hot-plasma environment. An enhanced energy transport into the solid results in higher temperatures and a larger fraction of He- and H-like Cu ions in the hot surface plasma. The absorption of the laser energy takes place in the density range close to the critical density and is dominated by collisionless absorption mechanisms

that produce electrons with quasi-Maxwellian energy spectra and temperatures from hundreds of keV to several MeV for all intensities discussed here.⁵⁰ The angular distribution is generally into the target. The electron source parameters vary with the local intensity and therefore also have a spatial pattern related to the laser focal-spot intensity pattern. Energy transport by these electrons is highly complicated and, up to now, not fully understood. Their binary collision range is generally much greater than the thin layer, which is strongly heated. Several processes may contribute to localizing energy deposition in a surface layer. Simple ohmic potential due to the cold electron return current can limit electron penetration, as discussed by Bell *et al.*¹⁹ Electrons can be trapped at the surface by their small Larmor radius in the surface region azimuthal thermoelectric B field generated by the axial increase of density and radial decrease of temperature (dB/dt scaling as $\nabla N \times \nabla T$), with the axial ambipolar electric field in the blowoff plasma causing a rapid radial drift (scaling as $E \times B$). This effect, well known from nanosecond experiments, particularly with CO₂ lasers, has been discussed in connection with petawatt-class, short-pulse experiments by Stephens *et al.*¹² and modeled recently by Mason *et al.*⁵¹ Three-dimensional PIC simulations by Sentoku *et al.*,¹⁶ have shown that there can be very strong collisionless energy deposition in a thin surface layer attributable to the “ohmic” heating effect of the return current due to anomalous resistivity induced by the scattering of the return current electrons on microscopic clumps of the B field generated by collisionless Weibel and two-stream instability. There is also evidence in PIC modeling by Adam *et al.*⁵² and Ruhl⁵³ that the strongest filamentation occurs in a thin surface layer. These processes may all contribute to the observed thin, high-temperature layer, but further work is needed to establish their relative importance.

The energy required to create a significant amount of He-like and H-like Cu ions is estimated by assuming the mass of the hot layer to be equivalent to an ~ 1 - μ m-thick layer at solid density, as determined from the overcoat experiments. For example, an energy of ~ 3.5 J is needed to heat a mass of solid copper contained in a disk with a 50- μ m diam and 1- μ m thickness to ~ 3 keV and the resulting average charge state of 27. This is small compared to laser energies of the order of 100 J.

It should be noted that the spectral measurements indicate that K _{α} and He _{α} are two distinctive lines with no significant continuum merged between them. This is supported by highly resolved measurements with a crystal spectrograph under similar experimental conditions.⁵⁴ The upshift of K _{α} emission from partially ionized Cu ions has been discussed by Gregori

*et al.*⁵⁴ There is a small spectral shift as M-shell electrons are removed because of the heating of the bulk of the target by binary collisions of hot electrons and ohmic heating by the return current. It is indistinguishable in our low-resolution K_α spectra. Removal of L-shell electrons at higher temperatures gives larger shifts as the hot layer is heated and emission occurs at each stage of ionization. The He-like ion is, however, present over a wide temperature range and, in particular, during the emission occurring after the initial heating, leading to a dominant He_α spectral feature in our spectra. This heating partially ionizes the bulk, resulting in a K_α emission shifted to higher energies.

Measurements of the K-shell emission as a function of foil thickness between $30\ \mu\text{m}$ and $1\ \mu\text{m}$ for a constant laser intensity of $\sim 3 \times 10^{18}\ \text{W}/\text{cm}^2$ show that the K_α emission remains about constant with diminishing foil thicknesses down to $3\ \mu\text{m}$. This is expected if no other hot-electron energy-loss mechanisms become significant; the electron temperature of the foil is so low that ionization does not significantly affect the L-shell, and the majority of the electrons are refluxing from an electrostatic sheath field. The decreasing yield for targets thinner than $3\ \mu\text{m}$ might imply that a significant amount of cold material is depleted. Another possible explanation is that, for very small volume targets, additional energy dissipation channels draining hot-electron energy might become important and influence the K_α signal. A possible channel is energy transfer into accelerated ions, which is enhanced in very thin targets.³⁶ The K_β yield is expected to be more sensitive to a temperature increase of the bulk of the target since K_β is eliminated when the M-shell is ionized, which might explain the decrease by factor of ~ 4 from $30\ \mu\text{m}$ to $20\ \mu\text{m}$ while no change is measured for K_α . The target volume changed by a factor of ~ 40 because a $500 \times 500\ \mu\text{m}^2$ foil area was used at $30\text{-}\mu\text{m}$ thickness while $100 \times 100\ \mu\text{m}^2$ was applied for the thinner targets. R. Snavely *et al.*, recently reported on similar observations and extensively discussed how the laser heating of very small target volumes affects the inner-shell emission.⁵⁵ The resonance-line emission from the $1\text{-}\mu\text{m}$ top layer is not expected to be significantly affected by the foil thickness. Nevertheless, varying He_α emission is observed with a peak at $5\text{-}\mu\text{m}$ thickness. This variability may be due to slight changes in the laser conditions from shot to shot. As shown in the measurement in Fig. 104.49, the He_α signal is more sensitive to the applied laser intensity than is the inner-shell emission.

2. Inner-Shell Emission

Implicit-hybrid PIC simulations with the code *LSP*⁵⁶ were performed to study inner-shell production with various foil areas in the range from $500 \times 500\ \mu\text{m}^2$ to $100 \times 100\ \mu\text{m}^2$ and thicknesses of $20\ \mu\text{m}$ to $5\ \mu\text{m}$, similar to the simulations recently reported by R. Town.⁴⁹ No significant change of K_α yield with the target area and thickness is calculated, which is attributed to the refluxing of most of the hot electrons at the target boundaries.³⁶ These calculations have solved the Maxwell equations coupled with the equations of motion for multiple particle species in a two-dimensional cylindrical geometry. The initially cold ions and bulk electrons of the target were modeled with fluid equations, and the hot laser-produced electrons were treated kinetically. The propagation and interaction of the high-intensity laser was not included, rather, the hot electrons were introduced into the calculation in an *ad hoc* manner by converting or “promoting” bulk electrons within a skin depth on the front of the target into the kinetic species. The kinetic electrons were given an isotropic Gaussian distribution in momentum space with a temperature that was determined by the ponderomotive potential of the local laser intensity.¹³ The local conversion rate was determined by assuming a 10% coupling efficiency from the local incident laser power into hot electrons. The laser spot shape was taken to be the same as in the experiment, both spatially and temporally. Although the heating of the target was modeled, the ionization of the target material was ignored.

The measured K_α photon numbers, per unit laser energy, are in general agreement with other experiments.^{20,24} In Ref. 20, $2 \times 10^{11}/\text{J}$ K_α photons were reported for $8\text{-}\mu\text{m}$ -thick Cu foil targets irradiated with 528-nm laser pulses at intensities of $\sim 10^{19}\ \text{W}/\text{cm}^2$. Similar numbers were reported in Ref. 24; however, these experiments used thick targets where the reabsorption of the K_α photons was strong, and the controlling mechanism was the interplay between electron-penetration depth relative to the K_α photon-attenuation length. With the targets considered here, reabsorption gives a modest correction; e.g., for solid copper, the transmission fraction f_{trans} is estimated to be 0.91, 0.69, and 0.58 for foil thicknesses of $d = 5, 20, \text{ and } 30\ \mu\text{m}$ respectively.

The expected number of photons generated N_k can be computed by integrating along the path of electrons whose initial energies are described by an energy distribution $f(E_0)$ so long

as the electron stays within the material, its energy loss is accurately described with a continuous slowing down formula (dE/ds), and that cold cross sections σ_k for K-shell ionization are appropriate (note that for copper, only direct K-shell ionization is significant³⁹). The yield N_k is then given by

$$N_k = N_e \int_0^\infty dE_0 f(E_0) \int_{E_0}^0 dE \omega_k n_{Cu} \sigma_k \left(\frac{dE}{ds} \right)^{-1}, \quad (1) \text{ and } (2)$$

$$= N_e \int_0^\infty dE_0 f(E_0) \int_0^{s(E_0)} ds \omega_k n_{Cu} \sigma_k,$$

where N_e is the total number of hot electrons, $\omega_k = 0.425$ is the fluorescence yield, and n_{Cu} is the number density of copper atoms in the target. From this model the electron-to- K_α photon-generation efficiency $\eta_{e \rightarrow k}$ is determined. This efficiency is defined according to $E_k = \eta_{e \rightarrow k} E_e$, where the energy in the electrons is given by $E_e = N_e \int E f(E) dE$ and in K_α photons by $E_k = \varepsilon_k N_k$ with ε_k being the fluorescence energy (8.05 keV for copper K_α). This simple model accounts only for the collisional energy loss and neglects ohmic effects and energy transfer to fast ions.

A direct comparison between the experimental production efficiency (yield/laser energy) and the calculated generation efficiency is not straightforward. The experimentally observable quantity is $N_{k,obs}$ from which the efficiency may be computed as

$$\eta_{e \rightarrow k} = \frac{\varepsilon_k (N_{k,obs} / f_{trans})}{E_L} \frac{1}{\eta_{L \rightarrow e}} \quad (3)$$

only if the transmission fraction and the hot-electron production efficiency $\eta_{L \rightarrow e} = E_e / E_L$ are known. Here, E_L is the energy in the laser pulse. The transmission fraction can be easily computed, but the electron-production efficiency is uncertain. Assuming that the hot-electron density within the foil is uniform, the K_α photon transmission fraction is estimated by $f_{trans} = (L_a/d) [1 - \exp(-d/L_a)]$ with the attenuation length $L_a = 25 \mu\text{m}$. The predicted efficiency, obtained using Eq. (1), further requires specification of the hot-electron spectrum $f(E)$.

The predicted total K_α energy of the model divided by the laser energy, together with experimental data, are shown in Fig. 104.57 for different $\eta_{L \rightarrow e}$ assuming exponentially distributed electron energies, $f(E) dE = (1/T) / \exp(-E/T) dE$, and

using slowing down and cross section data from the ITS code.⁵⁷ The total K-shell ionization cross section is from Ref. 58 and, unlike the cross section in Ref. 39, it is valid for relativistic electron energies. For highly relativistic electrons, the cross section increases with particle energy. In Ref. 59, an increased K_α yield was measured with laser intensities above 10^{19} W/cm^2 and attributed to an enhanced K-shell ionization cross section for relativistic electrons. In contrast to this work, an increase in the K_α yield with the laser intensity is not observed. Calculations have also been performed with a 3-D relativistic distribution function, leading to slightly higher predicted efficiencies, but with no change to our overall conclusions. Although different intensity temperature scaling appears in the literature,^{29,60} in Fig. 104.57 we have chosen the ponderomotive scaling of Wilks,^{13,61}

$$T_{\text{MeV}} = 0.511 \left[\left(1 + I_{18} \lambda_{\mu\text{m}}^2 / 1.37 \right)^{1/2} - 1 \right],$$

to connect the laser intensity to the hot-electron temperature. No spatial-laser intensity distribution was taken into account in this calculation.

In Fig. 104.57, the experimental data is almost independent of laser intensity, except at the highest laser intensity, $I = \sim 3 \times 10^{20} \text{ W/cm}^2$. This independence of efficiency on hot-electron temperature, over the experimental range of intensities, is a consequence of Eq. (1), displayed by the solid model curves. The efficiency is determined by the relative importance of energy loss due to nonionizing collisions and the cross section for K-shell ionization. The latter is quite flat for energies above 100 keV,⁶² while the collisional cross section drops with increasing energy. The electron range is not restricted by the target thickness for the solid curve in order to mimic the effect of electron refluxing. The net result is that the number of photons produced per unit electron energy is only a weakly increasing function. The solid curves can be made to agree quantitatively with the experimental data if we select an $\sim 8\%$ hot-electron coupling efficiency. This is lower than the $\eta_{L \rightarrow e} \sim (20\% \text{ to } 40\%)$ usually quoted in the literature for these intensities, e.g., in Ref. 4 (upper solid curve). Given the relative large uncertainty in the experimental points because of the CCD calibration uncertainty, the current measurement is in rough agreement with the previous measurements. In addition, the calculated 8% hot-electron coupling efficiency should be regarded as a lower bound because fast-electron energy loss into other channels, such as energy transfer into fast ions and ohmic effects, were not included in the model. Accounting for additional losses would shift the theoretical curves downward, leading to a higher $\eta_{L \rightarrow e}$ for the measurement.

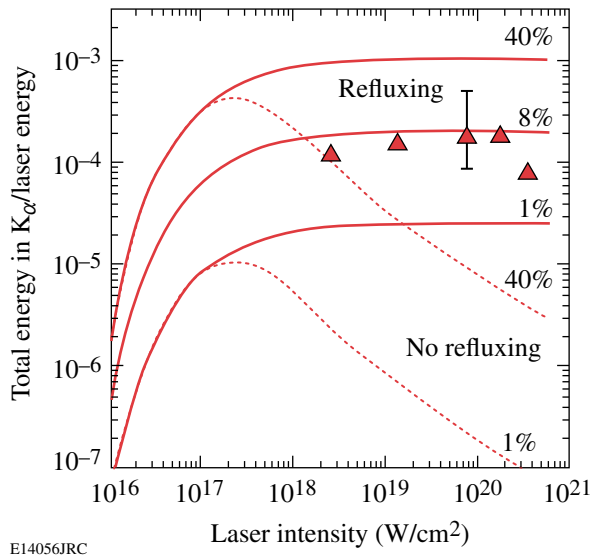


Figure 104.57

Total energy in K_{α} photons normalized to laser energy in the central laser spot as a function of laser intensity. The solid triangles are the experimental data points. The solid curves correspond to the model described in **Inner-Shell Emission** (p. 216) with perfect confinement of the hot electrons (refluxing) and with a hot-electron conversion efficiency of 40%, 8%, and 1%. The dotted curves correspond to the case (40% and 1%) with no refluxing, as described in the text. An 8% hot-electron coupling efficiency is calculated, which should be regarded as a lower bound because fast-electron energy loss into other channels, such as energy transfer into fast ions and ohmic effects, were not included in the model. A representative error bar shows the measured efficiency uncertainty.

The dotted curves illustrate the effect of truncating the electron path length s in the integral, Eq. (2), whenever it exceeds the target thickness $s(E_0) \rightarrow \min[s(E_0), d]$. Electrons in Cu have ranges from $\sim 1 \mu\text{m}$ to $\sim 700 \mu\text{m}$ for energies from 10 keV to 1 MeV.⁵⁷ Only a small fraction of the fastest electrons can escape out the foil, resulting in quickly charging up the target and confining the rest of the electrons that are reflected back from surface sheath fields. Refluxing has previously been discussed in the context of proton generation, showing the importance of the recirculation of the MeV electrons on the electrostatic fields that accelerate protons to multi-MeV energies.³⁶ As expected, ignoring refluxing in the model shows disagreement with the experimental data by an order of magnitude or more. Physically, the solid curves correspond to the case where hot electrons are confined within the target due to reflection or “refluxing” from surface sheath fields until it is stopped, whereas the dashed curves correspond to the case where the electron and its energy are lost as soon as its path length equals the target thickness. Refluxing has been observed in PIC calculations, leading to a yield that is independent of target volume.

The fact that the experimental efficiencies are lower than might be expected based on the simple refluxing model presented here might have several causes: refluxing might not be perfect. With a significant loss fraction, the range of the electrons might be overestimated (which leads to higher efficiencies) due to “anomalous” stopping mechanisms related to large, self-generated magnetic and electric field fluctuations, presumably becoming more important at higher intensities.¹⁶ Target heating might invalidate the use of the cold cross sections.

Summary and Conclusions

For the first time, He_{α} and Ly_{α} lines in the K-shell emission of solid Cu targets irradiated with a 0.7-ps petawatt laser beam were observed at intensities $>10^{20} \text{ W/cm}^2$. This is attributed to the formation of a ~ 2 to 3 keV near-solid-density hot plasma on the laser irradiation target side. A suppression of the ionic line emission is observed when the Cu targets are coated with either a $1\text{-}\mu\text{m}$ thin layer of aluminum or with a $0.5\text{-}\mu\text{m}$ tantalum layer, indicating that the strongest heating is confined to a thin layer.

Measurements of the K-shell emission as a function of foil thickness between $30 \mu\text{m}$ and $1 \mu\text{m}$ for a constant laser intensity of $\sim 3 \times 10^{18} \text{ W/cm}^2$ and $\sim 10\text{-ps}$ pulses show that the He_{α} emission varies by a factor of ~ 4 with a peak at $5\text{-}\mu\text{m}$ thickness, while the K_{α} yield stays about constant. A decreased K_{α} yield measured for targets thinner than $3 \mu\text{m}$ might be explained by a stronger heating of the small target volume and an increased hot-electron energy transfer into ions. Changing laser conditions especially affecting the surface layer could cause the variation of the He_{α} emission. The current data set is limited by its small sample size, and more shots are necessary to investigate this observation.

The K-shell emission of solid Cu foil targets was studied as a function of laser intensity between $2 \times 10^{18} \text{ W/cm}^2$ up to $3 \times 10^{20} \text{ W/cm}^2$ in low-area ($\sim 0.5 \times 0.5$ to $2 \times 2 \text{ mm}^2$) thin foils (~ 20 to $30 \mu\text{m}$) and 0.7-ps pulses. The yield of the ionic lines strongly increases with laser intensity such that, at the maximum intensity, the spectrum is dominated by the He_{α} emission. An approximately constant yield of $\sim 1 \times 10^{11}$ photons/J and $\sim 1 \times 10^{10}$ photons/J were measured for the K_{α} and K_{β} inner-shell emission, respectively, between intensities of $2 \times 10^{18} \text{ W/cm}^2$ and $1 \times 10^{20} \text{ W/cm}^2$. Above $1 \times 10^{20} \text{ W/cm}^2$, the inner-shell emission yield drops. A comparison of the measured intensity scaling of the K_{α} yield with a model shows that refluxing of suprathermal electrons and their confinement in the target volume is crucial to explain these results. Calculations that ignore refluxing show a strongly decreasing K_{α} yield with

laser intensity and disagree with the experimental data by more than an order of magnitude.

ACKNOWLEDGMENT

This work was supported by the U.S. Department of Energy Office of Inertial Confinement Fusion under Cooperative Agreement No. DE-FC52-92SF19460, the University of Rochester, the New York State Energy Research and Development Authority, and the University of California Lawrence Livermore National Laboratory under contract No. W-7405-Eng-48 UCRL_PRES213395. The support of DOE does not constitute an endorsement by DOE of the views expressed in this article.

REFERENCES

1. M. Tabak *et al.*, Phys. Plasmas **1**, 1626 (1994).
2. O. L. Landen *et al.*, Rev. Sci. Instrum. **72**, 627 (2001).
3. H.-S. Park *et al.*, Rev. Sci. Instrum. **75**, 4048 (2004).
4. K. B. Wharton *et al.*, Phys. Rev. Lett. **81**, 822 (1998).
5. S. P. Hatchett *et al.*, Phys. Plasmas **7**, 2076 (2000).
6. K. Yasuike *et al.*, Rev. Sci. Instrum. **72**, 1236 (2001).
7. R. Kodama *et al.*, Phys. Plasmas **8**, 2268 (2001).
8. M. H. Key, M. D. Cable, T. E. Cowan, K. G. Estabrook, B. A. Hammel, S. P. Hatchett, E. A. Henry, D. E. Hinkel, J. D. Kilkenny, J. A. Koch, W. L. Kruer, A. B. Langdon, B. F. Lasinski, R. W. Lee, B. J. MacGowan, A. MacKinnon, J. D. Moody, M. J. Moran, A. A. Offenberger, D. M. Pennington, M. D. Perry, T. J. Phillips, T. C. Sangster, M. S. Singh, M. A. Stoyer, M. Tabak, G. L. Tietbohl, M. Tsukamoto, K. Wharton, and S. C. Wilks, Phys. Plasmas **5**, 1966 (1998).
9. P. A. Norreys *et al.*, Phys. Plasmas **6**, 2150 (1999).
10. K. A. Tanaka *et al.*, Phys. Plasmas **7**, 2014 (2000).
11. J. A. Koch *et al.*, Phys. Rev. E **65**, 016410 (2001).
12. R. B. Stephens *et al.*, Phys. Rev. E **69**, 066414 (2004).
13. S. C. Wilks *et al.*, Phys. Rev. Lett. **69**, 1383 (1992).
14. B. F. Lasinski *et al.*, Phys. Plasmas **6**, 2041 (1999).
15. L. Gremillet, G. Bonnaud, and F. Amiranoff, Phys. Plasmas **9**, 941 (2002).
16. Y. Sentoku *et al.*, Phys. Rev. Lett. **90**, 155001 (2003).
17. A. R. Bell and R. J. Kingham, Phys. Rev. Lett. **91**, 035003 (2003).
18. A. J. Kemp *et al.*, Phys. Plasmas **11**, L69 (2004).
19. A. R. Bell *et al.*, Plasma Phys. Control. Fusion **39**, 653 (1997).
20. T. Feurer *et al.*, Phys. Rev. E **56**, 4608 (1997).
21. R. Kodama *et al.*, Nature **432**, 1005 (2004).
22. H. Chen, B. Soom, B. Yaakobi, S. Uchida, and D. D. Meyerhofer, Phys. Rev. Lett. **70**, 3431 (1993).
23. A. Rousse *et al.*, Phys. Rev. E **50**, 2200 (1994).
24. D. C. Eder *et al.*, Appl. Phys. B **70**, 211 (2000).
25. H. R. Griem, *Spectral Line Broadening by Plasmas* (Academic Press, New York, 1974).
26. J. L. Collier *et al.*, *Central Laser Facility Annual Report 2002/2003*, 168, Rutherford Appleton Laboratory, Chilton, Didcot, Oxon, England, RAL Report No. RAP-TR-2003-018 (2003).
27. C. N. Danson *et al.*, J. Mod. Opt. **45**, 1653 (1998).
28. P. K. Patel, M. H. Key, A. J. Mackinnon, H.-S. Park, R. Shepherd, H. Chen, R. A. Snavely, N. Izumi, J. Kuba, J. Koch, S. C. Wilks, M. May, R. Van Maren, J. A. King, B. Zhang, K. Akli, R. Freeman, S. Kar, L. Romagnani, M. Borghesi, C. Stoeckl, W. Theobald, R. Eagleton, M. Mead, R. J. Clarke, R. Heathcote, P. A. Brummitt, D. R. Neville, D. Neely, and R. Stephens, *Central Laser Facility Annual Report 2003/2004*, 34, Rutherford Appleton Laboratory, Chilton, Didcot, Oxon, England, RAL Report No. RAL-TR-2004-025 (2004).
29. F. N. Beg *et al.*, Phys. Plasmas **4**, 447 (1997).
30. C. Stoeckl, W. Theobald, T. C. Sangster, M. H. Key, P. Patel, B. B. Zhang, R. Clarke, S. Karsch, and P. Norreys, Rev. Sci. Instrum. **75**, 3705 (2004).
31. M. Nishiuchi *et al.*, in *EUV, X-Ray, and Gamma-Ray Instrumentation for Astronomy IX*, edited by O. H. Siegmund and M. A. Gummin (SPIE, Bellingham, WA, 1998), Vol. 3445, pp. 268–277.
32. D. H. Lumb and A. D. Holland, Nucl. Instrum. Methods Phys. Res. A **273**, 696 (1988).
33. H.-S. Park, Lawrence Livermore National Laboratory, private communication (2005).
34. J. A. Bearden, Rev. Mod. Phys. **39**, 78 (1967).
35. R. L. Kelly, J. Phys. Chem. Ref. Data **16**, 651 (1987).
36. A. J. Mackinnon *et al.*, Phys. Rev. Lett. **88**, 215006 (2002).
37. H. Habara *et al.*, Phys. Rev. E **70**, 046414 (2004).
38. D. E. Post *et al.*, At. Data Nucl. Data Tables **20**, 397 (1977).
39. M. Green, Solid-State Electron. **3**, 314 (1961); M. Green and V. E. Cosslett, J. Phys. D **1**, 425 (1968).
40. Prism Computational Sciences, Inc., Madison, WI, 53711.
41. J. J. MacFarlane *et al.*, in *Inertial Fusion Sciences and Applications 2003*, edited by B. A. Hammel *et al.* (American Nuclear Society, La Grange Park, IL, 2004), pp. 457–460.
42. H. K. Chung, Lawrence Livermore National Laboratory, private communication (2005).
43. G. J. Pert, J. Comput. Phys. **43**, 111 (1981).

44. M. I. K. Santala *et al.*, Phys. Rev. Lett. **84**, 1459 (2000).
45. M. Key *et al.*, presented at the 8th International Workshop on Fast Ignition of Fusion Targets, Tarragona, Spain, 29 June–1 July 2005.
46. S. Augst, D. Strickland, D. D. Meyerhofer, S. L. Chin, and J. H. Eberly, Phys. Rev. Lett. **63**, 2212 (1989).
47. L. Labate *et al.*, Phys. Plasmas **12**, 083101 (2005).
48. M. Key, Lawrence Livermore National Laboratory, private communication (2005).
49. R. P. J. Town, presented at the International Workshop on Fast Ignition and High Field Physics, Kyoto, Japan, 25–29 April 2004 (Paper P2633); R. P. J. Town, presented at the 8th International Workshop on Fast Ignition of Fusion Targets, Tarragona, Spain, 29 June–1 July 2005.
50. P. Gibbon and E. Förster, Plasma Phys. Control. Fusion **38**, 769 (1996).
51. R. J. Mason, E. S. Dodd, and B. J. Albright, Phys. Rev. E **72**, 015401(R) (2005).
52. J.-C. Adam, A. Héron, and G. Laval, presented at the International Workshop on Fast Ignition and High Field Physics (FIHFP 2004), Kyoto, Japan, 25–29 April 2004 (Paper P2630).
53. H. Ruhl *et al.*, presented at the International Workshop on Fast Ignition and High Field Physics (FIHFP 2004), Kyoto, Japan, 25–29 April 2004 (Paper P2631).
54. G. Gregori *et al.*, Contrib. Plasma Phys. **45**, 284 (2005).
55. R. Snively *et al.*, presented at the 8th International Workshop on Fast Ignition of Fusion Targets, Tarragona, Spain, 29 June–1 July 2005.
56. D. R. Welch *et al.*, Nucl. Instrum. Methods Phys. Res. A **464**, 134 (2001).
57. M. J. Berger, in *Methods in Computational Physics: Advances in Research and Applications*, edited by B. Alder, S. Fernbach, and M. Rotenberg, Volume 1: Statistical Physics (Academic Press, New York, 1963), pp. 135–215.
58. H. Kolbenstvedt, J. Appl. Phys. **38**, 4785 (1967).
59. F. Ewald, H. Schwoerer, and R. Sauerbrey, Europhys. Lett. **60**, 710 (2002).
60. D. W. Forslund, J. M. Kindel, and K. Lee, Phys. Rev. Lett. **39**, 284 (1977).
61. G. Malka and J. L. Miquel, Phys. Rev. Lett. **77**, 75 (1996).
62. C. Hombourger, J. Phys. B **31**, 3693 (1998).

LLE's Summer High School Research Program

During the summer of 2005, 15 students from Rochester-area high schools participated in the Laboratory for Laser Energetics' Summer High School Research Program. The goal of this program is to excite a group of high school students about careers in the areas of science and technology by exposing them to research in a state-of-the-art environment. Too often, students are exposed to "research" only through classroom laboratories, which have prescribed procedures and predictable results. In LLE's summer program, the students experience many of the trials, tribulations, and rewards of scientific research. By participating in research in a real environment, the students often become more excited about careers in science and technology. In addition, LLE gains from the contributions of the many highly talented students who are attracted to the program.

The students spent most of their time working on their individual research projects with members of LLE's technical staff. The projects were related to current research activities at LLE and covered a broad range of areas of interest including computational hydrodynamics modeling, cryogenic target fabrication and characterization, liquid crystal chemistry, materials science, the development and control of laser fusion diagnostics, and OMEGA EP Laser System design and engineering (see Table 104.II).

The students attended weekly seminars on technical topics associated with LLE's research. Topics this year included laser physics, fusion, holographic optics, fiber optics, and femtosecond lasers and their applications. The students also received safety training, learned how to give scientific presentations, and were introduced to LLE's resources, especially the computational facilities.

The program culminated on 24 August with the "High School Student Summer Research Symposium," at which the students presented the results of their research to an audience

including parents, teachers, and LLE staff. The students' written reports will be bound into a permanent record of their work that can be cited in scientific publications. These reports are available by contacting LLE.

One hundred ninety-one high school students have now participated in the program since it began in 1989. This year's students were selected from approximately 50 applicants.

At the symposium, LLE presented its ninth William D. Ryan Inspirational Teacher Award to Mr. Stephen Locke, a chemistry teacher at Byron-Bergen High School. This award is presented to a teacher who motivated one of the participants in LLE's Summer High School Research Program to study science, mathematics, or technology and includes a \$1000 cash prize. Teachers are nominated by alumni of the summer program. Mr. Locke had the rare distinction of receiving his nomination from a whole family—Christine Balonek (2002) and her brothers Gregory, Robert, and Daniel (2004). "In the classroom, Mr. Locke's wealth of knowledge and fervor for chemistry in combination with his sense of humor, patience, and dedication to his students create an ideal teacher," Christine Balonek writes in her nomination letter. "He is never too busy to help a student during a study hall or after school with any science work. His endless devotion to students and the community is one worthy of recognition." According to her brother, Robert, "Mr. Locke not only taught the material given by the state, he also brought in real-life applications. His teaching methods brought home for me the power of science and technology." David Pescrillo, principal of Byron-Bergen High School, added, "Stephen is an excellent teacher who expects the best from his students. He is very kids-oriented. He comes in during the summer, during the weekends, and after school hours on his own time to tutor the kids who need help. He is a phenomenal guy!"

Table 104.II: High School Students and Projects—Summer 2005.

Name	High School	Supervisor	Project Title
Mary Brummond	Honeoye Falls-Lima	M. Guardalben	OMEGA EP Pulse Compressor Modeling: Misalignment and Power Errors
Philip Chang	Pittsford Sutherland	K. Marshall	Computational Modeling and Analysis of Nickel Dithiolene Structures
Brandon Corbett	Allendale Columbia	T. Collins/ R. Bahukutumbi	Optimization of High-Gain ICF Targets for the National Ignition Facility
Adam DeJager	Greece Odyssey	S. Morse/ R. Kidder	Optical Time-Domain Reflectometry on the OMEGA EP Laser
Frank Fan	Webster Schroeder	S. Craxton	A Model for Cryogenic Target Layering
Alex Grammar	Brighton	R. Boni/ P. Jaanimagi	Relative Quantum Efficiency Measurements of Streak Camera Photocathodes
Stewart Laird	Harley School	J. Knauer	Characterization of a Compound Refractive Lens
Brian MacPherson	Penfield	R. Epstein	Dynamic Energy Grouping in Multigroup Radiation Transport Calculations
Karyn Muir	Honeoye Falls-Lima	J. Lambropoulos	Micromechanics and Microstructure in WC Hard Metals
Brian Pan	Penfield	W. Seka	Improving the Illumination Uniformity of Cryogenic Targets Inside a Layering Sphere
Nicholas Ramos	Palmyra-Macedon	S. Mott/ D. Lonobile	Automated X-Ray Framing Camera Characterization
Valerie Rapson	Greece Olympia	K. Marshall	Contaminant-Resistant Sol-Gel Coatings
Martin Wegman	McQuaid	W. Donaldson	Superconducting Electronics for the ICF Environment
Lauren Weiss	Brighton	L. Elasky	Categorization and Analysis of Defects in Cryogenic Targets
Rosie Wu	Brighton	D. Edgell/ S. Craxton	Analysis of Inner Ice Surface Perturbations Using Bright Ring Characterization

FY05 Laser Facility Report

The OMEGA Facility continued to operate extended shifts during select weeks in FY05, accommodating user demand by conducting 1461 target shots (see Table 104.III). Highlights of other FY05 achievements include the following:

- The SSD, main, and “backlighter” OMEGA laser sources were converted to integrated front-end sources (IFES). The IFES replaces the existing OMEGA master oscillators (OMO’s) and two pulse-shaping amplitude modulators. The IFES architecture consists of a single-frequency, continuous-wave (cw) fiber laser, a dual-amplitude modulator for pulse shaping, and a cw-pumped fiber amplifier that boosts the energy injected into OMEGA’s diode-pumped regenerative amplifier. The IFES system requires significantly less maintenance, is easier to operate, requires no optical alignment, has improved pulse-shaping stability, and is much more reliable than the OMO system. The “fiducial” laser source will be converted to the IFES architecture early in FY06.
- TIM-based target positioning systems (TTPS) were utilized on a number of experimental campaigns. These instruments were developed to improve the speed and accuracy of alignment for complex targets. Previously, high-magnification x-ray imaging pinhole arrays had been mounted on the same stalk as the primary target. This configuration put the burden of alignment on target fabrication and often required several metrology iterations to establish the angle of the pinhole substrate with respect to the primary target within allowable specifications. By using separate targets, overall time spent in target fabrication, metrology, and alignment has been reduced dramatically and target positioning precision has improved.
- The planar Moving Cryostat Transfer Cart (Cart 4), was modified to accommodate cryogenic hohlraum experiments. Cart 4 is used routinely to provide cryogenic solid/liquid D₂ targets for experiments on D₂ equation of state (EOS), multiple shock timing and convergence, and Rayleigh–Taylor instability growth. These experiments directly support the National Ignition Campaign. Cryogenic gas-filled (He and H) hohlraums are part of the indirect-drive ignition point design. Cart 4 was modified to field hohlraums at temperatures appropriate for the ignition point design. The first experimental series provided valuable temperature/density data. The target design is currently being modified for experiments in FY06 to minimize the target debris associated with the thermal mass in contact with the hohlraum.
- High-yield cryogenic DT experiments are expected in early FY06 following a successful tritium readiness review in June 2005. In anticipation of these experiments, a number of new high-yield diagnostic systems have been (or are being) implemented on OMEGA. These include the 12-m nTOF (neutron time-of-flight diagnostic 12 m from target chamber center), a chemical vapor deposition (CVD) diamond detector for bang time, a light-pipe–based neutron temporal diagnostic for reaction history and γ -ray bang time, a permanent neutron imaging capability, and a magnetic recoil spectrometer for neutron spectroscopy and areal density. The full implementation of this new instrumentation suite should be completed in FY06 and will give the facility diagnostic capabilities for high-yield DT implosions comparable to those for the lower yield standard D₂ implosions.
- A continuously pumped centralized vacuum system for OMEGA’s harmonic energy detector (HED) vacuum tubes was designed and installed. This system significantly increases the flexibility to refurbish and perform maintenance on the vacuum tubes, ensuring operational readiness. Approximately one-sixth of OMEGA is outfitted with the modified tube design, with the remainder to be installed in FY06.
- The east wall of the OMEGA Target Bay was modified to support transport of the OMEGA EP beams to the OMEGA target chamber. OMEGA Facility modifications planned for FY06 include the installation of OMEGA EP beam transport into OMEGA target chamber port H9 and the installation of the off-axis parabola inserter on port H7. This installation will remove the GMXI diagnostic from port H9 and TIM-2 from port H7.

Table 104:III: The OMEGA target shot summary for FY05.

Laboratory	Planned Number of Target Shots	Actual Number of Target Shots
LLE	715	701
LLNL	375	400
LANL	140	138
SNL	30	34
NLUF	120	130
CEA	30	34
NRL	20	24
Total	1430	1461
LLE ISE		303
LLE SSP		172
LLE RTI		95
LLE ASTRO		38
LLE DD		30
LLE CRYO		23
LLE DDI		16
LLE LPI		16
LLE PB		8
LLE Total		701

National Laser Users' Facility and External Users' Programs

During FY05, 760 target shots were taken on OMEGA for external users' experiments. The external users' shots accounted for 52% of the total OMEGA shots produced in FY05. External users in FY05 included seven collaborative teams under the National Laser Users' Facility (NLUF) program as well as collaborations led by scientists from the Lawrence Livermore National Laboratory (LLNL), Los Alamos National Laboratory (LANL), Sandia National Laboratory (SNL), the Naval Research Laboratory (NRL), and the Commissariat à l'Énergie Atomique (CEA) of France.

NLUF Program

FY05 was the first of a two-year period of performance for the eight NLUF projects approved for FY05 funding. Seven of these NLUF campaigns were allotted OMEGA shot time and received 130 shots on OMEGA in FY05. Table 104.IV lists the accepted proposals.

Isentropic Compression Experiments (ICE) for Measuring EOS on OMEGA

Principal Investigator: J. R. Asay (Washington State University)

This research is developing three new areas of high-pressure research. First, techniques to generate high-accuracy, quasi-isentropic equation of state data into the Mbar regime will be developed. This effort will enable, for the first time using lasers, "cold" equation of state curves for standard materials in the Mbar regime. Second, wave profile data on candidate materials (Bi and Fe) upon compression through both solid–solid and solid–liquid phase transitions will be measured and compared with similar data measured with different loading times on other platforms (Z data, gun data, diamond anvil data). These data will then be used to benchmark models for the time dependence of phase transitions being developed at WSU. Finally, to ensure the phase transitions observed in these dynamic experiments correspond to the same phases as observed in

Table 104.IV: FY05–FY06 Proposals.

Principal Investigator	Affiliation	Proposed Title
J. Asay	Washington State University	Isentropic Compression Experiments for Measuring EOS on OMEGA
H. Baldis	University of California, Davis	Laser–Plasma Interactions in High-Energy-Density Plasmas
R. P. Drake	University of Michigan	Experimental Astrophysics on the OMEGA Laser
R. Falcone	University of California, Berkeley	NLUF Proposal: Plasmon Density of States in Dense Matter (no target shots allocated in FY05)
P. Hartigan	Rice University	Astrophysical Jets and HED Laboratory Astrophysics
R. Jeanloz	University of California, Berkeley	Recreating Planetary Core Conditions on OMEGA
R. Mancini	University of Nevada, Reno	Three-Dimensional Study of the Spatial Structure of Direct-Drive Implosion Cores on OMEGA
R. D. Petrasso and C. K. Li	Massachusetts Institute of Technology	Implosion Dynamics and Symmetry from Proton Imaging, Spectrometry, and Temporal Measurements

static experiments, dynamic x-ray diffraction will be used to determine lattice structure. This past year the most difficult of these goals were achieved; we developed the platform to produce high-accuracy and high-pressure isentrope data on aluminum. In addition, it was observed that the elastic-plastic transition is much larger than expected from previous work at Z. This issue is being investigated.

Twelve shots were performed on isentropic compression targets in the past year (Feb. 22th: shots 38961–38966, June 14th: shots 40121–40127). The purpose of these initial campaigns was to (1) develop a shockless compression platform with a pressure drive of ~1% planarity over a several hundred micron region and (2) use this planar drive to extract a single-shot series of equation of state (EOS) data for Al to peak pressures in excess of 1 Mbar. The ICE-EOS package, as shown in Fig. 104.58, consists of a Au halfraum, a plastic reservoir followed by a vacuum gap, and a double-stepped Al target. Fifteen beams from the OMEGA laser at 0.35- μm wavelength, containing a combined energy of 5–6 kJ in a 2-ns temporally flat pulse, are focused symmetrically onto the inner walls of the Au hohlraum laser entrance hole (LEH): 1.7-mm; diameter: 2.2 mm; length: 1.7 mm). This confined high-Z geometry results in a near blackbody distribution of thermal x rays ($T_h \sim 120$ eV) with uniform temperature gradients over a spatial region close to the diameter of the hohlraum. The hohlraum is attached to a 180- μm -thick, 12% Br-doped polystyrene foil [$\text{C}_8\text{H}_6\text{Br}_2$]. The x-ray field within the hohlraum launches an ablatively driven shock through the foil. The initial region of planarity is expected to approach that of the diameter of

the halfraum and can extend over millimeters. The Bromine dopant absorbs the high-energy Au M-band x rays generated within the hohlraum, which otherwise could preheat the Al step sample. After breakout from the rear surface, shock heating and momentum cause the Br-CH to dissociate and unload across a 400- μm vacuum gap. Transit across the vacuum gap causes mass-density gradients along the target axis to relax as a function of distance from the original Br-CH/vacuum-gap interface. The unloading Br-CH monotonically loads up against the Al sample and the imparted momentum launches a ramp stress wave through the material. The temporal profile of the compression wave may be shaped by varying the size of the vacuum gap, the density of the reservoir, or the temperature within the hohlraum. In our FY05 experiments, the main targets consisted of 10-20-30- μm Al steps coated onto a well impedance-matched LiF window.

Probing through the LiF window, the time history of the Al/LiF interface acceleration is recorded with a line imaging velocity interferometer (velocity interferometry system for any reflector or VISAR) with two channels set at different sensitivities. The time-resolved fringe movement recorded by a streak camera is linearly proportional to the velocity of the reflecting surface, which in this case is the Al-LiF interface. This allows for accurate measurement of the particle velocity (after taking into account the refractive index of the LiF window) as a function of time. Shown in Fig. 104.59(a) is the streak camera output of the VISAR for the target conditions described in Fig. 104.58.

The image provides spatial resolution at the target plane over ~500 μm and temporal resolution of the interferometer fringe displacement over a 30-ns time window. We observe excellent planarity across the field of view with smooth ramp unloading from the 10-, 20-, and 30- μm Al samples at progressively later times. The velocity sensitivity (set by the resolving element within the VISAR) is 0.86 km/s/fringe shift. Using Fourier analysis, and after deconvolving the data for temporal and spatial distortions within the streak camera, the time-resolved particle velocity profile for each Al thickness [Fig. 104.59(b)] can be extracted.

The iterative analysis technique described by Rothman *et al.*¹ was used along with the particle velocity profiles in Fig. 104.59(b) to generate a path through stress-density space (Fig. 104.60). Also shown for comparison is the isentrope from the Mie-Grüneisen equation of state. The error bars on the experimentally determined σ - ρ curve are $\pm 5\%$ (stress space) and $\pm 2.5\%$ (density space) up to a peak stress of ~83 GPa.

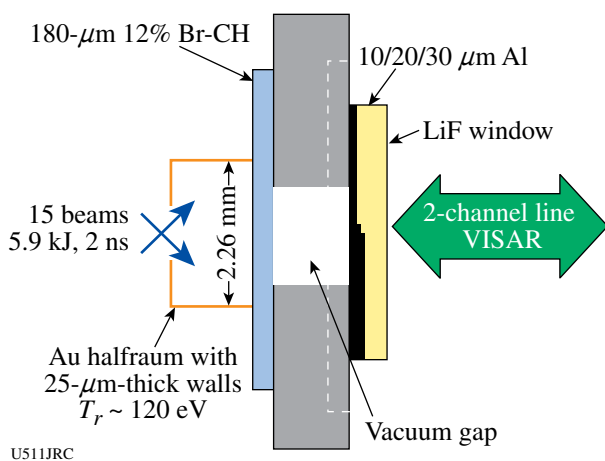


Figure 104.58
Standard ICE target design.

The errors are dominated by uncertainties in measuring of the (~0.1 km/s), time (~50 ps), step height (~1%), and initial density (0.6%) and are due to random noise within the system (poor fringe visibility). The error bars can be reduced linearly with increasing step height. This is the first such measurement on a laser platform and opens up the possibility of extracting EOS data well into the multi-Mbar regime. Note that the extracted stress-density path is stiffer than the predicted Al isentrope, which may be due to strength effects or potential systematic errors in the experiment.

Shockless compression was demonstrated over a range of peak pressures and rise times (Fig. 104.61). The highest achieved pressure was 210 GPa, which corresponds to a particle velocity of ~6 km/s. An enhanced elastic wave precursor was

observed, several times in excess of the reported Hugoniot elastic limit (HEL), for ramp compressions which occur over shorter time scales. This is not presently understood and is being investigated. If true, this is a significant discovery and it is expected that it will highlight the uniqueness of laser-driven ramp loading for measuring the yield strength of materials at high shockless strain rates. In the second year of the proposal,

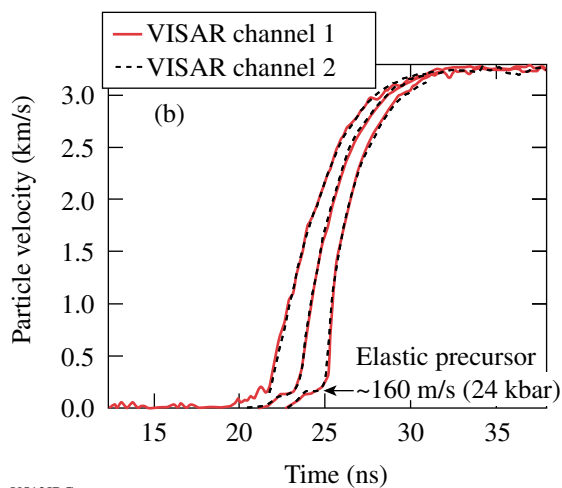
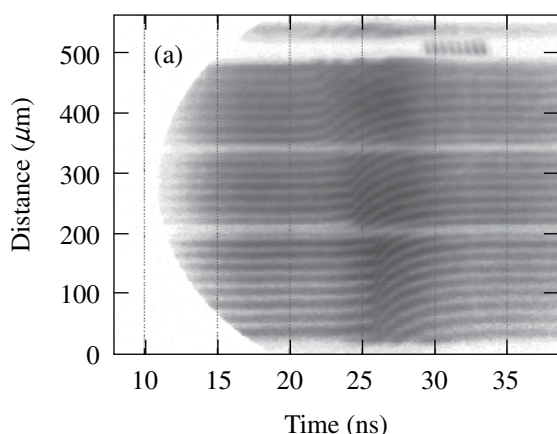


Figure 104.59
(a) Streak camera output of VISAR for shot 40127. (b) Extracted particle velocity profiles for shot 40127.

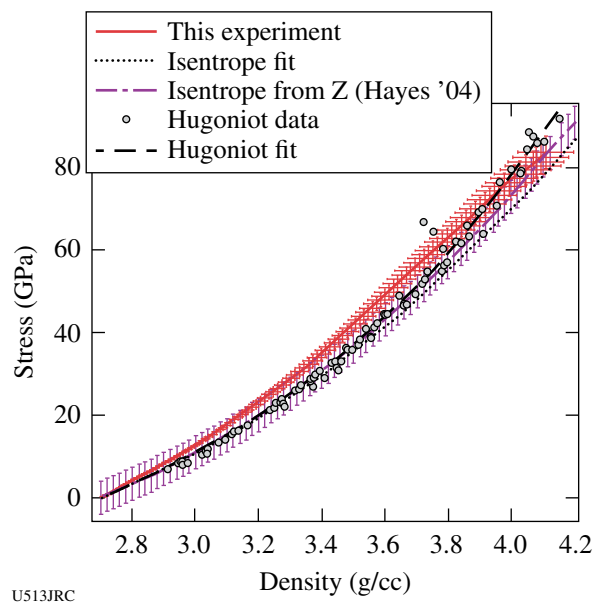


Figure 104.60
Stress-density path calculated from a double-stepped Al target.

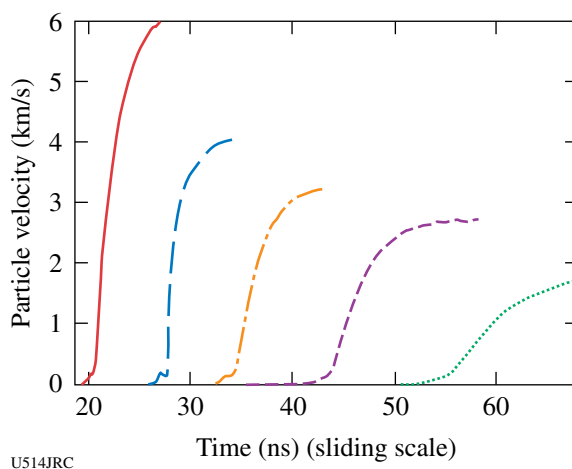


Figure 104.61
The compression of Al samples for different compression times shows a difference in the elastic-plastic structure with loading rate.

it is intended to extract EOS and strength information for free-surface Ta in excess of 1 Mbar and to determine the rate dependence of phase transformations for materials with multiple solid phases. A sophisticated analysis technique is also being developed to analyze free-surface stepped data so that a window material is not needed as a reference. Some effort will also be dedicated to develop techniques to shape the pressure profile of the compression wave.

Laser-Plasma Interactions in High-Energy-Density Plasmas
 Principal Investigator: H. Baldis (University of California, Davis)

Laser-plasma interactions in high-energy-density plasmas display a broad palette of features that prove useful in furthering the understanding and characterization of these unexplored plasma regimes. To access these regimes, reduced-size (below 1 mm in diameter and length), Au cylindrical enclosures are irradiated by intense laser beams at around 10-TW power in 1 ns. These hot hohlraums act as converters of laser energy into x-radiation, and because of the high power pumped into such a small target, the radiation temperature reaches high values, above 300 eV. The plasmas created into and around the laser channels are characterized by elevated electron temperatures (~10 keV), with densities varying up to the critical density (for 351 nm $n_{cr} = 9.1 \times 10^{20} \text{ cm}^{-3}$).

The intrinsic dependence of the stimulated Raman scattering (SRS) on plasma temperature and density gives the possibility of using the process as a plasma diagnostic tool. From the resonance condition coupled to the dispersion relation, one can infer the electron temperature in hot plasmas (above

5 keV) as the Bohm-Gross shift becomes significant and SRS wavelengths extend beyond 702 nm ($= 2\lambda_0$, where λ_0 is the laser wavelength). The hot hohlraum is irradiated by 19 OMEGA laser beams. Each beam carries ~500 J energy onto the target, in 1 ns pulses, at 351-nm wavelength. The beams are bundled in cones at ~23° (cone 1), ~48° (cone 2), and 59° to 62° (cone 3) as shown in Fig. 104.62.

Figure 104.63 illustrates a SRS spectrum measured by a full-aperture backscattering station (FABS) at OMEGA. The SRS wavelength rises quickly in the first half of the laser pulse, as the laser channel fills with plasma. The electron density

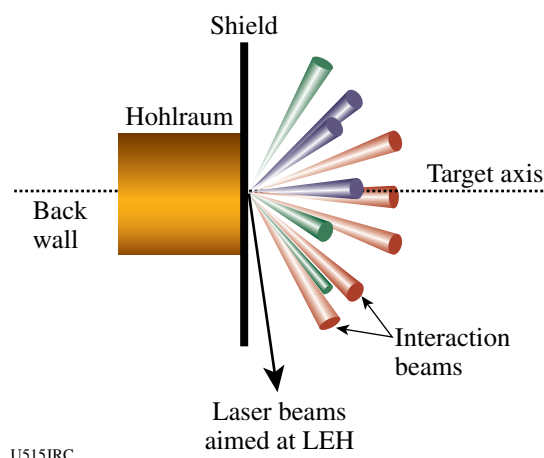


Figure 104.62
 Hohlraums irradiated by the OMEGA beams are used for new studies of laser-plasma interaction in high-energy density plasmas.

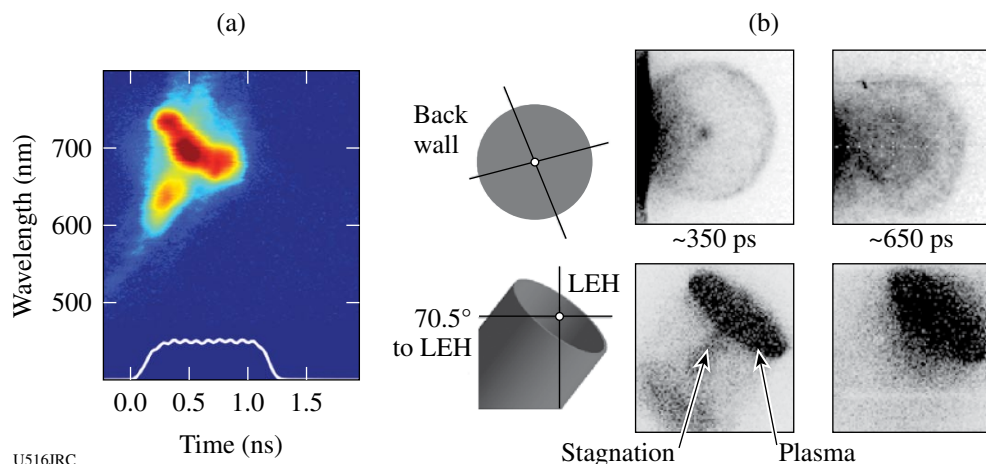


Figure 104.63
 (a) A time-resolved Raman spectrum measured in hot hohlraums is characterized by a wavelength above 702 nm. This is an indication of high electron temperatures. (b) Two different views (end-on and near side-on) of the Au plasma-emitting x-rays with photon energies above 7 keV. The stagnation on axis is visible at 350 ps, with the bright emission at the LEH.

increases above $0.1 n_{cr}$, and the plasma fill moves the laser energy deposition region to the laser entrance hole (LEH). Indications of plasma filling are given by the Raman spectra at the time when the SRS wavelength reaches its maximum and then stays constant or decreases. It is likely that SRS, occurring along a density gradient outside the target, is pushed to a lower density (shorter wavelength) as the laser beam filaments.

X-ray framing-camera images [Fig. 104.63(b)] confirm the filling time inferred from SRS spectra. The images were taken for x-ray photon energies above 7 keV, through the thin Au back wall of the hohlraum and also at 70.5° to the LEH. The Au plasma stagnation may be important for the scattering as it produces high electron temperatures ($T_e \sim 10$ keV). The stagnated plasma eventually moves to the LEH where it is further heated by the laser. This is reflected in the spectral shift that brings the SRS wavelength above 730 nm, which corresponds to $T_e \sim 8$ keV (as deduced from SRS dispersion relation). Time-integrated spectroscopic measurements of a Au L-band measured an average charge state of around 58 to 59, consistent with an average $T_e \sim 7$ to 8 keV.

Experimental Astrophysics on the OMEGA Laser

Principal Investigator: R. P. Drake (University of Michigan)

The OMEGA laser can address important issues in astrophysics because, through laser ablation, it can produce pressures of $\gg 10$ Mbars over areas of square millimeters. Two such issues, the contribution of hydrodynamic instabilities to the structure in supernovae and the dynamics of radiative shock waves, are the topics of this project. In experiments performed in this project, it was found that, under conditions well scaled to supernova explosions, spikes of dense material can penetrate much farther than previously anticipated. To explore this phenomenon, it was necessary to develop new radiographic diagnostics capable of improved imaging in two orthogonal directions. This goal was achieved (Fig. 104.64) and work is now proceeding to study the contributions of various initial modes to the enhanced spike penetration.

In the experiments, ten beams of the OMEGA laser irradiate a polyimide disk with UV light at an irradiance of $\sim 10^{15}$ W/cm² for 1 ns. This launches a 50-Mbar shock into the material, which later evolves to form a blast wave not unlike that produced during a supernova explosion. The blast wave crosses a structured interface to lower-density material, which is a surrogate for the structured interfaces that are present in a presupernova star. The subsequent, unstable evolution is monitored by radiographically detecting the structure of Bromine-doped

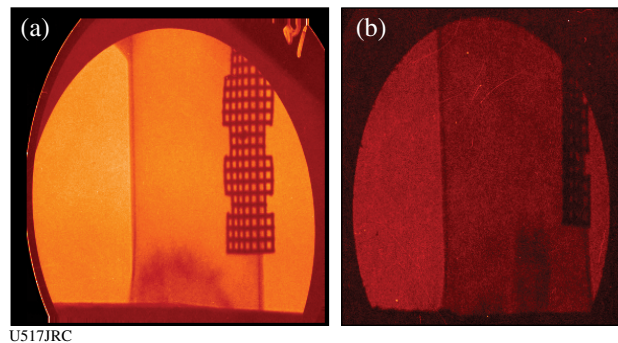


Figure 104.64

Data from the first experiments to obtain physics data using simultaneous, orthogonal, point-projection backlighting [viewing direction of image in (b) is orthogonal to that of (a)]. The data are obtained by using a brief (1 ns) x-ray source to project a signal onto an exposed piece of x-ray film. One can see on these images the structures that have evolved from an initial condition defined by $a_0 \sin(kx) \sin(ky)$, where $a_0 = 2.5 \mu\text{m}$, $k_x = k_y = 2\pi/(71 \mu\text{m})$. During the next year, the impact of a selected range of initial conditions will be studied.

material that was initially a strip within the high-density disk. The experiments can study some issues at a level of detail not possible in present-day simulations.

Astrophysical Jets and HED Laboratory Astrophysics

Principal Investigator: P. Hartigan (Rice University)

The series of experiments for the NLUF program on astrophysical jets and high-energy-density (HED) laboratory astrophysics was designed to explore what can be learned about astrophysical jets by simulating them in the laboratory while at the same time testing how well the advanced numerical codes *RAGE* and *PETRA* follow the evolution of shocked flows. In FY05, this program was granted one shot day on 25 May and another on 31 August. For the May shots, a series of baseline experiments were carried out to test the reproducibility of the jet creation. Results from these shots are shown in Fig. 104.65. The overall structure of the jet closely resembles that of the numerical simulations, and images taken at the same time from different shots are nearly identical in most cases. Hence, there is confidence that variations in the target construction are not dominating the experimental results. For the 31 August shots, a more advanced target design will be implemented in which a dense ball is embedded within the foam. This design shows many interesting shock waves in the numerical simulations and begins to address the astrophysical case of a jet deflecting from a dense molecular cloud or a jet entraining dense fragments within bow shocks. Such flows are of interest to astrophysicists as they are observed to occur in a variety of star formation

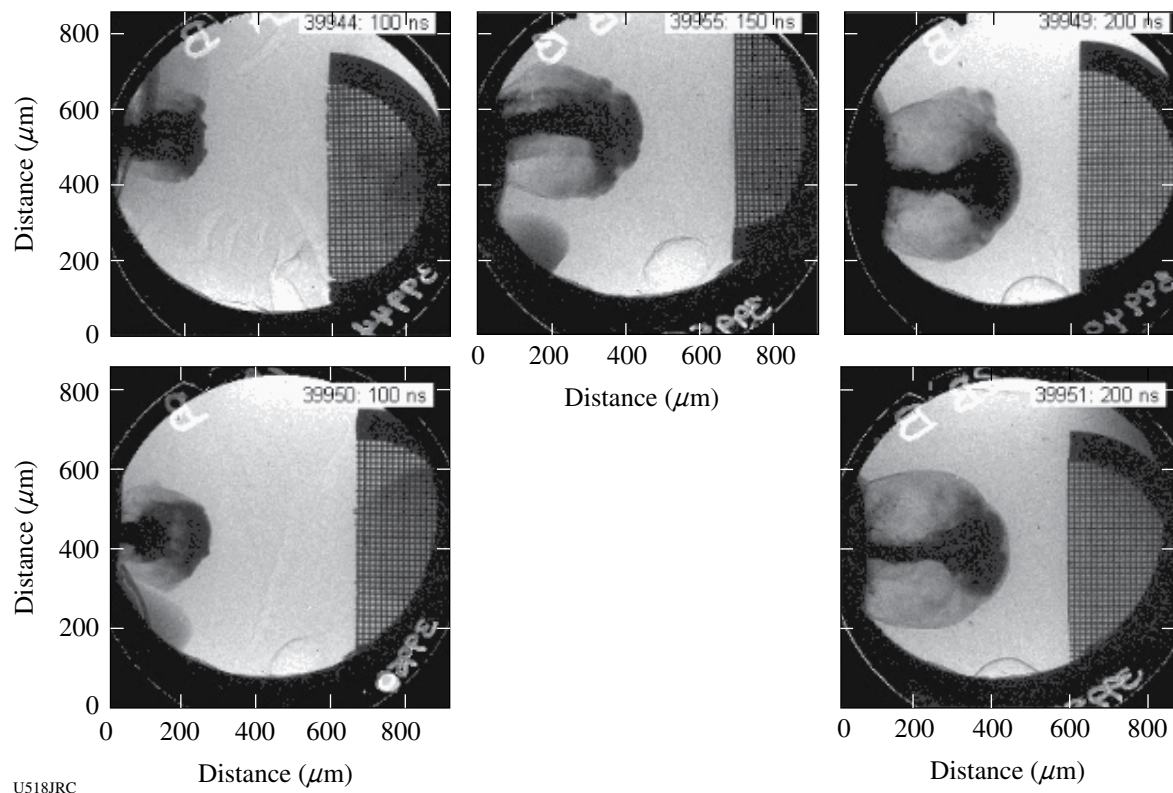


Figure 104.65

Time-framed x-ray backlit images showing the time evolution of jets on two OMEGA shots [39944 (top) and 39950 (bottom)].

settings and may help address issues such as the generation of turbulence in molecular clouds. The parameter space associated with dense clumps and shock waves is very rich, and it should be possible to explore a variety of phenomenon such as clump lifetimes, fragmentation, turbulence, and jet deflection for various sized clumps and impact parameters in future shots, provided these new targets perform as anticipated.

Creating the Core Conditions of Giant Planets in the Laboratory

Principal Investigator: R. Jeanloz (University of California, Berkeley)

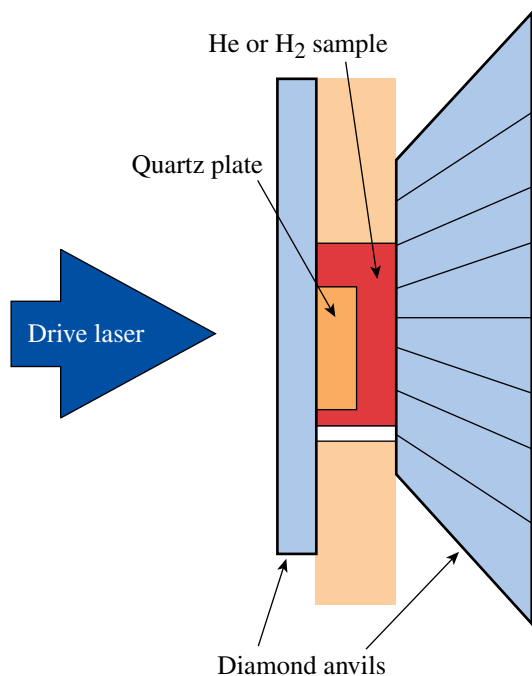
During the past year, 13 OMEGA shots were conducted on diamond anvil cells filled with H_2 , D_2 , He, and He/ H_2 mixtures. The primary focus of the work over the past year has been on dense He. Gas samples were precompressed (see Fig. 104.66) from 0.2 to 1.5 GPa and shocked to pressures as high as 200 GPa (2 Mbar). The experiments are designed to access the extreme densities of the interior regions of the giant

planets Jupiter and Saturn. The technique combines a diamond anvil cell target with a laser-driven shock. With this technique, the initial sample pressure is much higher than ambient (1 to 5 GPa), and the initial density may be from $1.5\times$ to $4\times$ higher than ambient (depending on the sample)—a large increase compared to nonpressurized preparation methods. Furthermore, in the important case of the He/ H_2 mixtures that compose giant planets, precompression is the only way to produce a uniform single-phase target sample for high-pressure/density experiments. The higher initial density results in a significantly larger final density and correspondingly lower temperature in the shock-compressed state.

Using the active shock breakout (ASBO)/shock optical pyrometers (SOP) diagnostic, it was possible to determine pressure and density in the shocked sample as well as its optical reflectance. The temperature is simultaneously measured with the pyrometer capability of the diagnostic. Such equation-of-state measurements provide crucial constraints on models that describe planetary structure (current internal state) and internal

evolution, which is a key requirement for understanding the origins of planets. Electrical conductivity inferred from optical reflectance measurements are used as input data for models of planetary magnetic-field generation.

A quartz reference technique was employed for all of the samples tested to produce quantitative measurements of the Hugoniot parameters (P , V , and E), temperature (T), and shock-front reflectivity (R) that can be related to electrical conductivity (σ). The recent experiments provide measurements of the properties of dense He to the highest pressures yet achieved under shock compression. Detailed data are now available on the insulator-conductor transition in He at conditions near 1 g/cm^3 and ~ 2 to 5 eV ; from these data it is estimated that the transition to metallic-like conducting states is near 360 GPa and 1 eV . This pressure is significantly lower than the estimated metallic transition along the cold compression curve ($\sim 1200 \text{ GPa}$). A significant data set on H_2 has also been collected at three different initial densities. These new data will provide an interesting comparison to the current extensive data set on cryogenic liquid deuterium. Finally, for the first time, two data points were produced on a 50% He/ H_2 mixture. The preliminary Hugoniot results indicate that the compressibility of the mixture is consistent with an idealized mixing model

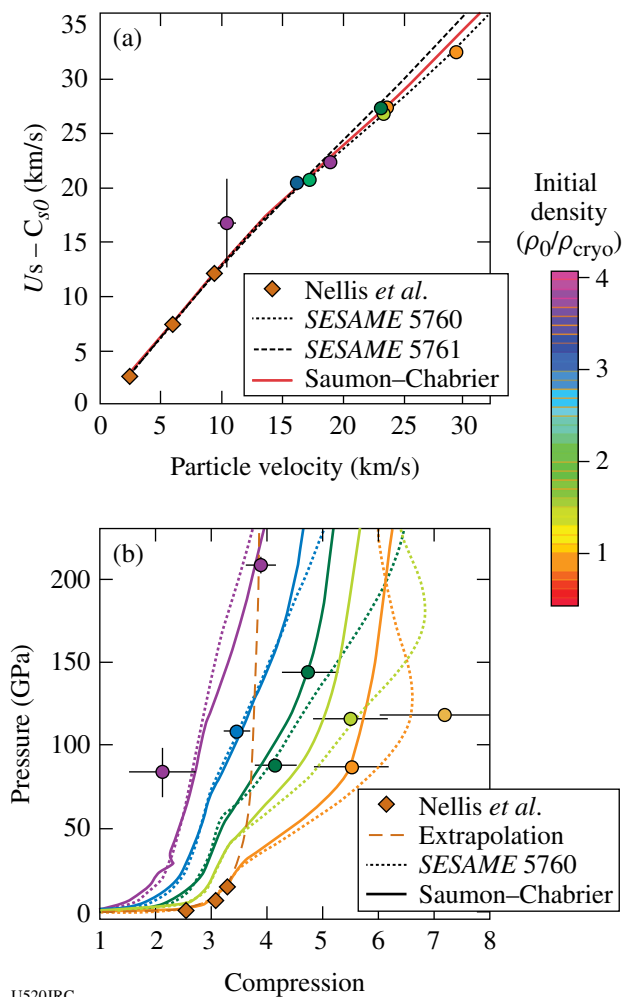


U519JRC

Figure 104.66
Schematic of the precompressed target arrangement.

based on the equations of state of pure He and H_2 ; it is planned to increase this data set with the future OMEGA experiments that are currently being planned.

Figure 104.67(a) shows a compact representation of the He Hugoniot data plotted as a function of the particle speed. It turns out that all available theoretical models predict that the family of Hugoniot curves corresponding to an ensemble of precompressed states are parallel to each other and offset from



U520JRC

Figure 104.67
(a) He Hugoniot measurements plotted in a reduced form. Shock velocity minus the sound velocity of the initial state is plotted as a function of particle velocity. The shades of the points indicate initial density relative to the cryogenic liquid density (0.122 g/cm^3), as indicated by the scale. (b) Pressure as a function of compression for shock-compressed He at three different initial densities. Points show our data, the solid curves are predictions from the SCVH EOS, and the dotted curves are from the SESAME 5760 table. The dashed curve is an extrapolation of a linear fit to the low-pressure EOS data.

the origin by the initial-state sound velocity. Different models predict different slopes for the Hugoniot, but all models are similar in that the Hugoniot for a range of precompressed states can be represented by a single average curve after the sound velocity offset is subtracted. Accordingly, the ordinate in Fig. 104.67(a) is given by the measured shock velocity minus the sound velocity of the initial state. As is evident in the figure, all of the data converge to a common reduced Hugoniot. Note that the slope of the high-pressure portion of the Hugoniot (particle velocity >10 km/s) is distinctly different from the slope of the low-pressure segment measured by Nellis *et al.*² The reduced slope observed for the high-pressure states indicates that the He Hugoniot undergoes a marked softening relative to its lower-pressure behavior. In this range, all the samples have become conducting, and thus the softening is probably associated with ionization.

Figure 104.67(b) shows the same data represented in terms of compression as a function of pressure. The near-vertical dashed line shows the behavior of the low-pressure Hugoniot if it is extrapolated to higher pressures—little can be said about compressions beyond about 3.5 because temperature dominates the pressure at this point (our precompression experiments avoid this problem). The solid curves show the behavior predicted by a commonly used astrophysical model calculated by Saumon, Chabrier, and van Horn (SCVH), and the solid curves show the same for the *SESAME 5760* table. The softening at high pressures is predicted by both the SCVH and *SESAME* models. In addition to the Hugoniot EOS data, we extracted temperature and shock-front reflectance for cases where the latter was observable. These data are summarized in Fig. 104.68 for all of our He data set. The temperature data also show broad agreement with the SCVH EOS for He. The reflectivity data are strongly correlated with temperature, indicating that the driving mechanism for the conductivity is a thermal activation process.

The reflectivity data have been fit to a simple semiconductor model of the ionizing fluid. From the fit it is estimated that metallic-like conditions in dense He will be achieved near 2.7 g/cm³ and 1-eV temperature, corresponding to ~ 360 GPa on the Jupiter isentrope. These data and the fit are also in good agreement with the data of Ternovoi *et al.*,³ who measured the conductivity of dense He with a reverberating shock technique, and with the plasma–chemical model of Forster *et al.*⁴ Figure 104.69(a) shows details of the fit to the semiconductor model; Fig. 104.69(b) shows the estimated metallization boundary on the pressure–temperature (P-T) phase plane.

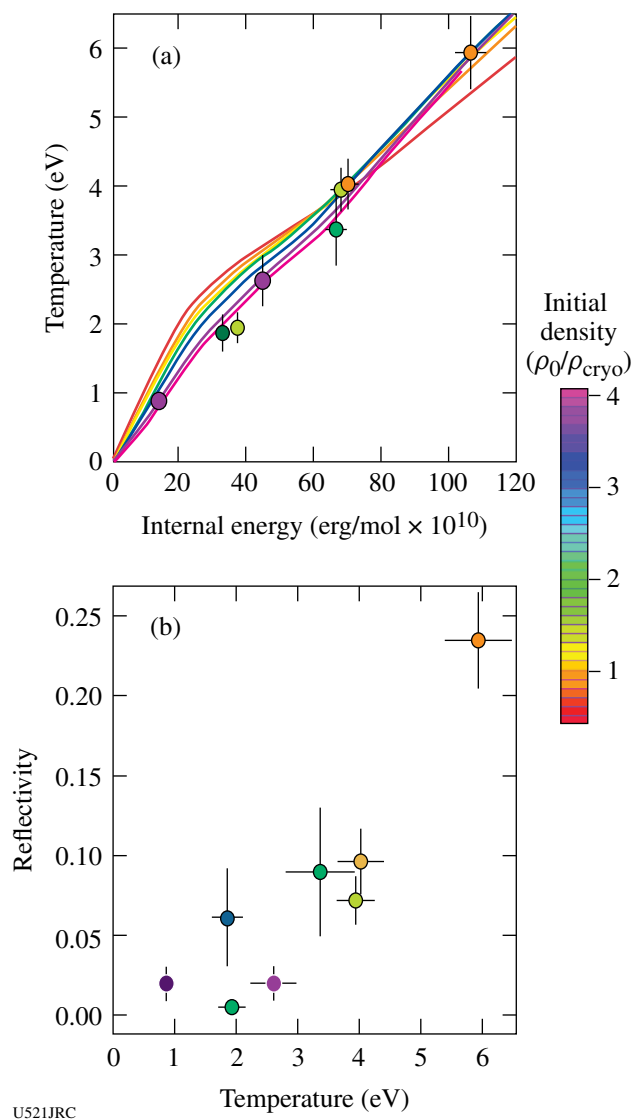


Figure 104.68

(a) Temperature as a function of internal energy for He (points) in comparison with the SCVH model (solid curves); the tone scheme is the same as described in Fig. 104.67. (b) Reflectivity as a function of temperature for shock-compressed He.

In addition to the He results, high-pressure data on H₂ continued to be collected, and Hugoniot data have been obtained, centered at three different initial densities (not shown here). Analysis of these data is ongoing, as the completion of an accurate model for the release response of the quartz standard is in progress. This will be the first high-pressure data set available to compare the high-pressure response of H₂ with the current extensive set of data for shock-compressed D₂.

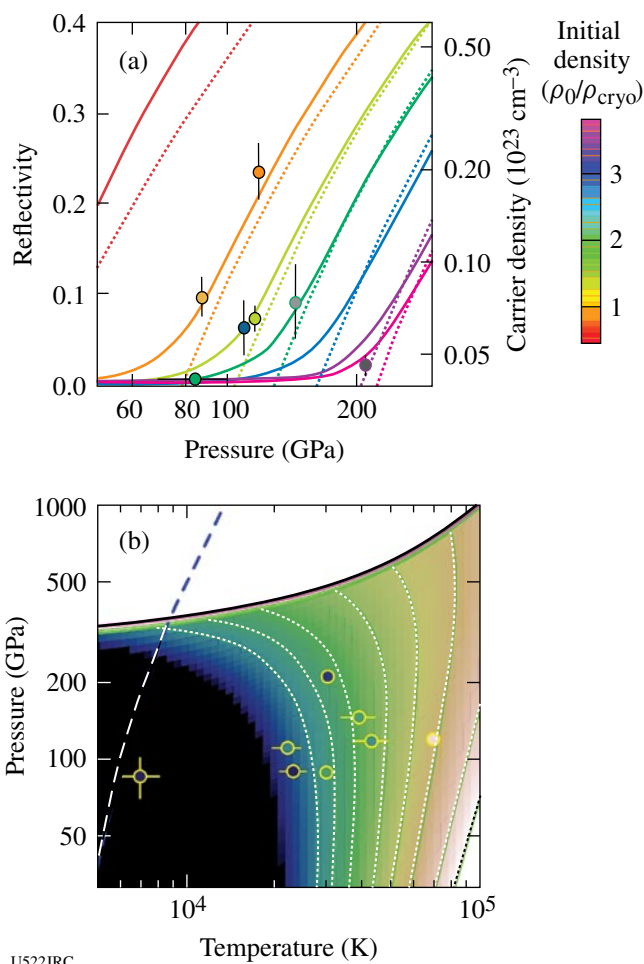


Figure 104.69

(a) Reflectivity of He as a function of shock pressure in comparison with a semiconductor model fit (solid curves). Dashed curves show the corresponding carrier density (right scale). (b) Points show the locations on the P-T plane of the data points in (a). The dotted curves and the tonal scale show contours of constant ionization from the model, the thick solid curve is the 2.7 g/cm³ isochore (indicating the metallization boundary), and the dashed curve is the Jupiter isentrope.

Finally, the first two experiments on He/H₂ mixtures have been completed. The Hugoniot results, shown in Fig. 104.70, indicate that the compression curve of the mixture is well modeled by an equation of state constructed by linear mixing of the SCVH He and Ross H₂ models. This is work in progress; considerably more analysis must be performed and more data collected before strong conclusions can be made.

Currently, a wide range of states in He and H₂ have been explored, and the first two experiments on He/H₂ mixtures

have been performed. For the coming year, this investigation will focus on He/H₂ mixtures. Because they are immiscible fluids, at ambient pressure and low temperature, these mixtures have never been studied at high pressures. The studies will begin to address the issues of He/H₂ miscibility, the transition to conducting states in the mixture, and the effect of the mixture on the equation of state. The conductivity (inferred from reflectance) in He/H₂ mixtures allows the determination of ionization properties. These data will provide insight on the electrical conductivity and the miscibility of He/H₂ mixtures in the giant planets.

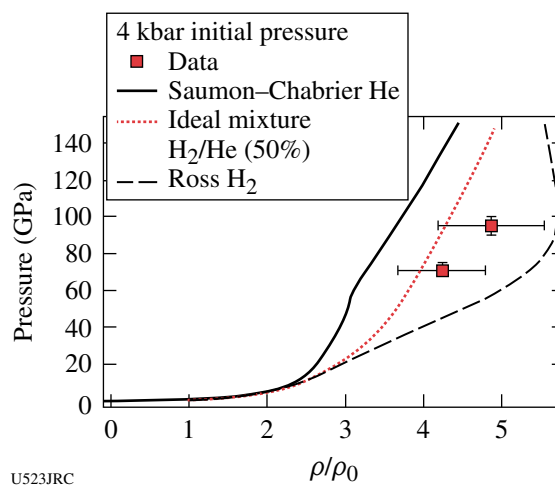


Figure 104.70

(a) Initial Hugoniot data on a 50% mixture of He/H₂, shown in comparison with a theoretical Hugoniot calculated based on ideal mixing of the SCVH-He model and the Ross H₂ model.

Three-Dimensional Study of the Spatial Structure of Direct-Drive Implosion Cores at OMEGA

Principal Investigator: R. Mancini (University of Nevada, Reno)

The goal of this project is to determine the three-dimensional spatial structure of temperature and density distributions in high-energy-density core plasmas arising from OMEGA direct-drive implosions. Targets are plastic shells with a gas fill made out of deuterium and a tracer amount of argon for spectroscopic diagnostics. The data for the analysis consists of space-integrated, time-resolved x-ray argon line spectra recorded with streaked crystal spectrometers and gated x-ray narrow-band images based on argon line spectral features obtained along three quasi-orthogonal directions.

Data modeling and analysis is performed using a spectral model that considers collisional-radiative level population kinetics, detailed Stark-broadened line shapes for both resonance- and satellite-line transitions, and radiation transport. Two analysis methods have been developed to extract temperature and density gradients from the data. On the one hand, using emissivity maps obtained from image data inversion temperatures are determined from narrow-band emissivity ratios and then densities are computed by solving a set of emissivity equations. On the other hand, a search and reconstruction algorithm driven by a Pareto genetic algorithm searches parameter space for the temperature and density gradients that yield the best simultaneous fits to the space-integrated line spectrum and a set of narrow-band emissivity maps and image intensity distributions, i.e., multi-objective data analysis.

Three multimonochromatic x-ray imagers (MMI) were designed, built, and fielded in OMEGA direct-drive implosion experiments during FY05. These (identical) instruments recorded gated narrow-band x-ray images of the core along three quasi-orthogonal directions at the collapse of the implosion based on the Ly_{α} , He_{β} , and Ly_{β} (and associated Li- and He-like satellites) line transitions of argon. In addition, a pre-existing x-ray imager at OMEGA was modified for better performance and fielded in the same experiments to obtain another Ly_{β} image along a direction diametrically opposite to one of the MMI's line of eight. This extra image permits an experimental check on the opacity of the Ly_{β} line emission in the core. Work is in progress in the analysis of the data.

Implosion Dynamics and Symmetry from Proton Imaging, Spectroscopy, and Temporal Measurements

Principal Investigator: R. D. Petrasso (Massachusetts Institute of Technology)

NLUF Proton Radiography Experiments

Initial experiments were conducted on OMEGA as part of this NLUF program to explore the use of proton radiography to study transient electric and magnetic fields generated by the interaction of OMEGA laser beams with plastic foils. In each experiment, a plastic foil was illuminated by a single OMEGA laser beam, and a projection radiograph was made of the foil using a source of nearly monoenergetic 14.7-MeV protons and a CR-39 area detector for image recording. The

protons passed through a wire mesh (see Fig. 104.71) before impinging on the foil, and the distortion in the mesh pattern at the detector shows how the proton trajectories were deflected through interaction with the fields generated by laser-plasma interaction at the foil.

The proton source for these experiments was formed by imploding a D^3He -filled, glass-shell capsule with 20 OMEGA laser beams in a 10-kJ, 1-ns pulse. The capsule diameter of the proton source target was unusually small, at about $440 \mu m$, in order to provide a smaller-than-usual burn radius for optimal spatial resolution in the radiograph; the full width at half maximum (FWHM) of the proton source was about $50 \mu m$, measured with proton emission imaging. The mesh was mounted on the foil assembly about 1 cm away, and the center-to-center spacing of the mesh wires was either $150 \mu m$ or $200 \mu m$. The CR-39 detector was about 36 cm away. The burn duration of the D^3He implosion was short (~ 100 ps) relative to the 1-ns duration of the foil illumination; adjusting the timing of the implosion relative to the foil illumination allows images to be recorded at different times. Sample images are shown in Fig. 104.72. Magnetic fields of the order of ~ 0.5 MG in the vicinity of the laser-irradiated foil are estimated on the basis of the proton deflection observed on these images (see Fig. 104.73).

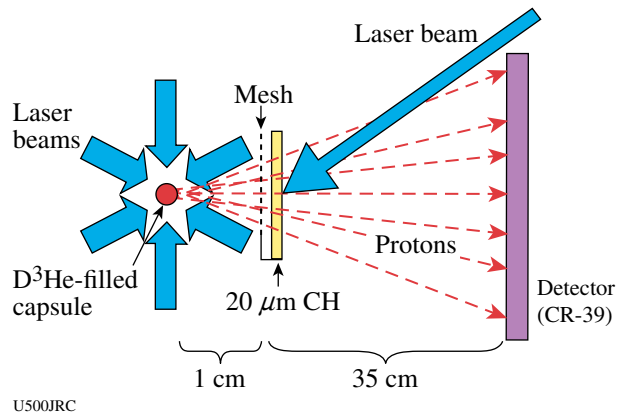


Figure 104.71 Physical arrangement of the proton backlighter (imploded D^3He -filled capsule), mesh, CH foil, CR-39 imaging detector, and OMEGA laser beams, as used for radiography.

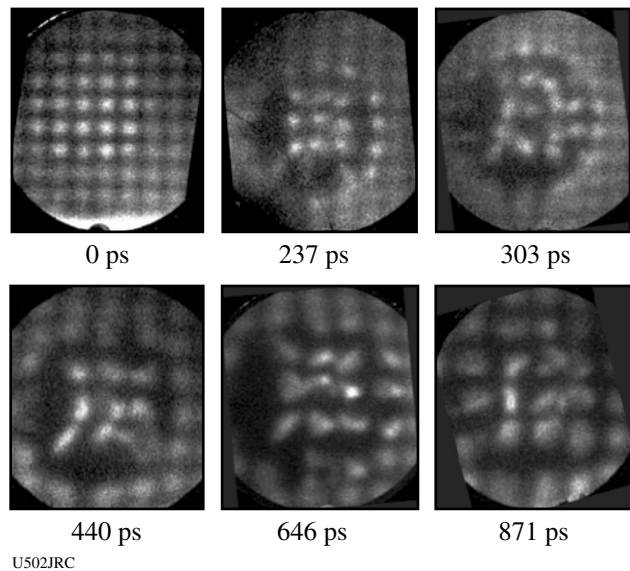


Figure 104.72
 Images recorded on the CR-39 detectors during different OMEGA shots. Each image is labeled by the difference between the time at which the protons passed the foil and the time when the foil was struck by a laser beam. The first three images were made using a mesh with 150- μm (center-to-center) spacing, while the last three were made with a 200- μm mesh.

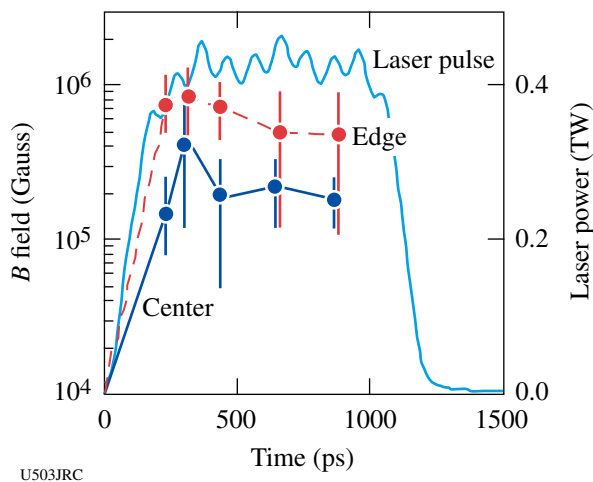


Figure 104.73
 Time evolution of magnetic-field amplitude at two locations on the laser-irradiated foil (center and edge of the laser beam)—referenced to the plasma-generating laser pulse (thick solid line).

LLNL Experiments on OMEGA in FY05

During FY05, LLNL was scheduled for 372 shots on OMEGA. These were distributed into 191 planned shots for the Inertial Confinement Fusion (ICF) program, and 181 planned shots for the High-Energy-Density Sciences (HEDS) program. The actual OMEGA performance averaged 7.5% more shots than scheduled (400 shots). A brief summary of the various campaigns follows, starting with HEDS experiments.

Hot Hohlraum Experiments: Hot hohlraum experiments were carried out; their objectives were to explore the laser-plasma interaction limits of very small half-hohlraums (“halfraums”) and to maximize the effective radiation temperature. Figure 104.74 shows x-ray images recorded at various times and photon energies, which show the hohlraum filling to overcritical densities.

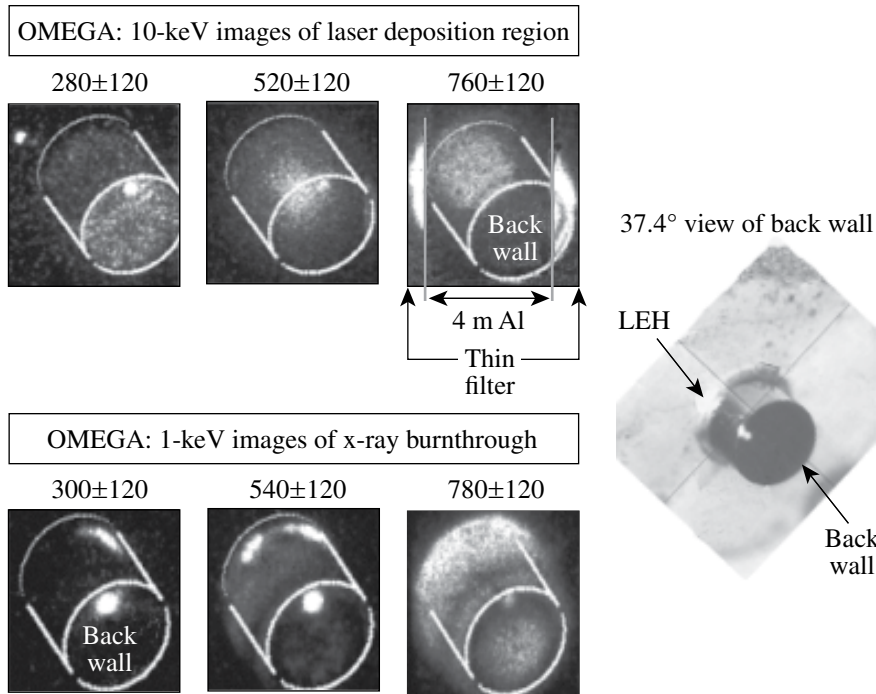
Hohlraum Development: In hohlraum development experiments, high-Z foam (approximately 5% of solid density) was substituted for solid gold for the hohlraum wall and measured a predicted increase in x-ray conversion efficiency.

Double-Shell Capsules: Pusher single-shell experiments used a glass capsule (coated with a plastic ablator) to explore physics issues associated with double-shell capsules.

Isentropic Compression Experiments (ICE): Isentropic compression experiments used a carefully shaped laser pulse to create a smoothly increasing, shockless compression of various target materials for equation of state measurements. These included diffraction experiments where x-ray diffraction from crystalline materials was used to diagnose change of state. Low-temperature Rayleigh-Taylor experiments also used the isentropic drive to investigate the hydrodynamic stability of solid materials under strong acceleration.

X-Ray Backlighting Development: Backlighter capability experiments were conducted with the aim of improving the x-ray backlighting capabilities. These experiments included backlit pinholes for point-projection measurements as well as various mid-Z (e.g., Ti) doped foams for increased x-ray conversion efficiency into multi-keV photons.

Radiation Flow: Radiation flow experiments continued from the previous year. These experiments used foam-filled hohlraums to measure x-ray propagation through various low-density materials.



U524JRC

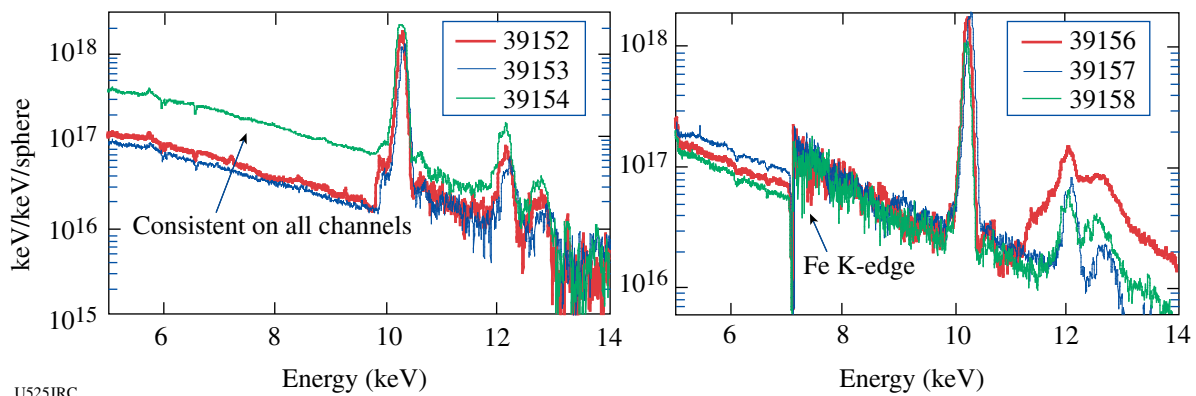
Figure 104.74

X-ray images of “halfraum” plasma fillings (view is 37.4° to the back wall). The time is given in picoseconds. The 10-keV images show that the laser deposition region moves from the back wall toward the LEH. The 1-keV images show that burnthrough occurs first near the LEH.

NWET: NWET (effects test) experiments concentrated on fielding multiple diagnostics to measure electromagnetic pulse and x rays from laser-driven hohlraums filled with low-density, mid-Z foams. These experiments were a collaboration between LLNL, LLE, and NRL and required the extensive installation of specialized diagnostics. Figure 104.75 shows the x-ray spectra recorded from 5-mg/cc aerogel (silicon dioxide) foam, doped with 20 atom-% Ge. Such targets produced an overall conversion efficiency of ~0.3% into x rays in the 9.4 to 13.8 keV range.

Opacity: An extensive opacity campaign was conducted on OMEGA. Early experiments were dedicated to developing appropriate x-ray backlighting sources, leading to future measurements of the opacity of warm materials.

Planar Double Shell: Planar double-shell experiments using a geometry that allowed diagnostic access were carried out to investigate the effects of x-ray preheat on the inner shell of a double-shell capsule.



U525JRC

Figure 104.75

Sample x-ray spectra obtained using the HENWAY spectrometer from targets containing SiO₂ foam (aerogel) at a density of ~4.8 mg/cc doped with 20 atom-% Ge. These data indicate x-ray yields ranging from 50 to 100 J for Ge K-shell radiation. On shots 39152 to 39154, the continuum is from 12-μm Al and 1-mil Be strips and $T_e \sim 2.5$ to 2.8 keV. On shots 39156 to 39158, the continuum features are due to a 12.6-μm Fe foil, $T_e \sim 2.0$ to 2.4 keV.

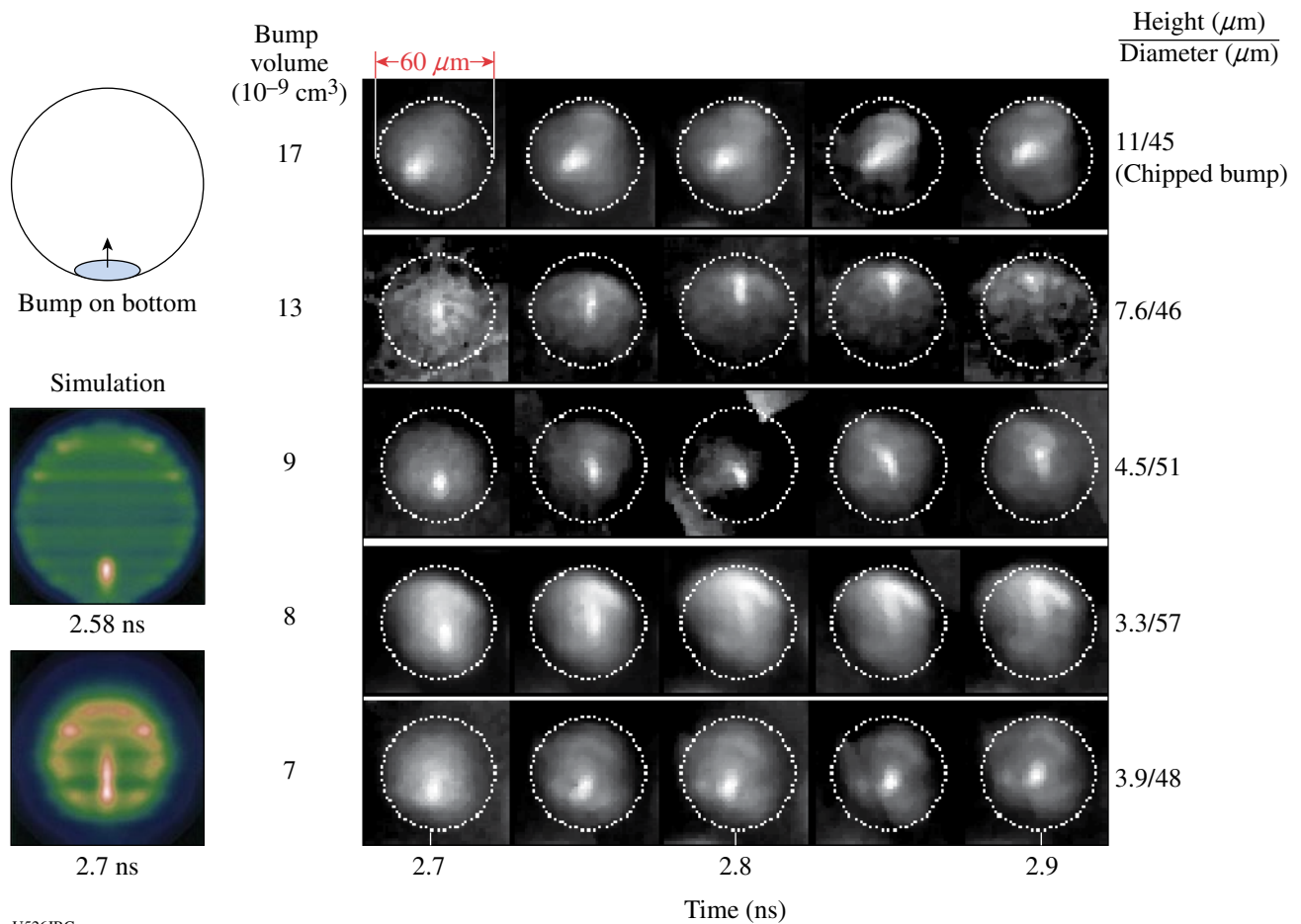
DPP: A series of experiments dubbed DPP investigated jets of material driven into foams with varying cell sizes. X-ray backlighting was used to measure the propagation of the jets into the foams.

Low- and Mid-Z Liners: The first ICF experiments of FY05 were designed to investigate laser-plasma issues and x-ray drive measurements of hohlraums with low- and mid-Z liners and foam fills. These liners and foams are designed to inhibit inward motion of the hohlraum walls and are an alternative to gas-filled designs.

Fill Tubes: A campaign was initiated to investigate the effects of fill tubes on capsules. These indirectly driven capsules used a single perturbation on the surface of the capsule to simulate, in a calculable way, the effect of an actual fill tube on the hydrodynamic stability of the shell. Figure 104.76 shows high-magnification x-ray images of such targets. The

perturbation grows and produces a jet of mid-Z material (originally implanted in the inner wall of the capsule). This material becomes visible in x-ray wavelengths as it is heated by the hot core.

Gas Hydro: "Gas-hydro" experiments were carried out using large, plastic, gas-filled hohlraums with a foam ball at the center. The objective of this campaign was to reduce the x-ray drive so that the direct, hydrodynamic effects of the laser-heated fill gas on a capsule could be observed and compared with simulations. Figure 104.77 shows the results of the first of such attempts. The shock front in the foam surrogate target, observed with x-ray backlighting, shows the effects of the laser-heated gas pressure for low initial fill pressures. Contrary to simulations, however, no effect was observed at higher initial fill pressures. A new experiment, designed to have reduced sensitivity to target alignment, will explore these issues.



U526JRC

Figure 104.76 Simulations (left) and x-ray framing camera images of capsules with imposed bumps that are used to simulate a fill tube.

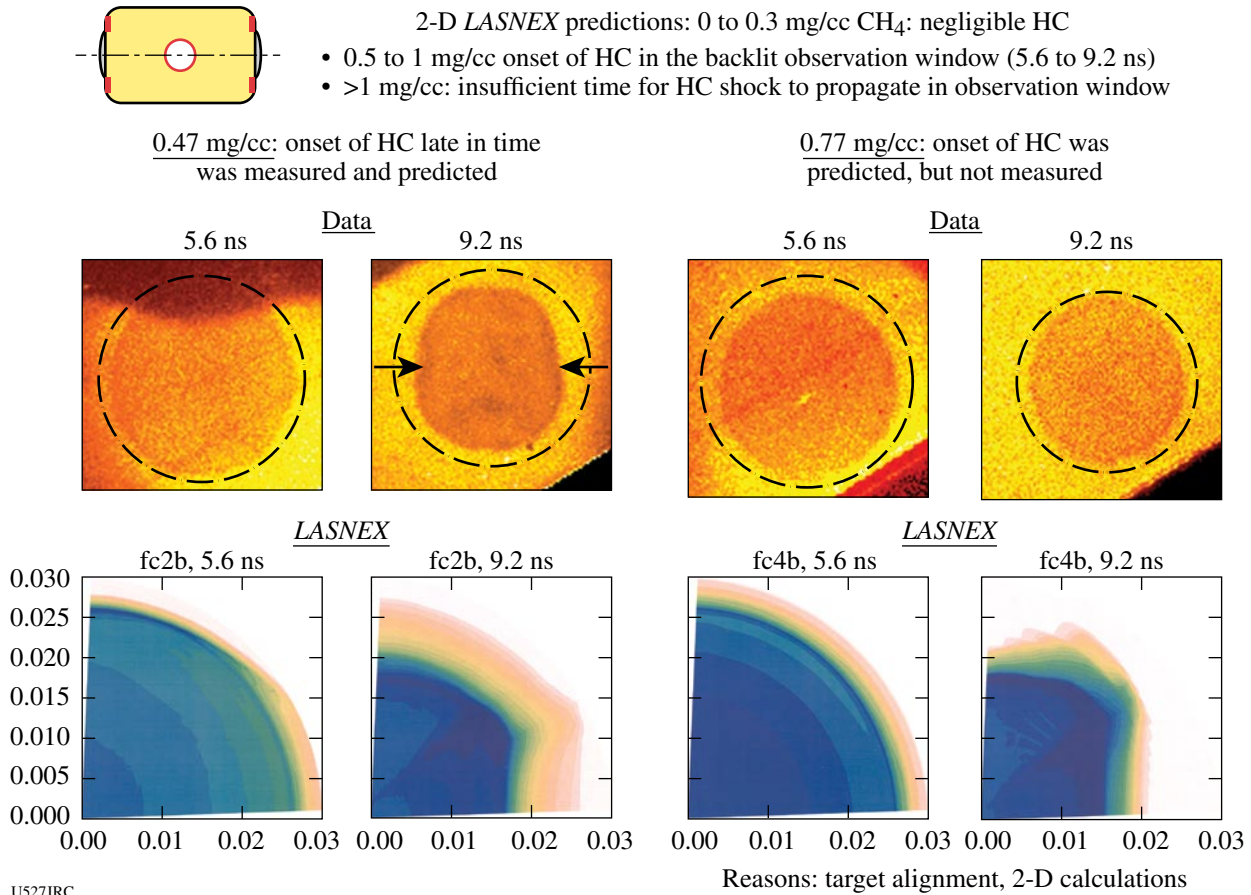


Figure 104.77

X-ray images from “gas-hydro” experiments. Top: X-ray backlit images of foam targets in 0.47 mg/cc and 0.77 mg/cc CH₄-filled hohlraums. Bottom: LASNEX simulations showing effects of gas hydrodynamics coupling to the implosion. The onset of hydrodynamic coupling was measured and predicted at low fill density but not observed at high density.

RTI in Be-Doped CH: Experiments were conducted to develop a Rayleigh–Taylor instability platform for accurately measuring the Rayleigh–Taylor growth rate of Be and Be doped with Cu ablaters in direct comparison with more traditional CH ablaters.

HEP-4: The HEP-4 series of implosions are integrated experiments that use standardized hohlraums and laser pulse shapes while varying the surface finish of the capsules by deliberately roughening them. The resulting neutron yields are compared to simulations with capsule-fuel mix models; the initial measured capsule perturbation spectrum is included in the simulation for each capsule to enable direct comparison with the experimental results. These experiments have been carried out on OMEGA for some time and were completed this year. Results are shown in Fig. 104.78.

Cocktail Experiments: “Cocktail” experiments were measurements of the effective x-ray drive power in hohlraums made of a mixture of high-Z materials (typically Au, Dy, U), in contrast to a single material. In FY05, considerable research and development from target fabrication at LLNL and GA was applied to reduce the impurity level of oxides in these targets, leading to measured unambiguous expected increases in x-ray flux (Fig. 104.79).

2ω LPI Experiments: A week of experiments was done with beam 25 converted to 2ω (530 nm). Measurements of laser–plasma interaction physics with “green” light were done in both hohlraum and open (using gas-bag targets) geometries. Figure 104.80 shows measurements from a 2ω beam that was propagated axially along a laser-heated hohlraum. Measurements of the 2ω beam transmission and stimulated backscatter

are shown. In addition, experiments were done with half-hohlraums to measure the overall x-ray conversion efficiency of 2ω light in direct, simultaneous comparison to the efficiency when using the 3ω light typical of OMEGA.

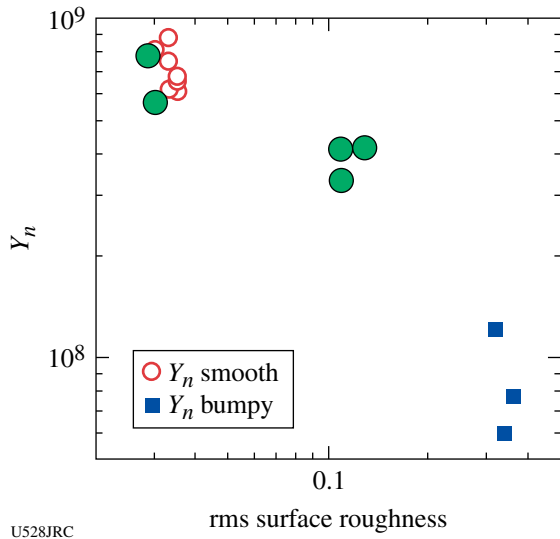


Figure 104.78 Neutron yield as a function of capsule roughness for HEP-4 experiments. Large filled data points were obtained in April 2005. Small open dots are smooth capsule data and square data were obtained in the prior campaigns.

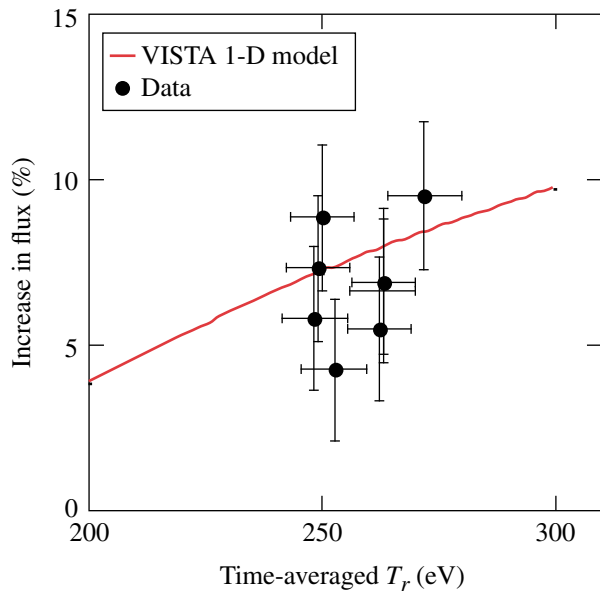


Figure 104.79 A plot of the measured (black dots) and VISTA 1-D model predicted an increase in x-ray flux of a cocktail hohlraum with a composition of $Au_{0.2}U_{0.6}Dy_{0.2}$ versus conventional Au hohlraums as a function of time-averaged radiation temperature (T_r).

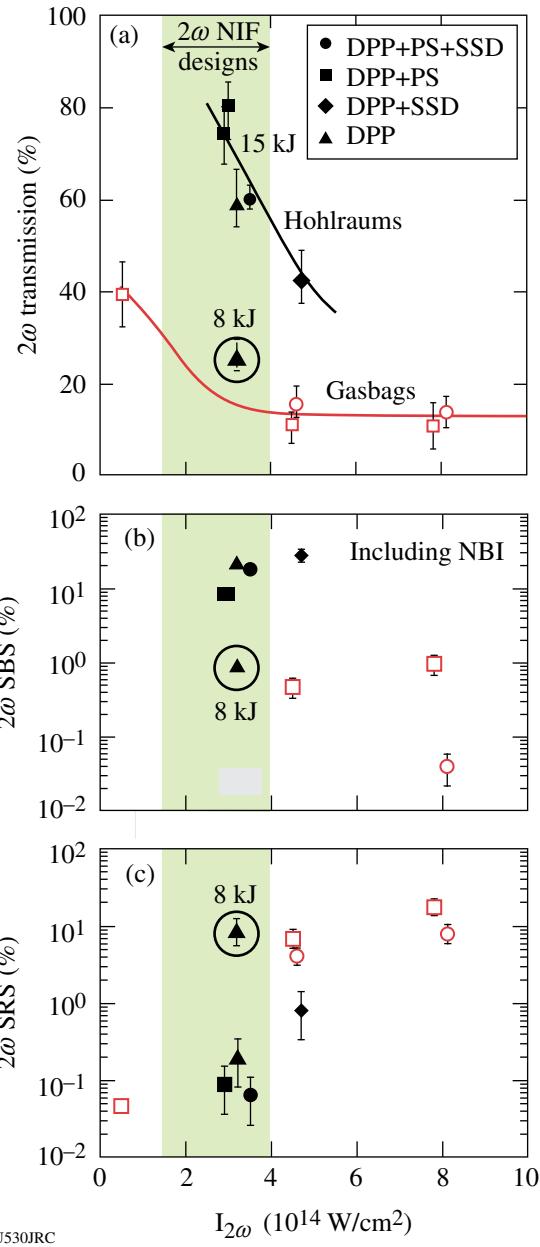


Figure 104.80 (a) Plots of 2ω beam transmission through a hohlraum (solid data points) and through gas bags (open points). Similar comparison for SBS (b) and SRS (c).

Plan "B": After encouraging laser-plasma interaction physics were obtained from SiO_2 foam-filled hohlraums, a series of foam-filled hohlraums with implosion capsules inside them were shot ("Plan B"). These yielded results similar to traditional vacuum hohlraums, indicating little or no deleterious effects on the x-ray drive for ICF-relevant foam fills.

X-Ray Thomson Scattering: X-ray scattering experiments were carried out, showing expected spectral features after scattering a strong line source from the hot plasma. The data were used to infer an electron temperature in the plasma.

4ω Thomson Scattering: A week of experiments was done with beam 25 converted to 4ω (260 nm). The principal focus was using the 4ω light for Thomson scattering measurements. Numerous improvements were made to the diagnostics from previous experiments, and the resulting data was of high quality, enabling the measurement of the electron temperature immediately external to a hohlraum laser entrance hole and from within a hohlraum. Figure 104.81 shows the Thomson-scattering-derived electron temperature from within a gas-filled hohlraum for three different laser energies. Careful characterization of these hohlraums is preliminary to their future use for LPI studies.

FY05 LANL OMEGA Experimental Programs

Los Alamos National Laboratory (LANL) successfully fielded a range of experiments on OMEGA during FY05 to study the physics relevant to inertial confinement fusion (ICF) and high-energy-density (HED) science in support of the National ignition effort. Many of these experiments were focused on developing underlying physics, diagnostics, and platforms for future experiments on the National Ignition Facility (NIF). LANL conducted a total of 138 target shots on OMEGA. Collaborations with LLNL, LLE, and AWE remain an important component of LANL's program on OMEGA. With the consolidation of ignition research in the United States into the National Ignition Campaign (NIC), healthy partnerships are required to achieve success in our National scientific objectives.

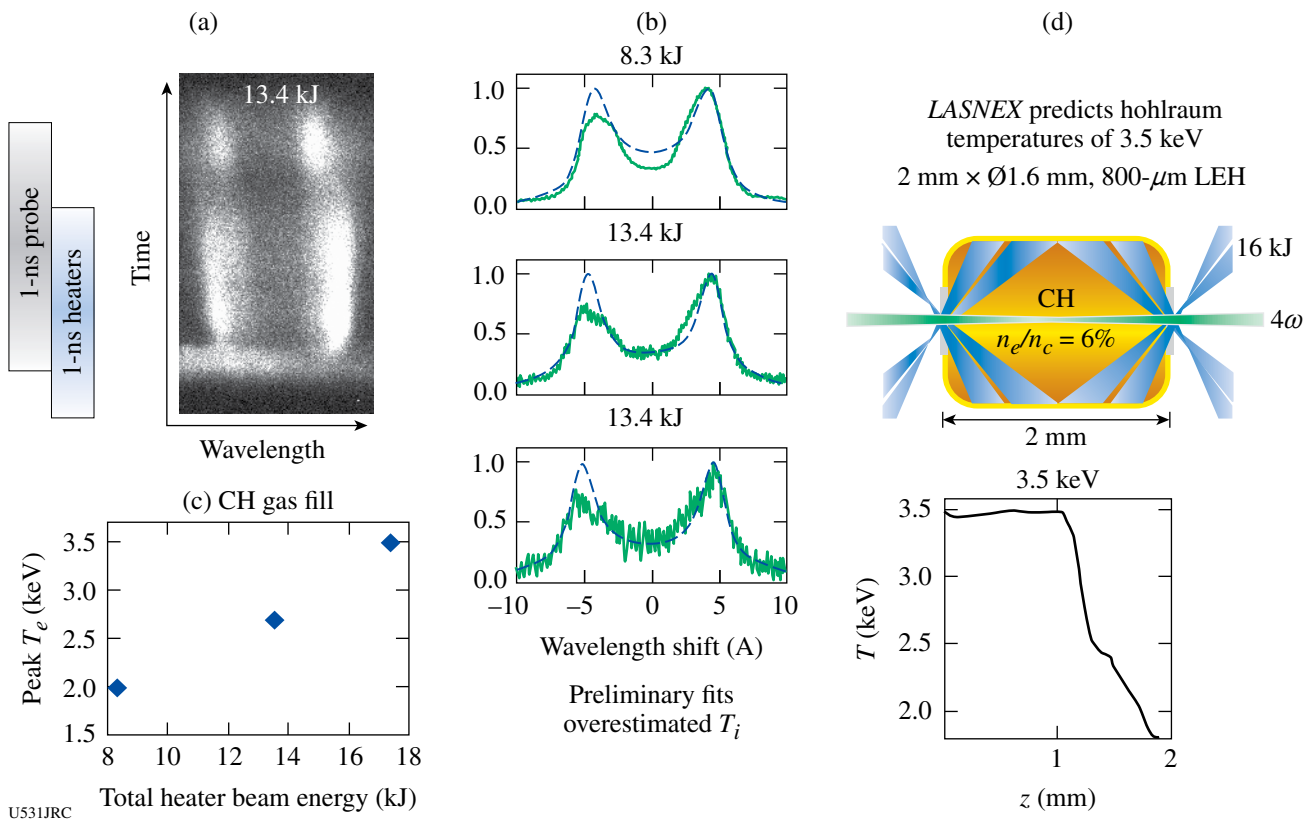


Figure 104.81

Data from 4ω Thomson scattering experiments: (a) streak camera record of spectrally resolved Thomson scattering spectrum, (b) scattering light spectra at various heater beam energies, (c) inferred electron temperature from these spectra, and (d) LASNEX predictions.

Beryllium Ablator Microstructure Stability (BAMS): The end goal of this project remains the delivery of a specification for the microstructure of ignition-capsule ablators to the National ICF program with the current focus on beryllium-copper ablators with 0.9% Cu by atom.

Two days of experiments using gas-filled hohlraums demonstrated the fabrication of small-amplitude Be sinusoids and measured growth of the sine wave perturbations in Be in a radiation-drive environment for the first time. The composite laser pulse consists of a combination of two separate OMEGA pulse shapes with a duration approaching 6 ns. Through VISAR measurements, a ~1-Mbar first shock in the Be (Cu) samples was observed. The methane gas fill held the Au walls of the hohlraum back for >10 ns to enable late-time, face-on x-ray radiography, thus demonstrating the growth of the sinusoid and evolution toward a spike-and-bubble behavior. Figure 104.82 shows a face-on, 1.7-keV radiograph of a sinusoid taken at 9.3 ns after the drive began. A lineout showing spike-and-bubble formation is illustrated in Fig. 104.83. The loss of laser energy to laser-plasma instabilities is modest (<10%), concentrated late in time, and clamps the radiation temperature near 145 eV.

In x-ray sidelighting experiments, differences between powder-pressed Be samples and sputtered samples as they are ejected from the hohlraum were observed. This difference may be related to excessive voids in the sputtered samples. The LANL theoretical group is modeling the shock breakout and

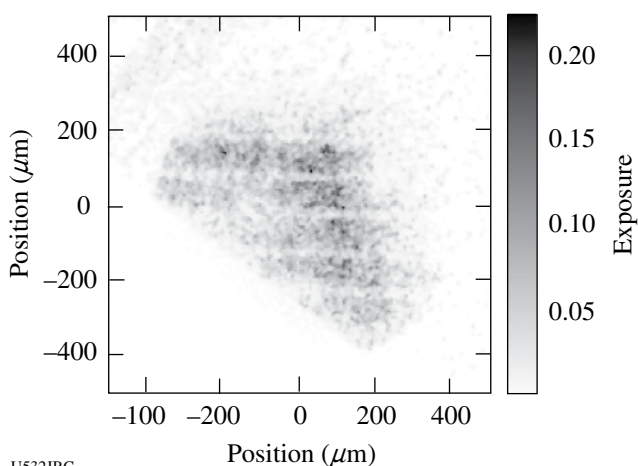


Figure 104.82
A face-on radiograph of a BeCu sinusoid (shot 39660) at 9.3 ns after the start of hohlraum drive.

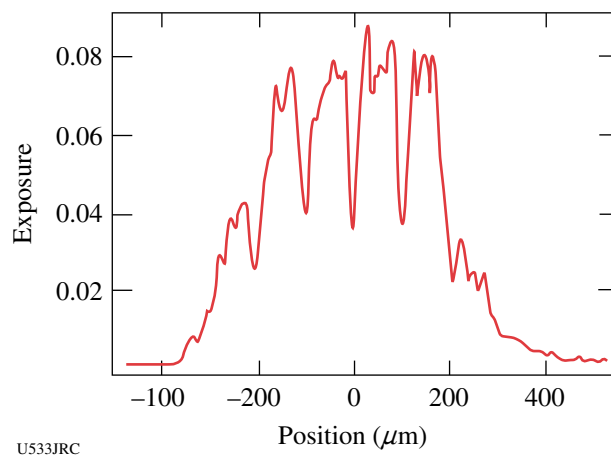


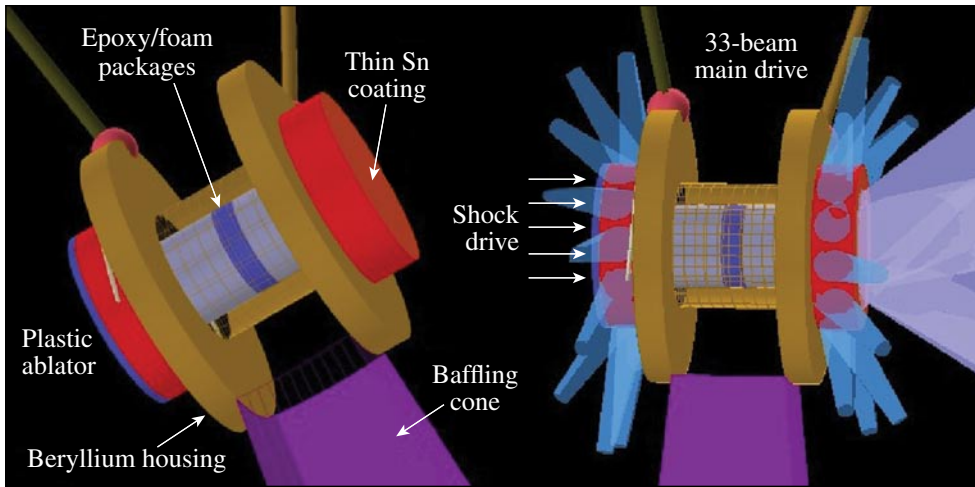
Figure 104.83
A lineout from the 9.3-ns data showing the growth of the sinusoidal perturbations and bubble-spike formation.

preheat of the BeCu samples to reproduce the as-measured radiation drive and to duplicate the “rollover” in growth rates of the instability growth with large-amplitude (2.5- μm) sinusoids.

Off-Hugoniot Stability: The off-Hugoniot (OH) campaign studies material dynamics under heated and shocked conditions. In ignition capsules, defects arising from the manufacturing process undergo significant evolution because of heating from Au M-band radiation prior to the passage of the main shock. It has not been demonstrated that the hydrocodes being used to model these experiments accurately capture the physics of this interaction. The OH platform provides the means to study the complex interactions between shocks and heated material.

The OH platform utilizes a Be housing that is coated with a thin layer of tin. Inside the housing are layers of foam and epoxy. Thirty-three beams strike the tin, produce L-shell radiation that permeates throughout the package, heating the epoxy and foam (Fig. 104.84). A short time later, seven beams launch a strong shock into the foam. As the heated epoxy expands in the foam, the shock interaction with this system is imaged radiographically.

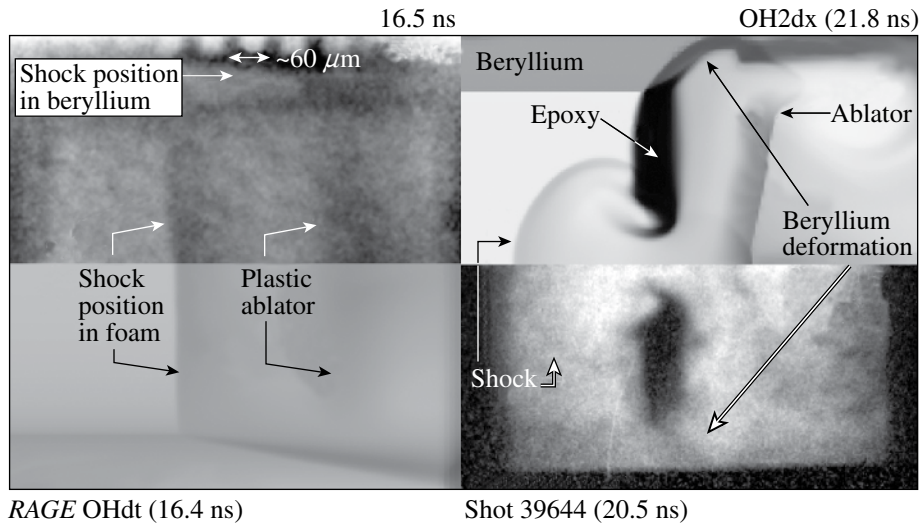
This year, the last phase of test bed development was completed in which shock planarity and speed were characterized and the interaction with an unheated defect was observed (Fig. 104.85). The next phase of campaign will advance to the fully integrated experiments of shock interaction with preheated material interfaces.



U534JRC

Figure 104.84

The target configuration for the off-Hugoniot experiment. A beryllium housing stuffed with layers of epoxy and foam are heated by exciting tin L-shell radiation. The evolution of the epoxy expanding into the foam is imaged via radiography.



U535JRC

Figure 104.85

(a) Comparisons between measurement and simulation (*RAGE*) of the shock position and planarity and (b) the unheated defect having experienced a strong shock.

Double-Shell Implosions: Double-shell implosions may provide a noncryogenic path ICF. Because of their complex implosion dynamics, however, double-shell capsules are much more sensitive to symmetry than their single-shell counterparts. Moreover, engineering defects, such as gaps formed during manufacturing, can play a large role in affecting their fusion yield.

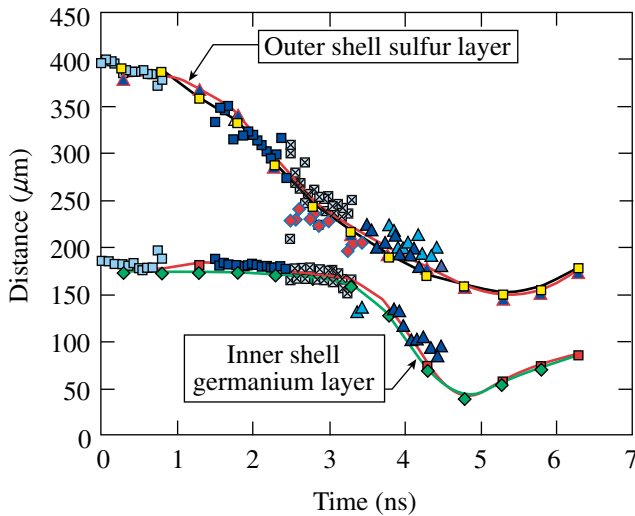
To better understand these issues, two experimental campaigns were conducted on OMEGA. The first characterized the zero-order implosion dynamics of a double-shell capsule implosion. The second measured how a gap purposefully machined in the outer shell evolved throughout the implosion. Selected results are presented.

Figure 104.86 shows the measurements of the inner and outer shell positions as compared with the simulated radiographs from *LASNEX*. Figure 104.87 displays a pre-shot radiograph and obtained shot data from a double-shell implosion with a deliberate engineering defect applied to the interior side of the outer surface. This data is used to quantify the defect's impact on the implosion symmetry.

Inhomogeneous Radiation Flow: Radiation transport calculations become greatly complicated in regions where two or more materials are inhomogeneously mixed. Laboratory experiments were performed to test the modeling of radiation transport through inhomogeneous plasmas.

A laser-driven hohlraum creates a radiation front, which propagates through a foam/gold particle mixture (Fig. 104.88). The position of the radiation front is measured as a function of time with a soft x-ray imager (Fig. 104.89). Three different foam-gold mixtures were examined experimentally (Fig. 104.90). One mixture was purely foam, another mixture was loaded with 2- μm -diam gold particles, and the last mixture

was loaded with 0.5- μm -diam gold particles. Each of the doped foams contained the same amount of gold volumetrically. Preliminary results from these experiments show the radiation front propagation slows in the presence of smaller gold particles. The next set of planned experiments have the objective of making a single temperature measurement of the radiation front.

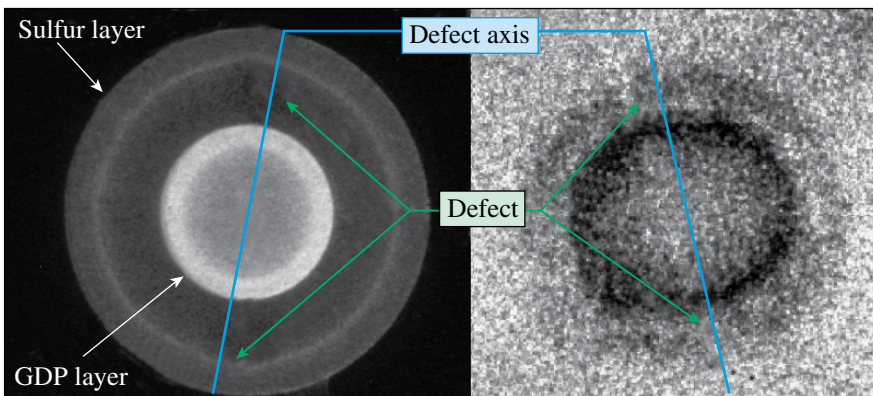


U536JRC

Figure 104.86 Measurements (symbols) of the outer and inner shell marker layers, showing collision near 3.6 ns. The solid lines are the *LASNEX* predictions as extracted from the simulated radiographs.

Beryllium Fill-Tube Defect Studies: Current ignition target designs for the NIF use a copper-doped beryllium (BeCu) ablator. Since DT cannot diffuse through the Be ablator, another filling method is required. The leading option is to use a fill tube, however, the tube provides a perturbation on the capsule that may affect the ignition capsule implosion. Initial experiments were performed that developed a planar platform to investigate the effect of a fill tube on ICF capsule performance.

The experimental configuration (Fig. 104.91) consists of a driven hohlraum, which heats and shocks the attached Be (0.9% Cu). Beryllium material then jets through the hole and into the surrounding vacuum. Two backlighters are used to image different aspects of the experiment. An iron backlighter resolves the shock position in the Be disk. A Teflon (C₂F₄) backlighter captures the jet with its C and F He- α lines (310 eV and 740 eV, respectively) using the soft x-ray imager. We also obtained images with the Teflon continuum. A definite jet was observed (Fig. 104.92) with a 30- μm -diam hole. This series of experiments validate the planar platform, which will be used by NIC in future experiments.



U537JRC

Figure 104.87
(a) A preshot radiograph of a defect capsule.
(b) An image of the implosion near 3.8 ns showing the interaction between the defect and inner shell.

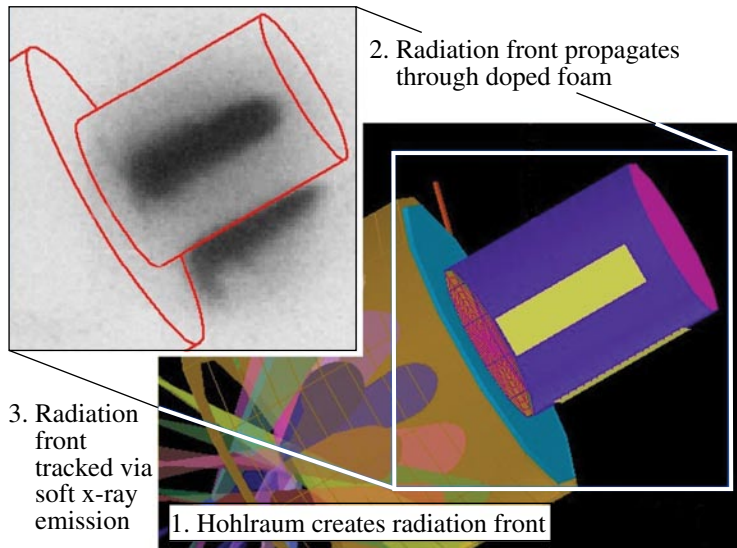


Figure 104.88

Sixteen beams heat a gold hohlraum, which produce a radiation front that propagates through the foam. Diagnostics slits allow measurement of the front's progression.

U538JRC

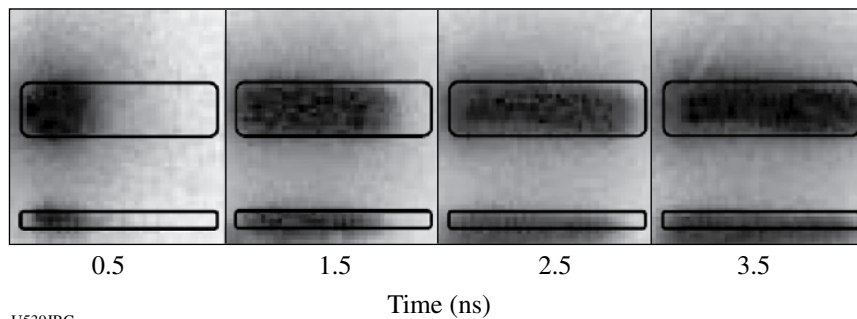


Figure 104.89

The temporal evolution of the radiation front as tracked by the soft x-ray emission.

U539JRC

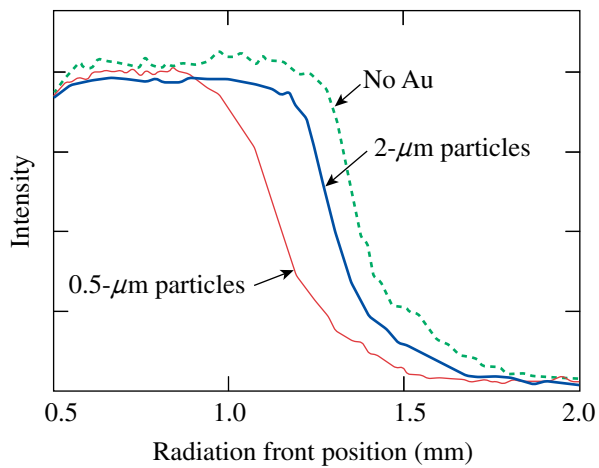
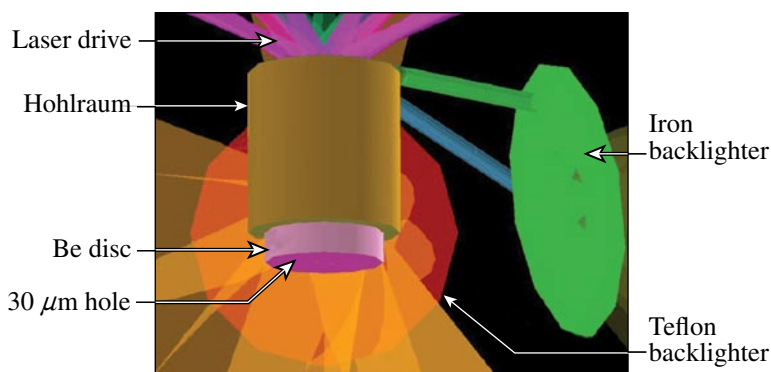


Figure 104.90

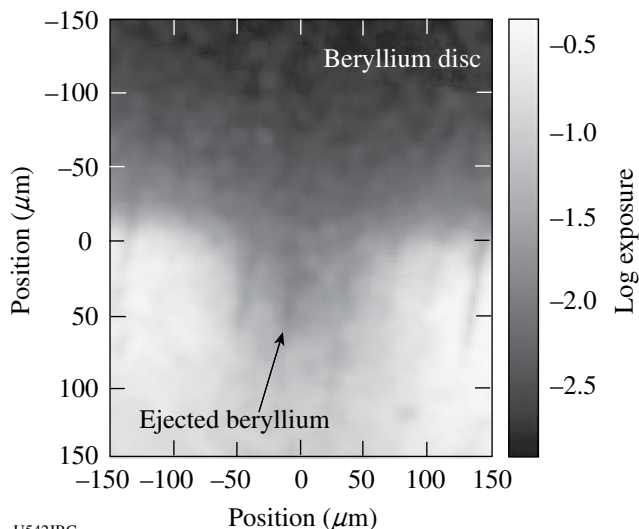
The radiation front position at 3.5 ns as it propagates through three foam types: no gold, 2- μm particles, and 0.5- μm particles. Data clearly show that propagation is slowed as gold particulates become smaller.

U540JRC



U541JRC

Figure 104.91
A heated gold hohlraum drives a shock into the beryllium disc creating a jet as the Be is forced out the small hole at the bottom. The Be jet and disc are imaged from two orthogonal directions.



U542JRC

Figure 104.92
Radiograph from shot 40407 showing the jetting of copper-doped (0.9%) beryllium at 4 ns. The central photon energy was 310 eV (C He- α). The jet has expanded about 100 μm into the vacuum.

ACE-D: The ACE-D experiment on OMEGA investigated several areas of radiation hydrodynamics in preparation for experiments using two bundles of the NIF. One research avenue was to decrease the size of the hohlraums to create higher radiation temperatures. Using 3/4-scale hohlraums, radiation temperatures of higher than 220 eV were reached. A second test was to line the hohlraum with a low-density (9 mg/cm^3) aerogel foam to decrease the influx of Au wall material into the radiographic line of sight. The liner noticeably prevented the wall from occluding the line of sight, but the radiation temperature was also reduced substantially. There was, however, no increase in backscattered energy due to either stimulated Raman scattering (SRS) or stimulated Brillouin scattering (SBS) as measured by the full-aperture backscatter (FABS) calorimeter.

Pinhole-Apertured, Point-Projection Backlighter (PAPBL) Studies: Imaging experiments at the NIF require the use of pinhole-apertured, point-projection backlighting (PAPBL) with gated instruments. Although this technique provides a much

more efficient use of backlighter photons, the absence of a pinhole array between the target and imaging system greatly enhances the susceptibility to extraneous noise sources. With this in mind, backlighter development experiments were performed at OMEGA to develop techniques to mitigate these undesired sources that degrade image quality.

The main objective of these experiments was to successfully image a driven hohlraum using zinc and germanium K-shell lines. The target consisted of a hohlraum with two gold grids mounted on the rear. Two orthogonal backlighters were used and a conical shield served to mitigate the noise source arising for the driven hohlraum (Fig. 104.93).

Images were obtained of the hohlraum's rear, including the grids for both undriven and driven hohlraums using a zinc backlighter. Moreover, we also obtained an undriven image of the hohlraum using a Ge (10.3 keV) backlighter (Fig. 104.94). This experiment's results provide confidence that orthogonal PAPBL imaging can be used successfully in the future.

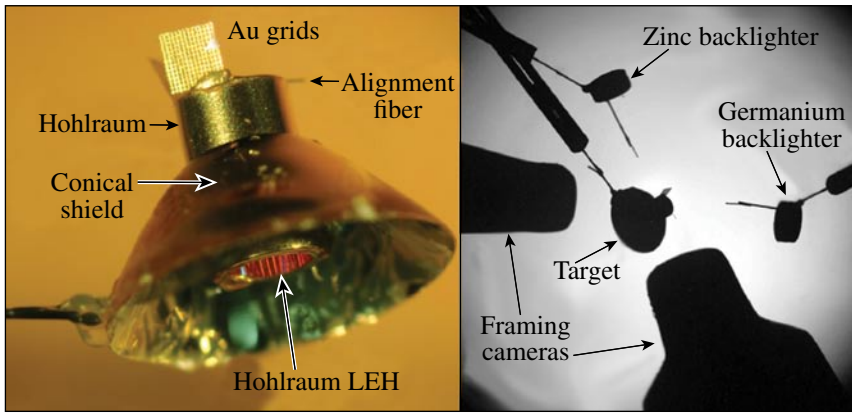
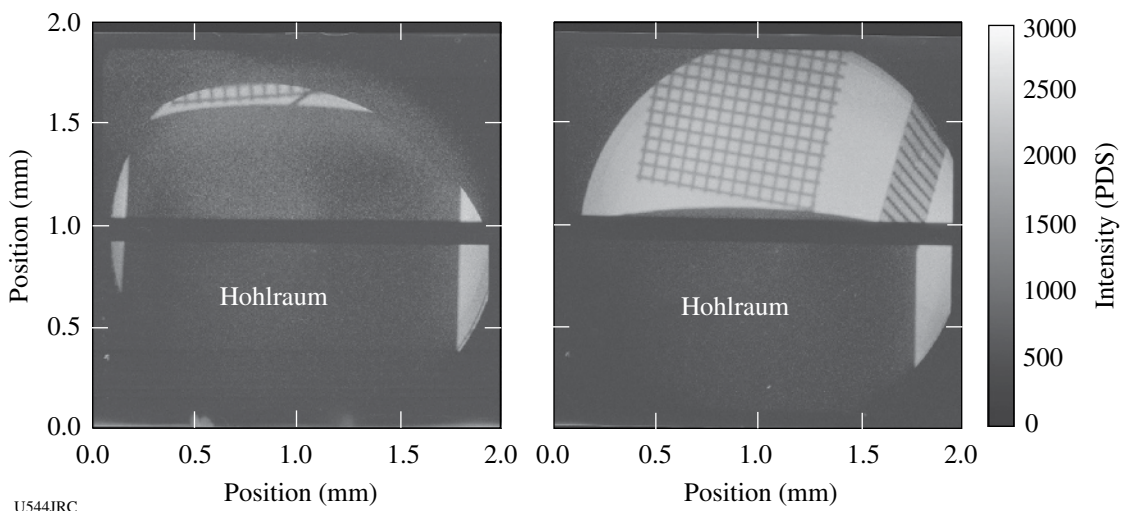


Figure 104.93

(a) An optical picture of the target showing the hohlraum, gold grids, and large gold conical shield. (b) The pre-shot target viewing system image of the experimental configuration showing the locations of the hohlraum, Zn and Ge backlighters, and two nose tips for the diagnostics.

U543JRC



U544JRC

Figure 104.94

(a) An image of a driven hohlraum with a Zn (~9 keV) backlighter. Some background noise from the driven hohlraum is still present, but the grid is still quite resolved. (b) An undriven hohlraum using a Ge backlighter (10.3 keV). As expected, the grids show very nice resolution.

High-Z Shell Implosions: Initial proof-of-principle experiments studying the effect of high-Z dopants on capsule burn were completed. These early experiments utilized deuterium-filled ignition capsules in which differing levels of krypton gas were introduced as a dopant. Previous experiments show that our hydrocodes calculate the effect of the high-Z dopant in ignition capsules poorly. Measurements of the neutron yield, ion temperature, and x-ray emission from the hot gas were obtained. Initial results indicate that the yield was lower than predicted, the ion temperature was higher than predicted, and the x-ray emission was lower than expected. More detailed analysis is being done to understand these results and to design FY06 experiments.

Time-Dependent Mix: The time-dependent mix campaign seeks to explore the mixing of shell material into the fuel of an inertial confinement fusion implosion. A thin layer of lightly doped titanium plastic is embedded into the inside surface of the plastic capsule. As the shell mixes into the fuel, the titanium heats up and radiates characteristic atomic lines that give information about the electron density and temperature in the vicinity of the titanium ions. The titanium was carefully chosen such that the ratio of more highly ionized to less ionized titanium could be used to infer the temperature at the point of emission, and thus tell us how far into the hot core the mix has reached at any particular time. The layer of titanium can be placed at the inside surface of the capsule or embedded

beneath the surface at a predefined depth. A series of capsules with progressively greater depths can tell us how much of the capsule material participates in mix. When the embedding depth is greater than the thickness of the layer that mixes, the hydrogenic titanium emission will disappear.

X-ray images of the capsule's implosion are shown in Fig. 104.95. The data clearly show the onset of K-shell emission arising from the titanium that has mixed into the core. We have determined that the amount of shell mix is between 0.5 and 1.0 μm and have also observed more mix than simulations would predict, thus constraining the parameters used in these models. This is apparent both from the nuclear yield and the amount of x-ray emission.

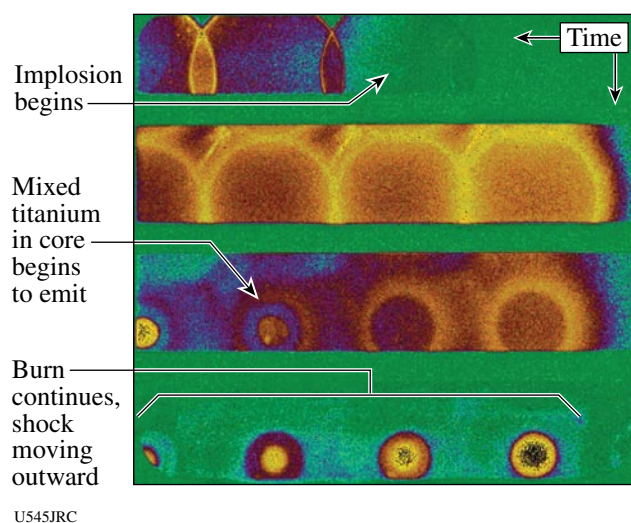


Figure 104.95
X-ray images of the capsule implosion showing the onset of titanium K-shell emission arising from the titanium that has mixed into the core.

FY05 Sandia National Laboratories Experiments on OMEGA

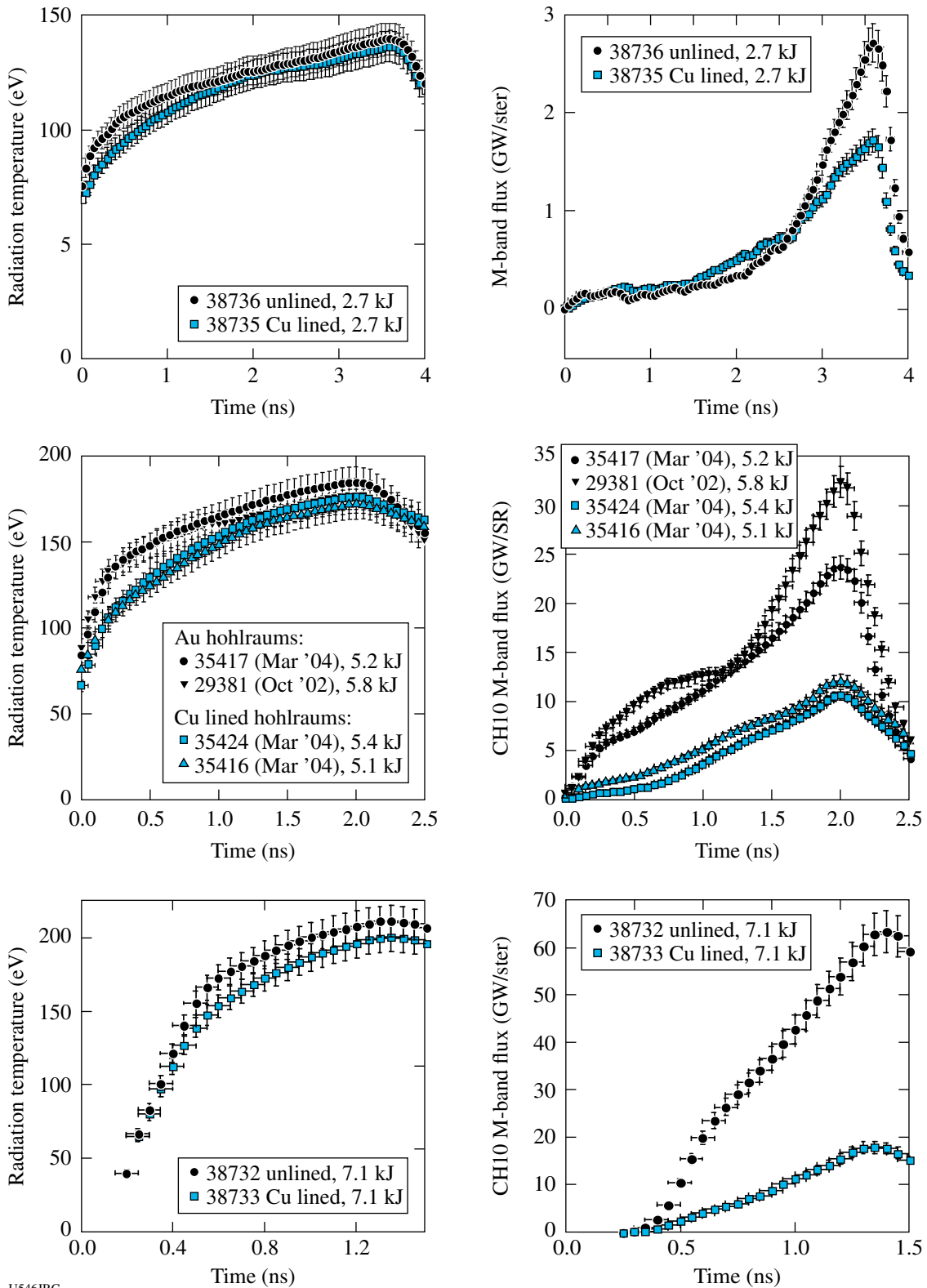
SNL performed 31 target shots on OMEGA in FY05.

Modification of a Laser Hohlraum Spectrum via a Mid-Z Wall Liner: A typical laser hohlraum has a radiation spectrum that includes a significant component of non-Planckian, high-energy photons (such as Au M-band x rays) that originate in and near the hot, low-density coronal plasma in which the laser light is absorbed and converted into x-rays. These hard x-rays can have undesirable effects for an inertial confinement fusion (ICF) application, such as causing preheat ahead of the shock front in the ablator of an indirect-drive capsule.⁵ In FY04 a

new concept was implemented for tailoring the spectrum in a hohlraum that uses a thin, mid-Z liner to supply plasma for the x-ray conversion with an underlying high-Z wall for x-ray containment.⁶ In a series of FY05 experiments performed at the OMEGA Laser Facility, this concept was demonstrated to be effective for a wide range of laser intensities and hohlraum temperatures. The DANTE unfolded radiation temperature shown in Fig. 104.96 illustrate the dramatic reduction in M-band flux as the associated hohlraum temperatures increase over the range of 120 to 200 eV.

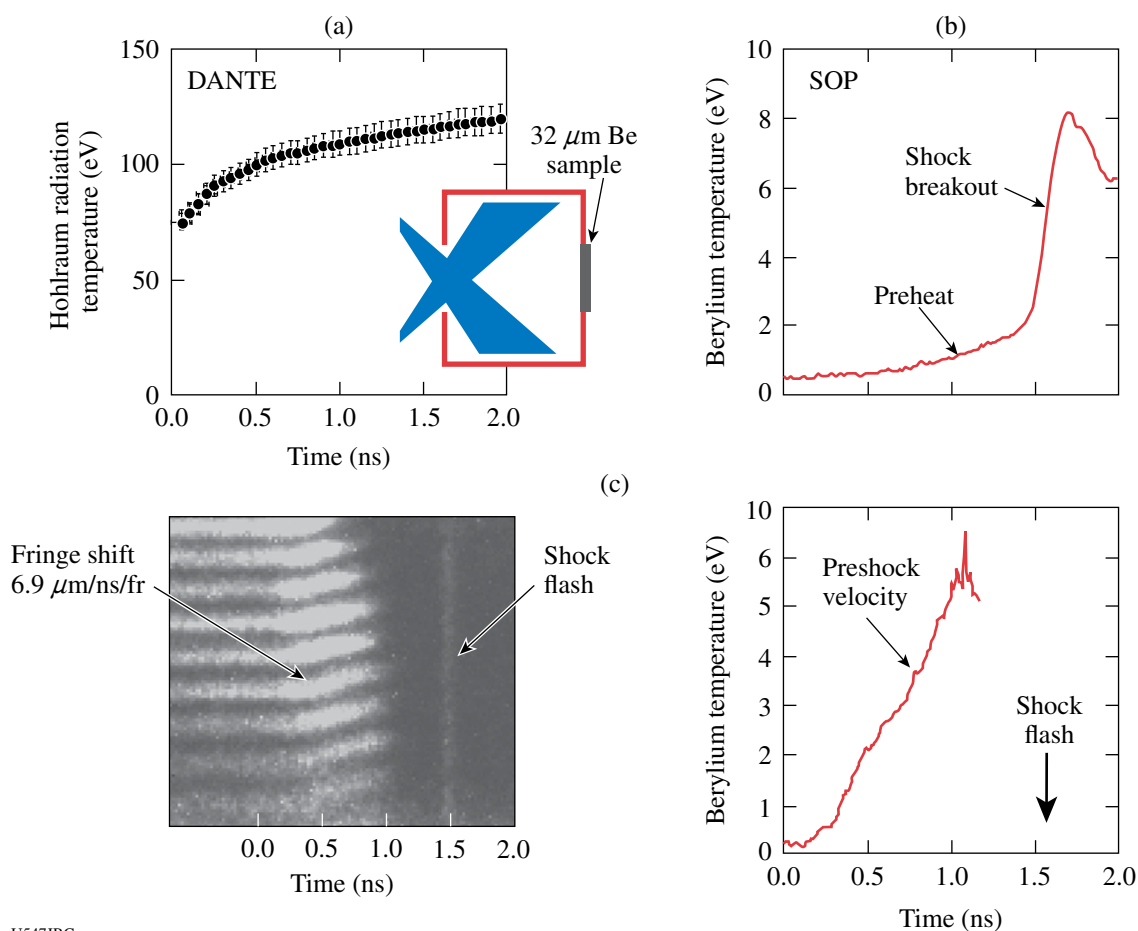
X-Ray Preheat in Indirect-Drive ICF Ablator Materials: In previous work⁵ measurements of ablator shock velocities, shock temperatures, and preheat temperatures were made using a 280-nm streaked optical pyrometer (SOP).⁷ More recent ablator experiments on OMEGA have extended this work by using an absolutely calibrated 600 to 800 nm SOP⁸ with a line-imaging velocity interferometer.⁹ Important new information has been obtained relating to ablator surface movement prior to shock breakout, ablator preheat temperature, and preheat effects on the anvil and window components of the shock-timing diagnostic system. Results from an experiment involving a 32- μm -thick beryllium ablator are shown in Fig. 104.97. In this experiment, 15 OMEGA beams delivered 2.8 kJ (in a 3.7-ns square pulse) into the interior of the hohlraum. The DANTE measurement of the hohlraum radiation temperature is shown in Fig. 104.97(a); the SOP measurement of the temperature of the exterior-facing side of the Be sample in Fig 104.97(b); and the VISAR measurement of the surface velocity of the Be sample in Fig 104.97(c). For all plots, time is relative to laser turn on at $t = 0$. Shock breakout occurs at ~ 1.5 ns with peak of the shock flash intensity occurring approximately 200 ps later. As indicated in Fig. 104.97(a), the hohlraum radiation temperature prior to $t = 1.5$ ns is in the range of 75 to 115 eV. Figure 104.97(b) indicates a pre-shock heating of the external Be surface to ~ 2 eV prior to shock breakout. Figure 104.97(d) indicates that the Be surface begins moving soon after the laser turn on and reaches a pre-shock velocity exceeding 6 $\mu\text{m}/\text{ns}$. As can be seen in Fig. 104.97(c), this velocity cannot be measured for times > 1.1 ns because of the loss of surface reflectivity. Per Fig. 104.97(b), the surface temperature at the time of reflectivity loss is approximately 1 eV.

Indirect-Drive ICF Shock Timing Diagnostic Development Experiments: Accurate measurements of shock timing and ablator x-ray burnthrough will be essential for the successful ignition of an indirect-drive ICF capsule. In FY05, we performed the initial tests of an experimental platform similar to the diagnostic proposed for accurate National Ignition Facility



U546JRC

Figure 104.96 DANTE-unfolded radiation temperature as a function of time for several hohlraum configurations (three plots on the left). M-band intensity versus time for the same shots (three plots on the right).



U547JRC

Figure 104.97

Indirect-drive experiment with a 32-mm-thick Be ablator. (a) DANTE measurement of hohlraum radiation temperature versus time, (b) SOP measurement of Be surface temperature versus time, (c) VISAR data showing fringe shift and shock flash, and (d) VISAR measurement of Be surface velocity.

(NIF) ignition shock-timing measurements.¹⁰ Full-scale ignition capsules and pre-ignition shock-timing experiments at the NIF will utilize Cu-doped Be ablators with a thickness of $\sim 150\ \mu\text{m}$. Our first attempts at testing the proposed shock-timing techniques utilized the geometry illustrated in Fig. 104.98. The $150\text{-}\mu\text{m}$ -thick ablator sample consisted of a pair of $75\text{-}\mu\text{m}$ -thick Be foils with a $0.5\text{-}\mu\text{m}$ -thick Cu foil sandwiched between the Be foils. In terms of overall ablator thickness and opacity, this approximates the proposed NIF ignition capsule ablator. A window was placed at a distance of $\sim 1\ \text{mm}$ from the ablator surface. In a few experiments, a liquid deuterium-filled cryostat was attached to the hohlraum, with the window at the same location (Fig. 104.99). Results from an experiment with a relatively low temperature hohlraum drive are shown in Fig. 104.98. In this experiment, the 15 OMEGA beams delivered 1.5 kJ (in a 3.7-ns square pulse) into the interior of the hohlraum. The DANTE measurement of hohlraum radiation

temperature is shown in Fig. 104.98(a), and the SOP measurement of the temperature of the exterior-facing side of the Be sample is shown in Fig. 104.98(b). As can be seen in the figure, the surface preheat begins soon after laser turn on and the surface temperature levels off at $\sim 3.7\ \text{ns}$, when the laser turns off. Shock breakout occurs at $\sim 7.2\ \text{ns}$. In relation to the experiment of Fig. 104.97, the reduced preheat level in Fig. 104.98 is consistent with the lower hohlraum temperature, the Cu component, and the thicker ablator. As explained in Ref. 5, the lower shock temperature is consistent with the reduced level of ablator preheat. An important finding in these experiments is that as hohlraum temperatures (and laser-spot intensities) are increased, the window is (apparently) also preheated and becomes opaque. A quartz window remained transparent throughout the laser pulse for hohlraum temperatures of up to 136 eV [Fig. 104.99(a)]. For hohlraum temperatures exceeding 140 eV (corresponding to laser intensities at the hohlraum

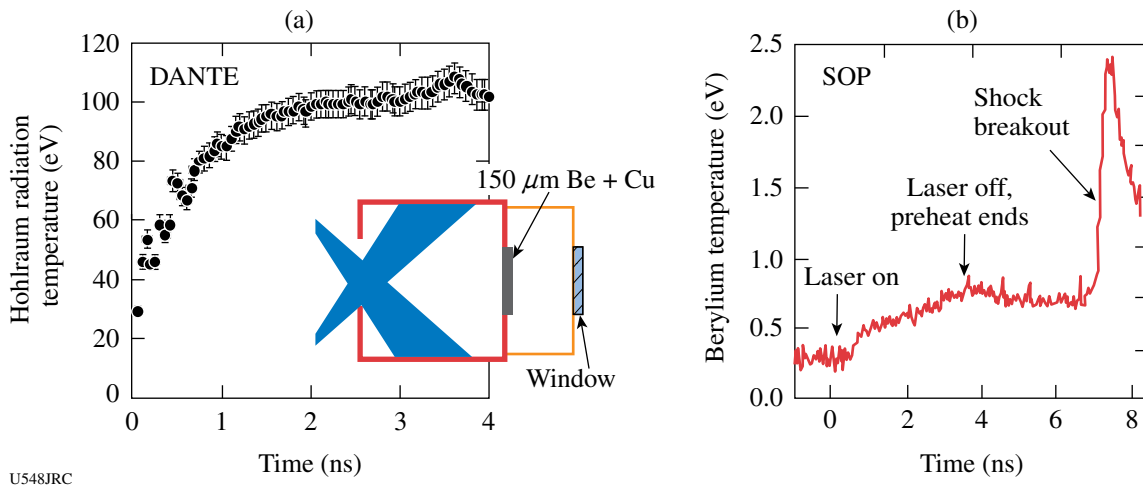


Figure 104.98 Shock breakout measurements: (a) DANTE-derived radiation temperature and (b) SOP-measured temperature of the exterior of the Be foil.

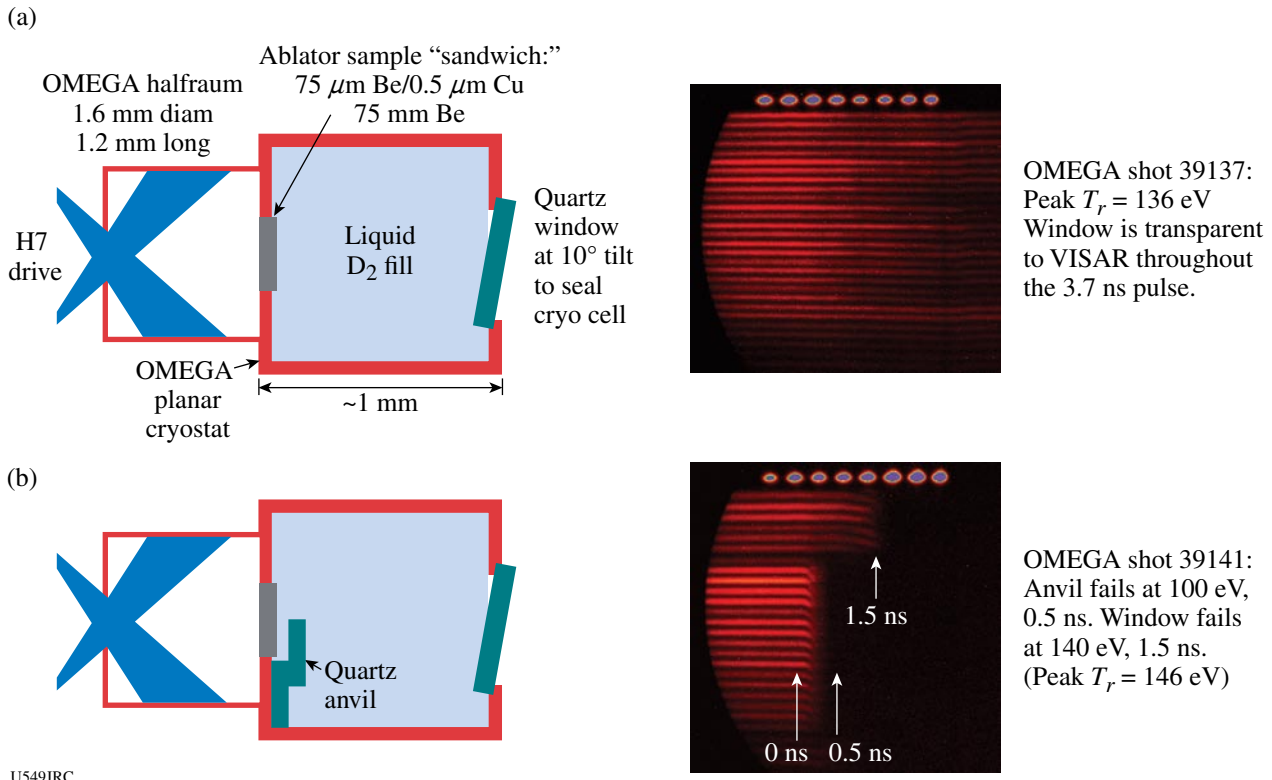
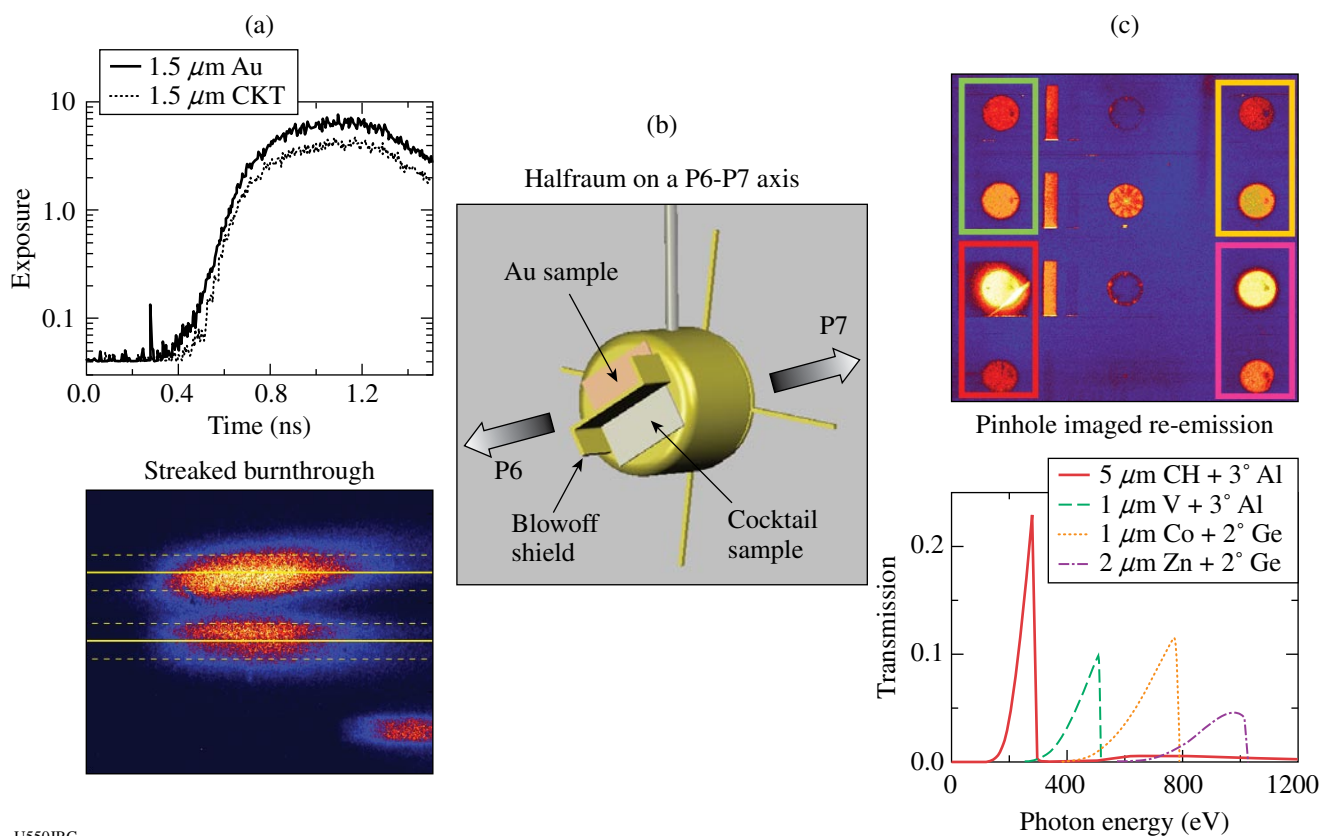


Figure 104.99 Window transparency: (a) quartz window maintains transparency up to $T_r \sim 136$ eV, (b) quartz anvil becomes opaque at $T_r > 100$ eV and window fails at 140 eV.

wall $\sim 1 \times 10^{14}$ W/cm²), however, windows and anvils became opaque soon after laser turn on [Fig. 104.99(b)]. In the near future, new window materials, laser smoothing, and geometric effects will be tested in an attempt to reduce window and anvil preheat effects to a level consistent with the requirements of the proposed NIF shock-timing diagnostic.

Cocktail Burnthrough and Re-emission: SNL conducted 11 shots in June 2005 to study the relative difference in burnthrough time and x-ray re-emission between thin cocktail and Au foils. Figure 104.100 shows the sample geometry and example data for the experiments. These were the first tests of the layered 75% U, 25% Au cocktail material made by General Atomics that is currently specified as the hohlraum wall material in the NIF point design. The experiments studied the difference in performance between cocktails and Au in hohl-

raums with peak radiation temperatures of 175 eV, 235 eV, and 270 eV. Preliminary results show that the difference in burnthrough between Au and cocktails at 550-eV photon energy is ~ 0 ps at $T_r = 170$ eV, and ~ 50 ps at $T_r = 230$ eV (the foils in the 270-eV hohlraums burnthrough at a time when the radiation temperature is ~ 230 eV). Time-gated x-ray pinhole camera measurements were configured with four different filter-mirror combinations to sample the wall re-emission across spectral ranges of ~ 200 to 250 eV, ~ 400 to 500 eV, ~ 600 to 800 eV, and ~ 800 to 1000 eV. Preliminary results show a $20 \pm 15\%$ increase in the re-emission from cocktails in the energy band from ~ 400 to 500 eV at hohlraum radiation temperatures > 220 eV and no statistically significant increase or decrease in any other energy band. Future work will include detailed comparisons between the experimental data and integrated *LASNEX* calculations with the best known opacities of Au and U.



U550JRC

Figure 104.100

Example data, (a) and (c), and geometry (b) from cocktail burnthrough and re-emission experiments conducted by SNL in June 2005. On the left is burnthrough data (b) taken with an x-ray streak camera at P6, and on the right (c) is x-ray framing camera data at P7 with four different mirrored channels.

2005 CEA Experiments on OMEGA

Scientists from CEA led several OMEGA experimental campaigns in FY05 including the development of neutron imaging and hohlraum symmetry experiments. A total of 34 OMEGA target shots were taken for CEA experiments in FY05.

Penumbra and Annular Imaging for Inertial Confinement Fusion Neutron Images

1. Introduction

In inertial confinement fusion experiments, laser energy is used to compress a millimeter-sized (diameter) target filled with deuterium and tritium. The compression results in the creation of a hot spot where the fusion reactions begin. On the NIF (U.S.A.) or LMJ (France), 14-MeV neutron images will be used to determine the dimensions and the shape of the hot spot. Since the dimensions of the hot spot will be $\sim 50 \mu\text{m}$, a spatial resolution below $10 \mu\text{m}$ will be required in a neutron image to distinguish between the different failure mechanisms of the implosion (symmetry, laser pulse shaping, etc.).

CEA developed a neutron imaging system (NIS) using a penumbral^{11,12} and, most recently, an annular¹³ imaging technique with a high-resolution neutron camera that was tested on OMEGA during high-neutron-yield shots. The images obtained with these tests attained a $20\text{-}\mu\text{m}$ spatial resolution with a high signal-to-noise ratio (SNR). With these results we can now consider a preliminary design for a NIS with a resolution of $10 \mu\text{m}$ on OMEGA and 6 to $7 \mu\text{m}$ on the NIF or LMJ.

2. Experimental Setup

Neutrons emitted by the target go through a coded aperture that is placed 26 cm from target chamber center (TCC). Two coded apertures can be used: a penumbral or an annular. Both are made of a biconical hole built in a 10-cm-long DENAL (Tungsten alloy) cylinder. The diameter at the intersection of the cones is $\sim 2 \text{ mm}$. The ring is obtained by placing a plug inside the hole so that the aperture is equivalent to a continuous assembly of $8\text{-}\mu\text{m}$ -diam pinholes distributed along a circle (Fig. 104.101).

An enlarged image of the coded aperture is projected on a neutron camera placed at a distance of $\sim 8 \text{ m}$ from TCC. The camera is composed of a coherent array of one-million glass capillaries, $85 \mu\text{m}$ in diameter, filled with a high-refractive-index organic liquid scintillator. Neutrons mainly interact by elastic scattering on hydrogen nuclei. As they lose kinetic energy, the recoil protons produce light, a part of which is guided through the stepped-index fiber optics made by glass

($n = 1.49$) and scintillator ($n = 1.56$). The image is then transported, intensified, and reduced to be registered on a one-million pixel CCD ($20 \times 20 \text{ mm}^2$).

The spatial resolution Δs of the overall system is given by

$$\Delta s = \sqrt{\left[\frac{\ln(2) \times FOV}{2 \times L_0 \times \mu} \right]^2 + \Delta s_{\text{det}}^2 \times \left(\frac{L_0}{L_1} \right)^2}, \quad (1)$$

where FOV is the field of view, L_0 and L_1 the target to aperture and target to detector distances, respectively, Δs_{det} is the resolution of the camera, and μ is the attenuation of neutrons in the DENAL cylinder. During the past few years, improvements in the detector design have led to the achievement of a camera resolution of $\sim 650\text{-}\mu\text{m}$ FWHM. Since the camera resolution is limited primarily by the recoil length of protons, this value can be reduced to $400 \mu\text{m}$ by replacing hydrogen atoms with deuterium in the scintillator.¹⁴

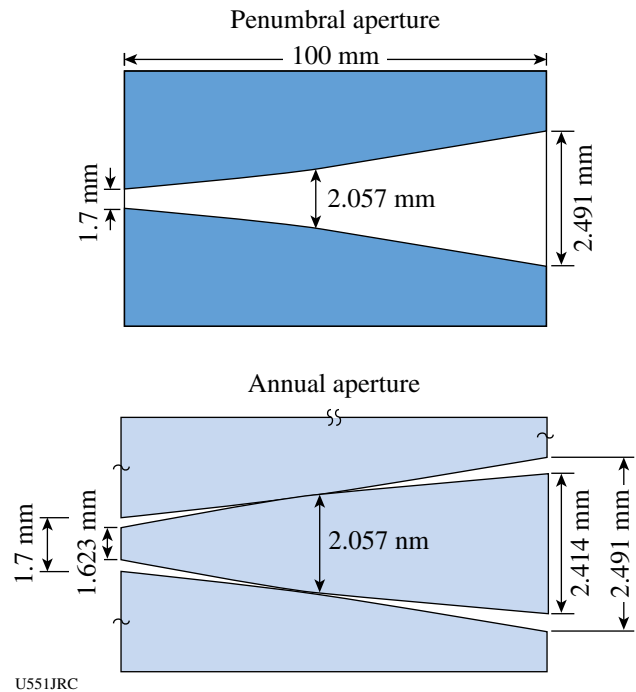


Figure 104.101 Sections of the penumbral- and annular-coded apertures. Both have the same dimensions. A plug is placed inside the second aperture to define a ring equivalent aperture.

3. 2005 High-Yield Shots

In 2004, neutron images were acquired with the penumbral technique. A spatial resolution of $20\ \mu\text{m}$ and a SNR of ~ 20 to 25 were demonstrated with this system. In 2005, the detector was unchanged except for replacement of the fiber optic reducer (taper) between the capillary array and the microchannel plate (MCP). The quality of this taper improved the uniformity and the transmission of the image on the whole field of view. The annular imaging technique was tested and compared with results obtained with the penumbral aperture for the same type of targets to prove the reliability of the technique. Figure 104.102 presents raw images, penumbral and annular, for plastic-shell targets and compares annular images for a plastic and a glass target. Glass targets produce a larger core than plastic ones. This is confirmed by observing the raw images as the thickness of the ring is directly related to the source diameter in one dimension. Figure 104.103 shows unfolded images for both techniques on DT(15)CH[15], DT(15)CH[20], and DT(15)SiO₂[2.5] targets. The images have a $20\text{-}\mu\text{m}$ spatial resolution. The corresponding neutron yields Y_n and SNR are written on each image. Plastic targets have a high convergence ratio for relatively high yields, which leads to very good SNR around 30 to 40. Though glass targets result in higher neutron yields, the larger cores produce images with a lower SNR of ~ 15 . Comparison of the penumbral and annular images shows that the dimensions and shape of the hot-spot dimensions are the same for similar targets. The ring technique was chosen because it will result in a high SNR in high-resolution images. This was confirmed by applying a $20\text{-}\mu\text{m}$ and then a $10\text{-}\mu\text{m}$ FWHM low-pass filter on the image for both techniques. The SNR of both penumbral and annular images was near 40 for a $20\text{-}\mu\text{m}$ filter, though it decreased to 14 in the penumbral image and still remained 28 in the ring image for a $10\text{-}\mu\text{m}$ filter.¹⁵

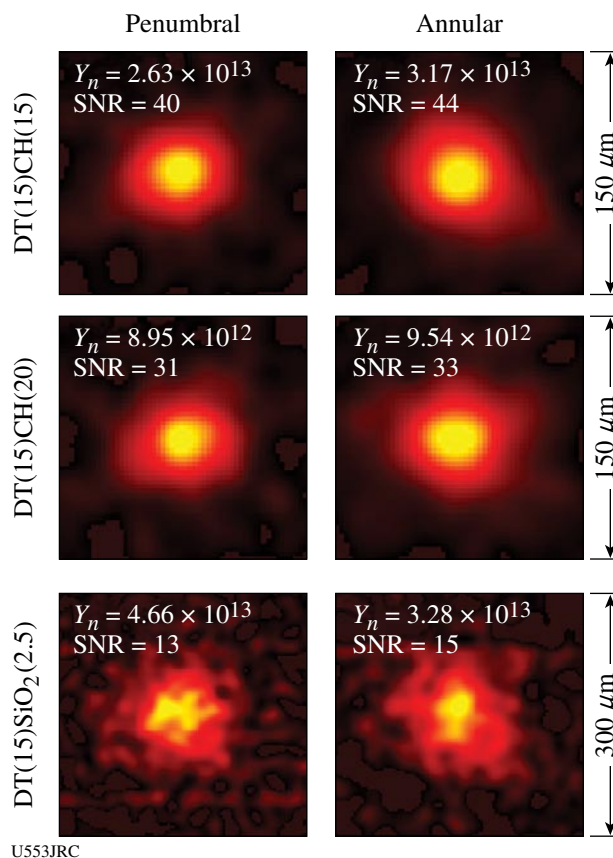
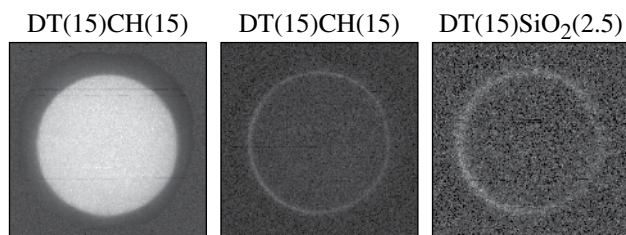


Figure 104.103 Unfolded images obtained during 2005 high-yield shots. Comparison between penumbral and annular techniques for three types of targets.



U552JRC

Figure 104.102 Raw images obtained with a penumbral (left) and an annular (center and right) apertures.

4. 2005 DD Shots

With 2.45-MeV DD neutrons, the recoil ion length in the scintillator is much shorter. As a consequence, the resolution of the detector is much better, $\sim 230 \mu\text{m}$ compared to $\sim 650 \mu\text{m}$ for DT neutrons. The improved sensitivity of the camera is sufficient to acquire a DD image with a neutron yield of about 10^{11} . Neutron images were thus registered on DD shots, including cryogenic targets. Figure 104.104 shows examples of neutron images obtained with a cryogenic target (left) and with a gas-filled plastic shell target (right). The resolution is set to $50 \mu\text{m}$ and $35 \mu\text{m}$, respectively, because of the low yield relatively close to the threshold of sensitivity of the camera, which implies a compromise between resolution and SNR.

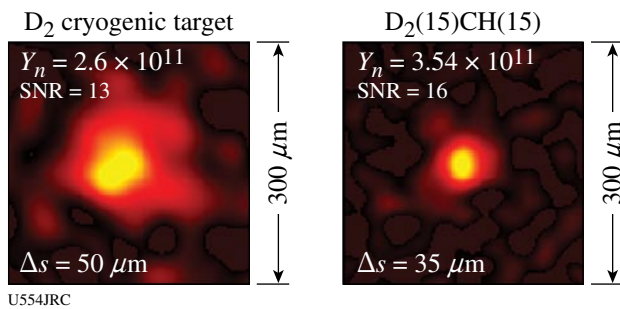


Figure 104.104
Neutron images of DD targets.

5. Conclusions

During the 2005 high-yield shots on OMEGA, DT neutron images were acquired with a $20\text{-}\mu\text{m}$ spatial resolution and very high SNR. The annular imaging technique was tested and demonstrated higher signal-to-noise ratio images compared to the penumbral imaging technique. With an enhanced detector and a ring-coded aperture, a $10\text{-}\mu\text{m}$ spatial resolution on OMEGA and $10\text{-}\mu\text{m}$ spatial resolution on the NIF or LMJ is now projected.

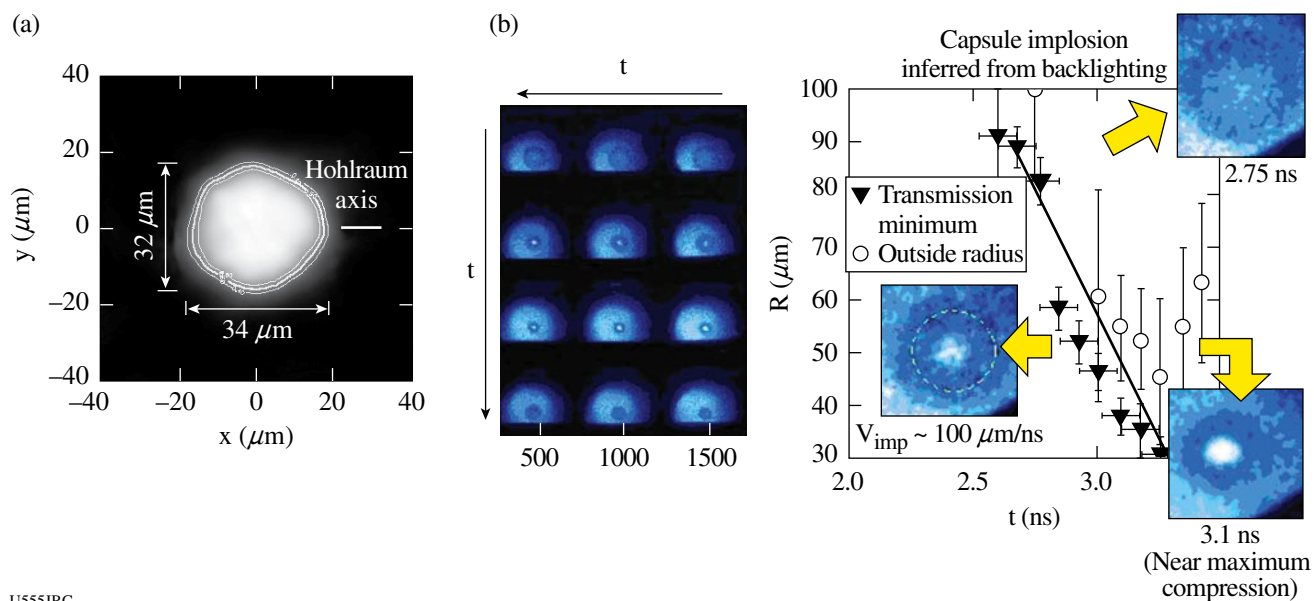
The neutron camera was sensitive enough to acquire DD images, but the low yield resulted in a reduction to the resolution to improve the quality of the image. A new detector design is now being considered to acquire DD neutron images. This camera will have an enhanced detection quantum efficiency with smaller dimensions to work with a lower magnification ratio.

CEA Symmetry Experiments

In previous years, CEA carried out an experimental campaign to study the irradiation symmetry of radiation-driven capsules in cylindrical hohlraums heated by a multicone arrangement of beams. In FY05, CEA experiments were carried out to characterize the symmetry by imaging the core x-ray emission¹⁶ of $500\text{-}\mu\text{m}$, 50-atm, D_2 -filled capsules doped with 0.1-atm argon. These capsules were produced by CEA/Valduc. Shell thickness variation was used to probe symmetry at different times during the implosion.

Figure 104.105(a) gives an example of a core image obtained with a $37\text{-}\mu\text{m}$ CH, 2% at., Ge-doped capsule. This image is obtained at an instant (3.1 ns) close to peak compression. The convergence ratio $\text{Cr} \sim 7$ can be determined on a similar capsule by backlighting the shell implosion. From Cr and core ellipticity, we can infer an irradiation P2 component of $\sim 1\%$ (Ref. 17), which is consistent with the expected symmetry from previous foam-ball experimental data, time-integrated evolution of flux P2 component in simulations, and also with data reported in Ref. 18.

Backlighting tests of imploding capsules were carried out. Figure 104.105(b) shows an example of a shot where a simultaneous image of core emission and backlighting of the dense shell is recorded. This provides valuable data to benchmark hydrodynamic simulations. We can infer from these data an implosion velocity of $\sim 100 \mu\text{m/ns}$ and a convergence ratio from the minimum radius of the dense part of the shell of ~ 7 .



U555JRC

Figure 104.105

(a) Example of an imploded core image. (b) Backlit image of imploding capsule showing, on the same data, an image of core emission and absorption through the dense part of the shell.

REFERENCES

1. S. D. Rothman *et al.*, *J. Phys. D* **38**, 733 (2005).
2. W. J. Nellis *et al.*, *Phys. Rev. Lett.* **53**, 1248 (1998).
3. V. Ya. Ternovoi *et al.*, in *Shock Compression of Condensed Matter, AIP Conference Proceedings 620*, edited by M. D. Furnish, N. N. Thadhani, and Y. Horie (American Institute of Physics, New York, 2002), pp. 107–110.
4. A. Forster, T. Kahlbaum, and W. Ebeling, *Laser Part. Beams* **10**, 253 (1992).
5. R. E. Olson *et al.*, *Phys. Rev. Lett.* **91**, 235002 (2003).
6. R. E. Olson *et al.*, *Bull. Am. Phys. Soc.* **49**, 24 (2004).
7. J. A. Oertel *et al.*, *Rev. Sci. Instrum.* **70**, 803 (1999).
8. J. Miller, T. R. Boehly, E. Vianello, W. J. Armstrong, C. Sorce, W. Theobald, D. D. Meyerhofer, J. Eggert, and D. G. Hicks, *Bull. Am. Phys. Soc.* **49**, 64 (2004).
9. P. M. Celliers, D. K. Bradley, G. W. Collins, D. G. Hicks, T. R. Boehly, and W. J. Armstrong, *Rev. Sci. Instrum.* **75**, 4916 (2004).
10. D. H. Munro *et al.*, *Phys. Plasmas* **8**, 2245 (2001).
11. A. Rouyer, *Rev. Sci. Instrum.* **74**, 1234 (2003).
12. R. A. Lerche *et al.*, *Laser Part. Beams* **9**, 99 (1991).
13. R. G. Simpson *et al.*, *Opt. Eng.* **14**, 490 (1975).
14. L. Disdier, R. A. Lerche, J. L. Bourgade, and V. Yu. Glebov, *Rev. Sci. Instrum.* **75**, 2134 (2004).
15. L. Disdier, A. Rouyer, I. Lantuejoul, O. Landuas, J. L. Bourgade, T. C. Sangster, V. Yu. Glebov, and R. A. Lerche, "Inertial Confinement Fusion Neutron Images," to be published in *Physics of Plasma*.
16. A. Hauer *et al.*, *Rev. Sci. Instrum.* **66**, 672 (1995).
17. J. D. Lindl *et al.*, *Phys. Plasmas* **11**, 339 (2004).
18. P. Amendt, R. E. Turner, and O. L. Landen, *Phys. Rev. Lett.* **89**, 165001 (2002).

Publications and Conference Presentations

Publications

- V. Bagnoud, "A Front End for Multipetawatt Lasers Based on a High-Energy, High-Average-Power Optical Parametric Chirped-Pulsed Amplifier," in *Frontiers in Optics 2004* (Optical Society of America, Rochester, NY, 2004), Paper FMM2.
- V. Bagnoud, I. A. Begishev, M. J. Guardalben, J. Puth, and J. D. Zuegel, "5 Hz, >250 mJ Optical Parametric Chirped-Pulse Amplifier at 1053 nm," *Opt. Lett.* **30**, 1843 (2005).
- V. Bagnoud, M. J. Guardalben, J. Puth, J. D. Zuegel, T. Mooney, and P. Dumas, "High-Energy, High-Average-Power Laser with Nd:YLF Rods Corrected by Magnetorheological Finishing," *Appl. Opt.* **44**, 282 (2005).
- V. Bagnoud, J. Puth, I. Begishev, M. Guardalben, J. D. Zuegel, N. Forget, and C. Le Blanc, "A Multiterawatt Laser Using a High-Contrast, Optical Parametric Chirped-Pulse Preamplifier," in *Conference on Lasers and Electro-Optics/Quantum Electronics and Laser Science and Photonic Applications, Systems and Technologies 2005* (Optical Society of America, Washington, DC, 2005), Paper JFA1.
- R. Betti, K. Anderson, J. Knauer, T. J. B. Collins, R. L. McCrory, P. W. McKenty, and S. Skupsky, "Theory of Laser-Induced Adiabatic Shaping in Inertial Confinement Fusion Implosions: The Relaxation Method," *Phys. Plasmas* **12**, 042703 (2005).
- C. Bouvier, J. C. Lambropoulos, and S. D. Jacobs, "Fracture Toughness of ULE, Zerodur, Astrosital and Corning 9600," in *Frontiers in Optics 2004*, OSA Technical Digest (Optical Society of America, Rochester, NY, 2004), Paper OTuA4.
- J. Carpenter and S. D. Jacobs, "In the Mood for Science," SPIE's *oemagazine*, March 2005, 35.
- A. C. A. Chen, S. Culligan, Y. Geng, S. H. Chen, K. P. Klubek, K. M. Vaeth, and C. W. Tang, "Glassy Nematic Conjugated Oligomers: Materials for Organic Light-Emitting Diodes," in *Liquid Crystals VIII*, edited by I.-C. Khoo (SPIE, Bellingham, WA, 2004), Vol. 5518, pp. 77–91.
- S. Chen, P. Zhang, W. Theobald, N. Saleh, M. Rever, A. Maksimchuk, and D. Umstadter, "Evidence of Ionization Blue Shift Seeding of Forward Raman Scattering," in *Advanced Accelerator Concepts: Eleventh Workshop*, edited by V. Yakimenko (American Institute of Physics, Melville, NY, 2004), Vol. 737, pp. 585–591.
- S. H. Chen, "Multifunctional Glassy Liquid Crystals for Photonics," *J. SID* **12**, 205 (2004).
- T. J. B. Collins, A. Poludnenko, A. Cunningham, and A. Frank, "Shock Propagation in Deuterium-Tritium-Saturated Foam," *Phys. Plasmas* **12**, 062705 (2005).
- S. Costea, S. Pisana, N. P. Kherani, F. Gaspari, T. Koteski, W. T. Shmayda, and S. Zukotynski, "Use of Tritium in the Study of Defects in Amorphous Silicon," *Fusion Sci. Technol.* **48**, 712 (2005).
- R. S. Craxton and D. W. Jacobs-Perkins, "The Saturn Target for Polar Direct Drive on the National Ignition Facility," *Phys. Rev. Lett.* **94**, 095002 (2005).
- R. S. Craxton, F. J. Marshall, M. J. Bonino, R. Epstein, P. W. McKenty, S. Skupsky, J. A. Delettrez, I. V. Igumenshchev, D. W. Jacobs-Perkins, J. P. Knauer, J. A. Marozas, P. B. Radha, and W. Seka, "Polar Direct Drive: Proof-of-Principle Experiments on OMEGA and Prospects for Ignition on the National Ignition Facility," *Phys. Plasmas* **12**, 056304 (2005) (invited).
- J. E. DeGroot, A. E. Marino, K. E. Spencer, and S. D. Jacobs, "Power Spectral Density Plots Inside MRF Spots Made with a Polishing Abrasive-Free MR Fluid," in *Optifab 2005* (SPIE, Bellingham, WA, 2005), Vol. TD03, pp. 134–138.

- J. E. DeGroot, S. N. Shafir, J. C. Lambropoulos, and S. D. Jacobs, "Surface Characterization of CVD ZnS Using Power Spectral Density," in *Frontiers in Optics 2004*, OSA Technical Digest (Optical Society of America, Rochester, NY, 2004), Paper OTuC2.
- W. R. Donaldson, M. Millicchia, and R. Keck, "A Multichannel, High-Resolution, UV Spectrometer for Laser-Fusion Applications," *Rev. Sci. Instrum.* **76**, 073106 (2005).
- R. Epstein, "On the Bell–Plesset Effects: The Effects of Uniform Compression and Geometrical Convergence on the Classical Rayleigh–Taylor Instability," *Phys. Plasmas* **11**, 5114 (2004).
- R. A. Forties and F. J. Marshall, "In Situ Characterization of High-Intensity Laser Beams on OMEGA," *Rev. Sci. Instrum.* **76**, 073505 (2005).
- S. Ghosh, R. Boni, and P. A. Jaanimagi, "Optical and X-Ray Streak Camera Gain Measurements," *Rev. Sci. Instrum.* **75**, 3956 (2004).
- V. Yu. Glebov, C. Stoeckl, T. C. Sangster, S. Roberts, R. A. Lerche, and G. J. Schmid, "NIF Neutron Bang Time Detector Prototype Test on OMEGA," *IEEE Trans. Plasma Sci.* **33**, 70 (2005).
- V. Yu. Glebov, C. Stoeckl, T. C. Sangster, S. Roberts, G. J. Schmid, R. A. Lerche, and M. J. Moran, "Prototypes of National Ignition Facility Neutron Time-of-Flight Detectors Tested on OMEGA," *Rev. Sci. Instrum.* **75**, 3559 (2004).
- J. E. Goldston, E. Quataert, and I. V. Igumenshchev, "Synchrotron Radiation from Radiatively Inefficient Accretion Flow Simulations: Applications to Sagittarius A*," *Astrophys. J.* **621**, 785 (2005).
- G. N. Gol'tsman, A. Korneev, I. Rubtsova, I. Milostnaya, G. Chulkova, O. Minaeva, K. Smirnov, B. Voronov, W. Słysz, A. Pearlman, A. Verevkin, and R. Sobolewski, "Ultrafast Superconducting Single-Photon Detectors for Near-Infrared-Wavelength Quantum Communications," *Phys. Stat. Sol. C* **2**, 1480 (2005).
- V. N. Goncharov and D. Li, "Effects of Temporal Density Variation and Convergent Geometry on Nonlinear Bubble in Classical Rayleigh–Taylor Instability," *Phys. Rev. E* **71**, 046306 (2005).
- V. N. Goncharov and G. Li, "Effect of Electric Fields on Electron Thermal Transport in Laser-Produced Plasmas," *Phys. Plasmas* **11**, 5680 (2004).
- O. V. Gotchev, P. A. Jaanimagi, J. P. Knauer, F. J. Marshall, and D. D. Meyerhofer, "KB–PJX—A Streaked Imager Based on a Versatile X-Ray Microscope Coupled to a High-Current Streak Tube," *Rev. Sci. Instrum.* **75**, 4063 (2004) (invited).
- L. Guazzotto and R. Betti, "Magnetohydrodynamics Equilibria with Toroidal and Poloidal Flow," *Phys. Plasmas* **12**, 056107 (2005) (invited).
- D. R. Harding, F.-Y. Tsai, E. L. Alfonso, S. H. Chen, A. K. Knight, and T. N. Blanton, "Properties of Vapor-Deposited Polyimides," in *Polyimides and Other High Temperature Polymers: Synthesis, Characterizations and Applications*, edited by K. L. Mittal (VSP, Utrecht, The Netherlands, 2005), Vol. 3, pp. 49–67 (invited).
- H. L. Helfer, "The Local Dark Matter," in *Progress in Dark Matter Research*, edited by J. Val Blain (Nova Science, New York, 2005), Chap. 4, pp. 121–147.
- B. Hu, R. Betti, and J. Manickam, "Application of the Low-Frequency Energy Principle to Wall Modes," *Phys. Plasmas* **12**, 057301 (2005).
- P. A. Jaanimagi, "Breaking the 100-fs Barrier with a Streak Camera," in *Fourth-Generation X-Ray Sources and Ultrafast X-Ray Detectors*, edited by R. O. Tatchyn, Z. Chang, J.-C. Kieffer, and J. B. Hastings (SPIE, Bellingham, WA, 2004), Vol. 5194, pp. 171–182.
- P. A. Jaanimagi, R. Boni, D. Butler, S. Ghosh, W. R. Donaldson, and R. L. Keck, "The Streak Camera Development Program at LLE," in the *26th International Congress on High-Speed Photography and Photonics*, edited by D. L. Paisley, S. Kleinfelder, D. R. Snyder, and B. J. Thompson (SPIE, Bellingham, WA, 2005), Vol. 5580, pp. 408–415.
- S. D. Jacobs, "Innovations in Optics Manufacturing," in *Frontiers in Optics 2004*, OSA Technical Digest (Optical Society of America, Rochester, NY, 2004), Paper OMA1.
- S. D. Jacobs, "International Innovations in Optical Finishing," in *Current Developments in Lens Design and Optical Engineering V*, edited by P. Z. Mouroulis, W. J. Smith, and

- R. B. Johnson (SPIE, Bellingham, WA, 2004), Vol. 5523, pp. 264–272 (invited).
- S. D. Jacobs and E. Kowaluk, “Glass Art ‘Sparkles’ at OSA–OF&T’s First Contest and Auction,” OSA Focal Point Newsletter, Winter 2004.
- Z. Jiang and J. R. Marciante, “Mode-Area Scaling of Helical-Core Dual-Clad Fiber Lasers and Amplifiers,” in *Conference on Lasers and Electro-Optics/Quantum Electronics and Laser Science and Photonic Applications, Systems and Technologies 2005* (Optical Society of America, Washington, DC, 2005), Paper CThR3.
- J. Keck, J. B. Oliver, V. Gruschow, J. Spaulding, and J. Howe, “Process Tuning of Silica Thin-Film Deposition,” in *Frontiers in Optics 2004*, OSA Technical Digest (Optical Society of America, Rochester, NY, 2004), Paper OMB4.
- J. Kitaygorsky, J. Zhang, A. Verevkin, A. Sergeev, A. Korneev, V. Matvienko, P. Kouminov, K. Smirnov, B. Voronov, G. Gol’tsman, and R. Sobolewski, “Origin of Dark Counts in Nanostructured NbN Single-Photon Detectors,” *IEEE Trans. Appl. Supercond.* **15**, 545 (2005).
- J. P. Knauer, K. Anderson, R. Betti, T. J. B. Collins, V. N. Goncharov, P. W. McKenty, D. D. Meyerhofer, P. B. Radha, S. P. Regan, T. C. Sangster, V. A. Smalyuk, J. A. Frenje, C. K. Li, R. D. Petrasso, and F. H. Séguin, “Improved Target Stability Using Picket Pulses to Increase and Shape the Ablator Adiabatic,” *Phys. Plasmas* **12**, 056306 (2005) (invited).
- J. P. Knauer and N. C. Gindele, “Temporal and Spectral Deconvolution of Data from Diamond, Photoconductive Devices,” *Rev. Sci. Instrum.* **75**, 3714 (2004).
- A. Korneev, V. Matvienko, O. Minaeva, I. Milostnaya, I. Rubtsova, G. Chulkova, K. Smirnov, V. Voronov, G. Gol’tsman, W. Słysz, A. Pearlman, A. Verevkin, and R. Sobolewski, “Quantum Efficiency and Noise Equivalent Power of Nanostructured, NbN, Single-Photon Detectors in the Wavelength Range from Visible to Infrared,” *IEEE Trans. Appl. Supercond.* **15**, 571 (2005).
- T. Z. Kosc, “Particle Display Technologies Become E-Paper,” *Opt. Photonics News* **16**, 18 (2005).
- T. Z. Kosc, K. L. Marshall, S. D. Jacobs, and J. C. Lambropoulos, “Polymer Cholesteric Liquid-Crystal Flake Reorientation in an Alternating-Current Electric Field,” *J. Appl. Phys.* **98**, 013509 (2005).
- T. Z. Kosc, K. L. Marshall, A. Trajkovska-Petkoska, E. Kimball, and S. D. Jacobs, “Progress in the Development of Polymer Cholesteric Liquid Crystal Flakes for Display Applications,” *Displays* **25**, 171 (2004).
- T. Z. Kosc, K. L. Marshall, A. Trajkovska-Petkoska, R. Varshneya, and S. D. Jacobs, “Development of Polymer Cholesteric Liquid Crystal Flakes for Electro-Optic Applications,” *Opt. Photonic News* **15**, 33 (2004).
- T. Kostas, N. P. Kherani, W. T. Shmayda, S. Costea, and S. Zukotynski, “Nuclear Batteries Using Tritium and Thin Film Hydrogenated Amorphous Silicon,” *Fusion Sci. Technol.* **48**, 700 (2005).
- I. A. Kozhinova, H. J. Romanofsky, S. D. Jacobs, W. I. Kordonski, and S. R. Gorodkin, “Polishing of Pre-Polished CVD ZnS Flats with Altered Magnetorheological (MR) Fluids,” in *Frontiers in Optics 2004*, OSA Technical Digest (Optical Society of America, Rochester, NY, 2004), Paper OMD2.
- I. A. Kozhinova, H. J. Romanofsky, A. Maltsev, S. D. Jacobs, W. I. Kordonski, and S. R. Gorodkin, “Minimizing Artifact Formation in Magnetorheological Finishing of Chemical Vapor Deposition ZnS Flats,” *Appl. Opt.* **44**, 4671 (2005).
- A. P. Küng, A. Agarwal, D. F. Grosz, S. Banerjee, and D. N. Maywar, “Analytical Solution of Transmission Performance Improvement in Fiber Spans With Forward Raman Gain and Its Application to Repeaterless Systems,” *J. Lightwave Technol.* **23**, 1182 (2005).
- J. C. Lambropoulos and R. Varshneya, “Glass Material Response to the Fabrication Process: Example from Lapping,” in *Frontiers in Optics 2004*, OSA Technical Digest (Optical Society of America, Rochester, NY, 2004), Paper OTuA1.
- X. Li, Y. Xu, Š. Chromik, V. Štrbík, P. Odier, D. De Barros, and R. Sobolewski, “Time-Resolved Carrier Dynamics in Hg-Based High-Temperature Superconducting Photodetectors,” *IEEE Trans. Appl. Supercond.* **15**, 622 (2005).
- J.-C. Lin, M. Z. Yates, A. Trajkovska-Petkoska, and S. D. Jacobs, “Electric-Field-Driven Assembly of Oriented Molecular-Sieve Films,” *Adv. Mater.* **16**, 1944 (2004).

- S. G. Lukishova, A. W. Schmid, R. Knox, P. Freivald, R. W. Boyd, C. R. Stroud, Jr., and K. L. Marshall, "Deterministically Polarized Fluorescence from Single Dye Molecules Aligned in Liquid Crystal Host," in *Conference on Lasers and Electro-Optics/Quantum Electronics and Laser Science and Photonic Applications, Systems and Technologies 2005* (Optical Society of America, Washington, DC, 2005), Paper QTuE6.
- J. R. Marciante, J. I. Hirsh, D. H. Raguin, and E. T. Prince, "Polarization-Insensitive, High-Dispersion TIR Diffraction Gratings," in *Frontiers in Optics 2004*, OSA Technical Digest (Optical Society of America, Rochester, NY, 2004), Paper DMA1.
- J. R. Marciante, J. I. Hirsh, D. H. Raguin, and E. T. Prince, "Polarization-Insensitive High-Dispersion Total Internal Reflection Diffraction Gratings," *J. Opt. Soc. Am. A* **22**, 299 (2005).
- J. R. Marciante and J. D. Zuegel, "High-Gain, Polarization-Preserving, Yb-Doped Fiber Amplifier for Low-Duty-Cycle Pulse Amplification," in *Conference on Lasers and Electro-Optics/Quantum Electronics and Laser Science and Photonic Applications, Systems and Technologies 2005* (Optical Society of America, Washington, DC, 2005), Paper JWB60.
- A. E. Marino, K. Spencer, J. E. DeGroote, and S. D. Jacobs, "Chemical Durability of Phosphate Laser Glasses," in *Frontiers in Optics 2004*, OSA Technical Digest (Optical Society of America, Rochester, NY, 2004), Paper OTuA7.
- F. J. Marshall, R. S. Craxton, J. A. Delettrez, D. H. Edgell, L. M. Elasky, R. Epstein, V. Yu. Glebov, V. N. Goncharov, D. R. Harding, R. Janezic, R. L. Keck, J. D. Kilkenny, J. P. Knauer, S. J. Loucks, L. D. Lund, R. L. McCrory, P. W. McKenty, D. D. Meyerhofer, P. B. Radha, S. P. Regan, T. C. Sangster, W. Seka, V. A. Smalyuk, J. M. Soures, C. Stoeckl, S. Skupsky, J. A. Frenje, C. K. Li, R. D. Petrasso, and F. H. Séguin, "Direct-Drive, Cryogenic Target Implosions on OMEGA," *Phys. Plasmas* **12**, 056302 (2005) (invited).
- F. J. Marshall, J. A. Oertel, and P. J. Walsh, "Framed, 16-Image, Kirkpatrick-Baez Microscope for Laser-Plasma X-Ray Emission," *Rev. Sci. Instrum.* **75**, 4045 (2004).
- K. L. Marshall, E. Kimball, S. McNamara, T. Z. Kosc, A. Trajkovska-Petkoska, and S. D. Jacobs, "Electro-Optical Behavior of Polymer Cholesteric Liquid Crystal Flake/Fluid Suspensions in a Microencapsulation Matrix," in *Liquid Crystals VIII*, edited by I.-C. Khoo (SPIE, Bellingham, WA, 2004), Vol. 5518, pp. 170–181.
- R. L. McCrory, "Recent Progress in Inertial Confinement Fusion in the United States," *Nucl. Fusion* **44**, S123 (2004).
- M. Mikulics, R. Adam, M. Marso, A. Förster, P. Kordoš, H. Lüth, S. Wu, X. Zheng, and R. Sobolewski, "Ultrafast Low-Temperature-Grown Epitaxial GaAs Photodetectors Transferred on Flexible Plastic Substrates," *IEEE Photonics Technol. Lett.* **17**, 1725 (2005).
- M. Mikulics, M. Marso, P. Javorka, P. Kordoš, H. Lüth, M. Kocan, A. Rizzi, S. Wu, and R. Sobolewski, "Ultrafast Metal-Semiconductor-Metal Photodetectors on Low-Temperature-Grown GaN," *Appl. Phys. Lett.* **86**, 211110 (2005).
- M. Mikulics, M. Marso, I. C. Mayorga, R. Güsten, S. Stancek, P. Kováč, S. Wu, X. Li, M. Khafizov, R. Sobolewski, E. A. Michael, R. Schieder, M. Wolter, D. Buca, A. Förster, P. Kordoš, and H. Lüth, "Photomixers Fabricated on Nitrogen-Ion-Implanted GaAs," *Appl. Phys. Lett.* **87**, 041106 (2005).
- F. H. Mrakovcic, J. A. Randi, J. C. Lambropoulos, and S. D. Jacobs, "Subsurface Damage in Single-Crystal Sapphire," in *Frontiers in Optics 2004* (Optical Society of America, Rochester, NY, 2004), Paper OTuA6.
- A. V. Okishev and J. D. Zuegel, "Highly Stable, All-Solid-State Nd:YLF Regenerative Amplifier," *Appl. Opt.* **43**, 6180 (2004).
- J. B. Oliver, "Thin-Film-Optics Design and Manufacturing Challenges for Large-Aperture High-Peak-Power, Short-Pulse Lasers," in *Frontiers in Optics 2004* (Optical Society of America, Rochester, NY, 2004), Paper OMB1.
- S. Papernov and A. W. Schmid, "High-Spatial-Resolution Studies of UV-Laser-Damage Morphology in SiO₂ Thin Films with Artificial Defects," in *Laser-Induced Damage in Optical Materials: 2004*, edited by G. J. Exarhos, A. H. Guenther, N. Kaiser, K. L. Lewis, M. J. Soileau, and C. J. Stolz (SPIE, Bellingham, WA, 2005), Vol. 5647, pp. 141–155.
- S. Papernov and A. W. Schmid, "Two Mechanisms of Crater Formation in Ultraviolet-Pulsed-Laser Irradiated SiO₂ Thin Films with Artificial Defects," *J. Appl. Phys.* **97**, 114906 (2005).
- L. Parlato, R. Latempa, G. Peluso, G. P. Pepe, R. Cristiano, and R. Sobolewski, "The Characteristic Electron-Phonon Coupling Time of Unconventional Superconductors and Implications for Optical Detectors," *Supercond. Sci. Technol.* **18**, 1244 (2005).

- A. Pearlman, A. Cross, W. Słysz, J. Zhang, A. Verevkin, M. Currie, A. Korneev, P. Kouminov, K. Smirnov, B. Voronov, G. Gol'tsman, and R. Sobolewski, "Gigahertz Counting Rates of NbN Single-Photon Detectors for Quantum Communications," *IEEE Trans. Appl. Supercond.* **15**, 579 (2005).
- G. P. Pepe, L. Parlato, R. Latempa, P. D'Acunto, N. Marrocco, C. De Lisio, C. Altucci, G. Peluso, A. Barone, T. Taneda, and R. Sobolewski, "Fabrication and Optical Properties of Ultrathin Ferromagnet/Superconductor Metallic Bilayers," *IEEE Trans. Appl. Supercond.* **15**, 2942 (2005).
- P. B. Radha, T. J. B. Collins, J. A. Delettrez, Y. Elbaz, R. Epstein, V. Yu. Glebov, V. N. Goncharov, R. L. Keck, J. P. Knauer, J. A. Marozas, F. J. Marshall, R. L. McCrory, P. W. McKenty, D. D. Meyerhofer, S. P. Regan, T. C. Sangster, W. Seka, D. Shvarts, S. Skupsky, Y. Srebro, and C. Stoeckl, "Multidimensional Analysis of Direct-Drive, Plastic-Shell Implosions on OMEGA," *Phys. Plasmas* **12**, 056307 (2005) (invited).
- P. B. Radha, V. N. Goncharov, T. J. B. Collins, J. A. Delettrez, Y. Elbaz, V. Yu. Glebov, R. L. Keck, D. E. Keller, J. P. Knauer, J. A. Marozas, F. J. Marshall, P. W. McKenty, D. D. Meyerhofer, S. P. Regan, T. C. Sangster, D. Shvarts, S. Skupsky, Y. Srebro, R. P. J. Town, and C. Stoeckl, "Two-Dimensional Simulations of Plastic-Shell, Direct-Drive Implosions on OMEGA," *Phys. Plasmas* **12**, 032702 (2005).
- J. A. Randi, J. C. Lambropoulos, and S. D. Jacobs, "Subsurface Damage in Some Single Crystalline Optical Materials," *Appl. Opt.* **44**, 2241 (2005).
- S. P. Regan, J. A. Marozas, R. S. Craxton, J. H. Kelly, W. R. Donaldson, P. A. Jaanimagi, D. Jacobs-Perkins, R. L. Keck, T. J. Kessler, D. D. Meyerhofer, T. C. Sangster, W. Seka, V. A. Smalyuk, S. Skupsky, and J. D. Zuegel, "Performance of a 1-THz-Bandwidth, Two-Dimensional Smoothing by Spectral Dispersion and Polarization Smoothing of High-Power, Solid-State Laser Beams," *J. Opt. Soc. Am. B* **22**, 998 (2005).
- S. P. Regan, T. C. Sangster, D. D. Meyerhofer, K. Anderson, R. Betti, T. R. Boehly, T. J. B. Collins, R. S. Craxton, J. A. Delettrez, R. Epstein, O. V. Gotchev, V. Yu. Glebov, V. N. Goncharov, D. R. Harding, P. A. Jaanimagi, J. P. Knauer, S. J. Loucks, L. D. Lund, J. A. Marozas, F. J. Marshall, R. L. McCrory, P. W. McKenty, S. F. B. Morse, P. B. Radha, W. Seka, S. Skupsky, H. Sawada, V. A. Smalyuk, J. M. Soures, C. Stoeckl, B. Yaakobi, J. A. Frenje, C. K. Li, R. D. Petrasso, and F. H. Séguin, "Direct-Drive Inertial Confinement Fusion Implosions on OMEGA," *Astrophys. Space Sci.* **298**, 227 (2005).
- R. Rey-de-Castro, D. Wang, A. Verevkin, A. Mycielski, and R. Sobolewski, "Cd_{1-x}Mn_xTe Semimagnetic Semiconductors for Ultrafast Spintronics and Magneto-optics," *IEEE Trans. Nanotech.* **4**, 106 (2005).
- R. Rey-de-Castro, D. Wang, X. Zheng, A. Verevkin, R. Sobolewski, M. Mikulics, R. Adam, P. Kordoš, and A. Mycielski, "Subpicosecond Faraday Effect in Cd_{1-x}Mn_xTe and Its Application in Magneto-Optical Sampling," *Appl. Phys. Lett.* **85**, 3806 (2004).
- A. Rigatti, "Cleaning Process Versus Laser Damage Threshold of Coated Optical Components," in *Frontiers in Optics 2004* (Optical Society of America, Rochester, NY, 2004), Paper OMB3.
- A. L. Rigatti, "Cleaning Process Versus Laser-Damage Threshold of Coated Optical Components," in *Laser-Induced Damage in Optical Materials: 2004*, edited by G. J. Exarhos, A. H. Guenther, N. Kaiser, K. L. Lewis, M. J. Soileau, and C. J. Stolz (SPIE, Bellingham, WA, 2005), Vol. 5647, pp. 136–140.
- J. Sanz and R. Betti, "Analytical Model of the Ablative Rayleigh–Taylor Instability in the Deceleration Phase," *Phys. Plasmas* **12**, 042704 (2005).
- J. Sanz, R. Betti, R. Ramis, and J. Ramírez, "Nonlinear Theory of the Ablative Rayleigh–Taylor Instability," *Plasma Phys. Control. Fusion* **46**, B367 (2004).
- S. N. Shafrir, J. C. Lambropoulos, and S. D. Jacobs, "Loose Abrasive Lapping of Optical Glass with Different Lapping Plates and Its Interpretation," in *Frontiers in Optics 2004* (Optical Society of America, Rochester, NY, 2004), Paper OMC4.
- R. W. Short and A. Simon, "Theory of Three-Wave Parametric Instabilities in Inhomogeneous Plasmas Revisited," *Phys. Plasmas* **11**, 5335 (2004).
- V. A. Smalyuk, J. A. Delettrez, S. B. Dumanis, R. Epstein, V. Yu. Glebov, D. D. Meyerhofer, P. B. Radha, S. P. Regan, T. C. Sangster, C. Stoeckl, N. C. Toscano, J. A. Frenje, C. K. Li, R. D. Petrasso, F. H. Séguin, and J. A. Koch, "Hot-Core Characterization of Direct-Drive Spherical Cryogenic D₂ Target Implosion," *Phys. Plasmas* **12**, 052706 (2005).

- V. A. Smalyuk, V. N. Goncharov, T. R. Boehly, J. A. Delettrez, D. Y. Li, J. A. Marozas, A. V. Maximov, D. D. Meyerhofer, S. P. Regan, and T. C. Sangster, "Measurements of Laser-Imprinting Sensitivity to Relative Beam Mistiming in Planar Plastic Foils Driven by Multiple Overlapping Laser Beams," *Phys. Plasmas* **12**, 072703 (2005).
- V. A. Smalyuk, V. N. Goncharov, T. R. Boehly, J. A. Delettrez, D. Y. Li, J. A. Marozas, D. D. Meyerhofer, S. P. Regan, and T. C. Sangster, "Angular Dependence of Imprinting Levels in Laser-Target Interactions on Planar CH Foils," *Phys. Plasmas* **12**, 040702 (2005).
- V. A. Smalyuk, V. N. Goncharov, T. R. Boehly, J. P. Knauer, D. D. Meyerhofer, and T. C. Sangster, "Self-Consistent Determination of Rayleigh–Taylor Growth Rates and Ablation-Front Density in Planar Targets Accelerated by Laser Light," *Phys. Plasmas* **11**, 5038 (2004).
- C. Stoeckl, W. Theobald, T. C. Sangster, M. H. Key, P. Patel, B. B. Zhang, R. Clarke, S. Karsch, and P. Norreys, "Operation of a Single-Photon–Counting X-Ray Charge–Coupled Device Camera Spectrometer in a Petawatt Environment," *Rev. Sci. Instrum.* **75**, 3705 (2004).
- X. Teng and H. Yang, "Synthesis of Magnetic Nanocomposites and Alloys from Platinum–Iron Oxide Core–Shell Nanoparticles," *Nanotechnology* **16**, S554 (2005).
- X. Teng and H. Yang, "Synthesis of Platinum Multipods: An Induced Anisotropic Growth," *Nano Lett.* **5**, 885 (2005).
- A. Trajkovska-Petkoska, R. Varshneya, T. Z. Kosc, K. L. Marshall, and S. D. Jacobs, "Enhanced Electro-Optic Behavior for Shaped Polymer Cholesteric Liquid-Crystal Flakes Made Using Soft Lithography," *Adv. Funct. Mater.* **15**, 217 (2005).
- N. G. Usechak and G. P. Agrawal, "An Analytic Technique for Investigating Mode-Locked Lasers," in *Conference on Lasers and Electro-Optics/Quantum Electronics and Laser Science and Photonic Applications, Systems and Technologies 2005* (Optical Society of America, Washington, DC, 2005), Paper CTuCC1.
- N. G. Usechak and G. P. Agrawal, "Pulse Switching and Stability in FM Mode-Locked Fiber Lasers," in *Conference on Lasers and Electro-Optics/Quantum Electronics and Laser Science and Photonic Applications, Systems and Technologies 2005* (Optical Society of America, Washington, DC, 2005), Paper JWB46.
- N. G. Usechak and G. P. Agrawal, "Semi-Analytic Technique for Analyzing Mode-Locked Lasers," *Opt. Express* **13**, 2075 (2005).
- D. Wang, A. Verevkin, R. Sobolewski, R. Adam, A. van der Hart, and R. Franchy, "Magneto-Optical Kerr Effect Measurements of Spin Dynamics in Cobalt Nanodots," *IEEE Trans. Nanotech.* **4**, 460 (2005).
- Y. Wang and H. Yang, "Synthesis of CoPt Nanorods in Ionic Liquids," *J. Am. Chem. Soc.* **127**, 5316 (2005).
- L. J. Waxer, D. N. Maywar, J. H. Kelly, T. J. Kessler, B. E. Kruschwitz, S. J. Loucks, R. L. McCrory, D. D. Meyerhofer, S. F. B. Morse, C. Stoeckl, and J. D. Zuegel, "High-Energy Petawatt Capability for the OMGA Laser," *Opt. Photonics News* **16**, 30 (2005).
- B. Yaakobi, T. R. Boehly, D. D. Meyerhofer, T. J. B. Collins, B. A. Remington, P. G. Allen, S. M. Pollaine, H. E. Lorenzana, and J. H. Eggert, "EXAFS Measurements of Iron bcc-to-hcp Phase Transformation in Nanosecond-Laser Shocks," *Phys. Rev. Lett.* **95**, 075501 (2005).
- B. Yaakobi, T. R. Boehly, D. D. Meyerhofer, T. J. B. Collins, B. A. Remington, P. G. Allen, S. M. Pollaine, H. E. Lorenzana, and J. H. Eggert, "Extended X-Ray Absorption Fine Structure Measurement of Phase Transformation in Iron Shocked by Nanosecond Laser," *Phys. Plasmas* **12**, 092703 (2005).
- B. Yaakobi, C. Stoeckl, W. Seka, J. A. Delettrez, T. C. Sangster, and D. D. Meyerhofer, "Measurement of Preheat Due to Fast Electrons in Laser Implosions of Cryogenic Deuterium Targets," *Phys. Plasmas* **12**, 062703 (2005).
- J. K. W. Yang, E. Dauler, A. Ferri, A. Pearlman, A. Verevkin, G. Gol'tsman, B. Voronov, R. Sobolewski, W. E. Keicher, and K. K. Berggren, "Fabrication Development for Nanowire GHz-Counting-Rate Single-Photon Detectors," *IEEE Trans. Appl. Supercond.* **15**, 626 (2005).
- T. Yasuda, K. Fujita, T. Tsutsui, Y. Geng, S. W. Culligan, and S. H. Chen, "Carrier Transport Properties of Monodisperse Glassy-Nematic Oligofluorenes in Organic Field-Effect Transistors," *Chem. Mater.* **17**, 264 (2005).
- L. Zheng, J. C. Lambropoulos, and A. W. Schmid, "UV-Laser-Induced Densification of Fused Silica: A Molecular Dynamics Study," *J. Non-Cryst. Solids* **347**, 144 (2004).

J. D. Zuegel, V. Bagnoud, T. Corso, P. Drew, G. J. Quarles, P. Dumas, J. T. Mooney, and S. D. O'Donohue, "Wavefront Correction Extends the Capabilities of Large-Aperture Nd:YLF Laser Rods," *Laser Focus World* **41**, 133 (2005).

OMEGA External Users' Publications

P. A. Amendt, H. F. Robey, H.-S. Park, R. E. Tipton, R. E. Turner, J. L. Milovich, M. Bono, R. Hibbard, H. Louis, R. Wallace, and V. Yu. Glebov, "Hohlraum-Driven Ignitionlike Double-Shell Implosions on the OMEGA Laser Facility," *Phys. Rev. Lett.* **94**, 065004 (2005).

B. E. Blue, J. F. Hansen, and H. F. Robey, "Improved Pinhole-Apertured Point-Projection Backlighter Geometry," *Rev. Sci. Instrum.* **75**, 3989 (2004).

B. E. Blue, J. F. Hansen, M. T. Tobin, D. C. Eder, and H. F. Robey, "Debris Mitigation in Pinhole-Apertured Point-Projection Backlit Imaging," *Rev. Sci. Instrum.* **75**, 4775 (2004).

D. K. Bradley, J. H. Eggert, D. G. Hicks, P. M. Celliers, S. J. Moon, R. C. Cauble, and G. W. Collins, "Shock Compressing Diamond to a Conducting Fluid," *Phys. Rev. Lett.* **93**, 195506 (2004).

D. K. Bradley, J. P. Holder, C. M. Damian, K. W. Piston, P. M. Bell, A. K. L. Dymoke-Bradshaw, and J. D. Hares, "Progress in the Development of a Single Line of Sight X-Ray Framing Camera," *Rev. Sci. Instrum.* **75**, 4054 (2004).

J. L. Bourgade, V. Allouche, J. Baggio, C. Bayer, F. Bonneau, C. Chollet, S. Darbon, L. Disdier, D. Gontier, M. Houry, H. P. Jacquet, J. P. Jadaud, J. L. Leray, I. Masclet-Gobin, J. P. Negre, J. Raimborg, B. Villette, I. Bertron, J. M. Chevalier, J. M. Favier, J. Gazave, J. C. Gomme, F. Malaise, J. P. Seaux, V. Yu. Glebov, P. Jaanimagi, C. Stoeckl, T. C. Sangster, G. Pien, R. A. Lerche, and E. R. Hodgson, "New Constraints for Plasma Diagnostics Development Due to the Harsh Environment of MJ Class Lasers," *Rev. Sci. Instrum.* **75**, 4204 (2004) (invited).

K. M. Campbell, F. A. Weber, E. L. Dewald, S. H. Glenzer, O. L. Landen, R. E. Turner, and P. A. Waide, "OMEGA Dante Soft X-Ray Power Diagnostic Component Calibration at the National Synchrotron Light Source," *Rev. Sci. Instrum.* **75**, 3768 (2004).

P. M. Celliers, D. K. Bradley, G. W. Collins, D. G. Hicks, T. R. Boehly, and W. J. Armstrong, "Line-Imaging Velocimeter for Shock Diagnostics at the OMEGA Laser Facility," *Rev. Sci. Instrum.* **75**, 4916 (2004).

C. Constantin, C. A. Back, K. B. Fournier, G. Gregori, O. L. Landen, S. H. Glenzer, E. L. Dewald, and M. C. Miller, "Supersonic Propagation of Ionization Waves in an Underdense, Laser-Produced Plasma," *Phys. Plasmas* **12**, 063104 (2005).

E. L. Dewald, K. M. Campbell, R. E. Turner, J. P. Holder, O. L. Landen, S. H. Glenzer, R. L. Kauffman, L. J. Suter, M. Landon, M. Rhodes, and D. Lee, "Dante Soft X-Ray Power Diagnostic for the National Ignition Facility," *Rev. Sci. Instrum.* **75**, 3759 (2004).

S. H. Glenzer, P. Arnold, G. Bardsley, R. L. Berger, G. Bonnano, T. Borger, D. E. Bower, M. Bowers, R. Bryant, S. Buckman, S. C. Burkhart, K. Campbell, M. P. Chrisp, B. I. Cohen, C. Constantin, F. Cooper, J. Cox, E. Dewald, L. Divol, S. Dixit, J. Duncan, D. Eder, J. Edwards, G. Erbert, B. Felker, J. Fornes, G. Frieders, D. H. Froula, S. D. Gardner, C. Gates, M. Gonzales, S. Grace, G. Gregori, A. Greenwood, R. Griffith, T. Hall, B. A. Hammel, C. Haynam, G. Heestand, M. Henesian, G. Hermes, D. Hinkel, J. Holder, F. Holdner, G. Holtmeier, W. Hsing, S. Huber, T. James, S. Johnson, O. S. Jones, D. Kalantar, J. H. Kamperschroer, R. Kauffman, T. Kelleher, J. Knight, R. K. Kirkwood, W. L. Kruer, W. Labiak, O. L. Landen, A. B. Langdon, S. Langer, D. Latray, A. Lee, F. D. Lee, D. Lund, B. MacGowan, S. Marshall, J. McBride, T. McCarville, L. McGrew, A. J. MacKinnon, S. Mahavandi, K. Manes, C. Marshall, J. Menapace, E. Mertens, N. Meezan, G. Miller, S. Montelongo, J. D. Moody, E. Moses, D. Munro, J. Murray, J. Neumann, M. Newton, E. Ng, C. Niemann, A. Nikitin, P. Opsahl, E. Padilla, T. Parham, G. Parrish, C. Petty, M. Polk, C. Powell, I. Reinbachs, V. Rekow, R. Rinnert, B. Riordan, M. Rhodes, V. Roberts, H. Robey, G. Ross, S. Sailors, R. Saunders, M. Schmitt, M. B. Schneider, S. Shiromizu, M. Spaeth, A. Stephens, B. Still, L. J. Suter,

G. Tietbohl, M. Tobin, J. Tuck, B. M. Van Wonterghem, R. Vidal, D. Voloshin, R. Wallace, P. Wegner, P. Whitman, E. A. Williams, K. Williams, K. Winward, K. Work, B. Young, P. E. Young, P. Zapata, R. E. Bahr, W. Seka, J. Fernandez, D. Montgomery, and H. Rose, "Progress in Long Scale Length Laser-Plasma Interactions," *Nucl. Fusion* **44**, S185 (2004).

D. G. Hicks, T. R. Boehly, P. M. Celliers, J. H. Eggert, E. Vianello, D. D. Meyerhofer, and G. W. Collins, "Shock Compression of Quartz in the High-Pressure Fluid Regime," *Phys. Plasmas* **12**, 082702 (2005).

D. E. Hinkel, M. B. Schneider, H. A. Baldis, G. Bonanno, D. E. Bower, K. M. Campbell, J. R. Celeste, S. Compton, R. Costa, E. L. Dewald, S. N. Dixit, M. J. Eckart, D. C. Eder, M. J. Edwards, A. Ellis, J. A. Emig, D. H. Froula, S. H. Glenzer, D. Hargrove, C. A. Haynam, R. F. Heeter, M. A. Hennesian, J. P. Holder, G. Holtmeier, L. James, K. S. Jancaitis, D. H. Kalantar, J. H. Kamperschroer, R. L. Kauffman, J. Kimbrough, R. K. Kirkwood, A. E. Koniges, O. L. Landen, M. Landon, A. B. Langdon, F. D. Lee, B. J. MacGowan, A. J. MacKinnon, K. R. Manes, C. Marshall, M. J. May, J. W. McDonald, J. Menapace, E. I. Moses, D. H. Munro, J. R. Murray, C. Niemann, D. Pellinen, V. Rekow, J. A. Ruppe, J. Schein, R. Shepherd, M. S. Singh, P. T. Springer, C. H. Still, L. J. Suter, G. L. Tietbohl, R. E. Turner, B. M. Van Wonterghem, R. J. Wallace, A. Warrick, P. Watts, F. Weber, P. J. Wegner, E. A. Williams, B. K. Young, and P. E. Young, "Laser Coupling to Reduced-Scale Hohlraum Targets at the Early Light Program of the National Ignition Facility," *Phys. Plasmas* **12**, 056035 (2005).

D. H. Kalantar, J. F. Belak, G. W. Collins, J. D. Colvin, H. M. Davies, J. H. Eggert, T. C. Germann, J. Hawreliak, B. L. Holian, K. Kadau, P. S. Lomdahl, H. E. Lorenzana, M. A. Meyers, K. Rosolankova, M. S. Schneider, J. Sheppard, J. S. Stölken, and J. S. Wark, "Direct Observation of the α - ϵ Transition in Shock-Compressed Iron via Nanosecond X-Ray Diffraction," *Phys. Rev. Lett.* **95**, 075502 (2005).

J. A. King, K. Akli, R. A. Snavely, B. Zhang, M. H. Key, C. D. Chen, M. Chen, S. P. Hatchett, J. A. Koch, A. J. MacKinnon, P. K. Patel, T. Phillips, R. P. J. Town, R. R. Freeman, M. Borghesi, L. Romagnani, M. Zepf, T. Cowan, R. Stephens, K. L. Lancaster, C. D. Murphy, P. Norreys, and C. Stoeckl, "Characterization of a Picosecond Laser Generated 4.5 keV Ti K -alpha Source for Pulsed Radiography," *Rev. Sci. Instrum.* **76**, 076102 (2005).

J. A. King, K. Akli, B. Zhang, R. R. Freeman, M. H. Key, C. D. Chen, S. P. Hatchett, J. A. Koch, A. J. MacKinnon, P. K. Patel, R. Snavely, R. P. J. Town, M. Borghesi, L. Romagnani, M. Zepf, T. Cowan, H. Habara, R. Kodama, Y. Toyama, S. Karsch, K. Lancaster, C. Murphy, P. Norreys, R. Stephens, and C. Stoeckl, "Ti K_{α} Radiography of Cu-Doped Plastic Microshell Implosions Via Spherically Bent Crystal Imaging," *Appl. Phys. Lett.* **86**, 191501 (2005).

J. A. Koch, T. W. Barbee, Jr., N. Izumi, R. Tommasini, R. C. Mancini, L. A. Welser, and F. J. Marshall, "Multispectral X-Ray Imaging with a Pinhole Array and a Flat Bragg Mirror," *Rev. Sci. Instrum.* **76**, 073708 (2005).

J. A. Koch, T. W. Barbee, Jr., S. Dalhed, S. Haan, N. Izumi, R. W. Lee, L. A. Welser, R. C. Mancini, F. J. Marshall, D. Meyerhofer, T. C. Sangster, V. A. Smalyuk, J. M. Soures, L. Klein, and I. Golovkin, "Core Temperature and Density Gradients in ICF," in the *14th APS Topical Conference on Atomic Processes in Plasmas*, edited by J. S. Cohen, S. Mazevet, and D. P. Kilcrease (American Institute of Physics, New York, 2004), Vol. 730, pp. 53–60.

M. Koenig, E. Henry, G. Huser, A. Benuzzi-Mounaix, B. Faral, E. Martinolli, S. Lepape, T. Vinci, D. Batani, M. Tomasini, B. Telaro, P. Loubeyre, T. Hall, P. Celliers, G. Collins, L. DaSilva, R. Cauble, D. Hicks, D. Bradley, A. MacKinnon, P. Patel, J. Eggert, J. Pasley, O. Willi, D. Neely, M. Notley, C. Danson, M. Borghesi, L. Romagnani, T. Boehly, and K. Lee, "High Pressures Generated by Laser Driven Shocks: Applications to Planetary Physics," *Nucl. Fusion* **44**, S208 (2004).

S. Kurebayashi, J. A. Frenje, F. H. Séguin, J. R. Rygg, C. K. Li, R. D. Petrasso, V. Yu. Glebov, J. A. Delettrez, T. C. Sangster, D. D. Meyerhofer, C. Stoeckl, J. M. Soures, P. A. Amendt, S. P. Hatchett, and R. E. Turner, "Using Nuclear Data and Monte Carlo Techniques to Study Areal Density and Mix in D_2 Implosions," *Phys. Plasmas* **12**, 032703 (2005).

G. A. Kyrala, S. H. Batha, J. B. Workman, J. R. Fincke, P. A. Keiter, J. Cobble, N. E. Lanier, T. Tierney, and C. Christensen, "High-Speed X-Ray Imaging in High-Power Laser Experiments," in the *26th International Congress on High-Speed Photography and Photonics*, edited by D. L. Paisley, S. Kleinfelder, D. R. Snyder, and B. J. Thompson (SPIE, Bellingham, WA, 2005), Vol. 5580, pp. 629–643.

- C. K. Li and R. D. Petrasso, "Stopping of Directed Energetic Electrons in High-Temperature Hydrogenic Plasmas," *Phys. Rev. E* **70**, 067401 (2004).
- K. T. Lorenz, M. J. Edwards, S. G. Glendinning, A. F. Jankowski, J. McNaney, S. M. Pollaine, and B. A. Remington, "Accessing Ultrahigh-Pressure, Quasi-Isentropic States of Matter," *Phys. Plasmas* **12**, 056309 (2005).
- A. J. MacKinnon, S. Shiromizu, G. Antonini, J. Auerbach, K. Haney, D. H. Froula, J. Moody, G. Gregori, C. Constantin, C. Sorce, L. Divol, R. L. Griffith, S. Glenzer, J. Satariano, P. K. Whitman, S. N. Locke, E. L. Miller, R. Huff, K. Thorp, W. Armstrong, R. Bahr, W. Seka, G. Pien, J. Mathers, S. Morse, S. Loucks, and S. Stagnitto, "Implementation of a High Energy 4ω Probe Beam on the OMEGA Laser," *Rev. Sci. Instrum.* **75**, 3906 (2004).
- A. R. Miles, M. J. Edwards, B. Blue, J. F. Hansen, H. F. Robey, R. P. Drake, C. Kuranz, and D. R. Leibbrandt, "The Effect of a Short-Wavelength Mode on the Evolution of a Long-Wavelength Perturbation Driven by a Strong Blast Wave," *Phys. Plasmas* **11**, 5507 (2004).
- A. R. Miles, B. Blue, M. J. Edwards, J. A. Greenough, J. F. Hansen, H. F. Robey, R. P. Drake, C. Kuranz, and D. R. Leibbrandt, "Transition to Turbulence and Effect of Initial Conditions on Three-Dimensional Compressible Mixing in Planar Blast-Wave-Driven Systems," *Phys. Plasmas* **12**, 056317 (2005).
- M. J. Moran, V. Yu. Glebov, C. Stoeckl, R. Rygg, and B. E. Schwartz, "PROTEX: A Proton-Recoil Detector for Inertial Confinement Fusion Neutrons," *Rev. Sci. Instrum.* **76**, 023506 (2005).
- J. R. Murray and J. M. Soures, "Fusion Laser Engineering," *Opt. Eng.* **43**, 2839 (2004) (Special Section Guest Editorial).
- C. Niemann, G. Antonini, S. Compton, S. H. Glenzer, D. Hargrove, J. D. Moody, R. K. Kirkwood, V. Rekow, J. Satariano, C. Sorce, W. Armstrong, R. Bahr, R. Keck, G. Pien, W. Seka, and K. Thorp, "Transmitted Laser Beam Diagnostic at the OMEGA Laser Facility," *Rev. Sci. Instrum.* **75**, 4171 (2004).
- C. Niemann, L. Divol, D. H. Froula, G. Gregori, O. Jones, R. K. Kirkwood, A. J. MacKinnon, N. B. Meezan, J. D. Moody, C. Sorce, R. Bahr, W. Seka, and S. H. Glenzer, "Intensity Limits for Propagation of $0.527\ \mu\text{m}$ Laser Beams Through Large-Scale-Length Plasmas for Inertial Confinement Fusion," *Phys. Rev. Lett.* **94**, 085005 (2005).
- C. Reverdin, A. S. Morlens, B. Angelier, J. L. Bourgade, J. Y. Boutin, M. Briat, G. Charles, A. Duval, A. Estadieu, C. Cholet, D. Gontier, D. Husson, H. P. Jacquet, J. P. LeBreton, G. Lidove, B. Marchet, R. Marmoret, R. Maroni, P. Millier, J. Raimbourg, C. Remond, R. Rosch, G. Souillé, P. Stemmler, P. Troussel, J. L. Ulmer, B. Villette, and R. Wrobel, "X-Ray Calibration of the Time Resolved Crystal Spectrometer SXDHR-It of the Ligne d'Intégration Laser," *Rev. Sci. Instrum.* **75**, 3730 (2004).
- H. F. Robey, T. S. Perry, H.-S. Park, P. Amendt, C. M. Sorce, S. M. Compton, K. M. Campbell, and J. P. Knauer, "Experimental Measurement of Au *M*-Band Flux in Indirectly Driven Double-Shell Implosions," *Phys. Plasmas* **12**, 072701 (2005).
- G. J. Schmid, J. A. Koch, M. J. Moran, T. W. Phillips, V. Yu. Glebov, T. C. Sangster, C. Stoeckl, S. A. Wender, and E. C. Morse, "Calibration of National Ignition Facility Neutron Detectors in the Energy Range $E < 14\ \text{MeV}$," *Rev. Sci. Instrum.* **75**, 3589 (2004).
- F. H. Séguin, J. L. DeCiantis, J. A. Frenje, S. Kurebayashi, C. K. Li, J. R. Rygg, C. Chen, V. Berube, B. E. Schwartz, R. D. Petrasso, V. A. Smalyuk, F. J. Marshall, J. P. Knauer, J. A. Delettrez, P. W. McKenty, D. D. Meyerhofer, S. Roberts, T. C. Sangster, K. Mikaelian, and H. S. Park, " D^3He -Proton Emission Imaging for Inertial-Confinement-Fusion Experiments," *Rev. Sci. Instrum.* **75**, 3520 (2004) (invited).
- R. B. Stephens, S. P. Hatchett, M. Tabak, C. Stoeckl, H. Shiraga, S. Fujioka, M. Bonino, A. Nikroo, R. Petrasso, T. C. Sangster, J. Smith, and K. A. Tanaka, "Implosion Hydrodynamics of Fast Ignition Targets" *Phys. Plasmas* **12**, 056312 (2005).
- J. Workman, J. R. Fincke, P. Keiter, G. A. Kyrala, T. Pierce, S. Sublett, J. P. Knauer, H. Robey, B. Blue, S. G. Glendinning, and O. L. Landen, "Development of Intense X-Ray Sources for Backlighting High Energy Density Experiments," *Rev. Sci. Instrum.* **75**, 3915 (2004) (invited).

Conference Presentations

The following presentations were made at the International Conference on Ultrahigh Intensity Lasers: Development, Science, and Emerging Applications, North Lake Tahoe, NV, 3–7 October 2004:

J. Bromage, J. D. Zuegel, D. Vickery, L. J. Waxer, D. Irwin, R. Boni, R. Jungquist, and C. Stoeckl, “High-Intensity Diagnostics for OMEGA EP.”

T. J. Kessler, J. Bunkenburg, H. Hu, C. Kellogg, L. S. Iwan, and W. Skulski, “Design Strategies and Technology Demonstrations for the Tiled Grating Compressor.”

A. W. Schmid, T. Z. Kosc, A. Kozlov, A. L. Rigatti, and J. B. Oliver, “A Short-Pulse, Laser-Damage Update on OMEGA EP.”

C. Stoeckl, “OMEGA EP: A High-Energy Petawatt Laser at LLE.”

J. D. Zuegel, V. Bagnoud, I. A. Begishev, M. J. Guardalben, and J. Puth, “Performance of the OMEGA EP’s Prototype—OPCPA Front End.”

J. R. Marciante, J. I. Hirsh, D. H. Raguin, and E. T. Prince, “Polarization-Insensitive, High-Dispersion TIR Diffraction Gratings,” *Diffraction Optics and Micro-Optics*, Rochester, NY, 10–13 October 2004.

The following presentations were made at *Optical Fabrication and Testing*, Rochester, NY, 10–13 October 2004:

C. Bouvier, J. C. Lambropoulos, and S. D. Jacobs, “Fracture Toughness of ULE, Zerodur, Astrosital, and Corning 9600.”

J. E. DeGroot, S. N. Shafir, J. C. Lambropoulos, and S. D. Jacobs, “Surface Characterization of CVD ZnS Using Power Spectral Density.”

S. D. Jacobs, “Innovations in Optics Manufacturing” (invited).

J. Keck, J. B. Oliver, V. Gruschow, J. Spaulding, and J. D. Howe, “Process Tuning of Silica Thin-Film Deposition.”

I. A. Kozhinova, H. J. Romanofsky, and S. D. Jacobs, “Polishing of Prepolished CVD ZnS Flats with Altered Magnetorheological (MR) Fluids.”

A. E. Marino, K. Spencer, J. E. DeGroot, and S. D. Jacobs, “Chemical Durability of Phosphate Laser Glasses.”

F. H. Mrakovcic, J. A. Randi, J. C. Lambropoulos, and S. D. Jacobs, “Subsurface Damage in Single-Crystal Sapphire.”

J. B. Oliver, “Thin-Film-Optics Design and Manufacturing Challenges for Large-Aperture, High-Peak-Power, Short-Pulse Lasers” (invited).

S. N. Shafir, J. C. Lambropoulos, and S. D. Jacobs, “Loose Abrasive Lapping of Optical Glass with Different Lapping Plates and Its Interpretation.”

The following presentations were made at *Frontiers in Optics, The 88th Annual Meeting—Laser Science XX*, Rochester, NY, 10–14 October 2004:

V. Bagnoud, “A Front End for Multipetawatt Lasers Based on a High-Energy, High-Average-Power Optical Parametric Chirped-Pulse Amplifier.”

S. G. Lukishova, A. W. Schmid, C. M. Supranowitz, A. J. McNamara, R. W. Boyd, and C. R. Stroud, Jr., “Dye-Doped, Liquid-Crystal, Room-Temperature, Single-Photon Source.”

D. D. Meyerhofer, “Progress in Direct-Drive Inertial Confinement Fusion” (invited).

B. Yaakobi, D. D. Meyerhofer, T. R. Boehly, J. J. Rehr, B. A. Remington, P. G. Allen, S. M. Pollaine, and R. C. Albers, “Dynamic EXAFS Probing of Laser-Driven Shock Waves and Crystal-Phase Transformations” (invited).

L. D. Merkle, M. Dubinskii, L. B. Glebov, L. N. Glebova, V. I. Smirnov, S. Papernov, and A. W. Schmid, “Photo-Thermo-Refractive Glass Resistance to Laser-Induced Damage Near

One Micron,” 7th Annual Directed Energy Symposium, Rockville, MD, 18–21 October 2004.

D. R. Harding, M. Bobeica, and R. Q. Gram, “Target Injection Studies,” 10th High Average Power Laser Meeting, Princeton, NJ, 27–27 October 2004.

B. Yaakobi, “EXAFS Study of Laser-Shocked Metals,” 11th International Workshop on Radiative Properties of Hot Dense Matter, Santa Barbara, CA, 1–5 November 2004.

R. L. McCrory, S. P. Regan, S. J. Loucks, D. D. Meyerhofer, S. Skupsky, R. Betti, T. R. Boehly, R. S. Craxton, T. J. B. Collins, J. A. Delettrez, D. H. Edgell, R. Epstein, V. Yu. Glebov, V. N. Goncharov, D. R. Harding, R. L. Keck, J. P. Knauer, J. Marciante, J. A. Marozas, F. J. Marshall, A. V. Maximov, P. W. McKenty, J. Myatt, P. B. Radha, T. C. Sangster, W. Seka, V. A. Smalyuk, J. M. Soures, C. Stoeckl, B. Yaakobi, J. D. Zuegel, C. K. Li, R. D. Petrasso, F. H. Séguin, J. A. Frenje, S. Padalino, C. Freeman, and K. Fletcher, “Direct-Drive Inertial Confinement Fusion Research at the Laboratory for Laser Energetics: Charting the Path to Thermonuclear Ignition,” 20th IAEA Fusion Energy Conference, Vilamoura, Portugal, 1–6 November 2004.

The following presentations were made at the 46th Annual Meeting of the APS Division of Plasma Physics, Savannah, GA, 15–19 November 2004:

K. Anderson, R. Betti, J. P. Knauer, V. A. Smalyuk, and V. N. Goncharov, “Simulations and Experiments on Adiabatic Shaping by Relaxation.”

R. Betti and J. Sanz, “Nonlinear Ablative Rayleigh–Taylor Instability.”

T. R. Boehly, E. Vianello, J. E. Miller, R. S. Craxton, V. N. Goncharov, I. V. Igumenshchev, D. D. Meyerhofer, D. G. Hicks, and P. M. Celliers, “Direct-Drive Shock-Timing Experiments Using Planar Targets.”

M. Canavan, J. A. Frenje, C. K. Li, C. Chen, J. L. DeCiantis, J. R. Rygg, F. H. Séguin, and R. D. Petrasso, “A Modified Accelerator for ICF Diagnostic Development.”

C. Chen, C. K. Li, J. A. Frenje, F. H. Séguin, R. D. Petrasso, T. C. Sangster, R. Betti, D. R. Harding, and D. D. Meyerhofer, “Monte Carlo Simulations and Planned Experiments for Studying Hot-Electron Transport in H₂ and D₂.”

T. J. B. Collins, S. Skupsky, A. Frank, A. Cunningham, and A. Poludnenko, “Shock Propagation in Wetted Foam.”

R. S. Craxton, F. J. Marshall, M. J. Bonino, R. Epstein, P. W. McKenty, S. Skupsky, J. A. Delettrez, I. V. Igumenshchev, D. W. Jacobs-Perkins, J. P. Knauer, J. A. Marozas, P. B. Radha, and W. Seka, “Polar Direct Drive—Proof-of-Principle Experiments on OMEGA and Prospects for Ignition on the NIF” (invited).

J. L. DeCiantis, F. H. Séguin, J. A. Frenje, C. Chen, C. K. Li, R. D. Petrasso, J. A. Delettrez, J. P. Knauer, F. J. Marshall, D. D. Meyerhofer, S. Roberts, T. C. Sangster, and C. Stoeckl, “Studying the Burn Region in ICF Implosions with Proton Emission Imaging.”

J. A. Delettrez, S. Skupsky, C. Stoeckl, J. Myatt, and P. B. Radha, “Simulation of Enhanced Neutron Production for OMEGA EP Cryogenic Implosions.”

D. H. Edgell, W. Seka, R. S. Craxton, L. M. Elasky, D. R. Harding, R. L. Keck, M. Pandina, M. D. Wittman, and A. Warrick, “Shadowgraphic Analysis Techniques for Cryogenic Ice-Layer Characterization at LLE.”

D. H. Edgell, W. Seka, R. S. Craxton, L. M. Elasky, D. R. Harding, R. L. Keck, M. Pandina, M. D. Wittman, and A. Warrick, “Three-Dimensional Characterization of Ice Layers for Cryogenic Targets at LLE.”

R. Epstein, R. S. Craxton, J. A. Delettrez, F. J. Marshall, J. A. Marozas, P. W. McKenty, P. B. Radha, and V. A. Smalyuk, “Simulations of X-Ray Core Images from OMEGA Implosions Driven with Controlled Polar Illumination.”

J. A. Frenje, C. K. Li, F. H. Séguin, J. L. DeCiantis, J. R. Rygg, M. Falk, R. D. Petrasso, J. A. Delettrez, V. Yu. Glebov, C. Stoeckl, F. J. Marshall, D. D. Meyerhofer, T. C. Sangster,

V. A. Smalyuk, and J. M. Soures, “Measurements of Time Evolution of Ion Temperature of D³He Implosions on OMEGA.”

M. C. Ghilea, D. D. Meyerhofer, T. C. Sangster, R. A. Lerche, and L. Disdier, “First Results from a Penumbra Imaging System Design Tool.”

V. Yu. Glebov, C. Stoeckl, T. C. Sangster, C. Mileham, S. Roberts, and R. A. Lerche, “NIF Neutron Bang-Time Detector Development on OMEGA.”

V. N. Goncharov, D. Li, and A. V. Maximov, “Effects of the Ponderomotive Terms in the Thermal Transport on the Hydrodynamic Flow in Inertial Confinement Fusion Experiments.”

O. V. Gotchev, T. J. B. Collins, V. N. Goncharov, J. P. Knauer, D. Li, and D. D. Meyerhofer, “Mass Ablation Rate and Self-Emission Measurements in Planar Experiments.”

L. Guazzotto, R. Betti, J. Manickam, S. Kaye, and J. L. Gauvreau, “Magnetorheological Equilibria with Toroidal and Poloidal Flow” (invited).

D. R. Harding, M. D. Wittman, L. M. Elasky, S. Verbridge, L. D. Lund, D. Jacobs-Perkins, W. Seka, D. H. Edgell, and D. D. Meyerhofer, “OMEGA Direct-Drive Cryogenic Deuterium Targets.”

I. V. Igumenshchev, “The Role of Viscosity in Simulations of Strong Shocks in Low-Density Foams.”

P. A. Jaanimagi, R. Boni, R. L. Keck, W. R. Donaldson, and D. D. Meyerhofer, “The Rochester Optical Streak System.”

J. P. Knauer, K. Anderson, P. B. Radha, R. Betti, T. J. B. Collins, V. N. Goncharov, P. W. McKenty, D. D. Meyerhofer, S. P. Regan, T. C. Sangster, and V. A. Smalyuk, “Improved Target Stability Using Picket Pulses to Increase and Shape the Ablator Adiat” (invited).

C. K. Li, C. Chen, J. A. Frenje, F. H. Séguin, R. D. Petrasso, J. A. Delettrez, R. Betti, D. D. Meyerhofer, J. Myatt, and S. Skupsky, “Linear-Energy Transfer and Blooming of Directed Energetic Electrons in Dense Hydrogenic Plasmas.”

D. Li and V. N. Goncharov, “Effects of the Temporal Density Variation and Convergent Geometry on Nonlinear Bubble Evolution in Classical Rayleigh–Taylor Instability.”

G. Li and V. N. Goncharov, “The Effect of Electromagnetic Fields on Electron-Thermal Transport in Laser-Produced Plasmas.”

J. A. Marozas, P. B. Radha, T. J. B. Collins, P. W. McKenty, and S. Skupsky, “Evolution of the Laser-Deposition Region in Polar-Direct-Drive Simulations on the National Ignition Facility (NIF).”

F. J. Marshall, R. S. Craxton, J. A. Delettrez, D. H. Edgell, L. M. Elasky, R. Epstein, V. Yu. Glebov, V. N. Goncharov, D. R. Harding, R. Janezic, J. P. Knauer, P. W. McKenty, D. D. Meyerhofer, P. B. Radha, S. P. Regan, W. Seka, V. A. Smalyuk, C. Stoeckl, J. A. Frenje, C. K. Li, R. D. Petrasso, and F. H. Séguin, “High-Performance, Direct-Drive, Cryogenic Target Implosions on OMEGA” (invited).

A. V. Maximov, J. Myatt, R. W. Short, W. Seka, and C. Stoeckl, “Two-Plasmon-Decay Instability in Plasmas Irradiated by Incoherent Laser Beams.”

D. D. Meyerhofer, B. Yaakobi, T. R. Boehly, T. J. B. Collins, H. Lorenzana, B. A. Remington, P. G. Allen, S. M. Pollaine, J. J. Rehr, and R. C. Albers, “Dynamic EXAFS Probing of Laser-Driven Shock Waves and Crystal Phase Transformations.”

J. E. Miller, W. J. Armstrong, T. R. Boehly, D. D. Meyerhofer, W. Theobald, E. Vianello, J. Eggert, D. G. Hicks, and C. Sorce, “Time-Resolved Measurement of Optical Self-Emission for Shock Wave and Equation of State Studies.”

J. Myatt, A. V. Maximov, R. W. Short, J. A. Delettrez, and C. Stoeckl, “Numerical Studies of MeV Electron Transport in Fast-Ignition Targets.”

P. B. Radha, T. J. B. Collins, J. A. Delettrez, Y. Elbaz, R. Epstein, V. Yu. Glebov, V. N. Goncharov, R. L. Keck, J. P. Knauer, J. A. Marozas, F. J. Marshall, R. L. McCrory, P. W. McKenty, D. D. Meyerhofer, S. P. Regan, T. C. Sangster, W. Seka, D. Shvarts, S. Skupsky, Y. Srebro, and C. Stoeckl, “Multidimensional Analysis of Direct-Drive Plastic-Shell Implosions on OMEGA” (invited).

S. P. Regan, J. A. Delettrez, V. Yu. Glebov, V. N. Goncharov, J. A. Marozas, F. J. Marshall, P. W. McKenty, D. D. Meyerhofer, P. B. Radha, T. C. Sangster, V. A. Smalyuk, C. Stoeckl, J. A. Frenje, C. K. Li, R. D. Petrasso, and F. H. Séguin, “Experimental Investigation of the Effects of Irradiation Nonuniformities on the Performance of Direct-Drive Spherical Implosions.”

J. R. Rygg, F. H. Séguin, C. K. Li, J. A. Frenje, J. L. DeCiantis, R. D. Petrasso, J. A. Delettrez, V. N. Goncharov, P. B. Radha, V. Yu. Glebov, D. D. Meyerhofer, and T. C. Sangster, "Inference of Imprint at Onset of Deceleration Phase Using Shock-Burn Measurements."

T. C. Sangster, J. A. Delettrez, V. Yu. Glebov, V. N. Goncharov, D. R. Harding, J. P. Knauer, F. J. Marshall, P. W. McKenty, D. D. Meyerhofer, P. B. Radha, S. P. Regan, S. Skupsky, V. A. Smalyuk, C. Stoeckl, J. A. Frenje, C. K. Li, R. D. Petrasso, and F. H. Séguin, "High-Areal-Density Cryogenic D₂ Implosions on OMEGA."

H. Sawada, S. P. Regan, T. R. Boehly, I. V. Igumenshchev, V. N. Goncharov, F. J. Marshall, B. Yaakobi, T. C. Sangster, D. D. Meyerhofer, D. Gregori, D. G. Hicks, S. G. Glenzer, and O. L. Landen, "Diagnosing Shock-Heated, Direct-Drive Plastic Targets with Spectrally Resolved X-Ray Scattering."

F. H. Séguin, J. L. DeCiantis, J. A. Frenje, C. K. Li, J. R. Rygg, C. Chen, R. D. Petrasso, V. A. Smalyuk, F. J. Marshall, J. A. Delettrez, J. P. Knauer, P. W. McKenty, D. D. Meyerhofer, S. Roberts, T. C. Sangster, K. Mikaleian, and H. S. Park, "Relationship of Asymmetries in Fusion Burn and ρR to Asymmetries in Laser Drive for ICF Implosions at OMEGA."

W. Seka, C. Stoeckl, V. N. Goncharov, R. E. Bahr, T. C. Sangster, R. S. Craxton, J. A. Delettrez, A. V. Maximov, J. Myatt, A. Simon, and R. W. Short, "Absorption Measurements in Spherical Implosions on OMEGA."

R. W. Short, "Convective Versus Absolute Two-Plasmon Decay in Inhomogeneous Plasmas."

V. A. Smalyuk, V. N. Goncharov, T. R. Boehly, D. Li, J. A. Marozas, D. D. Meyerhofer, S. P. Regan, and T. C. Sangster, "Measurements of Imprinting with Laser Beams at Various Angles of Incidence in Planar CH Foils."

J. M. Soures, F. J. Marshall, J. A. Delettrez, R. Epstein, R. Forties, V. Yu. Glebov, J. H. Kelly, T. J. Kessler, J. P. Knauer, P. W. McKenty, S. P. Regan, W. Seka, V. A. Smalyuk, C. Stoeckl, J. A. Frenje, C. K. Li, R. D. Petrasso, and F. H. Séguin, "Polar-Direct-Drive Experiments on OMEGA."

C. Stoeckl, W. Theobald, J. A. Delettrez, J. Myatt, S. P. Regan, H. Sawada, T. C. Sangster, M. H. Key, P. Patel, R. Snavely, R. Clarke, S. Karsch, and P. Norreys, "K-Shell Spectroscopy

Using a Single-Photon-Counting X-Ray CCD in Ultrafast Laser-Plasma Interaction Experiments."

S. Sublett, J. P. Knauer, I. V. Igumenshchev, D. D. Meyerhofer, A. Frank, P. A. Keiter, R. F. Coker, B. H. Wilde, B. E. Blue, T. S. Perry, J. M. Foster, and P. A. Rosen, "Hydrodynamic Jet Experiments on OMEGA."

W. Theobald, C. Stoeckl, T. C. Sangster, J. Kuba, R. Snavely, M. H. Key, R. Heathcoate, D. Neely, and P. Norreys, "X-Ray Line Emission Spectroscopy of 100-TW-Laser-Pulse-Generated Plasmas for Backlighter Development of Cryogenic Implosion Capsules."

E. Vianello, T. R. Boehly, R. S. Craxton, V. N. Goncharov, J. E. Miller, I. V. Igumenshchev, D. D. Meyerhofer, T. C. Sangster, D. G. Hicks, and P. M. Celliers, "The Effect of Incidence Angle on Laser-Driven Shock Strengths."

C. Zhou, J. Sanz, and R. Betti, "Asymptotic Bubble Evolution in the Bell-Plesset and Ablative Rayleigh-Taylor Instabilities."

C. W. Wu and D. R. Harding, "Growth of the Open-Networked Carbon Nanostructures at Low Temperature by Microwave Plasma Electron Cyclotron Resonance Chemical Vapor Deposition," 2004 MRS Fall Meeting, Boston, MA, 29 November-3 December 2004.

S. G. Lukishova, A. W. Schmid, R. S. Knox, P. Freivald, R. W. Boyd, and C. R. Stroud, Jr., "Deterministically Polarized Single-Photon Source," Quantum Optics II, Cozumel, Mexico, 6-9 December 2004.

H. L. Helfer, "The Dark Matter of Galactic Halos," 205th Meeting of the American Astronomical Society, San Diego, CA, 9-13 January 2005.

R. Betti, K. Anderson, J. P. Knauer, and V. N. Goncharov, "Hydrodynamics of Inertial Confinement Fusion Implosions: What's

Next?" 25th International Workshop on Physics of High Density in Matter, Hirschegg, Austria, 30 January–4 February 2005.

K. L. Marshall, T. Z. Kosc, A. Trajkovska-Petkoska, E. Kimball, and S. D. Jacobs, "Polymer Cholesteric Liquid Crystal (PCLC) Flake/Fluid Host Electro-Optic Suspensions and Their Applications in Flexible Reflective Displays," 4th Annual Flexible Microelectronics and Displays Conference, Phoenix, AZ, 1–3 February 2005.

P. B. Radha, "Direct-Drive Inertial Confinement Fusion: Status and Future," AAAS Annual Meeting, Washington, DC, 17–21 February 2005.

The following presentations were made at JOWOG 37, Albuquerque, NM, 21–25 February 2005:

D. D. Meyerhofer, B. Yaakobi, T. R. Boehly, T. J. B. Collins, H. Lorenzana, B. A. Remington, P. G. Allen, S. M. Pollaine, J. J. Rehr, and R. C. Albers, "Dynamic EXAFS Probing of Laser-Driven Shock Waves and Crystal Phase Transformations."

T. C. Sangster, T. R. Boehly, D. D. Meyerhofer, T. J. B. Collins, P. M. Celliers, G. W. Collins, J. H. Eggert, and D. G. Hicks, "Recent Results from EOS Experiments of Low-Density Foams and D₂."

R. L. McCrory, D. D. Meyerhofer, S. J. Loucks, S. Skupsky, J. M. Soures, R. Betti, T. R. Boehly, M. J. Bonino, R. S. Craxton, T. J. B. Collins, J. A. Delettrez, D. H. Edgell, R. Epstein, V. Yu. Glebov, V. N. Goncharov, D. R. Harding, R. L. Keck, J. H. Kelly, J. P. Knauer, L. D. Lund, D. Jacobs-Perkins, J. R. Marciano, J. A. Marozas, F. J. Marshall, A. V. Maximov, P. W. McKenty, S. F. B. Morse, J. Myatt, S. G. Noyes, P. B. Radha, T. C. Sangster, W. Seka, V. A. Smalyuk, C. Stoeckl, K. A. Thorp, M. D. Wittman, B. Yaakobi, J. D. Zuegel, K. A. Fletcher, C. Freeman, S. Padalino, J. A. Frenje, C. K. Li, R. D. Petrasso, and F. H. Séguin, "Direct-Drive Inertial Confinement Fusion Research at the Laboratory for Laser Energetics," 6th Symposium on Current Trends in International Fusion Research: A Review, Washington, DC, 7–11 March 2005.

L. Guazzotto, R. Betti, and J. P. Freidberg, "Progress in the Development of a Linear MHD Stability Code for Axisymmetric Plasmas with Arbitrary Equilibrium Flow," 2005 International Sherwood Fusion Theory Conference, Stateline, NV, 11–13 April 2005.

The following presentations were made at the 16th Target Fabrication Specialist's Meeting, Scottsdale, AZ, 1–5 May 2005:

M. J. Bonino, S. G. Noyes, F. J. Marshall, R. S. Craxton, D. W. Turner, and D. R. Harding, "Fabrication of Polar-Direct-Drive Targets for the National Ignition Facility."

D. H. Edgell, W. Seka, R. S. Craxton, L. M. Elasky, D. R. Harding, R. L. Keck, and M. D. Wittman, "Analysis of Cryogenic Target Shadowgraphs at LLE."

L. M. Elasky, S. Verbridge, D. H. Edgell, and D. R. Harding, "Improvements and Present Limitations of D₂ Ice Layers for OMEGA Cryogenic Targets."

R. Q. Gram and D. R. Harding, "Thermal Conductivity of Solid, Liquid, and Gaseous D₂ and Precise Thermometry Using an Embedded Pt Wire."

D. R. Harding, M. D. Wittman, L. M. Elasky, R. Q. Gram, M. J. Bonino, L. D. Lund, R. Janezic, S. Verbridge, S. Scarantino, and M. Bobeica, "Overview of Cryogenic Target Research at LLE."

A. K. Knight and D. R. Harding, "Modeling the Sensitivity of a Polymer Vapor Deposition Process to Different Operating Conditions and Parameters."

D. D. Meyerhofer, "Innovative Target Designs for Direct-Drive Ignition."

W. T. Shmayda, D. R. Harding, L. D. Lund, R. Janezic, and T. W. Duffy, "Handling Cryogenic DT Targets at the Laboratory for Laser Energetics."

D. Turner, M. J. Bonino, S. G. Noyes, R. Q. Gram, K. J. Lintz, S. Scarantino, S. Verbridge, and D. R. Harding, "Fabricating, Testing, and Fielding of Planar Cryogenic and X-Ray Scattering Targets."

M. D. Wittman and D. R. Harding, "Freezing Behavior of H₂-HD-D₂ Mixtures."

N. G. Usechak and G. P. Agrawal, "Pulse-Switching and Stability in FM Mode-Locked Fiber Lasers."

J. E. DeGroot, A. E. Marino, K. E. Spencer, and S. D. Jacobs, "Power Spectral Density Plots Inside MRF Spots Made with a Polishing Abrasive-Free MR Fluid," Optifab 2005, Rochester, NY, 2–5 May 2005.

S. G. Lukishova, A. W. Schmid, R. Knox, P. Freivald, R. W. Boyd, C. R. Stroud, Jr., and K. L. Marshall, "Deterministically Polarized Fluorescence from Single-Dye Molecules Aligned in Liquid Crystal Host," QELS 2005, Baltimore, MD, 22–27 May 2005.

The following presentations were made at ICONO/LAT 2005, St. Petersburg, Russia, 11–15 May 2005:

A. V. Okishev, "OMEGA EP (Extended Performance): Adding High-Energy, Short-Pulse Capability to the OMEGA Facility."

A. V. Okishev, K. P. Dolgaleva, and J. D. Zuegel, "Experimental Optimization of Diode-Pumped Yb:GdCOB Laser Performance for Broadband Amplification at 1053 nm."

A. V. Okishev, R. G. Roides, I. A. Begishev, and J. D. Zuegel, "All-Solid-State, Diode-Pumped, Multiharmonic Laser System for a Timing Fiducial."

The following presentations were made at the 32nd IEEE International Conference on Plasma Science, Monterey, CA, 18–23 June 2005:

V. Yu. Glebov, R. A. Lerche, C. Stoeckl, G. J. Schmid, T. C. Sangster, J. A. Koch, T. W. Phillips, C. Mileham, and S. Roberts, "Progress with CVD Diamond Detectors for ICF Time-of-Flight Applications."

W. Theobald, T. R. Boehly, E. Vianello, J. E. Miller, R. S. Craxton, V. N. Goncharov, I. V. Igumenshchev, D. D. Meyerhofer, D. G. Hicks, P. M. Celliers, and G. W. Collins, "Direct-Drive Shockwave-Timing Experiments in Planar Targets" (invited).

The following presentations were made at CLEO 2005, Baltimore, MD, 22–27 May 2005:

V. Bagnoud, J. Puth, I. A. Begishev, J. Bromage, M. J. Guardalben, and J. D. Zuegel, "A Multiterawatt Laser Using a High-Contrast, Optical Parametric Chirped-Pulse Pre-amplifier."

Z. Jiang and J. R. Marciante, "Mode-Area Scaling of Helical-Core, Dual-Clad Fiber Lasers and Amplifiers."

J. R. Marciante and J. D. Zuegel, "High-Gain, Polarization Preserving, Yb-Doped Fiber Amplifier for Low-Duty-Cycle Pulse Amplification."

N. G. Usechak and G. P. Agrawal, "An Analytic Technique for Investigating Mode-Locked Lasers."

The following presentations were made at the 35th Annual Anomalous Absorption Conference, Fajardo, Puerto Rico, 26 June–1 July 2005:

R. S. Craxton, F. J. Marshall, M. J. Bonino, V. Yu. Glebov, J. P. Knauer, S. G. Noyes, W. Seka, and V. A. Smalyuk, "Polar-Direct-Drive Experiments on OMEGA Using Saturn Targets."

R. Epstein, T. J. B. Collins, R. S. Craxton, J. A. Delettrez, I. V. Igumenshchev, F. J. Marshall, J. A. Marozas, P. W. McKenty, P. B. Radha, S. Skupsky, and V. A. Smalyuk, "Numerical Investigation of X-Ray Core Images from OMEGA Implosions Driven with Controlled Polar Illumination."

V. N. Goncharov, O. V. Gotchev, and C. Cherfils-Clérouin, "Ablative Richtmyer–Meshkov Instability as a Test of Thermal Conduction Models Used in Hydrosimulations of ICF Experiments."

A. V. Maximov, "Electron Heat Transport in the Laser Field in Direct-Drive ICF Plasmas."

S. P. Regan, H. Sawada, T. R. Boehly, I. V. Igumenshchev, V. N. Goncharov, T. C. Sangster, D. D. Meyerhofer, B. Yaakobi, G. Gregori, D. G. Hicks, S. H. Glenzer, and O. L. Landen, "Diagnosing Shock-Heated, Direct-Drive Plastic Targets with Spectrally Resolved X-Ray Scattering."

T. C. Sangster, R. S. Craxton, J. A. Delettrez, D. H. Edgell, R. Epstein, V. Yu. Glebov, V. N. Goncharov, D. R. Harding, D. Jacobs-Perkins, J. P. Knauer, S. J. Loucks, F. J. Marshall, R. L. McCrory, P. W. McKenty, D. D. Meyerhofer, P. B. Radha, S. P. Regan, W. Seka, V. A. Smalyuk, J. M. Soures, C. Stoeckl, J. A. Frenje, C. K. Li, R. D. Petrasso, and F. H. Séguin, "High-Performance Direct-Drive Implosions Using Cryogenic D₂ Fuel."

W. Seka, H. Baldis, A. V. Maximov, J. Myatt, R. W. Short, R. S. Craxton, R. E. Bahr, and T. C. Sangster, "Various Forms of Stimulated Brillouin Scattering in Long-Scale-Length Plasmas Relevant to Direct-Drive Inertial Confinement Fusion."

R. W. Short and J. Myatt, "Micro-Instabilities of Relativistic Electron Beams in Plasmas."

V. A. Smalyuk, O. Sadot, J. A. Delettrez, D. D. Meyerhofer, S. P. Regan, and T. C. Sangster, "Nonlinear Rayleigh–Taylor Growth Measurements on OMEGA."

The following presentations were made at the 8th International Workshop on Fast Ignition Targets, Tarragona, Spain, 29 June–1 July 2005:

J. A. Delettrez, J. Myatt, P. B. Radha, C. Stoeckl, S. Skupsky, and D. D. Meyerhofer, "Hydrodynamic Simulations of Integrated Experiments Planned for the OMEGA/OMEGA EP Laser Systems."

J. Myatt, J. A. Delettrez, W. Theobald, C. Stoeckl, A. V. Maximov, R. W. Short, M. Storm, T. C. Sangster, R. P. J. Town, and L. A. Cottrill, "Hybrid-Implicit PIC Calculations of Laser-Generated MeV Electrons in Copper Targets."

C. Stoeckl, T. R. Boehly, R. B. Stephens, J. A. Delettrez, S. P. Hatchett, J. A. Frenje, V. Yu. Glebov, C. K. Li, J. Miller, R. D. Petrasso, F. H. Séguin, V. A. Smalyuk, W. Theobald, B. Yaakobi, and T. C. Sangster, "Fuel-Assembly Experiments with Gas-Filled, Cone-in-Shell, Fast-Ignitor Targets on OMEGA."

S. G. Lukishova, A. W. Schmid, R. Knox, P. Freivald, R. W. Boyd, C. R. Stroud, Jr., and K. L. Marshall, "Deterministically Polarized Fluorescence from Single-Dye Molecules Aligned in Liquid Crystal Host," IQEC/CLEO 2005, Tokyo, Japan, 11–15 July 2005.

The following presentations were made at the SPIE 50th Annual Meeting, San Diego, CA, 31 July–4 August 2005:

A. C.-A. Chen, J. U. Wallace, L. Zeng, A. K.-H. Wei, and S. H. Chen, "Novel Light-Emitting Organic Materials with Variable Electron and Hole Conductivities."

J. E. DeGroote, A. E. Marino, J. P. Wilson, K. E. Spencer, and S. D. Jacobs, "Effects of Nanodiamond Abrasive Friability in Experimental MR Fluids with Phosphate Laser Glass LHG-8 and Other Optical Glasses."

E. Fess, J. Schoen, M. Bechtold, and D. Mohring, "Ultraform Finishing Process for Optical Materials."

M. Haurylau, S. P. Anderson, K. L. Marshall, and P. M. Fauchet, "Electrical Tuning of Silicon-Based 2-D Photonic Bandgap Structures."

K. L. Marshall, K. Adelsberger, B. Kolodzie, G. Mhyre, and D. W. Griffin, "A Second-Generation Liquid Crystal Phase-Shifting Point-Diffraction Interferometer Employing Structured Substrates."

A. G. Noto and K. L. Marshall, "Application of Computational Chemistry Methods to the Prediction of Chirality and Helical Twisting Power in Liquid Crystal Systems."

The following presentations were made at the 14th APS Topical Conference on Shock Compression of Condensed Matter, Baltimore, MD, 31 July–5 August 2005:

T. R. Boehly, D. G. Hicks, J. H. Eggert, E. Vianello, J. E. Miller, J. F. Hansen, P. M. Celliers, G. W. Collins, and D. D. Meyerhofer, “Direct-Density Measurements of Multi-Mbar Shock Waves for Absolute Equation-of-State Studies.”

D. D. Meyerhofer, “Creating Extreme Material Properties with High-Energy Laser Systems.”

J. E. Miller, T. R. Boehly, E. Vianello, W. J. Armstrong, C. Sorce, W. Theobald, D. D. Meyerhofer, D. G. Hicks, J. H. Eggert, and P. M. Celliers, “Streaked Optical Pyrometer for Shock Wave and EOS Studies.”

E. Vianello, T. R. Boehly, J. E. Miller, R. S. Craxton, V. N. Goncharov, I. V. Igumenshchev, D. D. Meyerhofer, D. G. Hicks, and P. M. Celliers, “Laser-Driven Shock-Timing Experiments in Planar CH and Cryogenic Deuterium Targets.”

The following presentations were made at IFSA 2005, Biarritz, France, 4–9 September 2005:

R. Betti and C. Zhou, “Low-Adiabatic Implosions for Fast-Ignition Inertial Confinement Fusion.”

J. Bromage, J. D. Zuegel, S.-W. Bahk, D. S. Vickery, L. J. Waxer, D. Irwin, V. Bagnoud, R. Boni, M. D. Moore, R. Jungquist, and C. Stoeckl, “High-Intensity Laser Diagnostics for OMEGA EP.”

D. H. Edgell, W. Seka, R. S. Craxton, L. M. Elasky, D. R. Harding, R. L. Keck, L. D. Lund, and M. D. Wittman, “Characterization of Cryogenic Direct-Drive ICF Targets During Layering Studies and Just Prior to Shot Time.”

V. N. Goncharov, O. V. Gotchev, R. L. McCrory, P. W. McKenty, D. D. Meyerhofer, T. C. Sangster, S. Skupsky, and C. Cherfils-Clérouin, “Ablative Richtmyer–Meshkov Instability: Theory and Experimental Results.”

J. H. Kelly, L. J. Waxer, V. Bagnoud, I. A. Begishev, J. Bromage, B. E. Kruschwitz, T. J. Kessler, S. J. Loucks, D. N. Maywar, R. L. McCrory, D. D. Meyerhofer, S. F. B. Morse, J. B. Oliver, A. L. Rigatti, A. W. Schmid, C. Stoeckl, S. Dalton, L. Folsbee, M. J. Guardalben, R. Jungquist, J. Puth, M. J. Shoup III, D. Weiner, and J. D. Zuegel, “OMEGA EP: High-Energy Petawatt Capability for the OMEGA Laser Facility.”

B. E. Kruschwitz, R. Jungquist, J. Qiao, S. Abbey, S. E. Dean, D. N. Maywar, M. D. Moore, L. J. Waxer, and M. E. Wilson, “Large-Aperture Deformable Mirror Correction of Tiled-Grating Wavefront Error.”

F. J. Marshall, R. S. Craxton, M. J. Bonino, R. Epstein, V. Yu. Glebov, D. Jacobs-Perkins, J. P. Knauer, J. A. Marozas, P. W. McKenty, S. G. Noyes, P. B. Radha, W. Seka, S. Skupsky, V. A. Smalyuk, J. A. Frenje, C. K. Li, R. D. Petrasso, and F. H. Séguin, “Polar-Direct-Drive Experiments on OMEGA.”

R. L. McCrory, D. D. Meyerhofer, S. J. Loucks, S. Skupsky, R. Betti, T. R. Boehly, T. J. B. Collins, R. S. Craxton, J. A. Delettrez, D. H. Edgell, R. Epstein, K. A. Fletcher, C. Freeman, J. A. Frenje, V. Yu. Glebov, V. N. Goncharov, D. R. Harding, I. V. Igumenshchev, R. L. Keck, J. D. Kilkenny, J. P. Knauer, C. K. Li, J. R. Marciante, J. A. Marozas, F. J. Marshall, A. V. Maximov, P. W. McKenty, S. F. B. Morse, J. Myatt, S. Padalino, R. D. Petrasso, P. B. Radha, S. P. Regan, T. C. Sangster, F. H. Séguin, W. Seka, V. A. Smalyuk, J. M. Soures, C. Stoeckl, B. Yaakobi, and J. D. Zuegel, “Progress in Direct-Drive Inertial Confinement Fusion Research at the Laboratory for Laser Energetics.”

S. Skupsky, R. S. Craxton, F. J. Marshall, R. Betti, T. J. B. Collins, R. Epstein, V. N. Goncharov, I. V. Igumenshchev, J. A. Marozas, P. W. McKenty, P. B. Radha, J. D. Kilkenny, D. D. Meyerhofer, T. C. Sangster, and R. L. McCrory, “Polar Direct Drive—Ignition at 1-MJ.”

J. D. Zuegel, V. Bagnoud, J. Bromage, I. A. Begishev, J. Puth, “High-Performance OPCPA Laser System.”

S. D. Allen, S. I. Kudryashov, S. Papernov, and A. W. Schmid, "Nano-Spallation on Silica Film Surfaces by Acoustic Wave Emitted by Laser-Heated Artificial Absorbing Inclusions," 8th International Conference on Laser Ablation, Banff, Canada, 11–16 September 2005.

The following presentations were made at the Boulder Damage Symposium XXXVII, Boulder, CO, 19–21 September 2005:

J. Keck, J. B. Oliver, T. J. Kessler, H. Huang, J. Barone, J. Hettrick, A. L. Rigatti, T. Hoover, K. L. Marshall, A. W. Schmid, A. Kozlov, and T. Z. Kosc, "Manufacture and Development of Multilayer Diffraction Gratings."

J. B. Oliver, T. J. Kessler, H. Huang, J. Keck, A. L. Rigatti, A. W. Schmid, A. Kozlov, and T. Z. Kosc, "Thin-Film Design for Multilayer Diffraction Gratings."

J. B. Oliver, A. L. Rigatti, J. D. Howe, J. Keck, J. Szczepanski, A. W. Schmid, S. Papernov, A. Kozlov, and T. Z. Kosc, "Thin-Film Polarizers for the OMEGA EP Laser System."

S. Papernov, A. W. Schmid, A. L. Rigatti, J. B. Oliver, and J. D. Howe, "Damage Behavior of HfO₂ Monolayer Film Containing Gold Nanoparticles as Artificial Absorbing Defects."

K. L. Marshall, A. Trajkovska-Petkoska, T. Z. Kosc, and S. D. Jacobs, "Polymer Cholesteric Liquid Crystal (PCLC) Flake/Fluid Host Suspensions: A Novel Electro-Optical Medium for

Reflective Color Display Applications," Eurodisplay 2005, Edinburgh, Scotland, 19–22 September 2005.

The following presentations were made at the 5th International Laser Operations Workshop, Livermore, CA, 20–22 September 2005:

M. J. Bonino, "Fielding Targets to Support OMEGA Experiments."

B. Kruschwitz, "High-Energy Capability for the OMEGA Laser Facility."

S. J. Loucks, "Laboratory for Laser Energetics Overview."

S. F. B. Morse, "Activation Operations Plan: OMEGA EP."

G. Pien, "Shot Specification Input Flow, Operational Use, and Lead Time Requirements."

K. A. Thorp, "OMEGA Availability and Experimental Effectiveness Data Collection and Analysis to Improve System Performance."

M. Bobeica, R. Q. Gram, and D. R. Harding, "An Experimental Method for Measuring the Response of a Target to the Thermal Environment of the Fusion Reaction Chamber," IEEE/NPSS Symposium on Fusion Engineering, Knoxville, TN, 26–29 September 2005.

UNIVERSITY OF
ROCHESTER